

Lecture Notes in Civil Engineering

Yeliz Yukselen-Aksoy  
Krishna R. Reddy  
Arvind Kumar Agnihotri *Editors*

# Sustainable Earth and Beyond

Proceedings of EGRWSE 2022

 Springer

# Lecture Notes in Civil Engineering

Volume 370

## Series Editors

Marco di Prisco, Politecnico di Milano, Milano, Italy

Sheng-Hong Chen, School of Water Resources and Hydropower Engineering,  
Wuhan University, Wuhan, China

Ioannis Vayas, Institute of Steel Structures, National Technical University of  
Athens, Athens, Greece

Sanjay Kumar Shukla, School of Engineering, Edith Cowan University, Joondalup,  
WA, Australia

Anuj Sharma, Iowa State University, Ames, IA, USA

Nagesh Kumar, Department of Civil Engineering, Indian Institute of Science  
Bangalore, Bengaluru, Karnataka, India

Chien Ming Wang, School of Civil Engineering, The University of Queensland,  
Brisbane, QLD, Australia

**Lecture Notes in Civil Engineering (LNCE)** publishes the latest developments in Civil Engineering—quickly, informally and in top quality. Though original research reported in proceedings and post-proceedings represents the core of LNCE, edited volumes of exceptionally high quality and interest may also be considered for publication. Volumes published in LNCE embrace all aspects and subfields of, as well as new challenges in, Civil Engineering. Topics in the series include:

- Construction and Structural Mechanics
- Building Materials
- Concrete, Steel and Timber Structures
- Geotechnical Engineering
- Earthquake Engineering
- Coastal Engineering
- Ocean and Offshore Engineering; Ships and Floating Structures
- Hydraulics, Hydrology and Water Resources Engineering
- Environmental Engineering and Sustainability
- Structural Health and Monitoring
- Surveying and Geographical Information Systems
- Indoor Environments
- Transportation and Traffic
- Risk Analysis
- Safety and Security

To submit a proposal or request further information, please contact the appropriate Springer Editor:

- Pierpaolo Riva at [pierpaolo.riva@springer.com](mailto:pierpaolo.riva@springer.com) (Europe and Americas);
- Swati Meherishi at [swati.meherishi@springer.com](mailto:swati.meherishi@springer.com) (Asia—except China, Australia, and New Zealand);
- Wayne Hu at [wayne.hu@springer.com](mailto:wayne.hu@springer.com) (China).

**All books in the series now indexed by Scopus and EI Compindex database!**

Yeliz Yukselen-Aksoy · Krishna R. Reddy ·  
Arvind Kumar Agnihotri  
Editors

# Sustainable Earth and Beyond

Proceedings of EGRWSE 2022

 Springer

*Editors*

Yeliz Yukselen-Aksoy  
Department of Civil Engineering  
Dokuz Eylül University  
İzmir, Türkiye

Krishna R. Reddy  
Department of Civil, Materials,  
and Environmental Engineering  
University of Illinois at Chicago  
Chicago, IL, USA

Arvind Kumar Agnihotri  
Department of Civil Engineering  
Dr. B. R. Ambedkar National Institute  
of Technology  
Jalandhar, Punjab, India

ISSN 2366-2557

ISSN 2366-2565 (electronic)

Lecture Notes in Civil Engineering

ISBN 978-981-99-4040-0

ISBN 978-981-99-4041-7 (eBook)

<https://doi.org/10.1007/978-981-99-4041-7>

© The Editor(s) (if applicable) and The Author(s), under exclusive license to Springer Nature Singapore Pte Ltd. 2023

This work is subject to copyright. All rights are solely and exclusively licensed by the Publisher, whether the whole or part of the material is concerned, specifically the rights of translation, reprinting, reuse of illustrations, recitation, broadcasting, reproduction on microfilms or in any other physical way, and transmission or information storage and retrieval, electronic adaptation, computer software, or by similar or dissimilar methodology now known or hereafter developed.

The use of general descriptive names, registered names, trademarks, service marks, etc. in this publication does not imply, even in the absence of a specific statement, that such names are exempt from the relevant protective laws and regulations and therefore free for general use.

The publisher, the authors, and the editors are safe to assume that the advice and information in this book are believed to be true and accurate at the date of publication. Neither the publisher nor the authors or the editors give a warranty, expressed or implied, with respect to the material contained herein or for any errors or omissions that may have been made. The publisher remains neutral with regard to jurisdictional claims in published maps and institutional affiliations.

This Springer imprint is published by the registered company Springer Nature Singapore Pte Ltd. The registered company address is: 152 Beach Road, #21-01/04 Gateway East, Singapore 189721, Singapore

# Preface

Environmental geotechnology is an interdisciplinary science that covers soil and rock and their interaction with environment, which includes behavior of the soil–water system. The importance of environmental geotechnology has been increasingly recognized because of environmental pollution. In order to enhance living standards, we need more advanced, applicable, and sustainable environmental technologies.

Recycling is the process of collecting and processing materials that would otherwise be thrown away as waste and turning them into new products. Various types of recyclable materials are currently in use in the construction industry. These include tire shreds, ground tire rubber, fly and bottom ash, blast-furnace slag, steel slag, cement kiln dust, silica fume, crushed glass, and other type of materials. Recycling is beneficial since it protects the environment and economically profitable. In order to elevate the use of recycled waste in civil engineering, research studies and documented field applications of recycled materials are needed.

Sustainable engineering, within the scope of civil engineering profession, may be defined as the process of designing structures in such a manner that energy and resources are consumed sustainably either during construction stages or thereafter. However, it should not be restricted in one discipline, sustainability should be incorporated with any discipline. Considering that earth's resources are rather limited in the face of population rise and demands of modern lifestyle that is keen on high life standards, the engineer is responsible of creating design work that does not only involve best strength and stiffness considerations but also has sustainable point of view so that we do not compromise our environment and undermine the future of next generations.

This proceeding book covers multidisciplinary articles which are related to research and case studies that cover environmental engineering, use of recycled materials in new design and construction, or retrofit of existing structures as well as sustainable engineering approaches and their field applications. The articles will

be useful for students, working professionals, practitioners, and researchers. Each article was reviewed by at least two distinguished reviewers. The editors are thankful to the authors and the reviewers for their contributions.

İzmir, Türkiye  
Chicago, USA  
Jalandhar, India

Yeliz Yukselen-Aksoy  
Krishna R. Reddy  
Arvind Kumar Agnihotri

# Contents

<b>Progressive Damage to GCLs Under Repeated Load Cycles</b> .....	1
Anjali G. Pillai and Gali Madhavi Latha	
<b>An Energy Dissipation Approach to Investigate the Liquefaction Resistance of Fine Sand Reinforced with Polyethylene Terephthalate Fibers</b> .....	11
Arpit Jain, Satyendra Mittal, and Sanjay Kumar Shukla	
<b>Variations in the Capacity of Driven Energy Piles in Clay</b> .....	25
Arvin Farid and Daniel P. Zimmerman	
<b>Designing of Self-sustain Electrokinetic Experiment for Saline Soil Treatment</b> .....	41
Öznur Karaca, Claudio Cameselle, Ayten Çalık, and Emin U. Uluggerli	
<b>Performance of Sand Bentonite Mixtures Under Leachate Percolation</b> .....	51
Kübra Fitnat Ayvalık, Ender Başarı, and Seda Durukan	
<b>Strength Performance of Tincal and Perlite Added Zeolite-Bentonite Mixtures Under High Temperature</b> .....	59
Sukran Gizem Alpaydin, İsa Cirkin, and Yeliz Yükselen-Aksoy	
<b>Geo-environmental Solution of Using Crushed Glass Waste to Improve Shear Strength Properties of Sandy Soil</b> .....	67
Mousa Attom, Zahid Khan, Naser Al Lozi, and Ahmed Eltayeb	
<b>Tannery Waste as a Partial Replacement of Cement in Mortar</b> .....	77
Md. Naimul Haque, Md. Adnan Haque Chowdhury, Rakibul Islam, Md. Shariful Alam, Bayzid Ahmed, and Sharif Mahmud Bhuiyan	
<b>Physio-chemical Investigations on MSWI Bottom Ash for Sustainable Use</b> .....	87
Davinder Singh and Sanjeev Kumar	



<b>Calculation of Strength Gain by Carbonate Precipitation in Crushed Granite Fines of Meghalaya</b> .....	97
Pranamee Baruah and Susmita Sharma	
<b>Mechanical Properties of Colemanite, Copper Slag and Glass Fiber Added Sand-Bentonite Mixtures as a Buffer Material for Energy Geo-structures</b> .....	107
Yusuf Batuge, Yeliz Yukselen-Aksoy, Cihat Asci, and Sukran Gizem Alpaydin	
<b>Strength Properties of Coffee Waste with Recycled Glass Geopolymers</b> .....	117
Tugba Eskisar	
<b>Research on the Contribution of Copper and Ferro-chrome Slags to the Thermal Conductivity of Buffer Materials Around Energy Geo-structures</b> .....	125
Cihat Asci and Yeliz Yukselen-Aksoy	
<b>Modeling Water Retention Curve of GCL Exposed to Pore Fluid with Solute Concentrations</b> .....	133
Ali Golaghaei Darzi, Hamed Sadeghi, Aysa Hedayati-Azar, and Poya Alipanahi	
<b>Compaction Properties of Soil Composite Fills: Sand, Silt, Clay and Polypropylene Fiber Mixtures</b> .....	145
Tanay Karademir	
<b>Sand Rubber Mixtures: 1D Compressibility Response</b> .....	157
Sabriye Ozkan, Erdin Ibrahim, and Andrea Diambra	
<b>Open Source Model Installation for Researching the Effect of Tides in the Izmir Gulf</b> .....	167
Doğuş Onur Bayram and Mustafa Doğan	
<b>Numerical Modelling of Soluble Contamination Transport in Landfills Based on Empirical Function of Membrane Efficiency</b> .....	183
Aysa Hedayati-Azar, Hamed Sadeghi, Ali Golaghaei Darzi, and Pouya AliPanahi	
<b>Investigation of Ferrochrome Fly Ash Reinforcement in Different Concrete Types</b> .....	199
Gökhan Başman, Şeyma Yüksel Sağman, Erdoğan Karip, and Tuğçe Özcan	
<b>Factors Affecting Cation Exchange Between Geosynthetic Clay Liners and Compacted Subsoils</b> .....	209
Yasin Karakuş, A. Hakan Ören, and B. Enes Taşkesti	

<b>Effects of Mixture Content of Paper Sludge Ash-Based Stabilizer on Accelerated Carbonation and Strength of Alkaline Construction Sludge</b> .....	221
Nguyen Duc Trung, Kimitoshi Hayano, and Hiromoto Yamauchi	
<b>3D Modeling of a Historical Mine Waste Site Using UAV Images: Estimation of Stockpile Volumes</b> .....	233
Okan Onal and Orhan Gunduz	
<b>Earthquake Analyses of Earthen Dams with an Emphasis on Sustainability</b> .....	243
Ali Gerçek and Gürkan Özden	
<b>Laboratory Study on Stabilization of Dredged Soil by Sustainable Materials</b> .....	253
Inci Develioglu and Hasan Firat Pulat	
<b>Particle Size Distribution of Finer Soil Particles Using Microscopic Image Analysis</b> .....	267
Pranjal Mandhaniya, Dhairya Singh Arya, and J. T. Shahu	
<b>Temperature Effect on the Shear Strength Behavior of Fiberglass Added Sand-Bentonite Mixtures</b> .....	275
Esra Güneri and Yeliz Yukselen-Aksoy	
<b>Investigation on the Vulnerability of Core Soils from Three Zoned Dams to Internal Erosion</b> .....	281
Ahmed Jalil, Ahmed Benamar, and Ebn Touhami Mohamed	
<b>Zeta Potential of Dispersed Nanocarbons by Sonication</b> .....	297
Mohd Raihan Taha and Jamal Mansour Alsharef	
<b>Slope Stability Under Extreme Rainfall Conditions</b> .....	307
Kübra Fitnat Ayvalik and Seda Durukan	
<b>Performance of Geocell Reinforced Expansive Soil Bed Under Circular Footing</b> .....	315
Sanjeev Kumar, Sanjeev Naval, and Anil Kumar Sahu	
<b>Recycling Excavated Clay to Produce ‘Sand-Like’ Material Through Sintering: Static Furnace Versus Rotary Kiln</b> .....	337
S. Subramanian, J. W. Koh, J. M. Soh, S. H. Chew, K. E. Chua, Y. C. Tan, C. S. Teo, M. Y. C. Koh, and T. H. H. Cheung	
<b>Field Implementation of EAF Steel Slag Mixtures in Clayey Subgrade Stabilization</b> .....	351
Irem Zeynep Yildirim and Monica Prezzi	
<b>An Experimental Investigation on Strength Behavior of Recycled Fine Aggregate (RCFA)-Treated Compacted Clayey Soils</b> .....	361
Hashem Kishko, Z. Nil Kutlu, Aykut Şenol, and A. Onur Pehlivan	

<b>Sodium Borohydride Assisted Catalytic Reduction of Toxic Pollutants by Carbon and Nitrogen Based Poly-meric Compounds: A Review</b> .....	369
Dimitra Das, Kalyan Kumar Chattopadhyay, and Somnath Mukherjee	
<b>Arsenate Adsorption on Goethite Nanorods in the Presence of Geochemical Constituents</b> .....	397
Leila Alidokht, Öznur Karaca, and Nasser Shirzadeh	
<b>A Case Study on Piping as a Mechanism Causing Collapse of an Earth Dam</b> .....	409
Ayşenur Altınsoy and Gürkan Özden	
<b>A Global Review of Environmental Management System Implementation in Construction Industry</b> .....	419
Hasan Eteraf, Zahra Delshad, and Viktoria Mikita	
<b>Changes Over Time in Geotechnical and Geoenvironmental Properties of a Recycled Construction and Demolition (C&amp;D) Waste</b> .....	435
Castorina S. Vieira, Paulo M. Pereira, and Nuno Cristelo	
<b>Removal of Phosphate from Stormwater Runoff Using Bench Scale Constructed Wetland</b> .....	443
Harsh Pipil, Shivani Yadav, Sonam Taneja, Harshit Chawla, Anil Kumar Haritash, and Krishna R. Reddy	
<b>Stabilization of Expansive Soil Using Rice Husk Ash</b> .....	451
Krupansh Patel and Bhargav Tewar	
<b>Geotechnical Characterization Methodology of Water Treatment Sludge for Production of Liner Material</b> .....	461
Leonardo Marchiori, Maria Vitoria Morais, António Albuquerque, and Victor Cavaleiro	
<b>A Low-cost Setup to Evaluate the Performance of a Methanotrophic Activity in Bio-augmented Systems at a Laboratory Scale</b> .....	471
Nivedita Sana, Dali Naidu Arnepalli, and Chandraraj Krishnan	
<b>An Assessment Focused on the Waste Energy Recovery by Co-processing of Oil Spilled in the Blue Amazon</b> .....	483
Érica Machado da Silva Guerreiro and André Felipe Simões	
<b>Sulfate Contamination in Groundwater Nearby Reclaimed Waste Management Site: Case Study</b> .....	493
Eugeniusz Koda, Anna Podlasek, Magdalena Daria Vaverková, and Petra Martínez Barroso	
<b>Challenges in Teaching Geoenvironmental Engineering Course</b> .....	503
Luis F. M. Ribeiro, Jyoti K. Chetri, and Krishna R. Reddy	

<b>Nanoremediation of Lindane Contaminated Soils</b> .....	517
Liang Zhao, Jyoti K. Chetri, Raksha Rai, Luis Fernando Martins Ribeiro, and Krishna R. Reddy	
<b>Water Treatment Sludge as Geotechnical Liner Material: State-of-Art</b> .....	529
Leonardo Marchiori, António Albuquerque, and Victor Cavaleiro	

# About the Editors

**Yeliz Yukselen-Aksoy** has been a full-time faculty member in the Geotechnical Engineering Division of Department of Civil Engineering at Dokuz Eylul University since 2015. Prior to that she was a full-time faculty member at the Celal Bayar University. She received a B.S. from Dokuz Eylul University in 1998 and an M.S. from the Dokuz Eylul University. She received her Ph.D. in Geotechnical Engineering from the Dokuz Eylul University in 2007. She was also at University of Illinois Chicago in Department of Civil and Materials Engineering for one year as a visiting professor. Her research efforts have focused on environmental geotechnics, ground improvement, surface properties of clay minerals, and remediation of contaminated soils. Dr. Yukselen-Aksoy published more than 40 papers, 1 book chapter, and approximately 35 conference proceedings. She was the recipient of the Turkish National and Scientific Research Council Scholarship. Dr. Yukselen-Aksoy has received several awards, many publication performance awards, and Fated Foundation Outstanding Achievement Award.

**Krishna R. Reddy** is a university scholar, a distinguished researcher, and the professor of Civil and Environmental Engineering, the director of both Sustainable Engineering Research Laboratory (SERL) and the Geotechnical and Geoenvironmental Engineering Laboratory (GAGEL) in the Department of Civil, Materials, and Environmental Engineering (CME) at the University of Illinois Chicago (UIC). Dr. Reddy received Ph.D. in Civil Engineering from the Illinois Institute of Technology, Chicago. He received gold medals for being first in both B.S. (Civil Engineering) at Osmania University, India, and M.S. (Civil Engineering) at the Indian Institute of Technology Roorkee. Dr. Reddy has more than 28 years of research, teaching, and consulting experience within the broad fields of civil, geotechnical, materials, environmental, and sustainable/resilient engineering, addressing the nexus among sustainability, resiliency, infrastructure, water, energy, and the environment. Dr. Reddy is the author of four major books, 272 journal papers, 28 edited books/conference proceedings, 23 book chapters, and 229 full conference papers. Dr. Reddy has served or currently serves as an associate editor or an editorial board member of over 10 different journals. Dr. Reddy has received several awards for excellence in

research and teaching, including ASCE Wesley W. Horner Award, ASTM Hogen-togler Award, UIC Distinguished Researcher Award, University of Illinois Scholar Award, and University of Illinois Award for Excellence in Teaching. He is a fellow of the American Society of Civil Engineers (FASCE), a diplomate of Geotechnical Engineering (DGE), and a board certified environmental engineer (BCEE). He is also a registered professional civil engineer (PE) and an Envision™ sustainability professional (ENV SP).

**Arvind Kumar Agnihotri** is a professor of Civil Engineering at NIT Jalandhar. He completed his Ph.D. from University of Roorkee (1998), M.Tech. from NIT Kurukshetra (1989), and B.E. from Panjab University, Chandigarh (1987). He possesses a work experience of around 32 years in research, teaching, and academic administration, with several years spent holding key leadership positions. His areas of interest are geotechnical and geoenvironmental engineering, reinforced earth (geosynthetics and geofibers), ground improvement and soil–structure interaction. He has supervised 12 Ph.D. theses, and 4 more are in progress. He has guided 52 M.Tech. dissertations. He has published more than 135 papers out of which about 85 in referred international and national journals and 50 in conferences and 5 edited books/conference proceedings. He served as the head of Civil Engineering, the dean academic, and the dean (Planning and Development) at prestigious Dr. B. R. Ambedkar National Institute of Technology, Jalandhar. He is a fellow/member of many professional organizations like ASCE, IGS, ISTE, Institution of Engineers, International Society of Soil Mechanics and Geotechnical Engineering, and Indian Roads Congress. He is a reviewer of many international journals of repute.

# Progressive Damage to GCLs Under Repeated Load Cycles



Anjali G. Pillai and Gali Madhavi Latha

**Abstract** Geosynthetic clay liner is used in the design of cover and barrier systems in engineered landfills. The shear strength at the interfaces is critical for slope stability. Though the interface shear characteristics of natural sand with GCLs are well established in literature, the recent problems of sand extraction and its harmful impact on coastal erosion has rendered it impractical. The geotechnical application of manufactured sand (Msand) is an uncharted field even though it has been approved as an admissible alternative to natural sand for manufacturing of concrete. The study involves analyzing the interface shear strength of GCLs with manufactured sand and compare them against river sand for identical loading conditions and identical gradations. The initial phase of study subjected the non-woven interface of GCL to interface shear tests with sands. To simulate the field conditions and to give an insight into the reduction of shear strength, same GCL specimen is subjected to repeated cycles of loading. Results showed continuous reduction in displacement values at which peak shear stress was attained. The interface shear strength parameters are evaluated for both interfaces. The assessment of surface changes of GCL due to the interaction with different type of sand is digital image analysis using MATLAB. The damage to the specimen is quantified on the reduction of shear strength over the cycles. Results from these studies provide conclusive indication to replace natural sand with Msand in landfills in terms of interface shear characteristics.

**Keywords** Interface shear strength · GCL liner · Image analysis · Manufactured sand

## 1 Introduction

The design of barrier systems with geosynthetic lining can involve interfaces with low shear strength. Translational failure is identified as a leading cause of landfill instability in several studies [1, 2]. Further, vertical expansions of existing landfills

---

A. G. Pillai (✉) · G. M. Latha  
Department of Civil Engineering, Indian Institute of Science, Bangalore, India  
e-mail: [anjalipillai@iisc.ac.in](mailto:anjalipillai@iisc.ac.in)

© The Author(s), under exclusive license to Springer Nature Singapore Pte Ltd. 2023  
Y. Yukselen-Aksoy et al. (eds.), *Sustainable Earth and Beyond*, Lecture Notes in Civil Engineering 370, [https://doi.org/10.1007/978-981-99-4041-7\\_1](https://doi.org/10.1007/978-981-99-4041-7_1)

by building new landfills on side slopes of older ones raises concerns of translational failure between old and new waste [3]. The interface shear resistance is required to assess the susceptibility of various interfaces to translational failures. Research has been performed to investigate the shear property of needle punched GCL through direct shear tests with normal stresses of 35–1050 kPa [3, 4] which demonstrated substantial increase in shear strength of GCL owing to reinforcing needle punched fibres. Studies highlighted that shear strength provided by reinforcing fibres is a liner function of normal stress. Another crucial aspect of design of landfill is the knowledge of friction present at interfaces of geosynthetics and between soil and geosynthetics. Failure is imminent if the slope stability aspect is not addressed properly as shown in several studies [5–9]. The base liner system involves placement of GCL on slopes of prepared subgrades. The fibre reinforcement structure of GCL is often challenged by gravitational weight of overlying material like soil or waste. Tension imposed by the shear stresses on the fibres need to be sustained for the time required by site specific conditions. The long-term testing and performance of GCL has not been investigated in an extensive manner.

This paper evaluates the variation to the interface shear strength exhibited by the GCL-sand interfaces under repeated cycles of load. The image analysis of the tested specimen using algorithm developed in MATLAB and high-resolution images, provides insight into the surface changes of the sheared GCL specimens. Evaluation of interface shear strength parameters for both interfaces, GCL-manufactured sand (MS) and GCL-river sand (RS) highlights their effectiveness. The test simulates actual field conditions where the laid GCL roll undergoes degradation due to imposed shear stress under varying normal load conditions due to waste disposal.

## 2 Experimental Setup

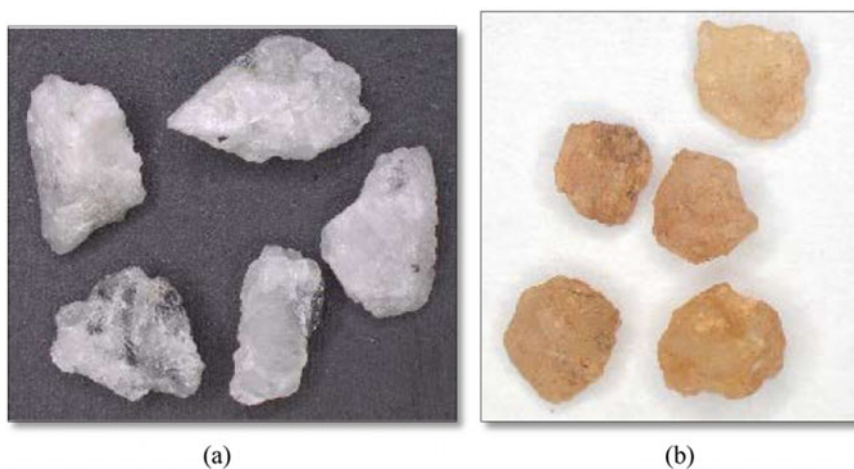
### 2.1 Test Materials

The geosynthetic clay liner used in this study has nonwoven upper layer, woven base layer and powdered sodium bentonite encapsulated between with needle-punched fibres. It is made of polypropylene. The study involved the use of two types of sands: river sand (RS) and manufactured sand (MS). To reduce the effect of particle size, an experimental gradation was obtained by collating fractions of different sizes in specific proportions for both sands. The properties of the RS and MS in their natural and graded state are listed in Table 1. Microscopic images of the particles were used for quantification of shape parameters as shown in Fig. 1. Sphericity, roundness, elongation and convexity values were computed [10]. For MS particles, the values of sphericity, roundness, elongation, and convexity was 0.78, 0.39, 0.80 and 0.34. For RS particles, the values are 0.85, 0.42, 0.87 and 0.23 respectively. The lower sphericity and roundness indicate irregular and rough texture of MS particles against RS particles. They are more elongated compared to RS particles.



**Table 1** Properties of sand—natural and experimental gradation

Property	Natural gradation		Experimental gradation	
	RS	MS	RS	MS
Gradation	Poorly graded	Well graded	Poorly graded	Well graded
Coefficient of curvature, $C_u$	4.375	9.374	5.80	5.80
Coefficient of curvature, $C_c$	0.55	1.4	1.10	1.10
Specific gravity	2.69	2.57	2.7	2.6
Size (mm)	Percentage finer by weight			
1.18	93.26	52.27	72.77	
0.6	49.50	30.89	40.18	
0.3	23.76	21.98	22.87	
0.075	0.79	2.97	1.88	

**Fig. 1** Microscopic images of sand particles taken at 16× magnification. **a** MS, **b** RS

## 2.2 Test Setup

The modified direct shear setup had a steel platform of dimensions 180 mm × 180 mm on rollers to which geosynthetic specimen was clamped [11]. The sand was filled in layers of three, hand compacted to maintain a relative density of 80%. Displacements were measured using LVDT and the applied shear load was monitored with load cell, both connected to the digital data acquisition system.

### ***2.3 Interface Shear Tests with Repeated Load Cycles***

The interface direct shear tests were conducted on GCL-sand interfaces to understand the effect of normal stress and repeated cycles of shear under constant normal stress on the developed shear strength. The normal stress was applied with the lever arm mechanism. Each interface was subjected to five repeated cycles of shear for each normal stress. Normal stresses of 100, 60 and 30 kPa was applied at constant displacement rate of 1.25 mm/min.

## **3 Results and Discussions**

The conventional approach is to perform single shear test on interface for different normal stresses and evaluate the interface shear strength parameters. The real field conditions result in mobilization of new shear stresses on already stressed specimens. The replacement of GCLs in a constructed facility is not feasible. So, to simulate the real field conditions and to understand the variations in reported interface parameters from conventional approach, the tests with repeated load cycles is designed. Further, the interface shear mechanisms were investigated with digital image analysis of the tested GCL interfaces. Results from various interface tests are presented and discussed in following sections.

### ***3.1 Shear Strength Parameters Under Repeated Load Cycles***

The data obtained from interface shear test of GCL-RS and GCL-MS was used to plot the shear stress-horizontal displacement response. Figure 2 shows a typical shear stress-displacement response for a normal stress of 30 kPa. For both GCL-MS and GCL-RS interface, the shear stress for load cycle-1 showed a gradual increase with increase in displacement. It was due to the frictional resistance mobilized between the sand particles and fibres of GCL specimen as the test progressed. The reinforcing needle punched fibres also resist the applied shear force and get stretched. The shear resistance of the GCL-MS interface was higher than GCL-RS interface due to efficient interlocking of MS particles with the fibres on nonwoven surface of GCL. The MS particles bond effectively with fibres due to the rougher texture and angularity in shape as compared to the RS particles (Fig. 1). However, it is observed that with increase in number of load cycles, there was considerable change in the shear stress-horizontal displacement response. It was observed that with number of load cycles to which the specimen was subjected to, there was increase in peak interface shear stress for GCL-sand interfaces. However, the displacement at which the peak shear stress was attained, reduced with the number of cycles. The critical observation was that the increased interface peak shear stress was reached at lower displacement values.

Similar response was observed for GCL-sand interfaces tested at normal stresses of 60 and 100 kPa, as well. Figures 3 and 4 show the reduction in displacement values at which peak shear stress attained for repeated cycles of shear.

The sudden increase of peak shear stress in load cycle 3 and 4 was attributed to the increased frictional resistance at the interface by higher sand-sand interaction offered by the entangled sand particles in the fibres of nonwoven GCL. However, with the continued shearing, the interlocking of sand with non-woven fibres reduced considerably due to tearing of fibres when subjected to repeated shear. This aspect was highlighted from the reduction in peak interface shear and low displacement values beyond load cycle-4 for all the normal stress conditions of GCL-sand interfaces.

To obtain a better understanding of the interface shear behavior under repeated load cycles, the evaluation of interface shear strength parameters at peak and residual stresses were done with Mohr–Coulomb failure criteria for each load cycle. The obtained values of shear strength parameters are listed in Table 2 for NGCL-sand interfaces. The interface friction at both peak shear stress and residual shear stress, showed a slight decrease initially and then increased to load cycle 4. This is due to the increased frictional resistance offered by the sand particles entangled with fibres on the surface of GCL with repeated shear. However, the effect of this increased sand-sand interaction on interface friction reduced, as the shear cycles induce tension

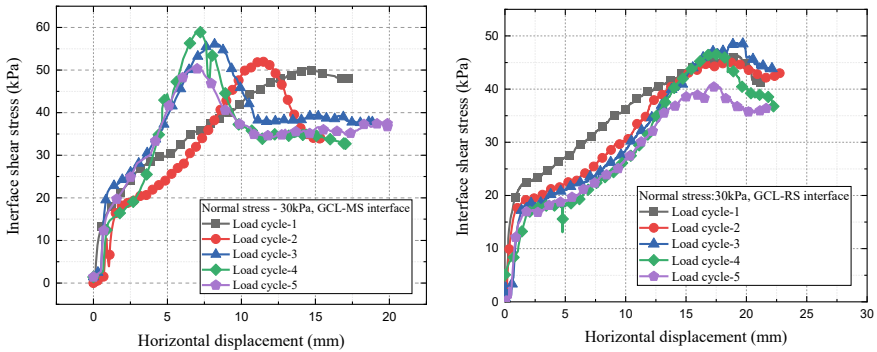


**Fig. 2** Typical shear stress–horizontal displacement at normal stress of 30 kPa for interfaces. **a** GCL-MS, **b** GCL-RS

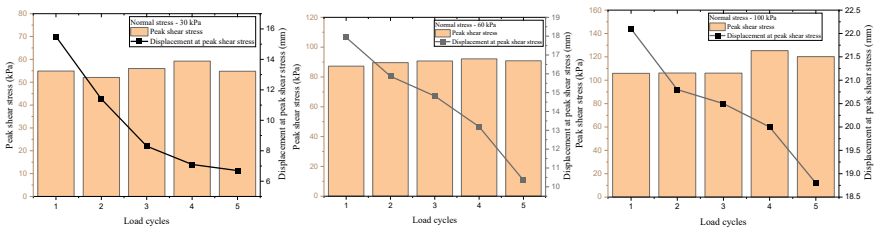


**Fig. 3** Variation of peak shear stress and displacement with load cycles for GCL-MS

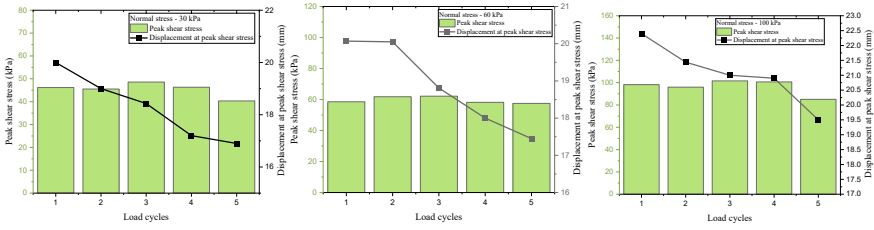


**Fig. 4** Variation of peak shear stress and displacement with load cycles for GCL-RS

**Table 2** Peak and residual shear strength parameters of the interfaces

Cycle number	Peak				Residual			
	GCL-MS		GCL-RS		GCL-MS		GCL-RS	
	$\phi_p$	$a_p$	$\phi_p$	$a_p$	$\phi_p$	$a_p$	$\phi_p$	$a_p$
1	35.33	37	34.8	35	33.08	37	32.39	35
2	40.51	30	35.58	25	38.01	30	36.86	25
3	35.95	35	37.08	30	35.15	35	35.61	30
4	46.44	35	38.63	30	42.08	35	33.42	30
5	42.7	30	33.88	25	41.01	30	30.96	25

on reinforcing fibres, weakening the internal structure of GCL along with rupture of surface fibres of GCL contributing to the damage of GCL. The effect was minimal for GCL-RS interface owing to the morphological differences of shape of particles. As observed, the performance of GCL-MS interface under all normal stress conditions and repeated load cycles showed improved shear resistance compared to GCL-RS interfaces. The effective interlocking abilities of the MS particles play an important role in providing additional frictional resistance in interlocking mechanism of fibres of GCL.

### 3.2 Image Analysis Studies

In this study the images of untested plain GCL and tested GCL specimens were captured using Sony HDR XR550 camera. For the tested GCL specimens, the images were captured after first and fifth cycles of shear under constant illumination source. The images were analyzed using MATLAB R2021b to examine the changes to the surface of GCL. To maintain contrast between fibres and sand particles, food colors in form of gel were used to color the sand.

To ensure proper analysis of the entangled sand particles and minimize the errors in results, the study ensured high contrast between sand particles and nonwoven fibres of GCL as shown in Fig. 5. For this purpose, the sieved-out proportions of

experimental gradation for both sands were subjected to coloring with food colors in form of gel. River sand (RS) was colored to dark green and manufactured sand (MS) was colored to indigo blue. The chosen colors had maximum contrast with the tested NGCL surface as shown in Fig. 5a, b. The shear area of tested GCL surfaces had a dimension of 120 mm × 100 mm. The entire area was divided into squares of 20 mm × 20 mm. This was done to obtain better resolution of images of the scanned area as shown in Fig. 5c.

**Image Analysis of Tested GCL**

The images for GCL surfaces prior to shear test was captured and analysed to account for the surface deformities that can result in errors during the evaluation of area of entangled sand particles. The tested nonwoven interfaces of GCL with RS and MS particles were analyzed to understand the influence of surface entanglement of particles on the interface shear stress. Figure 6a shows a typical captured image of tested GCL-RS interface of scan area of 20 mm × 20 mm with the high-resolution camera. The white fibres and green sand particles provided visual contrast in colors. Figure 6b shows the greyscale image of the NGCL-RS interface. In these images the grayscale intensity of entangled sand particles was obtained from data tip function of toolbox in MATLAB. Based on this intensity range the binary image is obtained from greyscale image using thresholding technique. Figure 6c shows the binary image of a typical GCL-RS interface with white region depicting the entangled sand particles. Similar approach was employed to obtain information about entangled MS particles in nonwoven GCL surfaces based on images of tested GCL-MS interfaces. Figure 7a shows the captured image of scan area 2 cm × 2 cm for a typical GCL-MS interface. The white fibres of non-woven GCL entangled the blue sand particles. The conversion into greyscale image is done using in-built function of image processing toolbox. Figure 7b shows the greyscale image of GCL-MS interface. The binary image is obtained by thresholding the greyscale image to extract the intensity values of sand particles. Figure 7c shows the analyzed binary image of tested NGCL-MS interface. From these images, the percentage area of coverage of sand particles within

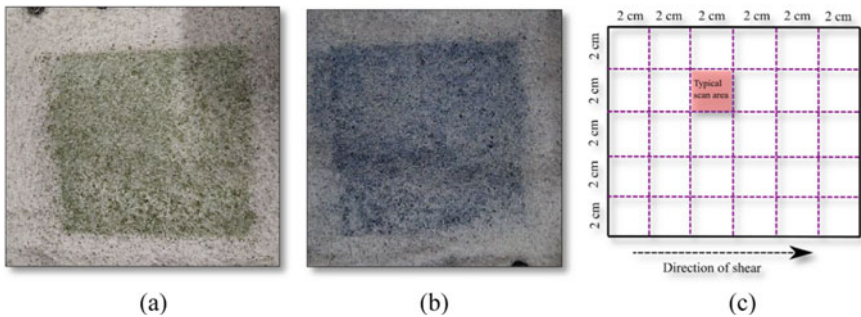


**Fig. 5** Sheared surface of tested GCL interfaces. **a** GCL-RS, **b** GCL-MS and **c** typical scan area of images

the sheared area of GCL surface was computed in MATLAB R2021a using region properties function.

### Effect of Sand Particle Entanglement

Table 3 shows that the sand particle entanglement on GCL-MS interfaces is lower than GCL-RS interface. It implied that despite the experimental gradation maintained for both sands during repeated shear, the effect of particle shape influenced the interaction mechanism at the interfaces. The results in Table 3 also shows the increase in sand particle entanglement from 1st to 5th cycle. It resulted in significant increase in interaction of sand on GCL surface and sand in the shear box at interface. This explained the increase of peak shear stress as seen in the previous plot for the interface shear-displacement response. But the repeated shear tests on single specimen damaged the surface and caused pullout of reinforcing fibres. This is evident with the lower displacement values at peak shear for each cycle of load. It is also shown that

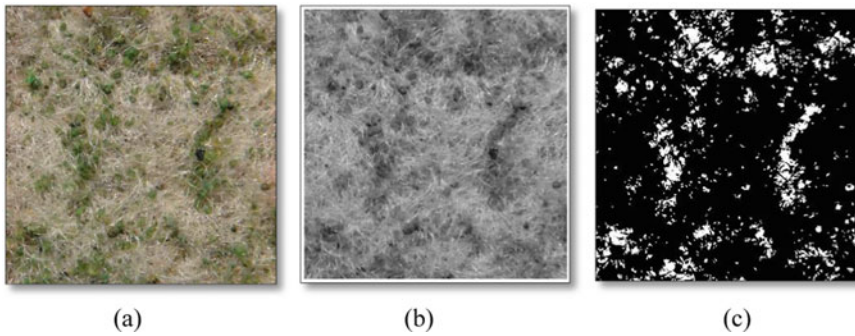


**Fig. 6** Images of tested interfaces of GCL-RS. **a** Original, **b** greyscale, **c** binary

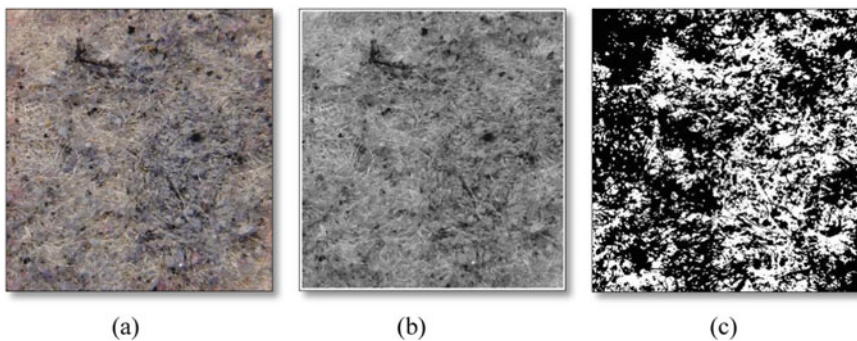


**Fig. 7** Images of tested interface of GCL-MS. **a** Original, **b** greyscale, **c** binary

**Table 3** Evaluation of area covered by sand particles

Interfaces	Normal stress (kPa)	Area of entangled particles after repeated cycles (%)	
		First cycle	Fifth cycle
NGCL-MS	30	7.42	10.38
	60	9.14	11.5
	100	11.43	14.43
NGCL-RS	30	8.21	10.62
	60	10.69	13.47
	100	12.59	19.17

even though entrapment of sand is increased, the effect of this on interface frictional resistance was reduced after 4th cycle in almost all tested interfaces.

## 4 Conclusions

The major conclusions drawn from the study are as following

1. The interface shear tests performed with repeated cycles of static normal stress showed a significant variation in shear stress-displacement response from the typical response obtained with conventional single shear test on specimens. Reduction in displacement values at peak shear stress indicated the loss of strength in GCL specimen. Beyond 4th cycle of shear, the shear strength reduced in both interfaces.
2. The GCL-MS interface offered higher frictional resistance and improved shear strength in all test conditions as indicated by the values of interface shear strength parameters. The MS particles has the potential to replace natural sand as they are crushed rocks like granite obtained from quarry and can even be manufactured in bulk for specific gradations as per requirements. They offer an alternative to the depleting river sand.
3. The image studies allowed investigation of the role sand particle entanglement and their influence on interface shear strength. It emphasized the limited role of increased sand-sand interaction on improved frictional resistance with repeated load cycles. Even though the entanglement of sand particles continued to increase, the damage to the reinforcing fibres due to repeated shear tests reduced the interface shear resistance beyond specific load cycle.

## References

1. Koerner RM, Soong TY (2000) Leachate in landfills: the stability issues. *Geotext Geomembr* 18(5):293–309
2. Bergado DT, Ramana GV, Sia HI (2006) Evaluation of interface shear strength of composite liner system and stability analysis for a landfill lining system in Thailand. *Geotext Geomembr* 24(6):371–393
3. Tano F, Olivier F, Touze-Foltz N, Dias D (2015) State-of-the-art of piggy-back landfills worldwide: comparison of containment barrier technical designs and performance analysis in terms of geosynthetics stability. In: *Geosynthetics*, Portland, USA, p 11
4. Siebken JR, Swan RH, Yuan Z (1997) Short-term and creep shear characteristics of a needle punched thermally locked geosynthetic clay liner. In: *Testing and acceptance criteria for geosynthetic clay liners*. ASTM International
5. Olsta JT, Swan Jr RH (2001) Internal shear strength of a geosynthetic clay liner at high normal loads. In: *Proceedings of tailings and mine wastes 2001*, Fort Collins, CO, pp 197–200
6. Blight GE (2007) Failures during construction of a landfill lining: a case analysis. *Waste Manage Res* 25(4):327–333
7. Stark TD, Newman EJ, Aust RL (2008) Back-analysis of a PVC geomembrane-lined pond failure. *Geosynth Int* 15(4):258–268
8. Wu W, Wang XT, Aschauer F (2008) Investigation on failure of a geosynthetic lined reservoir. *Geotext Geomembr* 26(4) 363–370
9. Eid HT (2011) Shear strength of geosynthetic composite systems for design of landfill liner and cover slopes. *Geotext Geomembr* 29(3):335–344
10. Pillai AG, Latha GM (2022) Role of particle shape on the shear strength of sand-GCL interfaces under dry and wet conditions. *Geotext Geomembr* 50(2):262–281
11. Vangla P, Latha GM (2015) Influence of particle size on the friction and interfacial shear strength of sands of similar morphology. *Int J Geosynth Ground Eng* 1(1):6



# An Energy Dissipation Approach to Investigate the Liquefaction Resistance of Fine Sand Reinforced with Polyethylene Terephthalate Fibers



Arpit Jain , Satyendra Mittal , and Sanjay Kumar Shukla 

**Abstract** The emerging sustainability trends in geotechnical engineering have shown the significant utilisation of waste products and recycled material through innovative approaches. Previous research studies have proven the appropriate usage of plastic bottles or polyethylene terephthalate (PET) fibers in mitigating liquefaction and related failures. In the present study, a series of consolidated undrained cyclic triaxial tests were performed on the unreinforced and PET fiber-reinforced fine sand to investigate the liquefaction phenomenon in the fiber-sand mixture. Three different fiber contents of 0.2, 0.4 and 0.6% were considered under loose and medium dense conditions at a confining pressure of 100 kPa. An energy dissipation approach has been considered to understand the failures triggered by liquefaction initiation. The amount of dissipated energy was the highest at the fiber content of 0.6% in loose specimens. With an increase in fiber content, the trends of dissipated energy were not similar under loose and medium-dense states. The outcomes obtained in the present research work will develop an understanding of the energy dissipation approaches in seismic failures and liquefaction mitigation through recycled wastes.

**Keywords** Cyclic triaxial · Liquefaction · Plastic fibers · Energy dissipation theory

---

A. Jain (✉) · S. Mittal  
Civil Engineering Department, IIT Roorkee, Roorkee 247667, India  
e-mail: [ajain4@ce.iitr.ac.in](mailto:ajain4@ce.iitr.ac.in)

S. K. Shukla  
School of Engineering, Edith Cowan University, Joondalup, Perth, Australia

Department of Civil Engineering, Adjunct Faculty, Indian Institute of Technology Madras, Chennai, India

## 1 Introduction

The accumulation of plastic waste has emerged as a global environmental challenge due to its severe effects on our ecosystem. Polyethylene terephthalate (PET) has affected the life of mankind at every level without its proper disposal or recycling process. It was estimated that out of 8.3 billion tonnes of virgin plastic produced, only 9% is recycled [10]. Many research studies have utilized industrial wastes in geotechnical engineering applications after improving the engineering properties of non-usable soils [13, 23]. Plastic fibres also act as a soil reinforcement which helps in mitigating the liquefaction phenomenon nearby slopes, man-made fills and embankments. The mechanical properties of soil can be improved using geosynthetics and fibre inclusion [7, 15, 25, 32]. Boominathan and Hari [4] performed stress-controlled cyclic triaxial tests to study the effect of randomly distributed polypropylene fibres and mesh elements on fly ash samples. Noorany and Uzdavines [21] investigated the resistance of fibre-soil mixtures against liquefaction using several cyclic triaxial tests. Liquefaction failure can lead to disastrous ground subsidence which can cause the loss of lives and property. Kazuhiro et al. [18] utilised liquefaction hazard maps to investigate the liquefaction-induced ground subsidence on a road network. The liquefaction resistance of fibre-reinforced silty sands was investigated by Ghadr et al. [11] using cyclic triaxial shear tests. Rasouli and Fatahi [26] utilised the reinforcement of recycled carpet fibre with sand and found a significant effect on the post-liquefaction resistance of the specimens. The investigations made by Zhang et al. [33] on the cyclic behaviour of fibre-reinforced soil suggested the significant role of fibre length, fibre content and cyclic stress ratio to govern the rate of pore-water development. Previous studies have explained the attainment of liquefaction through stress and strain-based theories where equivalent uniform shear stresses or strains and loading cycles were responsible to understand the occurrence of earthquake-related phenomena [8, 27]. Additionally, the energy per unit volume concept can be used to estimate the liquefaction potential correctly, as observed by Figueroa et al. [9] where the amount of energy dissipated during the hysteresis loop depicts the pore pressure changes occurring in the actual field. Using a variety of loading inputs, the energy-based approach provided a unique understanding of the liquefaction phenomenon [22, 24, 31]. The initial effective overburden pressure, relative density and mean grain size affect the liquefaction resistance as suggested by Baziar and Sharafi [3] through the strain energy-based model. Zhang et al. [33] and Amini and Noorzad [1] used the energy-based approach to understand the role of fibre inclusion on the liquefaction susceptibility of sandy soil and established their correlation between cumulative dissipated energy and fibre parameters. Kokusho [17] investigated the liquefaction triggering of Futsu sand with changes in the relative density and percentage of fine content using both stress and energy-based methods. The cyclic triaxial tests performed by Azeiteiro et al. [2] suggested the key role of density and axial strain rate on pore pressure development and energy dissipation in the fine-grained silica sand. The energy dissipation theory was also used by Davis and Berrill [5] to understand seismic liquefaction.

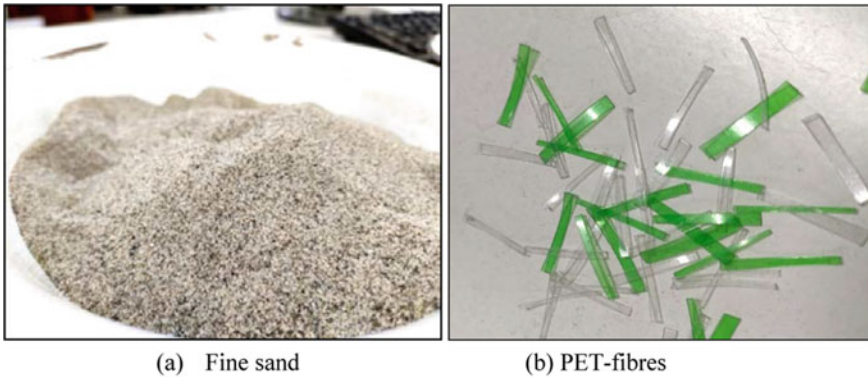


**Fig. 1** Materials used in the present study

The present study is based on the utilisation of polyethylene terephthalate fibres in mitigating the liquefaction phenomenon based on the energy dissipation approach. This new concept of energy dissipation was found to be more conservative than that of the other failures theory to understand the liquefaction triggering. A series of cyclic triaxial tests were performed where the amount of dissipated energy was found to be higher for the medium dense specimens than the loose specimens.

## 2 Materials Used and Testing Facility

### 2.1 Fine Sand

In this study, fine sand was collected from the bank of the Solani river (Roorkee, India) for experimental purposes. As per the Indian standard code (IS: 1498-1970), the fine sand falls in the category of SP soil type. The photographic image of fine sand is presented in Fig. 1a. The physical properties of Solani sand are presented in Table 1. The liquefaction-based study of Solani sand is very useful as the Roorkee region lies in seismic zone IV [14, 16].

### 2.2 PET Bottle Fibre

In the present study, the fibres obtained through the disposed of PET plastic bottles were used as reinforcement against liquefaction. These fibres had an aspect ratio ( $AR_f = l_f/b$ ) of 12 and width ( $b$ ) of 0.3 mm with which it lies within the upper bound of 100 [28] and lower bound of 10 [6]. The photographic images of fibre are

**Table 1** Physical properties of materials used

S. No.	Particulars	Notations	Sand	Silt
1.	Soil type	–	SP	ML
2.	Mean particle size	$D_{50}$	0.2 mm	0.017 mm
3.	Specific gravity	$G_s$	2.65	2.68
4.	Maximum void ratio	$(e_{max})$	0.88	1.27
5.	Minimum void ratio	$(e_{min})$	0.57	0.34
6.	Liquid limit	$w_l$	–	15%
7.	Plastic limit	$w_p$	–	12%

presented in Fig. 1b. The percentage of fibres well mixed into soil was 0.2, 0.4 and 0.6% of the oven-dry weight of soil.

### 2.3 Cyclic Triaxial Testing Facility

Cyclic triaxial testing facility was utilised to perform a series of consolidated undrained tests in accordance with ASTM D5311 under stress-controlled mode. This facility is pneumatically controlled and equipped with a complete data acquisition system enabled in both load and displacement-controlled modes. The frequency of the apparatus ranges from 0.1 to 10 Hz and has a maximum loading capacity of 50 kN. The apparatus allows several loading types like sinusoidal, impact and triangular. Linearly variable differential transducers (LVDT) were used to measure developed strains within  $\pm 50$  mm. Also, to calculate generated pore pressure, the pore pressure transducers (PPT) were used with a capacity of 2000 kPa.

## 3 Methodology Adopted and Parameters Considered

### 3.1 Methodology for Cyclic Triaxial Testing

The specimen was prepared in a latex membrane inside the mould to accommodate a specimen of size 70 mm in diameter and 140 in mm height, using a low vacuum of 5 kPa using a split mould. Moist tamping was considered as the specimen preparation technique for the preparation of unreinforced and fibre-reinforced specimens. The water content of sand was maintained at 6%, before the addition of fibres which was helpful in avoiding segregation and floating of fibres [11, 30]. The percentage of fibre is considered as the dry weight of soil which is denoted as  $\eta = W_f/W_s$ , where  $W_f$  and  $W_s$  are the weight of fibres and the weight of dry sand, respectively. Three different fibre contents ( $\eta$ ), 0.2, 0.4 and 0.6% by weight of dry soil, were used in the present

**Table 2** Test series of cyclic triaxial tests performed

Specimen No.	Fibre content ( $\eta$ , %)	Relative density (%)	CSR	$N_{cyc,L}$
S1	0	30	0.16	25
S2	0.2	30	0.16	28
S3	0.4	30	0.16	45
S4	0.6	30	0.16	58
S5	0	50	0.16	153
S6	0.2	50	0.16	225
S7	0.4	50	0.16	398
S8	0.6	50	0.16	663
S9	0.4	30	0.14	152
S10	0.4	30	0.20	27

study [19, 20]. A uniform sand-fibre mix was poured into the stretched membrane in five steps with slight compaction to obtain the required density. After the specimen preparation, carbon-di-oxide was percolated at low pressure of 1–2 kPa for 30 min. Then, distilled water was flushed from the bottom to the top of the specimen. In the present research work, the completion of saturation process was considered when the 'B' value (Skempton's pore pressure coefficient) reached 0.95 using the increment of 20 kPa in both confining and back pressures. Stress-controlled undrained cyclic triaxial tests were performed in the test series (Table 2).

### 3.2 Parameters Considered

After the completion of saturation process, the specimens were isotropically consolidated at an effective confining pressure of 100 kPa. Then, cyclic inputs were provided as sinusoidal loading at a frequency of 1 Hz. The adopted frequency ranges from 0.1 to 1.5 Hz for replicating small or large earthquakes [12, 14]. The fibre content ( $\eta$ ) was varied as provided in Table 2. Three cyclic stress ratio (CSR) values (0.14, 0.16 and 0.2) were considered, where CSR is defined as:

$$CSR = \frac{q_{cyc}}{2 \times \sigma'_c} \quad (1)$$

where  $q_{cyc}$  = cyclic deviatority stress and  $\sigma'_c$  = effective confining stress.

Table 2 details all the cyclic triaxial tests performed on both reinforced and unreinforced specimens. Relative densities of 30 and 50% were considered for both the reinforced and unreinforced specimens. These relative densities were chosen to investigate the influence of grain to grain contact and grain to fibre contact on the dissipation of energy. The densities higher than 50% were not considered in this study because the dense reinforced specimen possesses rare chances of liquefaction.

In this case, enormous energy is required to break the soil skeleton towards a failure state. This makes less significant liquefaction study for dense reinforced specimens. The significant parameters considered in the study are presented in Table 2.

### 3.3 Calculation of Dissipated Energy

In the present study, the dissipated energy per unit volume of soil specimen is calculated using the area under the stress–strain plot of the hysteresis loop. As suggested by Polito et al. [24], the combination of stress–strain in a loading cycle was used to calculate the energy dissipated after the application of cyclic deviator stresses using Eq. (2).

$$W = \sum_{i=1}^{j-1} \frac{1}{2} (q^i + q^{i+1}) \cdot (\epsilon_a^{i+1} - \epsilon_a^i) \quad (2)$$

where  $W$  = cumulative dissipated energy calculated from the beginning of the cyclic loading,  $j$  = total number of data points,  $q$  = deviator stress, and  $\epsilon$  = developed strain.

In order to counteract the effect of  $p_0$ , normalized dissipated energy seems to be more effective and can be calculated using Eq. (3). Here,  $p_0$  was taken as 100 kPa. In this study,  $W_n$  is utilized in predicting the triggering of the liquefaction phenomenon.

$$W_n = \frac{W}{p_0} \quad (3)$$

where  $W_n$  is the normalized dissipated energy with initial mean effective stress =  $p_0$ .

Normalized dissipated energy ( $W_n$ ) emerged as a key parameter in deciding the liquefaction susceptibility of the specimens. Also, the maximum normalized dissipated energy ( $W_{n,max}$ ) is the energy essential for the onset of the liquefaction phenomenon in all the specimens. A point where dissipated energy curve shows a sharp rise will be considered as a triggering point for the initiation of liquefaction phenomenon. In the present study, the values of  $W_{n,max}$  were compared for different fibre contents, cyclic stress ratios and relative densities. It was observed that a vulnerable specimen will dissipate low energy as less energy is required to break the bonds.

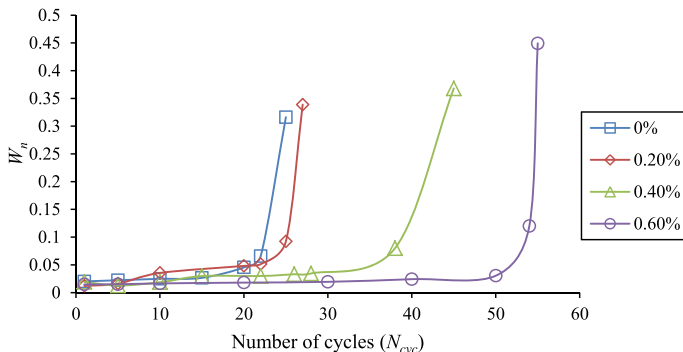


**Fig. 2** Variation of normalised dissipated energy ( $W_n$ ) with a number of cycles ( $N_{cyc}$ ) for different fibre content

## 4 Results and Discussion

### 4.1 Effect of Fibre Content on Liquefaction and Energy Dissipation

Fibres play a significant role in restricting the amount of pore pressure development [26]. It can be clearly observed in Fig. 2 where the dissipation energy required to cause liquefaction was highest for specimen S4. The matrix of fibre-sand was responsible for delaying the liquefaction failure by providing significant resistance. The non-reinforced specimen S1 failed in early least 25 cycles and with a  $W_{n,max}$  of 0.31. A similar phenomenon was also noticed in the previous research studies [1].

The rate of excess pore pressure development decreased with an increase in fibre content from 0 to 0.60%. The inter-pore spaces of the reinforced specimen receded the amount of pore water movement, which causes a reduction in excess pore pressure and delayed liquefaction, as shown in Fig. 3. Additionally, the amount of maximum dissipated energy ( $W_{n,max}$ ) was found to increase with an increase in fibre content as shown in Fig. 4.

### 4.2 Role of Density in Affecting the Energy Dissipation Characteristics

The packing arrangement of soil particles has a crucial role in controlling the energy dissipation characteristics. With an increase in relative density of the reinforced specimen, the grain-finer matrix possesses enough strength to counter liquefaction susceptibility. Therefore, the number of cycles was increased 8.8 times with an increase in relative density from 30 to 50% (Fig. 5).

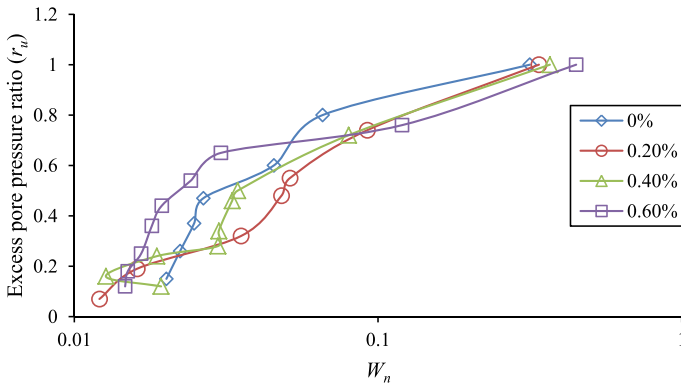


**Fig. 3** Variation of with excess pore pressure ratio ( $r_u$ ) with normalised dissipated energy ( $W_n$ ) for different fibre content

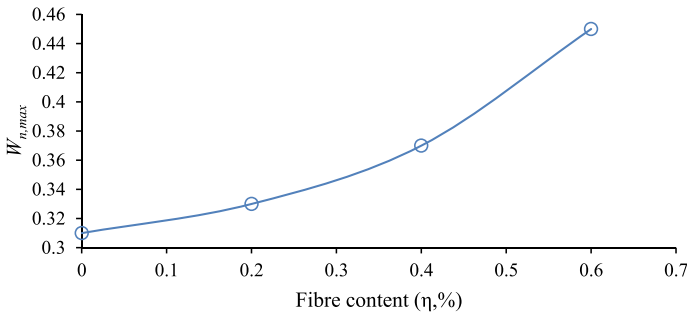


**Fig. 4** Variation of maximum normalized dissipated energy ( $W_n$ ) for different fibre content

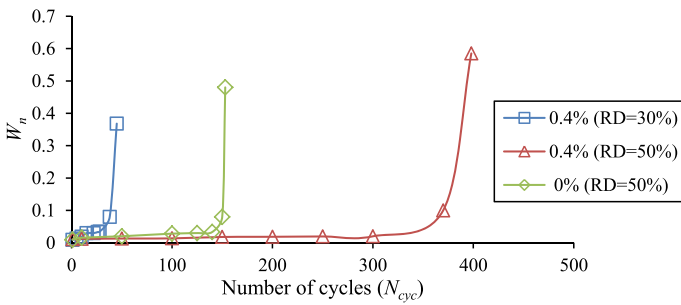


**Fig. 5** Variation of normalized dissipated energy ( $W_n$ ) with number of cycles ( $N_{cyc}$ ) at different relative densities



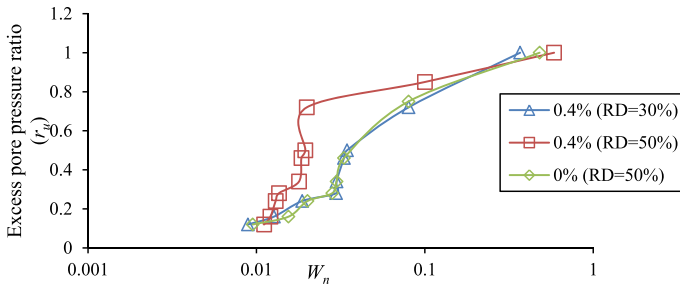


**Fig. 6** Variation of with excess pore pressure ratio ( $r_u$ ) with normalised dissipated energy ( $W_n$ ) at different densities

There was a reduction in excess pore pressure due to two main reasons, likely, the presence of fibre interlocking and the increment in grain-to-grain contact which is clearly visible in Fig. 6. It can be seen that the fibres are more effective in medium dense conditions rather than in the loose soil state.

### 4.3 Impact of Cyclic Stress Ratios (CSR) on the Energy-Dissipation

In order to replicate the real field conditions under the earthquakes of a variety of intensities, three different cyclic stress ratios were chosen at a fibre content of 0.4%. It can be clearly seen that the specimen S10 failed in just 27 cycles; therefore, the energy dissipated to cause liquefaction was minimum for S27 (Fig. 7). It can be seen in Fig. 7 that with an increase in CSR value,  $W_n$  decreases.

The increment in cyclic loading is responsible for causing the rise in pore pressure. At a fibre content of 0.4%, the CSR value increased from 0.14 to 0.2 to the number

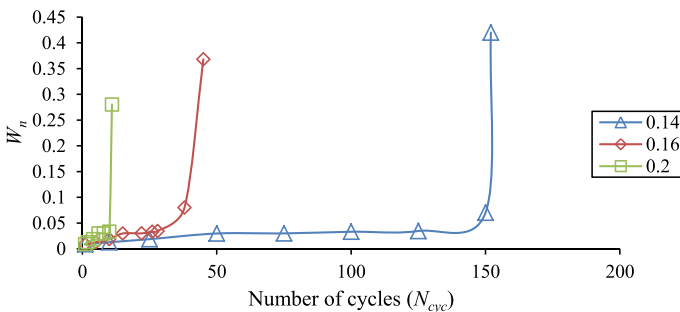


**Fig. 7** Variation of normalised dissipated energy ( $W_n$ ) with number of cycles ( $N_{cyc}$ ) at different cyclic stress ratios

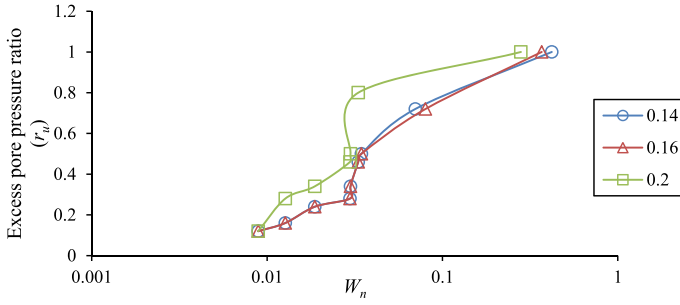


**Fig. 8** Variation of with excess pore pressure ratio ( $r_u$ ) with normalised dissipated energy ( $W_n$ ) at different cyclic stress ratios

of cycles decreased from 152 to 27 (Fig. 8). The reason behind this phenomenon is the instability triggered in a few cycles at higher deviator stresses.

#### 4.4 Comparison with the Previous Study

In the present study, the concept of energy dissipation has been used as the failure criteria to reach the liquefaction stage. In a similar study, Xueqian et al. [29] utilised the similar energy dissipation concept to justify the liquefaction-induced failures. Although, Xueqian et al. [29] performed the cyclic triaxial tests on the unreinforced specimen. As shown in Fig. 9, the curved of the present study lies rightward because the fibre-sand matrix caused the dissipation of energy in higher cycles. The pattern of both the studies follows a similar trend which justifies the utilisation of the energy dissipation concept to assess liquefaction and related failures of soil mass.

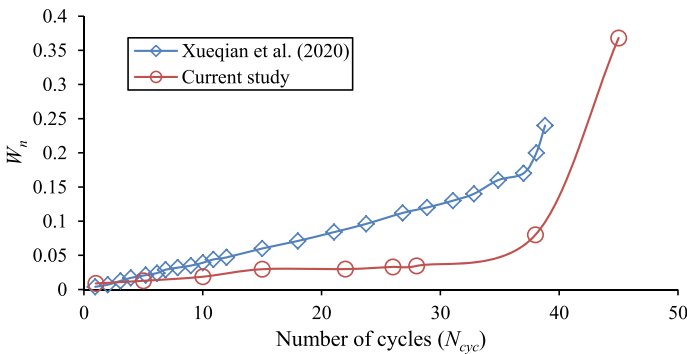


**Fig. 9** Comparison of energy variation with the previous study

## 5 Conclusions

The present research study is based on evaluating the liquefaction susceptibility of fibre reinforced and un-reinforced soil specimens using an energy dissipation approach. The outcomes obtained from the present study are given as follows:

1. The increment in fiber content from 0 to 0.6% in the loose specimen causes the 2.32 times increment in failure cycles or delayed liquefaction.
2. The amount of dissipated energy rose 8.84 times when the density of the fibre-reinforced specimen increased from 30 to 50%.
3. The value of maximum normalised dissipated energy ( $W_{n,max}$ ) reduced sharply when the cyclic stress ratios increased from 0.14 to 0.20. This was due to the sudden increase in the rate of pore pressure development.
4. The comparison of the current study with the previous research work also suggested the significant use of the energy dissipation approach instead of stress and strain-based failure theories.

**Acknowledgements** All the experiments in this study have been performed in the Geotechnical engineering laboratory, Indian Institute of Technology, Roorkee, India. This work was supported by the Ministry of Human Resource Development, Government of India, New Delhi (Grant No. MHR 002). There are no financial or non-financial competing interests between the authors.

## References

1. Amini PF, Noorzad R (2018) Energy-based evaluation of liquefaction of fiber-reinforced sand using cyclic triaxial testing. *Soil Dyn Earthq Eng* 104:45–53
2. Azeiteiro RJN, Coelho PALF, Taborada DMG, Grazina JCD (2017) Energy-based evaluation of liquefaction potential under non-uniform cyclic loading. *Soil Dyn Earthq Eng* 92:650–665
3. Baziar MH, Sharafi H (2011) Assessment of silty sand liquefaction potential using hollow torsional tests—an energy approach. *Soil Dyn Earthq Eng* 31(7):857–865
4. Boominathan A, Hari S (2002) Liquefaction strength of fly ash reinforced with randomly distributed fibres. *Soil Dyn Earthq Eng* 22(9–12):1027–1033
5. Davis RO, Berrill JB (1982) Energy dissipation and seismic liquefaction in sands. *Earthq Eng Struct Dyn* 10(1):59–68
6. Diambra A, Ibraim E (2015) Fibre-reinforced sand: interaction at the fibre and grain scale. *Geotechnique* 65:296–308
7. Debnath P, Dey AK (2017) Bearing capacity of geogrid reinforced sand over encased stone columns in soft clay. *Geotext Geomembr* 45:653–664
8. Dobry R, Ladd R, Yokel FY, Chung RM, Powell D (1982) Prediction of pore water pressure buildup and liquefaction of sands during earthquakes by the cyclic strain method. National Bureau of Standards, Gaithersburg, MD
9. Figueroa J, Saada A, Liang L, Dahisaria N (1994) Evaluation of soil liquefaction by energy principles. *J Geotech Eng* 120(9):1554–1569. [https://doi.org/10.1061/\(ASCE\)0733-9410\(1994\)120:9\(1554\)](https://doi.org/10.1061/(ASCE)0733-9410(1994)120:9(1554))

10. Geyer R, Jambeck JR, Law KL (2017) Production, use, and fate of all plastics ever made. *Sci Adv* 3:1–5. <https://doi.org/10.1126/sciadv.1700782>
11. Ghadr S, Samadzadeh A, Bahadori H, Assadi-Langroudi A (2020) Liquefaction resistance of fibre-reinforced silty sands under cyclic loading. *Geotext Geomembr* 48:812–827
12. Hussain H, Sachan A (2019) Dynamic characteristics of natural kutch sandy soils. *Soil Dyn Earthq Eng* 125:101517. <https://doi.org/10.1016/j.soildyn.2019.105717>
13. Jain A, Choudhary AK, Jha JN (2020) Influence of rice husk ash on the swelling and strength characteristics of expansive soil. *Geotech Geol Eng* 38:2293–2302. <https://doi.org/10.1007/s10706-019-01087-6>
14. Jain A, Mittal S, Shukla SK (2021) Effect of specimen preparation technique on the post-liquefaction behavior of fine sand under cyclic loading. *Indian Geotech J* 51:1026–1037. <https://doi.org/10.1007/s40098-021-00505-y>
15. Jain A, Mittal S, Shukla SK (2023) Use of polyethylene terephthalate fibres for mitigating the liquefaction-induced failures. *Geotext Geomembr* 51(1):245–258. <https://doi.org/10.1016/j.geotextmem.2022.11.002>
16. Kirar B, Maheshwari BK (2018) Dynamic properties of soils at large strains in Roorkee region using field and laboratory tests. *Indian Geotech J* 48:125–141. <https://doi.org/10.1007/s40098-017-0258-2>
17. Kokusho T (2013) Liquefaction potential evaluations: energy-based method versus stress-based method. *Can Geotech J* 50(10):1088–1099
18. Kazuhiro K, Okuda H, Kiyota T, Konagai K (2020) Mapping of liquefaction risk on road network based on relationship between liquefaction potential and liquefaction-induced road subsidence. *Soils Found* 60(5):1202–1214
19. Mercer FB, Andrawes KZ, McGown A, Hytiris N (1984) A new method of soil stabilization. In: *Polymer grid reinforcement*. Thomas Telford Publishing, pp 244–249
20. Noorzad R, Amini PF (2014) Liquefaction resistance of Babolsar sand reinforced with randomly distributed fibres under cyclic loading. *Soil Dyn Earthq Eng* 66:281–292
21. Noorany I, Uzdevaines M (1989) Dynamic behavior of saturated sand reinforced with geosynthetic fibres. In: *Proceedings of geosynthetics '89 conference*. North American Geosynthetics Society, pp 385–396
22. Nemat-Nasser S, Shakooch A (1979) A unified approach to densification and liquefaction of cohesionless sand in cyclic shearing. *Can Geotech J* 16(4):659–678
23. Patel SK, Singh B (2017) Experimental investigation on the behaviour of glass fibre-reinforced cohesive soil for application as pavement subgrade material. *Int J Geosynth Ground Eng* 3:13. <https://doi.org/10.1007/s40891-017-0090-x>
24. Polito C, Green RA, Dillon E, Sohn C (2013) Effect of load shape on relationship between dissipated energy and residual excess pore pressure generation in cyclic triaxial tests. *Can Geotech J* 50(11):1118–1128
25. Punthutaecha K, Puppala AJ, Vanapalli SK, Inyang H (2006) Volume change behaviors of expansive soils stabilized with recycled ashes and fibres. *J Mater Civ Eng* 18:295–306
26. Rasouli H, Fatahi B (2022) Liquefaction and post-liquefaction resistance of sand reinforced with recycled geofibre. *Geotext Geomembr* 50:69–81
27. Seed HB, Idriss IM (1971) Simplified procedure for evaluating soil liquefaction potential. *J Soil Mech Found Div* 97:249–74
28. Shukla SK (2017) *Fundamentals of fibre-reinforced soil engineering*. Springer, Singapore
29. Xueqian N, Bin Y, Zirui C, Guanlin Y (2020) Evaluation of the effects of initial deviatoric stress and cyclic stress amplitude on liquefaction potential of loose and medium-dense sands: an energy-based method. *Soil Dyn Earthq Eng* 136:106236
30. Ye B, Cheng ZR, Liu C, Zhang YD, Lu P (2017) Liquefaction resistance of sand reinforced with randomly distributed polypropylene fibres. *Geosynth Int* 24:625–636
31. Yang ZX, Pan K (2018) Energy-based approach to quantify cyclic resistance and pore pressure generation in anisotropically consolidated sand. *J Mater Civ Eng* 30(9):04018203

32. Yoo C, Abbas Q (2020) Laboratory investigation of the behavior of a geosynthetic encased stone column in sand under cyclic loading. *Geotext Geomembr* 48:431–442
33. Zhang J, Yang Z, Yang Q, Yang G, Li G, Liu J (2021) Liquefaction behavior of fiber-reinforced sand based on cyclic triaxial tests. *Geosynth Int* 28(3):316–326. <https://doi.org/10.1680/jgein.20.00045>

# Variations in the Capacity of Driven Energy Piles in Clay



Arvin Farid and Daniel P. Zimmerman

**Abstract** Energy piles are an emerging alternative for the reduction of energy consumption used to heat and cool buildings. Most of the research to date has been on thermodynamic properties or axial and radial stress and strain of piles. This paper focuses on the temperature-fluctuation effect on the capacity of vertically loaded driven energy piles in clayey soils. Consolidation of clay surrounding driven piles affects the pile capacity (i.e., set up in clay). The heating and cooling periods of energy piles can create the excess pore-water pressure (EPWP,  $u_e$ ) or relax the existing one (e.g., due to pile driving or previous thermal loads) in clayey soils (due to the contraction and expansion of water) affecting the pile capacity. In the meantime, the thermal expansion and contraction of the pile also generate or relax the EPWP in the soil, which can be computed using the cavity-expansion theory. This paper studies the resulting changes in the pile capacity due to the daily and seasonal thermal cycles. The results show that thermal cycles in an energy pile can cause a decrease in the pile capacity leading to a delay in reaching the capacity after a complete clay set up.

**Keywords** Energy · Geotechnology · Driven piles · Clay · Pile setup

## 1 Introduction

Energy piles are an emerging alternative for the reduction of fossil-fuel energy consumption to heat and cool buildings. Energy piles combine ground-sourced heating and cooling systems with the building's foundation. In recent history, heat exchange within the soil had been accomplished by horizontal heating and cooling beds, or heat sinks outside of the building footprint. The use of ground-source heat

---

A. Farid (✉) · D. P. Zimmerman  
Department of Civil Engineering, Boise State University, 1910 University Dr., MS. 2060, Boise,  
ID 83725-2060, USA  
e-mail: [arvinfarid@boisestate.edu](mailto:arvinfarid@boisestate.edu)

D. P. Zimmerman  
e-mail: [danielzimmerman@u.boisestate.edu](mailto:danielzimmerman@u.boisestate.edu)

pumps (GSHPs) requires additional ground surface area outside of the building footprint [5]. This requirement eliminates their use in most urban settings. While GSHPs require less energy to heat and cool structures, they have not been widely used in the United States due to higher installation costs than conventional heating and cooling methods [12]. Energy piles have advantages over separate foundation and GSHP systems, including lower installation costs and no requirement for additional space. Energy piles serve the dual purpose of supporting the structure and serving as a heat exchange medium. Energy piles have been installed in Austria and Switzerland for the last 30 years and are gaining popularity in other parts of Europe [6]. Energy piles have not yet been embraced by other developed countries more than the United States, mainly due to insufficient research concerning the effects of temperature fluctuation on the stress state of the foundation soils [12], initial construction cost, and the lack of U.S. requirements to utilize green energies in buildings, which is more common in Europe.

The adverse effect of energy piles may arise from the cyclic thermal loading of soils. In other words, the cyclic temperature change results in cyclic loading, which may potentially result in a reduction of the pile capacity. The cyclic thermal loading in fine-grained soils can affect the shear strength of soil since shear strength can be temperature dependent. However, in fine-grained soils such as clay, in addition to the temperature-dependent shear strength, the thermal cyclic loading can cause cyclic variations of the excess pore-water pressure (EPWP,  $u_e$ ). Cyclic variations of the EPWP cause cyclic variation of the effective stress, and the shear strength and volume changes triggered by the temperature cycles can reach a state of thermo-elasticity after the first few cycles. The focus of this paper is on the latter effect.

## 2 Scope and Methodology

### 2.1 Model

This paper uses the finite-difference method to analyze the impact of thermal cycles in an energy pile located within the clay. A coupled numerical model has been developed using principles of three-dimensional (3D, axisymmetric (radial), and vertical) primary consolidation of, and heat transfer through, saturated, slightly over-consolidated clay around a driven circular energy pile. The driving effect is captured through an increase in excess pore-water pressure ( $u_e$ ) and lateral stress modeled using the cavity expansion theory. The increase/decrease of  $u_e$  due to temperature variations in clay and the expansion or contraction of the pile were modeled and analyzed.

## 2.2 Modeling Material Properties and Pile Capacity

The temperature of the soil surface adjacent to the energy pile was varied to simulate seasonal heating and cooling demands. For the purpose of this paper, temperature changes adjacent to the pile were assumed on the order of 52 °C (− 1 to + 51 °C) between peak heating and peak cooling temperatures; however, temperature change estimated for energy piles in the U.S. are in the ± 15 °C range [2]. The model simulated the 3D dissipation of the  $u_e$  through the clay surrounding the pile. The resulting temporal variations of the pile capacity due to this cycling were computed. Thermal conductivity coefficients and specific heat capacities for the soil matrix were estimated using accepted values for soil and water found in the literature [8]. Coefficients of thermal expansion for the concrete piles, soil, and water were also assigned to the model according to accepted values found in the literature [8]. A driven energy pile that was modeled over a 2.5-year period with a constant-surface-temperature boundary condition and a transient-surface-temperature boundary condition assumed to be  $T = T_{med} + \left(\frac{T_h - T_l}{2}\right) * \cos\left[\frac{2\pi(t-212)}{364}\right]$  where time,  $t$ , is in days.

The purpose of the transient-surface temperature iteration is to simulate an energy pile that is near an exterior wall that may be subjected to seasonal temperature changes on the ground surface. A summary of results and conclusions will be discussed in the following.

The soil was modeled as a homogeneous layer of anisotropic clay for vertical and radial permeabilities. The study consists of three related, but stand-alone, models. Two of the models analyze a driven energy pile. One of these models includes transient ground-surface temperatures, and one assumes a constant surface soil temperature. Both of these driven-pile models assume the pile is driven six months before the HVAC system is turned on. The soil was modeled as a saturated, slightly over-consolidated clay of medium to high plasticity. The characteristics of the clay were similar to the Illite tested by Campanella and Mitchell [8] as shown in Table 1.

$e_0$  was the initial void ratio;  $k_{rr}$  is the horizontal (radial) hydraulic conductivity;  $k_{zz}$  was the vertical hydraulic conductivity;  $\gamma_{sat}$  was the void ratio was readjusted by the model as a result of the cavity expansion due to pile driving and soil expansion and contraction. The saturated unit weight was adjusted as the void ratio after the pile was driven or after soil expansion or contraction., but it is  $E_s$  was the Young's modulus for the soil;  $G_s$  was the specific gravity of the soil;  $\nu$  was the Poisson's ratio of the soil;  $s_u$  was the undrained shear strength of the clayey soil;  $\phi'$  was the angle

**Table 1** Properties of clay at 20 °C [8]

$\alpha_s$	$c_p$	K	$k_{rr}$	$k_{zz}$	$\gamma_{sat}$	$e_0$	
$3.3 \times 10^{-7}/$ °C	2462 J/kg °C	0.0042 W/m/ K	$7 \times 10^{-7}$ m/s	$4 \times 10^{-7}$ m/s	17 kN/m <sup>3</sup>	1.1	
$E_s$	$G_s$	$\nu_s$	$s_u$	$\phi'$	OCR	PL	LL
20 MPa	2.75	0.3	75 kPa	20°	1.1	17	52



of effective internal friction of the clay; OCR was the over-consolidation ratio; LL and PL were the liquid and plastic limits respectively.

$K$  was the heat conductivity coefficient for both vertical and radial directions;  $\alpha_s$  was the coefficient of thermal expansion for the saturated soil  $3.3 \times 10^{-7}/^\circ\text{C}$ ;  $c_p$  was the specific heat for the clay,  $c_p$ , is at  $20^\circ\text{C}$ , and the physicochemical coefficient of structural volume change is  $-0.5 \times 10^{-4}/^\circ\text{C}$  after Campanella and Mitchell [8].

The thermal expansion of the pile in the radial direction was calculated using the equation for the thermal expansion of an area,  $\Delta A = 2\alpha_T A_0 \Delta T$  where  $\Delta A$  is the change in the area,  $A_0$  is the original area,  $\alpha_T$  is the coefficient of linear thermal expansion, and  $\Delta T$  is the temperature change. The new radius,  $R_1$ , may be calculated based on the initial radius,  $R$ , as  $R_1 = [R^2 \times (1 + 2\alpha_T \Delta T)]^{0.5}$ .

The coefficient of thermal expansion,  $\alpha_{pile}$ , of the concrete for the driven pile was assumed  $14.5 \times 10^{-6}/^\circ\text{C}$ . The Young's Modulus for the concrete was assumed  $25 \text{ MN/m}^2$ . The coefficient of thermal expansion for water,  $\alpha_{H2O}$ , was set to  $0.207 \times 10^{-3}/^\circ\text{C}$ . Water density,  $\rho_w$ , is  $999.973 \text{ kg/m}^3$  at  $4^\circ\text{C}$  but was continually recalculated based upon the current temperature within the model. Dynamic viscosity is the measure of a fluid's resistance to deformation by shear or tensile stresses.

The Vogel–Fulcher–Tammann (VFT) model for dynamic viscosity,  $\mu$ , was used to find values for the variation of the dynamic viscosity of water with temperature [16]. The general form of the VFT model is as follows. Abdelaziz [1, 2] performed a sensitivity analysis that showed no significant impact of the minor change in the fluid properties on the thermal and mechanical response of energy piles. This is because the temperature range is small enough.

$$\mu = e^{(A + \frac{B}{C+T})}, \quad (1)$$

where  $T$  is the temperature in K; and coefficients  $A$ ,  $B$ , and  $C$  for water were obtained from the VFT-equation viscosity calculator for a variety of fluids. The VFT equation for the dynamic viscosity of water, with coefficients, is hence as follows.

$$\mu = e^{(-3.7188 + \frac{578.919}{-137.546+TK})} \quad (2)$$

Because the hydraulic conductivity changes when the temperature changes, the hydraulic conductivity is adjusted continuously within the model as follows.

$$k_T = K \frac{\gamma_T}{\mu_T} = \left( k_{20^\circ\text{C}} \frac{\mu_{20^\circ\text{C}}}{\gamma_{20^\circ\text{C}}} \right) \frac{\gamma_T}{\mu_T}, \quad (3)$$

where  $\gamma$  is the unit weight of the permeant fluid (here water), and  $\mu$  is the dynamic viscosity of the permeant fluid (here water). The subscripts represent the temperature in  $^\circ\text{C}$  [10]. Equation (3) inherently assumes that the change in the  $K$  depends only on the change of the viscosity. In other words, it does not consider changes in the microstructure of the soil (e.g., pore sizes and connectivity)

The coefficient of volumetric compressibility for water,  $m_v$ , was set at  $-0.364 \times 10^{-3} \text{ m}^2/\text{kg}$ . The coefficient of compressibility was selected so the  $u_e$  dissipation would be complete within 910 days such that the clay modeled in this work would have physical characteristics similar to the Illite studied by Campanella and Mitchell [8]. Consolidation was set to update on a daily basis within the model. The initial temperature of the soil was set to 15 °C (288 K).

The axisymmetric finite-difference mesh used to model the soil is a rectangular grid of 21 nodes wide and 31 nodes high, for a total of 651 nodes, as shown in Fig. 1. The width of the mesh was modeled at approximately 3.33 m (at increments of  $dr = 0.167 \text{ m}$ ), and the height of the mesh was modeled at 30 m (at increments of  $dz = 1 \text{ m}$ ). The driven pile was represented as a boundary condition from the top left corner of the mesh to mid-height. The pile was assumed to be 15 m long. The boundary condition below the pile to the bottom left corner is soil, assumed to be symmetrical to the soil below the pile. The bottom row of the mesh was modeled to be impermeable since the modeled soil was clay (and could be modeled symmetrically if the model soil were sand). This selection was made based on the hydraulic conductivity of the soil. The top of the mesh was assumed to have a concrete cover or pile cap over half of the surface near the pile. The other half of the top of the mesh was assumed to be exposed to the air.

The driven-pile model assumes that the structure built upon the energy piles will be built and operational, at least from the standpoint of HVAC system operation, exactly six months after pile installation. The modeled pile is representative of a

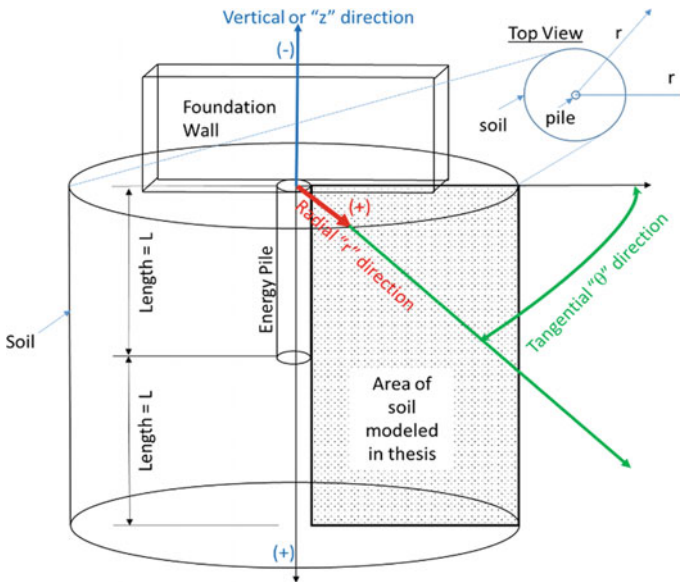


**Fig. 1** The layout of the model energy pile and simulated soil in cylindrical coordinates. Temperatures fluctuate between  $-1$  and  $+51$  °C in the soil adjacent to the energy pile

typical pile, and no distinction is made between an interior pile and an exterior (or perimeter) pile, except for the transient ground-surface temperature iteration of the model, which may be interpreted as an exterior pile. Consideration of the specifics of the construction of the building's foundation (within the pile) are beyond the scope of the model.

The model establishes a period through the initial six-month period prior to HVAC introduction, which allows for the dissipation of  $u_e$  and consolidation of the modeled soil. Both versions of the driven-pile model also calculate  $u_e$  dissipation for a period of two years plus six months, or 910 days, without HVAC system introduction, so that consolidation without conduction may be compared to consolidation with conduction.

As the six-month period begins within the time loop, the density and coefficient of thermal expansion of the water are calculated based on the in-situ temperature. Next, the physical state of the soil is changed due to pile driving. The initial void ratio,  $e_0$ , is recalculated to in-situ values using Eq. (4) for an element of unit length. In Eq. (4),  $C_c$  is the compression index;  $K_o$  is the at-rest lateral earth-pressure coefficient; and  $\gamma_{sat}$  is the initial saturated unit weight.

$$e_1 = e_0 - C_c [\log_{10}(K_o \cdot \gamma_{sat} \cdot z) - \log_{10}(K_o \gamma_{sat} \cdot (1))] \quad (4)$$

The installation of the pile will increase the radial stress based on Eq. (5). Equation (5) utilizes site-specific factors and restrrike data, that is, data obtained from driving the pile sometimes after driving has initially ceased, whether a few hours or several days. Re-striking is performed to either determine the capacity of the pile or to try to obtain additional penetration [14].

$$\frac{Q}{Q_0} = A \log_{10} \left( \frac{t}{t_0} \right) + 1, \quad (5)$$

where  $Q$  is the capacity of the pile at time  $t$ ;  $Q_0$  is the capacity of the pile at time  $= t_0$ , which is the time at which the dissipation of  $u_e$  becomes linear with the log of time [15]. The setup factor,  $A$ , is dimensionless and varies depending on soil conditions and the type of the pile [15]. The setup factor can range from 0.2 to greater than 1, where  $A = 0.6$  is typically used for clay, and  $t_0$  is typically valued at one day [18]. However, the Skov and Denver equation is not used to predict ultimate pile capacity. The Skov and Denver equation assumes a linear increase in pile capacity, and since pile capacity does not increase to infinity, it is only valid for a limited time after pile installation [17].

As seen in the flowchart of Fig. 2, a subroutine within the code recalculates the void ratio within the plastic zone based on the increase in stress. Once the void ratio and porosity are recalculated,  $\gamma_{sat}$  is also recalculated. After the density of water is calculated based on the temperature, its dynamic viscosity is calculated according to Eq. (2), and the absolute hydraulic conductivity is calculated according to Eq. (3). Therefore, Darcy's assumptions were violated so that the changes in the permeability due to temperature changes could be examined in the model. The next values to be

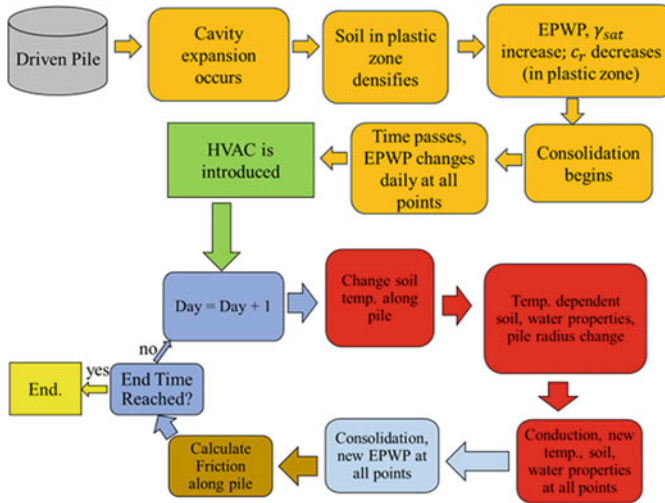


**Fig. 2** The process followed by the model for the driven-pile iterations

calculated by the model were the radial and vertical coefficients of consolidation,  $c_{rr}$  and  $c_{zz}$ , respectively. This calculation was performed using Eq. (6), and the unit of  $c_{rr}$  was converted to days.

$$c_{rr} = \frac{k_{rr}(86,400 \text{ s/day})}{m_v \rho_w g} \quad (6)$$

The  $u_e$  is then calculated. The boundary condition along the pile face is calculated using the logarithmic decay of Eq. (7) fitted to Bograd and Matlock (1990) and Banerjee [4] models [13]. Once the value of  $u_e$  in Eq. (7) reaches zero, the model limits the value of this boundary  $u_e$  to zero for cavity expansion.

$$u_e = 4.5 \cdot c_u \left[ 1 - \frac{\ln\left(\frac{c_r t}{R^2}\right)}{6} \right], \quad (7)$$

where  $t$  is time; and  $R$  is the lateral drainage path. Finally, the unit skin-friction resistance is calculated according to Eq. (8).

$$f_s = \beta \sigma'_z, \quad (8)$$

where  $\beta = K_0 \left( \frac{K}{K_0} \right) \tan \left[ \varphi' \left( \frac{\delta}{\varphi} \right) \right]$  where  $\varphi'$  is the effective stress friction angle, and  $\delta$  is the soil-foundation friction angle. The effective vertical stress,  $\sigma'_z$ , is calculated for each one-meter thickness of soil using Eq. (9). In Eq. (9), for the calculation of unit friction for a 1 m thick slice of soil at a depth of  $x$  m to a depth of  $(x + 1)$  m, the

value of the effective vertical stress is the overburden due to the above ( $x$ ) m plus the effective vertical stress at the midpoint between ( $x$ ) m and ( $x + 1$ ) m.

$$\sigma'_z = \gamma_{sat} \cdot (z - 1) + 0.5(\gamma_{sat} - \rho_w \cdot g), \quad (9)$$

where

$$K_0 = (1 - \sin \varphi') OCR^{\sin \varphi'}, \quad (10)$$

and where

$$K = 1.5 \cdot K_0 \quad (11)$$

where  $\left(\frac{K}{K_0}\right)$  values for a large displacement, driven pile range from 1.0 to 2.0 [9]. Values for the  $\left(\frac{\delta'}{\varphi'}\right)$  ratio are given at 0.8–1.0 for smooth concrete, such as the one seen in a precast pile, and 1.0 for rough concrete [9]. In the model,  $\left(\frac{K}{K_0}\right)$  is calculated using Eqs. (10) and (11), where  $\varphi'$  is  $20^\circ$ . The ratio  $\left(\frac{\delta'}{\varphi'}\right)$  is assumed to be equal to 0.8 in the model. Unit-circumference-friction is calculated using a ratio of  $u_e$  to initial  $u_{e0}$ , with the assumption that  $u_{e0}$  at Day 1 is equal to 1.25 times the deviator stress,  $\delta\sigma_r$ , as shown in Eq. (12). The unit friction calculated using Eq. (8) equals the friction along a unit length of the pile. Because the model calculates friction along the entire effective length of the pile, the frictional capacity calculation only requires multiplying the results by the perimeter of the pile. Therefore, the friction value computed by the model will, here on, be referred to as the unit-circumference friction value.

$$f = \left( \sum K_0 \cdot \sigma'_{z(ii)} \cdot \frac{K}{K_0} \cdot \tan \left[ \varphi' \left( \frac{\delta}{\varphi'} \right) \right] \right) * \left\{ 0.2 + 0.8 \left[ 1 - \left( \frac{u_{e(ii)}}{\left( \frac{\delta\sigma_r}{0.8} \right)} \right) \right] \right\} \quad (12)$$

After the six-month construction period, all three versions of the model loop through two years of simulated seasonal heating and cooling cycles. The heating and cooling cycles are cyclical in nature and separated into thirteen-week seasons. The details of this portion of the model are presented in Fig. 2.

After the initial six months, the  $u_e$  values are augmented by heat generated from the HVAC system. The HVAC system begins adding heat to the pile surface on the first day of summer. The heating of the energy pile through the convection of the heat-carrying fluid within the pile, as described by Brandl [6], is beyond the scope of this paper. Researchers such as Laloui et al. [11] and Brandl [6] present heating and cooling cycles that reach their maximum differential in a matter of days. The heat energy was added to and removed from the soil gradually in this model. In order to keep the quantity of heat added to the soil out of the model, a method of representing the gradual change in heat energy was devised. This gradual change in

heat energy introduced or removed from the soil is represented in a gradual change in the surface temperature of the soil adjacent to the energy pile. In addition, the gradual nature of the temperature change along the pile is meant to simulate the change in demand of the occupants of the theoretical building on the HVAC system throughout the calendar year. In the model, the highest demand on the cooling system would occur when the outside temperature was hottest. This time period is modeled to be in the middle of the summer season. Cooling of the building would pull heat from the occupied space and transfer that heat into the soil via the energy piles. This would then heat the soil. Conversely, the highest demand for heat would occur in the middle of the winter season, requiring the greatest amount of heat to be removed from the soil. The change between the demand for cooling and heating of the building occurs gradually and linearly, with a week in the middle of autumn and another in the middle of spring where neither heating nor cooling is required for the building. The seasons are simulated as shown in Fig. 3. Abdelaziz et al. [3] present a detailed analysis to form an ideal thermal cycle to model GSHP systems.

The total number of heating hours was calculated and then proportioned so that it could be distributed as shown in Fig. 3. The total range of temperature that the soil would see was decided upon prior to the creation of the model. The energy pile's face reaches a maximum temperature of slightly more than 50 °C and a minimum temperature of slightly less than 0 °C. The number of hours of heating was calculated using the method described above. The total number of heating hours was calculated to be 1344 heating hours.

When heat is added to the energy pile, the pile undergoes volumetric strain. However, the vertical dimension may be ignored in order to find the effect the thermal expansion has upon the horizontal cross-sectional area of the pile and pile radius. The increase in the pile radius may result in increased total stress on the soil, in the form of increased  $u_e$ ; the exception is the case of normally consolidated (NC) or slightly over-consolidated (OC) clays where the heating may cause thermal contraction of clay. The change in temperature between the in-situ temperature and the maximum soil temperature is 35 °C. Using the modulus of elasticity and coefficient of thermal expansion for concrete presented above and Eq. (13), the pile radius will expand 0.000076105 m during a change in temperature of 35 °C. Using Eq. (13) for a linear, compressive stress–strain relationship and assuming that since the stiffness of the concrete is much greater than that of the clay, the entirety of the strain from the thermal expansion of the energy pile is assumed to be transferred to the clay. The strain,  $\varepsilon$ , caused by the thermal expansion of the energy pile, represented by the right-hand side of Eq. (13), is equal to the strain due to the linear compression of the clay, represented by  $\frac{\sigma}{E_s}$  in Eq. (13). This assumes that first, the clay does not undergo any volume change due to heating, and the confining around the pile does not constrain the radial expansion of the pile, which may not be true in the case of NC or slightly OC clays where thermal contraction occurs.

$$\varepsilon = \frac{\sigma R_{clay}}{E_s} = R_{pile} \alpha_c \Delta T, \quad (13)$$

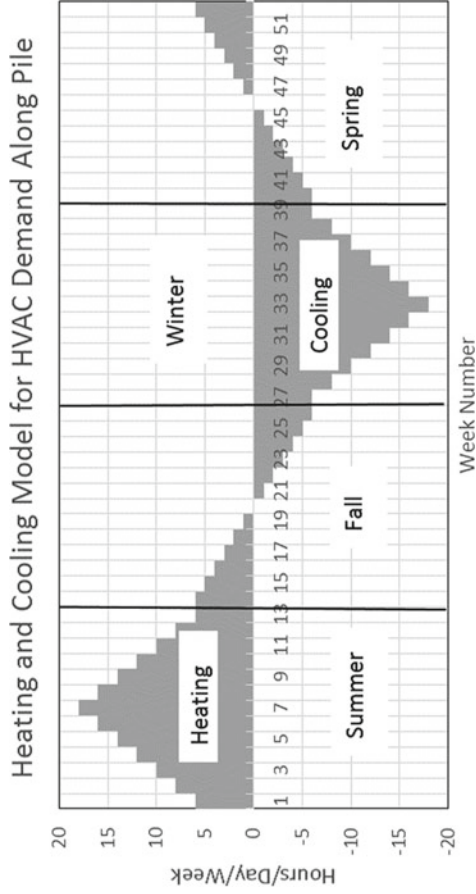


Fig. 3 A chart modeling the seasonal heating and cooling demand used to model temperature change for the temperature boundary condition along the pile

where it is assumed that the radius of the energy pile,  $R_{pile}$ , is equal to the length of clay being compressed,  $R_{clay}$ . Assuming that the stress created by the thermal expansion of the energy pile is then equal to the strain multiplied by the modulus of elasticity of the clay and that the stress,  $\sigma$ , is equal to an increase in the  $u_e$ , the  $u_e$  created by a temperature increase of 1 °C is calculated using Eq. (14).

$$u_{heat} = \frac{\varepsilon E_s}{\Delta T} = \frac{(7.6105 \times 10^{-5})20,000 \text{ kN/m}^2}{35 \text{ }^\circ\text{C}} = 0.0435 \frac{\text{kN}}{\text{m}^2 \text{ }^\circ\text{C}} \quad (14)$$

At this point in the model, the 182-day “construction phase” is over, and the model starts calculating the temperature change to the pile-soil boundary.

The value of  $u_{heat}$  in Eq. (14) is multiplied by the change in the temperature calculated for that day to obtain the amount of the  $u_e$  caused by the thermal expansion of the pile. This temperature change is added to the previous temperature, and the density and coefficient of thermal expansion values of water are then recalculated. At this point, the model starts to account for the changes to the soil characteristics caused by the change in the temperature that was not required during the “construction phase” because the temperature was constant. The model then recalculates the minor changes in the density of the soil,  $\rho_{clay}$ , and  $\rho_{satclay}$ . The specific heat is, thereafter, recalculated. The incremental temperature added to the previous day’s temperature is then removed because the temperature is added to the previous day’s temperature value in the part of the model that calculates conduction as a boundary condition along the pile face. This was necessary to prevent the change in temperature from being counted twice. Next, the  $u_e$  caused by the thermal expansion of the soil is calculated. The values of the dynamic viscosity and thermal expansion of water are then calculated, which are in turn used to calculate the hydraulic conductivity and coefficient of consolidation. The  $u_e$  is thus calculated for the day, and then the values of the  $u_e$  caused by thermal expansion of the pile and thermal expansion of the soil are added. This totals the  $u_e$  value for the day. The unit-circumference skin friction is then calculated and recorded, and the time value advances afterward.

### 3 Summary of Results

Figures 4 and 5 present the  $u_e$  data along the pile face at various depths. Figure 4 shows that the  $u_e$  at various depths experiences an initial rise in the value of approximately 14% immediately after pile installation. During this period,  $u_e$  values increase before consolidation begins—a dilatatory response of the soil that is similar to that described in Burns and Mayne [7]. The  $u_e$  decreases more rapidly around Day 200. This coincides with the beginning of soil heating. The increased soil temperature increases the hydraulic conductivity of the soil. Another reason for this can be the thermally-induced water flow since water flows from hot to cold regions. To examine the contribution of this, the change in PWP at points at a distance from the energy piles needs to be examined.



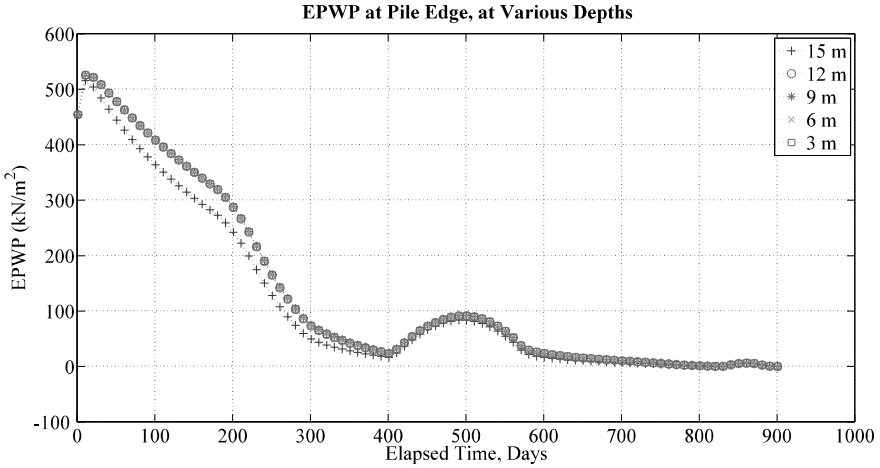


**Fig. 4** Excess pore-water pressure (EPWP,  $u_e$ ) at the pile surface at various depths, from the time of pile installation to the end of the model run. The ground-surface temperature is a constant 15 °C

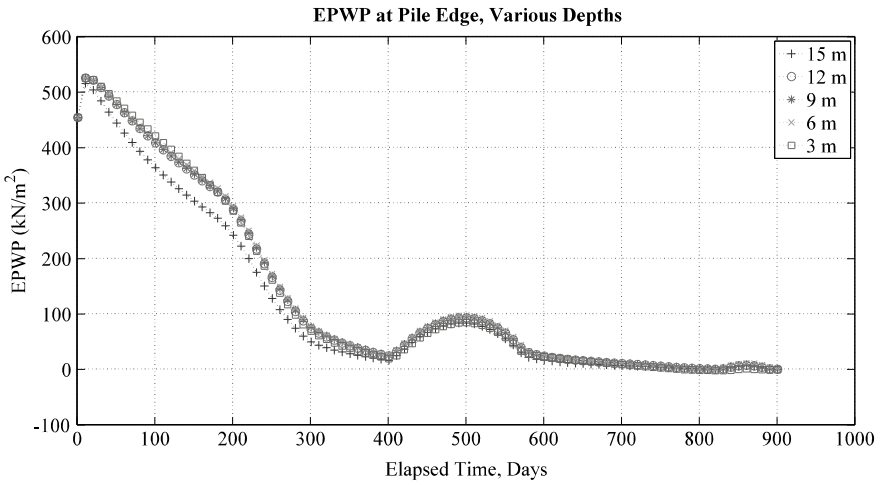


**Fig. 5** EPWP,  $u_e$ , at the pile surface at various depths, from the time of pile installation to the end of the model run, with transient ground-surface temperatures

There is a small schematic image of the model to the left of each figure with a thick solid line marking the locations for which the results in the figure are shown. Except for the 15 m case, other depths roughly coincide.

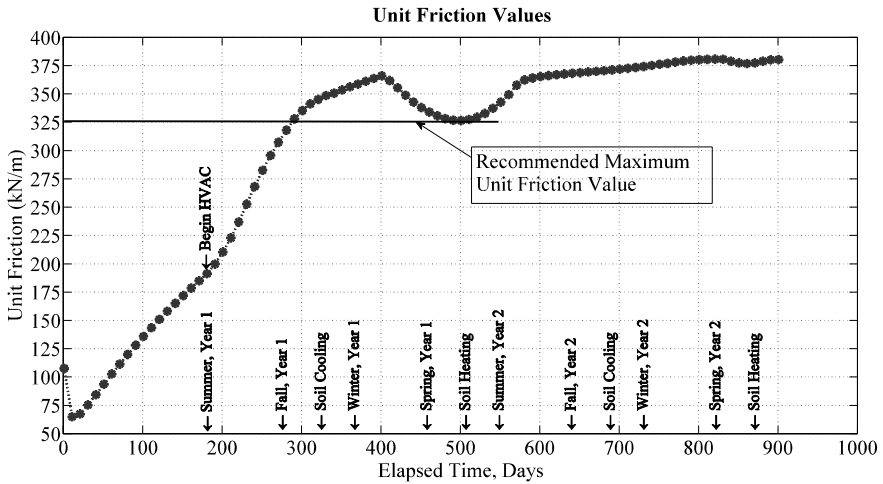


**Fig. 6** Unit-circumference-friction values from the time of pile installation to the end of the model run. The ground-surface temperature is a constant 15 °C

On Day 402, and peaking on Day 497, the  $u_e$  increases 67 kN/m<sup>2</sup>. This increase coincides with soil cooling during the winter season. There is another smaller increase in the  $u_e$  toward the end of Year 2. Figure 4 also shows that  $u_e$  values are almost equal along the pile face, except for the 15 m depth. This difference is likely due to the proximity of soil that has not undergone deformation due to cavity expansion within the assumptions of the model. In Fig. 5 (the more realistic case with a transient ground-surface temperature), the influence of the ground-surface temperature has caused the greater separation of the  $u_e$  values at the 3 m depth from the values at the other depths.

Results are available for other parameters at other locations at the same series of depths, which show more variations along the depth. However, those do not fit within the scope and limits of this paper.

The unit-circumference friction values are presented in Figs. 6 and 7. Friction values drop after Day 1 until approximately Day 10, then rise until approximately Day 400, and thereafter decrease due to the increased  $u_e$ . The initial decreased friction values coincide with the period of dilation in the soil, where the  $u_e$  values rise for a period of time before decreasing. Friction values drop slightly again due to soil heating during the spring of Year 2. Unit-circumference-friction values are slightly higher in Fig. 7 due to higher ground-surface temperatures. Although the friction capacity continues to increase until the end of the model run, the recommended unit-radius friction value is the value observed at the local minimum caused by soil cooling near the end of the first year of HVAC usage.

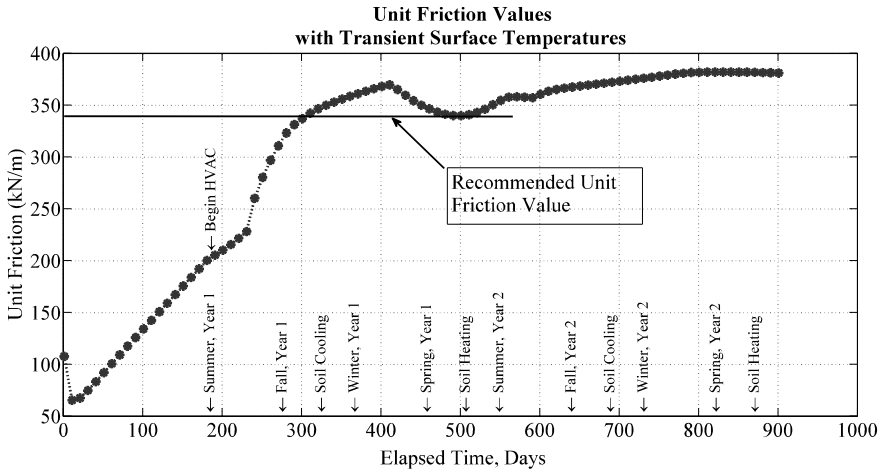


**Fig. 7** Unit-circumference-friction values from the time of pile installation to the end of the model run, with transient ground-surface temperatures

## 4 Conclusion

The purpose of this paper was to understand the soil-pile interaction of energy piles and to model the effects of temperature fluctuation on the capacity of a driven energy pile in clayey soils. The involved physical processes include the consolidation of clay around energy piles as well as conduction through the saturated clay soil. The consolidation of clay (due to the drainage of the excess pore-water pressure,  $u_e$ , in clay) surrounding the energy pile affects the capacity of the pile (i.e., pile setup in clay). This work simulates how temperature fluctuations within the soil surrounding the energy pile and fluctuations of the ground-surface temperature affect the drainage of  $u_e$  and thus the capacity of the energy pile.

The change in the  $u_e$  due to the thermal expansion and contraction of the energy pile and thermal expansion and contraction of the soil matrix were included in the model as well as the dissipation of the  $u_e$  generated by cavity expansion during pile driving.

The model analyzed the effect that variable temperatures had on the capacity of driven energy piles. The temperatures of both the soil at the surface of the pile and the ground surface varied sinusoidally to simulate seasonal demands on the energy pile and seasonal temperature changes, respectively.

The model assumed that the pile was driven on the first day of winter and the energy pile began operation on the first day of summer. The  $u_e$  dissipated at an increased rate during the period of time when the soil was heating. If the model conditions were flipped, i.e., the energy pile was constructed on the first day of summer and operational on the first day of winter, the  $u_e$  values would dissipate more slowly, likely leading to a longer period of consolidation and pile setup.

The influence of cyclical surface temperatures was observed in the results of the model. The offset in the cyclical surface-temperature equation placed the highest surface temperature in the middle of the summer, thus exaggerating the influence higher temperatures have on increasing consolidation rates because additional heat is present at the surface and is being conducted down into the soil at the same time the soil is heating due to HVAC usage. Consolidation rates would likely decrease more slowly if surface soil temperatures peaked during the period prior to the operation of the energy pile and during the period of soil cooling.

The unit-circumference-friction values computed by the model were calculated where the effective vertical stress was calculated along the depth. The unit-circumference-frictional values computed in the model led to allowable side-friction-capacity values that were similar in value to the allowable capacities that were calculated, where the effective vertical stress was calculated as a single full-depth clay layer.

## References

1. Abdelaziz SL (2013) Deep energy foundations: geotechnical challenges and design considerations. Ph.D. thesis, The Charles E. Via Department of Civil and Environmental Engineering, Virginia Polytechnic Institute and State University, p 368
2. Abdelaziz SL (2016) A sustainable perspective for the long-term behavior of energy pile groups. In: *Geo-Chicago 2016*. ASCE, Chicago, IL
3. Abdelaziz SL, Olgun CG, Martin JR (2015) Equivalent energy wave for long-term analysis of ground-coupled heat exchangers. *Geothermics* 53(1):67–84
4. Banerjee P.K. (1978) Analysis of axially and laterally loaded pile groups. *Developments in Soil Mechanics*. Applied Science Publisher, London, pp. 317–346
5. Brandl H (2006) Energy foundations and other thermo-active ground structures. *Geotechnique* 56(2):81–122
6. Brandl H (2009) Energy pile concepts. In: *Deep foundations on bored and auger piles*, pp 77–95
7. Burns S, Mayne P (1999) Pore pressure dissipation behavior surrounding driven piles and cone penetrometers. *Transp Res Rec* 1675:17–23
8. Campanella RG, Mitchell JK (1968) Influence of temperature variations on soil behavior. *ASCE J Soil Mech Found Div* 94(3):709–734
9. Coduto D (2001) *Foundation design: principles and practices*, 2nd edn. Prentice Hall, pp 402–558
10. Holtz B, Kovacs WD, Sheahan TC (2011) *An introduction to geotechnical engineering*. Prentice Hall, Hoboken, NJ
11. Laloui L, Nuth M, Vulliet L (2006) Experimental and numerical investigations of the behavior of a heat exchanger pile. *Int J Numer Anal Methods Geomech* 30:763–781
12. McCartney JS, Rosenberg JE (2011) Impact of heat exchange on side shear in thermo-active foundations. *ASCE Geotech Spec Publ* 211:488–498
13. Mirza UAA (2000) Consolidation parameters from axial pile load tests. In: *Proceedings of the tenth international offshore and polar engineering conference*, pp 395–402
14. Ng K, Roling M, AbdelSalam S, Suleiman M, Sritharan S (2013) Pile setup in cohesive soil. I: experimental investigation. *ASCE J Geotech Geoenviron Eng* 139(2):199–209
15. Steward EJ, Wang X (2011) Predicting pile setup (freeze): a new approach considering soil aging and pore pressure dissipation. *ASCE Geotech Spec Publ* 211:11–19

16. Trachenko K (2008) The Vogel–Fulcher–Tammann law in the elastic theory of glass transition. *J Non-Cryst Solids* 354:3093–3906
17. Wang X, Verma N, Tsai C, Zhang Z (2010) Setup prediction of piles driven into Louisiana soft clays. In: ASCE GeoFlorida 2010 conference: advances in analysis, modeling & design, vol 199. ASCE Geotechnical Special Publication, pp 1573–1582
18. Yang L, Liang R (2006) Incorporating set-up into reliability-based design of driven piles in clay. *Can Geotech J* 43(9):946–955

# Designing of Self-sustain Electrokinetic Experiment for Saline Soil Treatment



Öznur Karaca , Claudio Cameselle , Ayten Çalık ,  
and Emin U. Ulugergerli 

**Abstract** The lands stretching at the shorelines suffer from salinization which is one of the main environmental problems. Removing harmful salt contaminants requires an excessive amount of effort. The electrokinetic remediation (EKR) of soils away from urbanization is challenging since it requires a constant power supply. This research investigates the field scale effect of imposed electrical gradient (IEG) for the removal of salts from the soil with EKR using a solar panel-driven power supply. The testing soil was sampled in the Çanakkale-Dardanos Campus (CDC) area, in northwest Türkiye. The land in the CDC suffers from extreme saline water intrusion due to the excessive pumping of fresh water from multiple wells scattered in a relatively small area. The initial concentrations of salt ions were determined.  $\text{Ca}^{2+}$  showed the highest concentration (60,300 mg/kg) followed by  $\text{Mg}^{2+}$  (16,000 mg/kg),  $\text{K}^+$  (13,800 mg/kg), and  $\text{Na}^+$  ions (12,600 mg/kg). The most abundant anionic salt concentrations were  $\text{Cl}^-$  (674 mg/kg) and  $\text{SO}_4^{2-}$  (118 mg/kg). Lab-scale EKR studies showed that the EKR requires a minimum of 5-days to achieve satisfactory results. Therefore, we propose a mobile solar panel system and EKR as an innovative, sustainable, and environmentally friendly alternative to apply the EKR technology to saline soil. We will focus on designing the power supply system and fluid circulated electrodes. The results will be presented in due course.

**Keywords** Electrokinetic remediation · Saline soil · Solar energy

---

Ö. Karaca (✉) · A. Çalık

Geological Engineering Department, Canakkale Onsekiz Mart University, Çanakkale, Turkey  
e-mail: [oznurkaraca@comu.edu.tr](mailto:oznurkaraca@comu.edu.tr)

C. Cameselle

BiotechnIA, Department of Chemical Engineering, University of Vigo, Vigo, Spain

E. U. Ulugergerli

Geophysical Engineering Department, Canakkale Onsekiz Mart University, Çanakkale, Turkey

# 1 Introduction

Pollutant removal activities using electrokinetic remediation (EKR) technology have a weakness, in other words, some negative impact on the environment, which can be defined as the environmental footprint (EF) of EKR [1]. The application of the EKR technology requires a source of electrical energy, and disposal of electrode materials, wires, connectors, some substances, etc. [2]. Conventionally, each material, chemical substance, and also electrical energy are produced by the consumption of natural resources which cause gas emissions and pollution to the environment [3]. Paramitadevi et al. [1] presented a systematic literature review. They summarized the historical development and stated that the Sustainable Remediation Forum (SuRF) was established in the USA in 2006, then expanded to several countries such as Australia, the UK, Netherlands, Brazil, Canada, Taiwan, and Italy. The SuRF set the standards for remediation tools and assessed EKR as one of the green remediation technologies [3].

In order to reduce the EF, we focus on the production of electricity through solar panels. We are aware that the solar panel itself has EF. Our intention is to design and use a mobile, off-grid solar power system and use it in multiple sites so that EF in total will be less than permanent systems.

The main objectives of this study are as follows:

- Investigate the usability of solar panels to generate electricity for electrokinetic remediation applied on a field scale;
- Evaluate the effectiveness of electrokinetics for the remediation of salinized soil; and
- Examine the efficiency of different electrode configurations together with the conventional anode–cathode configuration.

For this purpose, we propose the following steps:

- An off-grid solar system shall supply necessary electrical power.
- Current, in turn, power need, shall be defined from the bulk resistivity of the geological unit.
- Multi-electrode system shall be employed for remediation.

We also need to solve the problems related to up-scaling the EKR application from lab to field scale. Some of the problems are keeping the moisturizing at an adequate level and also removing the pollutant from the system immediately to protect the electrodes.



**Fig. 1** The testing land is in the Çanakkale-Dardanos Campus (CDC) area, northwest Turkey

## 2 Testing Area

The testing land is in the Çanakkale-Dardanos Campus (CDC) area, northwest Turkey (Fig. 1). Main units in the area are sandstone and mudstone. Alluvium stretches along the shoreline. The land in the CDC suffers from extreme saline water intrusion due to excessive pumping of fresh water from multiple wells scattered in a relatively small area. As a reference, the concentrations of salt ions were determined as follows:  $\text{Ca}^{2+}$  was the highest (60,300 mg/kg) and  $\text{Mg}^{2+}$  (16,000 mg/kg),  $\text{K}^+$  (13,800 mg/kg), and  $\text{Na}^+$  ions (12,600 mg/kg) followed in this order. Anionic salt concentrations were  $\text{Cl}^-$ : 674 and  $\text{SO}_4^{2-}$ : 118 mg/kg.

Lab-scale EKR studies indicate that the experiment requires a minimum of 5-days for the results to be satisfactory [4]. Therefore, we propose to conduct a field test using an off-grid power system and EKR as an innovative, sustainable, and environmentally friendly alternative.

## 3 Designing an Off-Grid Power System

The simplified off-grid solar system is given in Fig. 2. The main components are the solar panel, battery pack, charge controller unit, and inverter. The number of solar panels and also the battery pack will depend on the power requirement.

We need to know the current intensity to be injected into the ground to estimate the power requirement. Therefore, we must have an idea about the electrical resistivity of the soil.



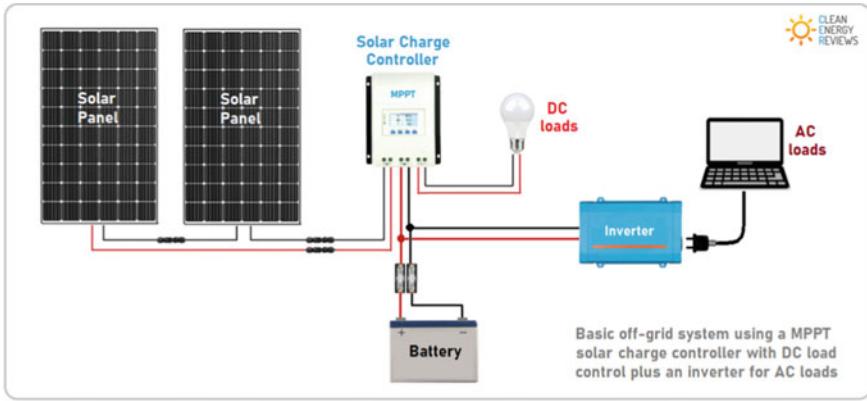


Fig. 2 Sample picture for solar system [5]

Working on the soil sample may not be adequate since the current will flow through a large volume. The bulk resistivity of the soil provides a better approximation to current soil conditions. The following sections will introduce a method to obtain bulk resistivity of the soil to be treated.

### 3.1 Direct Current Resistivity Method

In order to apply EKR, we need to figure out the bulk resistivity of the soil. We avoid getting it from hand-picked or core samples since the past agricultural activities created heterogeneity at the subsurface that varies from point to point. Hence, an in-situ method will be appropriate to define the bulk resistivity of the study area.

We propose the usage of the Direct Current resistivity (DCR) method of geophysics [6]. DCRM and EKR have similarities; both employ injected current through the electrode to the ground. EKR uses current flow to treat the subsurface while DCRM focuses on revealing the resistivity distribution of the subsurface.

The DCR data are acquired over the ground surface by injecting current ( $I_c$ ) from two electrodes, namely C1 and C2, and measuring the potential difference ( $\Delta V_p$ ) between another two electrodes (P1 and P2) for various intervals between the electrodes (Fig. 3).

The current ( $I_c$ ) and the potential drop values ( $\Delta V_p$ ) recorded at each survey point for each C1–C2, expansion along the profiles are converted to apparent resistivities;

$$\rho_a = k\Delta V_p/I_c \quad (1)$$

where  $k$  is a geometric factor obtained from the intervals of all electrodes.  $\rho_a$  represents both subsurface resistivity distribution and also the effect of the electrode positions.

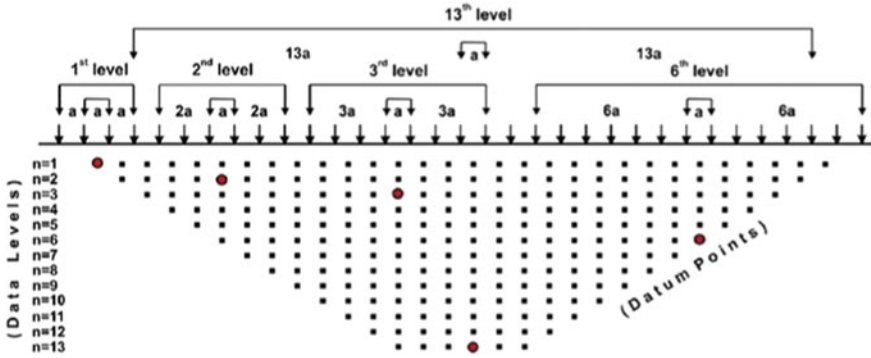


**Fig. 3** Multi-electrode system and DCR survey. Square dots show the hypothetical exploration depths. Red dots are the specific measurements related to electrode configuration given above (after [7])

These sets of apparent resistivities must be converted into pseudo images of soil material with true resistivities through inversion [8]. The data along the lines are evaluated with a Two-dimensional (2D) inversion scheme to obtain an electrical resistivity tomography (ERT) section for realistic evaluation [9–11]. Then, the resistivity values at various depths from the surface are extracted to map out the resistivity distribution of the study area at the depth of interest (Fig. 4).

Figure 4 clearly indicates that there is severe seawater intrusion (represented by <math>10 \Omega \text{ m}</math>) at the NW edge of the area (black rectangle). Targeting the area of interest, the bulk resistivity value is taken as  $\rho = 10 \Omega \text{ m}$ .

### 3.2 Power Requirement

We plan to use spike-like electrodes with an inline configuration. Electrode separation will be 100 + 100 cm (Fig. 5). Therefore, we need to apply 50 V for each side. Note that this configuration can be repeated multiple times to expand the coverage.

If the electrode interval is  $L = 100 \text{ cm}$  or 1 m while  $\rho = 10 \Omega \text{ m}$  then the resistance of the cube volume with a  $1 \text{ m}^2$  surface area

$$R = \rho * L/A = 10 * 1/1 = 10 \Omega.$$

The current requirement for each division is:

$$I = V/R = 50/10 = 5 \text{ A}$$

a



b

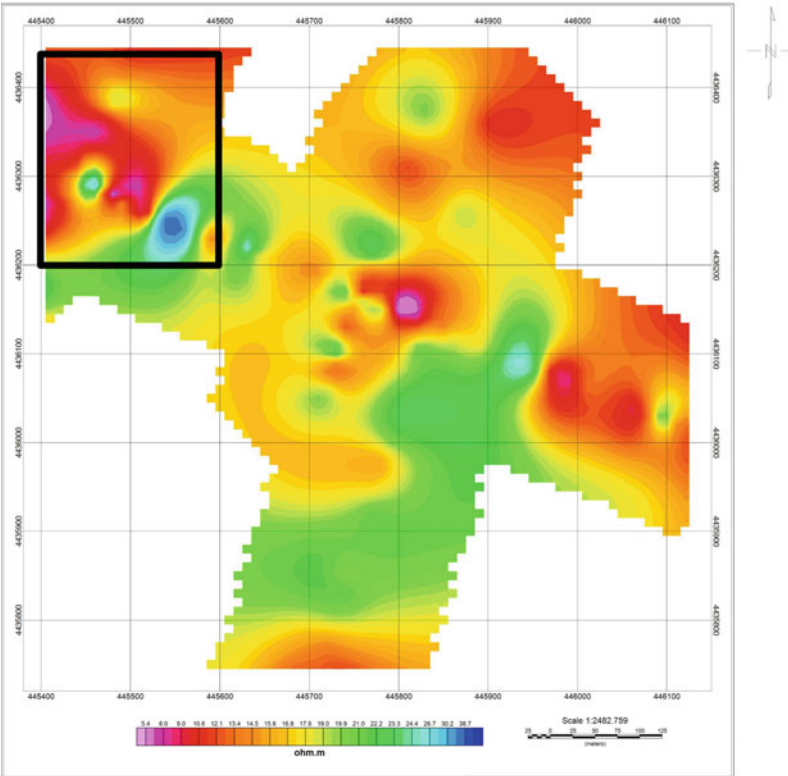


**Fig. 4** a Survey points, b distribution of the resistivity values at the 6 m depth from the surface in the study area extracted from the result of 2D inversion of DCR data along the various profiles

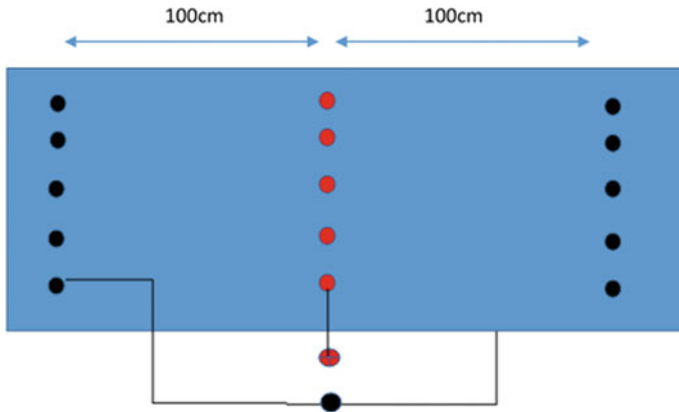


**Fig. 5** Electrode configuration for conceptual testing red dots anodes while black ones are cathodes

If we inject 5 A for both sides, then the power requirement is approximately:

$$P = V * I^2 = 50 * 10 * 10 = 5000 \text{ W}$$

Which is our minimum energy need for solar panels (Fig. 2).

### 3.3 Expected Energy Consumption

The accumulated consumption of electrical energy was calculated using the equation as follows:

$$E = \left( \int V I dt \right) / (VS) = (V / (VS)) \int dt \tag{2}$$

where V is the voltage applied (V), I is current intensity (A), and VS is the volume of soil (m<sup>3</sup>) [12].

The electrode configuration should be considered in the application of the electrokinetic technique because energy consumption is an important issue in electrokinetic remediation and electrode configuration influences significantly the total energy consumption.

### 3.4 Electrodes

Following Kim et al. [12], we will use hollow stainless steel with many holes for a cathode to facilitate the transport of electrolytes and pollutants. The anode is simpler

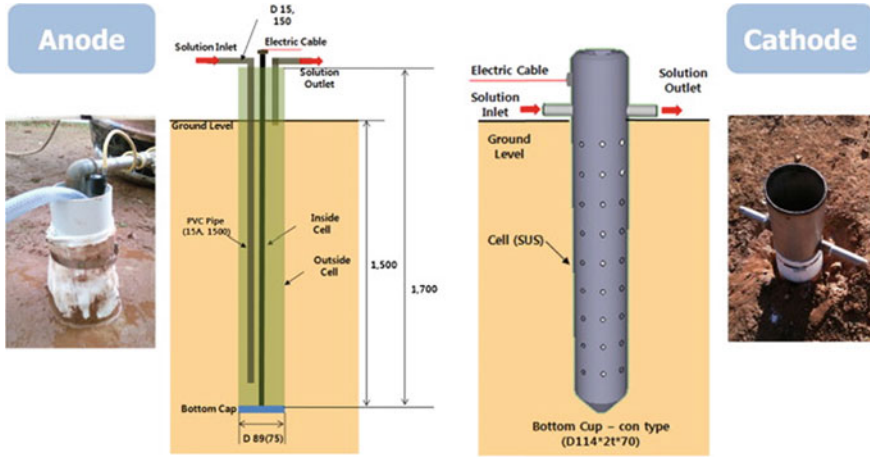


Fig. 6 Schematic diagram of electrode system (taken from Kim et al. [12])

than the cathode; polyvinyl chloride (PVC) casings with many holes housed the steel bars (Fig. 6).

We use NaOH as an anolyte conditioning agent while ethylenediamine tetraacetic acid (EDTA) as a catholyte processing fluid [11].

Each electrode will be wrapped with Gore-Tex and filtering textiles to prevent the leakage of electrolytes into the soil (Fig. 6). Circulation of electrolytes between the electrodes acts as a moisturizer of the electrode system.

### 4 Experiment

We will install the electrode configurations as described in Fig. 5 and Table 1. A constant voltage of 50 V will be applied, then the expected voltage gradient is 0.5 V/cm. The area covered by the electrode system was 2 m<sup>2</sup>.

Table 1 Experimental conditions for each electrode configuration (after Kim et al. [12])

Group	Size (m <sup>2</sup> )	Anolyte	Catholyte	A <sup>a</sup> (m)	B <sup>b</sup> (m)	The number of electrodes	
Empty cell	Empty cell	Empty cell	Empty cell	Empty cell	Empty cell	Anode	Cathode
A3	4 × 2	NaOH	EDTA	2	0.5	5	10
A4	2 × 4	NaOH	EDTA	1	1	5	10

<sup>a</sup> Anode–cathode spacing

<sup>b</sup> Same-polarity electrode spacing

To evaluate the influence of EDTA, tap water will be circulated as a catholyte conditioning agent. A thermometer will be installed to monitor the temperature change at the depth of 0.7 m below ground level [12].

Two soil samples will be taken from each configuration after 4 (1st sampling) and 14 weeks (2nd sampling). During the experimental period, current, temperature, and pH in electrolyte tanks will be monitored continuously. The electrode configuration should be considered, and the temperature of soil and groundwater flow should be monitored during the remediation to avoid unnecessary consumption of electrical energy and transport of contaminants by water flow.

## 5 Conclusions

This study outlines the design steps of a field scale EKR system. The power supply will rely on solar power while electrodes will be fluid-circulated holes. This design will be employed to perform in situ electrokinetic remediations on a pilot scale.

The removal of metals and salt are expected to be very slow because of the severe heterogeneity of soil and contamination and variation in groundwater levels. Thus we plan to run the test for up to 15 weeks. The results will be presented in due course.

## References

1. Paramitadevi YV, Ratnawati B, Effendi AJ, Hidayat S, Budihardjo MA, Ramadan BS (2022) Environmental footprint analysis tools of electrokinetic remediation (EKR): a bibliometric view of the literature. *IOP Conf Ser Earth Environ Sci* 950(1):012049. IOP Publishing
2. Kim DH, Yoo JC, Hwang BR, Yang JS, Baek K (2014) Environmental assessment on electrokinetic remediation of multimetal-contaminated site: a case study. *Environ Sci Pollut Res* 21(10):6751–6758
3. Ramadan BS, Sari GL, Rosmalina RT, Effendi AJ (2018) An overview of electrokinetic soil flushing and its effect on bioremediation of hydrocarbon contaminated soil. *J Environ Manage* 218:309–321
4. Bessaim MM, Karaca O, Missoum H, Bendani K, Laredj N, Bekkouche MS (2020) Effect of imposed electrical gradient on removal of toxic salt contaminants from alkali-saline low permeable soil during electrokinetic remediation. *Arab J Geosci* 13(14):1–12
5. <https://www.cleanenergyreviews.info/blog/2014/5/4/how-solar-works>
6. Telford WM, Geldart LP, Sheriff RE (eds) (1990) *Applied geophysics*. University Press, Cambridge
7. Ekinci YL, Türkeş M, Demirci A, Erginal AE (2013) Shallow and deep-seated regolith slides on deforested slopes in Çanakkale, NW Turkey. *Geomorphology* 201:70–79
8. Meju MA (1994) *Geophysical data analysis: understanding inverse problem theory and practice: SEG course notes series, 6*. SEG, Tulsa
9. Loke MH, Barker RD (1996) Rapid least-squares inversion of apparent resistivity pseudo sections by a quasi-Newton method. *Geophys Prospect* 44(1):131–152
10. Ulugergerli EU (2017) Marine effects on vertical electrical soundings along shorelines. *Turk J Earth Sci* 26(1):57–72

11. Roy A, Apparao A (1971) Depth of investigation in direct current methods. *Geophysics* 36(5):943–959
12. Kim WS, Park GY, Kim DH, Jung HB, Ko SH, Baek K (2012) In situ field scale electrokinetic remediation of multi-metals contaminated paddy soil: influence of electrode configuration. *Electrochim Acta* 86:89–95

# Performance of Sand Bentonite Mixtures Under Leachate Percolation



Kübra Fitnat Ayvalık , Ender Başarı , and Seda Durukan 

**Abstract** The permeability behavior of sand bentonite mixtures which were proposed for use of liner was investigated by using original leachate. In this regard, the 3-axial hydraulic conductivity tests were run while the chemical composition of the inlet and outlet leachate samples were identified. In addition, the adsorbed contaminants and the soil fabric of the mixtures were pictured via microscopic image technics. In literature, the conventional test procedures generally comprise the permeability values of the liner and/or filter materials which were determined by using tap water, this study suggested determining the hydraulic conductivities under the effect of leachate. Thus, leachate samples were taken from landfill sites located in Manisa Uzunburun municipal solid waste site. The pH of the environment for each test was found to be basic. The electrical conductivity values for each test were found to be under 1. This situation implies that the cation exchange process was not completed when the tests were ended. The hydraulic conductivity value of 10% sand-bentonite mixture sample was found to be higher when the inlet fluid was original leachate. When the inlet and outlet samples of leachates were investigated, it is found that sand-bentonite mixtures held  $\text{Ca}^{+2}$  while releasing  $\text{Na}^{+}$  which may be one of the main causes of the increase in hydraulic conductivity.

**Keywords** Landfill · Liner · Hydraulic conductivity · Leachate · Clay

## 1 Introduction

Environmental pollution rises due to the increase of the population and industry, the more the population and industry mean the more production of waste. Researchers have studied on prevention of pollution, especially subsurface contamination. Liners composed of clayey soils and synthetic membranes are used to inhibit the transition of contaminants to the groundwater. A liner is desired to contain the waste, prevent chemical attacks, act as a barrier against hazardous materials such as heavy metals

---

K. F. Ayvalık (✉) · E. Başarı · S. Durukan  
Manisa Celal Bayar University, Manisa, Türkiye  
e-mail: [kubrayvalik@gmail.com](mailto:kubrayvalik@gmail.com)

© The Author(s), under exclusive license to Springer Nature Singapore Pte Ltd. 2023  
Y. Yukselen-Aksoy et al. (eds.), *Sustainable Earth and Beyond*, Lecture Notes in Civil Engineering 370, [https://doi.org/10.1007/978-981-99-4041-7\\_5](https://doi.org/10.1007/978-981-99-4041-7_5)



and contain leachate produced by the waste. In other words, the aim of a liner is to prevent the transient flow of waste materials, and contaminants to the groundwater systems such as aquifers, and wells. In order to prevent dangerous leakage, a liner should have a required hydraulic conductivity that is less than or equal to  $10^{-9}$  m/s and other typical requirements were identified by many researchers [1–5].

Many studies have been conducted on impermeable layer or barrier applications and filtering studies in landfills [6–12]. In the light of the studies carried out to date, the desired properties in impermeable layers are; low hydraulic conductivity, high adsorption capacity, resistance to temperature changes, resistance to fluctuations in water content, and suitable mechanical properties to ensure continuity during and after construction, cheap cost and abundant availability. Clays are the first impermeable layer material that comes to mind with their low hydraulic conductivity and high adsorption capacity. However, studies have shown that; clays are highly affected by changes in temperature and water content; cracks occur in the impermeable material, and therefore the engineering parameters deviate from the desired level. Since clays did not give the desired result under the influence of temperature and water content changes, the idea of mixing them with sand was suggested. As a result, bentonite, which has the lowest hydraulic conductivity among the clay types, was mixed with sand. This mixture gave the desired result and, no cracks were observed under the influence of temperature and water content. Kleppe and Olson are cited as the pioneers of this practice [13]. Sand-bentonite mixtures (SBMs) are the most known bentonitic mixture that has widely been investigated by many researchers. A bentonite content of 10% was found to be sufficient in order to have a desirable hydraulic conductivity also avoiding volumetric shrinkage [14].

This study aimed to determine the adsorption and impermeability behavior of SBM against pollutants from landfill leachate. In this direction, it is aimed to determine the adsorption behavior of soil mixtures and the permeability values under the effect of leachate. Thus, the hydraulic conductivity of a SBM was measured using leachate directly. Since the chemical distribution of each landfill leachate is different, the leachate of solid waste landfill from Manisa was chosen as the target source.

When the adsorption studies in the literature are examined, the pollutants are tested one by one in the experiments carried out in the laboratories, whereas they are found in the form of a free mixture in landfills. This situation in laboratory research is far from reflecting the real conditions in the field. Besides, studies on hydraulic conductivity using mixtures of leachate and the uptake of these mixtures by impermeable layers are very few. In this study, the uptake behavior was determined for the original leachate, not for pollutants separately, by comparing the inlet and outlet fluids of the experiment.

Another important point is that, conventionally, tap water is used when determining hydraulic conductivity values in the literature. The values obtained using tap water are far from explaining the behavior in the field under the influence of leachate. In this study, soil mixtures were tested depending on the relevant leachate characterization and the hydraulic conductivity value was determined under the influence

of pollutants in the original leachate mixture. In addition, the chemical and physical effects of leachate on the structure of soils have been demonstrated by microscopic imaging techniques.

## 2 Materials and Method

Natural soils and leachate from Manisa Uzunburun Landfill were used as materials in the study. Sand (S) was supplied from Aydınlar Kum (Turgutlu-Manisa) where bentonite (B) was obtained from Karakaya Bentonit (Ankara). The mixtures were obtained by mixing the sieved sand (-No. 10) with the powdered bentonite (-No. 200). Some basic geotechnical properties of the materials to be used in soil mixtures were determined and presented in Table 1. The compaction parameters of the mixtures were determined with the standard Proctor energy, and the soil sample prepared at its wet of optimum state was then subjected to the flexible-wall hydraulic conductivity test where the water content of the sample was 22% and the dry unit weight was 15.4 kN/m<sup>3</sup>. Falling head protocol was followed during the hydraulic conductivity test. The confining pressure applied in the hydraulic conductivity test was 30 kPa, and the hydraulic gradient varied between 9 and 12.5. No additional treatment was carried out to ensure saturation before the experiment. Geotextiles were used for the porous layers, which would serve as upper and lower filters.

Scanning electron microscopy (SEM) was also used to visualize the initial and final conditions in the structure of the soil samples. EDX module was used to detect and display the contaminants in the samples. FEI Quanta 250 FEG type device was used in the SEM method, and Oxford Aztec Instruments was used during EDX

**Table 1** Summary of basic material characteristics

Properties	Bentonite	Sand
Mineralogy	Smectite (77%)	Quartz
	Cristobalite	
	Plagioclase	
<i>Particle size distribution</i>		
Gravel	0%	0%
Sand	4%	100%
Silt	21%	0%
Clay	75%	0%
<i>Atterberg limits</i>		
Liquid limit	405%	NA
Plastic limit	57%	
Plasticity index	348%	
<i>Specific gravity</i>	2.71	2.65

imaging. Chemical analysis of the leachate obtained from the landfill was carried out with inductively coupled argon plasma (ICP-OES). Agilent-5110 type device was used in ICP-OES analysis. The leachate, which was used as inlet fluid, and the effluent during the test were analyzed and compared.

### 3 Results

A flexible wall test was conducted where the influent was original leachate. During the test, such leachate samples were collected randomly to determine pH, and electrical conductivity (EC). The hydraulic conductivity was found to be within the limitation of  $10^{-9}$  m/s which is  $3 \times 10^{-10}$  m/s (see Fig. 1). The result was acceptable, however, the hydraulic conductivity value of the same soil sample with tap water was found to be  $2.6 \times 10^{-12}$  m/s in average in the study of Ören et al. [15]. A significant increase in hydraulic conductivity when the sample was subjected to leachate was obtained in contrast to some literature studies [16]. Then, to see the reason, SEM images of the samples were taken before and after the test as well as the ICP-OES analyses were done.

Scans were made on samples with (after the hydraulic conductivity test) and without (representing the initial condition) leachate and contaminants in the soil samples were detected. The initial compacted state of the samples with tap water before the exposure to the leachate was investigated by EDX and, Ba, Fe, Cr, and a small amount of Ni were observed in the SBM samples and it was determined that initial SBM samples already contained these contaminants (Fig. 2). Considering that natural bentonite was the only soil that can provide pollutant uptake in SBM samples, it has been determined that bentonite contained these elements in its natural state. It should be noted that the imaging process is done with very small soil samples. Therefore, there may be other contaminants present in the soil samples, which could not be visualized in their leachate-free state.

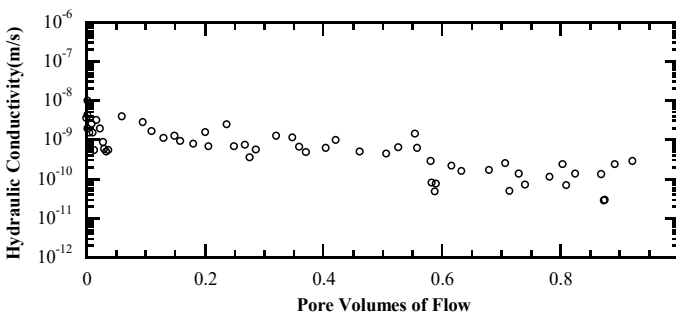
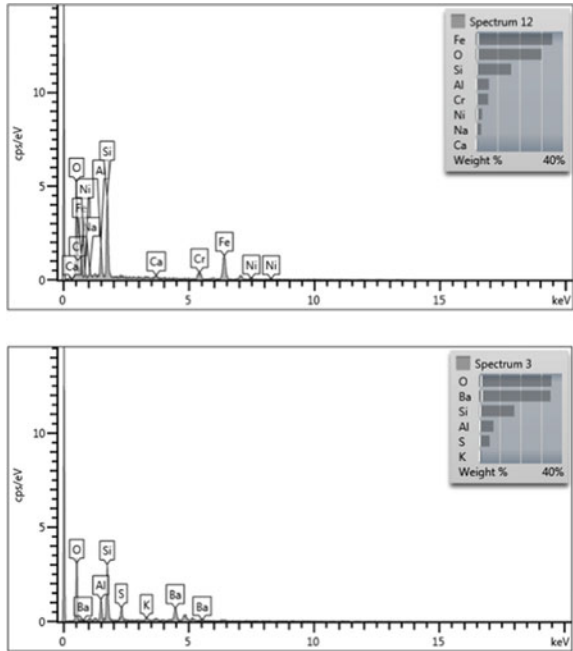


**Fig. 1** Hydraulic conductivity of SBM

**Fig. 2** Some pollutants detected in the initial state of SBM samples



Outflow leachate from soil samples was collected and pH and EC were measured at different times. The pH values of the effluent of SBM samples were found to be higher than 8 and sometimes even exceeded 9. The fact that the pH values are above 8 and sometimes even above 9 for the SBM samples indicates that the pH environment was not very efficient for the adsorption mechanism where precipitation occurs for metals. The change in the EC values of the outlet fluids is presented in Fig. 3 as the ratio of the EC value of the outlet fluids to the initial EC value. The ratio of the EC of the inlet fluid of the leachate to the EC of the sample’s outlet fluid remained below 1 in all conditions. This indicates that the cation exchange process did not end when the experiment was terminated.

It is very difficult to predict and follow the behavior of leachate, which has a very complex chemical content when it is percolated through soil samples. To see the elemental amount of alkali and alkaline-earth metals in leachate when percolated through a SBM sample ICP-OES analyses were conducted. Both the influent and effluent were analyzed. The variation in the amount of each exchangeable cation is given as the ratio of outlet concentration to inlet concentration ( $C_{out}/C_{in}$ ) of alkali and alkaline earth metals in the SBM sample (Fig. 4).

When the effluent of the SBM sample was examined, it was determined that it decreased up to 0.5 PVF, and then increased except for the Ca element. The element that increased according to the initial condition was Na. The displacement of  $Na^+$  and  $Ca^{+2}$  ions, which are closely related to permeability, and an increase in the Ca element in the effluent is expected behavior in clays because, generally speaking, the

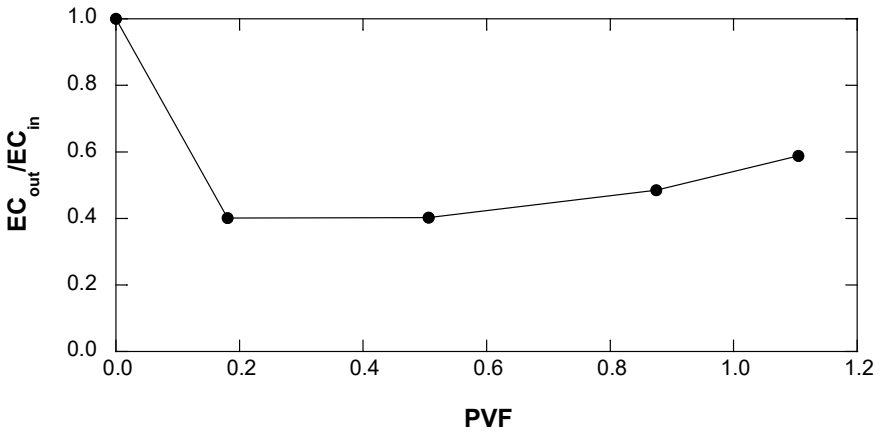


Fig. 3 The change of EC of SBM sample

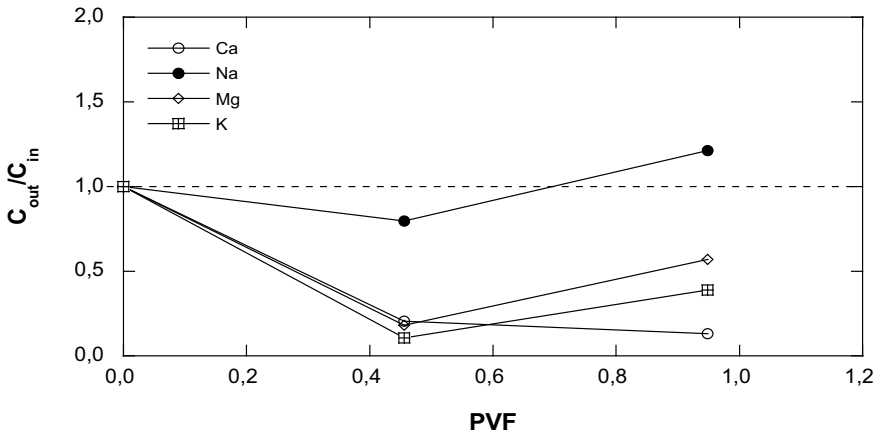


Fig. 4 The change in the alkali and alkaline-earth elements of the SBM sample

adsorption affinity of bivalent ions is greater than that of monovalent ions. Mostly, illitization occurs as a result of cation exchange due to the dissolution in the crystal structure of smectite-illite mixed layers which totally alters the behavior of the clay.

The exchange reaction of Na<sup>+</sup> and Ca<sup>2+</sup> ions has special importance as it directly affects the swelling capacity and permeability of bentonites (smectite group). The hydrated ion diameters of Na<sup>+</sup> and Ca<sup>2+</sup> are such that two hydrated Na<sup>+</sup> require more area than one Ca<sup>2+</sup>. Therefore, the replacement of Ca<sup>2+</sup> with Na<sup>+</sup> in the exchange areas causes an increase in the crystal lattice sizes of the clay. As a result, there is a decrease in permeability. When the effluent of 10% SBM sample was evaluated, a decrease in Ca ions and an increase in Na ions were determined. In other words,

the SBM sample absorbed Ca and released Na. Considering the hydraulic conductivity values of the SBM sample determined with tap water in previous studies which was  $10^{-12}$  m/s on average, it is seen that the hydraulic conductivity value increased and reached the order of  $10^{-10}$  m/s in SBM when percolated with Manisa leachate. The exchange of  $\text{Na}^+$  and  $\text{Ca}^{+2}$  ions which is already known to cause an increase in hydraulic conductivity can be accepted as one of the reasons for the increase in this study. The scope of this study was based on understanding the short-term hydraulic conductivity behavior, and for this testing duration, no bacterial formation was detected. It is recommended to investigate long-term behavior, including biological effects (bacteria).

## 4 Conclusions

The permeability behavior of sand bentonite mixtures which were proposed for use of liner was investigated by using original leachate. The hydraulic conductivity value of 10% sand-bentonite mixture sample was found to be higher when the inlet fluid was original leachate when compared to the result where the influent was tap water. The exchange of  $\text{Na}^+$  and  $\text{Ca}^{+2}$  ions was found possible to cause an increase in hydraulic conductivity. However, considering that this was a short-term hydraulic conductivity study and also no bacterial formation was detected at the end of the testing period, it is recommended to investigate the long-term behavior, including biological effects (bacteria) and the effect of organic matter.

**Acknowledgements** This study was supported by Manisa Celal Bayar University under Scientific Research Projects (Grant No: 2018:060). The authors are grateful for the funding source.

## References

1. Daniel DE, Benson CH (1990) Water content-density criteria for compacted soil liners. *J Geotech Eng* 119(2):223–237
2. Koch D (2002) Bentonites as a basic material for technical base liners and site encapsulation cut-off walls. *Appl Clay Sci* 21:1–11
3. Stewart DI, Cousens TW, Studds PG, Tay YY (1999) Design parameter for bentonite enhanced sand as a landfill liner. *Proc Inst Civ Eng Geotech Eng* 137(4):189–195
4. Pusch R (2015) Bentonite clay: environmental properties and applications. CRC Press, p 368
5. Chen YG, Cai YQ, Pan K, Ye WM, Wang Q (2021) Influence of dry density and water salinity on the swelling pressure and hydraulic conductivity of compacted GMZ01 bentonite–sand mixtures. *Acta Geotech*
6. Kraus JF, Benson CF, Erickson AE, Chamberlain EJ (1997) Freeze thaw cycling and hydraulic conductivity of bentonitic barriers. *J Geotech Geoenviron Eng* 123(3):229–238
7. Tay YY, Stewart DI, Cousens TW (2001) Shrinkage and desiccation cracking in bentonite-sand landfill liners. *Eng Geol* 20(1–4):263–274
8. Cho W-J, Lee JO, Kang C-H (2002) Hydraulic conductivity of compacted soil-bentonite mixture for a liner material in landfill facilities. *Korean Soc Environ Eng* 7(3):121–127

9. Komine H (2004) Simplified evaluation on hydraulic conductivities of sand–bentonite mixture backfill. *Appl Clay Sci* 26(1–4):13–19
10. Akgün H (2010) Geotechnical characterization and performance assessment of bentonite/sand mixtures for underground waste repository sealing. *Appl Clay Sci* 49(4):394–399
11. Akcanca F, Aytekin M (2014) Impact of wetting-drying cycles on the hydraulic conductivity of liners made of lime-stabilized sand-bentonite mixtures for sanitary landfills. *Environ Earth Sci* 72(1):59–66
12. Li B, Li LJ, Grace R (2015) Adsorption and hydraulic conductivity of landfill-leachate perfluorinated compounds in bentonite barrier mixtures. *J Environ Manage* 156:236–243
13. Kleppe JH, Olson RE (1985) Desiccation cracking of soil barriers. *ASTM Spec Tech Publ* 874:263–275
14. Kenney TC, van Veen WA, Swallow MA, Sungalia MA (1992) Hydraulic conductivity of compacted bentonite-sand mixtures. *Can Geotech J* 29:364–374
15. Ören AH, Durukan S, Kayalar AŞ (2014) Influence of compaction water content on the hydraulic conductivity of sand–bentonite and zeolite–bentonite mixtures. *Clay Miner* 49(1):109–121
16. Demdoun A, Gueddouda MK, Goual I (2017) Effect of water and leachate on hydraulic behavior of compacted bentonite, calcareous sand and tuff mixtures for engineering barriers. *Geotech Geol Eng* 35(6):2677–2696

# Strength Performance of Tincal and Perlite Added Zeolite-Bentonite Mixtures Under High Temperature



Sukran Gizem Alpaydin , İsa Cirkin , and Yeliz Yukselen-Aksoy 

**Abstract** In energy geo-structure and landfill applications, the effect of temperature on the behavior of soils should be considered. Some properties of soils surrounding structures which are nuclear waste disposal facilities, landfills, energy piles, etc. may change with increasing temperature. According to previous studies, properties of soils such as; volumetric deformation, shear strength, permeability are affected by high temperatures and thermal cycles. For that reason, in such geotechnical applications, there is a need for soils that are not negatively affected by high-temperatures, that is, that can maintain or improve their properties at high temperatures. Zeolite-bentonite mixtures may be proposed as an alternative to sand-bentonite mixtures in impervious barriers. Zeolite is preferred because of its high cation exchange capacity, which is not present in sands. In this study, 10% tincal and perlite were added to the mixtures which are bentonite/bentonite-zeolite ratio of 0.20 because of their superior properties at heat insulation. The compaction and direct shear tests were performed at room temperature and 80 °C.

**Keywords** Shear strength · Compaction · Temperature effect · Tincal · Perlite

## 1 Introduction

Compacted bentonite and sand-bentonite mixtures are attracting more attention as buffer materials for nuclear and urban waste repositories. Bentonite has high swelling capacity, low hydraulic conductivity and contaminant adsorption capacity. For that reason, bentonite forms an integral part of a liner and buffer material. Nevertheless, its use of concern due to its properties such as high compressibility, high desiccation shrinkage, low shear strength and low compaction density. It is preferred to

---

S. G. Alpaydin (✉) · İ. Cirkin  
The Graduate School of Natural and Applied Sciences, Dokuz Eylul University, İzmir, Turkey  
e-mail: [gizem.alpaydin@gmail.com](mailto:gizem.alpaydin@gmail.com)

Y. Yukselen-Aksoy  
Department of Civil Engineering, Dokuz Eylul University, İzmir, Turkey



mix bentonite with sand to improve certain engineering properties like maximum dry density, shrinkage, shear strength and thermal conductivity [1, 2]. However; since sand does not have a significant adsorption capability, the adsorption capacity decreases as the increase in sand content [3]. Therefore, as an alternative to sand, the zeolite may be considered as it is similar to bentonite in terms of adsorption capacity and sand in terms of mechanical properties. Natural zeolites consist of acidic and volcanic tuffs [4]. Zeolites have good physical and chemical properties such as large surface area, sieve-type molecular structure and high adsorption capacity. Zeolites are used as adsorbents for detergents, gas and oil processing, mining, and paper products. It was reported that zeolites have low compressibility and their hydraulic conductivity is appropriate for the limitation of landfill liners [5].

Former studies have shown that fluctuations in temperature affect the engineering characteristics of soils. It was reported that compacted San Francisco Bay mud had lower shear strength and higher pore pressure at higher temperatures [6]. In the study on silty clay, it was demonstrated that an increase in temperature resulted in lower shear strength, lower stiffness, and higher volume change during shear [7]. On the other hand, many studies revealed that an increase in temperature strengthened clay. For example, the shear strength of both illite and smectite-rich clay increased as the temperature increased [8].

Additives like boron minerals and perlite may be used to minimize the effects of temperature fluctuations on the engineering properties of buffer materials. Boron is a natural compound that consists of different proportions of boron oxides [9]. The most commonly boron minerals used in industry are tincal, colemanite and ulexite. Boron is strongly held by the aluminum or silicon tetrahedron in the clay structure [10]. In addition, boron minerals are suitable for use at high temperatures since they have low thermal expansion. Perlite is one of the materials widely used in the industry for heat resistance and heat insulation. Perlite expands greatly when heated sufficiently [11]. Perlite is used in many different fields such as construction, agriculture, medicine, chemistry, ceramics and glass industry.

The present study shows the compaction and direct shear test results of compacted zeolite-bentonite mixtures (ZBMs) in the presence of tincal and perlite at room temperature and 80 °C.

## 2 Materials and Methods

### 2.1 Materials

The soils used in this study are Na-bentonite and zeolite. Tincal and perlite were used as additive materials. ZBMs were in the ratio of 80:20 and added tincal/perlite of 10% were adopted. Bentonite, zeolite and additive materials were supplied by local companies. The mineralogical composition of the materials was analyzed by X-ray diffraction. The physical properties of the materials are summarized in Table 1.

**Table 1** Physical properties of the materials

	Zeolite	Bentonite	Tincal	Perlite
Mineralogy	Silicon dioxide, sodium tecto aluminosilicate hydroxide, silicon aluminum oxide, silicon oxide hydrate, clinoptilolite	Quartz, montmorillonite, illite	Borax, tincalconite, jadeite, silica	Aluminum oxide, iron oxide, calcium magnesium aluminum oxide and silicon dioxide
Specific gravity	2.30	2.70	1.67	1.50
Liquid limit (%)	42	476	61	375.1
Plastic limit (%)	–	70	43	–
Plasticity index (%)	–	406	18	–
pH	8.50	9.50	9.12	8.90
-No. 200 (%)	100.0	100.0	91.3	100.0

## 2.2 Experimental Methods

The compaction tests were performed in accordance with ASTM D698 [12]. The prepared samples were kept in an air-tight bag for 24 h. Subsequently, the compaction tests were performed by applying Standard Proctor energy by using an automatic compactor. The mixtures were compacted into two layers and 43 drops were applied to each layer to obtain the Standard Proctor energy.

The direct shear tests were performed on the samples of ZBMs in the presence of tincal and perlite (ZBTM and ZBPM) to determine the shear strength parameters [13]. The specimens were prepared under conditions of maximum dry density (MDD) and optimum moisture content (OMC) for the shear box test ( $6.0 \times 6.0 \times 2.0$  cm). The tests were performed with a strain-controlled shear box test machine. The shear stress and horizontal displacement were recorded.

The tests were carried out at different thermal conditions: room temperature (RT) and 80 °C. The conventional direct shear apparatus was modified for high temperature (Fig. 1). The modified test system consists of a conventional shear box, heat rod, thermostat, and K-type thermocouple. The specially designed heat rod indirectly heated the sample by heating the water. The thermostat was used to keep the temperature constant at 80 °C. The temperatures of the soil and water were controlled continuously via of K-type thermocouples.

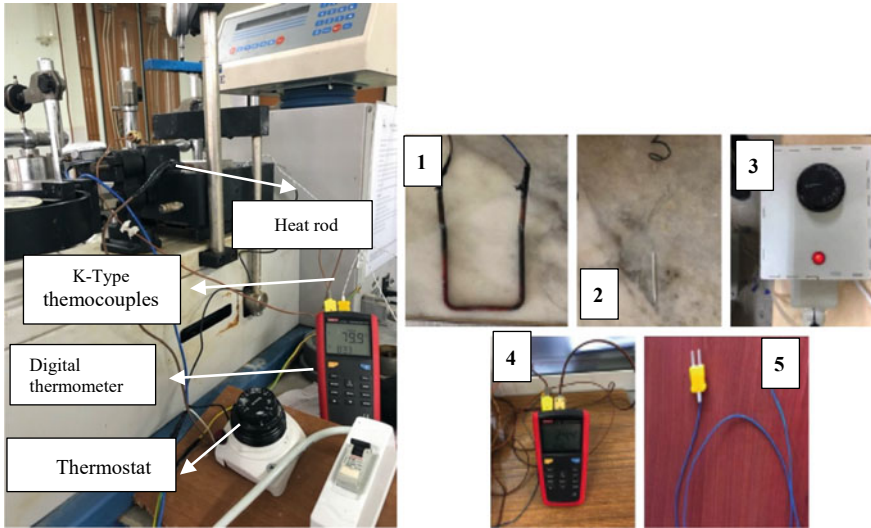


**Fig. 1** Photograph of the experimental set-up (1: heat rod, 2: thermostat, 3: thermostat box, 4: digital thermometer, 5: K-type thermocouple)

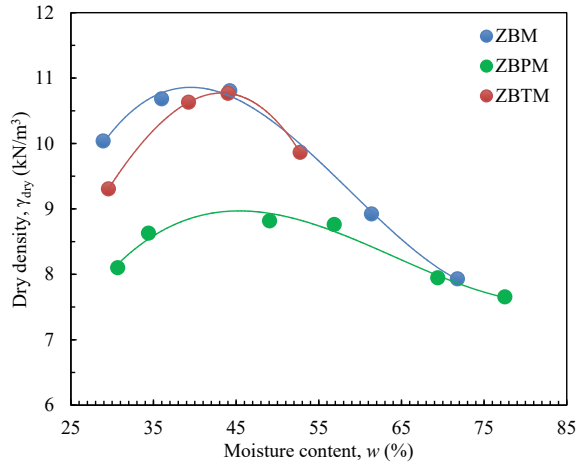
### 3 Results and Discussions

Figure 2 demonstrates the compaction curves of the three different mixtures compacted at same energy. The  $\gamma_{dry}$  (dry density) increased with increasing  $w$  (water content) with  $\gamma_{drymax}$  at the  $w_{opt}$  (optimum water content) (Fig. 2). The increase in the  $\gamma_{dry}$  with higher  $w$  may be due to variations in the particle orientation [14]. The particle orientation in bentonite increases as the moisture content increases, resulting in a higher dry density. At  $w$  values higher than the  $w_{opt}$  value,  $\gamma_{dry}$  decreases because swelling increases.

The  $w_{opt}$  of the ZBM increased slightly when perlite and tincal were added. Since additives were added to the mixture, the ratio of each material in the mixture changed. For example, while zeolite (low liquid limit) decreased, perlite (high liquid limit) increased. The OMC of the ZBM mixture, which was 42.0%, increased to 45.5% in the presence of perlite (Table 2). The slight increase is due to the displacement of materials. However, the  $\gamma_{drymax}$  value of the ZBM mixture, which was 10.2 kPa, did not show a significant change with the addition of tincal (10.8 kPa), but decreased significantly in the presence of perlite. Since perlite is a very light-weight material, even though 10% by dry weight was added to the mixture, it occupied more space by volume than other materials. This is the reason for the decrease in  $\gamma_{drymax}$  in the presence of perlite.

Figure 3 shows the variation of the shear stress versus shear displacement of all mixtures for  $\sigma_n' = 196$  kPa at both thermal conditions. While the shear stress of the ZBM decreased in the presence of tincal, it increased when perlite was added at both temperatures. The shear strength of ZBM and ZBTM increased at high temperature,

**Fig. 2** Compaction curves of zeolite-bentonite mixtures



**Table 2** Compaction parameters of all mixtures

Sample	$\gamma_{drymax}$ (kN/m <sup>3</sup> )	$w_{opt}$ (%)
ZBM	10.20	42.0
ZBPM	8.98	45.5
ZBTM	10.79	43.5

but the effect of temperature on ZBPM was insignificant. The peak shear stress of the ZBM increased from 103.7 to 118.5 kPa as temperature increased. Also, the failure of ZBM and ZBMT occurred at less shear displacement (Fig. 3). The shear stress of ZBPM was approximately 148 kPa at both temperatures.

Figure 4 shows the normal stress-shear stress relationship of the mixtures for both temperatures. According to the direct shear test results (Table 3), the  $c$  and  $\phi$  of all specimens range from 17 to 26 kPa and from 20° to 32°, respectively. The addition of tincal caused a decrease in the angle of internal friction both at room temperature and 80 °C. On the contrary, perlite additive increased the angle of internal friction. For example, while the angle of internal friction of ZBM was 27.8° at 80 °C, it increased to 32.3° with the addition of perlite. Among the mixtures, the highest  $\phi$  for both thermal conditions were determined in the ZBPM (32.3°) at 80 °C. The angle of internal friction values of all mixtures at 80 °C were higher than at room temperature. However, the increase in temperature decreased the cohesion values. However, it was clearly seen that the shear parameters of ZBPM were not significantly affected by the temperature.

As the temperature increases, the smectite mineral transforms into silicate phases by cementation and illitization [15]. For that reason, it is expected to increase in strength. In addition, it was reported that the clay showed a hardening behavior at

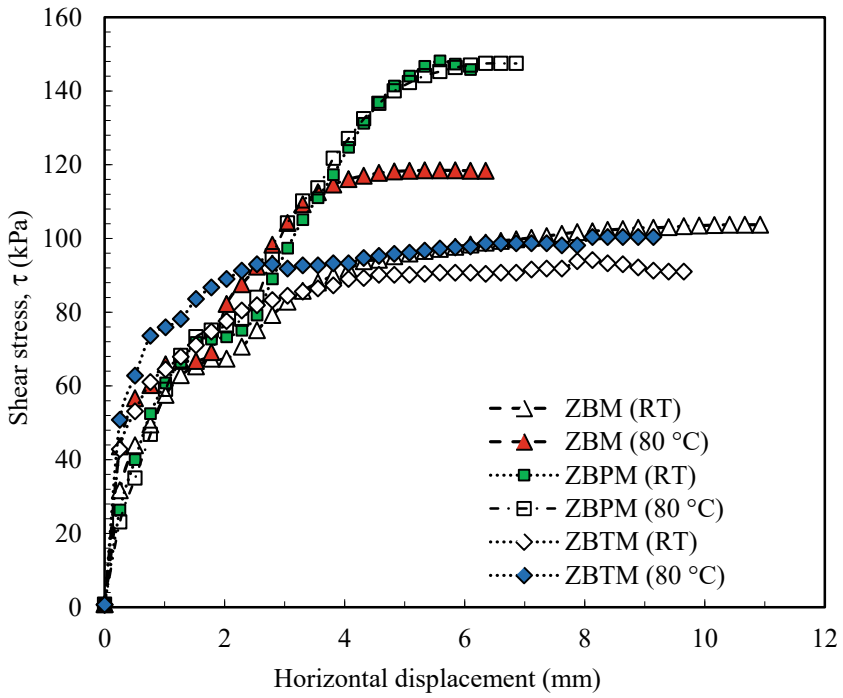


**Fig. 3** Effect of temperature on shear stress and shear displacement at 196 kPa effective normal stress

**Fig. 4** Shear stress against effective normal stress at RT and 80 °C

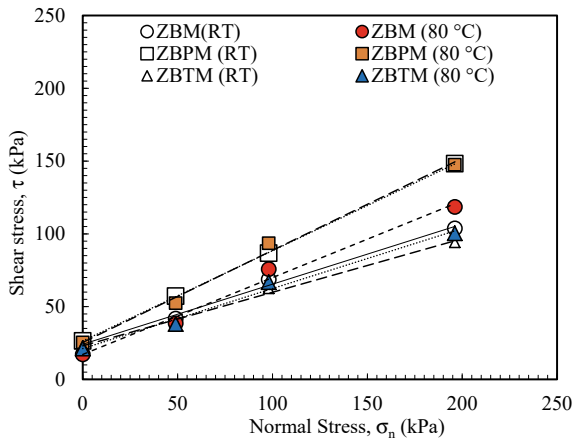


**Table 3** Shear strength parameters of the mixtures

Mixture	Room temperature		80 °C	
	$\phi$ (°)	c (kPa)	$\phi$ (°)	c (kPa)
ZBM	22.4	24.1	27.8	17.2
ZBTM	20.2	23.0	22.4	21.2
ZBPM	31.8	26.4	32.3	25.4

elevated temperatures [16]. Moreover, the zeolite skeleton generally shows a contraction behavior as temperature increases [17]. The reason for the increase in the shear stress of ZBM with high temperature may be the contraction behavior.

## 4 Conclusions

The effect of high temperature on the shear strength parameters of ZBMs in the presence of perlite and tincal was investigated. The temperature-controlled direct-shear test device was used to perform thermal tests. The following concluding remarks can be derived from compaction and direct shear tests:

- The  $w_{opt}$  of the ZBM increased slightly in the presence of perlite and tincal.
- The  $\gamma_{drymax}$  of the ZBM mixture did not change with tincal but decreased significantly in the presence of perlite.
- While the shear stress of the ZBM decreased with tincal addition, it increased with perlite addition at both temperatures.
- The shear strength of ZBM and ZBTM increased at high temperature.
- The effect of temperature on ZBPM was insignificant.

**Acknowledgements** This study is supported by The Scientific and Technological Research Council of Turkey (TUBITAK) (Grant no: 217M553). The authors are grateful for this support. The authors would like to thank 100/2000 The Council of Higher Education (YÖK) scholarship.

## References

1. Dixon DA, Gray MN, Thomas AW (1985) A study of the compaction properties of potential clay—sand buffer mixtures for use in nuclear fuel waste disposal. *Eng Geol* 21(3–4):247–255
2. Graham J, Saadat F, Gray MN, Dixon DA, Zhang QY (1989) Strength and volume change behaviour of a sand–bentonite mixture. *Can Geotech J* 26(2):292–305
3. Durukan S, Pulat HF, Yukselen-Aksoy Y (2014) Suction characteristics of compacted zeolite-bentonite and sand–bentonite mixtures. *Waste Manage Res* 32(2):149–156
4. Bish F, Guthrie GD (1993) Mineralogy of clay and zeolite dusts (exclusive of 1:1 layer silicates). In: Guthrie GD, Mossman BT (eds) Health effects of mineral dusts. *Rev Mineral* 28:139–184

5. Yükselen-Aksoy Y (2010) Characterization of two natural zeolites for geotechnical and geoenvironmental applications. *Appl Clay Sci* 50:130–136
6. Mitchell JK (1964) Shearing resistance of soils as a rate process. *J Soil Mech Found Eng Div ASCE* 90(1):231–251
7. Hueckel T, Baldi G (1990) Thermoplasticity of saturated clays: experimental constitute study. *J Geotech Geoenviron Eng ASCE* 116(12):1178–1769
8. Houston SL, Houston WN, Williams ND (1985) Thermo-mechanical behavior of seafloor sediments. *J Soil Mech Found Div ASCE* 111(11):1249–1263
9. Özkan ŞG, Çebi H, Delice MD (1997) Bor minerallerinin özellikleri ve madenciliği. 2 Endüstriyel Hammaddeler Sempozyumu. İzmir, Türkiye, pp 224–228
10. Privett K, Gillott JE (1987) Clay in engineering geology, 2nd edn. In: *Developments in geotechnical engineering*, vol 41. Elsevier Science Publishers, Amsterdam
11. Perlite. <https://www.perlite.org/>. Accessed 18 Aug 2021
12. ASTM D698-12 (2012) Standard test methods for laboratory compaction characteristics of soil using standard effort (12,400 ft-lbf/ft<sup>3</sup> (600 kN-m/m<sup>3</sup>)). ASTM International, West Conshohocken, PA, pp 1–13
13. ASTM D3080/D3080M (2018) Standard test method for direct shear test of soils under consolidated drained conditions. ASTM International, West Conshohocken, PA, pp 1–9
14. Lambe T (1958) The structure of compacted clay. *J Soil Mech Found Div* 84(2):1–33
15. Wersin P, Johnson LH, Snellman M (2006) Impact of iron released from steel components on the performance of the bentonite buffer: a preliminary assessment within the framework of the KBS-3H disposal concept. *MRS Proc* 932:117.1
16. Yavari N, Tang AM, Pereira J-M, Hassen G (2016) Effect of temperature on the shear strength of soils and the soil-structure interface. *Can Geotech J* 53(7):1186–1194
17. Tschaufeser P, Parker SC (1995) Thermal expansion behavior of zeolites and AlPO<sub>4</sub>s. *J Phys Chem* 99(26):10609–10615

# Geo-environmental Solution of Using Crushed Glass Waste to Improve Shear Strength Properties of Sandy Soil



Mousa Attom, Zahid Khan, Naser Al Lozi, and Ahmed Eltayeb

**Abstract** Millions of tons of glass waste are produced every year worldwide which has become an environmental hazard. This investigation proposes a promising geo-environmental solution to the hazards associated with glass waste materials. In this research, glass waste was crushed to three different sizes and mixed with sandy soil at four different percentages by dry weight of the sand. Specimens from the sand-glass waste mixtures were remolded at 90% relative compaction and optimum moisture content in the standard direct shear test mold. Direct shear test was performed to evaluate the shear strength properties of the sand mixed with crushed glass waste. Test results showed that the addition of the crushed glass waste decreased the optimum moisture content but had slight or no effect on the maximum dry density of the sand. The addition of crushed glass waste increased the shear strength of engineered sand at all percentages. The highest shear strength was noticed at 5% of sand-glass waste mixture at all crushed glass sizes. The main increase was noticed in the angle of internal friction of the sand. Additionally, the shear strength increased with an increase in the glass particle size.

**Keywords** Glass waste · Shear strength · Sandy soil · Angle of internal friction

## 1 Introduction

Numerous types of waste materials have been produced in massive amounts in recent years due to the adaptation of modern life. These main contributors to the generation of these waste materials are industrial wastes, agricultural wastes, hospital wastes, vehicular tires, and residential wastes such as glass, cans, metallic wastes, plastic

---

M. Attom (✉) · Z. Khan · A. Eltayeb  
American University of Sharjah, Sharjah, UAE  
e-mail: [mattom@aus.edu](mailto:mattom@aus.edu)

N. Al Lozi  
University of Exeter, Exeter, UK



wastes, etc. These materials impose various environmental issues and several challenges that involve locating appropriate disposing locations mainly if the materials are classified as non-biodegradable materials [1–4]. As a result, civil engineers have started to investigate the impacts of using such waste materials for different functions such as stabilization of soils, mixing with concrete, filling embankments, etc. Geotechnical engineers have been studying the influence of using glass wastes, fly ash, silica fumes, and shredded tire chips to enhance the soil properties and stabilize the soils. Soil stabilization is an engineering methodology that utilizes materials to improve the mechanical properties, shear strength and overcome the weak soil properties such as settlement, compressibility, expansion, etc. [5]. Stabilizations can be classified into mechanical stabilization which refers to adding material to the soil, or chemical stabilization which refers to the addition of additives that will chemically interact with the soil.

In recent years, many researchers have conducted studies to examine the impact of using solid wastes as stabilizing materials. Attom [5] investigate the influence of waste glass material on the soil swelling pressure. The author reported that the use of glass material led to a decrease both in swelling pressure and swell potential of the soil. Olufowobi et al. [6] have conducted a study to assess the stabilizing impact of adding powdered glass on clay soil. They reported that the powdered glass resulted in a significant improvement in the maximum dry density, cohesion, and internal friction angle. Attom et al. [7] investigated the use of glass waste and glass-cement waste in enhancing the mechanical properties of soil and found it successful. Phani Kumar and Sharma [8] have reported the effectiveness of fly ash in enhancing the engineering properties of expansive soils. Yadav and Tiwari [9] have conducted a study to evaluate the impact of the inclusion of waste rubber tire fibers on some of the geotechnical properties of uncemented and cemented clay. The study reported that the use of both elements led to a decrease in the swelling potential of the clay. Mahasneh [10] reported that using aluminum residue and recycled asphalt led to increasing the bearing capacity, dry density, and the unconfined shear strength of silty clay soil. Attom and Shatnawi [11] reported that adding wheat husk to the clay will result in improving the shear strength and reducing the expansion of clay. Islam et al. [12] have replaced the use of cement in concrete mixture with the use of waste glass additive. Canakci et al. [13] used the soda lime glass powder waste with clay and it showed a massive influence on the strength of the soil. Bairagi et al. [14] have reported that an increase in California bearing ratio, unconfined compressive strength, and a reduction in the expansion behavior of clay could be obtained by the addition of jute fiber. Al-Subari et al. [15] have investigated the utilization of waste rubber tire powder to improve the mechanical properties of cement-clay composites. Kalkan [16] performed an experimental work to evaluate the influence of silica fume–scrap tire rubber fiber mixture inclusion on the geotechnical properties of clayey soils. The outcomes have demonstrated that silica fume, fiber and silica fume–fiber mixture modification enhanced both the unconfined compression strength and strength parameters. Akbulut et al. [17] have conducted research to examine the

potential of waste fibers materials for the enhancement of clayey soils. The results shown that such materials can be used effectively to reinforce clayey soils. Yadav and Tiwari [18] reported that using crumb rubber in cemented clayey soil can sustainably overcome the brittleness of cemented clay in compression and tension.

The main objective of this paper is to investigate the effect of crushed glass waste on the shear strength properties of sand mainly the cohesion and the angle of internal friction angle.

## 2 Experimental Program

A well graded sandy soil was selected and the initial physical properties of the sand such as grain size distribution, specific gravity angle of internal friction and the apparent cohesion were determined in accordance of ASTM standard procedures. A glass was brought to the geotechnical laboratory and crushed and separated into three different sizes. The first size includes the particles that passed through sieve # 10 and retain in sieve # 20. The second size contain the particles that passed sieve # 20 and remained in sieve # 40 while the third size presents the particles that passed through sieve # 40. All these sizes were mixed with sand at four different percentages mainly 2.5, 5.0, 7.5, and 10% by dry weight of the sand and tested in the direct shear test by following the ASTM D3080 [19]. In this test, three identical specimens from each percentage were remolded in the standard direct shear test box at 90% relative compaction and optimum water content. Then the specimens are sheared at different normal loads (27.5, 55.0, and 110 kN/m<sup>2</sup>).

In accordance with the ASTM D698 [20], standard Proctor compaction test was also conducted on sand soil mixed with crushed sand at different percentages and different sizes. Data was collected and analyzed to show the influence of crushed glass waste on the shear strength and compaction properties of sandy soil.

## 3 Results and Discussion

### 3.1 *The Effect of Crushed Glass Waste on the Compaction Properties of Sand*

Figure 1 depicts the effect of glass waste on the optimum water content. The graph shows that the optimum water content tends to decrease as the percentage of glass waste increases for all sizes. The reduction is more pronounced when the larger-sized glass waste was added to the sandy soil. The optimum water content decreased from 12 to 9.2 and 8.5% at size passing sieve # 40 and size passed sieve # 10 and retained

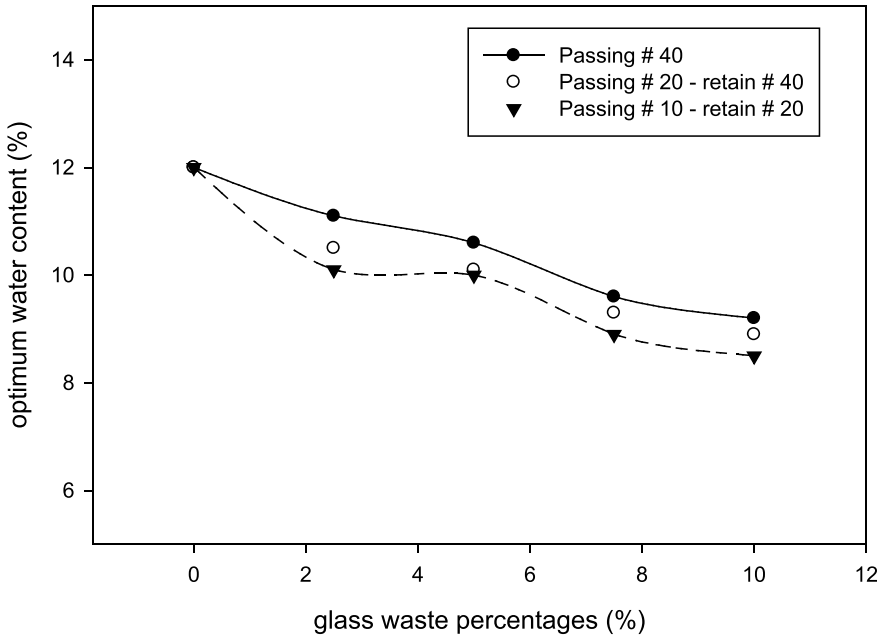


**Fig. 1** Effect of glass waste on the optimum water content

in sieve # 20, respectively when the percentages of the glass increased from 0.0 to 10%. The reason behind this effect is due to the replacement of sand by glass. Since glass doesn't absorb water, this led to less water absorption than sand which resulted in this behavior.

As it can be seen from Fig. 2 that increasing the percentage of glass waste has almost small or negligible impact on the maximum dry unit weight. This behavior is noticed for all the sizes. This can be explained since both sand and glass have almost similar specific gravities. Thus, replacing the sand with glass will not increase the weight per volume in the compaction mold and further will not lead to any changes in the dry unit weight.

### ***3.2 The Effect of Crushed Glass Waste on the Shear Stress of the Sand***

Figure 3 shows the effect of crushed glass waste on the shear stress-horizontal displacement curve obtained from direct shear test at 27.5 kN/m<sup>2</sup> normal load for sand mixed with glass waste passing sieve # 40. The graph reveals that increasing the percentage of glass waste up to 5% by the dry weight of the sand will lead to increase in the shear stress of the soil. However, further increase in the percentage of crushed

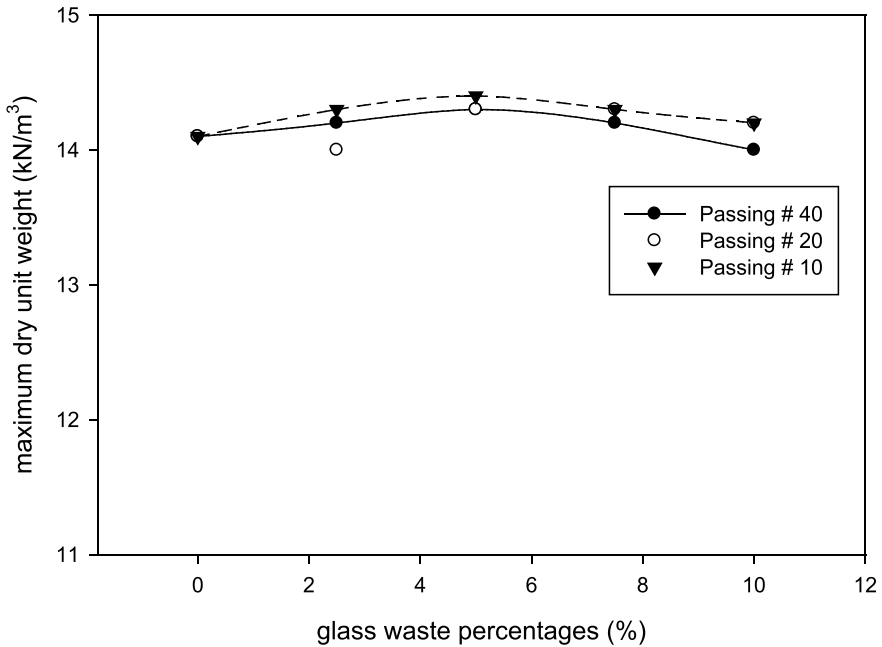


Fig. 2 Effect of glass waste on the maximum dry unit weight

glass in the sand caused to decrease in the shear stress. This trend was noticed in all glass sizes and at three normal loads used in the direct shear tests. This confirms that increasing the percentage of glass waste will initially lead to increase in the frictional force and further the shear stress. However, after 5%, the percentage of glass will become relatively high which will lead to reduce the compatibility of the mixture and thus the soil will become easier to shear. The increase in the percentages in the glass especially at larger sizes will result in less contact between the sand-sand particles and resulted in a reduction in shear stress. One more conclusion can be drawn out from Fig. 3. As it might be noticed that the slope of the shear stress-displacement curve increased as the percentages of the glass increased up to 5% which indicated that the elasticity modulus increased as the percent of glass becomes 5% and then decreased with further increase in the glass percentage.

### 3.3 The Effect of Crushed Glass Waste on the Shear Strength Parameters of the Sand

The results that obtained from shearing the specimens mixed with crushed glass at size passed sieve # 40 and under three normal loads are used to plot (Fig. 4). Figure 4 exhibits the influence of glass waste on the shear strength of sand mixed with glass

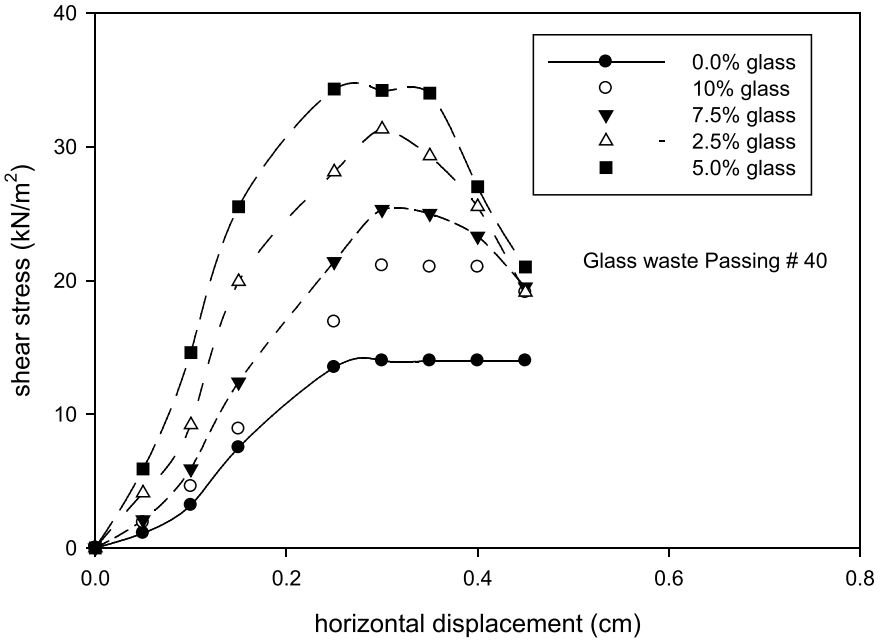


Fig. 3 Shear stress under 27.5 kN/m<sup>2</sup> normal load

passed sieve # 40. It seen from Fig. 4 that increasing the percentage of glass waste up to 5% by the dry weight of sand will lead to increase the slope of the line which represent the angle of internal friction angle. This implies that adding the crushed glass waste to the sand up to 5% will increase the angle of internal friction of the sand and further addition will decrease the angle of internal friction. Moreover, as it can also be seen that increasing the normal stress will lead to increase in the shear strength of the sand.

Figures 5 and 6 show the impact of particle size of the glass waste on the angle of internal friction and cohesion of sand, respectively. As seen in Fig. 5 increasing the percentage of glass waste will lead to increase in the frictional angle up to 5%. However, the amount of increase depends on the particle size of the glass waste. As the particle size of glass increased the angle of internal friction increased. Figure 6 depicts the impact of glass waste on the cohesion of sand. The graph showed that increasing the percentage of glass waste has negligible effect on the cohesion of the soil. Also, the particle size has no effect on the cohesion as well. A little variation is shown due to the change in the particle size of the glass. Yet, the effect is negligible.

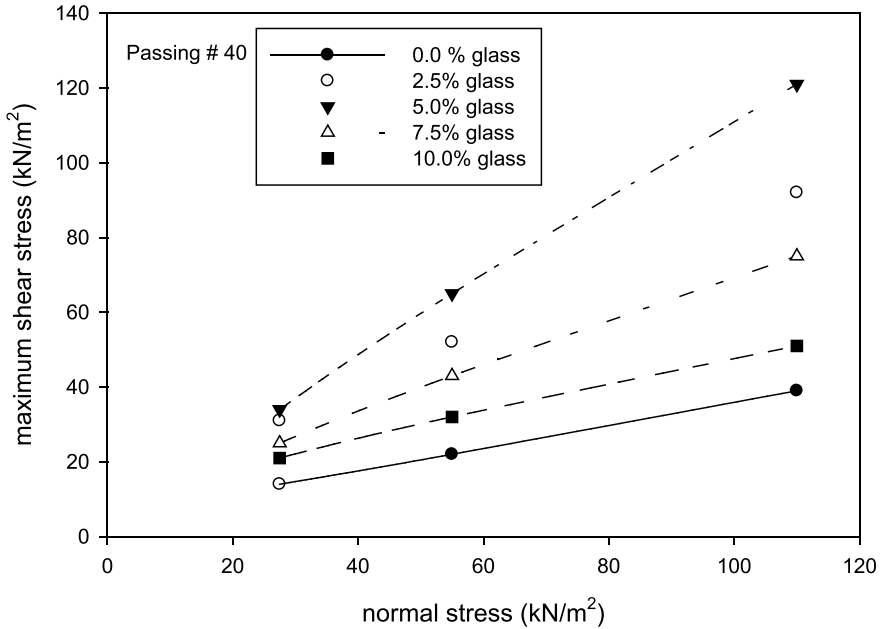


Fig. 4 Effect of glass waste on the maximum shear strength of the soil

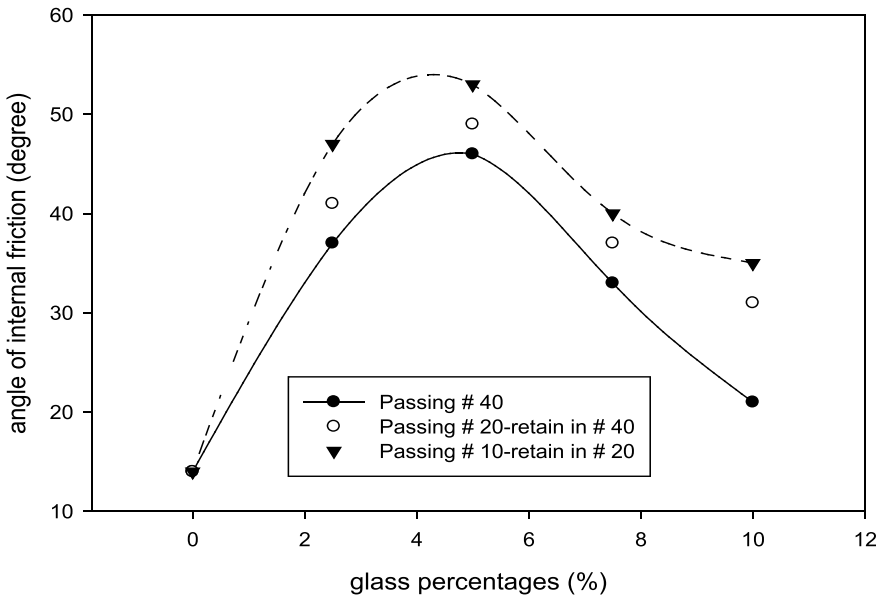
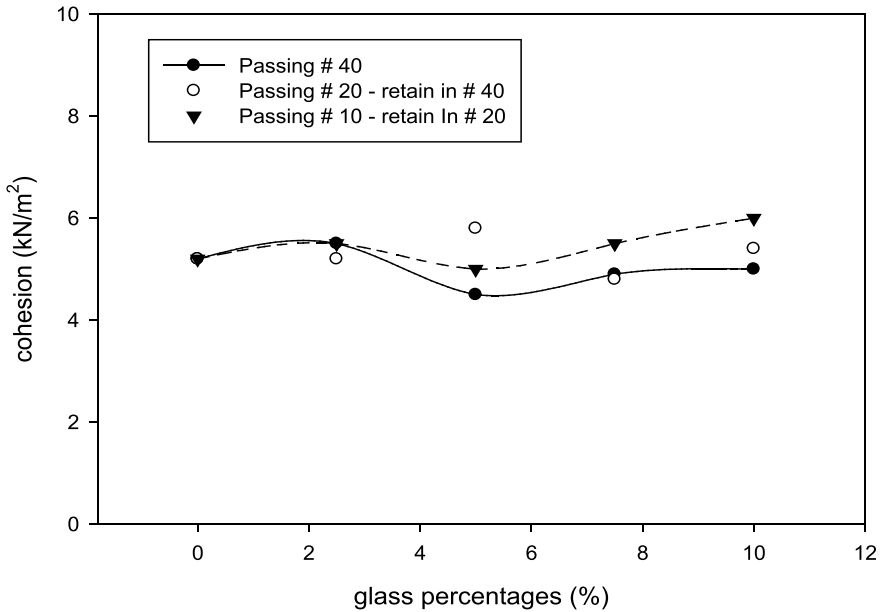


Fig. 5 Effect of glass waste size on the angle of internal friction



**Fig. 6** Effect of glass waste percentage (%) on the cohesion

## 4 Conclusion

Based on the test results, the following conclusions may be drawn out

- The addition of the crushed glass waste will increase the angle of internal friction of the sandy soil.
- The highest angle of internal friction was obtained at 5% of crushed glass waste. Further increase in the glass waste percentage will decrease the angle of internal friction.
- The glass waste has less or no effect on the apparent cohesion of the sand.
- The shear strength and angle of internal friction increased by increasing the glass size in the sand.

## References

1. Pastor J, Tomás R, Cano M, Riquelme A, Gutiérrez E (2019) Evaluation of the improvement effect of limestone powder waste in the stabilization of swelling clayey soil. Sustainability 11:1–14
2. Dang L, Fatahi B, Khabbaz H (2022) Behaviour of expansive soils stabilized with hydrated lime and bagasse fibres. In: International conference on transportation geotechnics (ICTG 2016), Guimarães

3. Taha R, Al-Rawas A, Al-Jabri K, Al-Harthy A, Hassan H, Al-Oraimi S (2004) An overview of waste materials recycling in the Sultanate of Oman. *Resour Conserv Recycl* 41:293–306
4. Pascual A, Tognonvi M, Tagnit-Hamou A (2014) Waste glass powder-based alkali-activated mortar. *Int J Res Eng Technol* 03:15–19
5. Attom M (2018) The use of waste glass material to control soil swelling pressure. In: *International conference on technological challenges for better world*. ScienceDZ, Cebu, pp 1–8
6. Olufowobi J, Ogundoku A, Michael B, Aderinlewo O (2014) Clay soil stabilization using powdered glass. *J Eng Sci Technol* 9:541–558
7. Attom M, Abed F, Vandanapu R (2019) Soil stabilization using glass-cement mixture. In: *International conference on technological challenges for better world*. ScienceDZ, Cebu, pp 1–7
8. Phani Kumar B, Sharma R (2004) Effect of fly ash on engineering properties of expansive soils. *J Geotech Geoenviron Eng* 130:764–767
9. Yadav J, Tiwari S (2017) Effect of waste rubber fibres on the geotechnical properties of clay stabilized with cement. *Appl Clay Sci* 149:97–110
10. Mahasneh B (2015) Assessment of using cement, Dead Sea sand and oil shale in treating soft clay soil. *Eur J Sci Res* 128:245–255
11. Attom M, Shatnawi M (2005) Stabilization of clayey soils using hay material. *J Solid Waste Technol Manag* 31:84–92
12. Islam G, Rahman M, Kazi N (2017) Waste glass powder as partial replacement of cement for sustainable concrete practice. *Int J Sustain Built Environ* 6:37–44
13. Canakci H, Al-Kaki A, Celik F (2016) Stabilization of clay with waste soda lime glass powder. *Procedia Eng* 161:600–605
14. Bairagi H, Yadav R, Jain R (2014) Effect of jute fibres on engineering properties of lime treated black cotton soil. *Int J Eng Res Technol* 3:1–3
15. Al-Subari L, Ekinci A, Aydın E (2021) The utilization of waste rubber tire powder to improve the mechanical properties of cement-clay composites. *Constr Build Mater* 300:1–16
16. Kalkan E (2013) Preparation of scrap tire rubber fiber–silica fume mixtures for modification of clayey soils. *Appl Clay Sci* 80–81:117–125
17. Akbulut S, Arasan S, Kalkan E (2007) Modification of clayey soils using scrap tire rubber and synthetic fibers. *Appl Clay Sci* 38:23–32
18. Yadav J, Tiwari S (2017) A study on the potential utilization of crumb rubber in cement treated soft clay. *J Build Eng* 9:177–191
19. ASTM International (1985) Standard test methods for direct shear test of soils under consolidated drained conditions, ASTM D3080. American Society of Testing Materials, West Conshohocken, PA
20. ASTM International (2007) Standard test methods for laboratory compaction characteristics of soil using standard effort (12,400 ft-lbf/ft<sup>3</sup> (600 kN-m/m<sup>3</sup>)), ASTM D698. American Society of Testing Materials, West Conshohocken, PA



# Tannery Waste as a Partial Replacement of Cement in Mortar



Md. Naimul Haque, Md. Adnan Haque Chowdhury, Rakibul Islam,  
Md. Shariful Alam, Bayzid Ahmed, and Sharif Mahmud Bhuiyan

**Abstract** The aim of this study is to investigate the strength characteristics of cement-sludge mortar. The cement content in mortar was replaced by tannery sludge in terms of weight for various quantities. The percentage of cement replaced in mortar by tannery sludge was 5, 10, 15 and 20%. Portland composite cement (Type-II) and river sand (4.75 mm down) was used. The tannery sludge was collected from BSCIC Tannery Industry Estate of Dhaka, Bangladesh. Moisture content, water absorption, compressive strength and tensile strength tests were carried out. It was found that the presence of tannery sludge has significant influence on the properties of cement mortar. The addition of tannery sludge reduced the mortar strength noticeably beyond a specific amount of cement replacement.

**Keywords** Tannery waste · Partial replacement · Cement mortar · Strength characteristics

## 1 Introduction

Managing industrial waste is a great challenge of the present time. With the rapid growth of the industry, the volume of industrial waste is also increasing day by day. Among the industrial waste produces in Bangladesh, tannery waste is one of the major types of waste and the most polluting one [1]. Yearly, approximately 78,000 tons solid wastes are produced from 207 tanneries in Bangladesh [2]. The waste production rate will increase even more in coming years as the demand of finished leather products are increasing now-a-days [3]. A proper disposal of this huge amount of toxic wastes is a great concern. Realizing the importance of the problem, the government of Bangladesh took an extensive project and shifted all the tannery companies to Savar

---

Md. N. Haque (✉) · Md. A. H. Chowdhury · R. Islam · Md. S. Alam · B. Ahmed  
East West University, A/2, Aftabnagar, Dhaka 1212, Bangladesh  
e-mail: [naimul@ewubd.edu](mailto:naimul@ewubd.edu)

S. M. Bhuiyan  
SAOCOL, Khulna 1212, Bangladesh

over a 200 acres area and established BSCIC Tannery Industry Estates. A Common Effluent Treatment Plant was established to treat approximately 20,000 m<sup>3</sup> of tannery effluent per day [4] and produces 80 tons of solid wastes per day out of which 8–10 tons are CETP sludge. As compared to the other wastes coming out from tannery industries, CETP sludge is less toxic [4]. The solid wastes are dumped in the solid waste dumping yard in a classified manner. However, the capacity of dumping zone is limited and this is going to finish very soon. This is a great problem how to manage this sludge once the dumping yard capacity finished as this waste can't be thrown here and there due to its adverse environmental effect. Therefore, it is necessary to find a recycling or consumption process of this CETP solid waste to save the environment from pollution and solve the scarcity of space.

One of the potential solutions could be recycling of this solid waste as a partial replacement of construction materials in concrete, brick, tiles or mortar. Partial replacement of constituent materials in concrete, brick and tiles using wastes is not a new idea [5–11]. However, past studies mainly focused on different type of wastes such as glass and textile sludge in preparation of brick and concrete. Only a few researches aimed to investigate the performance of tannery solid waste as a partial replacement of construction materials in concrete, brick and cement mortar [12–14]. Further, depending on the type of the tannery sludge, the performance in cement mortar may vary as well. In Bangladesh, no such kind of work has been carried out on the tannery sludge of BSCIC CETP.

Therefore, the aim of this study is to carry out a detailed study where the strength characteristics of cement mortar made of tannery sludge will be explored. The sample was collected from the dumping yard of BSCIC Tannery Industry Estates. The cement in mortar was replaced by tannery sludge for 5, 10, 15 and 20% by weight of cement. Along with the compressive and tensile strength tests, other important tests such as moisture content, pH, water absorption tests were also carried out. Based on the obtained results, a valid conclusion was drawn.

## 2 Working Procedure

Tannery sample was directly collected from the dumping yard of BSCIC Tannery Industry Estates. Figure 1 shows the process of sample collection from the dumping zone. Around 10 kg sample was collected from the site. After collection, the sample was then oven dried for 24 h at 105 °C. After oven dry, the color of the tannery sludge was changed from dark black to ash color and became hard as well. Figure 2 compares the picture of tannery sludge before and after the oven dry process. The hard tannery sample was then crushed into power to make it usable for partial replacement of cement in cement mortar (Fig. 3). This oven dried crushed sample was then mixed with cement mortar and the quantity of cement was gradually replaced by the tannery sludges. For mortar preparation, Portland composite cement (Type-II) was used and fine river sand passing from 4.75 mm sieve was used. For all the samples, the sand and cement ratio was 1:2.75 and a water-cement ratio of 0.485 was utilized. The

percentage of cement replacement by the crushed tannery sludge was 5, 10, 15 and 20% (in terms of weight) and named as cement-sludge mortar. Both for compressive and tensile strengths, 3, 7 and 28-days tests were carried out. Sample preparation, curing and strength testing process are shown in Fig. 4.

**Fig. 1** Collection of tannery waste from BSCIC Tannery Industry Estates



**Fig. 2** Color of tannery sample before and after the oven dry process



(a) Tannery sample before oven dry



(b) Tannery sample after oven dry



Fig. 3 Crushing of oven dry sludge to make it powder



(a) Making of sample



(b) Curing of Samples



(c) Compressive strength testing of mortar cube samples



(d) Tensile strength testing of mortar briquet samples

Fig. 4 Sample preparation and testing of samples

### **3 Results and Discussion**

#### ***3.1 Moisture Content and pH of Tannery Sludge***

Moisture content test was carried out by following the ASTM D2216 code. To test the moisture content of the tannery sludge, 2.5 g of tannery sludge was oven dried for 24 h at 105 °C. From weight difference, the moisture content was determined. The tannery sludge had a moisture content of 67%. The pH of the sludge was determined using a pH meter by following BS 1377 code. Around 25-gm sample was mixed with 75 ml distilled water and after mixing well using a magnetic stirrer the pH was determined. The tannery sludge had a pH value of 8.10 at 28 °C which seems that the dry tannery sludge is a basic.

#### ***3.2 Moisture Water Absorption of Cement-Sludge Mortar***

Water absorption test of cement mortar provides information about how porous the mortar is and which is closely connected to the durability of the mortar. To determine the water absorption capacity of the cement-sludge mortar, 1 set of cement-sludge mortar was tested after 7 days of curing by following the ASTM C642 specification. 2 in cement-sludge mortar cube was prepared and cured for 7 days. After 7 days of curing, the sample was oven dried. The oven dried sample was then immersed under water for 96 h. From weight difference of even dried and saturated samples, the water absorption was calculated. The water absorption of cement-sludge mortars are presented in Fig. 5. The water absorption is varying in between 9 and 12% and decreasing with the increase in cement replacement by sludge. This indicates that the incorporation of tannery sludge increases the compactness of the cement mortar. There is no recommended value of water absorption of cement, yet a good mortar should have water absorption capacity near about or less than 10% which is valid in case of cement-sludge mortar.

#### ***3.3 Compressive Strength of Cement-Sludge Mortar***

Compressive strength of cement-sludge mortar was prepared by following ASTM C109 code. The cement and sand ratio was 1:2.75. Three sets of sample for 3, 7 and 28 days curing period were considered. Figure 6 summarizes the results of compressive strength of cement-sludge mortar. As can be seen the compressive strength decreases with the increase in tannery sludge in the mortar. Regardless of curing days, the strength has a decreasing trend with the increase in tannery sludge. After 28 days of curing, the cement-sludge mortar with a cement replacement percentage of 10% and 15% had a compressive strength of 2190 psi and 1510 psi respectively. As

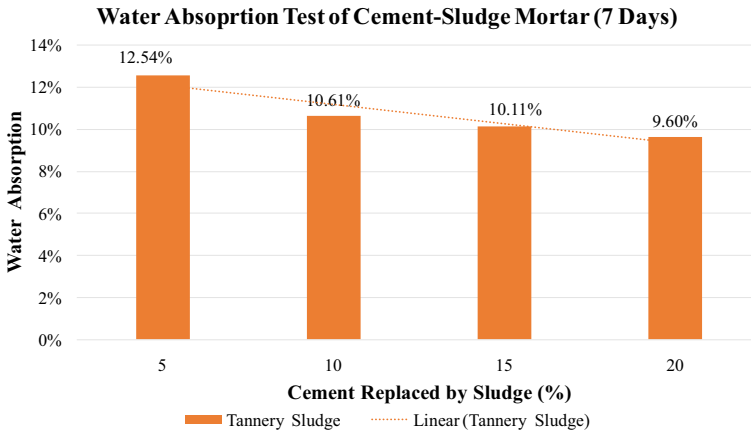


**Fig. 5** Water absorption of cement-sludge mortar after 7 days curing

per ASTM C270, for important construction work such as foundation wall, retaining wall and pavement works, the mortar compressive strength should be minimum 1800 psi. Based on this codal provision, the cement-sludge mortar can be used up to 10% replacement of cement for such kind of construction work.

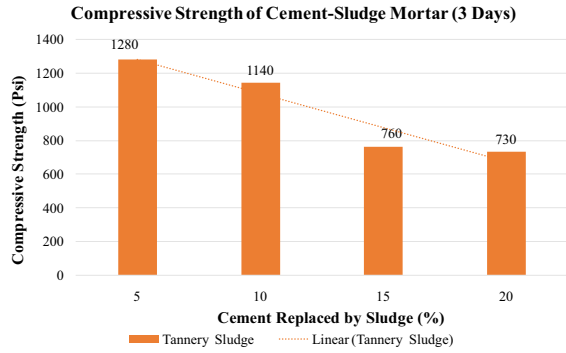
### **3.4 Tensile Strength of Cement-Sludge Mortar**

ASTM C307 was followed to determine the cement and cement-sludge mortar. The cement and sand ratio was maintained same as compressive strength test. Tensile strength test results 3, 7 and 28 days curing periods are plotted and compared in Fig. 7. Similar to the compressive strength, tensile strength of the cement-sludge mortar also decreases with the increase in tannery sludge content in the mortar for all three cases. Further, with the age of concrete, the mortar gains strength gradually. If a comparison is made with compressive strength of the mortar (Fig. 6), the tensile strength is approximately 15% of its compressive strength.

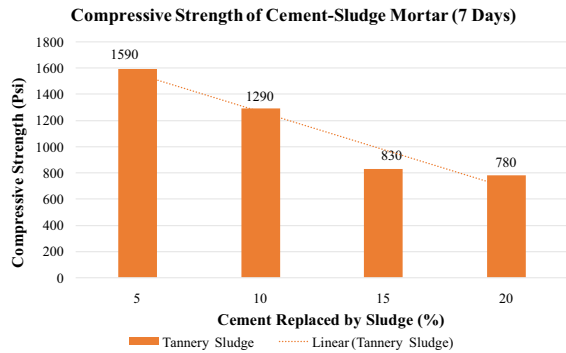
## **4 Conclusions**

This work aimed to observe the potentiality of using tannery sludge as a partial replacement of cement content in cement mortar. 5, 10, 15 and 20% by weight of cement, sludge was added in the mortar. Mainly the strength characteristics are explored for preliminary assessment of cement-sludge mortar. Based on the results

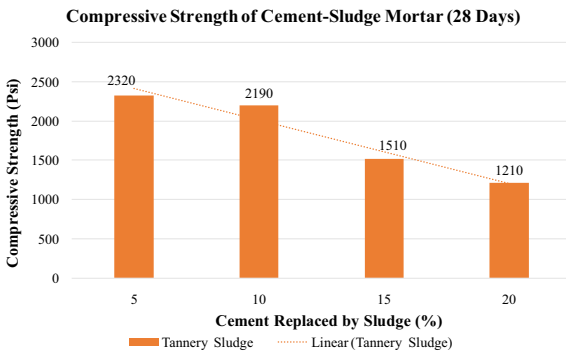
**Fig. 6** Compressive strength of cement-sludge mortar for different curing ages



(a) 3 days curing period



(b) 7 days curing period



(c) 28 days curing period

and discussion it is evident that the tannery sludge of BSCIC Tannery Industry has moisture content of 67% and it is basic in nature. Tannery sludge can be used in cement mortar for partial replacement of the cement in cement mortar. The presence of sludge in mortar doesn't affect the compactness of the mortar. Both the compressive and tensile strength of cement-sludge mortar decreases with the increase in cement replacement percentage. compressive strength point of view, a cement-sludge mortar

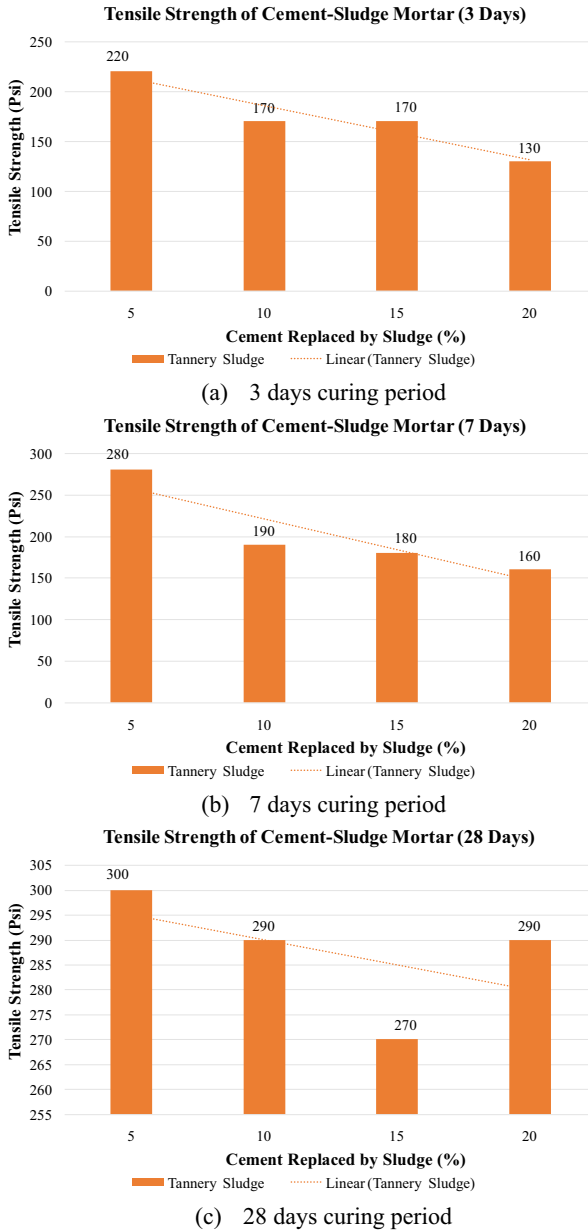


Fig. 7 Tensile strength of cement-sludge mortar for different curing ages



with 10% replacement of cement with sludge can be used for important masonry work such as foundation wall, retaining wall and footpath. The obtained tensile strength was approximately 15% of the compressive strength.

## References

1. Naher USB et al (2018) Challenges and prospects of tannery by-product industries (glue, gelatin, poultry and fish feed industries) in Bangladesh. *Int J Sci Eng Technol Res (IJSETR)* 7(12). ISSN: 2278-7798
2. Alam MN et al (2017) BOD reduction using spent tea waste from tannery wastewater. *J Sci Innov Res* 6(2):73–77
3. Mia MAS et al (2017) Footwear industry in Bangladesh: implementation of six sigma methodology. *Ind Eng Manage* 6(2)
4. Alamgir et al (2017) Solid waste management of Tannery Industrial Estate Dhaka. In: *Proceedings Sardinia 2017/sixteenth international waste management and landfill symposium*, 2–6 Oct 2017. S. Margherita di Pula, Cagliari, Italy
5. Begum SS et al (2013) Utilization of textile effluent wastewater treatment plant sludge as brick material. *J Mater Cycles Waste Manag* 15:564–570
6. Rahman A et al (2015) Effects of waste glass additions on quality of textile sludge-based bricks. *Environ Technol* 36(19):1–20
7. Al-Zboon K, Al-Zouby J (2015) Recycling of stone cutting slurry in concrete mixes. *J Mater Cycles Waste Manag* 17:324–335
8. Kazmi ML et al (2017) Feasibility of using waste glass sludge in production of ecofriendly clay bricks. *J Mater Civ Eng* 29(8)
9. Chen C, Wu H (2017) Lightweight bricks manufactured from ground soil, textile sludge, and coal ash. *Environ Technol* 39(11)
10. Goyel S et al (2019) Utilization of textile sludge in cement mortar and paste. *Constr Build Mater* 214:169–177
11. Ullah SMH et al (2020) Performance of industrial sludge-amended bricks manufactured in conventional kilns. *J Mater Cycles Waste Manag* 22:1932–1942
12. Reddy MVS et al (2016) Partial replacement of fine aggregate by tannery shredded waste in concrete. *Saudi J Eng Technol* 1(4):149–151
13. Malaiškiene J et al (2019) Study on tannery sludge as a raw material for cement mortar. *Materials* 12:1562
14. Partheeban P et al (2020) Strength properties of tannery slurry waste in geopolymer concrete. *J Crit Rev* 7(4):1113–1120

# Physio-chemical Investigations on MSWI Bottom Ash for Sustainable Use



Davinder Singh  and Sanjeev Kumar 

**Abstract** Incineration of MSW at a waste to energy conversion facility is now a common practice to scientifically deal with solid waste management issues. The process results in bottom ash (BA), Fly ash (FA), and air residues as significant byproducts. The paper targets the physical and chemical properties of these bottom ash procured from two different incineration plants. The investigation includes the chemical components and the specific gravity, optimum moisture content, and Loss of ignition values of these ashes that were compared. The study confirms that the material is highly heterogeneous and requires thorough investigations. The reliability and the applicability of the same were studied using scanning electron microscopy, X-ray diffraction, and pH analysis. The stabilization of freshly procured BA is advised before direct use.

**Keywords** Bottom ash · MSW · Incineration · Waste to energy · Sustainability

## 1 Introduction

With rapid technological advancements, waste management practices have also evolved. Anthropogenic activities result in the daily production of MSW in significant numbers; thus, dealing with such an amount of waste without causing danger to the environment is essential. Depending upon the complexity of the constituents, waste from municipal collection units goes through several stages before its final disposal in landfills [1]. Incineration of these high calorific waste constituents can serve an important role in resource conservation. Hence, developing nations invest in waste-to-energy (WtE) plants to consume the MSW waste after proper segregation and convert it into energy to meet power demands. Thus, WtE plants are being proposed to fulfil the waste management goals and conserve conventional energy production sources.

---

D. Singh (✉) · S. Kumar

Dr B R Ambedkar National Institute of Technology Jalandhar, Jalandhar, Punjab 144027, India

e-mail: [singhdj@nitj.ac.in](mailto:singhdj@nitj.ac.in)

The main objective of incineration at such a facility is to destroy and convert MSW into smaller residues that can be easily disposed of. It ensures the complete mineralization of organic compounds and the destruction of pathogens and other microorganisms. Bottom ash, fly ash, and air residue are the common effluent that must be treated before final disposal to the environment. To immobilize these residues, different means and technologies are involved. After the recovery of metals, bottom ash or BA needs to be chemically stable, and the concentration of heavy metals must be under the standard values. The disposal of BA is still a major concern; therefore, directly using it for engineering-based applications or as a raw material is suggested by researchers [2].

Being a heterogeneous material, the properties of MSW BA varies from batch to batch. It mainly depends on the type of waste fed to the incinerators as raw feed. Hence the chemical properties of the BA vary significantly. The literature confirms BA has a significant percentage of glass phases, and therefore different compositions of silicate minerals can be traced. Silicon, aluminum, calcium, and alkaline-earth metals are the major components of the BA from any WtE-based plant [3]. To avoid the leaching toxicity and propose MSW BA reuse, stabilization has been proposed by different possible means. It includes chemical agent extraction, calcination, washing, cement solidification, and chelating reagents [4–7]. Since the efficiency and resource value varies with the type of technology involved, it is needed to address this issue [8–10].

This work focuses on investigating the physicochemical properties of MSW BA procured from two different incineration plants for possible Geotechnical applications. MSWI BA is a heterogeneous, granular, and highly compactable material and its properties resemble cohesionless soils, i.e., sand, silty sand and other materials [11–13]. This paper emphasizes that the BA from both sources exhibits different properties and suitability for chemical stabilization with lime or cement. Parameters include specific gravity, density, particle size distribution, Loss of ignition, and density index. Due to possible pozzolanic reactions, future morphological studies such as FESEM, EDX, XRF, and XRD are conducted. Further, pH and morphological Studies regarding the potential environmental impacts of BA from incineration facilities conclude with the limited number of risks, thus favouring its engineering applications after preliminary treatments.

## 2 Materials and Methodology

### 2.1 Materials

One batch of MSWI BA was procured from the Incineration facility operational in Delhi, India, and another from Chandigarh, India, for the experimentation analysis. The BA was pretreated for three months in an open atmosphere away from direct moisture.

**Table 1** Procured MSW BA batch codes

MSW BA procured location	Code
Delhi, India	DB 1-1
Chandigarh, India	CB 2-1

## 2.2 Methodology

The MSW BA was sieved through sieve size 4 to remove large unnecessary, objectionable objects from ash, which are potentially a nuisance and can cause disruption in experiments to be conducted. The samples were prepared and tested following procedures mentioned in respective standard codes. Batch codes for MSW BA based on location are shown in Table 1. The testing was done on the same day as sample preparation, and precautions were taken against undesirable contamination.

## 3 Experimentation and Results

### 3.1 Chemical Characterisation of MSW BA

The chemical compositions for both batches of MSW BA are highly variable, given the incinerator type, method and temperature diversity. The samples contained phases of glasses, ceramic particles and burnt microplastics. The chemical composition of MSW BA for both batches is shown in Table 2.

**Table 2** Chemical composition

Chemical composition	DB 1-1	CB 2-1
Silicon dioxide	53.96	56.37
Aluminium oxide	18.63	9.20
Calcium oxide	11.34	19.39
Ferric oxide	6.87	4.93
Sulfur dioxide	2.07	1.53
Potassium oxide	0.74	0.43
Sodium oxide	0.33	0.24
Magnesium oxide	0.98	0.41
Others	5.08	7.5

### 3.2 Grain Size Distribution Analysis

The MSW-IBA oven-dried for 24 h at 103 °C was used in this test. Grain size distribution curve can be drawn using Sieve analysis and Hydrometer analysis. 500 g of sample was taken for dry sieve analysis. The sieves used in this test were 4.75, 2.36, 1.18, 0.850, 0.600, 0.425, 0.300, 0.150, 0.075 mm. The 50 g of sample passing 0.075 mm sieve was further taken for hydrometer analysis. Sodium hexametaphosphate and Sodium carbonate are used as dispersing agents. The temperature, meniscus, and dispersion agent corrections are applied to hydrometer readings accordingly. The procedure and guidance for grain size distribution analysis were followed as mentioned in ASTM D6913-04 [14]. The grain size distribution curve was drawn to classify the bottom ash.

The dry sieve analysis revealed that 83.972 and 84.615% of the particles ranged from 2.36 to 0.075 mm, indicating that most MSW-IBA is similar to fine-grained sand for both batches DB 1-1 and CB 2-1, respectively. The particle's effective sizes (D10) were 0.11 and 0.07 mm. The uniformity coefficients (Cu) were 6.36 and 6.14, while the curvature coefficients (Cc) were 0.80 and 1.46 for DB 1-1 and CB 2-1, respectively. According to the Unified Soil Classification System (USCS), the MSW BA batches showed poorly-graded and well-graded particle size distribution for DB 1-1 and CB 2-1, respectively. Figure 1 depicts the particle size distribution curve.

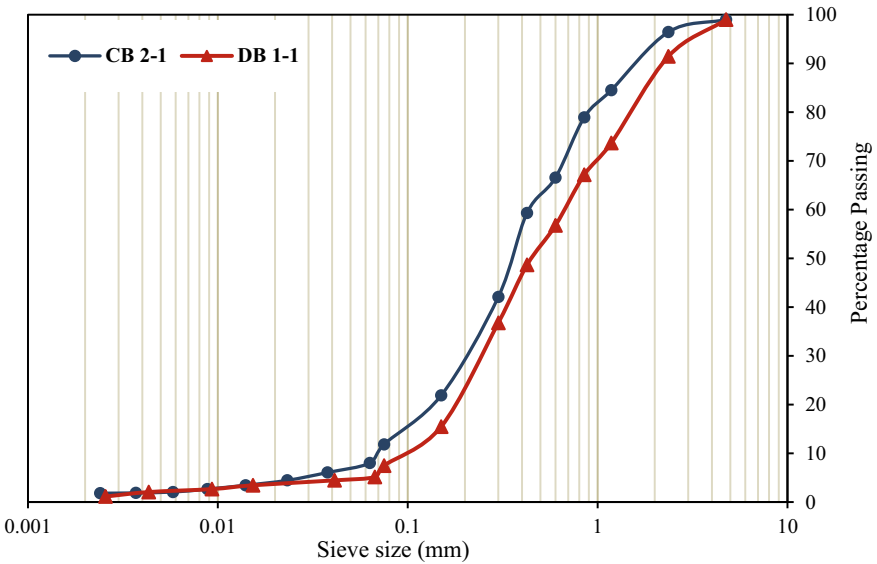


Fig. 1 Particle size distribution of MSW BA batches

### **3.3 Specific Gravity Test**

The specific gravity of a material is defined as the ratio of the unit weight of the given volume of material to the unit weight of water of equal volume of water at a standard temperature. The MSW BA was oven-dried at 103 °C for 24 h before testing. A density bottle of 50 ml was used in the experiment to determine specific gravity. The test procedure followed was as per ASTM D854-14 (2014).

The specific gravity test results indicated that MSW BA has a specific gravity of 2.05 and 2.07 for DB 1–1 and CB 2–1, respectively, which is less than any typical soil used in Geotechnical applications.

### **3.4 Loss of Ignition**

Loss is a given mass of material when ignited at higher temperatures in an open atmosphere is defined as Loss of ignition. It is frequently utilized because of its ease of usage. The test was carried out in line with the procedure mentioned in ASTM-D7348 (2021). The sample was kept in a muffle furnace for 2 h at 100 °C, then elevated to 500 and 1000 °C for another 2 h. The percentage change was measured using the initial weight (without any moisture) and the final weight when the sample was removed from the muffle furnace. This percentage change represents the Loss of ignition.

The Loss of ignition values of MSW BA was about 4.67 and 2.42% for batches DB 1–1 and CB 2–1, respectively. This LOI indicates that the organic and volatile matter in MSW BA is minute.

### **3.5 Density Index (Relative Density)**

The MSW BA was oven-dried at 103 °C for 24 h and used in this experiment. The cylindrical mould used in the experiment had a volume of 3000 cm<sup>3</sup>. The minimum and maximum density of material in a dry state were determined by following the procedure mentioned in ASTM D4254-00 (2017). The ash is coated with wax for the density of MSW BA particles and tested by the water displacement method as mentioned in code ASTM-D7263 (2021).

From this experiment, it has been observed that MSW BA from batch DB 1–1 had the minimum density and maximum density at 1.082 and 1.491. The values for MSW BA from batch CB 2–1 were 1.174 and 1.545 g/cm<sup>3</sup>, respectively. The particle densities for batches DB 1–1 and CB 2–1 were 1.235 and 1.307, respectively.

**Table 3** Physio-chemical and mechanical properties of MSW BA

MSW BA properties	DB 1-1	CB 2-1
Colour	Dark grey	Grey
Percentage of particles between 2.36 and 0.075 mm	83.97	84.61
Percentage passing 0.075 mm	7.47	11.83
The effective size of particle ( $D_{10}$ ), mm	0.11	0.07
The uniformity coefficients ( $C_u$ )	6.36	6.14
The curvature coefficients ( $C_c$ )	0.87	1.46
Type of particle size grading	Poorly-graded	Well-graded
Specific gravity (G)	2.05	2.07
Loss of Ignition (LoI), %	4.67	2.42
Density of particles, $g/cm^3$	1.235	1.307
Minimum density, $g/cm^3$	1.174	1.174
Maximum density, $g/cm^3$	1.545	1.545
The angle of internal friction ( $\phi$ )	36.5°	33.12°
Cohesion (C)	0	0
pH	8.11	7.6
The shape of MSW BA particles	Angular	Angular

### 3.6 pH Test

This test was brought to study due to the importance of alkalinity in the ash for dissociation of  $Al^{3+}$  and  $Si^{4+}$  ions for pozzolanic reactions and can be considered an assessment of environmental sustainability in the immediate future. The test was performed per ASTM D6276-19. The samples were sieved through 425  $\mu$ , and 30 g out of it was mixed with 75 ML of distilled water, stirred, and kept still for 1 h. After calibrating the pH meter by 3-point calibration, the test sample was tested. The pH values tested for both batches, DB 1-1 and CB 2-1, are 8.11 and 7.6, respectively.

All the data obtained from the above testing and observation for batches DB 1-1 and CB 2-1 is well represented in Table 3. The variation in properties can be seen vividly. The two batches were cohesionless, with angular particles for better interlocking properties.

### 3.7 Morphological Studies

**FESEM and EDS Analysis** The FESEM microstructure of MSW-IBA and its interaction with lime and fibre are observed. The photos are taken at various magnifications and angles to see the microbial structures better Fig. 2 shows the picture of MSW-IBA, which shows the angular shape of MSW-IBA particles. Due to the

oxidation of metals in MSW-IBA due to water, Fe-hydroxides can also be seen, and this resulted in excessive oxygen percentages in EDS analysis shown in Fig. 3.

**XRD Spectroscopy** It has been observed that the presence of quartz can be observed as the presence of peaks at  $2\theta = 20.8^\circ$  and  $26.7^\circ$  (Fig. 4).

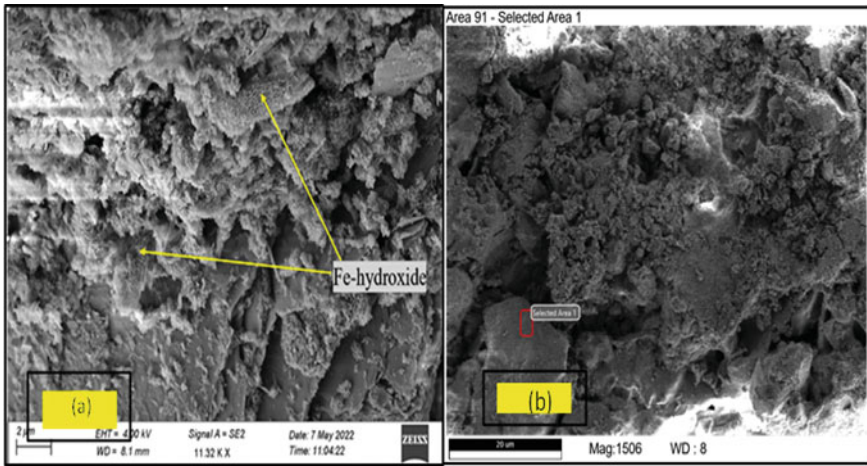


Fig. 2 Microstructural image of a MSW BA Batch CB 2-1 and b DB 1-1

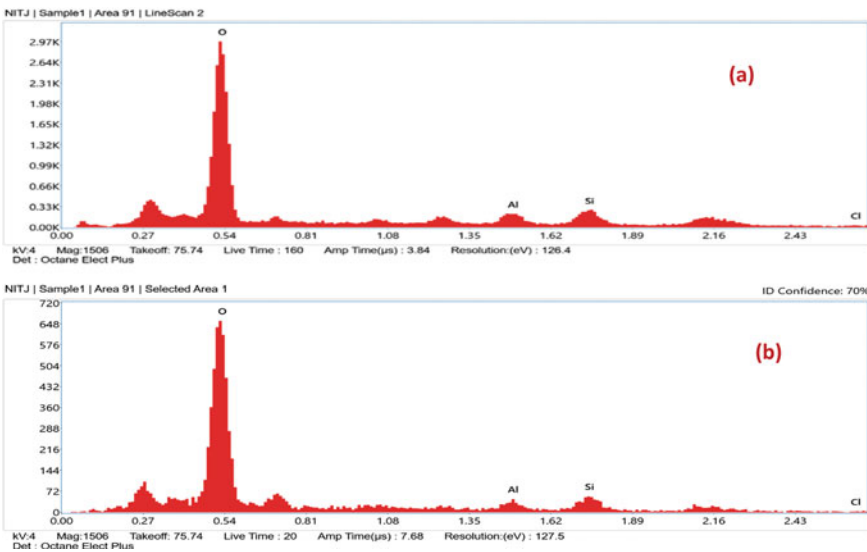


Fig. 3 EDS Spectrum of MSW BA Batch CB 2-1



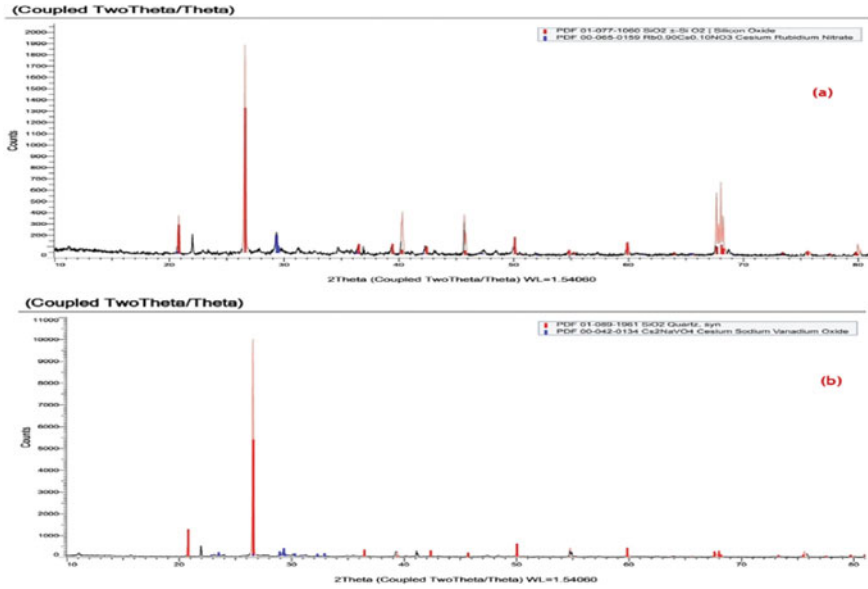


Fig. 4 XRD Spectrum for MSW BA for a MSW BA Batch CB 2-1 and b DB 1-1

### 4 Conclusions

By following the results from experimentation following conclusions are deduced,

- The variation in the chemical composition of both batches is insignificant to cause alteration in stabilizing mechanism.
- The batch DB 1-1 showed a poorly graded, and CB 2-1 showed well-graded particle size distribution and shape of particles being angular in both batches.
- From specific gravity tests, it can be concluded that particles from batch CB 2-1 were heavier than batch DB 1-1, and the ignition loss for both batches was minor (< 5%).
- The pH of MSW BA from batch CB 2-1 is lower than batch DB 1-1. It is because the pH of the material depends on the type of MSW in the feed, and it affects the leaching behaviour of the contaminants present in bottom ash.
- The presence of voids in the microstructural studies confirms both batches' heterogeneous nature. Thus, the voids can be removed by stabilizing the bottom ash with suitable material.

## References

1. Kumar S, Singh D (2021) Municipal solid waste incineration bottom ash: a competent raw material with new possibilities. *Innov Infrastruct Solut* 6:1–15
2. Gupta G, Datta M, Ramana GV, Alappat BJ (2021) MSW incineration bottom ash (MIBA) as a substitute to conventional materials in geotechnical applications: a characterization study from India and comparison with literature. *Constr Build Mater* 308:124925
3. Haiying Z, Youcai Z, Jingyu Q (2010) Thermal characterization of fly ash from one municipal solid waste incinerator (MSWI) in Shanghai. *Process Saf Environ Prot* 88:269–275
4. Zacco A, Borgese L, Gianoncelli A, Struis RPWJ, Depero LE, Bontempi E (2014) Review of fly ash inertisation treatments and recycling. *Environ Chem Lett* 12:153–175
5. Singh D, Kumar A (2019) Factors affecting properties of MSWI bottom ash employing cement and fiber for geotechnical applications. *Environ Dev Sustain* 22:6891–6905
6. Singh D, Kumar T, James BE, Hanifa M (2019) Utilization of MSWI ash for geotechnical applications: a review. *Lect Notes Civ Eng* 31:229–236
7. Alam P, Singh D, Kumar S (2021) Incinerated municipal solid waste bottom ash bricks: a sustainable and cost-efficient building material. *Mater Today Proc* 49:1566–1572
8. Zhu F, Xiong Y, Wang Y, Wei X, Zhu X, Yan F (2018) Heavy metal behavior in “washing-calcination-changing with bottom ash” system for recycling of four types of fly ashes. *Waste Manag* 75:215–225
9. Forteza R, Far M, Seguí C, Cerdá V (2004) Characterization of bottom ash in municipal solid waste incinerators for its use in road base. *Waste Manag* 24:899–909
10. Izquierdo M, Querol X, Vazquez E (2011) Procedural uncertainties of proctor compaction tests applied on MSWI bottom ash. *J Hazard Mater* 186:1639–1644
11. Lynn CJ, Ghataora GS, Dhir RK (2017) Municipal incinerated bottom ash (MIBA) characteristics and potential for use in road pavements. *Int J Pavement Res Technol* 10:185–201
12. Kim J, Tasneem K, Nam BH (2014) Material characterization of municipal solid waste incinerator (MSWI) ash as road construction material. *Pavement Perform Monit Model Manag* 14:100–108
13. Singh D, Kumar A (2017) Performance evaluation and geo-characterization of municipal solid waste incineration ash material amended with cement and fibre. *Int J Geosynth Gr Eng* 3:16
14. ASTM D6913 (2009) Standard test methods for particle-size distribution (gradation) of soils using sieve analysis

# Calculation of Strength Gain by Carbonate Precipitation in Crushed Granite Fines of Meghalaya



Pranamee Baruah and Susmita Sharma

**Abstract** Enzyme induced carbonate precipitation (EICP) is an emerging method to modify the mechanical properties of soils.EICP offers several advantages over Microbial induced carbonate precipitation (MICP), primarily urease enzyme being small in size; it can be adopted for a wider range of soils, with simpler processes of the application. In this context of soil modification, several developing countries have encountered strain in the supply of natural materials for infrastructural development; thus, using alternative materials which are locally available to the conventional ones as an alternative to sand is a sustainable solution. In this study, efforts were made to understand the effect of the single-phase premixed percolation method using purified urease enzyme for modifying the mechanical properties of Crushed Granite Fines (CGS) collected from a quarry in the Meghalaya region of Northeast India. The highest Calcium Carbonate ( $\text{CaCO}_3$ ) precipitation was established by studying the concentration and the ratio of cementation solution in a soil-less environment, which was later used to modify the CGS. The CGS predominantly contained  $\text{SiO}_2$  (~ 42.53% by wt.),  $\text{Al}_2\text{O}_3$  (~ 2.05% by wt.) with slight availability of  $\text{K}_2\text{O}$  (~ 0.57% by wt.). XRD investigated the Calcium Carbonate precipitation on the CGS, and the CGS micrograph confirmed the precipitation of  $\text{CaCO}_3$  crystals both in clusters and in unattached form. The amount of precipitation of  $\text{CaCO}_3$  and the Strength of the treated CGS were measured using acid digestion and Unconfined Compressive Strength (UCS) testing. It was observed that the single-phase method of treatment increased the compressive strength of CGS from 0 to 10.11 kPa and 17.88 kPa when extracted by two extraction methods viz. heavy extraction and light extraction respectively, which clearly indicated that the  $\text{CaCO}_3$  crystal facilitated load transfer between CGS grains. Thus, it is opined that EICP can also be used in unconventional materials for their mechanical stabilization.

**Keywords** EICP · Biocementation · Cementing solution · Unconfined compressive strength (UCS) · Soil improvement

---

P. Baruah · S. Sharma (✉)

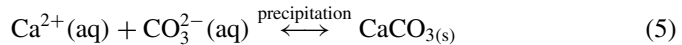
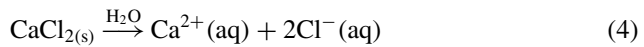
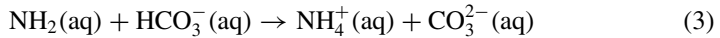
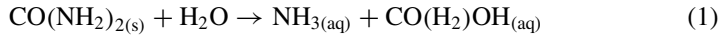
Department of Civil Engineering, NIT Meghalaya, Shillong, India

e-mail: [susmita.sharma4@nitm.ac.in](mailto:susmita.sharma4@nitm.ac.in)

## 1 Introduction

In a diversity of geological, biological and artificial systems, carbonate precipitation is an important phase in the biomineralization or biocementation process [1–3]. Enzyme Induced Carbonate Precipitation (EICP) is a biologically based ground improvement technique that uses a solution containing urea, calcium, and an activator urease enzyme to induce calcium carbonate precipitation in granular soil to improve its strength and stiffness, resulting in a long-lasting, consolidated material. Carbonate minerals are precipitated within the soil pores in this method of soil augmentation, cementing soil particles together and improving dilatancy. Furthermore, unlike other ground modification techniques that rely heavily on temperature change, EICP may be used in a wide range of temperatures (from 10 to 70 °C), making it appropriate for temperate to desert conditions.

Urease enzyme decomposes urea ( $\text{CO}(\text{NH}_2)_2$ ) through a chemical reaction, in which urea is hydrolysed into ammonia ( $\text{NH}_3$ ) and carbon dioxide ( $\text{CO}_2$ ) in the presence of water is known as urea hydrolysis. The enzyme can be added to the soil or generated in it by urease-producing microorganisms [1, 4–6]. In the presence of the urease enzyme, 1 mol of urea is hydrolyzed to 2 mol of ammonium. In the urea hydrolysis process, urea is degraded into ammonia,  $\text{NH}_3$ , and carbon dioxide,  $\text{CO}_2$ . The dissolution of ammonia,  $\text{NH}_3$ , in water produces ammonium ions ( $\text{NH}_4^+$ ) and hydroxide ions,  $\text{OH}^-$ , proceeds as per the following chemical reactions [7].



Meanwhile, the dissolution of  $\text{CO}_2$  into water generates bicarbonate ions,  $\text{HCO}_3^-$  and hydrogen ions,  $\text{H}^+$ . Bicarbonate ions ( $\text{HCO}_3^-$ ) reacts with the hydroxyl ions ( $\text{OH}^-$ ) to form carbonate ions ( $\text{CO}_3^{2-}$ ). Calcite (in form of  $\text{CaCO}_3$ ), most stable mineral is precipitated through the reaction between carbonate ions ( $\text{CO}_3^{2-}$ ) of urea hydrolysis and calcium ions ( $\text{Ca}^{2+}$ ) from the calcium chloride.

The  $\text{CaCO}_3$  that is precipitated and deposited into the soil grains strengthens the bonding between soil particles. Both plant and microorganism urease have been proven to cause carbonate precipitation [8]. Several studies have been conducted using  $\text{CaCO}_3$  precipitation facilitated by bacterial urease to support soil studies [1, 9].  $\text{CaCO}_3$  precipitation using free urease enzyme, i.e., EICP, has been used extensively

to study the critical factor and understand the MICP alternative for soil improvement in the last six years [10–16]. Almajed et al. [17] reported that using 0.67 M calcium and 1.0 M urea as cementation solution, the calcium conversion efficiency of EICP was about 70–95% within 7 days of curing. However, efforts to determine the most optimum precipitation and increase the calcium carbonate production efficiency in EICP are very limited in the literature. Generally, in soil, the experiments and factors affecting the increase in strength are carried out one parameter at a time. To achieve optimal conditions by this process, all tests must be repeated for all parameters, which leads to a considerable increase in the number of tests. To address these limitations, soil less test tubes experiments were carried out. It is opined that including the soil less test tube experiments with EICP soil treatment technology will increase the efficiency of the process and reduces the time of experimentation, provide better output results, and become more sustainable and cost-friendly for ground improvement. Additionally, the impact of optimized dosage of activator enzyme, Calcium carbonate and Urea is studied by observing the surface morphology of the soils.

## 2 Materials and Methods

The locally available soil is used for the study and named as  $W_1$ . This soil is collected from Meghalaya region. The soil has been chosen as the State of Meghalaya is endowed with large deposits of several valuable minerals such as coal, limestone, granite etc. Shillong Group of rocks comprising mainly quartzites are exposed in the central, eastern, and northern parts of the Meghalaya plateau. They are intruded by basic and ultrabasic intrusive and late tectonic granite plutons. Total Granitic reserves amounts to 50.0 million  $m^3$  in the region of Nongpoh in Ri-Bhoi, Myllem and Mawkyrat in Khasi Hills District, Rongjeng in East Garo Hills District. Due to this abundant availability effort were made to study the fine of granitic soils named as Crushed Granite Soils (CGS) is collected from quarry in the region (and named as  $W_1$ ). The physical and the chemical characterization of the two soils are done following ASTM/ASCE/APHA guidelines, the results are presented in Table 1. The primary materials such as Urea ( $CO(NH_2)_2$ ), Calcium Chloride dihydrate ( $CaCl_2 \cdot 2H_2O$ ), and Hydrochloric Acid (HCl) were obtained from Sigma Aldrich. The Activator Enzyme (AE) was obtained from Sisco Research Laboratory Pvt. Ltd.

The percentage of precipitation in soil is computed following. 5 gm of soil with Calcium precipitation, taken for analysis [17]. To this 20 ml of 1 M HCl is added and keep for 60 min for the dissociating precipitated  $CaCO_3$  from the soil to HCl

**Table 1** Physico-chemical characterization of the soil ( $W_1$ )

Physical properties							Chemical properties	
D10	D30	D60	Cc	Cu	> 75 $\mu$	< 75 $\mu$	EC ( $\mu$ S/cm)	pH
0.08	0.108	0.166	0.873	2.075	90.42%	9.58%	58.19	7.9

solution. The HCl washed soil is then filtered and oven dried weight is measured. Calcium Carbonate Precipitation (CCP) is calculated as.

$$\text{CCP}(\%) = 100 - \left( \frac{\text{Wt of the oven dried, HCL washed soil}}{\text{Wt of the original soil}} \right) \times 100\% \quad (6)$$

The Calcium precipitation in the Solution is identified using X-Ray Diffraction (XRD) analyzer (Make: PS-360/X-RAV Diffractometer). For the optimized control parameters that produced the highest CCP, efforts have been made to obtain the Unconfined compressive strength (UCS) of the soil. Soil columns (170 gm) were created in Polyvinyl Chloride (PVC) moulds of diameter 4.5 cm and height 12 cm and used for the study. The liquid to solid ratio is kept as 0.4 for all the soil samples. The samples were kept at a constant temperature of 30 °C for 7 days of curing time. Then the soil samples were extracted, using a heavy compaction hammer and a light compaction hammer to understand the change in strength with the extraction method. The samples were then, and oven dried for 24 h at 50 °C before UCS testing. The UCS tests were conducted at a strain rate of 1.250 mm/min.

### 3 Results and Discussion

The tables below depict the experiment program undertaken to get the maximum precipitate in the test tube. A total of 27 precipitation tests in 50-mL test tubes containing 25 mL of EICP solution without any soil to investigate the influence of the control factors on the calcium carbonate precipitation in the EICP treatment, were performed with three replicates and the average precipitation for each combination of Urea, CaCl<sub>2</sub> and Activator Enzyme was recorded. The pH and EC of the reaction solution in each tube was measured, at the end of the test period as tabulated in Table 2. As seen from the Table 2 the slight variation in the precipitation occurred in the test tube experiments as demonstrated by the std dev of results. The precipitation (CCP) in the test tubes have been analyzed for its mineralogy and the XRD plot is presented in Fig. 1.

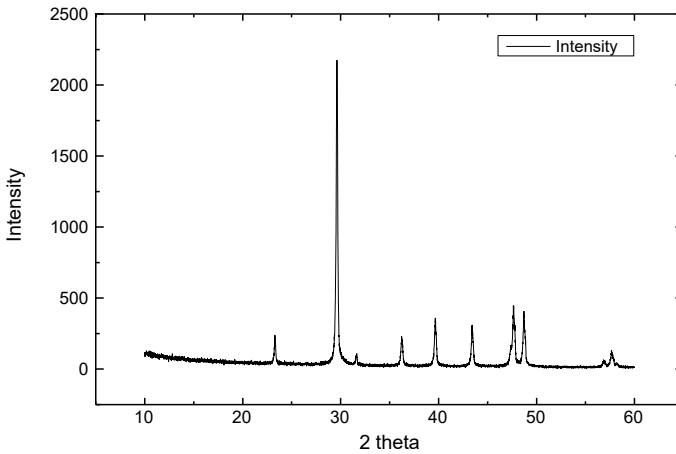
The effect of EICP treatment on CCP in the Soil W<sub>1</sub> was investigated using Unconfined Compressive Strength (UCS) testing. As obtained for the soil less experiments, maximum precipitated treatment solution is obtained as, 0.5 M Urea, 1 M CaCl<sub>2</sub> and 6 g/L activator enzyme and used for the soil modification study. The solution is added to the soil using Surface Percolation (SP) method. In SP method, the EICP solution is poured from top of the soil column. The moulds were wrapped with plastic, for no leakage. The samples were treated with the EICP cementing solution for 7 days in an Environmental Chamber at constant temperature and humidity. Then the soil samples were extracted UCS testing.

Figure 2 describes the stress–strains curves of the Soils W<sub>1</sub> display a linear elastic response followed by a decline in strength after reaching peak strength values of 10.11 and 17.88 kPa for heavy extractor and light extractor respectively. The average

**Table 2** Experimental results of the CaCO<sub>3</sub> precipitation in the test tubes

Parameters	Expt No1	Expt No2	Expt No3	Expt No4	Expt No5	Expt No6	Expt No7	Expt No8	Expt No9
CO(NH <sub>2</sub> ) <sub>2</sub> (M)	0.5	0.5	0.5	1	1	1	1.5	1.5	1.5
CaCl <sub>2</sub> (M)	0.6	0.8	1	0.6	0.8	1	0.6	0.8	1
AE (g/L)	1	3	6	1	3	6	1	3	6
Avg.PPT	0.20 (±0.01)	0.45 (±0.04)	0.51 (±0.09)	0.26 (±0)	0.33 (±0.03)	0.26 (±0.01)	0.26 (±0.02)	0.24 (±0.02)	0.43 (±0.03)
Avg.EC	22.83 (±0.4)	32.7 (±0.8)	39.73 (±0.4)	24.5 (±0.1)	30.2 (±0.3)	33.53 (±0.8)	23.16 (±0.2)	27.76 (±0.8)	35.3 (±1.0)
Avg.pH	7.16 (±0.1)	7.40 (±0.01)	7.22 (±0.03)	7.27 (±0.01)	7.37 (±0.1)	7.41 (±0.08)	7.30 (±0.06)	7.34 (±0.02)	7.30 (±0.02)

The numerical in Italics indicate the standard deviations of the experimental trails



**Fig. 1** XRD data showing Calcite crystal precipitated by EICP solution

mass of Calcium Carbonate precipitation for  $W_1$  is identified as  $\sim 4.6\%$ . The average precipitation in soil was less than the optimal precipitation (of 20.4 g/L) achieved in the test tube with the same concentrations of constituents. Figure 1 establishes the Calcite precipitation as the by-product. In case of soil  $W_1$ , less UCS strength may be due to presence of larger pore spaces, thereby having less opportunities for nucleation of calcite crystal. The nucleation of the calcite crystal and point to point load transfer, resulting in a higher UCS value [18].

Carbonate structure and size may have an impact on the treated CGS's strength. As seen in the SEM photos, the existence of agglomeration crystals in the precipitated materials may increase the adherence of the treated soil. The precipitated carbonate may form a covering over the CGS grains and bridges between them, causing the particles to bind together. The UCS steadily rose as the precipitated content increased. From the UCS plots it could be seen that, When the UCS samples were extracted using a heavy extractor the strength decreased. The reason could be that the heavy extractor created disturbance to the "soil-precipitated calcite" which broke the developed bonding between the soil particles.

Figure 3 represents the FESEM images of soil surfaces. For conducting the FESEM, a sputter coated with an ultrathin layer of gold of 15 milliamperes was necessary on surface under study. The calcium carbonate crystals are seen to be formed on CGS particles. The images highlight that rhombic calcium carbonate crystals are observed on the surface of the soils which are more stable in nature. Khodadadi et al. [19] emphasized that less stable calcium carbonate mineral phases will not be effective in improving the mechanical properties of the soil. As identified by the XRD data as given in Fig. 1, the calcite deposition has indicated a stable mineral deposition in the soil.



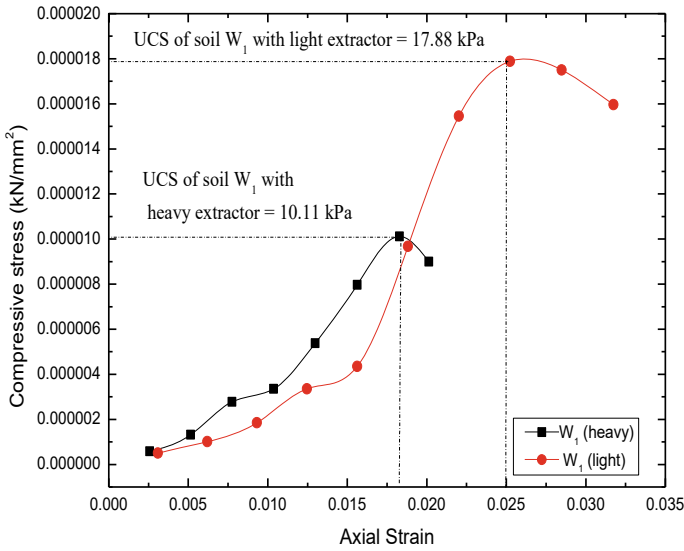


Fig. 2 UCS strength of the soil columns predicated by EICP solution

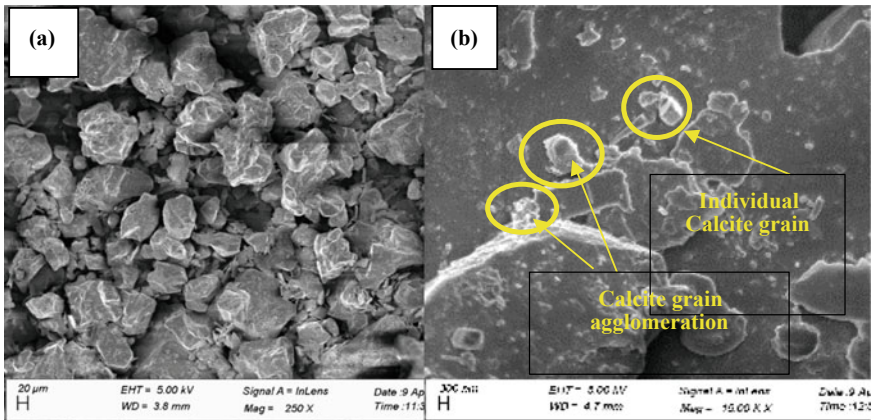


Fig. 3 FESEM images of  $W_1$  surfaces **a** virgin soil and **b** soil after Calcite deposition

The SEM images also shows agglomeration of precipitates along the surface of the  $W_1$  with calculated CCP as 2.2%. Similarly pattern of Calcium deposition is seen from EDX results where the surface deposition is discoursed as 3.83% (Fig. 4).

Element	Weight %	Atomic %
C K	1.81	3.25
O K	43.61	58.85
AlK	3.67	2.94
SiK	38.45	29.56
ClK	3.49	2.13
K K	1.47	0.81
<b>CaK</b>	<b>3.83</b>	<b>2.07</b>

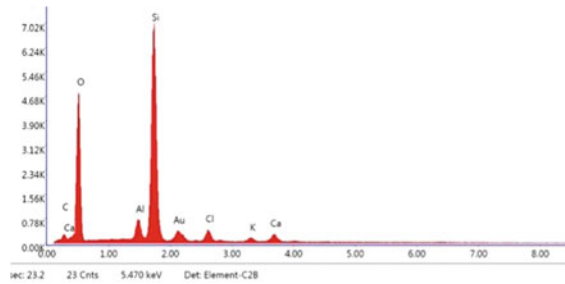


Fig. 4 EDX of soil columns surfaces for conforming Calcite deposition for W<sub>1</sub>

### 4 Conclusions

In this work, efforts have been made to determine the most optimum precipitation and increase the calcium carbonate production efficiency in EICP method of soil treatment. Soil less test tube experiments was implemented to find the optimum percentage of precipitation. The following observations are recorded as conclusion from the carried-out experiments,

1. The soil less experimental study suggests that a solution of 0.5 M urea, 1 M CaCl<sub>2</sub> and 6 g/L Activator Enzyme is recommended for optimal precipitation.
2. The obtained optimum cementing solution was used to treat soil specimens to confirm the efficiency Meghalayan soil W<sub>1</sub>. Two extraction methods were adopted as Heavy extractor and Light extractor.
3. For Heavy and Light extractor UCS strength for soil W<sub>1</sub> was obtained as 10.11 and 17.88 kPa respectively. The UCS strength increased up to 76.85% when samples were extracted using light extractor.
4. The calcium carbonate crystal produced in the CGS process is calcite, which is the most stable form of calcium carbonate. From the SEM images CaCO<sub>3</sub> agglomeration can be observed and in some sections the bridging effect between the soil particles can be seen.
5. The EDX images suggests that the virgin soil didn't have traces of Ca. Whereas the treated soil samples have results in a surface deposition of 3.83% for W<sub>1</sub>.

### References

1. Whiffin VS, van Paassen LA, Harkes MP (2007) Microbial carbonate precipitation as a soil improvement technique. *Geomicrobiol J* 24(5):417–423. <https://doi.org/10.1080/01490450701436505>

2. Harkes MP, van Paassen LA, Booster JL, Whiffin VS, van Loosdrecht MCM (2010) Fixation and distribution of bacterial activity in sand to induce carbonate precipitation for ground reinforcement. *Ecol Eng* 36(2):112–117. <https://doi.org/10.1016/j.ecoleng.2009.01.004>
3. Kulanthaivel P, Arun Kumar M, Krishnaraja AR, Kayalvizhi VS, Saranya K (2022) Applications of BCCP technology on civil engineering: a review. *Mater Proc* 65:1213–1221. <https://doi.org/10.1016/j.matpr.2022.04.179>
4. Nemati M, Voordouw G (2003) Modification of porous media permeability, using calcium carbonate produced enzymatically in situ. *Enzyme Microb Technol* 33(5):635–642. [https://doi.org/10.1016/S0141-0229\(03\)00191-1](https://doi.org/10.1016/S0141-0229(03)00191-1)
5. DeJong JT, Fritzges MB, Nüsslein K (2006) Microbially induced cementation to control sand response to undrained shear. *J Geotech Geoenviron Eng* 132(11):1381–1392. [https://doi.org/10.1061/\(ASCE\)1090-0241\(2006\)132:11\(1381\)](https://doi.org/10.1061/(ASCE)1090-0241(2006)132:11(1381))
6. Martinez BC, Barkouki TH, DeJong JD, Ginn TR (2011) Upscaling microbial induced calcite precipitation in 0.5 m columns: experimental and modeling results. *Geo-Frontiers* 2011:4049–4059. [https://doi.org/10.1061/41165\(397\)414](https://doi.org/10.1061/41165(397)414)
7. Ahenkorah I, Rahman MM, Karim MR, Beecham S (2021) Optimisation of chemical constituents on enzyme-induced carbonate precipitation in test-tube and soil. *Geotech Res* 8(3):66–84. <https://doi.org/10.1680/jgere.21.00006>
8. Stocks-Fischer S, Galinat JK, Bang SS (1999) Microbiological precipitation of CaCO<sub>3</sub>. *Soil Biol Biochem* 31(11):1563–1571. [https://doi.org/10.1016/S0038-0717\(99\)00082-6](https://doi.org/10.1016/S0038-0717(99)00082-6)
9. van Paassen L (2009) BiogROUT: ground improvement by microbially induced carbonate precipitation. Delft University of Technology, Delft
10. Ran D, Kawasaki S (2016) Effective use of plant-derived urease in the field of geoenvironmental/geotechnical engineering. *J Civil Environ Eng* 06(01):207. <https://doi.org/10.4172/2165-784x.1000207>
11. Hamdan NM (2015) Applications of enzyme induced carbonate precipitation (EICP) for soil improvement
12. Hamdan N, Kavazanjian E, Rittmann BE, Karatas I (2017) Carbonate mineral precipitation for soil improvement through microbial denitrification. *Geomicrobiol J* 34(2):139–146. <https://doi.org/10.1080/01490451.2016.1154117>
13. Neupane D, Yasuhara H, Kinoshita N (2013) Soil improvement through enzymatic calcite precipitation technique: small to large scale experiments. *Int J Lsl Environ* 1(1):65–66
14. Neupane D, Yasuhara H, Kinoshita N, Ando Y (2015) Distribution of mineralized carbonate and its quantification method in enzyme mediated calcite precipitation technique. *Soils Found* 55(2):447–457. <https://doi.org/10.1016/j.sandf.2015.02.018>
15. Putra H, Yasuhara H, Kinoshita N, Neupane D, Lu C-W (2016) “Effect of magnesium as substitute material in enzyme-mediated calcite precipitation for soil-improvement technique. *Front Bioeng Biotechnol* 4:3–10. <https://doi.org/10.3389/fbioe.2016.00037>
16. Yasuhara H, Neupane D, Hayashi K, Okamura M (2012) Experiments and predictions of physical properties of sand cemented by enzymatically-induced carbonate precipitation. *Soils Found* 52(3):539–549. <https://doi.org/10.1016/j.sandf.2012.05.011>
17. Almajed A, Khodadadi Tirkolaie H, Kavazanjian E (2018) Baseline investigation on enzyme-induced calcium carbonate precipitation. *J Geotech Geoenviron Eng* 144(11):04018081. [https://doi.org/10.1061/\(asce\)gt.1943-5606.0001973](https://doi.org/10.1061/(asce)gt.1943-5606.0001973)
18. Soon NW, Lee LM, Khun TC, Ling HS (2014) Factors affecting improvement in engineering properties of residual soil through microbial-induced calcite precipitation. *J Geotech Geoenviron Eng* 140(5):04014006. [https://doi.org/10.1061/\(asce\)gt.1943-5606.0001089](https://doi.org/10.1061/(asce)gt.1943-5606.0001089)
19. Khodadadi TH, Kavazanjian E, Bilsel H (2017) Mineralogy of calcium carbonate in MICP-treated soil using soaking and injection treatment methods. *Geotech Front* 2017:195–201. <https://doi.org/10.1061/9780784480441.021>

# Mechanical Properties of Colemanite, Copper Slag and Glass Fiber Added Sand-Bentonite Mixtures as a Buffer Material for Energy Geo-structures



Yusuf Batuge , Yeliz Yukselen-Aksoy , Cihat Asci ,  
and Sukran Gizem Alpaydin 

**Abstract** Soil stabilization methods are important in dealing with geotechnical engineering, especially for energy geo-structures. In the present study mechanical properties of reinforced and unreinforced sand-bentonite mixtures were evaluated by a series of laboratory tests such as unconfined compression test and direct shear tests. The bentonite ratio of the various test specimens was 20% and the proportions of colemanite, copper slag and glass fiber used as additives in the specimens were chosen as 1% for glass fiber and as 10% for copper slag and colemanite. Compaction tests were conducted to determine the optimum water content and maximum dry density of the mixtures. As a result of direct shear tests copper slag and glass fiber slightly increased and colemanite decreased the shear strength of the sand-bentonite mixture. Also, copper slag and colemanite decreased the unconfined compressive strength of the sand-bentonite mixtures whereas glass fiber increased.

**Keywords** Colemanite · Copper slag · Direct shear test · Glass fiber · Unconfined compression test · Sand-bentonite

## 1 Introduction

Compacted bentonite or sand-bentonite mixtures are frequently used in municipal landfills and nuclear waste repositories where low permeability and high mechanical properties are expected. Bentonite, with its low permeability and high swelling capacity, is used to prevent contaminants from contaminating the environment. The use of sand material mixed with bentonite plays a major role in improving the mechanical properties of the soil, as well as the disadvantage of increasing the

---

Y. Batuge (✉) · C. Asci · S. G. Alpaydin  
The Graduate School of Natural and Applied Sciences, Dokuz Eylul University, Izmir, Turkey  
e-mail: [ybatuge@hotmail.com](mailto:ybatuge@hotmail.com)

Y. Yukselen-Aksoy  
Department of Civil Engineering, Dokuz Eylul University, Izmir, Turkey

permeability. In addition, the use of different additives to improve soil properties has become widespread today. Among the soil parameters hydraulic conductivity, swelling, water retention characteristics, and mechanical properties are of prime importance. Moreover, the thermal conductivity is also important parameter for many energy geo-structures.

Glass fibers are a type of silica-based synthetic fiber with high tensile strength and elastic modulus. The use of natural or synthetic fibers for reinforcing the soils is a common method. It has been proven by the studies that the fibers reduce the desiccation cracking that may occur with the change in the moisture content of the soils, thanks to their mechanical properties, and increase the mechanical properties by holding the soil particles together due to their high tensile strength. Previous studies reported that the shear strength and compressive strength of the soils increased with the effect of glass fiber [1–4].

Colemanite is one of the boron minerals found in nature. Colemanite is a monoclinic mineral and is generally present in form of bright crystals. Typically, its color is white–gray and greenish gray. It is a very rich mineral in terms of boron. Colemanite has a chemical formula  $2\text{CaO}\cdot 3\text{B}_2\text{O}_3\cdot 5\text{H}_2\text{O}$  and  $\text{B}_2\text{O}_3$  content is about 30%. The country with the largest boron reserves in the world is Turkey. Colemanite was chosen as the soil reinforcement material in this study, due to its ease of availability and being one of the most widely used boron minerals in the industry. Among the purposes of using boron in industry, easy production, low thermal expansion value and light weight can be shown. Alpaydın and Yukselen-Aksoy [5] observed that the colemanite additive increased the compressibility behavior of sand bentonite mixtures. Also, in another study [6], it was observed that the addition of colemanite increased or decreased the shear strength parameter depending on the bentonite ratio of the mixtures. Çimen and Dereli [7] carried out Standard Proctor and unconfined compression tests by adding 2, 4, 6, 8 and 10% colemanite by dry weight of Na-Bentonite clay. According to the results, it was stated that the colemanite additive increased the unconfined compressive strength and the maximum dry unit weight and decreased the optimum water content value of the Na-Bentonite clay.

Copper slag is the name given to the oxidized copper that emerges when the lighter copper, which remains on top, encounters air after the unpurified copper is melted. Copper slag contains iron, alumina, calcium oxide, silica and traces of zinc, copper, manganese, and nickel. Approximately 2–3 tons of copper slag is obtained in the production of 1 ton of copper [8]. Previous studies on copper slag additives [9–12] concluded that copper slag additive of various soil specimens increased the maximum dry density, internal friction angle and unconfined compressive and decreased the optimum moisture content and cohesion values of the soil specimens.

In addition to improving the soil properties of additives, being easily available and inexpensive, serviceable, practical and environmentally friendly features are among the selection criteria. In this study, additives such as colemanite, copper slag and glass fiber were used because they meet the desired properties above. In the present study, the mechanical properties of sand-bentonite mixtures were investigated in the presence of colemanite, copper slag and glass fiber.

## 2 Materials and Methods

### 2.1 Materials

The materials used in this study are bentonite, sand, colemanite, copper slag and glass fiber, respectively (Fig. 2). The physical properties of the Ca-bentonite are given in Table 1. The grain size distribution of the sand material used is shown in Fig. 1 and the properties of the sand are presented in Table 2.

The glass fibers are used in this study were taken from the industrial raw materials of Dost Kimya Company. The physical properties of the glass fiber are given in Table 3.

The physico-chemical properties of colemanite and copper slag are given in Table 4.

**Table 1** Physical properties of bentonite

Ca-Bentonite	
Liquid limit (%)	270
Plastic limit (%)	60
Plasticity index (%)	210
Natural water content (%)	7.5
Specific gravity	2.6
USCS classification	CH

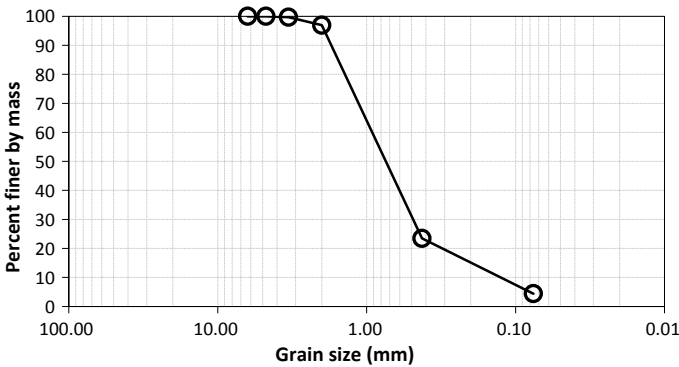


**Fig. 1** Grain size distribution of the sand



**Fig. 2** Materials used in the study. **a** Sand, **b** Ca-Bentonite, **c** Colemanite, **d** Copper slag, **e** Glass fiber

**Table 2** Physical properties of sand

Sand	
D <sub>60</sub> (mm)	0.92
D <sub>30</sub> (mm)	0.43
D <sub>10</sub> (mm)	0.19
Coefficient of uniformity (C <sub>u</sub> )	4.8
Coefficient of curvature (C <sub>c</sub> )	1.06
Specific gravity	2.7
USCS classification	SW

## 2.2 Methods

The compaction tests were performed according to ASTM D698 [13] standard. Bentonite in the natural water content was mixed with sand in proportions of 20% bentonite and 80% sand. 1% glass fiber and 10% copper slag and colemanite additives

**Table 3** Physical properties of glass fiber

Glass fiber	
Tensile strength (MPa)	3400
Elasticity modulus (GPa)	77
Specific gravity	2.60
Fiber length (mm)	3
Fiber diameter ( $\mu\text{m}$ )	13
Water absorption capacity	0

**Table 4** Physico-chemical properties of colemanite and copper slag

Color	Colemanite	Copper slag
	White gray-greenish gray	Blackish grey
Specific gravity	2.44	3.40
Natural water content (%)	1.0	1.0
Liquid limit (%)	37	–
Plastic limit (%)	26	–
pH	9.26	7–10
-No.200 (%)	100.0	–
-No.40 (%)	100.0	100.0

were added considering the dry weight of the mixtures. Tap water was added to the samples and mixed, then the samples were left for 24 h to obtain a uniform moisture distribution. Then, the maximum dry unit weight and optimum water content of the mixtures were determined according to Standard Proctor compaction test.

The direct shear tests were performed using the strain-controlled direct shear apparatus [14]. Consolidated drained (CD) direct shear tests were performed on  $6 \times 6$  cm and 2 cm height samples. Samples were sheared at 0.5 mm/min and three different normal stress levels, which are 49, 98 and 196 kPa.

The mixtures, which were prepared according to the optimum water content, were kept for 24 h in order to distribute the water homogeneously. Then, the samples were compacted at the maximum dry unit weight corresponding to the 3.76 cm diameter and 7.6 cm height mold. The sample was allowed to collapse at a rate of 0.5 mm/min velocity. At this stage, readings were taken from the deformation and load dials. Unconfined compression strength parameter was determined according to ASTM D2166 [15].



### 3 Results

#### 3.1 Compaction Characteristics

The compaction curves of the 80% sand–20% bentonite (SB20) obtained with the addition of copper slag, colemanite and glass fiber are shown in Fig. 3. While the maximum dry unit weight of the SB20 was 16.07 kN/m<sup>3</sup>, it increased to 16.37 and 16.27 kN/m<sup>3</sup> in the presence of 10% copper slag and 10% colemanite, respectively. In the presence of 1% glass fiber, the dry unit weight value decreased to 15.88 kN/m<sup>3</sup>. While the optimum water content was 18% in SB20, it decreased to 17.1 and 17.4% in the presence of 10% copper slag and colemanite, respectively and decreased to 17.5% in the presence of 1% glass fiber (Table 5).

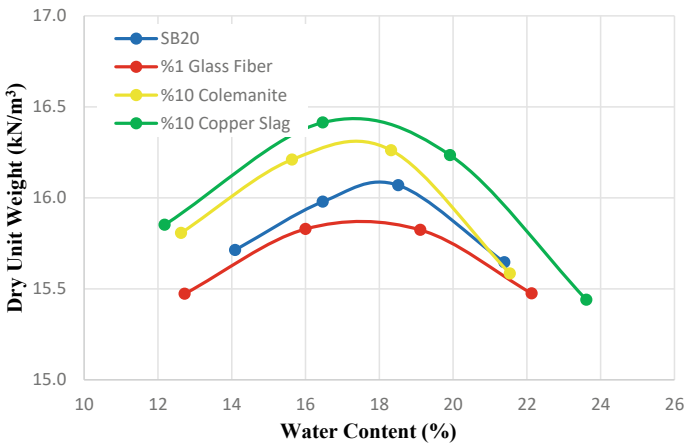
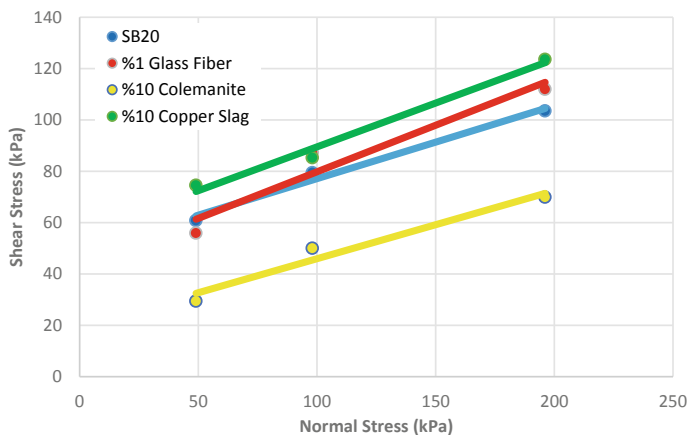


Fig. 3 Compaction curves of the mixtures

Table 5 Compaction data for the mixtures

Samples	Max. dry unit weight (kN/m <sup>3</sup> )	Optimum water content (%)
SB20	16.07	18.0
%1 Glass fiber	15.88	17.5
%10 Colemanite	16.27	17.4
%10 Copper slag	16.37	17.1



**Fig. 4** Shear strength behavior of the samples

**Table 6** Shear strength data for the mixtures

Mixture	$c'$ (kPa)	$\varphi$ (°)	$\tau_{\max}$ (kPa)
SB20	49.5	15.4	103.5
SB20—%1 G.F	45.4	18.7	111.9
SB-20—%10 C	20.6	14.1	69.9
SB20—%10 C.S	55.6	18.9	122.6

### 3.2 Shear Strength Characteristics

The results of the direct shear tests are as given in Fig. 4 and Table 6. The cohesion value of SB20 mixture was 49.5 kPa, the internal friction angle was 15.4°, and the maximum shear strength was 103.5 kPa. According to the results obtained from the experiments in the presence of colemanite, cohesion, angle of internal friction and maximum shear stress values decreased to 20.6 kPa, 14.1°, and 69.9 kPa, respectively. In the presence of 1% glass fiber, the cohesion value of the soil decreased slightly, the internal friction angle and shear strength increased (Table 6). An increase in the shear strength parameters was observed in the presence of 10% copper slag, as well. The cohesion value was 55.6 kPa, the angle of internal friction was 18.9°, and the maximum shear stress was 122.6 kPa (Fig. 5).

### 3.3 Unconfined Compression Strength Characteristics

The undrained shear strength ( $c_u$ ) and unit strain (%) values at the time of failure of the mixtures investigated by the unconfined compression tests are as shown in

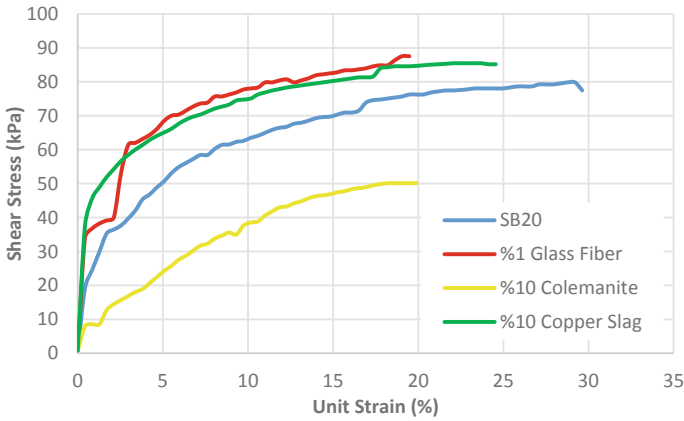


**Fig. 5** Shear strength behavior of the samples at 98 kPa normal stress

**Table 7** Unconfined compression test results

Samples	$c_u$ (kPa)	Failure strain (%)
SB20	106.6	1.84
SB20—%1 Glass fiber	109.7	1.50
SB20—%10 Colemanite	98.5	1.67
SB20—%10 Copper slag	98.7	1.50

Table 7. According to the results, while the undrained shear strength of the SB20 soil sample was 106.6 kPa, this value increased to 109.7 kPa in the presence of 1% glass fiber and in the presence of 10% colemanite and copper slag, it decreased to 98.5 and 98.7 kPa, respectively. The unit strain value at the time of failure was found to be 1.84% for SB20. This value was found to be 1.50, 1.67 and 1.50% for glass fiber, colemanite and copper slag additives, respectively. The stress–strain graphs of the mixtures are given in Fig. 6.

## 4 Conclusions

In the present study, boron mineral, namely colemanite, copper slag and glass fiber additives were used in order to improve the engineering properties of sand-bentonite mixtures. The compaction, shear strength and unconfined compressive strength behavior of SB20 mixtures were investigated in the presence of additives. The following results were drawn from the study:

- Copper slag (10%) increased shear strength, cohesion, and internal friction angle values of the SB20 mixtures. In addition, a decrease in the undrained shear strength parameter was observed.

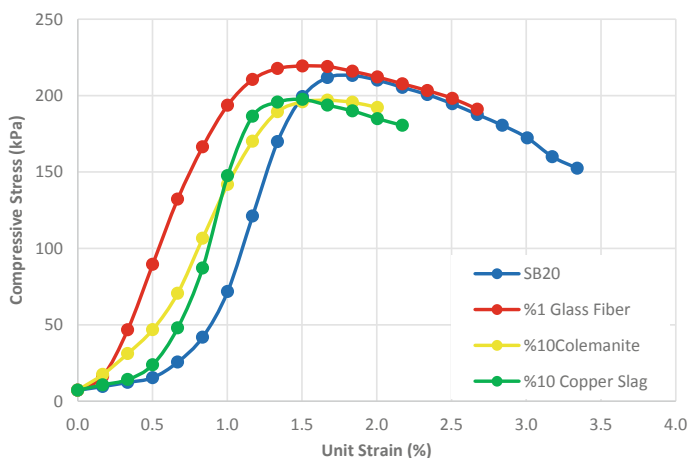


Fig. 6 Stress–strain behavior of the mixtures

- Addition of 10% colemanite to the SB20 decreased shear strength, cohesion, internal friction angle and undrained shear strength.
- Addition of 1% glass fiber to the SB20 increased shear strength, cohesion, internal friction angle and undrained shear strength.
- The results have shown that copper slag and glass fiber can be used as additive for SB20 mixtures, but further research is required for colemanite.

## References

1. Consoli NC, Prietto PD, Ulbrich LA (1998) Influence of fiber and cement addition on behavior of sandy soil. *J Geotech Geoenviron Eng* 124(12):1211–1214
2. Maher MH, Ho YC (1994) Mechanical properties of kaolinite/fiber soil composite. *J Geotech Eng* 120(8):1381–1393
3. Mukherjee K, Mishra AK (2019) Hydro-mechanical properties of sand-bentonite-glass fiber composite for landfill application. *KSCE J Civil Eng* 23(11):4631–4640
4. Mukherjee K, Mishra AK (2021) Impact of glass fibre on hydromechanical behaviour of compacted sand–bentonite mixture for landfill application. *Eur J Environ Civil Eng* 25(7):1179–1200
5. Alpaydın ŞG, Yukselen-Aksoy Y (2018) The effects of colemanite and ulexite additives on the geotechnical index properties of bentonite and sand-bentonite mixtures. In: *Proceedings of China-Europe conference on geotechnical engineering*. Springer, Cham, pp 778–781
6. Alpaydın ŞG (2019) An investigation of effects of boron additives on the permeability and shear strength behavior of sand-bentonite mixtures under high temperatures (Master's thesis, Fen Bilimleri Enstitüsü)
7. Çimen Ö, Dereli B (2019) Bentonitin Mühendislik Özelliklerine Mikronize Kolemanitin Etkisi. *Teknik Bilimler Dergisi* 4(2):12–17
8. Shi C, Meyer C, Behnood A (2008) Utilization of copper slag in cement and concrete. *Resour Conserv Recycl* 52(10):1115–1120

9. Gupta RC, Thomas BS, Gupta P, Rajan L, Thagriya D (2012) An experimental study of clayey soil stabilized by copper slag. *Int J Struct Civil Eng Res* 1(1):110–119
10. Havanagi VG, Mathur S, Prasad PS, Kamaraj C (2007) Feasibility of copper slag–fly ash–soil mix as a road construction material. *Transp Res Rec* 1989(1):13–20
11. Kavisri M, Senthilkumar P, Gurukumar MS, Pushparaj KJ (2018) Experimental study on effects of stabilization of clayey soil using copper slag and ggbs. *Rasayan J Chem* 11(1):111–117
12. Qureshi MA, Mistry HM, Patel VD (2015) Improvement in soil properties of expansive soil by using copper slag. *Int J Adv Res Sci Eng Technol* 2(7):125–130
13. ASTM D698 (2012) Standard test method for laboratory compaction characteristics of soil using standard effort (12400 ftlb/ft<sup>3</sup> \* 600 kN/m<sup>3</sup>). ASTM International, West Conshohocken
14. ASTM D3080 (2011) Standard test method for direct shear test of soils under consolidated drained conditions. ASTM Int West, Conshohocken
15. ASTM D 2166 (2006) Standard test method for unconfined compressive strength of cohesive soils, American Society for Testing and Materials, Philadelphia

# Strength Properties of Coffee Waste with Recycled Glass Geopolymers



Tugba Eskisar 

**Abstract** A sizable amount of coffee waste is dumped in the landfills every year. This study aims to investigate the possible use of coffee waste with recycled glass (CWRG) geopolymers as a green construction material for landfills. Coffee is an organic and a biodegradable material. Recycling glass reduces the landfill space that would be covered by many glass objects. Recycled glass is used in the construction industry and it has a property of replacing granular soils in construction works. In order to use coffee waste with recycled glass as a construction material, the strength development of CWRG geopolymers was observed. Fly ash was preferred as a precursor. Alkaline activators formed of sodium silicate and sodium hydroxide ( $\text{Na}_2\text{SiO}_3:\text{NaOH}$ ) were used to trigger the geopolymerization process. Three variables were tested, i.e. the ratio of  $\text{Na}_2\text{SiO}_3:\text{NaOH}$  in alkali activators; curing temperature and curing time on the strength development of CWRG geopolymers. By adding 30% of fly ash into CWRG with 90% $\text{Na}_2\text{SiO}_3:10\%\text{NaOH}$  provided the highest unconfined compressive strengths. The ratio of recycled glass in the geopolymer and the curing temperature were major factors that were found to considerably affect the performance of the geopolymers. This paper indicates that the geopolymerization products based on CWRG have the ability to transform the coffee waste into a non-degradable material, making geopolymers an alternative stabilization agent even for highly organic soils.

**Keywords** Geopolymer · Coffee waste · Recycled glass · Unconfined compression test

## 1 Introduction

Benefiting from recycled products in the construction industry is a relatively new topic as it provides an alternative way of creating a sustainable environment and boosting the economy. Bio-materials that have been recycled could be used to create environmentally friendly solutions. After coffee beans are dried, ground, and brewed,

---

T. Eskisar (✉)  
Ege University, 35100 Bornova, Izmir, Turkey  
e-mail: [tugba.eskisar@ege.edu.tr](mailto:tugba.eskisar@ege.edu.tr)

© The Author(s), under exclusive license to Springer Nature Singapore Pte Ltd. 2023  
Y. Yukselen-Aksoy et al. (eds.), *Sustainable Earth and Beyond*, Lecture Notes in Civil Engineering 370, [https://doi.org/10.1007/978-981-99-4041-7\\_12](https://doi.org/10.1007/978-981-99-4041-7_12)

117

an insoluble residue called “coffee waste” is left behind. The soluble coffee industry, which consumes over half of the annual worldwide coffee harvest, and cafes and the general public, who produce the remaining half, are the two sources of the waste produced by the coffee industry [1].

The International Coffee Organization (ICO) estimates that in the years 2020/21 global consumption of coffee is 166.35 million bags leading to almost 10 billion kilograms of coffee in total, the majority of which have been consumed in the EU, the USA, and Asia-Oceania [2]. The main issue is that producers discard considerable amount of coffee waste in landfills, which could have a negative impact on the local ecology [3].

Due to its high organic content, coffee waste could be regarded as an organic soil and should be analyzed using soil mechanics concepts when it is intended to be included in a geotechnical research. Average coffee waste has an organic content of 86–89%, a low shear strength, and a high compressibility [4].

Ground improvement methods or geopolymerization process could be different alternatives to treat coffee wastes and use them as fill materials in embankments. Geopolymers, which is an alternative binder based on fly ash that is activated by an alkaline activator, has a lower carbon footprint compared to cement [5]. According to IPCC data, ordinary Portland Cement responsible for about 7% of the total CO<sub>2</sub> emissions in the world [6]. For this reason, utilizing geopolymers may be a green solution for the coffee waste problem. Alkaline metals react with alumina rich and silica rich materials and produce a strong network of three dimensional aluminosilicates. Any natural mineral rich in alumina and silica, such as kaolinite and other clays, as well as wastes like fly ash and rice husk ash, could be used as the materials for the production of geopolymer stabilizers [7]. Arulrajah et al. [8] produced a geopolymer made of coffee waste and fly ash to develop a green engineering fill material. Later, Arulrajah et al. [9] showed that using recycled glass as a filler in coffee waste based geopolymers had a contribution to the mechanical strength.

Previously, the cement treatment of the coffee waste and the success of coffee waste based geopolymer was discussed by Eskisar and Altun [10]. The aim of this study was to evaluate the strength development of a geopolymer composed of coffee waste with recycled glass (CWRG) to determine the optimum material ratios to produce a coffee based geopolymer to be used in as a fill material in embankments. 7, 28 or 90 days of curing were applied to the specimens in a humidity controlled environment. Curing temperatures of  $20 \pm 2$  and  $38 \pm 2$  °C were considered for the efficiency of curing process of the geopolymers. The unconfined compressive strength (UCS) of the geopolymers was investigated. The findings of this study could help to find an alternative solution to stabilize highly organic waste materials/soils using geopolymers.

## 2 Materials and Testing Methods

Coffee waste was gathered from a branch of an American coffee chain store located in Turkey. It was noted that mold grew after 5 days since the waste that had been collected was moist. The waste was kept in sealed plastic containers in a cool location until it was transported to the laboratory, since the mold needs air and warmth to develop. Before air drying could begin, coffee waste had to be spread out flat on a sizable surface and separated from any other trash, such as paper cups, coffee filter paper, paper napkins, etc. The material was subsequently put into a drying oven. As a greater temperature might burn the organic material, an oven temperature of 90 °C was used.

This phase was accomplished in 4 days. Grain size distribution analysis was performed on the dry coffee waste (Fig. 1). The particle size distribution of dried coffee waste showed that 85% of the waste was sand size, and the rest of the material was silt and clay size. In this way, the grain size distribution of the waste was similar to silty sand, but this material was considered as a highly organic one. Class C fly-ash (FA) was derived from a coal plant, and recycled glass (RG) was derived from a local company in Turkey. While RG1 denotes the coarser gradation, RG2 denotes the finer gradation of the recycled glass used in this study.

Sukmak et al. [11] and Horpibulsuk et al. [12] achieved desired levels of unconfined compressive strength when 30% of ash by the dry weight of the soil was added to the silty clay specimens. Eskisar and Altun [10] also proposed using 30% fly ash in the geopolymerization process. Hereby, the ash content of 30% was kept constant during this study. A liquid alkali activator was used to trigger the geopolymerization process. The activator was composed of two compounds, i.e. NaOH and  $\text{Na}_2\text{SiO}_3$ . NaOH (with 97% purity) and  $\text{Na}_2\text{SiO}_3$  (3 modules—40 Baume) were commercially purchased. The concentration of NaOH was 8 molar in the water solution. Coffee waste, recycled glass and fly ash was dry mixed and the liquid alkali activator added to this mixture to achieve a homogenous mixture. Standard Proctor

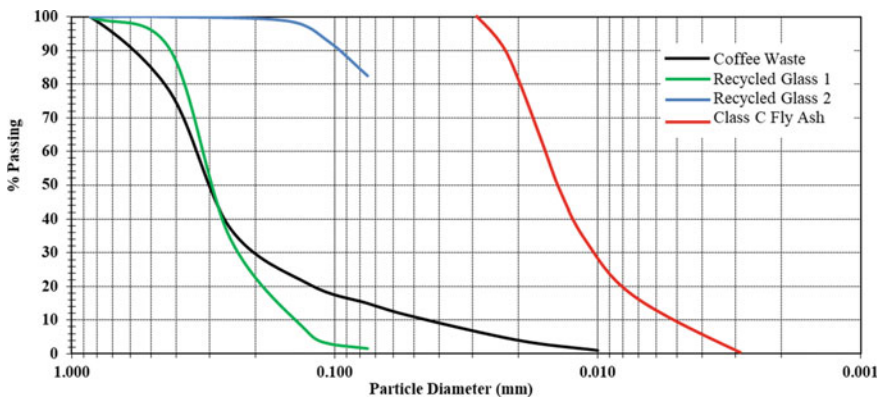


Fig. 1 Grain size distributions of the materials used in this study



tests were performed to achieve the optimum alkali activator contents according to ASTM D698 [13]. Cylindrical specimens with a diameter of 50 mm and a height of 100 mm were prepared for the unconfined compression tests. The specimens were wrapped and sealed to avoid moisture content loss and were cured for 7, 28 or 90 days. The unconfined compression tests were held on the specimens to observe the strength development following ASTM D2166 [14]. The load was applied so as to produce an axial strain at a rate of 1%/min. The rate of strain was chosen so that the time to failure did not exceed 15 min. The loading continued until the load values decreased with increasing strain, or until 15% strain was reached.

### 3 Results and Discussion

#### 3.1 Compaction Tests

The coffee waste (CW), recycled glass (RG) mixtures were treated with two different solutions of  $\text{Na}_2\text{SiO}_3:\text{NaOH}$ . Liquid activator 1 (LA1) and Liquid activator 2 (LA2) contained  $\text{Na}_2\text{SiO}_3:\text{NaOH}$  in ratios of 70–30% and 90–10%, respectively. Class C fly ash (FA) was used as a precursor for the liquid activators. The compaction tests were carried out to determine the optimum liquid activator contents for the specimens. Figure 2 shows the compaction curves of the CWRG geopolymers prepared with liquid activator 1 (LA1).

A point to be considered in this study is the interpretation of compaction results. In soil mechanics, compaction shows the relationship between the dry unit weight of the soil and the water content, while the values taken as a basis in this study express the relationship between the dry unit weight of the mixture and the liquid activator content. The solid part of the  $\text{Na}_2\text{SiO}_3:\text{NaOH}$  solution precipitated as the specimens dried, increasing the unit volume weight of the mixture. For this reason, the effect of the solid part was back calculated when presenting the dry unit weight-liquid activator content relationships in Fig. 2.

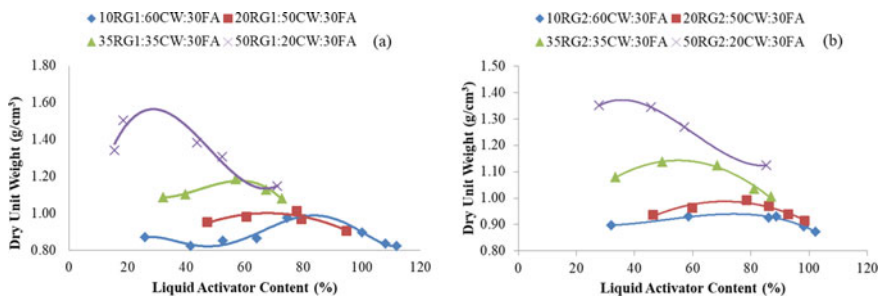


Fig. 2 Compaction curves of CWRG geopolymers a RG1 group and b RG2 group

When RG1 content of the geopolymer was up to 20%, the optimum liquid activator content was around 82% in the mixtures; the optimum amount of liquid activator decreased down to 30% as the amount of RG1 increased. While the optimum liquid activator content was 75% in the specimens with RG2 content up to 20%, it decreased to 49% in the specimens with higher RG2 contents (see 35RG2:35CW:30FA in Fig. 2b), and the change of optimum liquid activator was in a narrower range compared to that of specimens with RG1. The compaction curves of geopolymers containing both RG1 and RG2 tend to move down and to the right as the amount of coffee waste increased. The unit weight of coffee used in this study was 0.45–0.50 g/cm<sup>3</sup>. The addition of such a light material at increasing rates explains the decrease in the dry unit weight of the specimens.

### 3.2 Unconfined Compression Tests

Seven-days specimens were prepared with LA1 (70%Na<sub>2</sub>SiO<sub>3</sub>: 30%NaOH) and LA2 (90Na<sub>2</sub>SiO<sub>3</sub>:10NaOH%) liquid activators in order to evaluate the efficient liquid activator type among the CWRG specimens. RG1 and RG2 types of recycled glass were also separately used in specimen groups. Class C FA was 30% in all the specimens. Eskisar and Altun [10] reported that Class C FA caused an early strength development due to its high amount of calcium oxide casing cementing agents in the medium, therefore, the efficiency of the liquid activator type was evaluated on 7-day specimens.

In Fig. 3, CWRG specimens with LA1 had lower unconfined compressive strengths (UCS) compared to that of CWRG specimens with LA2. The improvement of the strength was emphasized with dashed lines. Figure 3a shows the UCS of specimens with RG1 and Fig. 3b shows the UCS of specimens with RG2.

When CW content was 60% in the geopolymer specimens, the requirement of the liquid activator was at its highest. The UCS of these specimens were relatively lower than the other specimens. On the contrary, when 20% CW was present in the geopolymer specimens, liquid activator need decreased resulting in higher UCS

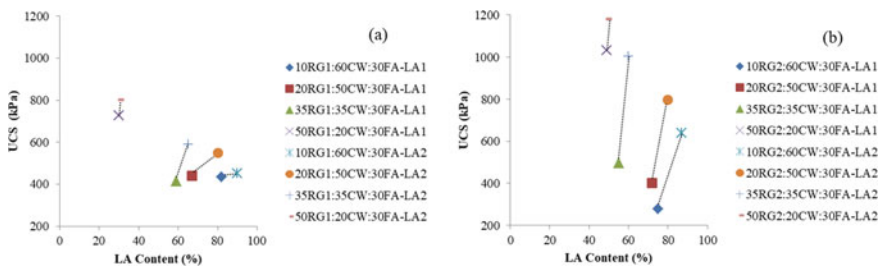


**Fig. 3** Unconfined compressive strength of specimens prepared with different activators **a** specimens with RG1 **b** specimens with RG2 (Class C FA was 30% in all the specimens)

compared to the other specimens. When the liquid activator type was changed from LA1 to LA2, there was a considerable increase in the UCS of the specimens with CW content more than 35%. However, the change of liquid activator was not very efficient on the specimens with a CW content of 20%. The change of the liquid activator from LA1 to LA2 resulted in UCS increase from 727 to 803 kPa in CWRG with RG1 and UCS increase from 1032 to 1182 kPa in CWRG with RG2. It was concluded that LA2 (90%Na<sub>2</sub>SiO<sub>3</sub>:10%NaOH) would provide better improvement by means of the strength. Besides, it was seen that in the early curing period of 7 days, RG2 performed better than RG1 in CWRG geopolymers.

### 3.3 Curing Temperature and Curing Period

The effect of curing temperature was considered in this study. The effective liquid activator and recycled glass types were addressed in the previous section as LA2 and RG2, respectively. The curing temperatures were chosen as  $20 \pm 2$  and  $38 \pm 2$  °C.  $20 \pm 2$  °C was the temperature of the moist room used for conventional curing and  $38 \pm 2$  °C corresponded to the average local summer conditions. The UCS of 28-day CWRG specimens was shown in Fig. 4a.

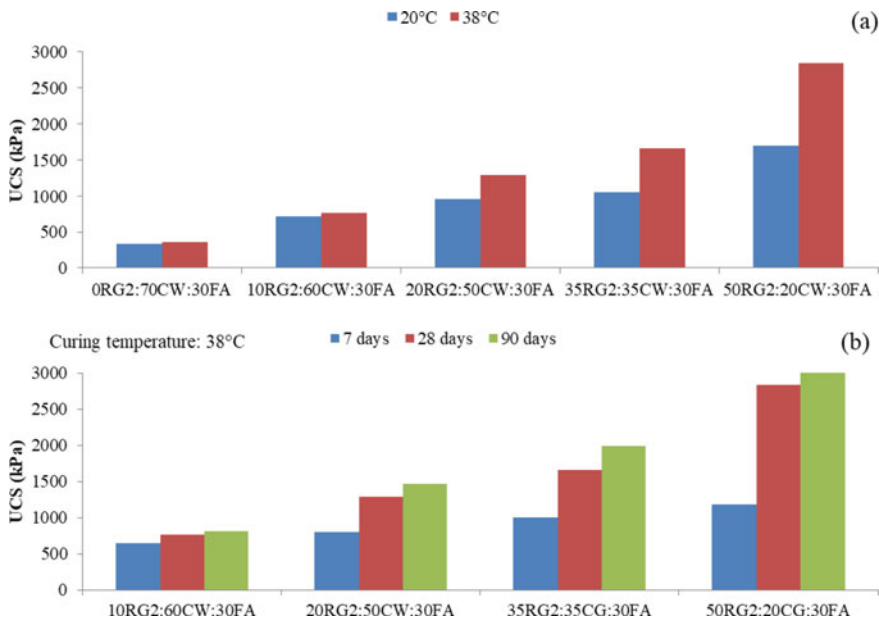


Fig. 4 The effects of a curing temperature and b curing period in CWRG specimens

The specimens cured at  $20 \pm 2$  °C resulted in relatively lower UCS than the specimens cured at  $38 \pm 2$  °C. The effect of temperature on the UCS of specimens was perceptible at 20% RG2 and becoming distinct at 35% RG2 and 50% RG2. When 50RG2:20CW:30FA specimen was cured at  $38 \pm 2$  °C for 28 days, it had a strength of 2847 kPa.

The long term strength development of CWRG specimens with RG2, 30% FA and optimum amount of LA2 were also investigated. The curing temperature was fixed to  $38 \pm 2$  °C. The strength development of the specimens after 28 and 90 days are shown in Fig. 4b. It is evident that geopolymerization is a longer process compared to the well-known methods of stabilization. Kua [15] reported that geopolymerization could be completed from 60 to 90 days. In this study, it was seen that there has been a rapid increment of strength up to 28 days, the increment of strength slowed down from 28 to 90 days. After 90 days, 35RG2:35CG:30FA and 50RG2:20CG:30FA specimens reached 1992 and 3089 kPa, respectively.

## 4 Conclusions

To determine whether CWRG geopolymers could be used as a fill material, their strength characteristics were assessed through unconfined compression tests. Additionally, the effectiveness of geopolymer stabilization in enhancing the mechanical behavior of highly organic waste materials was briefly addressed.

Coffee waste itself is an organic material and subject to biodegradation. However, in this study, it was stabilized with Class C fly ash and with  $\text{Na}_2\text{SiO}_3:\text{NaOH}$ . This process formed a strengthened medium, thus changing the degradation properties of the waste into a non degradable state. The strength development was found to be highest in specimens treated with 50% RG2 type recycled glass, 20% coffee waste and 30% fly ash. Combination of 35% RG2 with 35% coffee waste also gave promising results that could be applied in the field. The strength improvement continued up to 90 days, showing that geopolymerization is a long process compared to the traditional stabilization methods. Besides, importance of curing temperature was emphasized, showing that the field applications could benefit from high summer temperatures where it is available.

If a sustainable stabilization method is created, CWRG geopolymers may be able to remove a considerable amount of trash from landfills. This study demonstrates the feasibility of geopolymer stabilization as a technique for stabilizing highly organic soils, which can reduce the carbon impact of upcoming infrastructure projects.

## References

1. Scully DS, Jaiswal AK, Abu-Ghannam N (2016) An investigation into spent coffee waste as a renewable source of bioactive compounds and industrially important sugars. *Bioengineering* 3(4):33
2. International Coffee Organization (2022) Trade statistics. <https://www.ico.org/prices/new-consumption-table.pdf>. Accessed 01 May 2022
3. Cruz R, Cardoso MM, Fernandes L, Oliveira M, Mendes E, Baptista P, Morais S, Casal S (2012) Espresso coffee residues: a valuable source of unextracted compounds. *J Agricult Food Chem* 60:7777–7784
4. Arulrajah A, Maghoolpilehrood F, Disfani MM, Horpibulsuk S (2014) Spent coffee grounds as a non-structural embankment fill material: Engineering and environmental considerations. *J Clean Prod* 72(11):181–186
5. Turner LK, Collins FG (2013) Carbon dioxide equivalent (CO<sub>2</sub>-e) emissions: a comparison between geopolymer and OPC cement concrete. *Constr Build Mater* 43:125–130
6. Intergovernmental Panel on Climate Change (IPCC) (2005) Carbon dioxide capture and storage: special report. Cambridge University Press, New York
7. Akbari H, Mensah-biney R, Simms J (2015) Production of geopolymer binder from coal fly ash to make cement-less concrete. World of coal ash conferences WOCA. Nashville, USA, pp 1–8
8. Arulrajah A, Kua TA, Phetchuay C, Horpibulsuk S, Mahghoolpilehrood F, Disfani MM (2016) Spent coffee grounds–fly ash geopolymer used as an embankment structural fill material. *J Mater Civil Eng* 28(5):04015197
9. Arulrajah A, Kua TA, Horpibulsuk S, Mirzababaei M, Chinkulkijniwat A (2017) Recycled glass as a supplementary filler material in spent coffee grounds geopolymers. *Constr Build Mater* 151:18–27
10. Eskisar T (2021) Altun S (2021) Strength properties of coffee waste based geopolymers. In: Reddy KR, Agnihotri AK, Yukselen-Aksoy Y, Dubey BK, Bansal A (eds) Sustainable environment and infrastructure. Lecture notes in civil engineering, vol 90. Springer, Cham
11. Sukmak P, Horpibulsuk S, Chen SL (2013) Strength development in clay-fly ash geopolymer. *Constr Build Mater* 40(3):566–574
12. Horpibulsuk S, Suksiripattanapong C, Samingthong W, Rachan R, Arulrajah A (2016) Durability against wetting-drying cycles of water treatment sludge-fly ash geopolymer and water treatment sludge-cement and silty clay-cement systems. *J Mater Civil Eng* 28(1):04015078
13. ASTM D698 (2012) Standard test methods for laboratory compaction characteristics of soil using standard effort (12,400 ft-lbf/ft<sup>3</sup> (600 kN/m<sup>3</sup>)). ASTM International, West Conshohocken, PA
14. ASTM D2166 (2016) Standard test method for unconfined compressive strength of cohesive soil. ASTM International, West Conshohocken, PA
15. Kua TA (2017) Application of spent coffee ground as a road subgrade construction material. PhD Thesis, Swinburne University of Technology

# Research on the Contribution of Copper and Ferro-chrome Slags to the Thermal Conductivity of Buffer Materials Around Energy Geo-structures



Cihat Asci  and Yeliz Yukselen-Aksoy 

**Abstract** In the present study, it was aimed to develop a thermally conductive soil materials for energy geo structures so that increase the performance of energy geostructures. In general, slags are known as high level hazardous waste. However, copper slag and ferro-chrome slag were chosen as soil additives because their contaminant levels are low. In this research, slags were used in sand-bentonite and bentonite mixtures in order to increase thermal conductivity of soils for the geo-energy structures such as heat piles and nuclear waste repositories. The thermal conductivities of the samples were measured at various dry unit weight and optimum water content values and the thermal conductivity range of the mixtures will be given.

**Keywords** Copper slag · Ferro chrome slag · Thermal conductivity · Energy geo-structures

## 1 Introduction

Turkey is heavily dependent on foreign sources to meet its energy needs. According to the end of May 2022 data, the energy needs are provided by 31.3% hydraulic energy, 25.1% natural gas, 20.3% coal, 10.9% wind, 8.3% solar energy, 1.7% of geothermal and 2.4% of other resources [1]. In particular, Turkey continues to be dependent on foreign sources for fossil fuels such as oil and natural gas [2]. It is important to ensure energy supply security, reduce the risks of foreign dependency, protect the environment, and use energy efficiently and providently in the fight against

---

C. Asci (✉)

The Graduate School of Natural and Applied Sciences, Dokuz Eylül University, İzmir, Turkey  
e-mail: [asci.ahat@ogr.deu.edu.tr](mailto:asci.ahat@ogr.deu.edu.tr)

Y. Yukselen-Aksoy

Civil Engineering Department, Dokuz Eylül University, İzmir, Turkey  
e-mail: [yeliz.yukselen@deu.edu.tr](mailto:yeliz.yukselen@deu.edu.tr)

climate change [1]. It is aimed to meet 10% of the energy need with the establishment of nuclear power plants. It also plays an important role in the fight against climate change, with zero carbon emissions during operation [1].

It is targeted to increase the energy efficiency of energy geo-structures and to develop soil materials suitable for the nuclear waste disposal. Sand-bentonite and additives are used in energy geo-structures such as heat piles, high energy cables, ground heat exchange systems, as the soil is desired to have more strength. At the nuclear waste disposal area, bentonite and additives are used for providing properties of swelling, sealing, and low permeability [3].

The gradual increase in amount of industrial wastes and the high costs of waste disposal methods have made it common to use these wastes in different production processes [4]. Especially, blast furnace slag is no longer a waste material and has become an intermediate product with economic value [4]. Previous researches have shown that these slags can be mixed with natural soil and can be used as road embankment [5–13]. Slags possess properties such as high-volume mass, volume stability, good abrasion resistance to wear and crushability [13]. During copper production, ~ 2.2 tons of slag is produced from one ton of copper [5]. One ton of ferrochrome produces between 1.1 and 1.6 tons of slag [13]. The use and recycling of these slags is important in terms of sustainability, environmental health, and economy.

## 2 Literature Review

Past studies have proven that copper and ferrochrome slags are suitable for use in road construction [5]. These slags are used in sub-grade, sub-base, and bitumen mixes and are also suitable for use in soil improvement and fillings embankment construction, land reclamation [5–14]. Moreover, it could be used instead of sand used in backfill for retaining walls and shallow foundations as a construction material [5, 6, 8]. The grain size of the slag used by the researchers generally corresponds to aggregate or sand [5–8, 10, 11, 14]. Ferrochrome slag could be used in stone columns due to its high strength, hardness, and resistance to abrasion [11]. Copper slag could be used in place of sand in sand piles and sand drains, also it could obtain good results when mixing with expanding soils [5]. Copper slag increases the bearing capacity and stability due to angularity and high internal friction angle, it is also frost resistant and has high permeability [8, 10, 14]. Ferrochrome slag is also known to be resistant to freezing [12].

Yılmaz and Süttaş [4] compared natural aggregate and ferrochrome slag. According to the Los Angeles test results, ferrochrome slag showed higher wear resistance. Freeze–thaw resistance and CBR values of ferrochrome slag were 31% and 33% higher than natural aggregate, respectively. Maximum dry unit weight of ferrochrome slag was higher at optimum water content. In the mixtures made with binders, the unconfined compressive strength value was found to be considerably higher than the natural aggregate [4].

Lavaya et al. [6] reviewed on the mixtures of 30% copper slag, 70% local soil, and a small amount of fly ash. It was observed that plasticity index of soil decreased. Because the copper slag contains coarse particles, the free swelling index of the soil significantly reduced and provided to control the swelling properties of the expanding clays. According to the results of Proctor test, maximum dry unit weight increased, optimum water content decreased. A significant increase in CBR value was observed. Also, unconfined compressive strength of soil increased by 50%, due to the high internal friction angle of the copper slag [6]. Patel et al. [7] investigated the mixture of copper slag and fly ash for the use of the subbase course of the flexible pavements. Fly ash was added to the mixtures at a rate of 10–20–30–40%. Unconfined compressive strength value increased up to 30%, then decreased. It was observed that unconfined compressive strength increased with increasing curing time. It was determined that the CBR value increased with the curing time [7] with mixture of 70% copper slag-30% fly ash. It was found that as the copper slag ratio in the mixture increased, maximum dry unit weight increased, optimum water content decreased, liquid limit and plastic limit decreased, CBR and internal friction angle values increased [10]. Nawagamuwa and Madushanka [15] conducted experiments on mixing copper slag and soft soil in various proportions. It was observed that as the copper slag content was increased in the soil, the optimum water content decreased and the dry unit weight increased up to 35%. It was also reported that CBR value increased by 15%, so the soil became suitable for use as a sub-grade with addition of copper slag. According to the direct shear test results, the cohesion and the internal friction angle increased significantly [15].

It is known that the thermal conductivity values of soils depend on the degree of saturation, dry unit weight, mineralogy, void ratio, temperature, structure of the soil [3, 16, 17]. It can be said that the degree of saturation and dry unit weight are the parameters that most affect the thermal conductivity behavior [16]. Former studies have shown that the thermal conductivity value increases with the increase in degree of saturation and dry unit weight [3, 16]. When all the voids are filled with water, the change in the thermal conductivity value is negligible. The thermal conductivity value can be increased by increasing the contact surface between the particles by filling the voids with fine materials [18]. The thermal conductivity values of the materials that make up the structure of the soil are given in Table 1 [19].

**Table 1** Thermal conductivity of materials [19]

Material	Thermal conductivity (W/mK)
Quartz	8.8
Clay minerals	3
Organic matter	0.3
Water	0.57
Air	0.025
Ice	2.2



The thermal conductivity of the soil increases linearly as the temperature increases at positive temperatures [16]. At negative temperatures, with the freezing of water, the thermal conductivity of soils increases rapidly at first and then increases slowly [16]. This is because the thermal conductivity of ice is higher than water [16, 17].

### 3 Material and Method

#### 3.1 Material Characterization

Sand, bentonite, copper slag and ferrochrome slag were used in this study. The sand was taken from the Izmir region. Bentonite, a calcium bentonite activated with sodium bicarbonate, was obtained from Ünye Madencilik. Copper slag was supplied from Radöksan Metalurji ve Maden San. Tic. Ltd. Şti. Ferro chrome slag was supplied from Eti Krom A.Ş. The properties of the materials are given in the Table 2.

Most of the slags consist of oxides [16]. A typical copper slag consists of 30–40% Fe, 35–40% SiO<sub>2</sub>, ≤ 10% CaO, ≤ 10% Al<sub>2</sub>O<sub>3</sub>, 0.5–2% Cu and others (Co, Zn, Ni, Mn) [20]. The content of Ferrochrome slag received from Eti Krom A.Ş. is given in Table 3.

**Table 2** Physico-chemical properties of the materials

	Sand	Bentonite	Copper slag	Ferrochrome slag
Specific gravity	2.65	2.6	3.22	3.43
Liquid limit	–	270	–	–
Plastic limit	–	63	–	–
Sieve size	-No.6	-No.200	-No.40	-No.40
Natural water content (%)	0.8	6	0.8	1.2

**Table 3** Content of ferrochrome slag

	Al <sub>2</sub> O <sub>3</sub>	C	Cr <sub>2</sub> O <sub>3</sub>	SiO <sub>2</sub>	Cr/ Fe	CaO	Fe <sub>2</sub> O <sub>3</sub>	MgO	(MgOCaO)/ Al <sub>2</sub> O <sub>3</sub> )
	(%)								
Ferrochrome slag	24.34	0.32	3.63	31.94	2.88	0.69	1.23	37.68	1.58

**Fig. 1** Tempos and TR-3 probe



### ***3.2 Experimental Apparatus and Procedures***

TEMPOS thermal analyzer and TR-3 sensor (length: 10 cm width: 2.4 mm) were used for the thermal conductivity measurements. The TR-3 probe measurement range is 0.1 ~ 4.0 W/(mK), and the accuracy is  $\pm 10\%$  from 0.2 to 4.0 W/(mK) [21] (Fig. 1).

The soils and slags were used without drying. Samples were prepared at the targeted water content and kept in plastic bags for at least 16 h for uniform distribution of water in the soil samples. Samples were prepared at different water content values in order to get Proctor curve. The thermal conductivity values were measured by inserting the TR-3 sensor into the midpoint of the compacted samples. After waiting for at least 15 min for the sensor and the soil to reach thermal equilibrium, at least three measurements were taken within 15 min. Measurements were taken at room temperature and the sample was isolated from the external environment.

## **4 Results and Discussion**

In this study, the effect of copper and ferrochrome slags on the thermal conductivity of sand-bentonite mixtures was investigated. At least four samples were prepared for each curve according to the water contents and dry unit weight values obtained from the Standard Proctor tests. Thermal conductivity test results are shown in Table 5.

The sand-bentonite and sand-bentonite-slag mixtures were prepared according to their percentages. In this study, 80% sand-20% bentonite (80S-20B) mixtures were used. Slags were added as 10% in the mixtures. For example, when 10% slag is added to 80S-20B, 10 of 100 g of total sample is slag, 72 g is sand, 18 g is bentonite, and these mixtures are called 72S-18B-10CS/FS. The Standard Proctor test results of 80S-20B and 80S-20B-Slag mixtures are shown in Fig. 2.

Maximum dry unit weight and optimum water content values of 80S-20B and 80S-20B-slag mixtures are given in Table 4.

When copper and ferrochrome slag were added to sand-bentonite mixture as additives, it was seen that the maximum dry unit weight increased and the optimum water content decreased. Thermal conductivity test results of sand-bentonite and mixtures are shown in Table 5.

In 80S-20B mixtures, copper slag increased by 8% on average, while ferrochrome slag increased by 17% the thermal conductivity values. The study is in agreement with the previous results from literature. The variation of thermal conductivity values showed consistency depending on the dry unit weight and water content of the mixtures. The high water content zones of the Compaction curves where the dry unit weight decreases, the thermal conductivity values continue to increase. However, when the soil is saturated with water, the thermal conductivity values remain approximately constant or decrease depending on the dry unit weight.

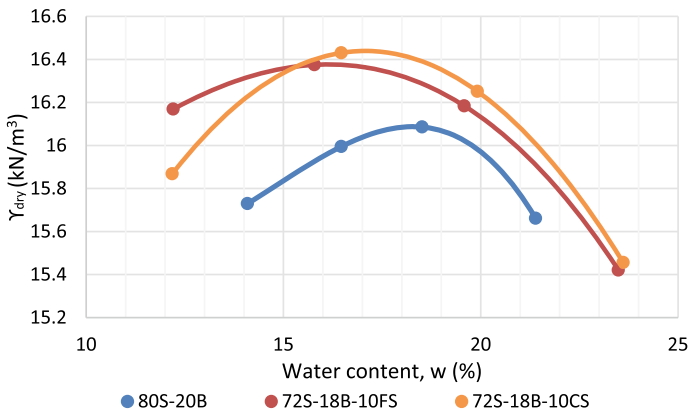


Fig. 2 80S-20B and 80S-20B-slag mixtures proctor results

Table 4 The optimum water content and maximum dry unit weight values of sand-bentonite and sand-bentonite mixtures

	80S-20B	72S-18B-10CS	72S-18B-10FS
$\gamma_{dry\ max}$ (kN/m <sup>3</sup> )	16,088	16,442	16,353
$w_{opt}$ (%)	18.3	17.1	16.0

**Table 5** Thermal conductivity results of sand-bentonite and sand-bentonite mixtures

Samples	$\gamma_{\text{dry}}$ (kN/m <sup>3</sup> )	Water content	$\gamma$ (kN/m <sup>3</sup> )	Thermal conductivity (W/mK)
80S-20B	15.79	0.14	18.05	1.531
	15.89	0.16	18.44	1.712
	16.09	0.18	19.03	1.906
	15.89	0.20	19.13	1.838
72S-18B-10CS	15.99	0.12	17.85	1.336
	16.58	0.16	19.13	1.860
	16.28	0.20	19.52	1.973
	15.50	0.24	19.13	1.877
72S-18B-10FS	16.19	0.12	18.15	1.604
	16.38	0.16	18.93	2.006
	16.09	0.20	19.33	2.052
	15.40	0.24	19.03	1.906

## 5 Conclusions and Recommendation

The results of the present study have shown that, slags increase the thermal conductivity, but the effect of ferrochrome slag on thermal conductivity is more pronounced than copper slag. According to the thermal conductivity values, copper slag increased by 8% on average whereas ferrochrome slag climbed by 17%.

In order to increase the thermal conductivity of sand-bentonite mixtures, the use of higher proportions of slag should be investigated. In addition, since these slags may affect the drainage conditions and the hydraulic conductivity value is an important parameter for nuclear disposal area, the effect of additives on the hydraulic conductivity should be investigated.

It is recommended to use sand-bentonite mixtures in applications where the soil requires strength. In order to adjust the desired hydraulic conductivity values of sand-bentonite mixtures, bentonite ratio may be changed. However, as the amount of bentonite increases, the thermal conductivity value will decrease, so it would be appropriate to increase the thermal conductivity values by using slag additives.

**Acknowledgements** This study is supported by The Scientific and Technological Research Council of Turkey (TÜBİTAK) (Grant no. 120M470). The authors are grateful for this support. Also appreciated to Radöksan Metalurji ve Maden San. Tic. Ltd. Şti. and Eti Krom A.Ş for the support of the slags.

## References

1. T.C. Enerji ve Tabii Kaynaklar Bakanlığı. <https://enerji.gov.tr/bilgi-merkezi-enerji-elektrik>. Accessed 01 July 2022
2. Kavaz İ (2019) Türkiye'nin Enerjide Gelecek Vizyonu. *Seta* 152:1–5
3. Chen Y, Liu X, Mu X, Ye W, Cui Y, Chen B, Wu D (2018) Thermal conductivity of compacted GO-GMZ bentonite used as buffer material for a high-level radioactive waste repository. *Adv Civil Eng* 1:1–11. <https://doi.org/10.1155/2018/9530813>
4. Yılmaz A, Süttaş İ (2008) Ferrokrom Cürufunun Yol Temel Malzemesi Olarak Kullanımı. *Teknik Dergi* 19:4455–4470
5. Tandel Y, Patel JB (2009) Review of utilisation of copper slag in highway construction. *Aust Geomech* 44:71–80
6. Lavanya C, Rao AS, Kumar ND (2011) A review on utilization of copper slag in geotechnical application. In: *Proceedings of Indian geotechnical conference, Kochi, India*, pp 445–448
7. Patel SR, Shahu JT, Senapati AK (2012) Feasibility of copper slag–fly ash mix as a road construction material. *ACEE Int J Transp Urban Dev* 2(1):11
8. Chandrshekar J, Chokshi TA, Chauhan DV (2015) A review on utilization of waste material “copper slag” in geotechnical applications. *IJIRST Int J Innov Res Sci Technol* 1(12):246–250
9. Poriya D, Pitroda J, Raval A (2019) Sustainable construction material—copper slag: a review. *Int J Eng Res* 8(4):10–15
10. Havanagi VG, Mathur S, Prasad PS, Kamaraj C (2007) Feasibility of copper slag–fly ash–soil mix as a road construction material. In: *Transportation research record: journal of the transportation research board*, No. 1989, Vol 2. Transportation Research Board of the National Academies, Washington, DC, pp 13–20. <https://doi.org/10.3141/1989-43>
11. Reddy CNV, Sanghamitra B (2017) Potential of ferro chrome slag as construction material. *Indian Highways* 45:11–17
12. Yılmaz A, Kardeşin M (2009) Mechanical properties of ferrochromium slag in granular layers of flexible pavements. *Mater Struct Materiaux et Constructions* 43:309–317. <https://doi.org/10.1617/s11527-009-9490-2>
13. Al-Jabri K (2018) Research on the use of Ferro-Chrome slag in civil engineering applications. *MATEC Web Conf* 149:01017. <https://doi.org/10.1051/mateconf/201714901017>
14. Vapur H, Top S, Teymen A, Türkmenoğlu M (2013) Elazığ Ferrokrom Tesisi Cürufunun Agregat Özelliklerinin Araştırılması. Investigation of the Aggregate Properties of Elazığ Ferrochrome Plant Slags, Çukurova Üniversitesi Mühendislik-Mimarlık Fakültesi Dergisi 28:77–88
15. Nawagamuwa U, Madushanka HK (2020) Ground improvement with waste copper slag. [https://www.researchgate.net/publication/344832088\\_Ground\\_Improvement\\_with\\_Waste\\_Copper\\_Slag](https://www.researchgate.net/publication/344832088_Ground_Improvement_with_Waste_Copper_Slag)
16. Nikoosokhan S, Nowamooz H, Chazallon C (2015) Effect of dry density, soil texture and time-spatial variable water content on the soil thermal conductivity. *Geomech Geoeng* 11:1–10. <https://doi.org/10.1080/17486025.2015.1048313>
17. Li R, Zhao L, Wu T, Wang Q-X, Ding Y, Yao J, Wu X, Hu G, Xiao Y, Du Y, Zhu X, Qin Y, Shuhua Y, Bai R, Erji D, Liu G, Zou D, Yongping Q, Shi J (2019) Soil thermal conductivity and its influencing factors at the Tanggula permafrost region on the Qinghai-Tibet Plateau. *Agricult For Meteorol* 264:235–246. <https://doi.org/10.1016/j.agrformet.2018.10.011>
18. Ahn J, Jung J (2017) Effects of fine particles on thermal conductivity of mixed silica sands. *Appl Sci* 7:650. <https://doi.org/10.3390/app7070650>
19. Ochsner T (2019) Rain or shine an introduction to soil physical properties and processes. Oklahoma State University Libraries, Oklahoma, p 283
20. Uysal F, Bahar S (2018) Cüruf Çeşitleri ve Kullanım Alanları. *Trakya Univ J Eng Sci* 19(1):37–52
21. METER Group, Inc. (2018) TEMPOS thermal analyzer manuel. Meter Group

# Modeling Water Retention Curve of GCL Exposed to Pore Fluid with Solute Concentrations



Ali Golaghaei Darzi, Hamed Sadeghi, Aysa Hedayati-Azar,  
and Poya Alipanahi

**Abstract** Geosynthetic clay liners (GCLs) are synthetic materials manufactured and widely used in geotechnical and geoenvironmental engineering due to their very low permeability and ease of use. As the most critical function of GCLs are their isolating features, it is of primary importance to precisely predict their water retention properties, especially when subjected to impure water having considerable solute concentrations because of landfill leachate. Despite numerous efforts on analytical modeling of bare soil-distilled water retention, less attention has been given to the retention characteristics of GCLs. Therefore, the current study's primary goal is to introduce a new analytical GCL-water retention model. More importantly, the selected experimental data for validation of the model comprises permeating solution with different molar concentrations along the wetting path to idealize leachate characteristics more reliably during the hydration process. The presented model is an extension of the original van Genuchten model for bare soil and pure water. The novelty of the proposed modeling approach is incorporating a new parameter, namely the pore fluid salinity index (PSI) through which, considering the influence of pore fluid chemistry on retention properties of different types of GCLs, becomes possible. The model can simply be calibrated by using a series of retention data in the presence of distilled water and one salinity level. The results also reveal the new model's robustness in capturing the retention behavior of GCLs under the influence of leachate.

**Keywords** Water retention · Isolating barrier · Leachate chemistry · Landfill

---

A. G. Darzi (✉) · H. Sadeghi · A. Hedayati-Azar · P. Alipanahi  
Sharif University of Technology, Tehran, Iran  
e-mail: [ali.golaghaei@sharif.edu](mailto:ali.golaghaei@sharif.edu)

H. Sadeghi  
e-mail: [hsadeghi@sharif.edu](mailto:hsadeghi@sharif.edu)

A. Hedayati-Azar  
e-mail: [aysa.hedayati9776@sharif.com](mailto:aysa.hedayati9776@sharif.com)

P. Alipanahi  
e-mail: [Pouya.alipanahi@sharif.edu](mailto:Pouya.alipanahi@sharif.edu)

## 1 Introduction

Geosynthetic clay liners (GCLs) are industry-manufactured materials that are broadly used in geotechnical and geoenvironmental engineering due to their very low permeability ( $<10^{-10}$  m/s) and ease of use [1]. They are usually used as geo-composite barrier systems for industrial artificial ponds, such as brine ponds on coal-seam gas extraction sites and solar ponds in thermal energy facilities [2, 3]. GCLs consists of a thin layer of bentonite (about 5–12 mm in thickness) sandwiched between two geosynthetic layers [4]. The geosynthetics used in GCLs can be both geotextile and geomembrane. In the first case, the GCLs are bonded with an adhesive, needle-punching, or stitch-bonding. It is worth noting that the needle punching process causes some fibers from the top geotextile to pass through the bentonite and bottom geotextile, bonding the whole structure together. Alternatively, the reinforcement by sewing the entire geotextiles bentonite composite and parallel rows of stitch-bonded yarns can be carried out. However, in the second case, the geomembrane is attached to the bentonite using a nonpolluting adhesive. In addition, a thin open weave spun-bound geotextile adhered to the bentonite, which is used for protection purposes during the installation process [5].

Some of the main advantages of GCLs are easy installation, cost-effectiveness, very low hydraulic conductivity to water, bearing large differential settlement of underlying soil or waste, no dependence on the availability of local soils, easy to repair, and low thickness. On the other hand, low shear strength of hydrated bentonite, punching during or after installation, bentonite loss during placement, the gas breakthrough at low moisture content, and potential stability problems at interfaces with other materials, the tendency to cations exchange. More importantly, significant changes in hydraulic and volumetric characteristics may occur due to exposure to different concentrations of salt existing in the landfill leachate [2–5].

GCLs are installed in a low saturation state and are allowed to reach the appropriate moisture level by absorbing water from the underlying subsoil [3, 6–10]. In other words, they are exposed to a hydration process until approaching the full saturation state. Indeed, the sealing behavior is not fully mobilized until the bentonite layer's gravimetric water content becomes more than 100% [7, 11]. The hydration process depends mainly on the availability of aqueous liquid adjacent to the GCL. Therefore, it can be inferred that the full hydration of GCL not only depends on its retention properties but also the hydraulic state of surrounding soils or wastes [7, 10–13].

Soil–water retention curve (SWRC), in a simple word, describes the relationship between soil suction and water content [14–16]. Due to the critical hydraulic behavioral facts mentioned in the previous paragraphs [3–5], it is essential to know the water retention behavior of GCLs, especially when exposed to a saline environment. Current modeling approaches in the literature considering different aspects of SWRC can be categorized into four general groups [16, 17]: parametric models, soil particle size-dependent models, soil pore size-dependent models, and pedotransfer functions. Although many models have been presented for the bare soils so far, only a few models are specifically developed for the water retention behavior of GCL.

Ghavam-Nasir et al. [18], for example, investigated the effects of temperature and volume change on both drying and wetting water retention branches of GCLs, using theories of Grant and Salehzadeh [19] and Gallipoli [20] in van Genuchten [21] and Fredlund and Xing [22] SWRC models. However, there has been no model so far for dealing with the retention behavior of GCLs exposed to various pore water salinity conditions. It is also worth mentioning that, according to the published experimental results, pore fluid chemistry causes a significant change in the retention characteristics of GCLs. Therefore, this study aims to provide a simplistic yet precise modeling approach to simulate GCL-water retention behavior based on minimal experimental data, excluding advanced testing requirements. The proposed model is purposely developed to simulate the hydration process of GCLs exposed to different salt solution concentrations with a new chemical-based parameter, namely the pore fluid salinity index (PSI). Details on the development, calibration procedure, and validation of the new model are presented and discussed in this paper.

## 2 Experimental Studies on the Water Retention of GCLs

Different laboratory methods have been proposed to study the retention behavior of GCLs, which can be generally classified into two groups [13]: suction control methods and moisture control methods. In suction control methods, the specimen is subjected to predetermined suction, while variations in water content and volume change are recorded. On the other hand, in moisture control methods, the water content is adjusted through a stepwise procedure while the corresponding suction and volume change are evaluated. Suction control methods include axis translation methods and osmotic and vapor equilibrium techniques. However, in moisture control methods, suction can be measured by various methods such as filter paper, tensiometer [23], thermocouple psychrometer, or relative humidity sensor [3, 6, 7, 13]. Abuel and Bouazza [13] reviewed both methods' performance and concluded that the moisture control method would be better for the GCLs configuration and conditions. Some of the laboratory approaches performed in the last decade are summarized in Table 1. The main differences between GCLs include the mineralogy and the type of bentonite (powder or granular and sodium or calcium, etc.) used in the GCL, the type of geotextile (woven or non-woven) or the addition of geomembranes, and the method of bonding. These cases are usually beneficial in the results of GCL retention behavior, and some of these cases were also mentioned in Table 1 [2, 6, 7, 13].

Many researchers have reported that in some site conditions where GCLs are installed, the subsoil has a high salt concentration in pore fluid [7]. However, several experimental studies have been conducted to evaluate the effect of pore water salinity on the hydraulic conductivity of GCLs, but research on hydraulic features of GCLs considering pore fluid salinity is somewhat limited [3]. On the other hand, recent experimental evidence proved the significant role of fluid salinity on SWRC, swelling and collapse potential, hydraulic conductivity, and compressibility [24–28].



**Table 1** Summary of the published experimental studies on GCL-water retention [6]

Paper	Suction measurement methods	Hydraulic path	Bentonite type	Cover geotextile	Carrier geotextile
Acikel et al. [32]	Filter paper	Wetting	Granular sodium	Non-woven	Woven
Bannour et al. [33]	Osmotic	Wetting	Granular sodium	Woven	Non-woven
Beddoe et al. [34]	High-capacity tensiometer and relative humidity sensors	Wetting and drying	Granular sodium	Woven and non-woven	Non-woven
Abuel-Naga and Bouazza [13]	Relatively humidity sensor and thermocouple psychrometer	Wetting	Powder sodium	Impregnated non-woven	Non-woven reinforced by silt fil
Southen and Rowe [35]	Axis translation	Drying	Granular and powder sodium	Virgin staple fiber	Slit-film woven
Bouazza et al. [36]	Thermocouple psychrometer	Wetting	Powder sodium	Impregnated non-woven	Non-woven reinforced by silt fil
Barroso et al. [37]	Filter paper	Wetting	Powder and granular	Non-woven	Woven
Lu et al. [3]	WP4C	Wetting	Powder sodium and granular sodium	Non-woven slit-film and woven	Woven and non-woven
Lu et al. [6]	WP4C	Wetting	Powder sodium	Non-woven	Woven
Yu1 and El-Zein [2]	Filter paper and vapour sorption analyzer test	Drying	Granular Na-bentonite and granular polymer	Non-woven	Woven and non-woven

Lu et al. [3, 6] investigated the wetting branches of GCL-WRC using a moisture control approach, implying that the corresponding total suction was measured using a WP4C device for different amounts of sodium chloride solution. The specimen was positioned in the device housing chamber under the sealed condition to achieve vapor equilibrium with the surrounding environment. The chamber included an infrared thermometer to measure the specimen temperature and a controlled cooled surface (chilled-mirror) to measure the dew-point using an optical sensor. According to Kelvin's equation, the total soil suction was determined. The experiments were conducted under constant volume conditions [6]. The results of this experiment will be discussed in more detail in Sect. 4.

Another recent experiment in this field was performed by Yu and El-Zein [2]. The WRC of three different types of GCLs hydrated with deionized water, and a 0.325 mol/L Na-based solution (NaCl, NaHCO<sub>3</sub>, and Na<sub>2</sub>CO<sub>3</sub>) was investigated. Higher air-entry values and steeper slopes of SWRCs between the two inflection points for the samples hydrated with synthetic brine are the most important result of this research. It is also worth mentioning that one of the samples was made of bentonite modified with polyacrylamide polymer. The results revealed that the polymer's addition increased the water retention of the GCL under both deionized water and brine hydration. However, it was shown that brine hydration caused a significant reduction in the bentonite's total liquid masses compared to deionized water.

According to some recent experimental evidence, it can be understood that the retention behavior of GCLs is of great importance. However, a few models have been presented so far to investigate this issue. Therefore, an attempt is made to present an approach based on precise but straightforward principles that can be used to investigate the wetting retention behavior of GCLs hydrated with different salts solution. In the next section, the theoretical framework for the new model is presented.

### 3 The Newly Proposed GCL-WRC Model for Different Salt Solution Concentrations

One of the pioneering SWRC models was proposed by van Genuchten [22], which is a smooth three-parameter model expressed according to Eq. (1):

$$w = w_r + (w_s - w_r) \left[ 1 + (a\psi)^n \right]^{-m} \quad (1)$$

where  $w$  is gravimetric water content,  $w_r$  is the residual gravimetric water content, and  $w_s$  is saturated gravimetric water content,  $\psi$  represents the soil suction,  $a$  is the model parameter related to air entry value,  $n$  is related to the pore size distribution, and  $m$  can reflect the overall symmetry of the retention curve, which also can be expressed as a function of parameter  $n$  [25, 29]. This model has been extensively used as a benchmark in the development of many subsequent SWRC models. For example, Gallipoli [20] modified the van Genuchten [21] model by considering the void ratio effects. Zhou et al. [30] also developed the model proposed by Gallipoli [20] to include microstructural evolution due to hydro-mechanical loading, determined from the MIP test results. According to Eq. (1), it can be understood that the three primary parameters of the van Genuchten model are the parameters  $a$ ,  $n$ , and  $m$ , used to define the water retention behavior mathematically. The implication is that a wide range of factors affecting retention behavior can be considered according to the literature if these three parameters are modified and enhanced. Based on this rationale, Eq. (1) is extended in this study to incorporate the influence of pore fluid salt concentration into the GCL-WRC modeling according to Eq. (2).

$$w = w_r + (w_s - w_r) \left[ 1 + (a^* \psi)^{n^*} \right]^{-m^*} \quad (2)$$

where  $a^*$ ,  $n^*$ , and  $m^*$  are the modified parameters of the van Genuchten model. These three parameters are defined as a function of a new parameter, namely pore fluid salinity index (PSI), according to Eqs. (3), (4), and (5), respectively.

$$a^* = a \text{PSI}^\alpha \quad (3)$$

$$n^* = n \text{PSI}^\beta \quad (4)$$

$$m^* = m \text{PSI}^\gamma \quad (5)$$

where  $\alpha$ ,  $\beta$ , and  $\gamma$  are three new model parameters used to consider the influence of solute concentrations on the original physics-based parameters of the van Genuchten model, i.e.,  $a$ ,  $n$ , and  $m$ . More importantly, the inclusion of PSI into the modified parameters makes it possible to consider the effects of osmotic suction caused by the pore fluid concentration. This new concept is formulated according to Eq. (6).

$$\text{PSI} = 1 + \frac{\pi}{\psi_0} \quad (6)$$

where  $\pi$  is the osmotic suction, and it can be calculated using the van't Hoff expression according to Eq. (7), and  $\psi_0$  denotes a reference suction (1 MPa in this study) with the same unit as the osmotic suction to make it dimensionless.

$$\pi = i R T M \quad (7)$$

where  $i$  is the number of ions for the salt dissolved in solution (e.g., 2 for NaCl),  $R$  is the universal gas constant equals to 8.32 J/(mol. K),  $T$  is the absolute temperature in Kelvin and  $M$  is the molar concentration [31]. It is also important to note that Eq. (6) has a smooth transition from positive concentration to the null value corresponding to the distilled water. In other words, the new model is smoothly transformed into the original form of the van Genuchten model with no extra effort. This issue is of primary importance for the application of the new model in numerical simulations.

It should be noted that there is no consensus on the interpretation and definition of the residual gravimetric water content ( $w_r$ ) in the literature. Some researchers consider this parameter only a fitting parameter with no specific physical meaning, while others consider it corresponding to a physical state where the water phase becomes discontinuous [16, 17]. According to the experimental observations, salinity mainly affects the water retention behavior at a suction range limited to the residual state. In contrast, all the retention curves are assumed to converge to that of the distilled water at a high suction range beyond the residual state independent of salt concentrations [25, 30].

Therefore, the value of  $w_r$  is assumed as a constant independent of salinity conditions. In other words, the retention data of distilled water is used to induce the residual water content for the GCLs under consideration. As a consequence, the present model contains three extra parameters to the original van Genuchten model or six parameters in total. The performance of this modeling approach in predicting the GCL-WRC in the presence of different salt solution concentrations is explained and validated in the following section.

## 4 Model Predictions and Validation Against Experimental Results

In this section, the validity of the new formulation presented in the previous section will be examined. For this purpose, the results of Lu et al. [6]'s experiment focusing on the determination of the wetting branch of the GCL water retention curve are employed. The retention data were evaluated following the moisture control method under constant volume conditions using a WP4C device. The results are available for six different concentrations of sodium chloride diffused to the Na bentonite, which has a cation exchange capacity of more than 70 meq/100 g. The approximate thickness of the GCL used was 5.4 mm, with a hydraulic conductivity of less than  $2 \times 10^{-11}$  m/s. Besides, the mass per unit area of the GCL varied from 4138 to 4452 g/m<sup>2</sup>. The needle-punched cover and carrier geotextile type used was non-woven and woven, respectively. To validate the proposed model, the following three steps must be taken. First, the value of  $w_r$  and  $w_s$  should be determined. According to Lu et al. [6],  $w_s$  are equal to 0.8, and  $w_r$  is equal to 0.04. According to the previous section's discussion, the value of  $w_r$  is assumed independent of the salt level, and so, it can be determined from the distilled water curve at a relatively high suction range (e.g., above 1400 kPa). Second, the van Genuchten model's three primary parameters, i.e.,  $a$ ,  $n$ , and  $m$ , should be calibrated according to the retention data corresponding to the distilled water. Third, using a series of SWRC for salt solution condition, the other parameter, namely  $\alpha$ ,  $\beta$ ,  $\gamma$ , by knowing the PSI value could be calibrated.

Figure 1a depicts the result of the fitting Eq. (2) to the specimen hydrated with distilled water. The values of the main three parameters are reported in Table 1. In the third step of model validation, the pore fluid salt solution's effects should be considered. In other words, three other parameters, namely  $\alpha$ ,  $\beta$ , and  $\gamma$ , should be evaluated. For this purpose, it is sufficient to use one series of retention data corresponding to a specific salt concentration level. For example, these new model parameters were calibrated and summarized in Table 1 using the water retention data of 0.5 mol/L, as shown in Fig. 1b. After completing the three-step procedure described, the model is fully calibrated, and hence it can be easily used to determine the GCL-WRC of any saline specimen having desired osmotic suction. Accordingly, Fig. 2a–e compare the predictions made by the model and the experimental measurements for a wide range of sodium chloride concentrations (i.e., 0.1, 0.2, 0.3, 0.4, and 2 mol/L).

**Table 2** Model parameters and its prediction capability for Lu et al. [6] dataset

$a$	$n$	$m$	$\alpha$	$B$	$\gamma$
0.72	97.60	0.009	0.9	0.1	0.0001
NaCl concentration (mol/L)		Osmotic suction (kPa)	PSI	RMSE	$R^2$
0		0	1.0	0.032	0.98
0.1		495	1.5	0.047	1.00
0.2		990	2.0	0.055	0.97
0.3		1486	2.5	0.029	1.00
0.4		1981	3.0	0.018	1.00
0.5		2476	3.5	0.042	0.98
2.0		9904	10.9	0.045	0.98

$$\text{RMSE} = 1 - \sqrt{\frac{\sum_{i=1}^n (w_i - w_i')^2}{n}} \quad (8)$$

$$R^2 = 1 - \frac{\sum_{i=1}^n (w_i - w_i')^2}{\sum_{i=1}^n (w_i - \bar{w})^2} \quad (9)$$

where  $n$  is the number of GCL-water retention data points for each test,  $w_i$  and  $w_i'$  are measured and predicted gravimetric water content of the  $i$ th data point, respectively, and  $\bar{w}$  is the mean value of the measured gravimetric water content for each test. According to the last two columns of Table 2, the  $R^2$  value is about 0.98, and the values of RMSE vary from 0.018 to 0.055 for all salt concentration levels. As a result, the present model can give excellent predictions of GCL water retention behavior's wetting branch as a function of pore fluid saline concentration.

## 5 Conclusions

For the first time, an analytical model was presented for simulating the wetting water retention curve of GCL considering pore fluid chemistry. The proposed model was originated and developed from the van Genuchten model [21]. It has six model parameters with specific physical interpretation. The newly introduced concept of PSI into the current modelling approach makes it possible to consider the effects of pore fluid salinity on the water retention behavior of GCLs. The validation analyses against some published experimental measurements indicated that the model has an

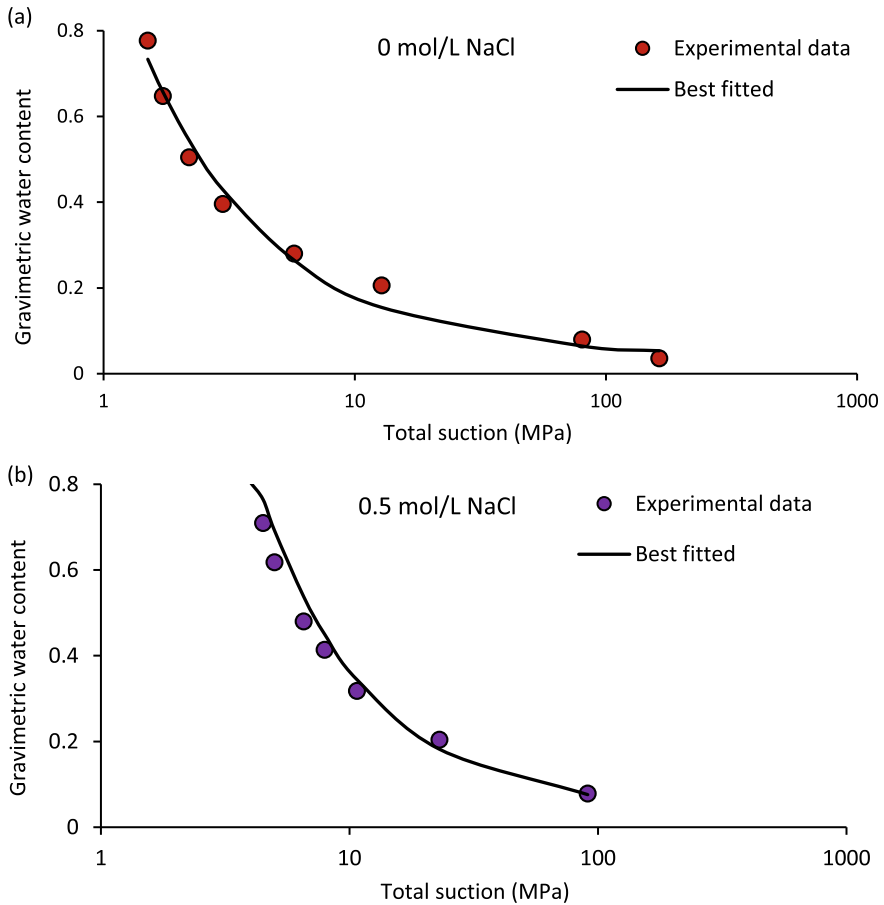
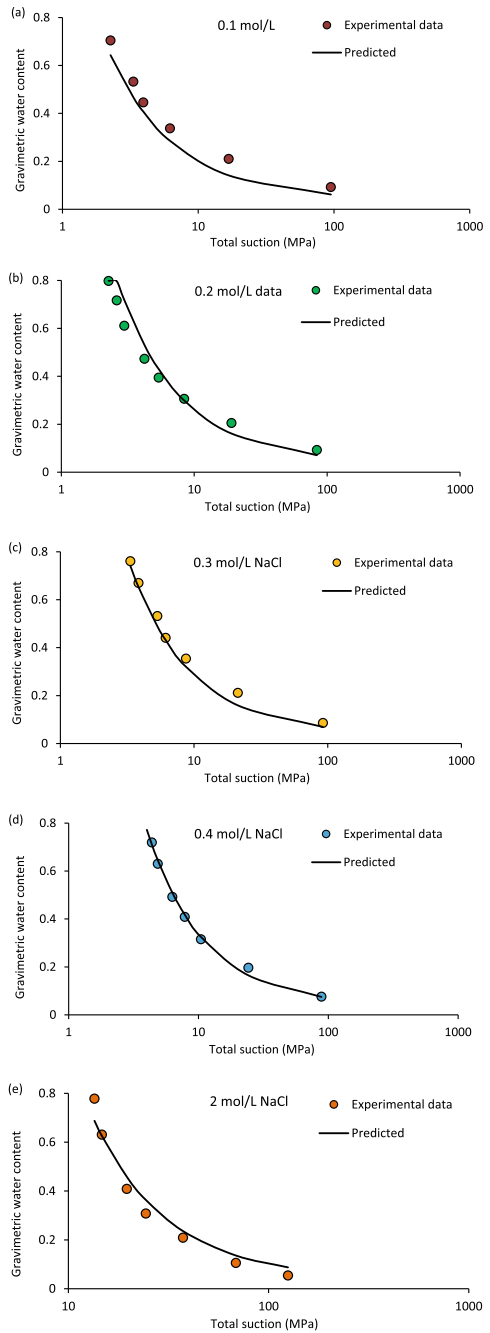


**Fig. 1** Calibration result based on 0 and 0.5 mol/L NaCl for Lu et al. [6] data set

impressive performance in the precise prediction of the GCL-water retention curve despite its simplicity. Some of the key findings of this study can be listed as follows:

1. The new model can predict the water retention behavior of GCLs during the hydration process to various solute concentrations, simulating the pore fluid exchange between GCLs and different leachates.
2. The proposed model relies only on data obtained from the conventional WRC tests. In other words, relatively advanced and costly experiments such as the MIP tests are not required.
3. The model has distinct merit of a simplistic nature and minimal model parameters compared with some available literature models. Therefore, it is recommended that this model be embedded into the numerical codes for the parametric study of contaminant transport under transient two-phase flow conditions.

**Fig. 2** Validation test results for Lu et al. [6] data set: **a–e** depicts the performance of the model prediction of SWRC data in terms of total suction for the five levels of NaCl molar concentrations



4. The new model's reliability was proved through a preliminary statistical analysis based on two decision-making criteria, revealing the high-accuracy prediction capabilities.

**Acknowledgements** The financial support provided by Research Grant Office at Sharif University of Technology for “fundamental investigation of flow characteristics through deformable porous media” via grant No. G970902 is gratefully acknowledged.

## References

1. Bouazza A (2002) Geosynthetic clay liners. *Geotext Geomembr* 20(1):3–17
2. Yu B, El-Zein A (2020) Water characteristic curves of geosynthetic clay liners hydrated by a saline solution. *Geosynth Int* 28:144–157
3. Lu Y, Abuel-Naga H, Bouazza A (2017) Water retention curve of GCLs using a modified sample holder in a chilled-mirror dew-point device. *Geotext Geomembr* 45(1):23–28
4. Hedayati-Azar A, Sadeghi H (2021) A review of research approaches for contaminant transport in saturated deformable clay under coupled hydro-chemico-mechanical processes. *Sharif J Mech Eng* 37:97–115
5. Hedayati-Azar A, Sadeghi H (2022) Semi-empirical modelling of hydraulic conductivity of clayey soils exposed to deionized and saline environments. *J Contam Hydrol* 249:104042
6. Lu Y, Abuel-Naga H, Leong E, Bouazza A, Lock P (2018) Effect of water salinity on the water retention curve of geosynthetic clay liners. *Geotext Geomembr* 46(6):707–714
7. Maubeuge V (1994) Needle punched geosynthetic clay liners. In: Proceedings of the 8th GRI conference, Philadelphia, pp 129–207
8. Anderson R, Rayhani MT, Rowe RK (2012) Laboratory investigation of GCL hydration from clayey sand subsoil. *Geotext Geomembr* 31:31–38
9. Chevrier B, Cazaux D, Didier G, Gamet M, Guyonnet D (2012) Influence of subgrade, temperature and confining pressure on GCL hydration. *Geotext Geomembr* 33:1–6
10. Bouazza A, Ali MA, Gates WP, Rowe RK (2017) No AccessNew insight on geosynthetic clay liner hydration: the key role of subsoils mineralogy. *Geosynth Int* 24(2):139–150
11. Rayhani M, Rowe R, Brachman R, Take W, Siemens G (2011) Factors affecting GCL hydration under isothermal conditions. *Geotext Geomembr* 29(6):525–533
12. Acikel A, Gates W, Singh R, Bouazza A, Rowe R (2018) Insufficient initial hydration of GCLs from some subgrades: factors and causes. *Geotext Geomembr* 46(6):770–781
13. Abuel-Naga H, Bouazza A (2010) No AccessA novel laboratory technique to determine the water retention curve of geosynthetic clay liners. *Geosynth Int* 17(5):313–322
14. Sadeghi H (2016) A micro-structural study on hydro-mechanical behavior of loess. Dual-Degree PhD thesis, Hong Kong University of Science and Technology and Sharif University of Technology
15. Ng CWW, Sadeghi H, Hossen SB, Chiu CF, Alonso EE, Baghbanrezvan S (2016) Water retention and volumetric characteristics of intact and re-compacted loess. *Can Geotech J* 53(8):1258–1269
16. Sadeghi, H., Golaghaei Darzi, A. (2021). A review of different approaches to analytical modeling of soil-water retention curves. *Sharif J Civil Eng* 37.2(3.1), 111–123.
17. Assouline S, Or D (2013) Conceptual and parametric representation of soil hydraulic properties: a review. *Vadose Zone J* 12(4):121
18. Ghavam-Nasiri A, El-Zein A, Airey D, Rowe RK (2019) Water retention of geosynthetics clay liners: dependence on void ratio and temperature. *Geotext Geomembr* 47(2):255–268



19. Grant SA, Salehzadeh A (1996) Calculation of temperature effects on wetting coefficients of porous solids and their capillary pressure functions. *Water Resour Res* 32(2):261–270
20. Gallipoli D (2012) A hysteretic soil-water retention model accounting for cyclic variations of suction and void ratio. *Géotechnique* 62(7):605–616
21. van Genuchten M (1980) A closed-form equation for predicting the hydraulic conductivity of unsaturated soils. *Soil Sci Soc Am J* 44(5):892–898
22. Fredlund D, Xing A (1994) Equations for the soil-water characteristic curve. *Can Geotech J* 31(4):521–532
23. Sadeghi H, Chiu CF, Ng CWW, Jafarzadeh F (2020) A vacuum-refilled tensiometer for deep monitoring of in-situ pore water pressure. *Sci Iran* 27(2):596–606
24. Sadeghi H, Golaghaei Darzi A (2021) Modelling of soil-water retention curve considering the effects of existing salt solution in the pore fluid. In: *MATEC web of conferences*, vol 337. EDP Sciences, p 02001
25. He Y, Zhang K-N, Wu D-Y (2019) Experimental and modeling study of soil water retention curves of compacted bentonite considering salt solution effects. *Geofluids* 2019:1–11
26. Sadeghi H, Nasiri H (2021) Hysteresis of soil water retention and shrinkage behaviour for various salt concentrations. *Géotech Lett* 11(1):21–29
27. Ye W-M, Zhang F, Chen Y-G, Chen B, Cui Y-J (2017) Influences of salt solutions and salinization-desalinization processes on the volume change of compacted GMZ01 bentonite. *Eng Geol* 222:140–145
28. Sadeghi H, AliPanahi P (2020) Saturated hydraulic conductivity of problematic soils measured by a newly developed low-compliance triaxial permeameter. *Eng Geol* 278:105827
29. van Genuchten MT, Leij FJ, Yates SR (1991) The RETC code for quantifying the hydraulic functions of unsaturated soils. U. S. Salinity Laboratory, U.S. Department of Agriculture, Agricultural Research Service, Riverside, California 9250 1
30. Kolahdooz A, Sadeghi H, Ahmadi MM (2020) A numerical study on the effect of salinity on stability of an unsaturated railway embankment under rainfall. In: Accepted for oral presentation in The 4th European conference on unsaturated soils (E-UNSAT 2020), Oct. 2020, Portugal, E3S web conference, vol 195, p 01004
31. Li X-Y, Xu Y-F (2020) Determination and application of osmotic suction of saline solution in clay. *Environ Earth Sci* 79(48):1–14
32. Acikel A, Singh R, Bouazza A, Gates W, Rowe R (2015) Applicability and accuracy of the initially dry and initially wet contact filter paper tests for matric suction measurement of geosynthetic clay liners. *Geotechnique* 65(9):780–787
33. Bannour H, Stoltz G, Delage P, Touze-Foltz N (2014) Effect of stress on water retention of needlepunched geosynthetic clay liners. *Geotext Geomembr* 42(6):629–640
34. Beddoe R, Take W, Rowe R (2011) Water-retention behavior of geosynthetic clay liners. *J Geotech Geoenviron* 137(11):1028–1038
35. Southen J, Rowe R (2007) Evaluation of the water retention curve for geosynthetic clay liners. *Geotext Geomembr* 25(1):2–9
36. Bouazza A, Vangpaisal T (2006) Laboratory investigation of gas leakage rate through a GM/GCL composite liner due to a circular defect in the geomembrane. *Geosynth Int* 11(4):110–115
37. Barroso M, Touze-Foltz N, Saidi F, Kuwano J, Koseki J (2006) Validation of the use of filter paper suction measurements for the determination of GCLs water retention curves. In: *Proceedings of the 8th international conference on geosynthetics (8ICG)*, Japan, pp 171–174

# Compaction Properties of Soil Composite Fills: Sand, Silt, Clay and Polypropylene Fiber Mixtures



Tanay Karademir 

**Abstract** A laboratory experimental program including a series of compaction tests on various soil composite fill samples prepared by using sand, silt, clay and polypropylene (PP) fiber at different dry weight proportions was performed. As a result of the tests, the compaction curves were developed for distinct soil composite fill samples so as that the two most crucial and critical compaction engineering design parameters: maximum dry unit weight ( $\gamma_{d-max}$ ) and optimum moisture content ( $w_{opt}$ ) were determined. The change in the detected values of  $\gamma_{d-max}$  and  $w_{opt}$  was investigated by addition of; (i) silt, (ii) clay, (iii) PP fiber, (iv) or selected two of them, (v) or all of them into sand, and thus, the behavior in those two important compaction characteristics ( $\gamma_{d-max}$ ,  $w_{opt}$ ), that are decisive properties in design and construction of soil fill infrastructures, was identified for various different soil composite fill samples including different materials studied. It was seen that the  $\gamma_{d-max}$  decreases, whereas, the  $w_{opt}$  increases as a result of adding silt and/or clay into pure sandy soil. The greater change in the values was observed for clay inclusion compared to that of silt. On the other hand, the inclusion of PP fiber into sandy soil resulted in an increase in the measured values of  $\gamma_{d-max}$ , while a decrease in the detected values of  $w_{opt}$ . Consequently, the PP fiber served a relative advantage in comparison to the two other materials (silt, clay) by facilitating enhanced compaction properties for the improvement of the characteristics of soil composite fill under loading, and thereby, enabling highly densification or more desirable compaction of the fill not only at larger  $\gamma_{d-max}$  but also at lower  $w_{opt}$  so as to better comply with common design criteria in practice for the application of compaction procedure in the field during construction as well as to achieve higher bearing capacity (larger load-carrying resistance), and hence, superior performance during operation of the infrastructure built from this soil composite fill.

**Keywords** Soil composite fills · Compaction properties · Soil mixtures · PP fibers

---

T. Karademir (✉)  
Istanbul Bilgi University, Istanbul 34060, Turkey  
e-mail: [tanay.karademir@bilgi.edu.tr](mailto:tanay.karademir@bilgi.edu.tr)

## 1 Introduction and Relevant Literature

The advancements in geotechnical engineering urge engineers to explore innovative enhanced materials as well as to develop new alternative methods for design and construction of soil composite fills. To this end, the mechanical characteristic such as compaction properties of the fill materials requires to be improved to fulfill and satisfy the prevailing standards of today's advanced construction technology (i.e. higher quality) by demonstrating not only superior physical and strength properties in the course of construction but also better performance and durability characteristics during operation. In this regard, compaction is the densification of soils by the expulsion of air using mechanical methods or water or both that is accomplished very quickly in the field as the compactive effort applied on soil reduces the volume of air existing in the void space (i.e. pore space). Soil composite fills are designed to construct foundations for; (i) buildings such as houses, commercial and industrial complexes, and (ii) roads and highways. Additionally, the compaction of soil fill is performed for construction of; (i) earth retaining systems such as retaining walls, and (ii) water retaining systems such as earth and rock fill dams. Soil composite fills are generally constructed by following the engineering methodology of soil improvement techniques including mechanical compaction. Soil compaction, being not only the oldest but also the most widely preferred soil modification method, is perhaps the least expensive method of improving soils for enhanced mechanical properties and superior deformation characteristics under load applications. Further, it is a common practice in the construction of all types of infrastructural systems on and within soils.

Over the decades, soil compaction has been becoming a global concern such that the improper application of compaction technique in the field can impact and reduce the quality of soil. This results in jeopardizing sustainability of soil composite fills [1]. Further, the quality of compaction as well as the type of materials used in construction of soil composite fills control and govern the hydraulic properties and mechanical characteristics in terms of load carrying capacity (i.e. strength) and settlement performance (i.e. deformation behavior) [2].

Moreover, the alternative methods to traditional materials for subsoil stabilization and embankments were examined by several researchers [1, 3–5]. The extensive use of natural materials along with soft soil stabilization using hydraulic binders in construction of infrastructural projects is required according to geotechnical specifications. To this end, in order to benefit from refuse materials instead of consuming natural resources, the utilization of waste materials including fly ash and slag for earthworks such as soil composite fills was experimentally studied by Vukicevic et al. [3]. As such, they reported the results of high plasticity clay stabilization using fly ash by investigating engineering properties of ash and ash-slag mixtures with emphasis on the application in road subgrade and embankment construction as a result of determination of physical and mechanical properties. The results of their laboratory study indicated the favorable influence of the clay stabilization using fly ash for increasing strength and stiffness of soil fill as well as for reducing an undesirable property of soil fills being expansivity. Consequently, it was pointed out that fly

ashes and ash-slag mixtures possess comparable mechanical properties with sands that accompanied by multiple other benefits including lower energy consumption and CO<sub>2</sub> emission, preserving natural materials, and additionally, facilitating the production of less amount of refuse, and thus, enabling smaller waste landfill areas owing to the utilization of the refuse in soil composite fills. Therefore, those refuse materials can become suitable as fill materials for embankments, particularly considering the necessity in practice for sustainable development [3–5]. In this regard, in an attempt to investigate soil composite mixture having enhanced and improved mechanical and hydraulic properties as a fill material, a laboratory experimental program has been conducted by performing a series of proctor compaction test on sand, silt, clay and PP fiber mixtures at different dry weight proportions so as to develop the optimum density-moisture relationship for a selected soil composite fills having superior compaction properties.

## 2 Experimental Methods and Tested Materials

### 2.1 Materials Used in Laboratory Testing Program

In the laboratory experimental program, four different materials including three different soil types such as sand, silt and clay as well as one polymeric fiber made from polypropylene (PP) were used (Fig. 1). Those distinct natural materials (i.e. soils) and synthetic material (i.e. PP fiber) were mixed at various dry weight proportions in order to investigate the relatively superior mixture possessing enhanced compaction properties, and thus, improved higher quality features as a soil composite fill.

**Fig. 1** Materials tested in the experimental program



## 2.2 Testing Equipments, Experimental Procedures and Data Reduction

The standard proctor compaction test [6] was performed on different soil composite mixture fill specimens. The compaction of the specimens in the mold was accomplished at three different layers such that each layer was subjected to be compacted by 25 hammer blows (Fig. 2). The volume of the mold in which the mixture specimens were compacted, and thus, soil composite fill samples were prepared was  $9.44 \times 10^{-4} \text{ m}^3$ .

Furthermore, in order to develop compaction curves appropriately for each specimen, every compaction experiment was conducted at five different water contents such that five proctor tests were repeated by adding moisture (i.e. water) to the original soil composite fill specimen prepared at the beginning of the experiment. The dry unit weight ( $\gamma_d$ ) at each water content ( $w, \%$ ) was calculated (Eq. 1) so as that the compaction curve consisting of a plot of  $\gamma_d$  versus  $w (\%)$  for each tested specimen was developed. After that, the peak in the compaction curve was identified such that the coordinates of peak have given optimum water content ( $w_{\text{opt}}$ ) (i.e. abscissa) and maximum dry unit weight ( $\gamma_{d-\text{max}}$ ) (i.e. ordinate) that is the maximum unit weight a soil can attain employing a specified means of compaction methodology. Further, the designation of optimum moisture content is required such that it is the water content needed to enable a soil to reach its maximum dry unit weight following a compaction technique. To this end, the determination of  $\gamma_{d-\text{max}}$  and  $w_{\text{opt}}$  are of importance as they serve a reference for site specifications of practical applications of the compaction process in the field by incorporating a relative compaction (RC) (Eq. 2) particularly specified for the construction project.

**Fig. 2** Compacted soil composite mixture specimen in the mold



$$\gamma_{\text{bulk}} = \frac{W_{\text{wet-soil-in-mold}}}{V_{\text{mold}}} \tag{1a}$$

$$\gamma_d = \frac{\gamma_{\text{bulk}}}{1 + w} \tag{1b}$$

$$\text{RC} (\%) = \frac{\gamma_{d-\text{max-in-field}}}{\gamma_{d-\text{max-in-lab}}} \cdot 100\% \tag{2}$$

where

$\gamma_{\text{bulk}}$ : Bulk unit weight of wet soil in mold

$W_{\text{wet-soil-in-mold}}$ : Weight of wet soil in mold

$V_{\text{mold}}$ : Volume of wet soil in mold

$\gamma_d$ : Dry unit weight of soil in mold

$w$ : Water content of soil in mold

RC (%): Relative compaction

$\gamma_{d-\text{max-in-field}}$ : Maximum dry unit weight that can be reached in the field as specified by relative compaction required for the construction project

$\gamma_{d-\text{max-in-lab}}$ : Maximum dry unit weight that was obtained in the laboratory environment as a result of Proctor Test applied on soil sample

### 2.3 Testing Program

The laboratory experimental program consisted of a series standard proctor compaction tests on the soil specimens including sand, silt, clay and PP fiber. Those materials were mixed at different dry weight proportions for which the details are presented in Table 1.

**Table 1** Laboratory testing program

Specimen	1	2	3	4	5	6
	75% sand-25% silt	75% sand-25% clay	50% sand-25% silt-25% clay	25% sand-50% silt-25% clay	50% sand-24% silt-24% clay-2% PP fiber	98% sand-2% PP fiber

### 3 Experimental Findings

The experimental findings of the laboratory testing program including a series of compaction tests on various soil composite fill samples prepared by using sand, silt, clay and PP fiber at different dry weight proportions will be presented. As a result of the proctor tests, the compaction curves developed for distinct soil composite fill samples will be shown so as that the two most crucial and critical compaction engineering design parameters:  $\gamma_{d-max}$  and  $w_{opt}$  determined from the compaction curves will be comparatively analyzed for those different soil composite fill specimens prepared in the laboratory. The change in the detected values of  $\gamma_{d-max}$  and  $w_{opt}$  investigated by addition of; (i) silt, (ii) clay, (iii) PP fiber, (iv) or selected two of them, (v) or all of them into sand will be displayed, and thus, the behavior in  $\gamma_{d-max}$  and  $w_{opt}$  which are decisive properties in design and construction of soil fill infrastructures, will be identified for various different soil composite fill samples including various materials studied.

#### 3.1 Compaction Curves

The compaction curves, showing the relationship between two important compaction properties such as dry unit weight,  $\gamma_d$  ( $\text{kN/m}^3$ ) and moisture content,  $w(\%)$  were developed for different soil composite fill materials as a result of the standard proctor test applied on the various specimens, are presented in Fig. 3. The effect of moisture content during compaction on soil fabric is evident from the developed compaction curves such that prior to optimum water content, water replaces air and helps to rearrange soil particles into denser configuration, whereas, subsequent to optimum water content, water replaces soil particles which are denser than water, that is why the density then decreases.

The compaction behavior exhibited for all soil composite mixtures appears to be similar by displaying an increase in dry unit weight with an increase in water content in the mixture at dry side of optimum prior to arriving to peak that is  $\gamma_{d-max}$  ( $\text{kN/m}^3$ ) which could be attained by specific means of compaction (i.e. applied compactive effort). Subsequent to peak (i.e.  $\gamma_{d-max}$ ), there occurs a decrease in the values of  $\gamma_d$  ( $\text{kN/m}^3$ ) with a further increase in moisture content in the mixture. However, the magnitude of that reduction in the values of  $\gamma_d$  was different for the distinct soil composite mixtures. Therefore, it could be inferred that the compaction behavior at wet side of optimum after peak is not analogous such that a substantial diminish in the values of  $\gamma_d$  demonstrated with an increase in clay content in the mixtures, whereas, a marginal decline in the values of  $\gamma_d$  exhibited with an increase in silt content.

Moreover, the addition of PP fiber into the soil composite fill material results in attaining higher  $\gamma_{d-max}$  values in the mixtures, and also, having the ability to reach  $\gamma_{d-max}$  at lower water contents. This shows a decrease in the detected values of  $w_{opt}$

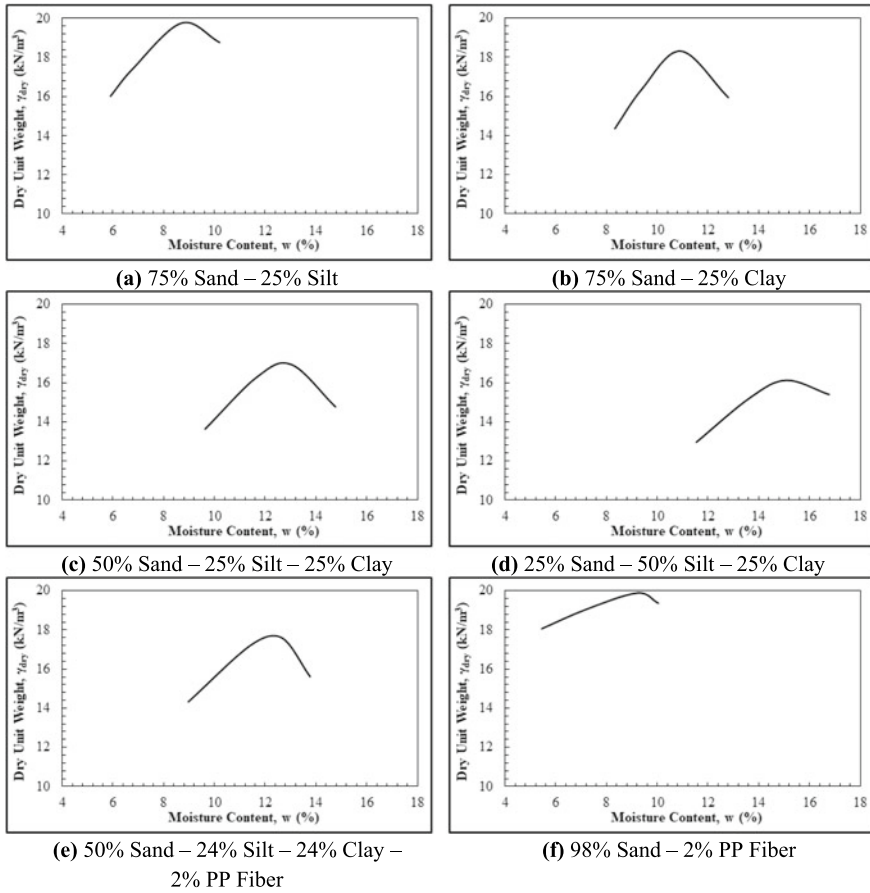


**Fig. 3** Compaction curves for different soil composite mixtures

(%) which is favorable in field applications of compaction for the construction of soil composite fills. Furthermore, the incorporation of PP fiber into the soil fill material enables the occurrence of relatively smaller drops after  $\gamma_{d-max}$  at wet side of optimum such that the progression of trivial decline in the values of  $\gamma_d$  following the peak is a result of PP fiber inclusion into the soil. Further, when the PP fiber was mixed into pure sand, it was observed from the developed compaction behavior that the sand becomes densified, firm and intact by displaying the largest  $\gamma_{d-max}$  as well as the lowest  $w_{opt}$  (%) among all the tested soil composite mixtures along with a flatter compaction curve generated in displaying minor changes in the values of  $\gamma_d$  with addition of moisture (water) into the mixture.

To sum up, the incorporation of clay results in the development of appropriate bell-shaped compaction curves, while, the addition of silt brings about the mobilization of inverted check mark type compaction curves. Further, the involvement of PP fiber



into the soil mixture facilitates the flattening of the compaction curves by enabling marginal changes and/or variations in the detected values of  $\gamma_d$  with an increase in the moisture content.

### 3.2 Comparison of Test Results

The two compaction engineering design parameters  $\gamma_{d-max}$  and  $w_{opt}$  (%) were determined based on compaction curves developed for different soil composite mixtures tested throughout the entire laboratory experimental program by applying standard proctor test (Table 2). As explicitly known, the ultimate goal of conducting the proctor test in the laboratory is to detect and obtain those two vital compaction properties to be utilized in engineering design of infrastructures for which the compaction process needs to be carried out during construction operations. The values of  $\gamma_{d-max}$  and  $w_{opt}$  (%) tabulated in Table 2 will benefit the design engineers on this perspective to relatively evaluate the magnitudes of those parameters for different soil mixtures as well as will extend an understanding on the variation of those compaction properties due to the change in weight proportions of distinct soil types.

Figure 4 provides the results of a comparative analysis performed on the compaction engineering design parameters for  $\gamma_{d-max}$  and  $w_{opt}$  (%) as presented in Fig. 4a, b, respectively. The  $\gamma_{d-max}$  decreases with an increase in clay content (i.e. dry weight proportion) in the mixture. An analogous behavior is observed for the case of silt content such that the increase in the weight proportion results in diminishing the  $\gamma_{d-max}$ . Consequently, the incorporation of fine grained materials including silty and/or clayey soils into the compacted soil fills leads to the improvement of hydraulic properties when a fluid barrier (i.e. flow resistant) system is aimed to be constructed in the field; however, causes deteriorating mechanical strength properties including bearing capacity (i.e. load carrying resistance). On the other hand, the addition of PP fiber into the mixture contributes the increment of the  $\gamma_{d-max}$ . This shows the

**Table 2** The detected compaction engineering design parameters

Test specimen	Max. dry unit weight, $\gamma_{d-max}$ (kN/m <sup>3</sup> )	Optimum moisture content, $w_{opt}$ (%)
75% sand–25% silt	19.75	8.70
75% sand–25% clay	18.32	10.93
50% sand–25% silt–25% clay	16.94	13.03
25% sand–50% silt–25% clay	16.13	15.09
50% sand–24% silt–24% clay–2% PP fiber	17.60	12.65
98% sand–2% PP fiber	19.89	9.21

enhancement of the quality of compaction operations in the field during construction so that the relatively improved densification of soil composite fill could be accomplished. Furthermore, the detected value of  $\gamma_{d-max}$  was  $16.94 \text{ kN/m}^3$  for the 50% sand–25% silt–25% clay specimen, and owing to the addition of 2% PP fiber, the measured value of  $\gamma_{d-max}$  has risen up to  $17.60 \text{ kN/m}^3$  for the 50% sand–24% silt–24% clay–2% PP fiber specimen with a resulting raise of  $\sim 4\%$  in the magnitude of  $\gamma_{d-max}$ . Moreover, the largest value of  $\gamma_{d-max}$  was attained for the 98% sand–2% PP fiber specimen whereas the smallest value of  $\gamma_{d-max}$  was obtained for the 25% sand–50% silt–25% clay specimen (see Fig. 4a).

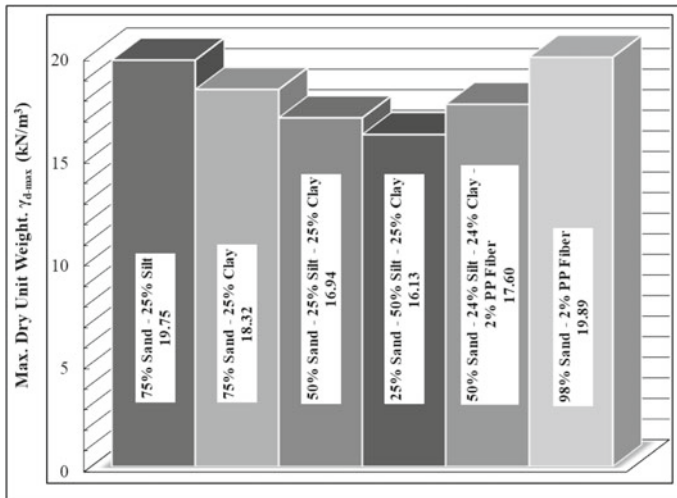
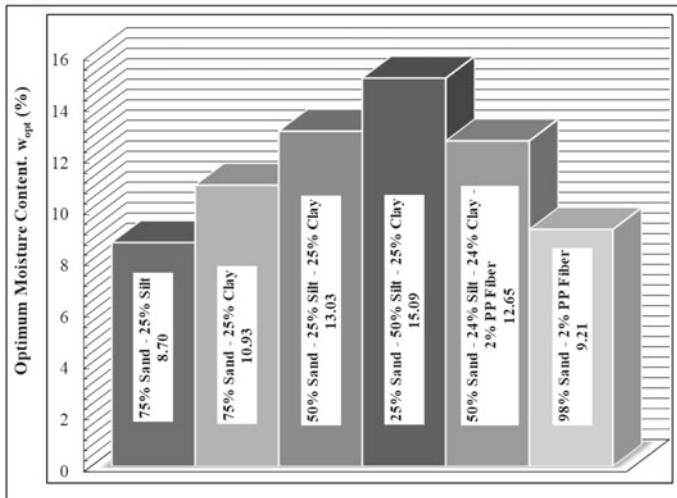
The largest value of  $w_{opt}$  (%) was observed for the 25% sand–50% silt–25% clay specimen that is 15.09% whereas the smallest value of  $w_{opt}$  (%) was seen for the 75% sand–25% silt specimen that is 8.70%. In particular, the addition of clay into the mixture specimens resulted in an increase of the  $w_{opt}$  (%) due to high water absorption capacity of clay compared to sand and silt. Further, a similar behavior was evidently seen that the increase in the content of silt causes the rise of  $w_{opt}$  (%) for the mixture.

As per the strength perspectives of soil fill materials, the increment in the value of  $w_{opt}$  (%) is unfavorable for engineering design approaches, and thus, undesirable to be applied in the field during construction operations. On the other hand, the addition of PP fiber improves optimum moisture content property of the mixtures such that the  $w_{opt}$  (%) decreased from 13.03% down to 12.65% (with a  $\sim 3\%$  decline) for the 50% sand–25% silt–25% clay specimen when only 2% PP fiber had been added into the mixture for which the modified weight proportions became as 50% sand–24% silt–24% clay–2% PP fiber. This is favorable for the soil composite fill materials such that they could be compacted by a specific means of compaction to attain the maximum dry unit weight during construction works at lower optimum moisture contents in order to build safer, sustainable and most importantly highly stabilized soil filling leading to more strengthened soil composite fills (Fig. 4b).

## 4 Conclusions

The densification of the mixture specimens by means of compaction was achieved in each proctor test at different water contents for every compaction experiment performed on distinct soil composite fill samples. The results of the Proctor tests serve as the reference for field specifications of compaction.

It was seen that the  $\gamma_{d-max}$  decreases, whereas, the  $w_{opt}$  increases as a result of adding silt and/or clay into pure sandy soil. The greater change in the values was observed for clay inclusion compared to that of silt. On the other hand, the inclusion of PP fiber into sandy soil resulted in an increase in the measured values of  $\gamma_{d-max}$ , while a decrease in the detected values of  $w_{opt}$ . Consequently, the PP fiber served a relative advantage in comparison to the two other materials (silt, clay) by facilitating enhanced compaction properties for the improvement of the characteristics of soil composite fill under loading, and thereby, enabling highly densification or more

(a) Maximum Dry Unit Weight,  $\gamma_{d-max}$  (kN/m<sup>3</sup>)(b) Optimum Moisture Content,  $w_{opt}$  (%)

**Fig. 4** Comparative analysis on compaction engineering design parameters for different soil composite mixtures **a** Maximum dry unit weight,  $\gamma_{d-max}$  (kN/m<sup>3</sup>) and **b** Optimum moisture content,  $w_{opt}$  (%)

desirable compaction of the fill not only at larger  $\gamma_{d-max}$  but also at lower  $w_{opt}$  so as to better comply with common design criteria in practice for the application of compaction procedure in the field during construction as well as to achieve higher bearing capacity (larger load-carrying resistance), and hence, superior performance during operation of the infrastructure built from this soil composite fill.

## References

1. Van Verseveld CJW, Gebert J (2020) Effect of compaction and soil moisture on the effective permeability of sands for use in methane oxidation systems. *Waste Manag* 107(2020):44–53
2. Wang L, Wang H, Tian Z, Lu Y, Gao W, Ren T (2020) Structural changes of compacted soil layers in Northeast China due to Freezing-Thawing Processes. *Sustainability* 12(1587):1–13
3. Vukicevic M, Marjanovic M, Pujevic V, Jockovic S (2019) The alternatives to traditional materials for subsoil stabilization and embankments. *Materials* 12(3018):1–21
4. Çokça E (2001) Use of class C fly ashes for the stabilization of an expansive soil. *J Geotech Geoenviron Eng* 127(5):568–573
5. Acosta HA, Edil TB, Benson CH (2003) Soil stabilization and drying using fly ash. In: *GeoEngineerin report (3)*, geoen지니어ing program, University of Wisconsin-Madison, Madison, WI
6. ASTM D698-12 (2021) Standard test methods for laboratory compaction characteristics of soil using standard effort. ASTM International, Book of Standards Volume: 04.08

# Sand Rubber Mixtures: 1D Compressibility Response



Sabriye Ozkan, Erdin Ibraim, and Andrea Diambra

**Abstract** The number of scrap tyres is growing all around the world due to increasing number of vehicles on the roads. This creates significant environmental and economic concerns. The usage of recycled and reused scrap tyres in civil and geotechnical engineering projects is an alternative way to help with decreasing number of stockpiled scrap tyres. The tyre derived material is commonly mixed with sand in different proportions and used as an alternative material in engineering projects. This paper presents a series of laboratory experimental work on sand-rubber mixtures under one-dimensional confined compression loading. It is aimed to investigate the response of mixture and the effect of increasing volumetric fraction of rubber on results. Samples were tested with seven different volumetric fractions of rubber ranging from 0 (SR0-pure sand) to 100% (SR100- pure rubber). The results of conducted laboratory experiments indicate that the one-dimensional response of mixtures change with rubber fraction. Samples with higher rubber fraction indicate higher compressibility and lower stiffness whereas specimen with lower rubber fraction demonstrate higher stiffness and less compressible behaviour which is related to the material properties of rubber particles.

**Keywords** Sand-rubber mixtures · Recycled tyres · Compressibility

## 1 Introduction

Increasing number of scrap tyres has been a growing environmental and economical concern worldwide. To decrease these impacts, scrap tyres have been recycled and reused in civil and geotechnical engineering projects in recent decades. Scrap tyres are mostly processed into rubber crumbs in variety of sizes and mixed with soils. Mixing soil and rubber particles generates an alternative material to soils alone which may help improving the properties of sand particles [1] and solving the problems related to settlement and bearing capacity of soils [2]. Sand-rubber mixtures can be

---

S. Ozkan (✉) · E. Ibraim · A. Diambra  
Queens Building, Faculty of Engineering, University of Bristol, Bristol BS8 1TR, UK  
e-mail: [sabriye.ozkan@bristol.ac.uk](mailto:sabriye.ozkan@bristol.ac.uk)

© The Author(s), under exclusive license to Springer Nature Singapore Pte Ltd. 2023  
Y. Yukselen-Aksoy et al. (eds.), *Sustainable Earth and Beyond*, Lecture Notes in Civil Engineering 370, [https://doi.org/10.1007/978-981-99-4041-7\\_16](https://doi.org/10.1007/978-981-99-4041-7_16)

157

used as soft ground material, pavement and road embankments material due to their high damping ratio and elastic deformability [2–5]. It is also suggested that recycled tyres can be used as lightweight material for embankments [3, 6]. Recycled tyres can be also used to reduce vibration on structures [7]. Feng and Sutter [7] analysed the dynamic properties of sand-rubber mixtures with different rubber fractions and pointed out that rubber material can be used for reducing vibration as rubber has a higher damping ratio in comparison with soils. Experimental and numerical analyses have been conducted to define the behaviour of sand-rubber mixtures which suggests that mixtures can be used as drainage layers and filtration layers [8].

Rubber material has a great potential to be an applicable alternative material in engineering projects which will also be beneficial in terms of dealing with rapidly increasing number of scrap tyres both from an environmental and economic perspective. Recycling and reusing scrap tyres in engineering projects can also address the demand for construction materials [9]. However, it is important to understand well their behaviour under a variety of loading conditions and mixing ratios, as rubber particles are much softer compared to sand particles which leads further deformability of the mixtures. Many researchers have analysed the response of sand-rubber mixtures from different perspectives and under a variety of conditions. This research aims to analyse and present the response of sand-rubber mixtures under one-dimensional confined compression and explore how this response is affected by the fraction of rubber materials. A series of laboratory experiments on sand-rubber mixtures are therefore conducted, and results presented. Further analyses and experimental works are planned for mitigation options to improve the properties of sand-rubber mixtures as a part of this research.

## 2 Material and Methods

### 2.1 Materials

Leighton Buzzard Sand (Fraction-A) is used for the experimental work. The mean grain size ratio between sand and rubber materials is one of the main factors which affects the response of sand-rubber mixtures [10–13]. To avoid these possible effects, and isolate the effects of the rubber content, the rubber particulate material was designed to have the same particle size distribution as the sand (Fig. 1). The rubber particles of a wide range of sizes have been sieved, sorted and mixed again in certain percentages to obtain the same particle size distribution as the sand material. The properties of sand and rubber materials are presented in Table 1.

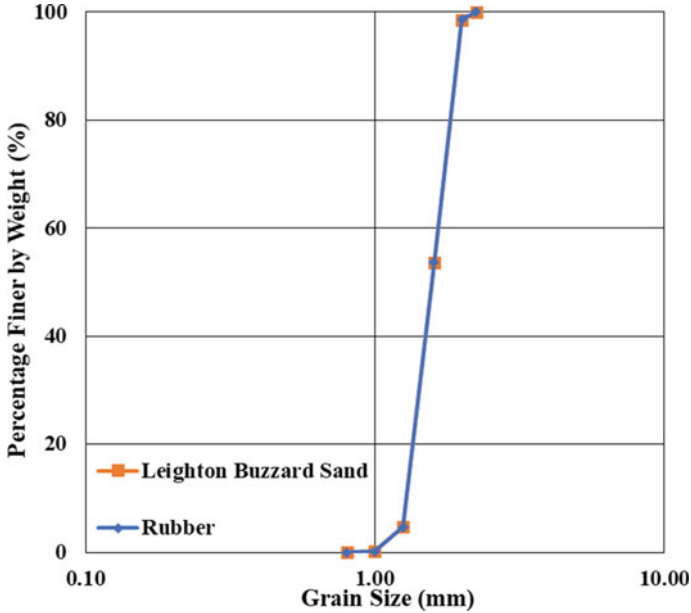


**Fig. 1** Particle size distributions of sand and rubber materials obtained from sieve analysis

**Table 1** Properties of sand and rubber materials

	Leighton buzzard sand (S)	Rubber (R)
Specific gravity [14]	2.65	1.04
Mean grain size-D <sub>50</sub> (mm)	1.57	1.57
Coefficient of uniformity (C <sub>u</sub> )	1.29	1.29
Coefficient of gradation (C <sub>g</sub> )	0.95	0.95

## 2.2 Sample Preparation and Testing Procedure

Sand and rubber materials were mixed in 7 different volumetric rubber fractions (F<sub>R</sub>): 0 (pure sand), 10, 20, 30, 50, 70 and 100% (pure rubber), where (F<sub>R</sub>) is defined according to Eq. 1.

$$F_R = \frac{V_{rubber}}{V_{rubber} + V_{sand}} \tag{1}$$

where V<sub>rubber</sub>, and V<sub>sand</sub> stands for volume of rubber and volume of sand, respectively.

The minimum and maximum void ratio of Leighton Buzzard sand were determined as 0.55 and 0.83 respectively [14], and a target fabrication void ratio of 0.646 was aimed to for all the sample tested in this study. The sample with 100% rubber fraction (SR100) has a higher fabrication void ratio due to damping properties of rubber.

An oedometric sample cell with 75 mm diameter and 60 mm height was used. The initial height for all samples was set to be 58 mm. All samples were prepared in two volumetrically equal layers to avoid any possible segregation. A circular bowl, a stainless-steel spoon, a steel rod tamper with a diameter of 35 mm, a digital calliper with resolution of 0.01 mm, and a digital scale readable to 0.01 g were used for sample preparation. The weighted materials were firstly mixed with a spoon in the bowl in dry conditions, and then 10% water was added, and materials were carefully mixed. When all materials were mixed properly and as homogeneous as possible, the mixture was transferred to with a spoon into the sample cell with a zero drop height to avoid particle segregation. Once all material was transferred to the sample cell, it was compacted with a steel rod tamper until it reached the required height corresponding to the target fabrication void ratio. When both layers were completed, the height of the sample was measured and noted. The loading cap was placed, and the settlement of the sample due to its weight measured. The sample was then placed in the oedometer device for testing. The samples were loaded automatically under strain-controlled mode at a displacement rate of 1.0 mm/min. A load cell with a maximum capacity of 10 kN load which gives a maximum normal pressure of 2250 kPa for a sample with 75 mm diameter was employed. An LVDT with a 25 mm measurement range was used for displacement readings. A data acquisition system was employed, and data were monitored on the computer in regular intervals of time.

### 3 Results and Discussions

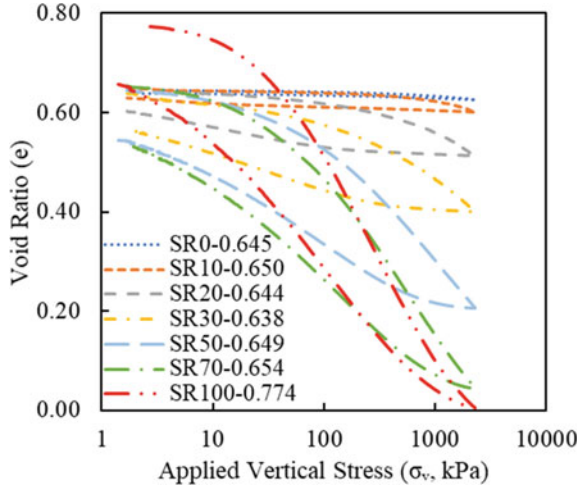
The experimental results of sand-rubber mixtures under one-dimensional confined compression are analysed and presented considering the compressibility and stiffness of mixtures and the effect of rubber fraction.

#### 3.1 *Compressibility of Mixtures*

This section presents compressibility of Leighton buzzard sand mixed with rubber tested under one-dimensional confined compression. Figure 2 presents the compressibility curves of sand rubber mixtures for the variety of rubber fractions employed in this study. For the higher rubber contents (i.e.  $F_R$  higher than 30–50%), some curvature of the one-dimensional response is starting to show at high stresses above about 1 MPa. The swelling curves for the sand–rubber mixtures have also distinct S-shape, as also observed by other researchers [10–14] and this is apparent for samples starting



**Fig. 2** The relationship between void-ratio and logarithm of stress for all applied rubber fractions. Samples are named as SRX-Y where SR is sand-rubber, and X and Y stands for rubber fraction (%) and initial void ratio, respectively



with  $F_R$  values above 20%. The results clearly indicate that the mixtures becomes more compressible with increasing the rubber fractions which leads further deformations, in agreement with results observed by other researchers (i.e. [6, 10, 11, 13, 15, 16]). For samples with higher rubber contents above 50%, the void ratio seems to tend to zero, the voids seem saturated by the deformable rubber. Additionally, it is observed that the remanent deformation at the end of the unloading stage is also increasing with the rubber fraction. One-dimensional loading–unloading–reloading cycle tests are currently performed to explore the extent of the remanent deformations and their implications for the design of such soil mixtures.

The compression ( $CC = \Delta e / \Delta \sigma_v$ ) and swelling ( $CS = \Delta e / \Delta \sigma_v$ ) indexes for all rubber fractions were calculated from the slope of the linear portion of loading and unloading curves of stress-void ratio graphs, respectively. Figure 3 shows the compression and swelling indexes as a function of the rubber fractions. The compression and swelling indexes for sand-rubber mixtures show almost a linear variation with increasing rubber content.

### 3.2 Stiffness of Mixtures and the Effect of Rubber Inclusion

To enable the analysis of the stiffness of the sand-rubber mixtures, the results of oedometer tests have been plotted in vertical strain-vertical stress graphs in Fig. 4. The one-dimensional incremental confined stiffness ( $M$ ) of mixtures was calculated from the slope of this curves ( $M = \Delta \sigma_v / \Delta \epsilon_v$ ) following equal stress–strain increments for each sample, as given by relation Eq. 2:

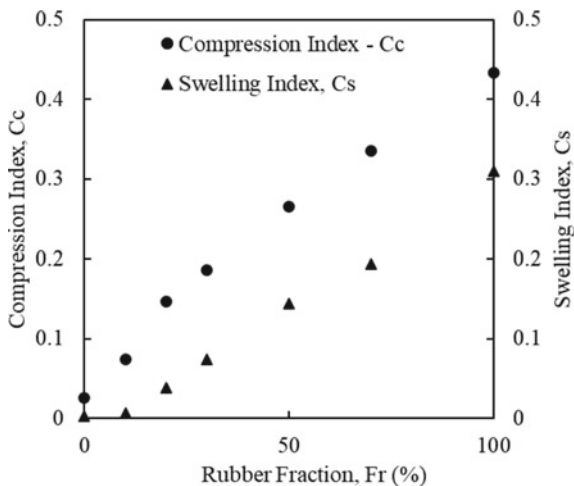


**Fig. 3** Compression and swelling indexes against rubber fractions

$$\frac{M}{\sigma_a} = \chi * \left( \frac{\sigma_v}{\sigma_a} \right)^\alpha \quad (2)$$

where  $\sigma_a$  is a reference stress, while  $\chi$  and  $\alpha$  are material parameters. The parameter  $\chi$ , known as modulus number, gives the magnitude of the confined stiffness at the reference pressure, while  $\alpha$  describes the stress dependency of stiffness [16].

One-dimensional incremental stiffness ( $M$ ) and vertical stresses normalised with a reference stress of  $\sigma_a = 100$  kPa are plotted in Fig. 5. The curves for rubber fractions higher than 30% in Fig. 5 are rather grouped at the lower end of the y-axis, showing lower stiffness and lower rates of increase with the stress level. Madhusudhan et al. [17] analysed the stiffness of sand-rubber mixtures in terms of constrained modulus, and they observed a similar trend for higher rubber fractions. For mixtures with lower rubber fractions, the trend is more similar to granular soils responses.

$\chi$  and  $\alpha$  values for all samples are plotted against rubber fractions in Fig. 6. Higher  $\chi$  modulus numbers would represent stiffer material properties [16] and these results reflect the sand-like behaviour with more dominant rigid sand-sand contacts for mixtures with lower rubber content, below 20%. As the rubber content increases, rubber-to-rubber contacts are becoming more dominant, rubberlike behaviour is prevalent and lower modulus numbers are recorded. The  $\alpha$  component increases with increasing rubber fractions tending towards unity value which, for a given high rubber content, would signify a constrained modulus proportional with the stress level. The magnitude of stiffness of the mixtures decreases greatly with increasing rubber fraction. Similar observations were made in Kim and Santamarina [13].

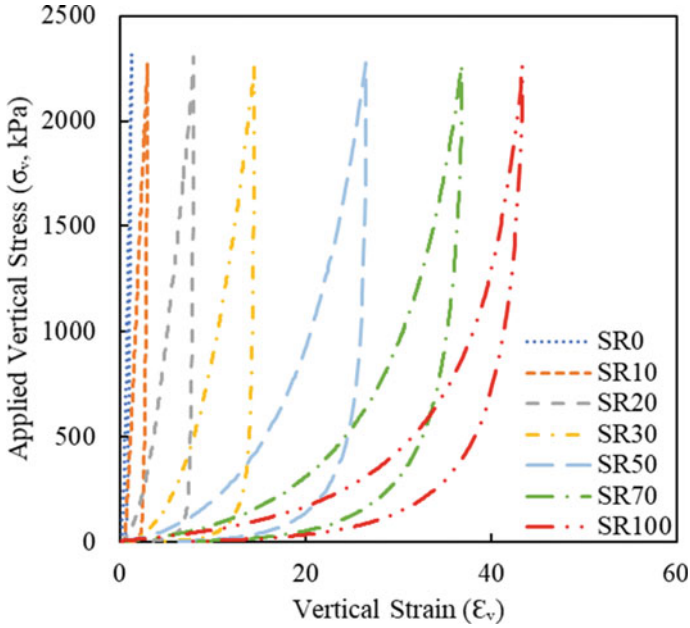


**Fig. 4** Vertical strain–vertical stress graphs for sand–rubber mixtures. Samples names as SRX where SR and X stands for sand–rubber and rubber fraction, respectively

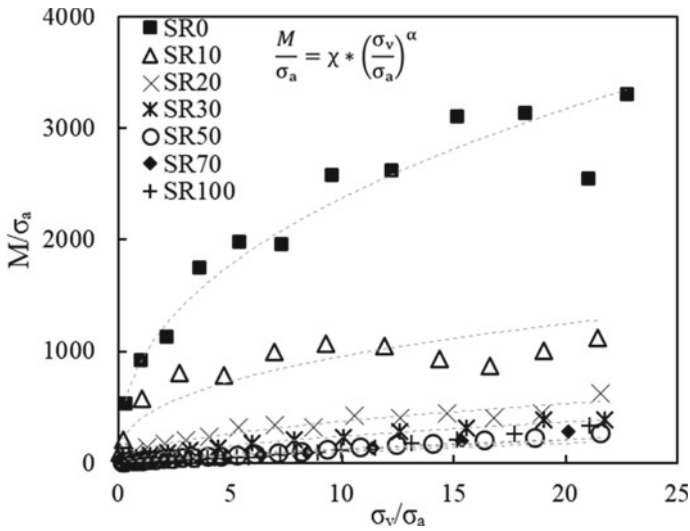


**Fig. 5** Normalised stiffness and stress relation of sand–rubber mixtures under confined compression

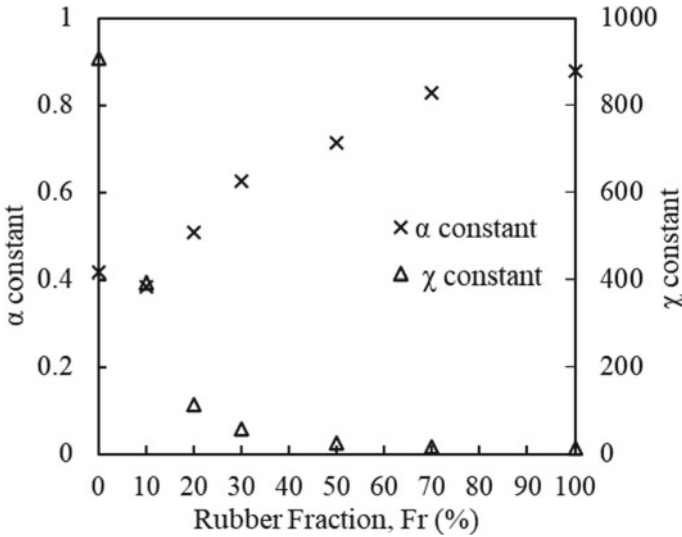


Fig. 6 Stiffness parameters as a function of rubber fractions

The stiffness exponent of different soils are plotted against the specific volume,  $v = 1 + e$ , following [16] in Fig. 7. The  $\chi$  and  $\alpha$  parameter values for sand-rubber mixtures resulted from the oedometer tests are also presented in Fig. 7 for comparison. As can be observed, the values of  $\alpha$  and  $\chi$  move upwards and downwards, respectively, from a sand-like behaviour to a much softer rubber-like behaviour, both within the limits defined by various soils.

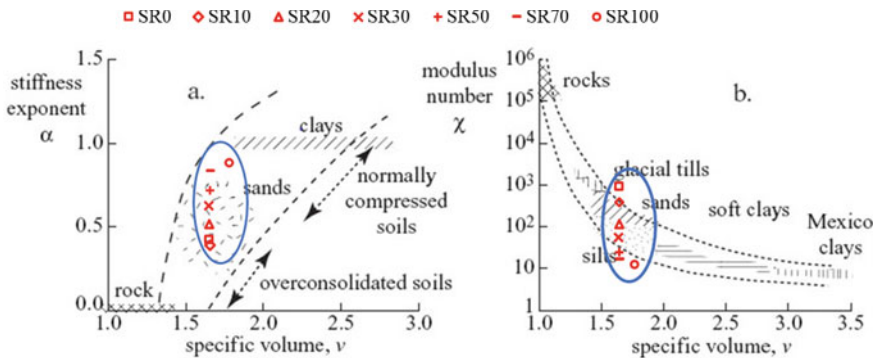


Fig. 7 Stiffness parameters against specific volume for different soil types from Muir-Wood [16]. Stiffness parameters for sand-rubber mixtures are plotted over the parameters from Muir-Wood [16]

## 4 Conclusion

The response of sand-rubber mixtures under one-dimensional confined compression conditions has been analysed and the compressibility response and one-dimensional stiffness parameters of mixtures have been deduced. The following conclusions can be drawn from this research:

- The compressibility and deformability of mixtures increases with increasing rubber fraction. Rubber is a softer material, and the properties of the mixture become dominated by rubber-to-rubber particle contacts.
- The stiffness of mixtures decreases with increasing rubber fractions. One-dimensional incremental stiffness of the mixture becomes more proportional with the stress level for higher rubber fractions.

This research will be followed by one-dimensional cyclic loading tests, as well as the analysis of time-dependency. Mitigation measures to reduce the compressibility of sand-rubber mixtures for higher rubber contents in the range of 20–40% will also be considered.

**Acknowledgements** This research is funded by The Ministry of National Educational of Turkey, and this financial support is gratefully acknowledged.

## References

1. Tatlısoz N, Benson CH, Edil TB (1997) Effect of fines on mechanical properties of soil-tire chip mixtures. *Test Soil Mixed Waste Recycl Mater* 1275:93–108
2. Ahmed I (1993) Laboratory study on properties of rubber soils, in school of civil engineering, Purdue University, West Lafayette
3. Bosscher PJ, Edil TB, Kuraoka S (1997) Design of highway embankments using tire chips. *J Geotech Geoenviron Eng* 123(4):295–304
4. Edinçliler A, Baykal G, Dengili K (2004) Determination of static and dynamic behavior of recycled materials for highways. *Resour Conser Recycl* 42(3):223–237
5. Edinçliler A, Baykal G, Saygili A (2010) Influence of different processing techniques on the mechanical properties of used tires in embankment construction. *Waste Manag* 30(6):1073–1080
6. Edil TB, Bosscher PJ (1994) Engineering properties of tire chips and soil mixtures. *Geotech Test J* 17(4):453–464
7. Feng ZY, Sutter KG (2000) Dynamic properties of granulated rubber/sand mixtures. *Geotech Test J* 23(3):338–344
8. Valdes JR, Evans TM (2008) Sand-rubber mixtures: experiments and numerical simulations. *Can Geotech J* 45(4):588–595
9. Wang ZY et al (2018) Influence of sand-rubber mixtures backfill on mechanical properties of bridge abutment and foundation piles. *Soil Mech Found Eng* 55(2):139–139
10. Sheikh MN et al (2013) Shear and compressibility behavior of sand-tire crumb mixtures. *J Mater Civil Eng* 25(10):1366–1374
11. Lee C, Shin H, Lee JS (2014) Behavior of sand-rubber particle mixtures: experimental observations and numerical simulations. *Int J Numer Anal Methods Geomech* 38(16):1651–1663

12. Lee JS, Dodds J, Santamarina JC (2007) Behavior of rigid-soft particle mixtures. *J Mater Civil Eng* 19(2):179–184
13. Kim HK, Santamarina J (2008) Sand-rubber mixtures (large rubber chips). *Can Geotech J* 45(10):1457–1466
14. Rouhanifar S (2017) Mechanics of soft-rigid soil mixtures. In: Department of civil engineering. University of Bristol, Bristol
15. Liu L, Cai G, Liu S (2018) Compression properties and micro-mechanisms of rubber-sand particle mixtures considering grain breakage. *Constr Build Mater* 187:1061–1072
16. Muir-Wood D, Stiffness S (2009) Soil mechanics: a one-dimensional introduction. Cambridge University Press, New York, pp 67–89
17. Madhusudhan BR, Boominathan A, Banerjee S (2019) Engineering properties of sand–rubber tire shred mixtures. *Int J Geotech Eng*

# Open Source Model Installation for Researching the Effect of Tides in the Izmir Gulf



Doğuş Onur Bayram and Mustafa Doğan

**Abstract** Monitoring and modeling of changes in sea levels and sea characteristics due to global warming, climate changes and other reasons have gained importance in terms of the sustainability of seas and cities. Open source code ADCIRC model has been applied in order to predict the water movements due to tide in İzmir Bay. The source code of the ADCIRC model was obtained with the approval of the relevant institute and installed on a local computer, the preparation of the input files required for the model to work, the creation of the calculation grid, the coefficients representing the open boundary conditions, and the obtaining of the bathymetry data were again made with open source code utilities and models. Cloud-based and open-access DesignSafe CI environment was also used to run the model. The results obtained by making simulations of different time intervals and periods were graphed with the help of open source code visualization tools.

**Keywords** ADCIRC · Modelling · Sea · Sustainability · Tide

---

D. O. Bayram (✉) · M. Doğan  
Dokuz Eylül University, Izmir, Turkey  
e-mail: [dogus.bayram@ogr.deu.edu.tr](mailto:dogus.bayram@ogr.deu.edu.tr)

M. Doğan  
e-mail: [mustafa.dogan@deu.edu.tr](mailto:mustafa.dogan@deu.edu.tr)

## 1 Introduction

Monitoring, modelling and assessing changes in the ocean and coastal regions has become essential to keep coastal communities, economies, and ecosystems healthy, resilient and sustainable. Tides and meteorological forces are the main effects on changes in ocean and major topics in sea modelling.

Tides are long period waves generated by gravitational forces of the sun and the moon on the ocean waters [1]. The period, wavelength, and amplitude characteristics of the tide depend on geometric properties of a specific water body, i.e., the coastal outline and bathymetric profile. Tidally generated water heights and currents can be the dominant feature in a coastal area, or they may serve as background circulation that contributes in an influential manner to overall coastal dynamics.

Coastal and estuarine systems are home to more than 50% of the human population as well as many biological species [2]. Tidal predictions are a necessary component of any description of the coastal environment for navigational purposes, coastal fisheries, and military operations, to name a few applications [3].

İzmir, the 3rd largest city of Turkey is also a coastal city which resides coast of İzmir Gulf, and an important trade center with its port. İzmir Gulf is one of the great natural gulfs of the Aegean Sea. The gulf is roughly “L” shaped with a total length 64 km and opens to the Aegean Sea in the north. There are series of islands parallel to the west coast of the gulf [4]. Observation and modeling of the İzmir Gulf and sea is important for predictability, safety and sustainability.

## 2 Methodology

Using a numerical model is a popular and innovative way to predict sea level, water velocities and other changes in the ocean caused by tide or meteorological effects by means of commercial or open source software and tools.

Open source modelling has several advantages comparing to modelling with commercial software;

- Flexibility
- Cost Effectiveness
- Transparency and Security
- Innovation via Community
- Sustainability



## 2.1 ADCIRC—Advanced Circulation Model

ADCIRC is a system of computer programs for solving time dependent, free surface circulation and transport problems in two and three dimensions. These programs utilize the finite element method in space allowing the use of highly flexible, unstructured grids. Typical ADCIRC applications have included [5]:

- Prediction of storm surge and flooding
- Modeling tides and wind driven circulation
- Larval transport studies
- Near shore marine operations
- Dredging feasibility and material disposal studies

**Formulation.** ADCIRC solves forms of the shallow-water equations (SWE) for water levels  $\zeta$  and the vertically integrated momentum equations for currents  $\vec{U}$ . The model applies the continuous Galerkin finite-element method with linear  $C_0$  triangular elements to discretize and solve the SWE on unstructured meshes, and thus it allows localized refinement in regions where the solution gradients are largest.

ADCIRC computes water levels via the solution of the Generalized Wave Continuity Equation (GWCE), which is a combined and differentiated form of the continuity and momentum equations:

$$\frac{\partial^2 \zeta}{\partial t^2} + \tau_0 \frac{\partial \zeta}{\partial t} + S_p \frac{\partial \tilde{J}_\lambda}{\partial \lambda} + \frac{\partial \tilde{J}_\phi}{\partial \phi} - S_p U H \frac{\partial \tau_0}{\partial \lambda} - V H \frac{\partial \tau_0}{\partial \phi} = 0 \quad (1)$$

where:

$$\begin{aligned} \tilde{J}_\lambda = & -S_p Q_\lambda \frac{\partial U}{\partial \lambda} - Q_\phi \frac{\partial U}{\partial \phi} + f Q_\phi - \frac{g}{2} S_p \frac{\partial \zeta^2}{\partial \lambda} \\ & - g S_p H \frac{\partial}{\partial \lambda} \left[ \frac{P_s}{g \rho_0} - \alpha \eta \right] + \frac{\tau_{S\lambda, winds} + \tau_{S\lambda, waves} - \tau_{b\lambda}}{\rho_0} \\ & + (M_\lambda - D_\lambda) + U \frac{\partial \zeta}{\partial t} + \tau_0 Q_\lambda - g S_p H \frac{\partial \zeta}{\partial \lambda} \end{aligned} \quad (2)$$

and

$$\begin{aligned} \tilde{J}_\phi = & -S_p Q_\lambda \frac{\partial V}{\partial \lambda} - Q_\phi \frac{\partial V}{\partial \phi} + f Q_\lambda - \frac{g}{2} S_p \frac{\partial \zeta^2}{\partial \phi} \\ & - g S_p H \frac{\partial}{\partial \phi} \left[ \frac{P_s}{g \rho_0} - \alpha \eta \right] + \frac{\tau_{S\phi, winds} + \tau_{S\phi, waves} - \tau_{b\phi}}{\rho_0} \\ & + (M_\phi - D_\phi) + V \frac{\partial \zeta}{\partial t} + \tau_0 Q_\phi - g H \frac{\partial \zeta}{\partial \phi} \end{aligned} \quad (3)$$

and the currents are obtained from the vertically-integrated momentum equations:

$$\begin{aligned} & \frac{\partial U}{\partial t} + S_p U \frac{\partial U}{\partial \lambda} + V \frac{\partial U}{\partial \varphi} - fV \\ &= -gS_p \frac{\partial}{\partial \lambda} \left[ \zeta + \frac{P_s}{g\rho_0} - \alpha\eta \right] + \frac{\tau_{S\lambda,winds} + \tau_{S\lambda,waves} - \tau_{b\lambda}}{\rho_0 H} + \frac{M_\lambda - D_\lambda}{H} \end{aligned} \quad (4)$$

and

$$\begin{aligned} & \frac{\partial V}{\partial t} + S_p U \frac{\partial V}{\partial \lambda} + V \frac{\partial V}{\partial \varphi} + fU \\ &= -gS_p \frac{\partial}{\partial \varphi} \left[ \zeta + \frac{P_s}{g\rho_0} - \alpha\eta \right] + \frac{\tau_{S\varphi,winds} + \tau_{S\varphi,waves} - \tau_{b\varphi}}{\rho_0 H} + \frac{M_\varphi - D_\varphi}{H} \end{aligned} \quad (5)$$

where  $H = h + \zeta$  is total water depth;  $\zeta$  is the deviation of the water surface from the mean;  $h$  is bathymetric depth;  $S_p = \cos \varphi_0 / \cos \varphi$  is a spherical coordinate conversion factor and  $\varphi_0$ : is a reference latitude;  $U$ ,  $V$  are depth-integrated currents in the  $x$ ,  $y$  directions, respectively;  $Q_\lambda = UH$ ;  $Q_\varphi = VH$  are fluxes per unit width;  $f$  is the Coriolis parameter;  $g$  is gravitational acceleration;  $P_s$  is atmospheric pressure at the surface;  $\rho_0$  is the reference density of water;  $\eta$  is the Newtonian equilibrium tidal potential and  $\alpha$  is the effective earth elasticity factor;  $\tau_{S\lambda,winds}$ ,  $\tau_{S\lambda,waves}$  are surface stresses due to winds and waves, respectively;  $\tau_b$  is bottom stress;  $M$  are lateral stress gradients;  $D$  are momentum dispersion terms; and  $\tau_0$  is a numerical parameter that optimizes the phase propagation properties [6].

**Obtaining the Source Code.** The ADCIRC source code is developed and accessed by the University of North Carolina at Chapel Hill. Within the scope of the study, the necessary correspondence for the examination and use of the model was made with the university official and access to the resource folder was provided. Use for academic purposes is permitted provided the model source code is not distributed to third parties. The source folder was accessed as a result of e-mail conversations with UNC officials.

**Creating the Executable ADCIRC Components with “cmake”.** The configuration required for the installation of the ADCIRC model is provided by the cmake software. There are options such as serial or parallel configuration, inclusion of SWAN model, configuration settings required for output in NetCDF format. A folder named “build” is created in the source folder and the “cmake”. command is run and the configuration is completed by following the path below.

```

$ cmake ..

EMPTY CACHE:
Keys: [enter] Edit an entry [d] Delete an entry
Cmake Version 3.20.0
  [l] Show log output    [c] Configure
  [h] Help                [q] Quit without generating
  [t] Toggle advanced mode (currently off)

ADDITIONAL_FLAGS_ADCIRC      *
ADDITIONAL_FLAGS_ADCPREP     *
ADDITIONAL_FLAGS_ASWIP       *
ADDITIONAL_FLAGS_SWAN        *
ADDITIONAL_FLAGS_UTILITIES   *
BUILD_ADCIRC                  *ON
BUILD_ADCSWAN                 *ON
BUILD_ASWIP                   *ON
BUILD_SWAN                    *ON
BUILD_UTILITIES               *ON
CMAKE_BUILD_TYPE              *Release
CMAKE_CXX_COMPILER            */usr/bin/c++.exe
CMAKE_CXX_FLAGS_DEBUG         *-g
CMAKE_CXX_FLAGS_RELEASE       *-O3 -DNDEBUG
CMAKE_C_COMPILER              */usr/bin/cc
CMAKE_C_FLAGS_DEBUG           *-g
CMAKE_C_FLAGS_RELEASE         *-O3 -DNDEBUG
CMAKE_Fortran_COMPILER        */usr/bin/gfortran.exe
CMAKE_Fortran_FLAGS_DEBUG     *-g
CMAKE_Fortran_FLAGS_RELEASE   *-O3 -DNDEBUG -O3
CMAKE_INSTALL_PREFIX          */adcirc_v53releasev53.04/bin
DEBUG_ALL_TRACE               *OFF
DEBUG_FLUSH_MESSAGES          *OFF
DEBUG_FULL_STACK              *OFF
DEBUG_LOG_LEVEL               *OFF
ENABLE_OUTPUT_NETCDF          *ON
ENABLE_WARN_ELEV_DEBUG        *OFF
Fortran_COMPILER_SPECIFIC_FLAG *-mcmode1=medium
Fortran_LINELENGTH_FLAG       *-ffixed-line-length-none
PERL                           */usr/bin/perl.exe

```

```

CMAKE_INSTALL_PREFIX: Install path prefix, prepended onto install
directories.
Keys: [enter] Edit an entry [d] Delete an entry
Cmake Version 3.20.0
  [l] Show log output    [c] Configure      [g] Generate
  [h] Help                [q] Quit without generating
  [t] Toggle advanced mode (currently off)

```

Here, the necessary selections are made and the “g (Generate)” key is pressed and the “Makefile” file is created by cmake to perform the installation. Then, the model is configured by running the “make” and “make install” commands in the terminal and executable components of ADCIRC model has created. The created executable files are essential parts of ADCIRC model.

## 2.2 Unstructured Grid Generation

ADCIRC model requires an unstructured grid model of the region. In the calculation network compatible with the ADCIRC model, there are triangular calculation elements and nodes determined based on the finite element method. These points are expressed with the coordinate information of a predetermined georeference system and the elevation values obtained from the bathymetry data. Various commercial software or open source scripts prepared in various programming languages are used to create this model.

**Oceanmesh2D.** OceanMesh2D is a MATLAB-based, object-oriented and open-source software used to create two-dimensional computational networks for sea, coastal and shallow water flow models [7]. It can create an ADCIRC compatible irregular network model with defined geographical coordinates, coastline data, topography and bathymetry information.

OceanMesh2D program written with an object-oriented approach and it contains the 4 basic classes as follows.

1. Geodata: Processes geospatial data.
2. Edgex: Configures the mesh size functions.
3. Meshgen: It creates the meshgen according to the mesh size functions and model boundaries.
4. Msh: It is used to store, write, read, analyze and visualize computational networks and auxiliary components for numerical simulation.

*GSHHS Shoreline Data and SRTM15 + V2.1 DEM Data.* GSHHS (A Global Self-consistent, Hierarchical, High-resolution Shoreline) is a globally consistent, hierarchical, high-resolution shoreline database [8]. SRTM15 + is a digital elevation model that contains bathymetry and topography data at a global scale, with a sampling interval of 15 angle-seconds, and a resolution of approximately 500 m × 500 m per pixel on the equator [9].

It is aimed to clear some indentations in the coastline data and to create a smoother calculation area. These regions in the coastline data were cleaned with the help of QGIS software and coastline in Fig. 1 obtained. SRTM15 + V2.1.nc DEM bathymetry data assimilated to grid shown in Fig. 2 and unstructured grid in Fig. 3.

## 2.3 Tidal Parameters

It is necessary to know the tidal parameters of the open boundary calculation points in order to calculate the level change and velocity values caused by the tidal effect in İzmir Bay with the help of the ADCIRC model. MATLAB based TMD (Tidal Model Driver) used to determine amplitude and phase values in open boundary nodes and “tide\_fac.f” FORTRAN code used to obtain nodal attributes for calculation date and



Fig. 1 Coastline data

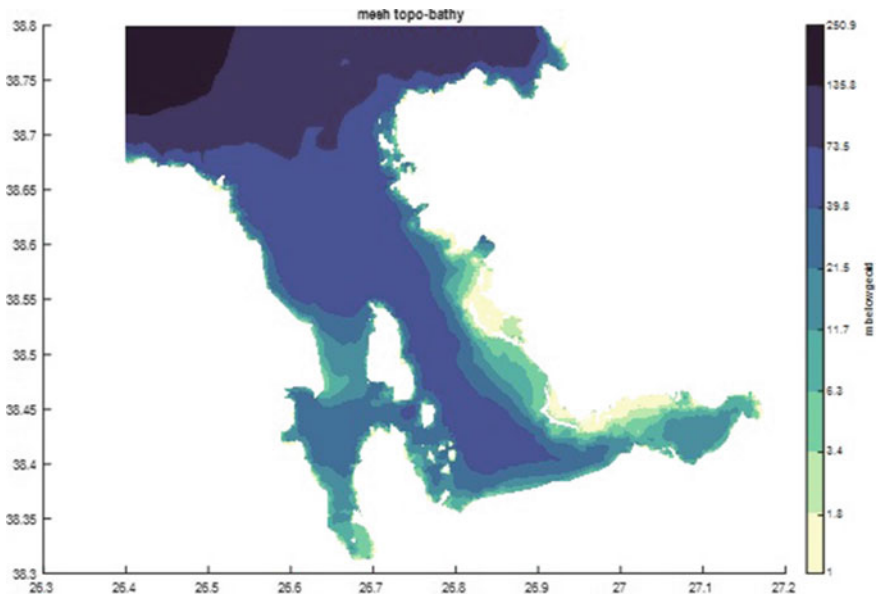


Fig. 2 SRTM15 + V2.1 bathymetry

length. This information will be processed into the fort.15 input file containing the model parameters.

**TMD (Tidal Model Driver).** “TMD (Tidal Model Driver) Tide Toolbox” is a MATLAB package created to access the harmonic components of the ESR/OSU family of tide models and make predictions for tide height and currents [10]. TMD MATLAB interface shown in Fig. 4.

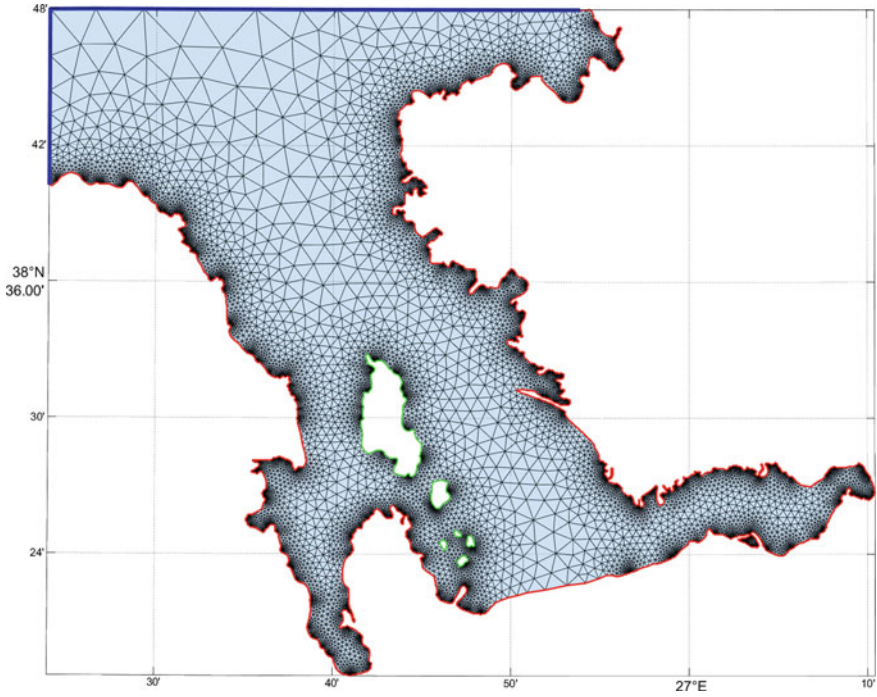


Fig. 3 Unstructured grid

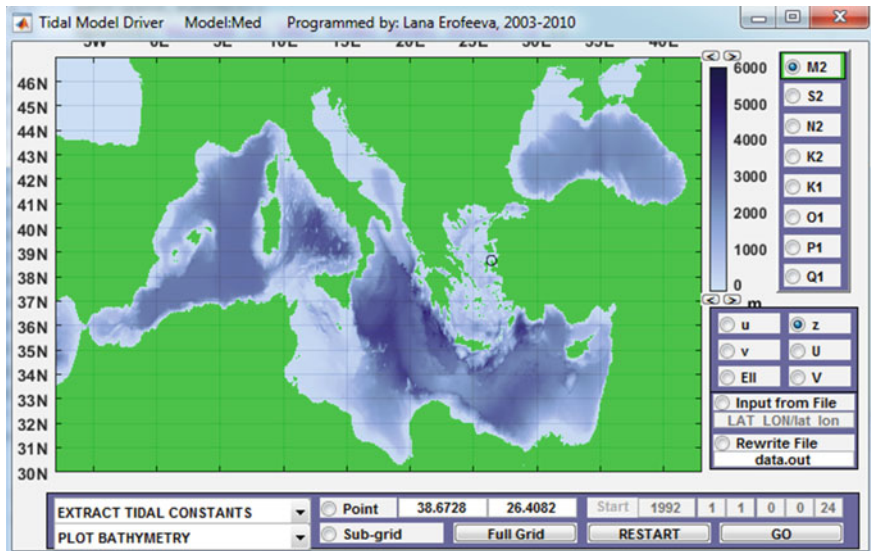
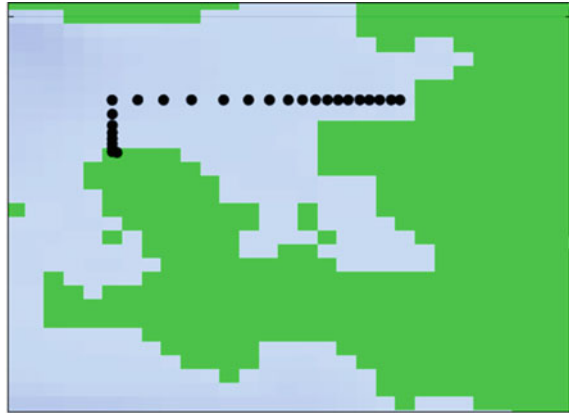


Fig. 4 TMD MATLAB interface

**Fig. 5** Open boundary nodes–TMD



Coordinates of boundary nodes in the grid recorded to “lat\_lon” text file as a list and amplitude and phase values for selected tidal constituents and applied in TMD. Open boundary nodes of the grid has shown in Fig. 5.

*Tidal Constituents.* 5 major tidal constituents selected for this model to determine tidal boundary conditions; properties of these constituents shown in Table 1.

*OSU TPXO-OTIS Regional Mediterranean Tidal Model.* TPXO is a global, regional and local, barotropic tide model. The methods have been implemented in the “OTIS (OSU Tidal Inversion Software)” software. All global, regional and local models were obtained by assimilating satellite altimetry and other data with OTIS [11].

The “Mediterranean” model in the “Regional Models” section was used to calculate the amplitude and phase values of the Izmir Bay. The model file is downloaded and imported into the TMD MATLAB source file. General information about the OSU TPXO-OTIS Regional Mediterranean Tidal Model shown in Fig. 6.

**Table 1** Properties of 5 major tidal constituents in model

Darwin symbol	Type	Period (h)	Speed (°/h)	Doodson number	NOAA order
M2	Principal lunar semidiurnal	12.4206012	28.9841042	255.555	<b>1</b>
S2	Principal solar semidiurnal	12	30	273.555	<b>2</b>
N2	Larger lunar elliptic s.diurnal	12.65834751	28.4397295	245.655	<b>3</b>
K1	Lunar diurnal	23.93447213	15.0410686	165.555	<b>4</b>
O1	Lunar diurnal	25.81933871	13.9430356	145.555	<b>6</b>

NOAA order: National Oceanic and Atmospheric Administration orders are durable intra-agency directives that remain effective until superseded or canceled by appropriate action

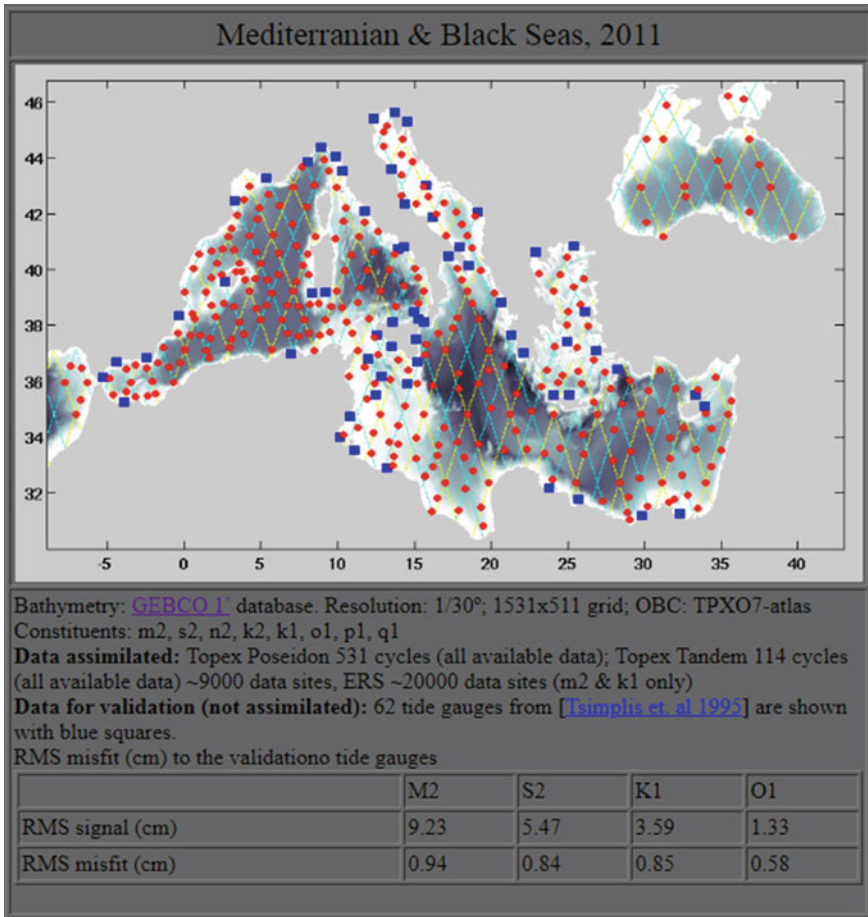


Fig. 6 OSU TPXO-OTIS regional mediterranean tidal model information

**Nodal Parameters with “tide\_fac.f” Fortran Program.** The nodal parameters to be used in tide calculation are calculated with the help of Fortran program “tide\_fac.f”, which is among the ADCIRC model auxiliary tools. An example run of the code for 30 days of simulation starting at 00:00, 01.01.2020 shown below.



```

$ ./tide_fac.exe
ENTER LENGTH OF RUN TIME (DAYS)
30
ENTER START TIME - BHR, IDAY, IMO, IYR (IYR e.g. 1992)
00,01,01,2020
TIDAL FACTORS STARTING: HR- 0.00, DAY- 1, MONTH- 1 YEAR- 2020

FOR A RUN LASTING 30.00 DAYS

CONST   NODE   EQ ARG (ref GM)
NAME    FACTOR  (DEG)
K1      0.99979  1.23
O1      0.99946  230.34
P1      1.00000  349.87
Q1      0.99946  62.13
N2      1.00497  59.27
M2      1.00497  227.48
S2      1.00000  0.00
K2      0.97870  182.43

```

## 2.4 *DesignSafe CI*

The Natural Hazards Engineering Research Infrastructure (NHERI) is a multi-user facility that aims to provide advanced technology infrastructure to engineers doing research on natural hazards. It is funded by the “National Science Foundation (NSF)”. NHERI aims to develop innovations that help prevent natural hazards from occurring by enabling researchers to conduct research to protect homes, businesses and infrastructure lifelines from the effects of earthquake, wind and water hazards.

DesignSafe is the CI component of the NHERI collaboration. DesignSafe adopts the cloud strategy for big data generated in natural hazards engineering research. It supports research workflows, data analysis and visualization. ADCIRC model can also be used within this infrastructure.

ADCIRC module in DesignSafe infrastructure is mostly used for simulations and supported with ADCIRC compiled on PC which explained in Sect. 2.1.

## 2.5 *FigureGen*

FigureGen is a Fortran program that creates images for ADCIRC files. It reads grid files (fort.14, etc.), nodal attributes files (fort.13, etc.) and output files (fort.63, fort.64, maxele.63, etc.). It plots contours, contour lines, and vectors. Using FigureGen, you can go directly from the ADCIRC input and output files to figures, for one- or multiple-time snaps. “maxele.63” output files of simulations are visualized with FigureGen to show maximum water levels during each of 30 days simulations for whole Izmir Gulf area with contour lines filled with and color related a color legend with 1 mm precision.

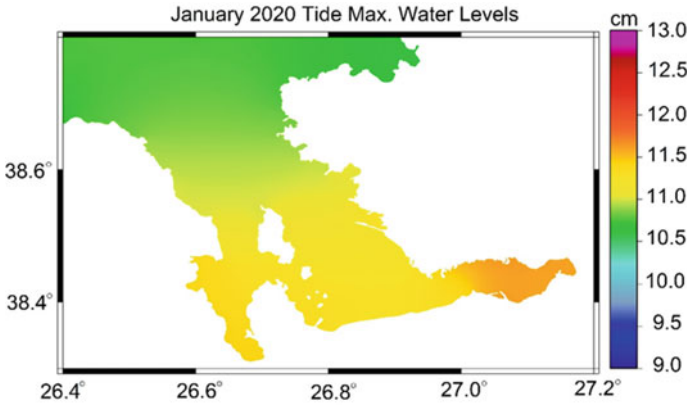


**Fig. 7** January 2020 max. Water levels due to tide effects

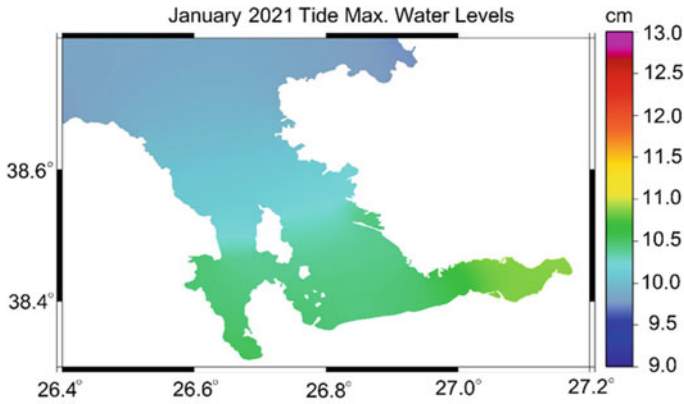


**Fig. 8** January 2021 max. Water levels due to tide effects

### 3 Results

Simulations performed for 30 days from beginning of each month, for 2 years, 2020 and 2021. Maximum water levels due to tidal constituents obtained from TMD for each open boundary node of calculation grid used as boundary conditions.

30 Days of Simulations Performed from Beginning of January, April, July and October 2020–2021 in Figs. 7, 8, 9, 10, 11, 12, 13 and 14 Respectively.

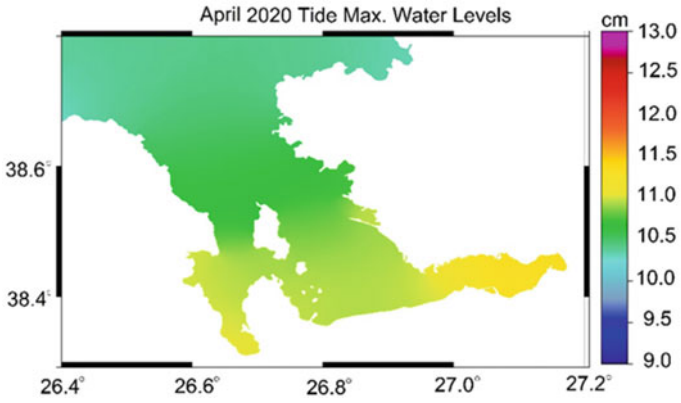


Fig. 9 April 2020 max. Water levels due to tide effects

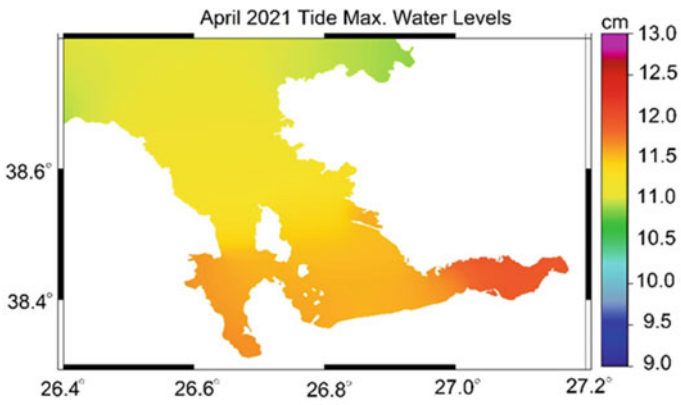


Fig. 10 April 2021 max. Water levels due to tide effects

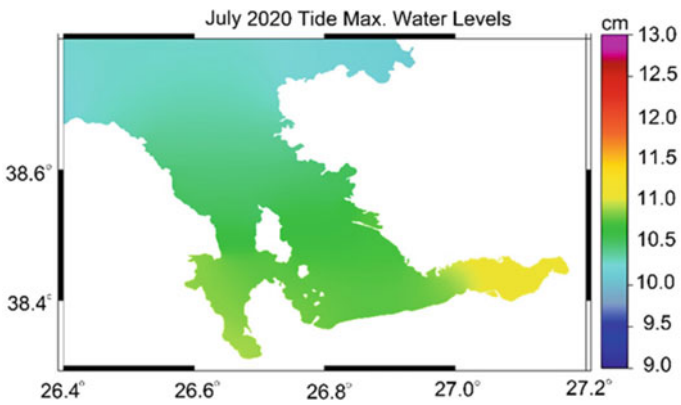


Fig. 11 July 2020 max. Water levels due to tide effects

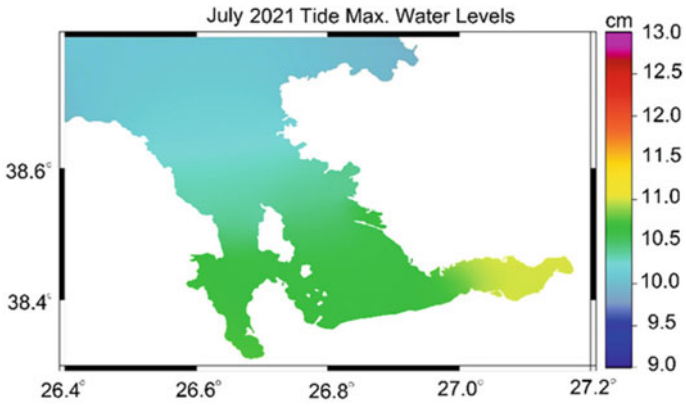


Fig. 12 July 2021 max. Water levels due to tide effects

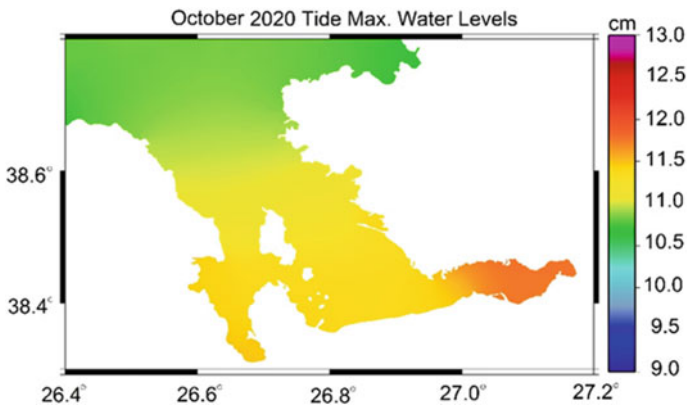


Fig. 13 October 2020 max. Water levels due to tide effects

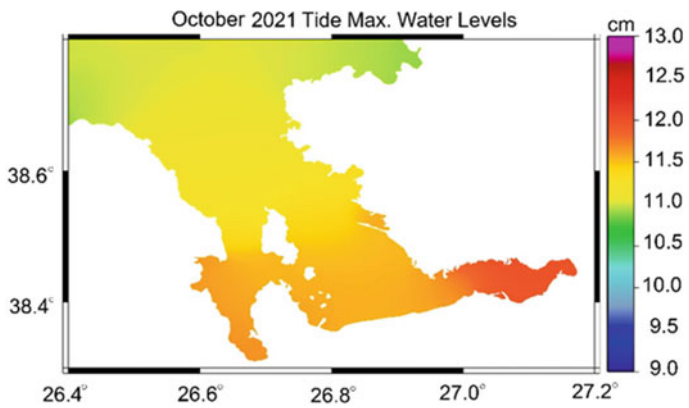


Fig. 14 October 2021 max. Water levels due to tide effects

## 4 Conclusion

Open source ADCIRC model performed on İzmir Gulf driven with tidal open boundary conditions obtained from TMD with calculation grid generated with Ocean-mesh2D. 30 days of simulation runs performed for each month in 2020 and 2021. Maximum water levels occurred only with 5 major tide effects obtained and visualized by FigureGen. Maximum water level changes between 10–12 cm and different sections can be observed from figures.

By combining tidal effects with meteorological forces obtained from ERA5 database (wind and atmospheric pressure), simulations with coupled ADCIRC-SWAN model is also planned for future of this work.

## References

1. Hendershott MC (2016) Long waves and ocean tides. *Evol Phys* Author F.: Article Title. J 2(5):99–110
2. Yanagi T (1999) *Coastal Oceanography*. Terrapub, Tokyo, p 172
3. Blain CA, Rogers WE (1998) Coastal tide prediction using the ADCIRC-2DDI Hydrodynamic Finite Element Model: Model Validation and Sensitivity Analyses in the Southern North Sea/English Channel, "NRL/FR/7322--98-9682, Naval Research Laboratory, Stennis Space Center, MS
4. Sayın E, Pazi I, Eronat C (2006) Investigation of water masses in İzmir Bay, Western Turkey. *Turkish J Earth Sci* 15:343–372
5. ADCIRC Homepage. <https://adcirc.org/>. Last accessed 14 Sep 2022
6. Dietrich JC, Tanaka S, Westerink JJ, Dawson CN, Luettich RA, Zijlema M, Holthuijsen LH, Smith JM, Westerink LG, Westerink HJ (2011) Performance of the unstructured-mesh, SWAN+ ADCIRC model in computing hurricane waves and surge
7. Roberts KJ, Pringle WJ, Westerink JJ (2019) OceanMesh2D 1.0: MATLAB-based software for two-dimensional unstructured mesh generation in coastal ocean modelling. *Geosci Model Dev* 12:1847–1868. <https://doi.org/10.5194/gmd-12-1847-2019>
8. Wessel P, Smith WHF (1996) A global, self-consistent, hierarchical, high-resolution shoreline database. *J Geophys Res* 101(B4):8741–8743. <https://doi.org/10.1029/96JB00104>
9. Tozer B, Sandwell DT, Smith WHF, Olson C, Beale JR, Wessel P (2019) Global bathymetry and topography at 15 arc sec: SRTM15+. *Earth Space Sci* 6. <https://doi.org/10.1029/2019EA000658>
10. Erofeeva SY, Padman L, Howard SL (2020) Tide Model Driver (TMD) version 2.5, Toolbox for Matlab
11. [https://www.github.com/EarthAndSpaceResearch/TMD\\_Matlab\\_Toolbox\\_v2.5](https://www.github.com/EarthAndSpaceResearch/TMD_Matlab_Toolbox_v2.5)

# Numerical Modelling of Soluble Contamination Transport in Landfills Based on Empirical Function of Membrane Efficiency



Aysa Hedayati-Azar, Hamed Sadeghi, Ali Golaghaei Darzi, and Pouya AliPanahi

**Abstract** Clayey soils are widely used as barriers to control leachate leakage in landfills. Chemico-osmosis is one of the important phenomena influencing soluble contamination transport through clay barriers acting as a membrane. The membrane ability to restrict contamination transport is referred to as membrane efficiency. Experimental reports have revealed that membrane efficiency is a function of soil void ratio and contamination concentration. However, the currently used empirical function expresses the membrane efficiency simply in terms of average concentration. Therefore, the merit of this study is to enhance the reliability of this function to take into account various concentrations and void ratios for Na-bentonite soil by using the dataset reported by Malusis and Shakelford (2002). In order to highlight the significance of the newly proposed function, a numerical simulation has been conducted to compare three different approaches of applying membrane efficiency including (1) constant, (2) point, and (3) average value. The results show that membrane efficiency from the point approach is less than the constant value at shallower depths but more at deeper depths in the early years. More importantly, membrane efficiency by point and average approaches decrease over time, resulting in higher contamination concentration compared to a constant value. The implication is that current design practice based on constant membrane efficiency is not conservative. According to the results of time-dependent contamination concentration, the required thickness and an efficient lifetime of the landfill barriers should be adjusted by simulation results of more reliable point and average approaches.

---

A. Hedayati-Azar · H. Sadeghi · A. G. Darzi (✉) · P. AliPanahi  
Department of Civil Engineering, Sharif University of Technology, Tehran, Iran  
e-mail: [ali.golaghaei@sharif.edu](mailto:ali.golaghaei@sharif.edu)

A. Hedayati-Azar  
e-mail: [aysa.hedayati9776@sharif.edu](mailto:aysa.hedayati9776@sharif.edu)

H. Sadeghi  
e-mail: [hsadeghi@sharif.edu](mailto:hsadeghi@sharif.edu)

P. AliPanahi  
e-mail: [Pouya.alipanahi@sharif.edu](mailto:Pouya.alipanahi@sharif.edu)

**Keywords** Contaminant transport · Membrane efficiency · Numerical modelling · Solute-clay interactions

## 1 Introduction

Managing municipal solid waste is one of the crucial environmental issues, because it challenges most countries in the world. Municipal solid waste contains contaminants which are harmful for plants, animals, and humans' lives. Burying wastes in an isolated layer of soil is one way to control leachate leakage into ground water. Fine-grained compacted clayey soils are used to act as the isolating layer which is also referred to as clay barriers, because of their low hydraulic conductivity and membrane behavior [1]. However, there is still a chance for leachate to infiltrate into soil and to deteriorate fresh water quality, depending on the porosity, and mineralogy of the barrier as well as the chemical compositions in the leachate. Although the influence of solute concentrations on some aspects of soil behavior such as water retention [2–4], volumetric behavior [5], hydraulic conductivity [6], and slope stability [7] has been the focus of recent studies, less attention has been given to solute transport under a more realistic field condition. Therefore, understanding of the influencing factors on liquid and contaminants transport process in clay-rich barriers is profitable for improving barrier design [8–10].

Coupled flow phenomena cause contaminants and liquid transport in clayey barriers. Hydraulic conduction (Darcy's law) and chemico-osmosis flow cause liquid to flow as a result of hydraulic gradient and concentration gradient, respectively. On the other hand, advection and diffusion cause chemical species to transport [11, 12]. Clayey soils show semi-permeable membrane behavior which is the reason of chemico-osmosis flow across barrier. Membrane behavior of clayey soils are quantified by membrane efficiency coefficient. This coefficient reflects the restriction ability of clay-rich soils and it varies from 0 to 1. "Zero" implies no membrane behavior while "unity" connotes perfect restriction on contaminants transport. There are lots of experimental tests on membrane efficiency of different kinds of clayey soils including compacted clays, natural clays, geosynthetic clay liners (GCLs), bentonite-based soils, etc. It has been shown that membrane efficiency can change as a function of solute concentration and void ratio of soil [13–18].

If a clay barrier would act as a perfect membrane, there would be no possibility of chemical species transport through diffusion and advection mechanisms. Therefore, it can be concluded that membrane efficiency influences advection and diffusion rate [19, 20]. Moreover, there are some experimental tests indicating the influence of membrane efficiency on effective diffusion coefficient. Theoretical equations for coupled flow show role of membrane efficiency as well [17, 20, 21]. There are some numerical modellings based on theoretical equations. The results confirmed the great influence of membrane efficiency on concentration profile, exit flux rate, and so forth. Indeed, increasing membrane efficiency cause decreasing concentration profile and exit flux and downward liquid velocity [19, 22, 23]. More importantly,

some experimental test results strongly support the variations in this coefficient by concentration. Nevertheless, in these numerical models, membrane efficiency was assumed to be constant during analysis.

Therefore, the main objective of this study is the realistic modelling of one-dimensional contaminant transport through a 1-m saturated bentonite liner by considering hydraulic conduction, chemico-osmosis flow, diffusion, and advection phenomena. In order to achieve more reliable outcomes, a new empirical membrane efficiency function is first derived based on reliable experimental database in the literature. The new function is distinctive in taking into consideration the influence of both porosity and concentration on the membrane efficiency. Afterwards, the new function is embedded into the simulation modelling and results of more realistic variations in the concentration profile including two approaches are compared with the conventional constant profile assumption. Eventually, some new insights are provided with implication for the prospective amendment of clay barrier design.

## 2 A New Membrane Efficiency Function

There are some theoretical functions for membrane efficiency in the literature [24–27]. Furthermore, there is an empirical function for membrane efficiency based on experimental test results [28]. In this function, membrane efficiency is a linear semi-log function of average concentration across clayey membrane. As a result, most of test results were reported in this format [28]. This function describes membrane efficiency for limited range of concentration with high coefficient of determination,  $R^2$ . Although this equation cannot predict a correct value for limiting concentration where membrane behavior disappears, it can be used for limited range of solute concentration [17, 29].

### 2.1 Data Presentation

As mentioned before, there are some data sets for membrane efficiency, which are divided into several categories based on their test procedures, test devices, soil types, and solute types. In this study, the experimental database of Malusis and Shakelford [22] are used. It should be noted that the data were reported for potassium chloride (KCl) permeating through Na-bentonite soil in a rigid-wall device [14]. In order to obtain the new empirical function, a similar regression-based approach as employed in previous research is used for correlating the membrane efficiency to the average concentration for each void ratio. Afterwards, the constant parameters in Eq. (1), namely  $a$  and  $b$  are optimized to best-fit the measured experimental data at specific void ratio. It is also noted that membrane efficiency coefficients are determined and adjusted by water activity equation [30].



$$\omega = a \times \ln(C_{avg}) + b \quad (1)$$

$\omega$  membrane efficiency coefficient

$C_{avg}$  average concentration

$a, b$  fitting parameters for in semi-log space.

## 2.2 Empirical Function for Membrane Efficiency

Based on best fitting curve of Eq. (1), constant parameters were obtained for each void ratio, and reported in Table 1. Measured data points along with the best-fit lines are shown in Fig. 1 for each void ratio. According to the results, semi-log trend lines are in an excellent agreement with data points in the concentration range considered (i.e. from 3.9 to 47 mM).

In the next step, the fitting parameters of Eq. (1) are correlated linearly to void ratio. Comparison between the measurements and predictions are made in Fig. 2. Both fitting parameters ( $a$  and  $b$ ) take negative values and increase with void ratio. Similar to the results of Fig. 1, linear best-fit trends can give excellent predictions for the empirical constant values of  $a$  and  $b$ . Details of correlations for  $a$  and  $b$  are given in Table 1. Eventually, these correlations are implemented into the general function of membrane efficiency according to Eq. (2). This newly derived empirical function based on high quality experimental measurements are used in numerical simulations to take into account the real time dependency of membrane efficiency on both void ratio and solute concentration.

$$\omega = (0.015e - 0.256) \times \ln(C_{avg}) + 0.037e - 0.753 \quad (2)$$

$e$  void ratio.

## 3 Numerical Simulation

### 3.1 Different Approaches for Applying Membrane Efficiency

Many numerical analyses have been done considering constant membrane efficiency condition [19, 22, 23, 31]. Different simulation methods including explicit (E), implicit (I), explicit/implicit (EI) and no membrane behavior (NM) from Malusis and Shakelford [22] have shown that changing membrane efficiency influences exit flux and concentration profile widely. In explicit analysis, apparent tortuosity factor was constant and membrane efficiency changed as a function of solute concentration. In implicit method, membrane efficiency was constant and apparent tortuosity changed as a function of solute source concentration. In explicit/implicit method,

**Table 1** Summary of results for empirical membrane efficiency function

$e$	$\omega = a \times \ln(C_{avg}) + b$	$a = a_a e + b_a$	$b = a_b e + b_b$	$R^2$ of Eq. (2)
2.85	$-0.218 \times \ln(C_{avg}) - 0.665$ $R^2 = 0.99$	$a = 0.015e - 0.256$ $R^2 = 0.97$	$b = 0.037e - 0.753$ $R^2 = 0.90$	0.99
3.76	$-0.196 \times \ln(C_{avg}) - 0.593$ $R^2 = 0.99$			0.99
6.14	$-0.168 \times \ln(C_{avg}) - 0.535$ $R^2 = 0.98$			0.98

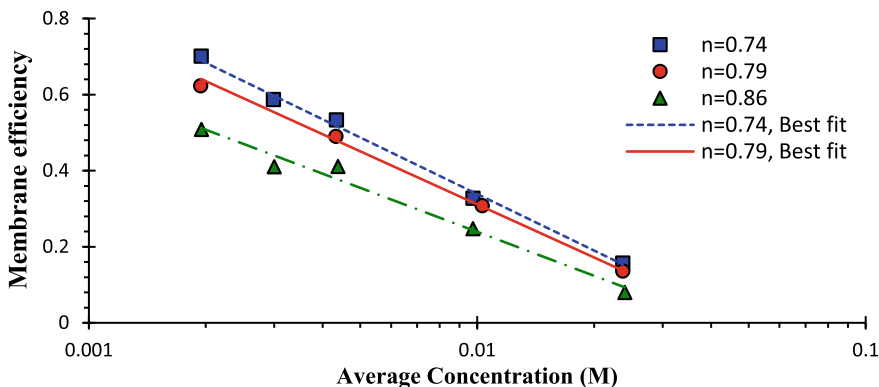


Fig. 1 Membrane efficiency as a function of average concentration across barrier (data points from [22])

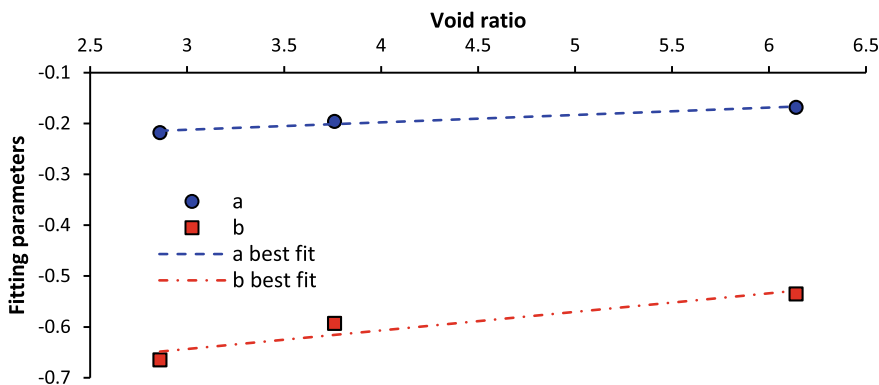


Fig. 2 Fitting parameters as a function of void ratio

both of them changed with concentration. It was revealed that considering both of these coefficients as a function of concentration, eventuates more realistic results in the perfect membrane behavior condition ( $\omega = 1$ ) [22].

Numerical simulation results have shown that concentration profile changes over time [19, 22, 23, 31]. In numerical simulation of Malusis and Shakelford [22], membrane efficiency was constant during analysis in all 3 approaches (E, I, EI). However, membrane efficiency changes with respect to concentration profile over time.

Regrading to importance of membrane efficiency in solute transport, three different approaches are considered for applying membrane efficiency during analysis in this study:

**Constant Membrane Efficiency:** Based on Malusis and Shakelford [22] test results, a constant value is assumed and it remains constant during numerical analysis. This

**Table 2** Model parameters

Parameters	$e = 2.85$
$D_{0s}$ (m <sup>2</sup> /s)	$19.93 \times 10^{-10}$
$K_h$ (m/s)	$6.24 \times 10^{-12}$
$\omega_{\text{constant}}$	0.16
$C_0$ (mol/m <sup>3</sup> )	0.047
$i_h$	10
T (k)	298
R (J/mol/K)	8.314
$\rho$ (kg/m <sup>3</sup> )	1371.8
M	0.5
$C_{\omega=0}$	0.0478
$C_{\omega=1}$	0.00044

constant value is chosen based on source concentration and void ratio of barrier. This approach is referred to as constant approach in this paper.

**Point Membrane Efficiency:** In this approach, membrane efficiency is applied for each point of barrier based on the corresponding solute concentration. Accordingly, membrane efficiency is calculated by Eq. (2) for each point. Since this equation may give some values more than 1 or less than 0 which are not acceptable, an operative solute concentration range is defined. Membrane efficiency coefficient for concentration less than this range (upper boundary of membrane efficiency) is assumed to be 1 and for concentration more than this range (lower boundary of membrane efficiency) is assumed to be 0. These limiting boundaries are reported in Table 2 as  $C_{\omega=1}$  and  $C_{\omega=0}$  respectively. This approach is referred to as point approach in the following analyses.

**Average Membrane Efficiency:** In this approach, an average value of membrane efficiency is applied for part of barrier which contains solute. Average solute concentration of this part is calculated by Eq. (3) at each time step and membrane efficiency is obtained by Eq. (2) and applied to that part. Membrane efficiency for rest of barrier with no solute, is assumed to be 1. Operative concentration range is applicable in this approach as well. This approach is referred to as average approach in simulations.

$$C_{sa} = \frac{\int_{z=0}^{d_s} C dz}{d_s} \tag{3}$$

$C_{sa}$  average solute concentration for part of barrier with solute content  
 $d_z$  barrier's depth with solute content.

### 3.2 Driving Equations for Solute Transport

Diffusion, advection, hydraulic conduction, and chemico-osmosis are considered as coupled flow phenomena for solute transport in this study. Driving equations of liquid flow and solute species transport through a saturated porous membrane are expressed as follow [12, 32–35]:

$$q = q_h + q_\pi = K_h i_h + \omega K_h i_\pi = -K_h \frac{\partial h}{\partial z} + \frac{\omega K_h}{\gamma_w} \frac{\partial \pi}{\partial z} \quad (4)$$

$$J_j = J_{ha,j} + J_{\pi,j} + J_j^d = (1 - \omega)q_h C_j + (1 - \omega)q_\pi C_j - nD_{sj}^* \frac{\partial C_j}{\partial z} \quad (5)$$

$q$	total fluid flow
$q_h$	hydraulic liquid flux
$q_\pi$	chemico-osmosis liquid flux
$K_h$	hydraulic conductivity
$i_h$	hydraulic pressure gradient
$i_\pi$	chemico-osmosis pressure gradient
$h$	hydraulic head
$\pi$	chemico-osmosis pressure
$\gamma_w$	unit weight of pore water
$J_j$	flux of solute species
$J_{ha,j}$	hyperfiltration advection flux solute species
$J_{\pi,j}$	chemico-osmosis flux with regard to solute species
$J_j^d$	diffusion flux of solute species
$D_{sj}^*$	effective salt-diffusion coefficient of species
$C_j$	Concentration of solute species j

Parameters in these equations are defined as follow [20, 36–39]:

$$\pi = RT \sum_{j=1}^M C_j \quad (6)$$

$$D_{sc}^* = D_{sa}^* = D_s^* = \tau_a \frac{D_{0c} D_{0a} (|z_a| + |z_c|)}{D_{0a} |z_a| + D_{0c} |z_c|} = \tau_a D_{0s} \quad (7)$$

$R$	universal gas constant
$T$	absolute temperature
$M$	solute number
$D_{0c}$	self-diffusion coefficients of the cation
$D_{0a}$	self-diffusion coefficients of the anion
$ z_c $	cation valence

$|z_a|$  anion valence

By considering membrane behavior, apparent tortuosity factor can be defined as follow [29]:

$$\tau_a = \tau_m \tau_r = \tau_m (1 - \omega) = n^m (1 - \omega) \quad (8)$$

$\tau_a$  apparent tortuosity factor  
 $\tau_m$  matrix tortuosity factor  
 $\tau_r$  restrictive tortuosity factor  
 $n$  porosity  
 $m$  empirical coefficient

As shown in the series of Eqs. (4), (5), and (8), membrane efficiency has a great impact on solute transport process.

### 3.3 Simulation Assumptions

Figure 3 shows a schematic model of the 1-m thick Na-bentonite layer. Potassium chloride (KCl) is assumed as the soluble contaminant, consistent with the experimental dataset. Numerical analyses are done in order to compare results of different approaches. Table 2 shows the details of assumed model parameters. Moreover, the boundary conditions of the model are summarized in Table 3. Fixed concentration is applied at the top boundary and a secondary boundary condition is applied at the bottom boundary. It is noted that volume changes are neglected in this study for the sake of simplicity. As discussed before, the semi-log empirical function for membrane efficiency reports incorrect values for higher range of concentration. Therefore, source solute concentration in this study is assumed to be the highest KCl concentration of Malusis and Shakelford [22] tests which is 47 mM [14]. This study uses COMSOL Multiphysics for numerical modelling.

## 4 Interpretation of the Results

In this section, the most important numerical outputs are reported and explained. Membrane efficiency profile, concentration profile, and concentration changes at the bottom boundary during time are considered specifically and results of three different approaches are compared.

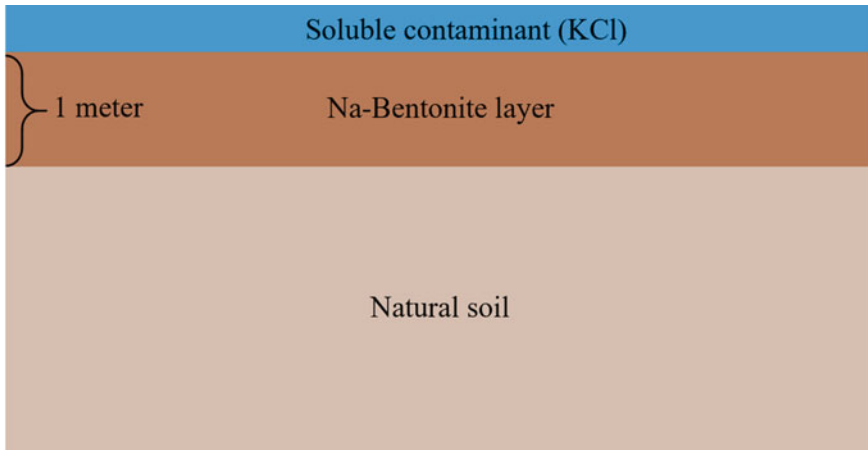


**Fig. 3** A schematic model of the Na-bentonite membrane barrier

**Table 3** Model boundary and initial conditions

Time	Location	Boundary and initial condition
$t \geq 0$	$z = 0$	$C_0 = 0.047$
$t = 0$	$z > 0$	$C = 0$
$t \geq 0$	$z = 1$	$\frac{\partial C}{\partial z} = 0$

### 4.1 Membrane Efficiency Profile

The main objective of this study was to compare different approaches of applying membrane efficiency function to barrier. Since membrane efficiency based on point and average approaches changes across barrier and over time, it is important to investigate that.

Figure 4 shows membrane efficiency changes across barrier in 3rd month, 5th year, and 10th year. According to Fig. 4a, membrane efficiency in average approach is more than constant value across barrier in 3rd months. However, it decreases during time by referring to the results of Fig. 4b and c. It can be seen that in 5th year, it is almost equal to constant value and in 10th year it is equal to half of that (Fig. 4b and c). Since chemico-osmosis phenomenon cause slower rate of solute transport during time [19, 23], the results of current study reveal that using constant approach cause conservative barrier design in the first 5 year, but non-conservative design after that compared to average approach.

Figure 4a also shows lower values of membrane efficiency for point approach compared to constant value, up to depth of 0.12 m in 3rd month. For deeper depths, however, point approach results in higher predictions. It causes higher rate of solute

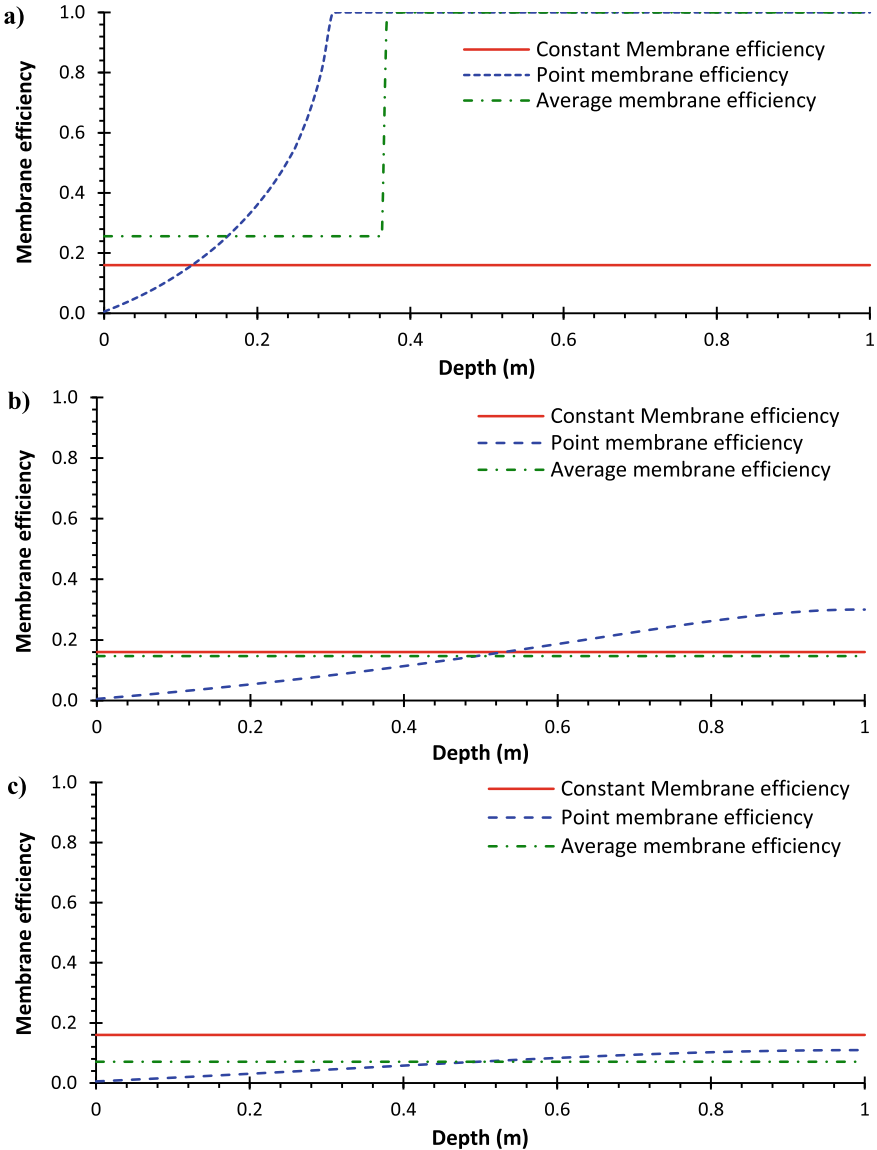


Fig. 4 Membrane efficiency profile at a) 3rd month, b) 5th year, c) 10th year

transport in shallower depths and lower rate in deeper depths compared to constant approach. According to the results of Fig. 4b and c, this critical depth increases over time: 0.5 m in 5th year and more than 1 m in 10th year, respectively. The implication is that membrane efficiency obtained from point approach is generally lower than the constant one after 10 years. It also shows that membrane efficiency from point



approach is less than average approach at shallower depths. This depth increases over time as well. Furthermore, results show that differences between point and average approach decrease over time.

## 4.2 Concentration Profile

Figure 5a shows that Infiltration depth based on constant and point approaches are respectively 0.4 m and 0.3 m in 3rd month. Solute concentration of bottom boundary is less by point approach in 5th year as well. Nonetheless, solute concentration based on point approach is more at shallower depths compared to constant approach in 3rd month and 5th year and across the whole depth of barrier in 10th year. It can be interpreted by means of membrane efficiency changes (Fig. 4). Membrane efficiency based on point approach is less at shallower depths and more at deeper depths compared to constant approach. It causes more rate of infiltration at shallower depths and less rate of that at deeper depths in 3rd months and 5th year according to Fig. 5a and b, respectively. Membrane efficiency based on point approach is less than constant value in 10th year which causes higher solute concentration across the whole depth of barrier as shown in Fig. 5c.

Concentration profile based on average approach is close to constant approach and differences can be neglected. Concentration profile based on average approach is marginally less than constant approach in the 3rd month and 5th year (Fig. 5a and b) and a little more in the 10th year (Fig. 5c).

## 4.3 Concentration Changes at Bottom Boundary

Figure 6 shows solute concentration changes during 20 years at the bottom boundary of barrier. Solute existence at the bottom boundary of barrier can be seen around 1st year based on constant approach and 2nd year based on point approach. All three approaches report same solute concentration around 6th year. Point approach reports more solute concentration value after that. Furthermore, it can be seen that difference between approaches increases after that (around 4.96% and 3.73% more solute concentration respectively for point and average approaches compare to constant approach). Average approach reports solute concentration values between constant and point approach over time.

In case, solute concentration of bottom boundary is a design criterion, it can be seen that up to 0.02 mM solute concentration, point value guarantees more utilizable years than constant and average approach. However, for higher solute concentration criterion, constant approach reports more utilizable years. It should be noted that using constant value for solute concentration varieties is intrinsically wrong based on analytical functions and empirical tests results.

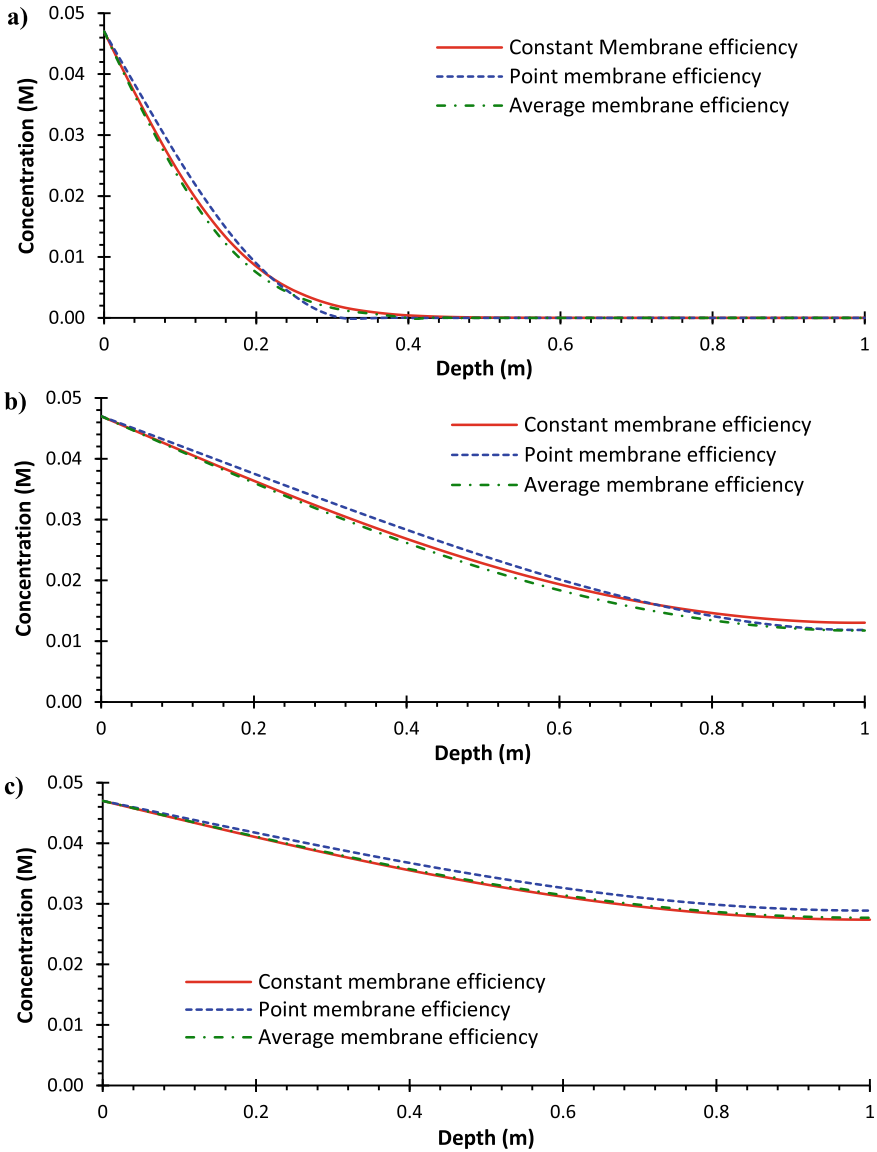
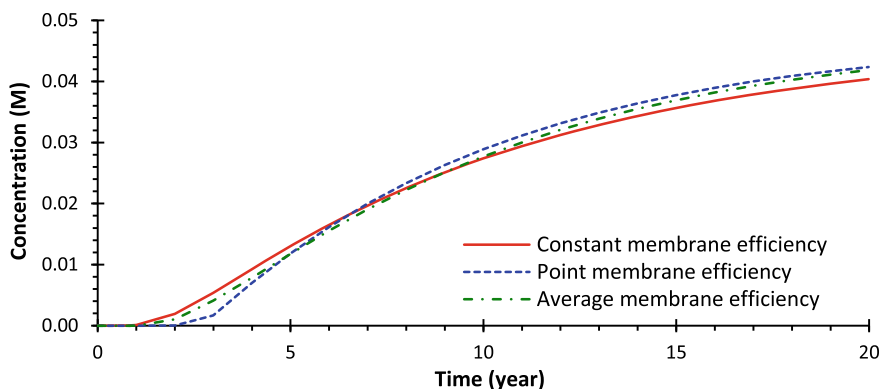


Fig. 5 Concentration profile at a) 3rd month, b) 5th year, c) 10th year

## 5 Conclusion

Clay-based soil or composite barriers are used to decrease leachate infiltration rate into the surrounding environment especially the fresh water. These barriers perform as membrane which causes chemico-osmosis flow. The properties of this type of



**Fig. 6** Concentration changes at the bottom of Na-bentonite layer during 20 years

flow plays a notable role in reducing liquid and solute transport through barriers as a result of concentration gradient. Previous experimental studies revealed that membrane efficiency coefficient is a key factor in the design of barriers. Although this coefficient is a function of void ratio and solute concentration, most of previous numerical simulations assumed a constant value for it during the life span of the barrier.

Therefore, this study was carried out to address the foresaid limitation by considering the dependency of membrane efficiency on porosity and concentration through introducing a new and simple, yet realistic empirical function for numerical simulations. In other words, a novel regression-based semi-log function was defined in this study based on the experimental results of Malusis and Shakelford [14]. Eventually, a numerical study was planned to compare the outcomes of three approaches of (1) constant, (2) point, and (3) average membrane efficiency in simulating chemico-osmosis phenomenon.

Results show that membrane efficiency calculated by point approach is less than constant approach at shallower depths, but more at deeper depths until year 6th from the beginning of transport. However, lower membrane efficiency was calculated for point approach compared to the constant one for the whole layer after 10 years consistently. The practical implication is that less amount of leakage be predicted for short-term performance of barrier while deterioration of membrane can cause a rise in leakage in long-term if the more realistic point approach be prioritized over conventional constant type of analysis. Regarding the average membrane efficiency, on the other hand, the results mostly lay between those of the other two approaches with some exceptions. The results also revealed that concentration profiles were more or less similar at different time intervals independent of the chosen approach. At the bottom boundary, however, relatively less changes in concentration were calculated based on point approach compared with the constant approach until year 6 while the trends became the other way around afterwards. One should note that different

behavior can be expected compared to this study, depending on initial concentration level, void ratio, thickness of barrier, and boundary conditions.

**Acknowledgements** The financial support provided by Research Grant Office at Sharif University of Technology for “fundamental investigation of flow characteristics through deformable porous media” via grant No. G970902 is gratefully acknowledged.

## References

1. Sadeghi H, AliPanahi P (2020) Saturated hydraulic conductivity of problematic soils measured by a newly developed low-compliance triaxial permeameter. *Eng Geol* 278:105827
2. Sadeghi H, Darzi AG (2021) Modelling of soil-water retention curve considering the effects of existing salt solution in the pore fluid. In: MATEC web of conferences. EDP Sciences, pp 02001
3. Golaghaei Darzi A, Sadeghi H (2021) A review of different approaches to analytical modeling of soil-water retention curves. *Sharif J Civil Eng*
4. Sadeghi H, Nasiri H (2021) Hysteresis of soil water retention and shrinkage behaviour for various salt concentrations. *Géotech Lett* 11(1):1–9
5. Sadeghi H et al (2019) Geotechnical characterization and collapsibility of a natural dispersive loess. *Eng Geol* 250:89–100
6. Hedayati-Azar A, Sadeghi H (2022) Semi-empirical modelling of hydraulic conductivity of clayey soils exposed to deionized and saline environments. *J Contam Hydrol* 104042
7. Kolahdooz A, Sadeghi H, Ahmadi MM (2020) A numerical study on the effect of salinity on stability of an unsaturated railway embankment under rainfall. In: E3S web of conferences. EDP Sciences, pp 01004
8. Nelles M et al. (2017) Recycling and recovery of the biogenic fractions from municipal solid waste in the PR of China. Study by University of Rostock
9. Keijzer TJ, Kleingeld P, Loch J (1999) Chemical osmosis in compacted clayey material and the prediction of water transport. *Eng Geol* 53(2):151–159
10. Elango L (2011) Hydraulic conductivity: issues, determination and applications. BoD–Books on Demand
11. Mitchell J (1991) Conduction phenomena: from theory to geotechnical practice. *Geotechnique* 41(3):299–340
12. Hedayati-Azar A, Sadeghi H (2021) A review of research approaches for contaminant transport in saturated deformable clay under coupled hydro-chemico-mechanical processes. *Sharif J Mech Eng*
13. Keijzer TJ, Loch J (2001) Chemical osmosis in compacted dredging sludge. *Soil Sci Soc Am J* 65(4):1045–1055
14. Malusis MA, Shackelford CD (2002) Chemico-osmotic efficiency of a geosynthetic clay liner. *J Geotech Geoenviron Eng* 128(2):97–106
15. Bohnhoff GL, Shackelford CD (2013) Improving membrane performance via bentonite polymer nanocomposite. *Appl Clay Sci* 86:83–98
16. Tang Q et al. (2014) Influence of compaction degree on membrane behavior of compacted clay amended with bentonite. In: Geo-congress 2014: geo-characterization and modeling for sustainability, pp 1880–1889
17. Shackelford CD, Meier A, Sample-Lord K (2016) Limiting membrane and diffusion behavior of a geosynthetic clay liner. *Geotext Geomembr* 44(5):707–718
18. Dominijanni A, Guarena N, Manassero M (2018) Laboratory assessment of semi-permeable properties of a natural sodium bentonite. *Can Geotech J* 55(11):1611–1631

19. Manassero M, Dominijanni A (2003) Modelling the osmosis effect on solute migration through porous media. *Geotechnique* 53(5):481–492
20. Malusis MA, Shackelford CD (2002) Coupling effects during steady-state solute diffusion through a semipermeable clay membrane. *Environ Sci Technol* 36(6):1312–1319
21. Malusis MA, Kang J-B, Shackelford CD (2015) Restricted salt diffusion in a geosynthetic clay liner. *Environ Geotech* 2(2):68–77
22. Malusis MA, Shackelford CD (2004) Explicit and implicit coupling during solute transport through clay membrane barriers. *J Contam Hydrol* 72(1–4):259–285
23. Zhang Z, Tian G, Han L (2020) Influence of chemical osmosis on solute transport and fluid velocity in clay soils. *Open Chem J* 18(1):232–238
24. Fritz SJ (1986) Ideality of clay membranes in osmotic processes: a review. *Clays Clay Miner* 34(2):214–223
25. Bolt G (1979) Electrochemical phenomena in soil and clay systems. *Develop Soil Sci* vol. 5. Elsevier, pp 387–432
26. Bresler E (1973) Anion exclusion and coupling effects in nonsteady transport through unsaturated soils: I. Theory. *Soil Sci Soc Am J* 37(5):663–669
27. Dominijanni A, Manassero M (2012) Modelling the swelling and osmotic properties of clay soils. Part II: the physical approach. *Int J Eng Sci* 51:51–73
28. Shackelford C (2012) Membrane behavior of engineered clay barriers for geoenvironmental containment: state of the art. In: *Geocongress 2012: state of the art and practice in geotechnical engineering*, pp 3419–3428
29. Meier A et al. (2014) Persistence of semipermeable membrane behavior for a geosynthetic clay liner. In: *Proceedings, 7th international conference on environmental geotechnics*. Melbourne, Australia, pp 10–14
30. Fritz CJ et al (2020) Determining maximum chemico-osmotic pressure difference across clay membranes. *J Geotech Geoenviron Eng* 146(1):06019018
31. Zhang Z et al (2018) Modeling fully coupled hydraulic-mechanical-chemical processes in a natural clay liner under mechanical and chemico-osmotic consolidation. *Environ Sci Pollut Res* 25(36):36173–36183
32. Yeung AT (1990) Coupled flow equations for water, electricity and ionic contaminants through clayey soils under hydraulic, electrical and chemical gradients. *J Non-Equilib Thermodyn* 15(3)
33. Mitchell JK, Soga K (2005) *Fundamentals of soil behavior*. vol 3, John Wiley & Sons, New York
34. Katchalsky A, Curran PF (2013) *Nonequilibrium thermodynamics in biophysics*. Harvard University Press
35. Shackelford CD et al. (2019) Research challenges involving coupled flows in geotechnical engineering. *Geotech Fundam Addressing New World Challenges* 237–274
36. Shackelford CD, Daniel DE (1991) Diffusion in saturated soil. I: Background. *J Geotech Eng* 117(3):467–484
37. Malusis MA, Shackelford CD (2002) Theory for reactive solute transport through clay membrane barriers. *J Contam Hydrol* 59(3–4):291–316
38. Shackelford CD, Moore SM (2013) Fickian diffusion of radionuclides for engineered containment barriers: diffusion coefficients, porosities, and complicating issues. *Eng Geol* 152(1):133–147
39. Shackelford CD (1989) Diffusion of contaminants through waste containment barriers. *Trans Res Record* 1219

# Investigation of Ferrochrome Fly Ash Reinforcement in Different Concrete Types



Gökhan Başman, Şeyma Yüksel Sağman, Erdoğan Karip, and Tuğçe Özcan

**Abstract** The evaluation of industrial wastes is one of the issues that increase its importance day by day in terms of both reducing environmental impacts and increasing economic contributions. In this study, it was aimed to create an alternative usage area for ferrochrome fly ash by adding ferrochrome fly ash wastes to different types of concrete such as filled concrete, road concrete and C 25/30 concrete. Samples were prepared by adding 5–20% by weight ferrochrome fly ash to different concrete types. Compression tests and Cr (VI) amounts were analyzed by keeping the samples in curing water for 7, 14 and 28 days. As a result, it was observed that the compressive strength of the sample with the addition of ferrochrome fly ash (10% by wt.) to the filled concrete gave similar values to the standard filled concrete. It was observed that the compressive stresses for the concrete sample with the addition of ferrochrome fly ash (7.5% by wt.) of road concrete were 34.21, 37.96 and 40.01 MPA (7, 14 and 28 days), respectively. This value was observed as 30.1, 35.1 and 36.82 MPa for the sample to which ferrochrome fly ash (12.5% by wt.) was added to C 25/30 concrete, respectively. When the environmental effects of the samples were analyzed, it was observed that the samples using ferrochrome fly ash did not exceed the limits according to the Water Pollution Regulation.

**Keywords** Ferrochrome · Fly ash · Concrete

## 1 Introduction

Concrete is the most extensively utilized construction material around the globe owing to its inherent strength, durability, cheap cost, raw material availability, and potential for fire resistance [1–3]. The main bulk resources used in conventional concrete are natural aggregate and cement. Aggregates constitute around 70–80% of the total volume of concrete [4]. The enormous demand for aggregate may lead to a rapid run out of natural resources. Furthermore, the use of cement in concrete is

---

G. Başman (✉) · Ş. Y. Sağman · E. Karip · T. Özcan  
Eti Chrome INC., R&D Center, Antalya, Türkiye  
e-mail: [gokhan.basman@etikrom.com](mailto:gokhan.basman@etikrom.com)

© The Author(s), under exclusive license to Springer Nature Singapore Pte Ltd. 2023  
Y. Yukselen-Aksoy et al. (eds.), *Sustainable Earth and Beyond*, Lecture Notes in Civil Engineering 370, [https://doi.org/10.1007/978-981-99-4041-7\\_19](https://doi.org/10.1007/978-981-99-4041-7_19)

199

another key contributor to increased greenhouse gas emissions [5]. Climate change mitigation and resource efficiency have emerged as crucial challenges for long-term sustainability of concrete. Implementing circular approach through waste valorization in concrete production with eco-efficient mix design is an efficient mitigation pathway to combat natural resources depletion and environmental issues [6]. In recent decades, efforts have been undertaken to combine the waste and concrete sectors in a synergistic manner to reduce the downsides associated with conventional concrete production [7, 8]. For this reason, the evaluation of waste materials with useful recycling mechanisms gains importance in terms of cost and at the same time in terms of improving environmental impacts [9]. It is thought that the recycling of industrial waste materials such as fly ash, silica fume and flue dust, which can cause environmental problems and are used in the construction sector, will make great contributions to humanity both in terms of the environment and in terms of improving the properties of concrete.

The construction sector is the leading sector in which industrial wastes such as chimney dust and fly ash are evaluated. In addition, it is used in various fields such as chemistry, ceramics, glass, glass-ceramic, casting metal industry, soil improvement in agriculture, environment, drilling works, prevention of icing and fillers in mines [10]. Also, these wastes are used as additives and substitutes in both cement and concrete production, as they are pozzolans [11]. Fly ash behave like all pozzolanic materials in fine-grained state with alumina and siliceous structure. When mixed with calcium hydroxide and combined with water, they provide the formation of C-S-H gels as a result of hydration, as in Portland cement and can gain binding properties [12]. Çelik et al. emphasized in their study that the effect caused by the fly ash being composed of very fine particles is more important in increasing the compressive strength [13]. The fly ash particles are mostly spherical in shape and their size varies between 1 and 200  $\mu\text{m}$ . Generally, 85% of flue dusts are  $\text{SiO}_2$ ,  $\text{Al}_2\text{O}_3$ ,  $\text{Fe}_2\text{O}_3$ ,  $\text{CaO}$  and  $\text{MgO}$  [14].

In this study, it is aimed to create an alternative usage area for ferrochrome fly ash by adding ferrochrome fly ash wastes to different types of concrete such as filled concrete, road concrete and C 25/30 concrete. Samples were prepared by adding 5–20% by weight ferrochrome fly ash to different concrete types. The uniaxial concrete compressive strength of the obtained samples and the Cr (VI) amounts of the curing waters of the concrete samples were analyzed. As a result, it was observed that the compressive strength of the concrete increased with the addition of ferrochrome fly ash, and the Cr (VI) amounts remained below the values expressed in the Water Pollution Regulation.

## 2 Material and Method

In this study, ferrochrome fly ash (FFA) was added to different types of concrete in order to create an alternative usage area of ferrochrome fly ash. Three types of concrete such as filled concrete, road concrete and C 25/30 concrete were used.

Standard prescriptions for filling concrete, road concrete and C 25/30 concrete made within Eti Concrete INC., are given in Table 1. Chemical analysis of ferrochrome slag (FS) used in meat concrete is given in Table 2. FFA reinforced into different concrete types was obtained from Elazig Eti Chrome INC. facilities. Chemical analysis of FFA is given in Table 3. Concrete samples were prepared by adding 5, 7.5, 10, 12.5, 15, 17.5 and 20 wt. % FFA to different concrete types. Concrete recipes produced by adding FFA to different types of concrete are given in Table 4.

Samples were mixed in accordance with the prescriptions given in Table 4. The mixer in the R&D center laboratory was used for the mixing process. The resulting mortars were taken into molds measuring  $15 \times 15 \times 15$  cm. The poured concretes were kept in the laboratory environment for 24–48 h, then they were taken into the curing water. Setting times varied according to the amount of FFA and the type of concrete. The samples were kept in the curing water for 7, 14 and 28 days. Uniaxial compression tests of the samples taken from the curing water were analyzed. In

**Table 1** Filling concrete, road concrete and C 25/30 concrete standard prescriptions produced in Eti Concrete INC

	Filled concrete	Road concrete	C 25/30 concrete
Raw material	Amount (kg)	Amount (kg)	amount (kg)
Limestone (0-5 mm)	2150.5	1200	1100
FS (7–14 mm)	0	730	390
FS (14–24 mm)	0	0	470
Cement	200	350	310
Water	150	220	170

**Table 2** Chemical analysis of FS

Simple	S	C	Cr <sub>2</sub> O <sub>3</sub>	SiO <sub>2</sub>	Cr/ Fe	CaO	Fe <sub>2</sub> O <sub>3</sub>	MgO	MgO/ SiO <sub>2</sub>	(MgO,CaO) /Al <sub>2</sub> O <sub>3</sub>	Al <sub>2</sub> O <sub>3</sub>
FS (7–14 mm)	0.135	0.32	3.63	31.94	2.88	0.69	1.23	37.68	1.18	1.58	24.34
FS (14–28 mm)	0.129	0.14	3.22	32.7	2.79	0.68	1.13	38.04	1.16	1.63	23.73

**Table 3** Chemical analysis of FFA

%	CaO	TiO <sub>2</sub>	Fe <sub>2</sub> O <sub>3</sub>	K <sub>2</sub> O	SO <sub>3</sub>	Cl	Br
FFA	1.16	0.87	7.13	16.57	6.42	0.9	0.03
	Na <sub>2</sub> O	MgO	Al <sub>2</sub> O <sub>3</sub>	SiO <sub>2</sub>	P <sub>2</sub> O <sub>5</sub>	CuO	Cr <sub>2</sub> O <sub>3</sub>
	0.00	12.16	2.51	21.40	0.021	0.02	10.97
	MnO	ZnO	NiO	As <sub>2</sub> O <sub>3</sub>	SeO <sub>2</sub>	Ga <sub>2</sub> O <sub>3</sub>	Rb <sub>2</sub> O
0.64	19.23	0.12	0.11	0.03	0.25	0.24	



**Table 4** Prescription prepared with the addition of FFA

<i>Filling concrete prescription with the addition of FFA</i>							
Raw material	Raw material (kg)						
	%5 FFA	%7.5 FFA	%10 FFA	%12.5 FFA	%15 FFA	%17.5 FFA	%20 FFA
Limestone (0–5 mm)	25.8	25.8	25.8	25.8	25.8	25.8	25.8
Cement	2.28	2.22	2.16	2.10	2.04	1.98	1.92
FFA	0.12	0.18	0.24	0.30	0.36	0.42	0.48
Water (L)	2	2	2	2	2	2	2
Setting time	24	24	24	27	41	41	46
<i>Road concrete prescription with the addition of FFA</i>							
Raw material	Raw material (kg)						
	%5 FFA	%7.5 FFA	%10 FFA	%12.5 FFA	%15 FFA	%17.5 FFA	%20 FFA
Limestone (0–5 mm)	14.4	14.4	14.4	14.4	14.4	14.4	14.4
FS (7–14 mm)	8.76	8.76	8.76	8.76	8.76	8.76	8.76
Cement	3.99	3.885	3.78	3.675	3.57	3.465	3.36
FFA	0.21	0.315	0.42	0.525	0.63	0.735	0.84
Water (L)	3	3	3	3	3	3	3
Setting time	24	24	24	24	40	44	46
<i>C 25/30 concrete prescription with the addition of FFA</i>							
Raw material	Raw material (kg)						
	%5 FFA	%7.5 FFA	%10 FFA	%12.5 FFA	%15 FFA	%17.5 FFA	%20 FFA
Limestone (0–5 mm)	13.2	13.2	13.2	13.2	13.2	13.2	13.2
FS (7–14 mm)	4.68	4.68	4.68	4.68	4.68	4.68	4.68
FS (14–24 mm)	5.64	5.64	5.64	5.64	5.64	5.64	5.64
Cement	3.534	3.441	3.348	3.255	3.255	3.069	2.976
FFA	0.186	0.279	0.372	0.465	0.558	0.651	0.744
Water (L)	2.50	2.50	2.50	2.50	2.50	2.50	2.50
Setting time	18	19	21	24	24	48	48

addition, Cr (VI) analyzes were performed to examine the environmental effects of the water taken from the curing water.

### 3 Finding and Discussion

In this study, the addition of FFA wastes to different concrete types is aimed both to reduce the cost by reducing the amount of cement and to create an alternative use of waste powders. The uniaxial compression tests result of different concrete type with the addition of FFA are given in Table 5.

Standard compressive strengths for filled concrete in Eti Concrete INC. are 16.14, 16.02 and 16.63 MPa (for curing times of 7, 14 and 28 days, respectively). It is seen that the compressive strength of the samples obtained when 5 and 7.5% FFA by wt. is added to the filled concrete is approximate with the standard compression range of Eti Concrete INC. (Table 5). For the filled concrete, the best compressive strength was observed in the sample with 10% FFA additive by weight. However, it partially decreased in samples kept in curing water for 14 days. It was also observed that the compressive strength decreased with the increase of FFA addition. This result shows that up to 10% by weight of FFA can be used in filled concrete.

Cr (VI) analyzes of the samples prepared by adding FFA to different concrete types were made. In the Cr (VI) analyzes performed for the filled concrete with FFA addition, it was observed that the Cr (VI) amount varied in the range of 0.106–0.489 mg/L. According to the Water Pollution Regulation, the Cr (VI) limit is 0.3 mg/L in the metal industry and 0.5 mg/L in the coal industry. These results are in line with the Water Pollution Regulation. According to the analyzes made, the addition of FFA at the rate of 5–10% by weight in the filled concrete is very important because of the reasons such as reducing the cement cost, not causing environmental pollution and

**Table 5** Filled concrete, road concrete and C 25/30 concrete compression tests analysis

Reinforcement	Filled concrete			Road concrete			C 25/30 concrete		
	Compression tests (MPa)			Compression tests (MPa)			Compression tests (MPa)		
	7 days	14 days	28 days	7 days	14 days	28 days	7 days	14 days	28 days
%5 FFA	17.12	8.52	13.56	29.82	35.85	37.87	28.47	29.17	33.46
%7.5 FFA	15.17	15.16	16.77	34.21	37.96	40.01	23.37	27.69	38.68
%10 FFA	16.82	14.67	17.28	30.15	32.81	30.35	29.65	30.01	33.52
%12.5 FFA	18.53	15.25	12.44	28.66	33.11	35.2	30.1	35.1	36.82
%15 FFA	12.3	12.34	10.83	27.13	31.96	30.19	31.92	32.3	37.2
%17.5 FFA	6.65	10.13	9.07	24.5	28.15	29.13	26.9	27.56	31.22
%20 FFA	8.55	11.17	8.94	22.72	26.13	27.52	27.2	24.81	30.15

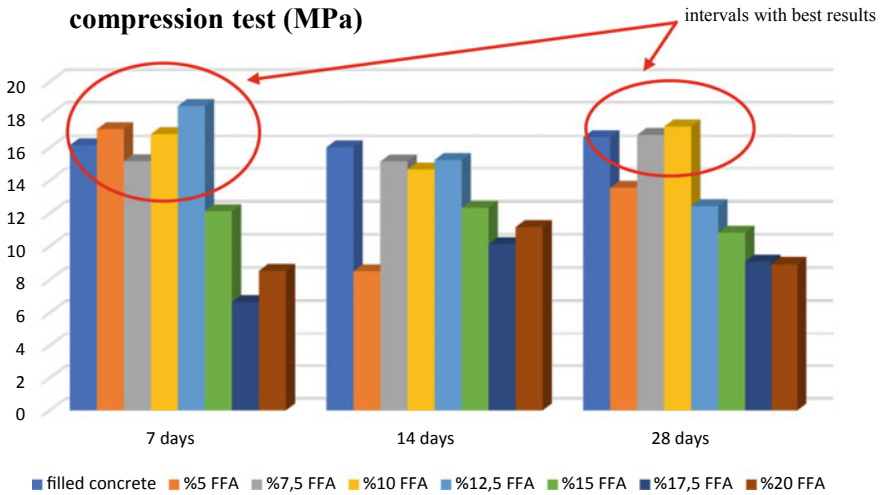


**Fig. 1** Comparison of the compressive strength of the filled concrete produced according to the standards of Eti Concrete INC. and the filled concrete with the addition of FFA

evaluating the wastes. Comparison of the results obtained from the addition of FFA to the filled concrete and the results obtained according to the standards of Eti Concrete INC., is given in Fig. 1. In particular, it is seen in Fig. 1. that the compressive strength of the sample cured for 7 days and 28 days is higher than the standard concrete.

The comparison of FFA reinforced road concrete and standard road concrete is given in Fig. 2. Standard compressive strengths for road concrete in Eti Concrete INC. are 29.40, 33.44 and 39.26 MPa (for curing times of 7, 14 and 28 days, respectively). The compressive strength of FFA reinforced (%5 and %7.5 wt.) road concrete yielded similar results with Eti Concrete INC concrete (Fig. 2). It was observed that this value was better especially in the sample to which 7.5% by wt. FFA. It was also observed that the compressive strength increased as the curing time increased (%7.5 FFA). It is seen that the compressive strength values decrease as the FFA addition pass 10% by wt. (Fig. 2). In the analyzes made for road concrete, it was observed that the amount of Cr (VI) was in the range of 0.055–0.475 mg/L. These values are in line with the Water Pollution Regulation.

In Fig. 3, compression strength results of the effect of standard C25/30 concrete and FFA reinforcement are given.

Standard compressive strengths for C 25/30 concrete in Eti Concrete INC. are 24.06, 35.03 and 36.65 MPa (for curing times of 7, 14 and 28 days, respectively). According to the Turkish Standards Institute (TS EN 206) standards, their compressive strength is 26, 32.3 and 33.1 MPa. It was observed that the compressive strength of all values waiting for 7 days in curing was higher than the Eti Concrete standards. According to Fig. 3., the addition of 12.5% by weight FFA gave the best compression strength result. However, compressive strength decreased in all samples with 14 days curing time (except 12.5% FFA). It was also observed that Cr (VI) release was in the

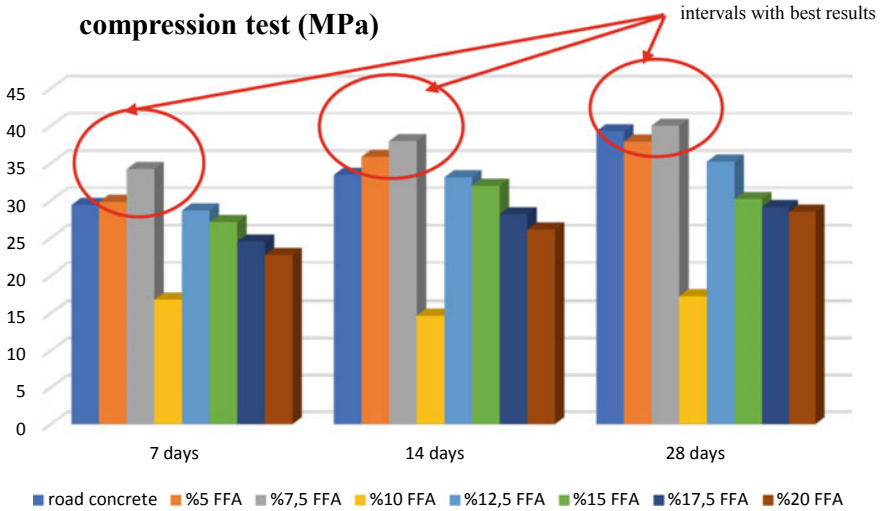


**Fig. 2** Comparison of the compressive strength of the filled concrete produced according to the standards of Eti Concrete INC. and the road concrete with the addition of FFA

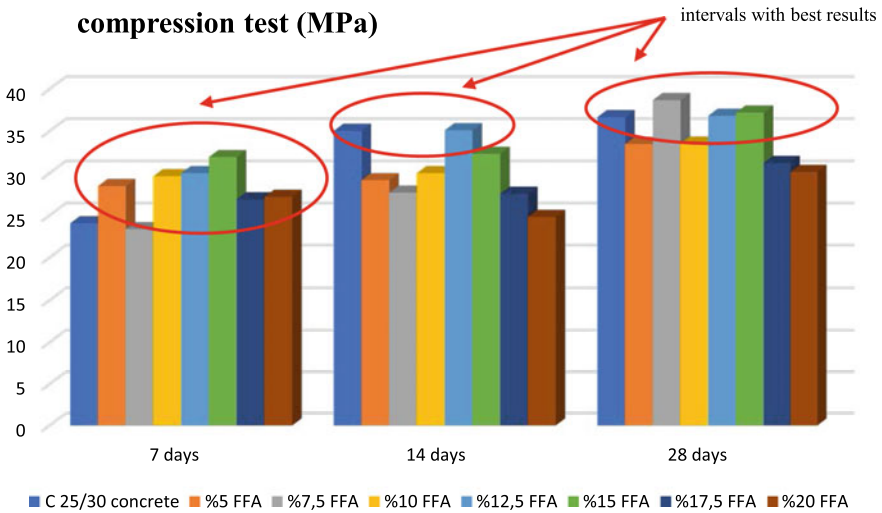


**Fig. 3** Comparison of the compressive strength of the filled concrete produced according to the standards of Eti Concrete INC. and the C 25/30 concrete with the addition of ferrochrome fly ash

range of 0.02–0.37 mg/L. This value is lower than the value determined by the water pollution control regulation.

## 4 Conclusion

In this study, samples were prepared by adding ferrochrome fly ash wastes to different concrete types. It is aimed to create an alternative usage area of ferrochrome fly ash. As a result:

- The best compressive strength for the filled concrete was observed in the sample to which 10% by weight ferrochrome fly ash was added. But it decreased partially in the sample kept in curing for 14 days.
- The best compressive strength in road concrete was measured as 34.21, 37.96 and 40.01 in samples kept for 7, 14 and 28 days, respectively (% 7.5 by wt. fly ash).
- It was observed that the addition of 12.5% by weight ferrochrome fly ash gave the best compression strength result for C 25/30. In addition, it was observed that the compressive strength of all samples was higher than the standards (for curing time of 7 days).
- It was observed that the Cr (VI) release of ferrochrome fly ash addition for different concrete types was below the values determined by the water pollution control regulation (0.5 mg/L).

These results showed that the use of ferrochrome fly ash in different concrete types is cost effective, does not harm the environment and can be used in the evaluation of waste.

**Acknowledgements** The authors gratefully acknowledge the support from the Eti Chrome Management INC. for this study. Also, the authors gratefully acknowledge Eti Chrome R&D unit technician Cengiz Yaşın for his contributions.

## References

1. Valipour M, Yekkalar M, Shekarchi M, Panahi S (2014) Environmental assessment of green concrete containing natural zeolite on the global warming index in marine environments. *J Clean Prod* (65):418–423
2. Makul N, Rattanadecho P, Agrawal DK (2014) Applications of microwave energy in cement and concrete—a review. *Renew Sustain Energy Rev* (37):715–733
3. Serres N, Braymand S, Feugeas F (2016) Environmental evaluation of concrete made from recycled concrete aggregate implementing life cycle assessment. *J Build Eng* (5):24–33
4. Pradhan S, Tiwari BR, Kumar S, Barai SV (2019) Comparative LCA of recycled and natural aggregate concrete using Particle Packing Method and conventional method of design mix. *J Clean Prod* (228):679–691. <https://doi.org/10.1016/j.jclepro.2019.04.328>
5. Panesar DK, Kanraj D, Abualrous Y (2019) Effect of transportation of fly ash: life cycle assessment and life cycle cost analysis of concrete. *Cem Concr Compos* (99):214–224. <https://doi.org/10.1016/j.cemconcomp.2019.03.019>
6. Das P, Cheela VRS, Mistri A, Chakraborty S, Dubey B, Barai SV (2022) Performance assessment and life cycle analysis of concrete containing ferrochrome slag and fly ash as replacement materials—a circular approach. *Constr Build Mater*. (347):128609

7. Turk J, Coti'c Z, Mladenovi'c A, Sajna A (2015) Environmental evaluation of green concretes versus conventional concrete by means of LCA. *Waste Manag* (45):194–205. <https://doi.org/10.1016/j.wasman.2015.06.035>
8. Ortiz O, Castells F, Sonnemann G (2009) Sustainability in the construction industry: a review of recent developments based on LCA. *Constr Build Mater* 23(1):28–29
9. Tulga İ, Kılınç K (2018) Effect of fly ash use on the mechanical and durability properties of concretes which have different strength level. *Kırklareli Univ J Eng Sci* 4 (2):212–236
10. Aruntaş Y (2006) Uçucu Küllerin İnşaat Sektöründe Kullanım Potansiyeli. *Gazi Üniv Müh Mim Fak Der Cilt* 21(1):193–203
11. Yaprak H, Şimşek O, Aruntaş Y (2004) Uçucu Kül ve Yüksek Fırın Cürufunun Süper Akışkanlaştırıcı Katkılı Beton Özelliklerine Etkisi. *Beton Kongresi*. İstanbul. Türkiye, pp 707–715 (10–13 Haziran 2004).
12. Subaşı S, İşbilir, B. Ercan İ (2011) Effect of high temperature on mechanical properties of cement samples with fly ash substitution. *J Polytech* 14(2):141–148
13. Çelik Ö, Yurter G, Kan S, Yeprem A (2004) Farklı Puzolanik Katkıların Çimento Harçlarının Mekanik Özellikleri Üzerine Etkisi. *Doğuş Üniversitesi Dergisi* 5(2):147–154
14. Baradan B (2004) Portland Çimentosu-Uçucu Kül-Yüksek Fırın Cürufu Esaslı Bağlayıcıların Yüksek Sıcaklık Davranışının İncelenmesi. *Dokuz Eylül Üniversitesi İnşaat Mühendisliği Bölümü*. İzmir. Türkiye. TÜBİTAK Proje no. 103I003/2004-373

# Factors Affecting Cation Exchange Between Geosynthetic Clay Liners and Compacted Subsoils



Yasin Karakuş, A. Hakan Ören, and B. Enes Taşkesti

**Abstract** The hydration behavior of geosynthetic clay liner (Na-GCL) was investigated to assess the hydration duration, vertical stress, and subsoil water content on cation exchange. Na-GCL with 4.0 and 5.0 kg/m<sup>2</sup> MPUA were hydrated over silty sand compacted at four moisture contents. For each Na-GCLs considered, increasing in vertical stress led to a decrease in the final water content of the GCLs. In the meantime, Na-GCL absorbed water from the subsoil for up to 40 days. Afterward, the water content of GCLs does not change significantly. Besides, it was observed that increasing subsoil water content increases the final water content of the Na-GCLs. Cation exchange was observed significantly in the first 30 days of hydration. On the other hand, it was observed that an increase in vertical stress increased the cation exchange. Additionally, when the subsoil water content effect on cation exchange in terms of change in mole fractions, it was observed that the GCLs hydrated on the subsoils compacted at the wet side of the optimum water content, exposed more cation exchange.

**Keywords** Geosynthetic clay liner · Subsoil water content · Vertical stress · Cation exchange

---

Y. Karakuş (✉) · B. E. Taşkesti  
Graduate School of Natural and Applied Sciences, Dokuz Eylul University, Izmir, Turkey  
e-mail: [karakus.yasin@ogr.deu.edu.tr](mailto:karakus.yasin@ogr.deu.edu.tr)

B. E. Taşkesti  
e-mail: [enes.taskesti@ogr.deu.edu.tr](mailto:enes.taskesti@ogr.deu.edu.tr)

A. H. Ören  
Department of Civil Engineering, Dokuz Eylul University, Izmir, Turkey  
e-mail: [ali.oren@deu.edu.tr](mailto:ali.oren@deu.edu.tr)

# 1 Introduction

GCLs are composite materials with a thickness between 5 and 10 mm, produced by sandwiching bentonite between two geotextiles. GCLs have many advantages when compared to the compacted clay liners. Due to their capacity to hold water up to 10 times of their weight and low permeability ( $\sim 2 \times 10^{-11}$  m/s), GCLs are used extensively as a barrier material in solid waste and hazardous waste storage areas, irrigation canals, water transmission lines, and in ponds [1, 8, 12, 13], Rowe et al. 2011, [17].

Hydration can be addressed in two phases: crystalline and osmotic swelling. These phases can be explained in terms of hydration solution. Different types of hydration solutions can cause different types of hydrations. For instance, crystalline swelling occurs when clays are subjected to a solution consisting of divalent or multivalent cations [19]. On the other hand, if the clays expose to a dilute solution in which monovalent cations are concentrated, this situation leads to strong thrust between the layers and thus to osmotic swelling [18]. Karakuş et al. [9] showed that significant exchange among the cations occurs between  $\text{Na}^+$  and calcium ( $\text{Ca}^{2+}$ ) cations; hence, the water content of the GCL decreases. As a result of these decreases, hydraulic conductivity, the governing parameter affecting the GCL performance, may decrease.

There are valuable studies investigating the cation exchange that occurs during hydration of GCLs [6, 15, 14]. However, none of these studies investigate the parameters affecting cation exchange reaction. For this reason, this study aims to investigate some parameters such as hydration time, subsoil water content ( $w_{\text{subsoil}}$ ), and vertical stress, affecting the cation exchange reaction. A sodium-rich GCL (i.e., Na-GCL), with MPUA of  $4.0 \text{ kg/m}^2$  was hydrated for 30, 90, 180, and 360 days and the influence of  $w_{\text{subsoil}}$  was investigated on this GCL. The influence of  $w_{\text{subsoil}}$  is evaluated for the long-term hydration duration herein (i.e., 180 and 365 days). For this purpose, the silty sand subsoil was again compacted at four different water contents: 8, 11, 14, and 17%. Finally, the effect of vertical stress on the cation exchange reaction of Na-GCL was determined by applying 1, 2, 5, and 10 kPa stress.

## 1.1 Background

Rayhani et al. (2011) reported the factors influencing GCL hydration. Hydration tests were conducted with three types of GCLs and on two different subsoils. One of the factors considered was the subsoil water content. The silty sand subsoil was compacted at 5, 10, 16, and 21% water contents. Based on the results, an increase in the  $w_{\text{subsoil}}$  led to increase the final moisture content ( $w_{\text{final}}$ ) of GCLs.

Sarabadani et al. [16] conducted hydration tests on two subsoils (sand and clay). The stress range applied in these tests is between zero and 28 kPa. The results showed that the hydration rate increases as the vertical stress increases. Chevrier et al. [7] argued that increasing vertical stress provides good contact between GCL



and subsoil. However, considering the equilibrium water contents of the GCLs in Sarabadani et al. [16], they found that the stress between 2 and 5 kPa increase the performance of GCL hydration.

Bradshaw et al. [6] evaluated the cation exchange by conducting the hydration test on Na-GCLs. GCL with MPUA of  $3.7 \text{ kg/m}^2$  was hydrated on four subgrades, namely Torpedo sand, Red Wing clay, Boardman silt, and Cedar Rapids clay. As a consequence, it was reported that cation exchange occurs in the first 30 days of hydration. This outcome shows that cation exchange starts in the early stages of hydration. To reduce the cation exchange, it was recommended to compact subsoil on its wet side of optimum water content.

Rowe et al. [15] investigated the effects of the water content of the subgrade on the long-term hydration of five GCLs. GCLs were prehydrated on silty sand subsoil at two distinct water contents (5 and 16%) to show the effect of  $w_{\text{subsoil}}$  on cation exchange before hydraulic conductivity tests. MPUA of the GCLs was within the range of  $4.4\text{--}5.2 \text{ kg/m}^2$ . They reported that since cation exchange could not occur via vapor transport, the monovalent fraction of GCLs which were hydrated in dry subsoils was greater than the monovalent fractions of the GCLs hydrated in wet subsoils (e.g.,  $\sim 64$  vs.  $35\%$  for Na-GCL).

Özdamar Kul and Ören [11] investigated the hydration performance of two GCLs which were hydrated over compacted zeolite. The MPUA was within the range of  $3.2\text{--}4.3 \text{ kg/m}^2$  for LP-GCL and  $2.7\text{--}3.0 \text{ kg/m}^2$  for HP-GCL. LP and HP denote for “low performance” and “high performance”, respectively. The cation exchange takes places for LP-GCL in the early-stages of the hydration. For LP-GCL, monovalent cation fractions decreased from 0.87 to 0.76 and to 0.61, after 30 and 90 days of hydration, respectively.

## 2 Materials and Methods

### 2.1 Materials

#### Geosynthetic Clay Liner

The Na-GCL investigated were taken from a local manufacturer. Mass per unit area (MPUA) of the Na-GCLs were ranged between  $3.8$  and  $5.1 \text{ kg/m}^2$ . The liquid limit of the bentonite was determined by following ASTM D4318 and was  $231\%$ . The swell index was  $21.5 \text{ mL/2 g}$ .

The GCL investigated in this study had been manufactured by needle-punching. GCLs had nonwoven cover geotextile and woven carrier geotextile. The average initial thickness of the GCLs were varied between  $5.6$  and  $6.5 \text{ mm}$ . This Na-GCL has powdered sodium bentonite ( $D_{60} = 0.0048 \text{ mm}$ ). The properties of GCLs investigated are summarized in Table 1.

**Table 1** Properties of GCLs investigated

GCL Properties	Na-GCL
MPUA (kg/m <sup>2</sup> )	3.8–5.1
Carrier geotextile	Woven
Cover geotextile	Non-woven
Initial water content (%)	12.6 ± 4.7%
Liquid limit, w <sub>L</sub> (%)	231
Plastic limit, w <sub>P</sub> (%)	61
Clay fraction (%)	45
Swell index (mL/2 g)	21.5
Manufacture type	Needle-punched

### Subsoil

Silty sand taken from a landfill was used as the subsoil in hydration tests. The grain size distribution curve of subsoil was obtained following [4]. As a result of the wet sieving and hydrometer tests, the fine content of the subsoil was determined 41.5%. Liquid and plastic limits of the subsoil [2] were determined 31% and non-plastic (NP). Subsoil was compacted with Standard Proctor compaction effort using PVC mold [3]. The optimum water content ( $w_{opt}$ ) and maximum dry unit weight of the subsoil ( $\gamma_{max}$ ) were obtained as 12% and 19.1 kN/m<sup>3</sup>, respectively.

## 2.2 Methods

### Hydration Test Setup

Circular Na-GCLs were cut from the roll using a 110-mm diameter steel ring. After GCL was removed from the roll, the GCL was reduced to 100-mm in diameter using scissors. The sides of the GCL were slightly wetted with DIW to prevent bentonite loss. Then, GCL was air-dried until the weight change was insignificant.

Hydration tests were conducted in isothermal conditions. Firstly, silty sand subsoil was oven-dried at 105 ± 5°C. After that, the subsoil was wetted by using a tap water filled spray bottle to bring the water content of the subsoil to the target water content. Subsoil left for conditioning for one night to ensure the homogeneous distribution of water within the soil. Then, subsoil was compacted with Standard Proctor Compaction Energy. Once the subsoil was prepared, GCLs, which were priory cut in 100-mm diameter form the roll, was placed on the compacted subsoil. Finally, a 20 mm-thick polyoxymethylene (POM) cap was placed on the GCL to imitate the geomembrane in the field applications and to provide a basement for the applied vertical load. To provide the isothermal conditions, PVC molds were wrapped with plastic bags. O-rings were attached to the top and bottom of the mold to solidify the impermeability of the air. Additionally, in order to supply a sufficient contact

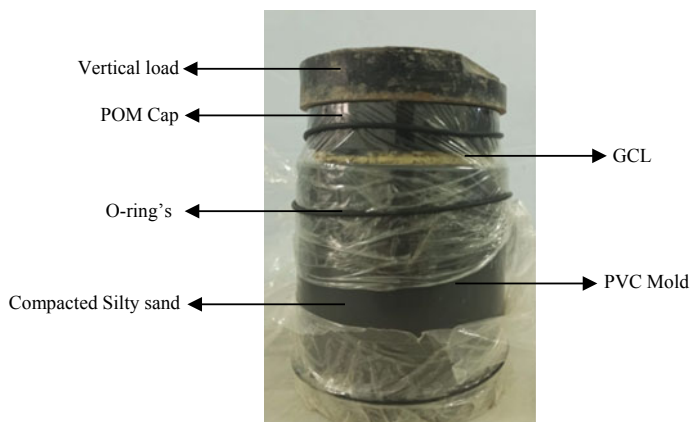


**Fig. 1** Isothermal hydration test setup [10]

between GCLs and subsoils, 1 kPa vertical stress was applied. In addition to 1, 2, 5, and 10 kPa stresses were also applied to investigate the influence of vertical stress. A picture of the hydration test setup is given in Fig. 1. Hydration test setup was open periodically to measure the mass of the GCLs. At the end of the hydration durations, GCLs were oven-dried to determine the water contents.

### Bound Cation Tests

Bound cation tests were conducted on virgin and hydrated bentonite extracted from the GCLs [5]. For this purpose, 1 M ammonium acetate ( $\text{NH}_4\text{OAc}$ ) stock solution was prepared in a volumetric flask. Initially, 10 g of air-dry bentonite and 40 ml of  $\text{NH}_4\text{OAc}$  was mixed vigorously in a plastic bottle and the suspension was shaken in an end-over-end shaker at 30 rpm for 5 min. Then, the suspension was left curing for 24 h. After 24 h, the suspension was shaken for another 15 min at 30 rpm. The suspension was filtered through a 2.5  $\mu\text{m}$  ashless filter paper which was placed on a Buchner funnel. Bentonite was further washed with 30 ml of  $\text{NH}_4\text{OAc}$  solution four times by applying 10 kPa vacuum pressure. The filtrate was analyzed in inductively coupled plasma optical emission spectrophotometry (ICP-OES) to determine the major bound cations (i.e.,  $\text{Na}^+$ ,  $\text{K}^+$ ,  $\text{Ca}^{2+}$ , and  $\text{Mg}^{2+}$ ).

## 3 Results and Discussions

### 3.1 Hydration Behavior of the Na-GCL

Water contents of the Na-GCL hydrated for 30, 90, 180, and 360 days on a silty sand subsoil were determined by recording the mass of GCLs at specific time intervals (Table 2). During the first week of hydration, the GCL swelled due to the rapid uptake

of water from the subsoil due to the high suction pressure difference between the subsoil and the GCL. As the suction pressure difference decreased, the hydration rate of the GCLs decreased, and water contents came to equilibrium after approximately 30 days (Table 2). These results are consistent with those reported in the literature [1, 13, 14].

To see the effect of  $w_{\text{subsoil}}$  on hydration, Na-GCL with MPUA of  $4.0 \text{ kg/m}^2$  was hydrated for 180 days over the subsoil compacted at four different water contents. Note that one of a sample was hydrated for 360 days. As a result of hydration tests, it was observed that  $w_{\text{final}}$  of Na-GCL increased as the  $w_{\text{subsoil}}$  increased. It was also observed that the hydration rate was more for greater  $w_{\text{subsoil}}$  than for lower  $w_{\text{subsoil}}$ . The  $w_{\text{final}}$  of Na-GCL was 60.4% when  $w_{\text{subsoil}}$  was 8.3% and was 69.6% when  $w_{\text{subsoil}}$  was 11.0%. The effect of  $w_{\text{subsoil}}$  was being more pronounced on the wet side of the optimum. For example,  $w_{\text{final}}$  was 78% when  $w_{\text{subsoil}}$  was 14%; and 104.2% when  $w_{\text{subsoil}}$  was 17%.

Another factor affecting the hydration behavior of Na-GCL is vertical stress. To see the effect of vertical stress, Na-GCL with MPUA of  $5.0 \text{ kg/m}^2$  was hydrated for 180 days under 1, 2, 5, and 10 kPa. Based on the findings, no significant difference was observed between the  $w_{\text{final}}$  of Na-GCL hydrated under 1, 2, and 5 kPa stresses (76.6%, 76.7%, and 75.3%, respectively). However, the  $w_{\text{final}}$  for Na-GCL hydrated under 10 kPa decreased to 71.9%, which is slightly less than  $w_{\text{final}}$  obtained under other stresses studied.

**Table 2** Summary of hydration test results conducted on Na-GCLs

MPUA ( $\text{kg/m}^2$ )	Vertical Stress ( $\text{kN/m}^2$ )	$w_{\text{subsoil}}$ (%)	Hydration duration (day)	$w_{\text{final}}$ (%)	Test no#
4.16	1	8.3	180	60.6	SB3
4.05	1	11.0	180	69.9	SB23
3.91	1	13.9	30	97.3	SB12
4.31	1	3.8	90	84.2	SB19
3.91	1	14.5	180	78.0	SB20
3.91	1	14.5	360	61.9	SB24
4.02	1	16.6	180	104.2	SB6
4.72	1	13.9	180	76.6	SB22
5.34	2	13.0	180	76.7	SB25
5.00	5	14.3	180	75.3	SB26
5.33	10	13.8	180	71.9	SB27

### 3.2 Cation Exchange During Hydration

The major bound cations ( $\text{Na}^+$ ,  $\text{Ca}^{2+}$ ,  $\text{K}^+$ , and  $\text{Mg}^{2+}$ ) were detected for virgin and hydrated Na-GCL. The results from the bound cation tests are summarized in Table 3.

The cation exchange in the bound cations occurred mainly within the first 30 days. The monovalent mole fraction of bentonite ( $X_M$ ) for virgin Na-GCL was 81%.  $X_M$  then decreased to 70% after 30 days of hydration. In the meantime, the divalent mole fraction ( $X_D$ ) increased from 19 to 30%. The percentages of bound cations remained almost the same for 90 days and 180 days of hydration. For example,  $X_M$  was 71 and 70% at 90 days and 180 days of hydration, respectively. The cation exchange over the long-term (i.e., 360 days) negligibly changed. These results were consistent with the literature [6]. The reason why no cation exchange was observed after 90 days of hydration is probably due to the relatively low number of multivalent cations in the subsoil pore water.

The effect of  $w_{\text{subsoil}}$  on cation exchange is shown in Fig. 2 in terms of mole fraction of bound cations.  $X_M$  of Na-GCL was 71, 77, 70, 72% when hydrated over a subsoil compacted at 8, 11, 14, and 17% water content (Fig. 2).

Another parameter that is thought to affect the cation exchange between the subsoil and Na-GCL is the vertical stress. When the results of the experiments conducted at the end of the hydration period with bound cations were examined in terms of mole fraction, no obvious difference was observed between vertical stresses. For example,  $X_M$  of Na-GCL was 70 and 72% when hydrated under 1 and 10 kPa stress, respectively. For the tests conducted under 2 and 5 kPa vertical stress,  $X_M$  was determined 72% and 73%, respectively (Fig. 3). It is known that at higher vertical stresses, there is a good contact between GCL and the subsoil. With the good contact, it is expected that the cations can be easily transported because water is present in the subsoil to allow hydration of the GCL in the liquid phase. Therefore, it is expected that more cation exchange occurs at high vertical stress level. However, Fig. 3 shows that this effect is negligible.

## 4 Conclusions

In this study, the cation exchange between Na-GCL and compacted subsoil was investigated as a function of  $w_{\text{subsoil}}$ , hydration time, and vertical stress. To investigate the influence of hydration time, Na-GCL was hydrated with MPUA of  $4.0 \text{ kg/m}^2$  for 30, 90, 180, and 360 days. To investigate the effect of the  $w_{\text{subsoil}}$ , silty sand was compacted at 8, 11, 14, and 17% water contents, and Na-GCLs were hydrated on these subsoils. Finally, to investigate the effect of vertical stress, Na-GCL with MPUA of  $5.0 \text{ kg/m}^2$  was subjected to 1, 2, 5, and 10 kPa vertical stresses during the 180-day

**Table 3** Bound cation concentrations and fractions of Na-GCLs

MPUA (kg/m <sup>2</sup> )	Vertical stress (kN/m <sup>2</sup> )	w <sub>subsoil</sub> (%)	Hydration duration (days)	Bound Cations (%)					
				Na <sup>+</sup>	Ca <sup>2+</sup>	Mg <sup>2+</sup>	K <sup>+</sup>	X <sub>M</sub>	X <sub>b</sub>
Virgin	-	-	-	78.8	14.7	4.7	1.7	80.5	19.4
4.40	1	8.3	180	64.7	25.1	7.8	2.4	67.1	32.9
4.05	1	11.0	180	69.3	23.8	5.1	1.8	71.1	28.9
3.91	1	13.9	30	75.2	18.1	4.7	2.1	77.3	22.8
4.31	1	13.8	90	68.4	22.7	7.0	1.9	70.3	29.7
3.91	1	14.5	180	68.7	22.2	6.8	2.3	71.0	29.0
3.91	1	14.5	360	68.1	23.1	6.6	2.2	70.3	29.7
4.02	1	16.8	180	66.7	22.5	9.4	1.4	68.1	31.9
4.72	1	13.9	180	70.3	21.2	6.4	2.1	72.4	27.6
5.34	2	13.0	180	69.3	22.7	7.0	1.0	70.3	29.7
5.00	5	14.3	180	70.8	19.8	8.0	1.4	72.2	27.8
5.33	10	13.8	180	71.7	18.5	8.2	1.6	73.3	26.7

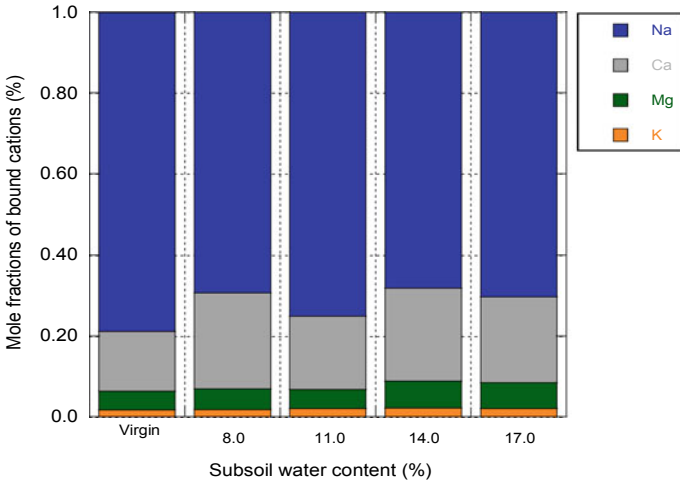


**Fig. 2** Investigating the subsoil water content ( $w_{\text{subsoil}}$ ) effect on cation exchange with Na-GCL with MPUA 4.0 kg/m<sup>2</sup> in terms of mole fraction

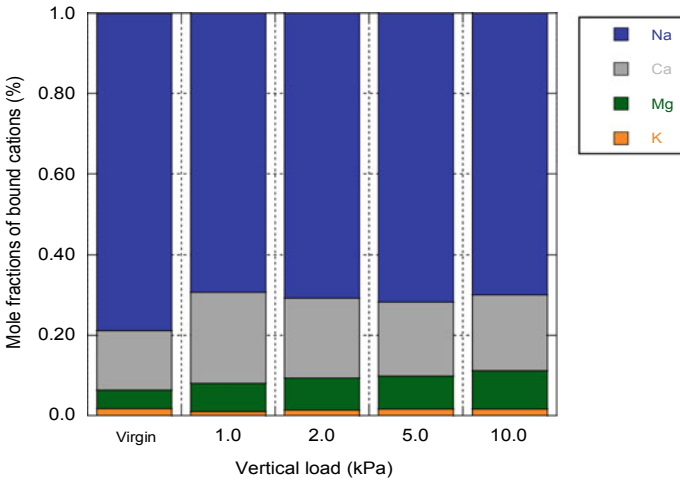


**Fig. 3** Investigating the vertical stress effect on cation exchange of Na-GCL with MPUA 5.0 kg/m<sup>2</sup> in terms of mole fraction

hydration period. At the end of the hydration duration, the major bound cations of the bentonites were determined. The results were examined in terms of both mole fraction and cation concentration.

Based on the findings, the following conclusions can be made:

- As  $w_{\text{subsoil}}$  increases, the  $w_{\text{final}}$  of the Na-GCL increases.

- The effect of vertical stress on GCL hydration is negligibly important. When considering the  $w_{\text{final}}$ , it can be seen that increase in vertical stress limits the swelling of the GCLs, resulting in a slight decrease in the  $w_{\text{final}}$ .
- When examining the effect of hydration time on cation exchange, it was found that cation exchange between the Na-GCL and subsoil was rapid during the first 90 days of hydration and did not change significantly thereafter. The reason why cation exchange was not observed after 90 days of hydration is probably due to relatively low number of divalent cations in the pore water of subsoil.
- The effect of vertical stress on the cation exchange is negligible. It is expected that good contact would be satisfied when vertical stress increased. However, such effect on cation exchange was not observed.

**Acknowledgements** This study has been financially supported by the Scientific and Technological Research Council of Turkey (TUBITAK) with a Grant No: 119R044. The authors are grateful to TUBITAK for this valuable support.

## References

1. Anderson R, Rayhani MT, Rowe RK (2012) Laboratory investigation of GCL hydration from clayey sand subsoil. *Geotext Geomembr* 31:31–38
2. ASTM D4318 (2005) Standard test methods for liquid limit, plastic limit, and plasticity index of soils. Report 04:1–14
3. ASTM D698-12 (2020) Standard test methods for laboratory compaction characteristics of soil using standard effort 1. ASTM Int West Conshohocken PA USA 1–13
4. ASTM D6913 (2017) Standard test methods for particle-size distribution (Gradation) of soils using sieve analysis. ASTM Int West Conshohocken PA
5. ASTM D7503. Standard test method for measuring the exchange complex and cation exchange capacity of inorganic fine-grained soils 1. ASTM Int West Conshohocken, PA, USA 1–5. <https://doi.org/10.1520/D7503>
6. Bradshaw SL, Benson CH, Scalia J (2013) Hydration and cation exchange during subgrade hydration and effect on hydraulic conductivity of geosynthetic clay liners. *J Geotech Geoenviron Eng* 139:526–538. [https://doi.org/10.1061/\(ASCE\)GT.1943-5606.0000793](https://doi.org/10.1061/(ASCE)GT.1943-5606.0000793)
7. Chevrier B, Cazaux D, Didier G, Gamet M, Guyonnet D (2012) Influence of subgrade, temperature and confining pressure on GCL hydration. *Geotext Geomembranes* 33:1–6
8. Estornell P, Daniel DEDE (1992) Hydraulic conductivity of three geosynthetic clay liners. *J Geotech Eng* 118:1592–1606. [https://doi.org/10.1061/\(ASCE\)0733-9410\(1992\)118:10\(1592\)](https://doi.org/10.1061/(ASCE)0733-9410(1992)118:10(1592))
9. Karakuş Y, Taşkesti BE, Ören AH (2022) Combined influence of subgrade moisture content and mass per unit area on cation exchange behavior of geosynthetic clay liners. *Geotext Geomembr* 50:174–182
10. Karakuş Y (2021) Factors controlling the cation exchange between geosynthetic clay liners and compacted subsoils during hydration. Thesis, The Graduate School of Natural Applied Sciences, Dokuz Eylül University, M.Sc
11. Özdamar Kul T, Ören AH (2019) Hydration of geosynthetic clay liners (GCLs) on compacted zeolite. *Geosynth Int* 26. <https://doi.org/10.1680/jgein.18.00038>
12. Petrov RJ, Rowe RK (1997) Geosynthetic clay liner (GCL)—chemical compatibility by hydraulic conductivity testing and factors impacting its performance. *Can Geotech J* 34:863–885



13. Rayhani MT, Rowe RK, Brachman RWI, Take WA, Siemens G (2011) Factors affecting GCL hydration under isothermal conditions. *Geotext Geomembr* 29:525–533
14. Rowe RK, Abdelatty K (2012) Effect of a Calcium-rich soil on the performance of an overlying GCL. *J Geotech Geoenviron Eng* 138:423–431. [https://doi.org/10.1061/\(ASCE\)GT.1943-5606.0000614](https://doi.org/10.1061/(ASCE)GT.1943-5606.0000614)
15. Rowe RK, Garcia JDD, Brachman RWI, Hosney MS (2019) Chemical interaction and hydraulic performance of geosynthetic clay liners isothermally hydrated from silty sand subgrade. *Geotext Geomembranes* 47:740–754. <https://doi.org/10.1016/j.geotexmem.2019.103486>
16. Sarabadani H, Rayhani MT (2014) Influence of normal stress on hydration of GCLs from subsoil. *J Solid Waste Technol Manag* 39:292–303. <https://doi.org/10.5276/JSWTM.2013.292>
17. Scalia J IV, Benson CH (2010) Effect of permeant moisture on the hydraulic conductivity of exhumed GCLs. *Geotech Test J* 33:201–211
18. Yesiller N, Hanson JL, Risken JL, Benson CH, Abichou T, Darius JB (2019) Hydration fluid and field exposure effects on moisture-suction response of geosynthetic clay liners. *J Geotech Geoenviron Eng* 145:04019010
19. Zhou Z (1995) Construction and application of clay-swelling diagrams by use of XRD methods. *JPT J Pet Technol* 47:306

# Effects of Mixture Content of Paper Sludge Ash-Based Stabilizer on Accelerated Carbonation and Strength of Alkaline Construction Sludge



Nguyen Duc Trung, Kimitoshi Hayano, and Hiromoto Yamauchi

**Abstract** In Japan, cement- or lime-based stabilizer is commonly used to treat in-situ construction sludge. This process generally produces alkaline construction sludge due to the high alkalinity of the stabilizer. The condition does not often satisfy the environmental regulation. To overcome this, in this study, alkaline construction sludge was exposed to pure carbon dioxide at a high concentration percent to accelerate the pH neutralization. For further enhancement, paper sludge ash-based stabilizer (PSAS) was added to alkaline construction sludge to granulate the alkaline sludge to shorten the pH neutralized period. Moreover, effect of particle sizes of alkaline construction sludge treated by PSAS on accelerated carbonation was investigated. Aiming to be used as a recycling material, it is necessary to evaluate the strength development of the carbonated construction sludge. In this scenario, a series of cone index tests were also conducted to investigate the strength development of carbonated construction sludge. It was found that the strength of sludge treated with PSAS was significantly improved due to the water absorption and retention performance of PSAS. In addition, an attempt to shorten the pH neutralized period and improve the strength of sludge was carried out by crumbling the sludges and then curing them under atmospheric conditions for 1 day prior to the accelerated carbonation. It was found that the pH neutralization period could be shortened by the crumbling and that the cone index,  $q_c$  showed the enhancement in strength of the crumbled sludges undergone air curing.

---

N. D. Trung (✉)

Graduate School of Urban Innovation, Yokohama National University, Yokohama, Japan  
e-mail: [nguyen-trung-hy@ynu.jp](mailto:nguyen-trung-hy@ynu.jp)

K. Hayano

Faculty of Urban Innovation, Yokohama National University, Yokohama, Japan  
e-mail: [hayano-kimitoshi-hg@ynu.ac.jp](mailto:hayano-kimitoshi-hg@ynu.ac.jp)

H. Yamauchi

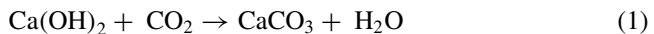
DOMI Environmental Solutions, Sodegaura, Chiba, Japan  
e-mail: [yamauchi@domi-es.jp](mailto:yamauchi@domi-es.jp)

**Keywords** Alkaline construction sludge · pH neutralization · Accelerated carbonation · Paper sludge ash-based stabilizer · Strength improvement · Recycled material

## 1 Introduction

Construction industry is generating a huge amount of construction wastes. One of those is construction sludge generated from the process of excavating underground construction projects [1]. The construction sludge is frequently seen with a high-water content that often being treated on-site with cement or lime for hardening to be loaded on a dump truck. However, the addition of cement or lime often increases the alkalinity of treated sludge. The condition does not often satisfy the environmental regulation in Japan. In an effort to reduce the alkalinity of the sludge, the use of CO<sub>2</sub> gas to accelerate carbonation of alkaline sludge has been widely studied [2–4].

In atmospheric conditions, CO<sub>2</sub> at the concentration of 0.03% [5] can also neutralize the pH of construction sludge but under a very slow reaction rate of carbonation that requires a longtime curing [2, 6] and does not adapt the demand of the practical treatment. For this reason, exposing alkaline construction sludge to CO<sub>2</sub> gas at a high concentration can significantly shorten the pH neutralization curing period. Hence, the authors propose a pH treated method to promote the accelerated carbonation of alkaline construction sludge by exposing it to pure CO<sub>2</sub> gas in an underground pit as presented in Fig. 1. The rapid pH neutralization is expected by the reaction of CO<sub>2</sub> with the cement hydrates such as calcium hydroxide (Ca(OH)<sub>2</sub>) and calcium silicate hydrate (C-S-H) to form calcium carbonate (CaCO<sub>3</sub>) as the following chemical reactions:



Water is one of the crucial reactants for these chemical reactions [7]. With an appropriate water content, the reactions involved in the carbonation of hydrated cement can be occurred following three main steps: (i) dissolution of Ca(OH)<sub>2</sub>, (ii) CO<sub>2</sub> absorption and formation of carbonate ions, and (iii) chemical reaction and precipitation [8].

The carbonation of alkaline construction sludge was successfully accelerated by curing it under the high CO<sub>2</sub> concentration conditions [2, 9]. It was concluded that a concentration degree of CO<sub>2</sub> higher than 10% was not effective in further accelerating the pH neutralization of alkaline construction sludge and the low initial water content of sludge facilitated the accelerated carbonation [2]. In addition, another review [10] reported that the liquid to solid (L/S) ratio of alkaline waste plays an important factor influencing the acceleration of pH neutralization, and the water content ranges from

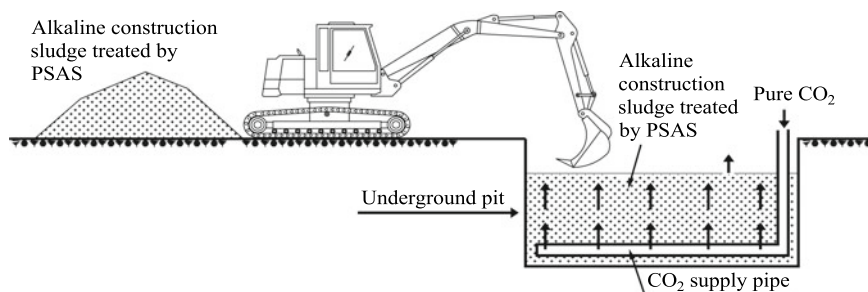


**Fig. 1** Schematic illustration of alkaline treated system for alkaline construction sludge

0.2 to 0.4 was the optimum L/S ratio depending on the characteristics of alkaline waste [10].

Inspired by such attempts, paper sludge ash-based stabilizer (PSAS) having water absorption function was successfully used to reduce the water content of alkaline construction sludge. In addition, due to the water absorption during the mixing, PSAS could granulate alkaline construction sludge [11] and generate the particle size that significantly shortened the pH neutralization periods of constructions sludge [4].

Moreover, the granulation by PSAS can strengthen the soft construction sludge with the aim of using it as a recycled material. The previous study used an alkaline construction sludge prepared from Ao clay (categorized as clay of low plasticity) and blast furnace cement type B (BFCB) to accelerate the carbonation and evaluated the strength development. It was concluded that PSAS did not only shorten the pH neutralization period but also significantly enhance the strength of construction sludge [4]. The pH neutralization period is facilitated by the produced particle size. Although the particle size is reduced with the addition amount of PSAS, a large additional amount PSAS could induce negative impact on alkaline treatment because PSAS itself is an alkaline material. This implies that PSAS treated sludge with small amount PSAS and small particle size could further enhance the efficiency in both accelerated carbonation as well as strengthening the mud.

From that point of view, this study aims to investigate the effects of additional amount of PSAS on the pH neutralization of alkaline construction sludge prepared from Kasaoka clay (clay of high plasticity). To shorten the pH neutralized period further and enhance the strength improvement of alkaline construction sludge by using PSAS, crumbling method is introduced to reduce the particle size of sludge treated by small amount of PSAS. The PSAS treated sludges were crumbled and cured under air curing for 1 day prior to the accelerated carbonation. Subsequently, the cone index test was applied to carbonated sludges to evaluate the strength development as well as the effectiveness of crumbling.

## 2 Material Preparation

Alkaline construction sludge was prepared in the laboratory by mixing Kasaoka clay at liquid limit state ( $w_L = 60.4\%$ ) with an amount of 3% by weight of blast furnace cement type B. Finally, different proportions of PSAS were added to the alkaline sludge to produce PSAS treated sludge.

### 2.1 Material

The Kasaoka clay is categorized into CH (clay (high liquid limit)), according to the Japan Unified soil Classification. The liquid limit ( $w_L$ ), plastic limit ( $w_P$ ), and dry density ( $\rho_d$ ) of Kasaoka clay are 60.4%, 26.0%, and 2.680 g/cm<sup>3</sup>, respectively. In order to form a clay slurry, distilled water is mixed with Kasaoka Clay.

To simulate alkaline construction sludge, Kasaoka clay was mixed with blast furnace cement type B (BFCB). BFCB ( $\rho_s = 3.04$  g/cm<sup>3</sup>, pH = 12.3) is a mixture of ground granulated blast furnace slag (BFS) and Portland cement with the amount of BFS ranging between 30%–60% as specified in JIS R 5211: “Blast Furnace Slag Cements” by Japanese Standards Association (JSA). BFCB was chosen because the change in the addition of BFCB changes slowly with change in pH compared to ordinary Portland cement, making it easier to adjust the pH of alkaline sludge.

Paper sludge ash-based stabilizer ( $\rho_s = 2.603$  g/cm<sup>3</sup>, pH = 11.7) is obtained from the PS ash, the cinder generated from the incineration of paper sludge. The main advantage of PSAS is its high-water absorption performance as mentioned previously. Moreover, adding PSAS granulates the new composite mixture, thereby increasing the surface area and thus effectively accelerating the alkaline neutralization. The particle size distribution of Kasaoka clay, PSAS, and PSAS sludge with different amounts of PSAS ( $A_{PS}$ ) are shown in Fig. 2. Note that the particle size distribution of  $A_{PS} = 0, 10, \text{ and } 20\%$  sludges could not be determined since the mixture was not granulated. The typical chemical compositions of BFCB and PSAS are shown in Table 1.

### 2.2 Sludge Samples Preparation

First, dry Kasaoka clay was stirred with an appropriate amount of distilled water for 3 min to attain the liquid limit state,  $w_L$  by using a bench-top mixer. Then, BFCB was added and continuously stirred for 7 more minutes. Sequentially, the PSAS treated sludge was simulated by adding different ratios of PSAS to the alkaline sludge, and the new composite mixture was then stirred for 5 more minutes. Simulated sludges

**Fig. 2** Particle size distribution of PSAS treated sludges

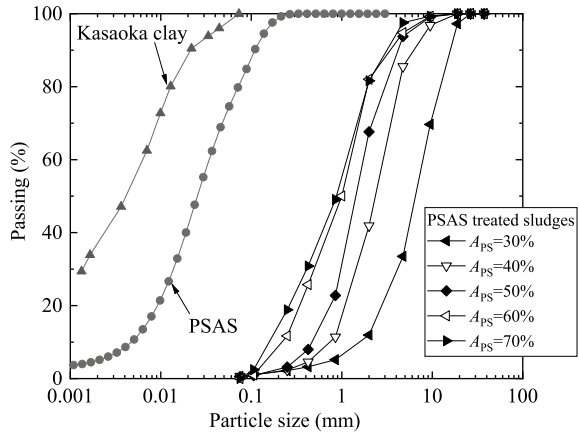


**Table 1** Chemical compositions of materials (%mass ratio)

(a) Paper sludge ash-based stabilizer (PSAS)									
CaO	SiO <sub>2</sub>	Al <sub>2</sub> O <sub>3</sub>	SO <sub>3</sub>	Fe <sub>2</sub> O <sub>4</sub>	TiO <sub>2</sub>	MgO	P <sub>2</sub> O <sub>5</sub>	Others	
63.9	13.5	6.9	6.1	3.3	3.0	1.3	1.0	1.0	
(b) Blast furnace cement type B (BFCB)									
CaO	SiO <sub>2</sub>	Al <sub>2</sub> O <sub>3</sub>	SO <sub>3</sub>	Fe <sub>2</sub> O <sub>3</sub>	MgO	TiO <sub>2</sub>	MnO	P <sub>2</sub> O <sub>5</sub>	Others
65.6	19.1	5.3	4.0	2.9	2.0	0.6	0.2	0.2	0.1

were then stored in plastic bags for curing under sealed conditions. After 7 days of sealed curing time, the resultant simulated sludge was taken out to conduct the experiments.

### 3 The Effect of PSAS on pH Neutralization of Alkaline Construction Sludge

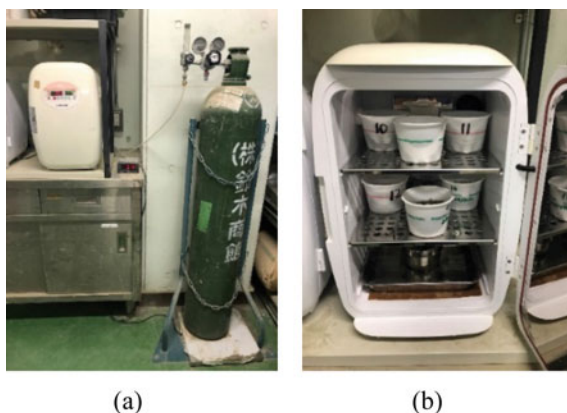
Previous studies reported that the particle size [4, 10] and initial water content [2] strongly affect the accelerated carbonation of alkaline construction sludge. From this point of view, this study focused on the effects of additional amount of PSAS on accelerating the pH neutralization of PSAS treated sludge.

After the preparation with the mixture conditions shown in Table 2, each specimen was stored in a plastic bag and placed in room at the temperature of 25 °C for sealed curing. After the 7 days of sealed curing, the sludges were sequentially placed into plastic cups at zero-high and the height of mixtures in cups was adjusted to around 30 mm. Specimens were then placed in a CO<sub>2</sub> incubator which sets up the temperature, CO<sub>2</sub> concentration, and humidity to be 25 °C, 10%, and more than

**Table 2** Mixture condition

Types of sludge	Ratio of BFCB to clay in weight, $A_c$ (%)	Ratio of PSAS to clay in weight, $A_{PS}$ (%)
Alkaline construction sludge	3	0
PSAS treated sludge	3	10, 20, 30, 40, 50, 60, 70

**Fig. 3** Accelerated carbonation equipment: **a** CO<sub>2</sub> incubator supplied by CO<sub>2</sub> tank; **b** Sludge samples in cups placed in CO<sub>2</sub> incubator



90%, respectively as shown in Fig. 3. It is noteworthy that the  $A_{PS} = 0\%$  and  $A_{PS} = 10\%$  sludges were not granulated and hence, they were separated into two parts which some were undergone deliberately crumbling process prior to the accelerated carbonation, and some were not.

After arbitrary CO<sub>2</sub> curing periods, cups were taken out to measure the pH of specimens. The relationship between pH and accelerated carbonation period is shown in Fig. 4. It can be seen that the sludges with the  $A_{PS}$  higher than 30% produced the higher pH neutralization rate. It is because the high  $A_{PS}$  sludges having smaller particle size as shown in Fig. 2 facilitated the accelerated carbonation and their pH quickly fell to less than 8.6.

To assess the effectiveness of using CO<sub>2</sub> to treat the alkalinity of construction sludge, the neutralization completion period,  $t_N$  was proposed and identified as the needed CO<sub>2</sub> curing period to neutralize pH to 8.6 as shown in Fig. 5 because this pH value satisfies the current Japanese regulation.

As mentioned above, the particle size produced by the addition of PSAS significantly accelerated the pH neutralization. Figure 6 presents the relationship between  $t_N$ , amount of PSAS,  $A_{PS}$ , and mean of particle size,  $D_{50}$ . The result showed that the granulated sludge with the reduction of  $D_{50}$  caused by PSAS strongly shortened  $t_N$ . Without PSAS,  $t_N$  of the  $A_{PS} = 0\%$  sludge could not be obtained. In addition, sludges with  $A_{PS} = 10$  or 20% were not granulated, and hence, their  $t_N$  were very long which was 80–90 h compared to those of the sludges with the  $A_{PS} \geq 40\%$ .

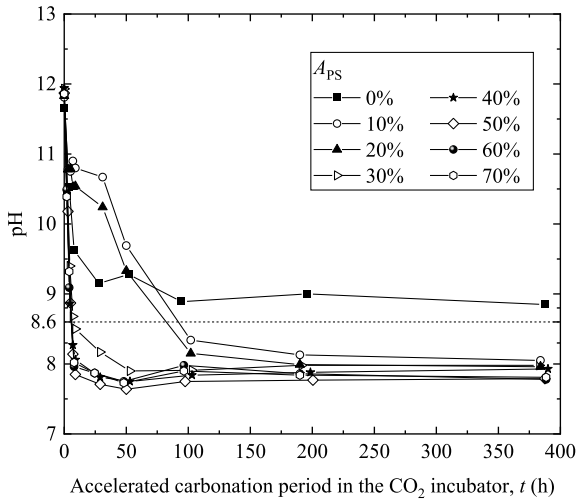


Fig. 4 The relationship of pH and accelerated carbonation period

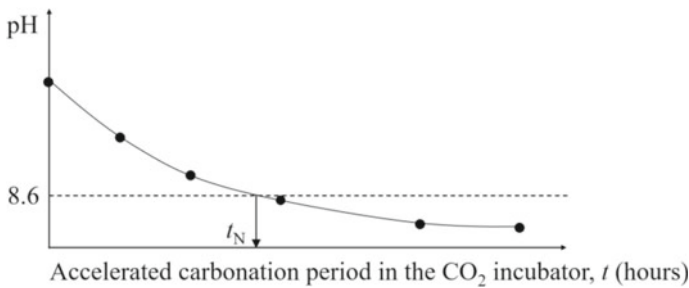
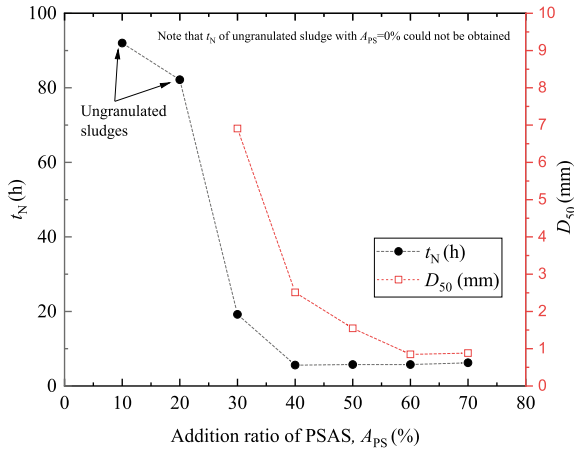


Fig. 5 Neutralization completion period,  $t_N$

#### 4 Strength Improvement of Carbonated PSAS Treated Sludge

Together with the effect on accelerated carbonation of alkaline construction sludge, PSAS could strengthen alkaline construction sludge by its water absorption and retention performance [12]. The strength improvement of PSAS treated sludge undergone  $CO_2$  curing was investigated by using Ao clay (categorized as low plasticity clay) as the main material [4]. In this study, a further investigation on strength improvement will be focused on alkaline construction sludge created by Kasaoka clay (categorized as high plasticity clay) by conducting a series of cone index tests. Moreover, an attempt to reduce the amount of PSAS while maintaining the strength development was carried out.





**Fig. 6** Relationship between  $A_{PS}$  with  $t_N$  and  $D_{50}$

#### 4.1 Material Preparation

The strength improvement effect of PSAS was investigated by carrying out the experiments on 4 types of sludge with the  $A_{PS} = 0, 20$ , and  $40\%$ . To investigate the impact of accelerated carbonation on strength development, the cone index test was applied to sludge samples.

The alkaline sludge and PSAS treated sludges were also prepared as mentioned above. Dry Kasaoka clay was stirred with distilled water to achieve the desired liquid limit state,  $w_L$ . Subsequently, BFCB was added to the clay, and the mixture was stirred thoroughly to obtain alkaline sludge. PSAS treated sludges were then sequentially produced by adding PSAS with different  $A_{PS}$  to the alkaline sludge. Each sludge sample was then cured under sealed conditions at room temperature ( $25\text{ }^\circ\text{C}$ ) for 7 days. After sealed curing, the  $A_{PS} = 0$ , and  $20\%$  sludges were separated into 2 categories. One was crumbled and cured under air curing conditions (which is called pre-air curing) for 1 day prior to the accelerated carbonation. This process is expected to reduce the water content of sludge which promotes accelerated carbonation as well as improves strength. The another was crumbled only before conducting  $\text{CO}_2$  curing.

#### 4.2 Cone Index Test Procedures

After sealed curing and pre-air curing (PAC) conditions for the  $A_{PS} = 0$ , and  $20\%$  sludges, all sludge samples were then cured under  $\text{CO}_2$  curing. Again, the  $\text{CO}_2$  concentration, temperature, and humidity in the  $\text{CO}_2$  incubator were set to  $10\%$ ,  $25\text{ }^\circ\text{C}$ , and  $90\%$  or higher, respectively. The curing period was set to 7 h, and once

the pH of sludges decreased to approximately 8.6 or lower, the sludges were immediately removed from the CO<sub>2</sub> incubator, and cone index tests were conducted on the specimens based on the Japanese Geotechnical Society Standards (JGS 0716). The cone index tests require specimen compaction followed by the Japanese Geotechnical Society Standards (JGS 0711). Therefore, each specimen was placed in a 10 cm mold by first dividing the sludge into three equal layers, where each layer was sequentially added to the mold and compacted 25 times by dropping a 2.5-kg hammer from a height of 30 cm. After full compaction, the cone index test was conducted by penetrating the tip cone at a speed of 1 cm/s into each compacted specimen held in a 10 cm mold. The force acting on the cone when the tip cone penetrated 5, 7.5, and 10 cm from the top surface of the specimen was used to calculate the cone index value,  $q_c$  as shown in Fig. 7. The sludge samples were then cured under air curing conditions. During this process, the cone index test was applied to sludge samples to determine the strength at 0, 3, 7, 14, and 28 days.

It can be seen that the cone index values of all sludges increase during the air curing conditions. The crumbling followed by PAC probably speeded up the strength development of sludge since the  $A_{PS} = 0\%$  sludge undergone crumbling and PAC showed a higher  $q_c$  than that of without PAC. In addition, the higher  $A_{PS}$  sludges produced higher  $q_c$ . As shown in Fig. 8, by crumbling and curing under PAC prior to accelerated carbonation,  $q_c$  of sludge was improved. In this study,  $q_c$  of the  $A_{PS} = 20\%$  sludge sample was significantly improved and tended to be equal to that of

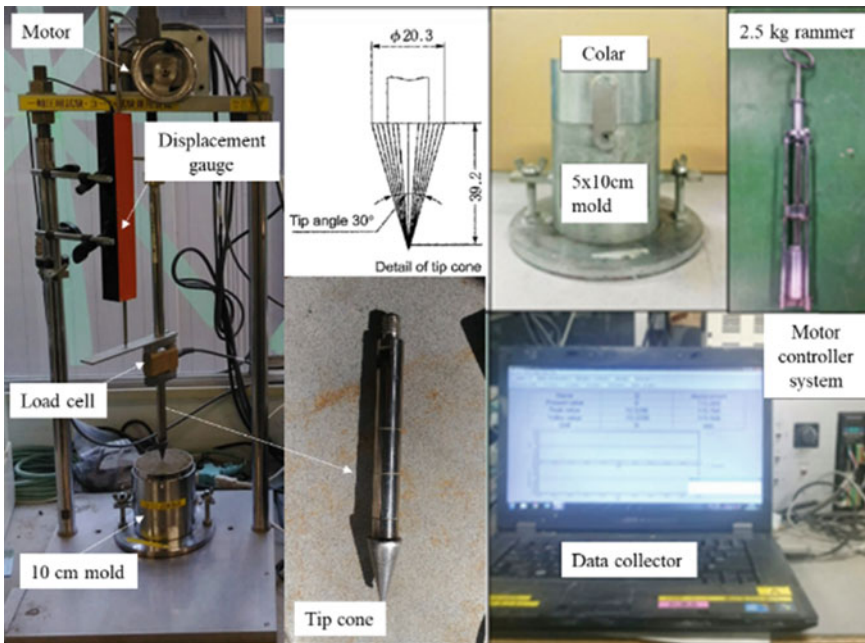
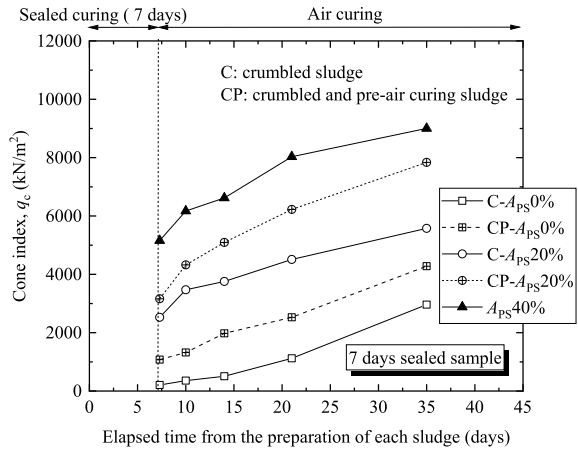


Fig. 7 Cone index test

the  $A_{PS} = 40\%$  sludge after 28 days of air curing. The reduction of water content by adding PSAS, crumbling, and air curing could improve the strength of alkaline sludge effectively as presented in Fig. 9. In addition, for the  $A_{PS} = 0\%$  sludge, it can be seen that water content reduction is the factor contributing to the strength development. However, Fig. 10 shows that with the same water content, the higher  $A_{PS}$  showed a higher  $q_c$ , which implies that not only water reduction but the contribution of PSAS to strength development was also significant.

**Fig. 8** Cone index,  $q_c$  of sludges based on time elapsed after their preparation



**Fig. 9** Water content,  $w_{sludge}$  of sludges based on time elapsed after their preparation

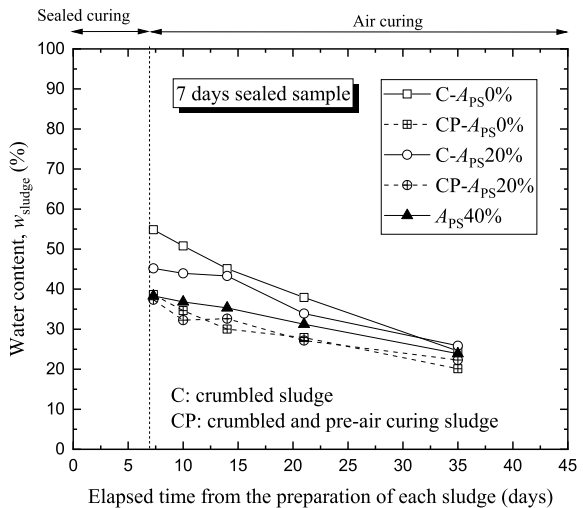
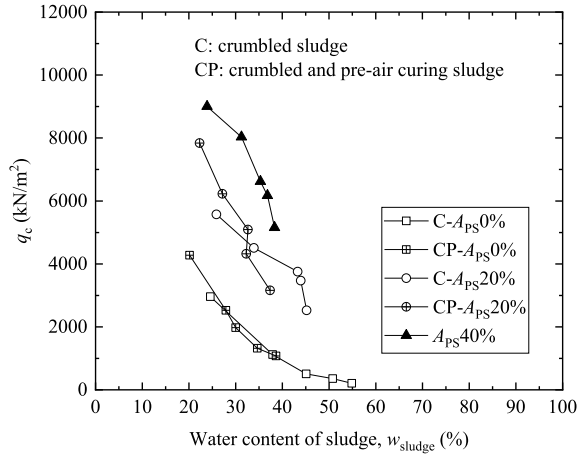


**Fig. 10** Relationship between cone index,  $q_c$  and water content,  $w_{\text{sludge}}$



## 5 Conclusions

In this study, the pH neutralization of alkaline construction sludge treated with paper sludge ash-based stabilizer (PSAS) was experimentally investigated. Moreover, the strength of PSAS treated sludges was studied by conducting a series of cone index tests. Based on the experimental results, the following conclusions can be drawn:

The pH neutralization rate of alkaline construction sludge was significantly improved by the addition of PSAS. By mixing with PSAS, the lumpy alkaline construction sludge was granulated, and the particle size was reduced. This increased the surface area that facilitate the accelerated carbonation of alkaline construction sludge. Without PSAS,  $t_N$  of alkaline construction sludge could not be obtained even after being intentionally crumbled to be granulated. Once granulated by PSAS, the  $t_N$  of PSAS treated sludge was significantly reduced.

The addition of PSAS effectively improved the strength of alkaline sludge. The larger amount of PSAS, the higher  $q_c$  can be obtained. However, by crumbling and curing under air conditions prior to accelerated carbonation, the strength of sludge could be further improved. For instance, the strength of the  $A_{\text{PS}} = 20\%$  sludge undergone crumbling and pre-air curing could be improved and tended to be equal to that of  $A_{\text{PS}} = 40\%$  sludge after 28 days of air curing. In addition, not only water reduction but the addition of PSAS also contributed to strengthening improvement of sludges since with the same water content, the higher  $A_{\text{PS}}$  sludge showed a higher  $q_c$ .

## References

1. Murakami O, Masuda T, Hanada O, Tamura T, Kamao S, Takezawa M (2012) Recycling and treatment of construction sludge. In: Pacetti M, Passerini G, Brebbia CA, Latini G (eds) *The sustainable city VII*. Wit Press, pp 1129–1138
2. Imai K, Hayano K, Yamauchi H (2020) Fundamental study on the acceleration of the neutralization of alkaline construction sludge using a CO<sub>2</sub> incubator. *Soils Found* 60(4):800–810
3. Trung ND, Hayano K, Yamauchi H (2021) Fundamental study on the effect of CO<sub>2</sub> curing on the strength development of alkaline construction sludge. In: *BT - advances in sustainable construction and resource management*, pp 95–105
4. Trung ND, Ogasawara T, Hayano K, Yamauchi H (2021) Accelerated carbonation of alkaline construction sludge by paper sludge ash-based stabilizer and carbon dioxide. *Soils Found* 61(5):1273–1286
5. Nakarai K, Yoshida T (2015) Effect of carbonation on strength development of cement-treated Toyoura silica sand. *Soils Found* 55(4):857–865
6. Otieboame Djangjeme M, Hayano K, Yamauchi H, Maqsood Z (2022) Swelling and strength characteristics of sand treated with paper sludge ash-based stabilizer. *Constr Build Mater* 341:127849
7. Saetta AV, Schrefler BA, Vitaliani RV (1993) The carbonation of concrete and the mechanism of moisture, heat and carbon dioxide flow through porous materials. *Cement Concr Res* 23(4):761–772
8. García-González CA et al (2006) Modification of composition and microstructure of portland cement pastes as a result of natural and supercritical carbonation procedures. *Ind Eng Chem Res* 45(14):4985–4992
9. Inasaka K, Duc Trung N, Hayano K, Yamauchi H (2021) Evaluation of CO<sub>2</sub> captured in alkaline construction sludge associated with pH neutralization. *Soils Found* 61(6):1699–1707
10. Pan S-Y, Chang EE, Chiang P-C (2012) CO<sub>2</sub> capture by accelerated carbonation of alkaline wastes: a review on its principles and applications. *Aerosol Air Quality Res* 12(5):770–791
11. Watanabe Y, Nguyen Binh P, Hayano K, Yamauchi H (2021) New mixture design approach to paper sludge ash-based stabilizers for treatment of potential irrigation earth dam materials with high water contents. *Soils Found* 61(5):1370–1385
12. Phan NB, Hayano K, Mochizuki Y, Yamauchi H (2021) Mixture design concept and mechanical characteristics of PS ash–cement-treated clay based on the water absorption and retention performance of PS ash. *Soils Found* 61(3):692–707

# 3D Modeling of a Historical Mine Waste Site Using UAV Images: Estimation of Stockpile Volumes



Okan Onal  and Orhan Gunduz 

**Abstract** In recent decades, the use of Unmanned Aerial Vehicles (UAV) for land surveying became very popular because of their simplicity and low cost. Aerial images of the site can be used for the reconstruction of the site's 3D digital model. Once proper calibrations are made, these digital models can be used for several purposes including stockpile volume estimation, stability analyses, forensic engineering and archiving, etc. In this study, the 3D model of an abandoned historical mine waste disposal site located in Balıkesir-Turkey was reconstructed for the estimation of the waste stockpile volumes. The historical mine site is a facility that was abandoned more than 80 years ago. Mine wastes of different quality were disposed of in and around the site along the hydrologically intermittent creek that passes through the site. No engineered precautions were taken at the site to reduce the environmental impacts and all waste piles were exposed to the natural eroding effect of precipitation and wind. The total amount of the waste volume is not known accurately, which prevents researchers to quantify the potential impacts associated with different waste stockpiles. Thus, a 3D digital model of the site was created by using UAV data obtained from a quadcopter and later processed to obtain a digital topography of the site with an improved accuracy value of  $\pm 2$  cm. The stockpiles were later analyzed with geographic information systems to characterize the magnitude of mine wastes and to propose alternative engineering solutions for environmental mitigation.

**Keywords** Mine waste stockpile volume · Historical mine site · Photogrammetry

---

O. Onal (✉)

Department of Civil Engineering Izmir, Dokuz Eylul University, Izmir, Turkey  
e-mail: [Okan.onal@deu.edu.tr](mailto:Okan.onal@deu.edu.tr)

O. Gunduz

Department of Environmental Engineering, Izmir Institute of Technology, Izmir, Turkey

# 1 Introduction

The historical lead–zinc (Pb–Zn) mine located within the borders of Balya District in Balıkesir-Turkey and the uncontrolled process wastes of this mine pose a risk for the deterioration of the surface and subsurface water quality of the region. Lead and zinc, which form the main ore of the Balya mine, are among the oldest metals used in human history. Since ancient times, metallic lead is obtained by smelting very high-grade lead ores following manual extraction. Mining activities in Balya region continued for many years and eventually the mine and process wastes were abandoned at the site along the intermittent creek that passes through the site. No engineered precautions were taken in the site to reduce the environmental impacts and all waste piles were exposed to natural eroding effect of precipitation and wind. In order to determine the effects of abandoned mines and their wastes on the surface and subsurface waters in the field's impact area, it is necessary to determine the amount of waste in the field. Thus, field observations and high-resolution images obtained by unmanned aerial vehicles were used to quantify the amount of process wastes abandoned at different points in the mine area. A 3D digital model of the site was created by using UAV data obtained from a quadcopter and later processed to obtain a digital topography of the site with an improved accuracy value of  $\pm 2$  cm. Although used for many years as a disposal area, no topological survey data has been found about the waste disposal area. Balya Mine, which is very close to the Balya district center, is in a position that directly affects the Manyas Dam Lake and Manyas Lake-Bird Sanctuary, as it is within the watershed of Madra and Kocacay streams (Fig. 1).

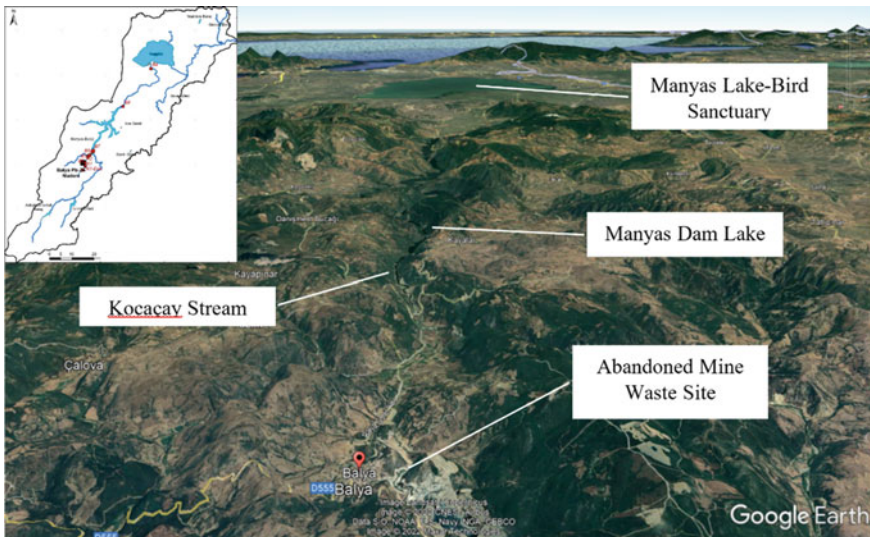


**Fig. 1** Location of the study area

The Manyas Lake Bird Sanctuary was declared as a national park in 1959, covering an area of 17,800 ha, due to its diverse bird communities, plant populations and unique wildlife. The effects of the Balya mine on Lake Manyas have been known for many years and various studies have been carried out in the past on this subject [1–4].

## 2 A Brief History of Balya Mine

The existence of the Pb–Zn ores in Balya has been known since ancient times. It is stated that the site has been operated since the period of Pericles (494–429 BC) [1, 5, 6]. It is rumored that the mine was operated under the name of “Christian Mines” during the Roman period [7]. The most reliable records of the operation of the mine are from the Ottoman period. It is known that during the reign of Mehmet IV (1648–1687) and Selim III (1789–1807), the mine was operated. Later, between 1839 and 1849, the mining operation was given to a company called “Balya Mining Enterprises”, whose nationality is unknown [7]. It is known that in 1868, a German citizen named Reiser transferred the operating rights of the mine to the “Lorium” company, and subsequently, in 1878, a French citizen named Riol received the privilege of operating the mine for 99 years [7]. According to the available records, it is seen that the first modern operation in the field was started by a French company named Balya Karaaydın Mines in 1880. It is known that the Balya mine was one of the largest lead deposits in the world in the early 1900s before the First World War. It is stated that the field reached the highest level of operation in 1913 with 140,300 tons of raw ore processing and 13,800 tons of lead production. It is estimated that after the company’s transition to modern operations, it has processed around 4 million tons of ore, from which approximately 400,000 tons of lead metal has been produced [4, 6]. It is known that there was intensive production in the Balya mining enterprise until the Second World War, but on the eve of the war, the production stopped completely in 1939 due to the falling metal prices and the changing political and economic conditions of the period. The mine was nationalized in 1940 by Turkish Government but could not be operated again. However, it is also known that enrichment and production studies were carried out by a private company between 1966 and 1970 using the abandoned mine wastes found in the field [5]. Balya mine field was licensed by the General Directorate of Mining and Petroleum Affairs in the 2000s and given to Eczacıbaşı ESAN and Dedeman Mining Industry corporations. Both companies continue production in Balya today [8].

## 3 Estimation of Stockpile Volumes Using UAV Images

During the field investigations, 9 different waste areas were identified, one of which was formed by natural river deposition (B1 region) and 8 of them (B2–B9) were formed during the former operation of the Balya mine. The waste accumulation





**Fig. 2** Waste accumulation area B1 and other waste disposal areas (B2–B9)

area B1, which is estimated to be formed by river sediment transport, is located at the northernmost point of the site and is located at the south edge point of Manyas Dam Lake. B1 point is within the lake area of Manyas Dam. It has been determined that if the dam reaches the maximum water level, this area will be inundated (Fig. 2). For this study, the stockpile estimation of the B1 region was established by manual measurement methods. For the other regions, an aerial imaging approach was adopted.

Images were taken on the waste sites with a DJI Phantom 3 model unmanned aerial vehicle. Since the waste is spread over a very large area including a high hill in the middle of the zone, the flight was completed in two phases. For both phases, the flight times were approximately 20 min. Before aerial images were acquired, six ground control points for flight zone 1 and seven ground control points for flight zone 2 were established (Fig. 3).

The flights were performed at an altitude of 120 m for both flight zones, resulting 5 cm ground sampling distance (5 pixel/cm) and 305 images. The images were obtained by 80% overlap on flight direction and 60% side lap for the other direction. The aerial images were then transformed from the copter to a hard-drive and analyses were performed in the office.

The photogrammetric analysis was performed using a commercial photogrammetry software package i.e. Agisoft Metashape. Since the aerial images were tagged by the embedded GPS of the quadcopter, the approximate coordinates of the images were used at the import process. These coordinates were used in the initial processes of the photogrammetric operations for accelerating the calculations.

In order to establish a coarse 3D cloud point model, a computationally demanding process call as photo alignment has to be performed [9]. In this stage, the identical



**Fig. 3** Ground control point and surveying

features in the image matrixes were examined and the tie points between the overlapping images were detected [10]. At the end of this process a sparse cloud point, in which the topography may be seen in 3D was established (Fig. 4).

Overall, the space cloud consists of 112,450 points in a 3D environment with an inherent scale and orientation. The exact locations of the ground control points were used to locate and scale the topographical model. To do this, all ground control points were marked in the aerial images and an iterative calibration procedure was performed by optimizing the measured and marked ground control point coordinates. Hence, average errors between field measurements and image analysis coordinates

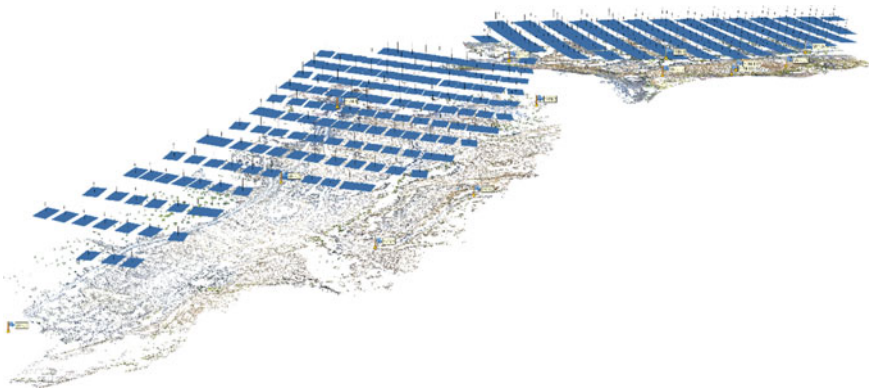


**Fig. 4** Sparse cloud point of zone 1 and zone 2



**Fig. 5** Waste disposal areas (B2–B8)

were computed as 2 cm for the GCP of two topographical models. After optimizing the 3D point cloud of the areas, a dense point cloud having 16 million of points was processed using multi view stereo algorithms. Finally, a dense mesh surface was calculated by using the dense point cloud data, in order to establish a 3D mesh model.

Waste disposal areas (B2–B8) were marked as polygons in the 3D environment by considering field observations and high-resolution aerial images for the stockpile volume determinations (Fig. 5).

Since the topography of the site before the landfill is not known, it is not possible to calculate the amount of waste with a method based on calculating the difference between the two surfaces. For this reason, it would be a realistic approach to determine the limit values that will constitute the lower and upper limits for the determination of the amount of waste stored. For this purpose, in determining the lower limit of the waste amount, the surface areas of the waste piles in the fields and the average value of the waste material thickness obtained from the observation wells drilled in previous studies in the stockpiles were used. Total waste weights were calculated by multiplying the volumes obtained with the average material densities.

On the other hand, although a detailed surface model (waste top surface) is obtained in photogrammetric analysis, there is no old topography of the area that will form the basis for the volume calculations. Therefore, horizontal planes that were considered to pass through the minimum waste material level were determined separately for each area in order to determine the amount of waste material disposed. In this second approach, the amount of waste material was obtained by determining the volumes between the detailed surface topographies limited by areal polygons and the minimum elevation plane of waste stockpiles, which were considered to contain waste materials. The weights were obtained by multiplying the volumes with the material densities. While the amounts obtained by this method can precisely estimate the amount of wastes stacked on a nearly flat horizontal plane without slope, they can slightly overestimate the amount of waste in areas with a more sloping topography. For this reason, it would be appropriate to accept the amount of waste calculated by the second method as an upper limit for the waste areas in the field.

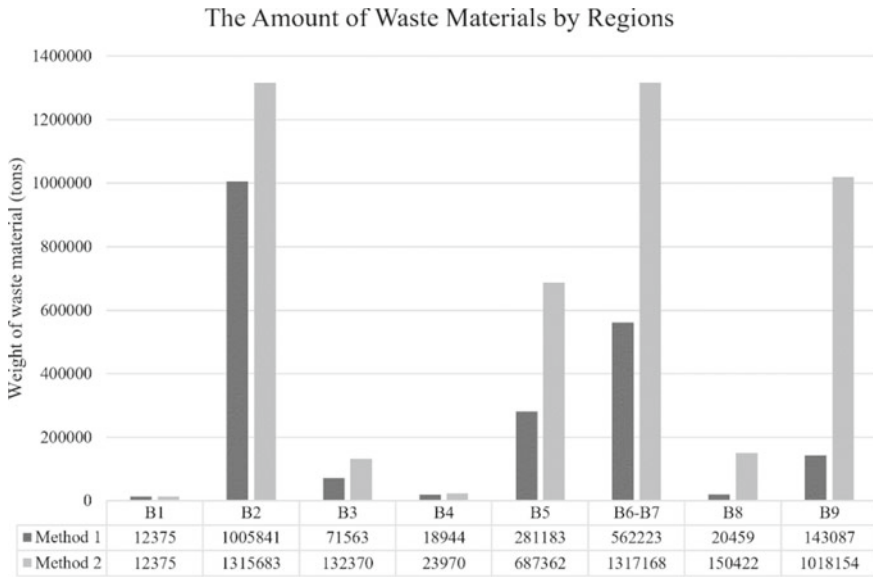


**Fig. 6** The amount of waste materials for regions by two approaches

The amounts of waste by regions calculated based on both approaches are given in Fig. 6. As can be seen here, the second method yields more waste for all sites. Since there are no UAV images for the B1 region, an approximate estimation based on field observation and satellite images was presented. Using the approaches outlined above, the amount of waste material found in the entire Balya mine site was calculated to be between 2,110,000 tons and 4,660,000 tons (Fig. 7).

## 4 Conclusions

This study was carried out on the abandoned Lead–Zinc (Pb–Zn) mine located within the borders of Balya District of Balıkesir Province, Turkey to determine the total amount of mine wastes abandoned at the mine site in uncontrolled conditions. These wastes pose a risk for the deterioration of the quality of surface and subsurface waters within and downstream the mine. In the study, data were obtained to determine whether the site still actively affects the water resources despite a period of nearly 100 years since its abandonment. For that purpose, a photogrammetric process was adopted, in which the aerial images of the regions were used to obtain a detailed surface topology. The aerial images were acquired by a quadcopter and ground control points were used in order to calibrate the 3D model of the waste disposal sites. Since there is no old topography of the area that will form the basis for the volume calculations, the waste stockpile volumes were estimated by determining the

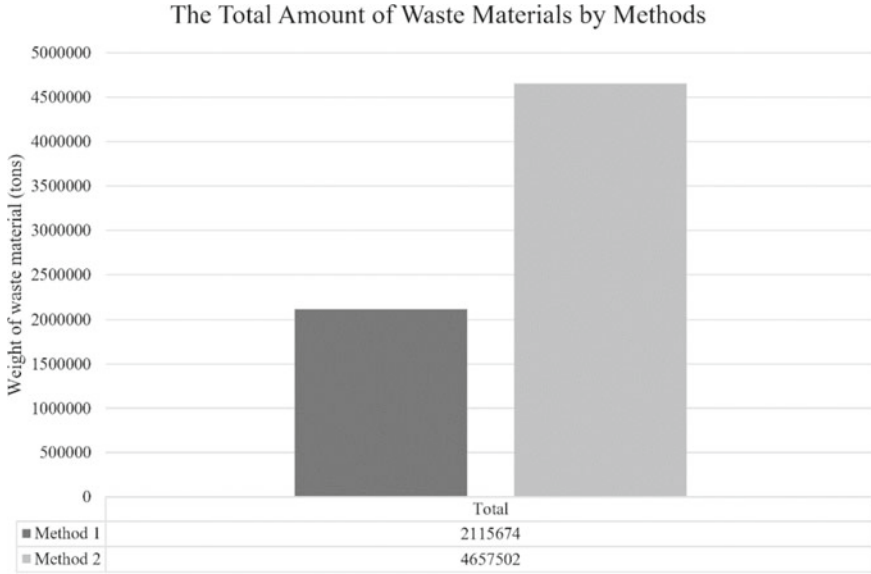


**Fig. 7** The total amount of waste materials for upper and lower limits

upper and lower bound values. The results of this study were later used to assess the overall impacts of the mine wastes in the region with respect to soil and water resources. The findings of the study are thought to be important for determining the general environmental effects of abandoned and/or expired old mining sites.

## References

1. Bukowski V (1892) Die geologischen Verhaeltnisse der Umgebung von Balya Maden im nordwestlichen Kleinasien, Wien
2. Baştürk A (2017) Balya (Balıkesir) Civarındaki Flotasyon ve İzabe Atıklarının Özelliklerinin Belirlenmesi ve Rezervinin Hesaplanması, Yüksek Lisans Tezi, Balıkesir Üniversitesi Fen Bilimleri Enstitüsü, Balıkesir
3. Aykol A, Budakoğlu M, Kumral M, Gültekin AH, Turhan M, Esenli V, Yavuz F, Örgün Y (2003) Heavy metal pollution and acid drainage from abandoned Balya Pb-Zn sulfite mine, NW Anatolia, Turkey. *Environ Geol* 45:198–208
4. Agdemir N, Kirikoglu MS, Lehmann B, Tietze J (1994) Petrology and alteration geochemistry of the epithermal Balya Pb-Zn-Ag deposit, NW Turkey. *Miner Deposita* 29(4):366–371
5. Akyol Z (1977) Balıkesir-Balya (Pb-Zn) Artıklarının Yurt Ekonomisi Açısından Önemi, *Jeoloji Mühendisliği Dergisi*, Cilt: 1, Sayı: 2, s.13–16
6. Kovenko V (1940) Balya kurşun madenleri. MTA Mecmuası. s. 4/2, Ankara
7. Madencilik Bülteni (2010) Balya Madenlerinin Tarihi, İnceleme, Madencilik Bülteni, Temmuz Eylül 2020, Sayı: 094, s.54–57
8. T.C. Çevre ve Şehircilik Bakanlığı - Balıkesir İli Balya İlçesinde Terk Edilmiş Maden Sahasında Bulunan Atıkların Çevreye Etkilerinin Araştırılması, Dokuz Eylül Üniversitesi (2020)

9. Dyer C (2001) Volumetric scene reconstruction from multiple views. In: Davis LS (ed) Foundations of image understanding. Kluwer, pp 469–189
10. Lowe DG (2004) Distinctive image features from scale-invariant keypoints. *Int J Comput Vision* 60(2):91–110

# Earthquake Analyses of Earthen Dams with an Emphasis on Sustainability



Ali Gerçek  and Gürkan Özden 

**Abstract** For sustainable development, engineering structures should be manufactured safely using the most economical method and with minor environmental damage. While designing a structure or infrastructure, it is crucial to use our limited resources most efficiently and not compromise on safety while making these savings so that our future generations can live in prosperity. Earth-fill dams are preferred because of the use of natural materials of the surrounding area, the smaller carbon footprint of the soil material compared to concrete, and therefore being less damaging to nature than reinforced concrete dams. Based on this information, choosing earth-fill dams is more advantageous from the point of sustainability view. The safe design of earth-fill dams under seismic effects dates back to the 1930s, while the safety of dams built before this date against seismic effects was still a mystery. While site-specific earthquake hazard analyses and dynamic analyses in time domain are primarily performed in the design of large dams, these issues are ignored in medium and small-size dams, and their safety against earthquake hazards is calculated using pseudo-static or conventional equivalent static methods. With the use of these methods in dams of medium and small sizes, designs that are heavily conservative and less economic are being made. This study performed analyses on a sample earth-fill dam using conventional equivalent static, nonlinear pseudo-static, and nonlinear time domain solutions. Nonlinear analyses were made by means of finite element method. It was seen that the time history solutions promise more economic designs that are still stay on the safe side provided that nonlinear material parameters are correctly determined.

**Keywords** Earth fill dams · Sustainability · Earthquake · Time domain analyses

---

A. Gerçek (✉) · G. Özden

Graduate School of Natural and Applied Sciences, Department of Civil Engineering, Dokuz Eylül University, Izmir, Turkey

e-mail: [gercek.ali@ogr.deu.edu.tr](mailto:gercek.ali@ogr.deu.edu.tr)

Faculty of Engineering Department of Civil Engineering, Dokuz Eylül University, Izmir, Turkey

## 1 Introduction

The safety of dams under seismic effects is a problem that has been researched since the 1930s. While site-specific seismic hazard analyzes and dynamic analyses in time domain are performed in the construction of large-scale dams, they are mostly ignored in medium and small-scale dams, and the analyses of these dams under dynamic effects are carried out with equivalent static methods or pseudo-static methods. Regardless of the dam's dimensions, analyses made with non-linear soil models in time domain yield the most realistic results today. The safety values calculated by pseudo-static and equivalent static methods are generally calculated lower than the actual safety of the dam, and therefore, the designs made with these methods generally move away from the economy. This situation causes unnecessary overuse of limited resources at our disposal.

For sustainable development, engineering structures should be constructed in a way that has the least impact on the environment. Earth-fill dams create less carbon footprint than reinforced concrete dams because they are constructed with natural materials in and around the area where they would be made. Therefore, earth dams should be preferred more than reinforced concrete dams in terms of sustainability.

Until the 1960s, the design of earth-fill dams under earthquake loads was pursued with the help of seismic coefficients. The calculation method was to evaluate the force value, which is the result of multiplying the sliding mass ( $W$ ) on the fill slope with an acceleration coefficient ( $k$ ) in the range of 0.05–0.5 times the gravitational acceleration [1], as the maximum lateral force that would occur during an earthquake ( $F = k * W$ ). The coefficient  $k$  mentioned in this calculation is referred to as the effective horizontal acceleration in the literature. Some horizontal seismic “ $k$ ” coefficients suggested in the literature are given in Table 1.

With the development of technology, the use of the finite element method has increased. The first finite element analysis of embankment dams is due Clough and Chopra [2]. The material models of the period were visco-elastic total stress-based. Therefore, such models could not calculate the excess pore water pressures developed in the soil during dynamic effects. In the San Fernando Earthquake that took place in 1971, a large part of the upstream of the San Fernando dam liquefied after the earthquake as a result of redistribution of excess pore water pressure induced in the dam body [3]. The development of dynamic finite element models has been of great interest to researchers since then.

In this study, we investigated the behavior of a medium-sized earth-fill dam in Italy under seismic effects to observe the economy that would be provided by time domain analyses. For the analyses to be made in the time domain, a selected earthquake record was scaled spectrally according to the design level earthquake, which is likely to occur once in 1460 years in the region where the dam is located. The earthquake was applied at the engineering bedrock of the analysis model. Plane-strain finite element runs were performed in the time domain and pseudo-static analyses, as well as quasi-static method calculations based on limit equilibrium approach.



**Table 1** Recommended horizontal seismic  $k$  coefficients [1]

Horizontal seismic coefficient, $k_h$	Description	
0.10	“Large” Earthquakes	Terzaghi
0.20	“Strong, destructive” Earthquakes	
0.50	“Catastrophic” Earthquakes	
0.10	Large Earthquakes for $FS > 1.0$	U.S. Corps of Engineers
0.15	Large Earthquakes	
0.05–0.15	America	
0.12–0.25	Japan	
0.10–0.20	Seed, for $FS \geq 1.15$	
1/2–1/3 of PGA	Marcuson 1981, $FS > 1.0$	
1/2 of PGA	Hynes-Griffin and Franklin 1984, $FS > 1.0$	

FS = Factor of Safety. PGA = Peak Ground Acceleration

## 2 Analyses Models

The dam discussed herein is located in the Arezzo region of Italy. This dam selected since it was well studied by previous researchers and adequate data were available in the published literature [4]. The dam consists of two main zones: the clay core and the sand-gravel zone fill. On the ground where the dam sits, there is ophiolitic engineering rock under the alluvial ground with a thickness of about 5 m. In order to reduce the leakages to occur in the dam, the alluvial ground under the clay core was excavated and the core base was placed on the bedrock. The height of the earth-fill dam is  $H = 64$  m, and the slopes on the upstream and downstream sides are 1:2.5 and 1:2.25, respectively. The maximum water capacity height of the dam is  $h_w = 62$  m. A section of the dam is given in Fig. 1, the parameters assigned to the finite element, and limit equilibrium models are presented in Tables 2 and 3.

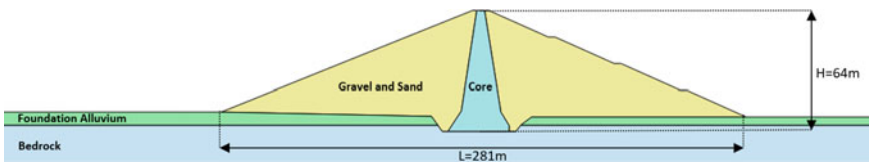


**Fig. 1** Geometry of the dam [4]

**Table 2** Parameters assigned to the finite element model

Identification	Unit	Bedrock	Alluvium foundation	Sand-gravel shield	Core
Material model		Linear elastic	Linear elastic	HS small	HS small
Drainage type		UD-A	UD-A	UD-A	UD-A
$\gamma_{\text{unsat}}$	kN/m <sup>3</sup>	25.0	22.0	24.2	20.7
$\gamma_{\text{sat}}$	kN/m <sup>3</sup>	25.5	22.5	25.0	21.0
$e_{\text{init}}$		0.20	0.37	0.36	0.53
E	kN/m <sup>2</sup>	$1.25 \times 10^7$	$4.02 \times 10^6$	–	–
N		0.35	0.40	–	–
$E_{50,\text{ref}}$	kN/m <sup>2</sup>	–	–	$5 \times 10^4$	$1 \times 10^4$
$E_{\text{oed,ref}}$	kN/m <sup>2</sup>	–	–	$5 \times 10^4$	$1 \times 10^4$
$E_{\text{ur,ref}}$	kN/m <sup>2</sup>	–	–	$1.5 \times 10^5$	$3 \times 10^4$
power(m)		–	–	0.5	0.5
$c'_{\text{ref}}$	kN/m <sup>2</sup>	–	–	1	10
$\phi'$ (fi)	°	–	–	40	25
$\psi$ (psi)	°	–	–	10	0
$\gamma_{0.7}$		–	–	0.0222	0.0438
$G_{0,\text{ref}}$	kN/m <sup>2</sup>	$4.64 \times 10^6$	$1.44 \times 10^6$	$1.09 \times 10^6$	$2.30 \times 10^5$
$k_{o,x} = k_{o,y}$		0.5	0.5	0.36	0.58
OCR		1	1	1	1
$k_x$	m/day	$2.59 \times 10^{-5}$	2.59	2.59	$2.59 \times 10^{-5}$
$k_y$	m/day	$2.59 \times 10^{-5}$	2.59	2.59	$2.59 \times 10^{-5}$

**Table 3** Parameters assigned to the limit equilibrium model

Identification	Unit	Bedrock	Alluvium foundation	Sand-gravel shield	Core
Material model		Bedrock	Mohr-coulomb	Mohr-coulomb	Mohr-coulomb
Unit weight	kN/m <sup>3</sup>	–	22.5	25.0	21.0
Cohesion	kPa	–	1.0	1.0	10.0
Friction angle	°	–	40.0	40.0	25.0

Hardening small strain material model [4] was the preferred one since the degradation of the initial shear modulus with strain could be accounted for during the analyses. As can be seen from the table, the shear strength parameters of the materials used in the model are the parameters calculated according to the Mohr–Coulomb

failure criterion. The same strength values were also chosen for the limit equilibrium analysis. This selection shows that the results of the force-based calculations shall converge to the same value regardless the finite element or the limit equilibrium approach is used.

### 3 Record Used for Dynamic Analyses

In the analysis, the San Fernando Earthquake ( $M_w = 6.6$ ), which occurred in 1971, was chosen as the earthquake record (Lake Hughes #4 station of PEER NGA-West2 database) with an effective duration of  $D_{5-95} = 13$  s. The shear wave velocity of the station in the first 30 m is  $V_{s,30} = 600$  m/s. The earthquake occurred on a strike-slip fault and the closest distance to the station is 19.45 km. The selected earthquake motion is spectrally matched according to the region where the dam is located. The target spectrum defines an earthquake with a 2% probability of occurring in 75 years, which is the service life of the dam. Baseline correction was applied to eliminate permanent displacements that occur during spectral matching. Since this application prolongs the recording time, only the effective duration of the earthquake was used to save analysis time. The acceleration-time and displacement-time graphs of the earthquake record after scaling are given in Figs. 2 and 3. Spectra are presented in Fig. 4.

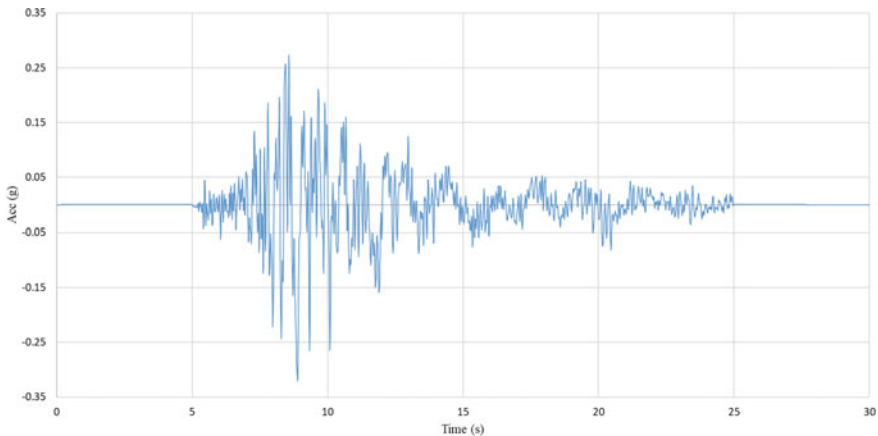


Fig. 2 Input motion acceleration-time graph

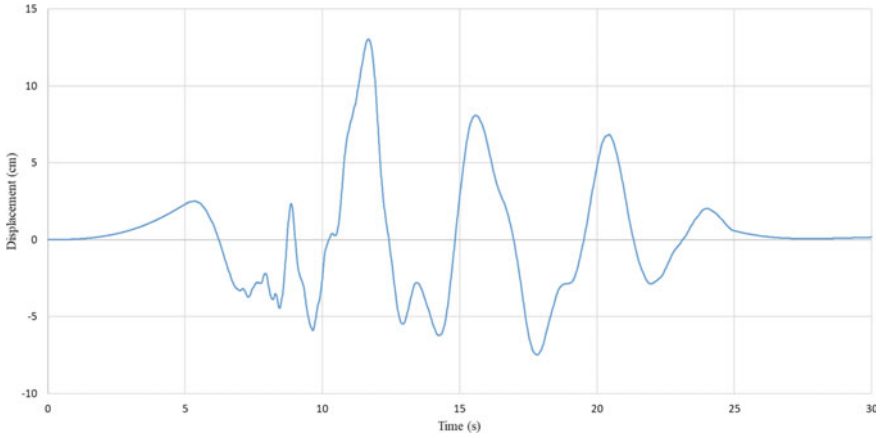


Fig. 3 Input motion displacement–time graph

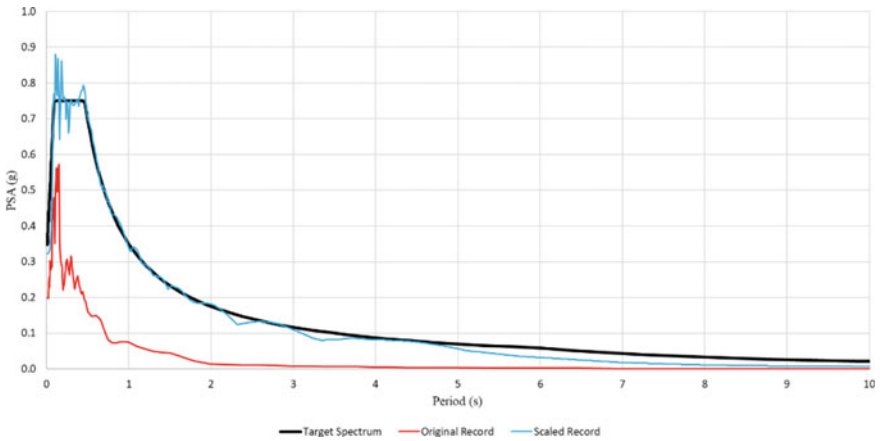


Fig. 4 Input earthquake, original record and target spectrum

### 4 Finite Element and Limit Equilibrium Analysis Results

Since the failure criteria for the hardening small strain material model the limit equilibrium analysis are the same, the safety coefficients of the slope stability are expected to be close to each other. According to the results of the analyses, the safety factor against slope failure was found to be  $F_S = 2.0$  for the finite element analysis under gravity forces. According to the limit balance analysis, the safety factor of the circular slip surface is also  $F_S = 2.0$ . On the downstream side of the dam model, there are 4 slopes with equal slope and height, separated from each other by three

benches (see Fig. 1). Since the geometry of these four different slopes is the same and the critical slip circles do not interfere, the safety factors against slipping are found to be equal.

No permanent deformation was found in the downstream slope of the dam with the Newmark sliding block method in the limit equilibrium analysis. The reason for this is that the maximum acceleration value (0.32 g) of the earthquake remains below the limit acceleration coefficient that would cause permanent deformation ( $a_y = 0.33$  g). This value represents the amount of horizontal force needed to decrease the factor of to unity. Any acceleration above this value results in permanent displacement for the sliding mass.

In the results of the analysis made with the finite element method, 9.7 mm permanent deformation was calculated at the apex of the dam. At first glance, it can be said that the results of the permanent deformation calculated by the Newmark sliding block method and the finite element method agree. The absence of permanent deformation in the dam body reduced the hysteretic behavior of the material and reduced the damping of the system. Due to the geometry of the dam and the non-linear behavior of the dam, the earthquake acceleration values were amplified along the dam body. The increase in spectral acceleration during the progression of the input acceleration inside the dam core can be seen in Fig. 5. As one may notice in Fig. 5, the embankment dam amplifies the high-frequency content of the earthquake. In particular, it increased the maximum ground acceleration, which is one of the most defining features of the earthquake, by 3.1 times. The earthquake amplification between the clay core base and the crest of the dam is given in Fig. 6.

As can be followed in Fig. 6, the dam body amplifies short-period excitations. Peak ground acceleration value increased to 1.01 g at the dam crest from 0.32 g at the base of the model. The acceleration-time and displacement-time graphs of the crest region are given in Figs. 7 and 8.

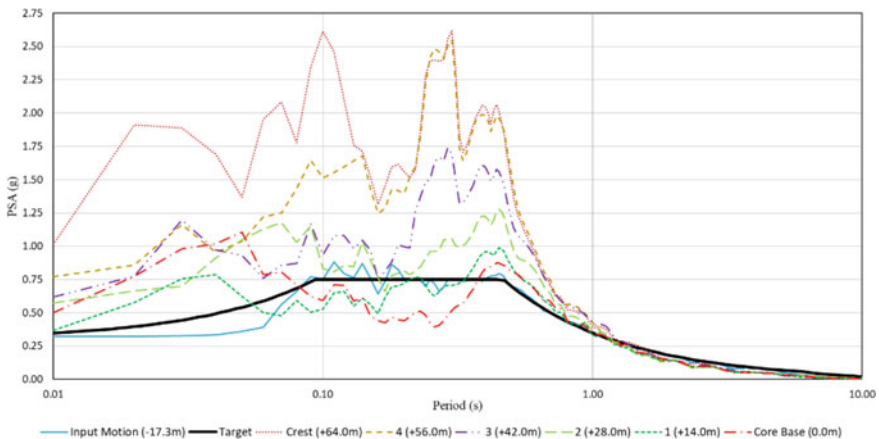


Fig. 5 Changes of input motion spectral magnitudes in the dam core

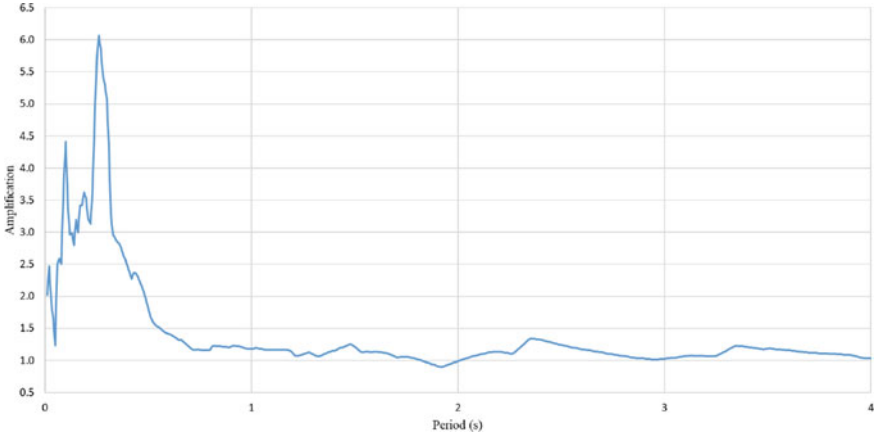


Fig. 6 Magnification factors between clay core base and crest

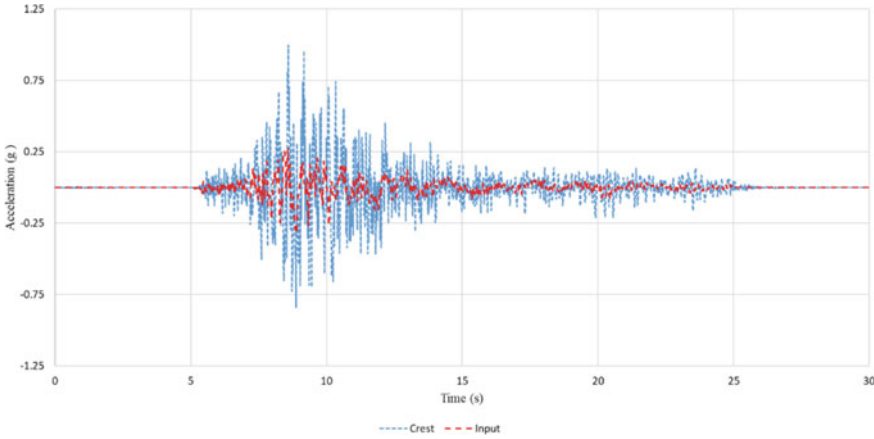
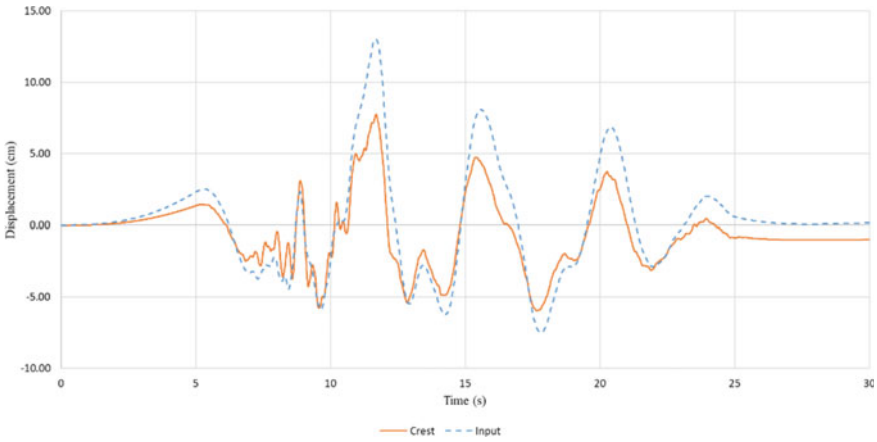


Fig. 7 Input motion and crest region acceleration-time records

The pseudo-static earthquake acceleration coefficient was chosen as 0.21 g according to Turkish Building Code 2018. Although dams are outside the scope of this code it involves some regulations about dynamic slope stability. The formulae for calculating horizontal force acting on the slope according to the code is expressed in Eq. 1 where  $S_{DS} = 0.75$  as short period spectral acceleration,  $S_T = 1.4$  as topographic amplification coefficient and  $W$  is the weight of the sliding mass.

$$F_h = 0.5 * W * (0.4 * S_{DS} * S_T) \tag{1}$$

According to the results of the pseudo-static analysis by means of the finite element method, 9.2 mm permanent lateral displacement took place at the crest of the dam.



**Fig. 8** Input motion and crest region displacement–time records

This value is very close to the outcome of the analyses made in time domain. Even though the deformations are compatible, the factor of safety values for time domain and pseudo static analyses considerably differ from each other. In time domain analyses, factor of safety against sliding happens to be  $F_S = 2.0$ , which is 1.16 for the pseudo static. This may be attributed to the fact that seismic coefficient applies to the entire dam body in pseudo-static analyses whereas major accelerations affect the dam couple cycles in the time domain. Influence of analyses with constant seismic coefficient is best reflected by the distribution of induced plastic points over the dam section, which is quite unlikely in real earthquake conditions unless downstream and upstream slopes undergo liquefaction or piping (Fig. 9).

This time dependent variation of the motion along the dam section cannot be observed if pseudo-static and equivalent static methods are preferred over the time domain analyses. These methods assume that the seismic coefficient  $k$  affects all zones of the dam with a constant value. The safety of the downstream slopes that have same inclination and same height is found to be equal using these methods.



**Fig. 9** Distribution of plastic points over the dam section in FEM pseudo-static analysis

However, since the acceleration value increases gradually along the dam, slopes are exposed to higher accelerations towards the crest. In the middle of the uppermost slope, for instance, the peak acceleration rises to 0.76 g. This value remains above the critical acceleration calculated in the limit equilibrium analysis. If the actual acceleration records in this zone are used in Newmark sliding block analysis, the permanent displacement increases to 3 cm.

## 5 Conclusions

In this study, influence of three different analyses methods on dam response is studied under seismic loading conditions. In this respect a well-documented earth-fill dam in Arezzo, Italy, was chosen as a case study. The earthquake record used for time domain analysis was scaled to the level of an earthquake that could occur once in 1460 years in the area (OBE level) where the dam is located. According to the results of the analyses using a single earthquake motion, it can be said that the dam was not damaged during the earthquake, a statement well matches with the response of the dam in a country with high seismic activity. Pseudo-static analyses, on the other hand, yielded factor of safety values considerably smaller than those found in time domain analyses. One may note that the seismic coefficient applied was  $k = 0.21$ , which was in accordance with the expected operation based earthquake loading. Therefore, it may be concluded that more economic dam designs will be possible with time domain based nonlinear analyses helping to provide a sustainable environment for future generations provided that nonlinear material model parameters are determined correctly. Beneficial effects of nonlinear analyses in time domain will be better observed for maximum credible earthquake level motions (MCE). Besides, it should be noted that time domain approach would also enable to catch critical zones of the dam especially nearby the crest since amplification of the earthquake motion can be captured with this approach.

## References

1. Cetin K (2014) C.81 Dolgu barajlar için sismik tasarım ve performans kriterleri Seismic design and performance criteria for earthfill and rockfill dams
2. Clough RW, Chopra AK (1966) Earthquake stress analysis in earth dams Proceedings 92(EM2)
3. Seed HB (1979) Considerations in the earthquake-resistant design of earth and rockfill dams. Geotechnique 29(3):215–263
4. Lanzo G, Pagliaroli A, Scasserra G (2015) Selection of ground motion time histories for the nonlinear analysis of earth dams



# Laboratory Study on Stabilization of Dredged Soil by Sustainable Materials



Inci Develioglu and Hasan Firat Pulat

**Abstract** Considering the dredging activity in ports and channels, large amounts of sediment are generated as waste materials to be disposed of. The administration of such sediments is a major environmental problem for many countries worldwide. Environmental impacts caused by dredging, such as turbidity and disruption of the marine ecosystem, have increased the demand for the reuse of dredged soil in civil engineering applications. Typically, dredged soils have a low bearing capacity and low shear strength, hence the dredged soils should be strengthened up by solidification. Also, the dredged soils have organic matter, so they have high compressibility. This study aims to improve the compressibility behavior of dredged soil obtained from Izmir Bay in Turkey. Also, the effects of organic matter content (OM) on the geotechnical and compressibility properties of dredged soil were investigated. Different percentages of lime (L), thermal power plant fly ash (T), and silica fume (S), namely 5, 10, 15, and 20% were used using a dry mixing method to improve the compressibility behavior of dredged soil and then 1D consolidation tests were conducted with these samples. Also sieve analysis, consistency limit, specific gravity, pH determination, scanning electron microscope (SEM), Fourier transform infrared spectroscopy (FTIR) and 1D consolidation tests have been performed for dredged samples which have various OM (0, 4, 7, 11%). The test results have shown that change in the void ratio ( $\Delta e$ ), compression index, and liquid and plastic limit of natural samples increased with the OM increasing. For L additive samples, compression index ( $C_c$ ) and axial strain ( $\epsilon$ ) values decreased with the OM increasing but swelling index ( $C_s$ ) values decreased with the OM increasing for only 11% OM (11OM) samples. The T additive had a positive effect on the  $C_c$  and  $\epsilon$  values for all samples and  $C_s$  values for 7OM and 11OM samples. The S showed a positive effect of up to 10% for 11OM samples only. It was found to have a negative effect on all samples from 15% addition.

**Keywords** Compressibility · Dredged soil · Lime · Silica fume · Thermal power plant fly ash

---

I. Develioglu (✉) · H. F. Pulat  
Izmir Katip Celebi University, Izmir 35620, Turkey  
e-mail: [inci.develioglu@ikc.edu.tr](mailto:inci.develioglu@ikc.edu.tr)

## 1 Introduction

Advances in industry, urban planning, and tourism lead to the emergence of landmarks and skyscrapers. With the scarcity of land, the reclamation of land becomes increasingly important. Therefore, more land is needed to drive this development.

Dredging is the removal of sediment and debris from the bottom of rivers, harbors, lakes, and other bodies of water. Hundreds of millions of cubic meters of sediment are dredged every year to widen the river and harbor channels, facilitate access to ports and marinas, and control flooding [1–4]. The structural properties of the dredged material are related to current and past land use in the harbor basin and behave differently depending on time and place [5]. The dredged marine soils are reused as fill material, for the construction of roads and foundations, as building materials, and for the creation of wildlife habitats, as they are largely clean materials [6, 7]. It is known that these soils have high compressibility and low shear strength due to their organic matter content [8–10]. Therefore, the geotechnical properties and compressibility behavior of this dredged material should be studied in detail before using it in these areas.

Examining the literature, many studies have been conducted to determine the geotechnical index properties of dredged soils. Yu et al. [11] studied the physico-chemical properties of dredged soil treated with Class C self-cementing fly ash. The dredged material was from the port of Milwaukee, Wisconsin in the USA. Untreated samples were mixed with 10, 20, and 30% fly ash and the curing process was carried out for 2 h, 7 days, and 28 days. The unconfined compressive strength (UCS) values remained constant up to a fly ash content of 20% and then increased. The CBR values increased with increasing fly ash content and ranged from 1.5 to 20. The average UCS value was proportional to the fly ash content, and the increase in UCS value increased with increasing curing time. Anisuzzaman and Arifuzzaman [12] studied the geotechnical index properties, compressibility parameters, and shear strength properties of soft organic soils underlying dredged fill. The specific gravity ranged from 2.25 to 2.55, and the liquid limit and plasticity index ranged from 45 to 192% and from 18 to 63%, respectively. Organic matter content varied between 4.7 and 9.4%. According to USCS, the soil was classified as OH and OL. According to the test results, the ultimate strain and unconfined compressive strength (UCS) varied between 9 and 15% and 6 and 58 kPa, respectively. The initial void ratio ( $e_0$ ) and coefficient of primary strain ( $c_v$ ) ranged from 1.5 to 3.88, 0.20 to 10.89  $m^2/y$ , respectively. The compression index ( $C_c$ ) and recompression index ( $C_r$ ) varied between 0.44 and 1.25, 0.05 and 0.44, respectively.

It is well known that the OM of the dredged material has numerous effects on the geotechnical and strength parameters of the soil. Malasavage et al. [8] used steel slag fill (SSF) as a stabilization material. The excavated soil and SSF were mixed in the ratios of 80/20, 60/40, 50/50, 40/60, and 20/80, and laboratory tests were conducted. The plastic and liquid limits ranged from 37 to 49% and 74 to 140%, respectively. The clay content of the samples ranged from 21.7 to 98.8%. The internal friction angle of the natural dredged soil was 27.3°, which increased to a peak value of 45° when mixed 50/50.

The stabilization of dredged soils with various additives is also popular among researchers. Jaditager and Sivakugan [2] studied the sedimentation behavior of dredged mud from Townsville Harbor, Queensland, Australia. A fly ash-based geopolymer binder was used for stabilization. Tests were conducted with settling columns, and sedimentation was found to increase as the stabilization ratio of fly ash-based geopolymers increased. In addition, the results showed that there is no chemical reactivity between the fly ash-based geopolymer matrix and the dredged soil particles. Nguyen et al. [10] investigated the physical index properties of treated and untreated clayey dredged soil. Hydrated lime, quicklime, Class F fly ash, and Portland cement were used as additive materials. These additive materials were mixed with the dry soil sample at a ratio of 6, 12, 7.5, 6%, respectively. The Atterberg limits, UCS value, and optimum moisture content were determined for both the treated and untreated samples. According to the test results, the plasticity index, liquid limit, and optimum moisture content values decreased with the increase of quicklime, hydrated lime, and fly ash and the decrease of Portland cement. Quicklime was the additive that increased the optimum moisture content the most. UCS values also increased as the percentage of stabilizers increased. In other words, while Portland cement had the most positive effect on geotechnical properties, fly ash had the least effect.

In this study, the effect of OM on the physical index properties and compressibility behavior of dredged soil was examined. It was aimed to improve the compressibility parameters of the dredged soil material by using different additives (lime, silica fume, thermal power plant fly ash). Fourier transform infrared spectroscopy (FTIR) and Scanning electron microscope (SEM) and were used to investigate the internal structure of the dredged soil. Geotechnical characteristics were determined by laboratory tests such as specific gravity, sieve analysis, Atterberg limits, and pH tests. A one dimensional consolidation test was performed to obtain the compressibility parameters of natural and stabilized samples. The stabilizers were added at 5, 10, 15, and 20% of the dry weight of the soil sample.

## 2 Materials and Methods

### 2.1 Materials

The dredged material used in this study was from İzmir Bay (İzmir, Turkey). Mechanical and hydraulic systems were used in the dredging process. In the mechanical system, the dredged material is transported to the storage site by barges. In the hydraulic system, the dredged material is transported to the storage area by pipes as a slurry solution. The excess water of the dredged material was drained and transported in sealed boxes from the storage area to the Soil Mechanics Laboratory of Katip Çelebi University in İzmir. To improve the geotechnical properties and

compressibility behavior of the dredged material, lime (L), thermal power plant fly ash (T), and silica fume (S) were used as additives. The specific gravities of L, T, and S are 2.48, 2.66, and 2.21, respectively.

## 2.2 Methods

The OM of dredged soil was determined by ignition at 440° C in a furnace according to ASTM D2974 [13]. First, the natural OM was determined (11%), then samples were fired at 440° C for predefined times (1440, 70, and 20 min) to obtain different OM samples (0, 4, 7, and 11%) (Fig. 1).

The specific gravity of the samples was determined according to ASTM D854 using the pycnometer method [14]. The pH values of the samples were determined using a digital pH meter. The suspension was prepared by mixing 50 g of sample and 125 ml of distilled water. The pH measurement was performed 24 h after preparation [15]. Particle size distributions for four dredged material samples with different OM were determined by wet sieve analysis according to ASTM D422 and ASTM D6913 [16, 17]. The liquid limit was determined using the falling cone method [18]. The

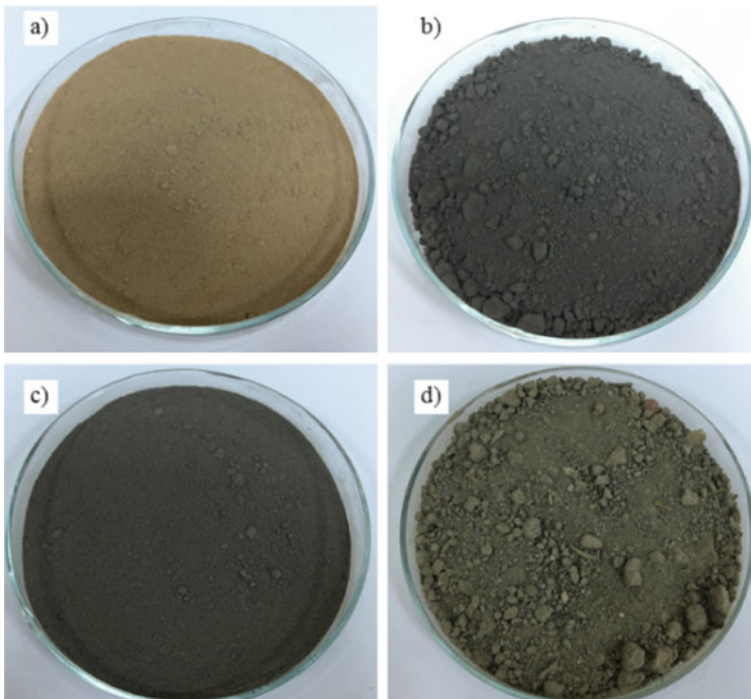


**Fig. 1** Dredged soil samples **a** 0% OM, **b** 4% OM, **c** 7% OM, **d** 11% OM

plastic limit test was performed according to ASTM D4318 [19]. The dredged soil samples were classified using Atterberg limits and particle size analyses according to ASTM D2487 [20].

The SEM analysis was performed to determine the internal structure of the dredged soil sieved from No. 40 (0.425 mm). The analysis was performed at the Central Research Laboratory of İzmir Katip Celebi University. Since the sample is not a conductive material, it tends to become charged during scanning, so it is coated with gold, a conductive material, at a thickness of 5 nm. Then the sample holder was placed and analyzed using the Sigma 300 VP model from Zeiss. In this analysis, both microscopic image scanning and elemental analysis were performed.

FTIR analysis was performed to obtain a characterization of the molecular bonds of natural and stabilized samples in the mid-infrared region ( $4000\text{--}400\text{ cm}^{-1}$ ). The analysis was performed at the Central Research Laboratory of Katip Celebi University, Izmir, passing the dry sample over a No. 40 sieve (0.425 mm). The sample was placed on the sample plate and the head was brought into contact with the sample. After that, the analysis was performed using the Thermo iS50 FT-IR model instrument.

The 1D consolidation test was performed to determine the compressibility parameters of the dredged soil according to ASTM D2435 [21]. Each sample was prepared at its liquid limit to obtain uniform samples. The seating pressure of 5 kPa was applied before starting the test. The specimen was loaded with vertical stresses of 24.5, 49, 98, 196, 392, and 784 kPa. Subsequently, the same specimen was relieved of 196 and 49 kPa vertical stresses to determine swelling behavior. The consolidation experiments were repeated twice for each specimen to check repeatability.

Following the consolidation experiments with natural samples, consolidation experiments were performed with additional samples (L, T, S). The excavated soil material was mixed at 5, 10, 15, and 20% (dry weight of additive relative to the dry weight of excavated soil material) for a one-dimensional consolidation test. The samples were again prepared at their liquid limits. The samples, mixing ratios, and abbreviations are listed in Table 1.

### 3 Results and Discussion

#### 3.1 Geotechnical Properties of Natural Dredged Samples

The grain size distributions of dredged materials having different OM are shown in Fig. 2. The grain size distributions of all samples were obtained as very similar to each other. It was also observed that more than half of the sample fell through sieve No. 200.

The relation between OM and  $G_s$  obtained from the literature and present studies has been shown in Fig. 3. As a result of the specific gravity tests, it was determined that as the amount of OM increased, the specific gravity decreased. The reason for

**Table 1** Samples, abbreviations, and mixture ratios

Dredged soil	Additive content (%)			
	Lime			
	5	10	15	20
0% OM	0OM5L	0OM10L	0OM15L	0OM20L
4% OM	4OM5L	4OM10L	4OM15L	4OM20L
7% OM	7OM5L	7OM10L	7OM15L	7OM20L
11% OM	11OM5L	11OM10L	11OM15L	11OM20L
<i>Thermal power plant fly ash</i>				
0% OM	0OM5T	0OM10T	0OM15T	0OM20T
4% OM	4OM5T	4OM10T	4OM15T	4OM20T
7% OM	7OM5T	7OM10T	7OM15T	7OM20T
11% OM	11OM5T	11OM10T	11OM15T	11OM20T
<i>Silica fume</i>				
0% OM	0OM5S	0OM10S	0OM15S	0OM20S
4% OM	4OM5S	4OM10S	4OM15S	4OM20S
7% OM	7OM5S	7OM10S	7OM15S	7OM20S
11% OM	11OM5S	11OM10S	11OM15S	11OM20S

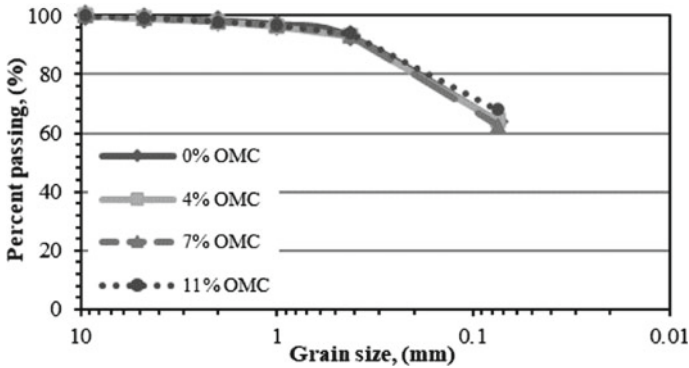


**Fig. 2** Particle size distributions of dredged soil

this situation is that the carbon content increases with the increase in OM, thus weakening the internal structure [8, 22–25].

The Atterberg limits indicate the moisture content at the transition from solid to plastic and liquid consistency. Clay type and content, type of exchangeable cations, and OM affect the consistency limits. OM can affect the consistency limits differently; the plastic limit is reduced by the oxidation of organics with hydrogen peroxide. In addition, organics have a high adsorption capacity for water. After the hydration of the organic matter is complete, sufficient water can wrap around the mineral particles

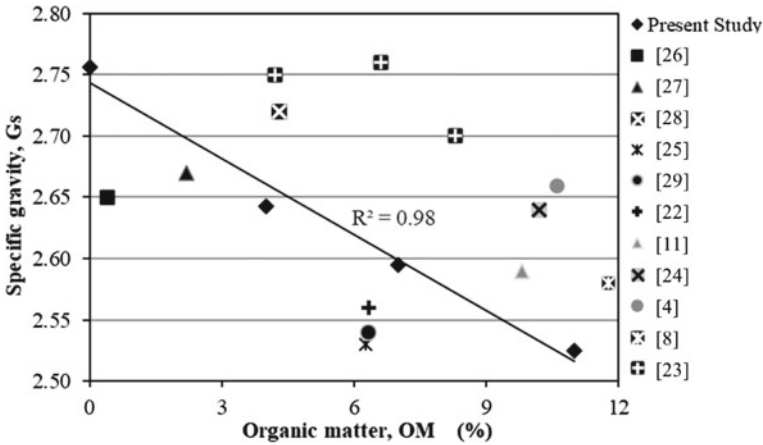


Fig. 3 The relation between Gs and OM

like a film. Figure 4 shows that the values of LL and PL generally increase with an increase in OM. The liquid limit values range from 33 to 40, and the plastic limit values range from 26 to 31. Similar results can also be found in the literature [9, 26].

Soil pH varies depending on many parameters such as mineral content, soil texture, climate, vegetation, and pore water chemistry. Organic material increases alkalinity and counteracts acidity. The pH values of the dredged soil material ranged from 7.2 to 8.9 and ranged from slightly alkaline (7–8) to moderately alkaline (8–9). The dredged soil samples were classified as OL (organic soil with low plasticity) based on the particle size distribution curve and consistency limits according to USCS.

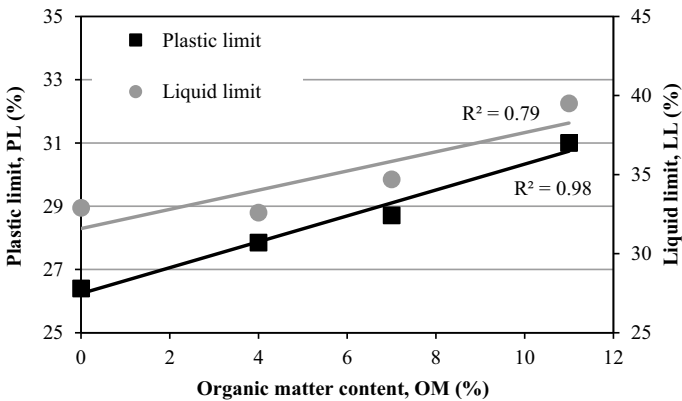


Fig. 4 The relations between LL, PL, and OM

### 3.2 The Internal Structure of Natural Dredged Samples

The dredged material contains slender particles such as twigs, bones, and algae that are much larger than the other two dimensions and were observed in the SEM analysis. However, the two dimensional sieve analysis was insufficient for the size distribution of the dredged soil. For this reason, the sieve analysis was supplemented by the SEM analysis. SEM Analyzes were performed with 0OM and 11OM samples to see in detail the OM effect on particle size. The result of the SEM analysis is shown in Fig. 4. While the naturally dredged sample contains organic materials (Fig. 5b), there are no organic materials in the 0OM sample (Fig. 5a).

Typical FTIR spectra from FTIR analysis are shown in Fig. 6 for samples 0OM, 11OM, 0OM10T, 4OM5S, and 7OM15L.

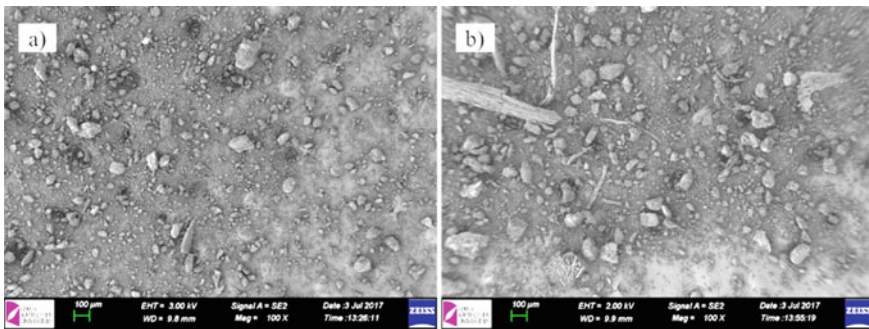


Fig. 5 SEM analysis of a) 0OM sample, b) 11OM sample [27]

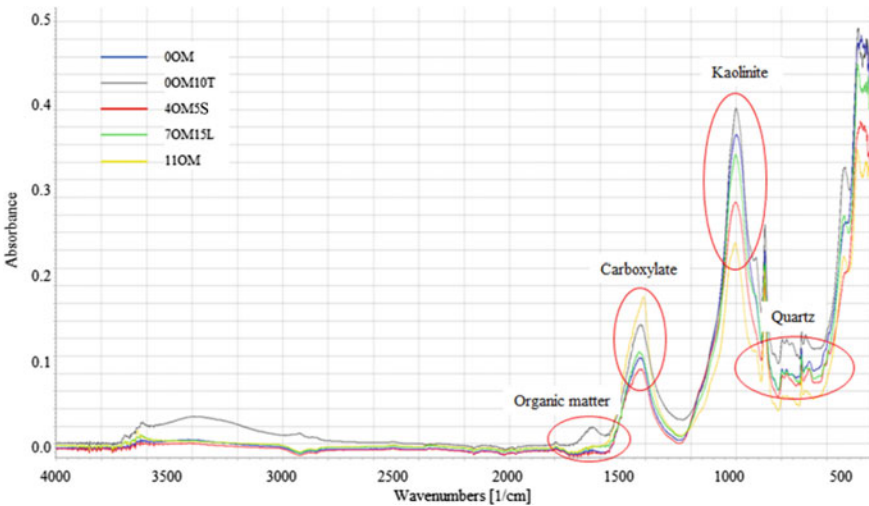


Fig. 6 FTIR spectra of samples



Although soil is a very complex and variable material, the situation is even more complex when it also contains organic matter. As can be seen in Fig. 6, the spectra of all samples are quite similar.

### 3.3 Compressibility Behavior of Dredged Samples

#### Compressibility Behavior of Natural Dredged Samples

The curves of void ratio ( $e$ ) and effective vertical stress ( $\sigma'_v$ ) are shown in Fig. 7. The largest change in void content ( $\Delta e = e_0 - e_1$ ) was observed for the 11OM sample ( $\Delta e_{11OM} = 0.38$ ). The change in void ratio was proportional to OM ( $\Delta e_{7OM} = 0.23$ ,  $\Delta e_{4OM} = 0.20$ ,  $\Delta e_{0OM} = 0.11$ ).

It was found that the ignited soil samples (0OM, 4OM, 7OM) did not have a breakpoint (the point at which the slope of the curve rises sharply) on the  $e-\sigma'_v$  curve, while the natural dredged material (11OM) had a breakpoint. The steepest slope of the swelling curve and the maximum swelling potential belong to a natural soil sample with the highest OM.

The relation between the compression index ( $C_c$ ), swelling index ( $C_s$ ), and OM from the consolidation test is shown in Fig. 8.

The results show that with the increase in OM, there is an increase in  $C_c$  and  $C_s$ . The consolidation test assumes that the volume of soil particles remains constant, so the change in total volume is due to the change in water volume. The adsorbed

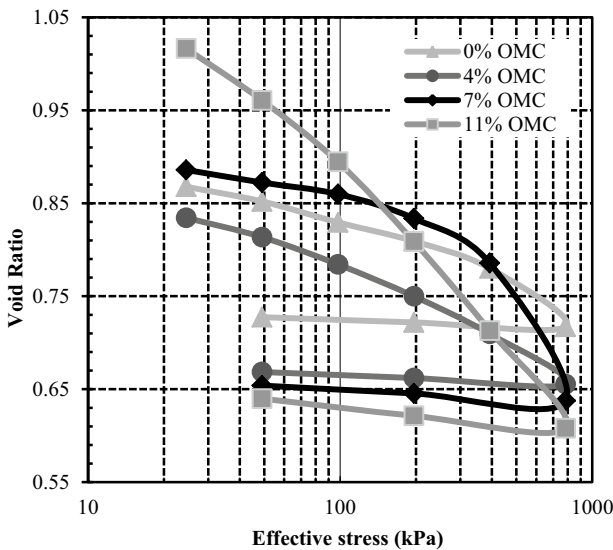
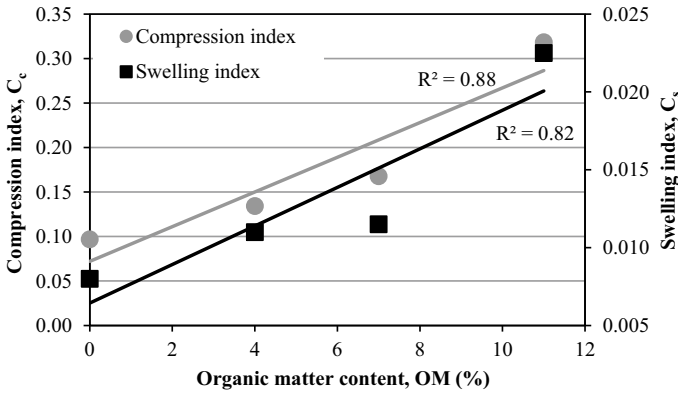


Fig. 7 Void ratio ( $e$ )—effective vertical stress ( $\sigma'_v$ )



**Fig. 8** The relation between  $C_c$ ,  $C_s$ , and OM

water surrounded the organic matter and dewatered with the increased normal stress, so a crucial axial deformation was observed. In addition, organic matter is more deformable compared to solid particles and has a higher pore fraction. Therefore, as the amount of organic matter increases, the change in pore fraction also increases. The correlation shows that the  $R^2$  values are 0.88 and 0.82, respectively.

**Compressibility Behavior of Lime Added Dredged Samples**

The relation between compression index ( $C_c$ ) and lime content is shown in Fig. 9.

$C_c$  values tend to decrease with increasing lime content and range from 0.043 to 0.247 for all samples. The strongest effect was observed in the natural dredge sample (11OM), which had the highest water and organic matter content.

**Fig. 9** The relation between  $C_c$  and lime content

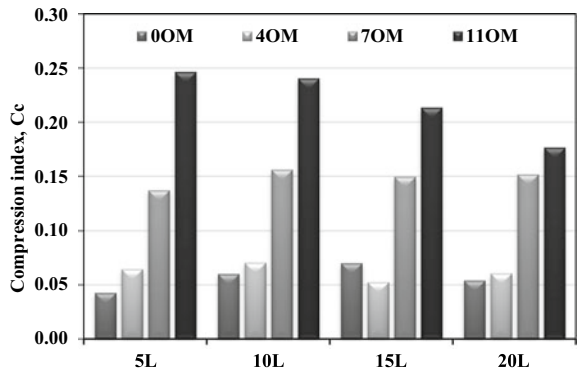
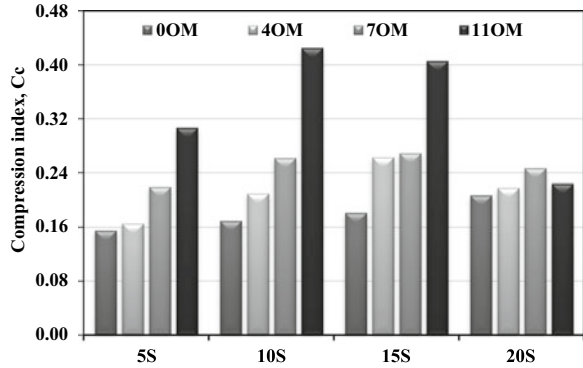


**Fig. 10** The relation between  $C_c$  and silica fume content



**Compressibility Behavior of Silica Fume Added Dredged Samples**

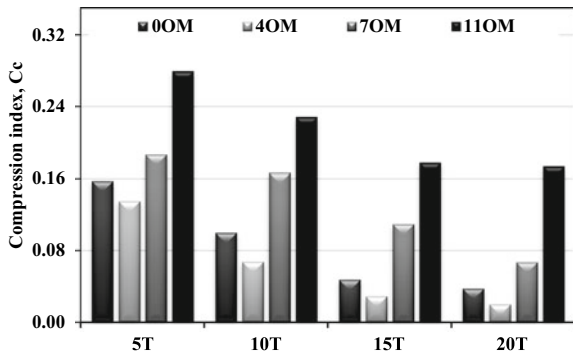
The diagram showing the change in compression index as a function of silica fume content is shown in Fig. 10 for all samples. The  $C_c$  values were proportional to the S content except for 11OM samples and had values between 0.156 and 0.426.

**Compressibility Behavior of Thermal Power Plant Fly Ash Added Dredged Samples**

The relation between compression index ( $C_c$ ) and thermal power plant fly ash content has shown in Fig. 11.

It can be observed that the value of  $C_c$  decreases with increasing T. Fly ash is a very fine-grained, spongy-textured, porous, and non-porous particle. As a result of the consolidation test, it was calculated that the porosity of the mixed samples was higher than that of the natural dredged samples. The adsorbed water was divided between the organic materials and the fly ash of the thermal power plant so that the density increased, and the plasticity decreased. For this reason, lower vertical deformations and changes in the void ratio were observed as the amount of additive increased. The  $C_c$  values ranged from 0.021 to 0.318 for all samples.

**Fig. 11** The relation between  $C_c$  and thermal power plant fly ash content



## 4 Conclusion

In this study, the physical index properties, and compressibility behavior of dredged material from İzmir Bay were examined under different conditions. Firstly, the effect of OM on geotechnical properties and compressibility behavior of dredged soil was investigated. Secondly, the effect of L, S, and T on the compressibility behavior of the dredged soil was determined.

For natural samples:

- Atterberg limit values increase with the increase of OM by 20% and 17.4%, respectively.
- Specific gravity increases by 9.1% as OM decreases.
- The maximum change in the void ratio ( $\Delta e = e_0 - e_1$ ) is observed for the sample with the highest OM ( $\Delta e_{11OM} = 0.38$ ). As OM decreases, the difference in void ratio also decreases.
- The compression indices of the dredged material range from 0.32 to 0.10. The compression index increases with the increase of OM.

For samples stabilized with lime:

- The addition of lime has a positive effect on the compression resistance.
- $C_c$  values tend to decrease as lime content increases.
- Lime additions of 5–10% have more effective compressibility performance than 15–20%.

For samples stabilized with silica fume:

- Stabilization with silica fume had a negative impact on the compressibility performance of the dredged soil.
- The values of the compression index were proportional to the silica fume content, except for sample 11OM.
- According to these results, this type of stabilizer is not suitable to improve the compressibility behavior of dredged material for samples 0OM, 4OM, and 7OM, but it is suitable for sample 11OM.

For samples stabilized with thermal power plant fly ash:

- The  $C_c$  values decrease with an increasing proportion of thermal power plant fly ash.
- No significant effect is observed when 5% thermal power plant ash is added.
- The minimum elongation value is generally reached at an additive content of 20% for each sample.

## References

1. Rezik B, Boutouil M (2009) Geotechnical properties of dredged marine sediments treated at high water/cement ratio. *Geo-Marine Lett* 29:171–179
2. Jaditager M, Sivakugan N (2017) Influence of fly ash-based geopolymer binder on the sedimentation behaviour of dredged mud. *J Waterw Port Coast Ocean Eng* 143(5):1–9
3. Shahri Z, Chan CM (2015) On the characterization of dredged marine soils from Malaysian waters: physical properties. *Environ Pollut* 4:1–9
4. Kalianan S, Chan C (2017) 1-D compressibility parameters of lightly solidified dredged marine soil (DMS) using cement, GGBS and coarse sand. *Int J GEOMATE* 12:167–171
5. Pebbles V, Throp S (2001) Waste to resource: beneficial use of great lakes dredged material. Great Lake Commiss
6. Limeria J, Agullo L, Etxeberria M (2010) Dredged marine sand as construction material. *Journées Nationales Genie Cotier–Genie Civil. Les Sables d’Olonne, France, 22–25 June*
7. Ganesalingam D, Arulrajah A, Ameratunga J, Boyle P, Sivakugan N (2011) Geotechnical properties of reconstituted dredged mud. In: *Proceeding from the Pan-AM CGS geotechnical conference*. Toronto, Canada, pp 1–7
8. Malasavage NE, Jagupilla S, Grubb DG, Wazne M, Coon WP (2012) Geotechnical performance of dredged material – steel slag fines blends: laboratory and field evaluation. *J Geotech Geoenviron Eng* 8:981–991
9. Thiyyakkandi S, Annex S (2011) Effect of organic content on geotechnical properties of Kuttanan clay. *Electron J Geotech Eng* 16:1653–1663
10. Nguyen T, Janik LJ, Raupach M (1991) Diffuse reflectance infrared Fourier transform (DRIFT) spectroscopy in soil studies. *Soil Res* 29(1):49–67
11. Yu H, Yin J, Soleimanbeigi A, Likos WJ (2017) Effects of curing time and fly ash content on properties of stabilized dredged material. *J Mater Civ Eng* 29(10):1–11
12. Anisuzzaman M, Arifuzzaman M (2013) Engineering properties of soft organic soil underlying dredge fill areas of Dhaka, Bangladesh. In: *International conference on transport, environment and civil engineering*. Phnom Penh, Cambodia, 25–26 Sept
13. ASTM D2974-14 (2014) Standard test methods for moisture, ash, and organic matter of peat and other organic soils, ASTM International, West Conshohocken, PA. [www.astm.org](http://www.astm.org)
14. ASTM D854-14 (2014) Standard test methods for specific gravity of soil solids by water pycnometer, ASTM International, West Conshohocken, PA. [www.astm.org](http://www.astm.org)
15. Kocasoy G (1994) Atıksu arıtma çamuru ve katı atık ve kompost örneklerinin analiz yöntemleri. ISBN-13: 978-975-518-083-0, ISBN: 975-518-083-4
16. ASTM D422-63e2 (2007) Standard test method for particle-size analysis of soils (Withdrawn 2016), ASTM International, West Conshohocken, PA. [www.astm.org](http://www.astm.org)
17. ASTM D6913-04e1 (2009) Standard test methods for particle-size distribution (Gradation) of soils using sieve analysis, ASTM International, West Conshohocken, PA. [www.astm.org](http://www.astm.org)
18. British Standard Institution BS 1377-1 (2016) Methods of test for soils for civil engineering purposes, London
19. ASTM D4318-10e1 (2010) Standard test methods for liquid limit, plastic limit, and plasticity index of soils, ASTM International, West Conshohocken, PA. [www.astm.org](http://www.astm.org)
20. ASTM D2487-11 (2011) Standard practice for classification of soils for engineering purposes (Unified Soil Classification System), ASTM International, West Conshohocken, PA. [www.astm.org](http://www.astm.org)
21. ASTM D2435/D2435M-11 (2011) Standard test methods for one-dimensional consolidation properties of soils using incremental loading, ASTM International, West Conshohocken, PA. [www.astm.org](http://www.astm.org)
22. Chan C (2016) Geo-parametric study of dredged marine clay with solidification for potential reuse as good engineering soil. *Environ Earth Sci* 75:941–955
23. Kang G, Tsuchida T, Athapaththu AMRG (2016) Engineering behaviour of cement-treated marine dredged clay during early and later stages of curing. *Eng Geol* 209:163–174

24. Kang G, Tsuchida T, Kim Y (2017) Strength and stiffness of cement-treated marine dredged clay at various curing stages. *Constr Build Mater* 132:71–84
25. Wang D, Abriak NE, Zentar R (2015) One-dimensional consolidation of lime-treated dredged harbour sediments. *Euro J Environ Civil Eng* 19:199–218
26. Develioglu I, Pulat HF (2017) Geotechnical properties and compressibility behavior of organic dredged soils. In: *Proceedings 19th international conference on earthquake geotechnical engineering*, pp 194–198
27. Develioglu I, Pulat HF (2019) Compressibility behaviour of natural and stabilized dredged soils in different organic matter contents. *Constr Build Mater* 228:1–11

# Particle Size Distribution of Finer Soil Particles Using Microscopic Image Analysis



Pranjal Mandhaniya , Dhairya Singh Arya, and J. T. Shahu

**Abstract** Particle size distribution of soil is the most basic geotechnical property of soil which affects its overall behavior. Determinations of particle sizes of soil can be done by sieving but particles smaller than 75 microns (clay and silt) are analyzed by hydrometer or pipette analysis. Smaller particles of soil are flakier due to clay minerals present in it. This makes the use of sieve analysis uneasy. Hydrometer analysis uses the principle of settlement of a spherical particle in a viscous fluid. The density of a soil–water suspension is measured with time to calculate the particle sizes of finer particles. The experiment time for hydrometer analysis can vary from a day to a week. There are very high chances of error from the human side as well as changes in laboratory conditions. There is a demand for newer testing methods for fine soil particle size determination. X-rays and lasers can be used and were used by researchers to determine the particle size of finer soil spectrum. In the present study, a microscopic image analysis-based approach is used for the PSD of finer soil. Soil samples from the pan for sieve analysis (soil particles smaller than 75 microns) are sprayed into a glass slide of standard dimensions and the images of the slide are extracted under a standard microscope. These images are then analyzed to find the particle size using image processing. Particle size and its occurrence are recorded in a data table which is used to plot a standard PSD curve. The results are compared to the standard hydrometer analysis results. The study shows that microscopic image analysis can provide a good alternative to hydrometer analysis for soil particle size analysis.

**Keywords** Particle size distribution · Hydrometer analysis · Microscopic image analysis · Image processing · Geotechnical testing

---

P. Mandhaniya (✉) · J. T. Shahu  
Department of Civil Engineering, IIT Delhi, Delhi 110016, India  
e-mail: [pranjalmandhaniya@gmail.com](mailto:pranjalmandhaniya@gmail.com)

D. S. Arya  
CSIR-Central Scientific Instruments Organisation, Chandigarh 160030, India

## 1 Introduction

The particle size distribution of soil is intrinsic to its classification. Gradation of soil is necessary to define its geotechnical properties and receptive tests to be performed on it. Getting to know what a soil sample consists of will give a general estimate of its strength. Coarse grain (4.75 mm–75 microns) distribution of a soil sample can be acquired by sieve analysis. However, the soil particles under 75 microns can not be sieved as the loss of material and too much retention of particles on sieves gives out erroneous results. Thus, hydrometer analysis is performed on the finer particles which are based on Stoke's Law. Hydrometer analysis considers two major assumptions.

1. The disturbance due to inter-particle interference and wall boundary of the sedimentation vessel is negligible.
2. The particles are settling under a laminar flow regime.
3. Settling particles are smooth spheres.

As discussed in Lu et al. [1], the first assumption is valid as the soil sample of 50 g is small enough for negligible interaction between particles and vessel walls. The second assumption is also fine as the fine particles do not cause flow with higher Reynolds numbers. However, the third assumption is criticized by Parslow and Jennings [2], who used a Sedigraph 5000 to analyze the PSD of anisodiametric particles. A Sedigraph employs X-ray absorption and laser diffraction to acquire the particle size distribution. They stated that smaller particles of the soil generally contain clay minerals that are flaky in shape; thus, assuming a spherical form will be a great deviation. This criticism of hydrometer analysis can be seen in the works of Vitton et al. [3] and Chaney et al. [4], who compared the sedigraph results of a soil suspension with the hydrometer results. Wen et al. [5] also compared the hydrometer results from laser diffraction analysis on a soil suspension. Ghasemy et al. [6] compared the hydrometer results of soil samples with that of spectrophotometry analysis on a soil suspension. However, the Brownian motion of particles in a soil suspension will cause some variability in laser and X-ray outputs. The particles in suspension will settle by facing their smaller dimension downwards which will maximize the kinetic energy. Thus, the larger dimension of a flaky particle will be hard to determine using this method. Several modern developments suggest that an alternative and more accurate method can be used to replace the hydrometer method. Raschke and Hryciw [7] applied a computer vision technique to obtain the particle size distribution of dry soil samples. Sudarsan et al. [8] analyzed the PSD of dry soil samples from large agricultural fields using wavelet analysis of microscopic images. Deguchi [9] proposed a new technique for high-speed image processing of 2D images of multiple particles of different sizes.

It can be seen in the literature that particle size analysis on dry samples without soil suspension is more advantageous as it reduces the error due to Brownian motion and coagulation. Further, the assumption of spherical shape can be ignored as irregular images can be obtained in a two-dimensional plane. Thus, in the present study, a dry soil sample was used for the image analysis under a microscope.



## 2 Materials and Method

The hydrometer and microscopic method outputs of four soil samples were compared. The first sample was obtained from a local site at Ankleshwar, Gujrat. This sample was named Ankleshwar soil. However, the soil was identified as red lateritic soil. The second sample was collected locally in the IIT Delhi campus and named Delhi silt based on its origin. The third sample was obtained from north-western India; thus, named Dhanaury clay. The fourth sample was industrial Kaolinite. The raw images of these four soil samples are shown in Fig. 1. The hydrometer test and microscopic analysis were performed on particles smaller than 75 microns, which are retained after sieve analysis from all four samples.

The microscopic images were acquired by spreading the soil particles over a glass slide and placing the images under a microscope. Zeiss Primotech microscope was used at 10X for acquiring the images. The soil spread glass slide is manually moved randomly to add variability in image acquisition.

These images were then analyzed using a MATLAB program to get the dimensions of the captured particles. This data is then plotted as a histogram and merged compared with the output of performed hydrometer data. Scanning electron microscope imaging was also performed to verify the relative particle sizes of soil samples. Further X-ray diffraction was performed to check the rough elemental structure of soil samples. The whole process of data acquisition and analysis is outlined in Fig. 2.



**Fig. 1** Images of soil samples

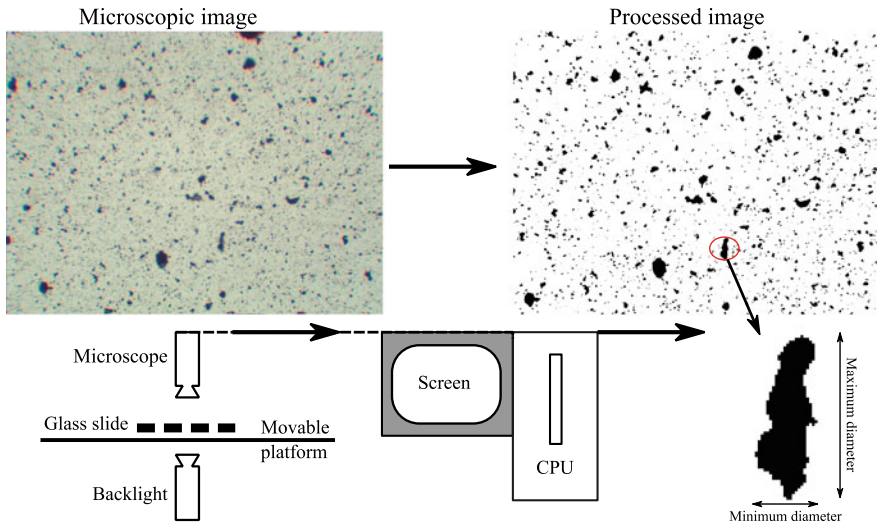


**Fig. 2** Image acquisition and analysis

### 3 Results and Discussion

The output of the hydrometer and the microscopic image analysis is trimmed to cover the particle size between 1 and 7 microns. It was seen in the experimentation that larger particles do not stick properly to the glass slide; thus, the range limitation was applied. The maximum and minimum diameter of each particle captured in images is recorded and the mean of these two values is calculated. This mean is plotted as a cumulative histogram and compared with the results of hydrometer analysis as shown in Fig. 3.

It can be seen in the plots that the microscopic image analysis slightly overestimates the overall particle size distribution. However, it is also visible that the gap between the two datasets is almost constant. Figure 4 shows the images of soil samples taken under a scanning electron microscope. All images were taken at 500X resolution except Delhi silt (350X).

Kaolinite and Dhanaury clay samples contain finer particles as compared to the Ankleshwar soil and Delhi silt. Further, X-ray diffraction analysis was done to carefully look at the elemental structure of these four soil samples. The results of which are given in Table 1.

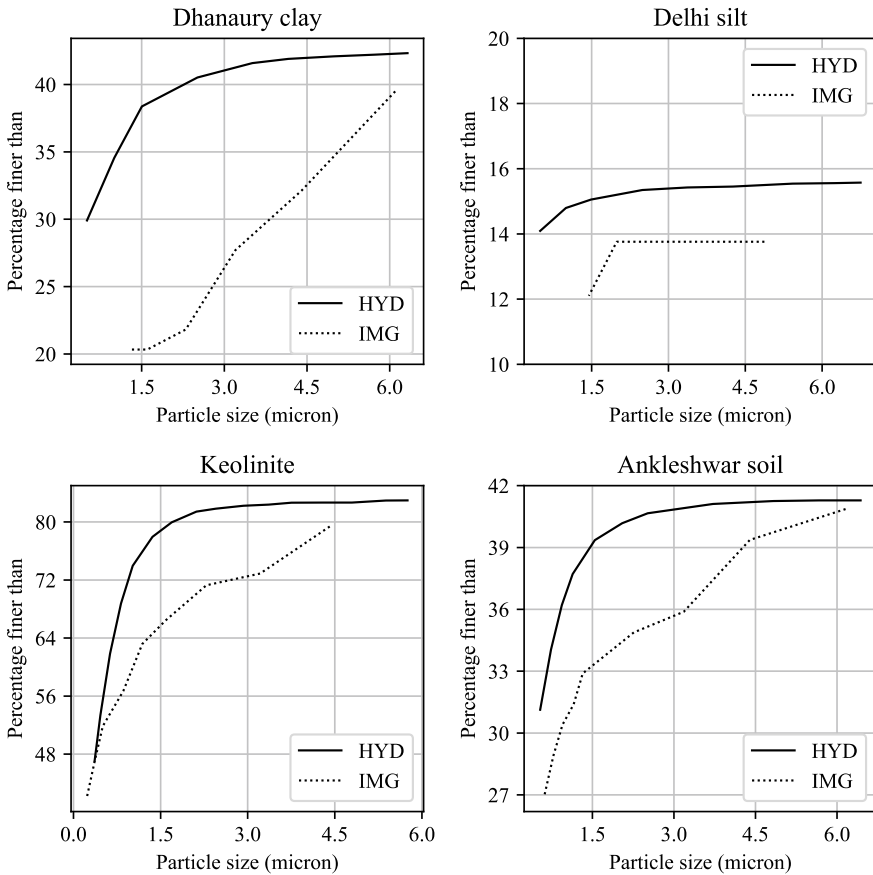


Fig. 3 PSD comparison of hydrometer and microscopic image analysis

### 4 Conclusions

The main objective of the present study is to show that microscopic image analysis can be useful for obtaining the particle size distribution of soil samples. Taking hydrometer results as the reference, image analysis for particle sizes lower than 5 microns shows the least error. Based on XRD analysis and soil colors, it can be said that the color of the soil sample generally goes lighter as the count of finer particles increases. However, the count of finer particles is independent of any element abundance in any soil sample. Kaolinite is hydrous Aluminum Silicate but the elemental composition of Dhanaury clay is similar to Ankleshwar soil and Delhi silt. However, the particle size of kaolinite and Dhanaury clay are very similar.

From this study, it can be concluded that a handheld electronic device can modeled for soil PSD, which can perform in situ drying and sieving. Further, the device can

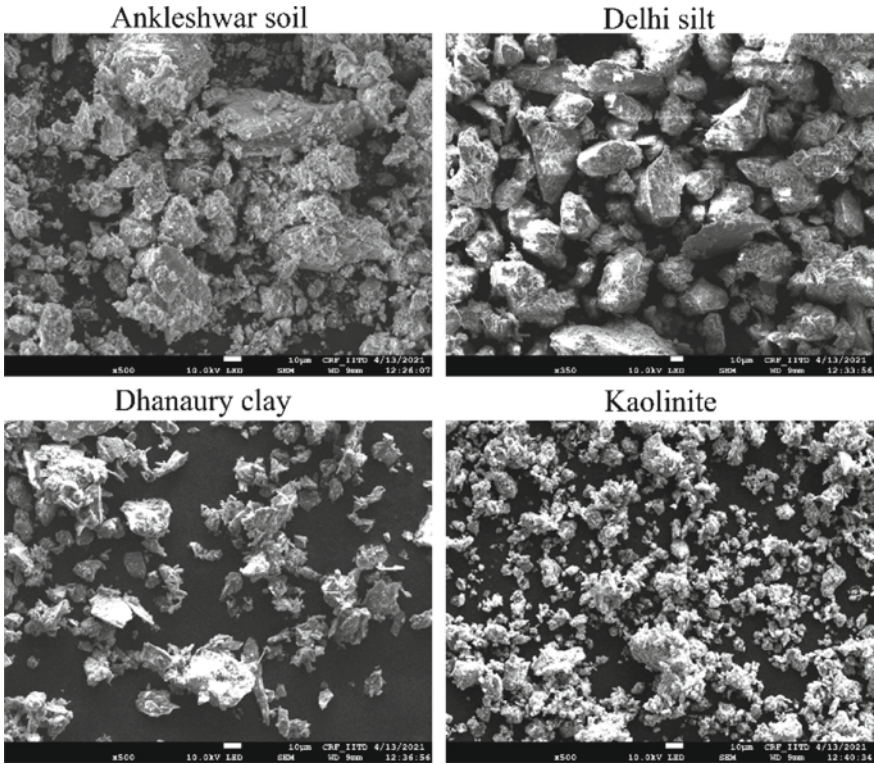


Fig. 4 SEM images of soil samples

Table 1 XRD Data of soil samples

Sample	Al	Si	Ca	Fe
Ankleshwar soil	14.16	18.75	0.39	10.18
Delhi silt	8.96	22.24	5.57	8.72
Dhanaury clay	8.90	23.77	1.57	10.72
Kaolinite	8.43	8.91	0.14	0.65

be equipped with a small microscope with a randomisation mechanism to perform image analysis to get the particle size distribution of soil samples.

## References

1. Lu N, Ristow GH, Likos WJ (2000) The accuracy of hydrometer analysis for fine-grained clay particles. *Geotech Test J* 23:487–495. <https://doi.org/10.1520/gtj11069j>

2. Parslow K, Jennings BR (1986) Simultaneous size and thickness measurements for heterogeneous micrometre-sized particles. *J Phys D Appl Phys* 19:1233–1243. <https://doi.org/10.1088/0022-3727/19/7/013>
3. Vitton SJ, Nesbitt CC, Sadler LY (1997) Soil particle size analysis using X-ray absorption. *Transp Res Rec* 1548:51–59. <https://doi.org/10.1177/0361198196154800108>
4. Chaney R, Demars K, Vitton S, Sadler L (1997) Particle-size analysis of soils using laser light scattering and X-ray absorption technology. *Geotech Test J* 20:63. <https://doi.org/10.1520/gtj11421j>
5. Wen B, Aydin A, Duzgoren-Aydin NS (2002) A comparative study of particle size analyses by sieve-hydrometer and laser diffraction methods. *Geotech Test J* 25:434–442. <https://doi.org/10.1520/gtj11289j>
6. Ghasemy A, Rahimi E, Malekzadeh A (2019) Introduction of a new method for determining the particle-size distribution of fine-grained soils. *Measur J Int Measur Confederation* 132:79–86 (2019). <https://doi.org/10.1016/j.measurement.2018.09.041>
7. Raschke SA, Hryciw RD (1997) Grain-size distribution of granular soils by computer vision. *Geotech Test J* 20:433–442. <https://doi.org/10.1520/gtj10410j>
8. Sudarsan B, Ji W, Adamchuk V, Biswas A (2018) Characterizing soil particle sizes using wavelet analysis of microscope images. *Comput Electron Agric* 148:217–225. <https://doi.org/10.1016/j.compag.2018.03.019>
9. Deguchi K (1986) An image processing technique for high-speed measurement of particle-size distributions. *Measurement* 4:128–133. [https://doi.org/10.1016/0263-2241\(86\)90003-5](https://doi.org/10.1016/0263-2241(86)90003-5)

# Temperature Effect on the Shear Strength Behavior of Fiberglass Added Sand-Bentonite Mixtures



Esra Güneri  and Yeliz Yukselen-Aksoy 

**Abstract** The behavior of soils under high temperature is very important. Previous studies have revealed that engineering properties of soils change depending on temperature. For instance, increase in temperature generally increases volumetric deformation and hydraulic conductivity of soils. In this study, in order to stabilize these changes and optimize engineering properties of buffer soils, fiberglass additives were added to the sand-bentonite mixtures and shear strength behavior under room and high temperatures was investigated. Fiberglass is widely used in the construction industry and many other industries for thermal insulation purposes. The test results showed that the shear strength of fiberglass added sand-bentonite mixtures changed negligibly under high temperature compared with under room temperature.

**Keywords** Fiberglass · Sand-bentonite mixtures · Shear strength

## 1 Introduction

Considering the cost of fossil fuels and the harmful effects on the environment, the need for sustainable energy sources is increasing. Accordingly, an increase is observed in the number of energy geo-structures. The main energy structures that cause temperature changes on the soils are heat piles, buried power cables, solid waste and nuclear waste storage areas, geothermal energy facilities.

Many studies investigated the thermal behavior of soils and reported that the volumetric deformation behavior of soils, shear strength, hydraulic conductivity and the structure of soils change depending on temperature. Laloui investigated that the temperature affects the thermal hardening and temperature differences affect the shear strength of the samples by changing the internal friction angle [1]. Cekerevac

---

E. Güneri (✉)

Dokuz Eylül University the Graduate School of Natural and Applied Sciences, Izmir, Turkey  
e-mail: [esra\\_cetinorgu@hotmail.com](mailto:esra_cetinorgu@hotmail.com)

Y. Yukselen-Aksoy

Department of Civil Engineering, Dokuz Eylül University, Izmir, Turkey

and Laloui reached a higher shear strength value with the triaxial test performed under high temperature using kaolin [2]. On the other hand, Hueckel and Baldi observed decrease in strength when the temperature was increased from 18° to 115 °C with Pontida clay [3].

The literature studies show that bentonite or sand-bentonite mixtures are used as buffer material around energy geo-structures [4]. The high impermeability of bentonite, and the shrinkage-limiting effect of sand-bentonite mixtures compared to bentonite are some of the reasons for using these materials as buffers. Fiberglass is a SiO<sub>2</sub>-based material, which is frequently used for insulation in the construction industry, and is formed by melting glass at high temperatures and has many types [5]. Guo et al., determined with XRD analyses that fiberglass includes alumina in the structure [6]. Also, fiberglass mainly contains silica. The superior properties of fiber glass under high temperatures may contribute to the performance of buffer material under high temperatures. In the present study, fiberglass added sand-bentonite mixtures were used as a candidate buffer material for energy geo-structures. Within the scope of this study, direct shear tests of fiberglass added sand-bentonite mixtures under room and high temperatures were conducted.

## 2 Materials and Methods

### 2.1 Material Characterization

In this study, the fiber glass was added to sand-bentonite mixtures in two different proportions. Fiberglass additive was obtained from a local supplier (Fig. 1). Bentonite was supplied from the local supplier and sodium bentonite was used in the tests. The physico-chemical properties of materials used in the study are shown in Table 1. When naming mixtures, it is briefly denoted by fiberglass “FG”, sand “S” and bentonite “B”. Sand and bentonite were used after drying in the oven at 105 °C.

As a buffer material the additive free and 30% bentonite + 70% sand mixtures were used. Fiberglass additive rates were chosen as 1.0 and 0.5%. In the mixtures, the additive was first weighed and then 30% of the remaining weight was added as bentonite and the remaining amount was added as sand amount to the mixture.

### 2.2 Methods

In this study, Standard Proctor test of 30B-70S mixtures was performed according to ASTM D698-12 [7] and maximum dry unit weight value was determined as 14.6 kN/m<sup>3</sup> and optimum water content was 22.5%. Since the fiberglass additive ratios were very low, the effect of fiber glass to compaction parameters was insignificant.

**Fig. 1** Fiberglass (3 mm) used in the tests



**Table 1** The physico-chemical properties of the samples

	Bentonite	Sand	Fiberglass
Specific gravity	2.70	2.63	2.60
Liquid limit (%)	476	–	–
Plastic limit (%)	70	–	–
pH	9.5	–	–
Length (mm)/diameter ( $\mu$ )	–	–	3/13

Direct shear tests were performed according to ASTM D3080 [8]. Direct shear tests were carried out under two different conditions, room and high temperatures. Test samples were prepared on the 2% wet side of the optimum water content. The shearing rate of the samples was determined as 0.003 mm/min in both tests (room and high temperatures).

The samples were left to consolidation for 24 h, then shearing stage was started. In the tests which were performed under high temperatures, the samples were also exposed to heat during the consolidation phase. In order to provide the high temperature, the heat rod designed for the shear box (Fig. 2). In order to prevent water evaporation from the cell, a rectangular black membrane was covered on the top of the cell. In addition, water supply was provided through pipes from a water reservoir and the water level was kept constant during the tests. A thermostat was used to keep the water temperature constant at 80 °C. All experiments were carried out under normal stresses of 49, 98 and 196 kPa.



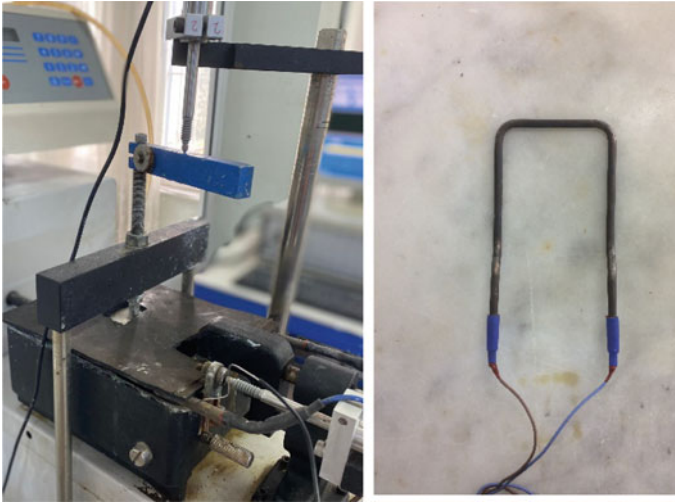


**Fig. 2** Direct shear test equipment used in the tests at high temperature (80 °C)

### 3 Results

In this study, direct shear tests of 0.5 and 1% fiberglass added sand-bentonite mixtures were carried out under room temperature and high temperature (80 °C). The obtained results are given in Table 2. Test results showed that 1% fiberglass additive slightly increased the internal friction angle of the additive-free mixture under room temperature. It was observed that the cohesion value decreased due to the decrease in the proportion of bentonite in the mixture.

In the direct shear tests, which were under high temperature, it was observed that the internal friction angles of the mixtures did not change significantly. It was determined that there was almost no change in the internal friction angle and shear stress values when the temperature was increased from room temperature to high temperature.

As a result of direct shear tests, it was observed that the internal friction angle almost did not change in the presence of fiberglass additive and under high temperature and the maximum shear stress increased slightly at the normal stress level of

**Table 2** Internal friction angles and cohesion values of sand-bentonite mixtures with fiberglass additives under room and high temperatures

Mixtures	Room temperature		80 °C	
	$\phi'$ (°)	$c'$ (kPa)	$\phi'$ (°)	$c'$ (kPa)
30B-70S	28.6	12.7	31.1	15.0
0.5% GF	28.0	8.3	30.3	14.2
1.0% GF	31.3	5.9	31.8	12.5

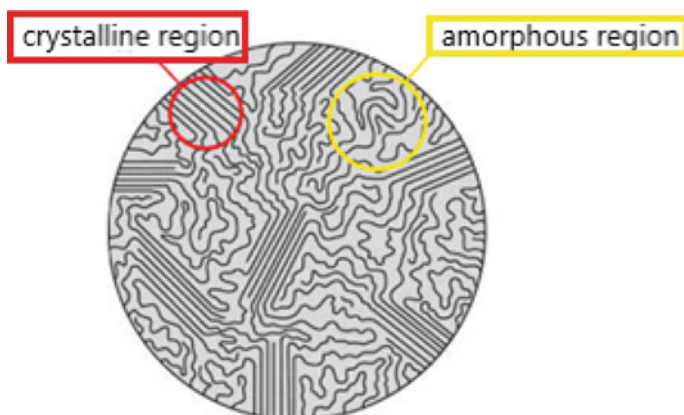


**Fig. 3** Display of fiber structure of fiberglass [11]

196 kPa but still did not change significantly. Harmancıoğlu (1981) reported that the strength of fiberglass increases after 250 °C [9]. At the same time, the crystalline and amorphous regions forming the structure of the fibers affect the behavior of the fiber in the presence of temperature (Fig. 3). The amorphous region is a softer region with a lower melting point than the crystalline region, and the amorphous region may lose its strength when exposed to high temperatures. After the amorphous region adsorbs a certain temperature, it can also affect the crystalline region, causing a complete loss of strength and acting like a low-viscosity material to lose its strength. Therefore, the ratio and behavior of these two regions in the fiber structure used in the tests affected the increase or decrease in shear strength [10].

Table 3 shows that the maximum shear stress values of fiberglass added sand-bentonite mixtures at room and high temperatures. It was observed that 0.5% fiberglass additive had the highest increase in shear stress value under 196 kPa stress under high temperature. It was determined that both additives caused a slight increase at the same stress level at room temperature.

## 4 Conclusions

In the present study, direct shear tests of 0.5 and 1.0% fiberglass added sand-bentonite mixtures were conducted at room temperature and high temperature (80 °C). The test results revealed that the internal friction angle values almost did not change when changing from room temperature to high temperature for fiber added sand-bentonite mixtures. It was observed that the cohesion values decreased insignificantly depending on the decrease in the amount of bentonite. It was determined that the maximum shear stresses increased slightly at some stress levels depending on the applied normal stress. The tests carried out support the use of fiberglass additive with

**Table 3** Maximum shear stress values of the mixtures under room and high temperatures

Mixtures	Normal stress (kPa)	RT	80 °C
		Max. shear stress (kPa)	Max. shear stress (kPa)
30B-70S	49	37.5	44.4
	98	69.3	74.6
	196	118.2	133.3
	49	38.3	40.9
0.5FG-30B-70S	98	68.8	70.3
	196	128.8	117.8
	49	33.9	41
1.0FG-30B-70S	98	68.2	76.3
	196	124.3	133.1

sand-bentonite mixtures as it keeps its durability stable against high temperature. The effect higher fiber glass contents should be investigated.

## References

- Laloui L (2001) Thermo-mechanical behavior of soils. *Revue Française de Genie Civil* 5(6):809–843
- Cekerevac C, Laloui L (2004) Experimental study of thermal effects on the mechanical behaviour of a clay. *Int J Numer Anal Methods Geomech.* <https://doi.org/10.1002/nag.332>
- Hueckel T, Baldi G (1990) Thermoplasticity of saturated clays: experimental constitutive study. *J Geotech Eng* 116(12):1778–1796. [https://doi.org/10.1061/\(ASCE\)0733-9410\(1990\)116:12\(1778\)](https://doi.org/10.1061/(ASCE)0733-9410(1990)116:12(1778))
- Smith MJ et al (1980) Engineered barrier development for a nuclear waste repository in basalt: an integration of current knowledge. In: RHO-BWI-ST-7, Rockwell Hanford Operations, WA
- Wallenberger FT, Bingham PA (2010) Fiberglass and glass technology. Pittsburgh, USA
- Guo Y-G, Lee J-S, Hu Y-S, Maier J (2007) AgI nanoplates in unusual 7H/9R structures highly ionically conducting polytype heterostructures. *J Electrochem Soc* 154:K51–K60
- ASTM: D698–12 (2012) Standard test methods for laboratory compaction characteristics of soil using standard effort. *ASTM Int.* <https://doi.org/10.1520/D0698-12.1>
- ASTM (2011) D3080/D3080M-11. Standard test method for direct shear test of soils under consolidated drained conditions. *ASTM Int.* <https://doi.org/10.1520/D3080>
- Harmancıoğlu M (1981) *Tekstil maddeleri 2, Rejenere ve sentetik lifler* s 338–347
- Hammadde Kurutma. <https://www.hammaddekurutma.com/kutuphane/amorf-ve-kristalin-plastik-ne-demektir-26>. Last Accessed 22 July 2022
- Borche Machinery Homepage. <https://www.borche.com.tr/bilgi-kutuphanesi/123/kristalizotoler>. Last Accessed 22 July 2022

# Investigation on the Vulnerability of Core Soils from Three Zoned Dams to Internal Erosion



Ahmed Jalil, Ahmed Benamar, and Ebn Touhami Mohamed

**Abstract** Global warming (due to climate change) can lead to a decrease in rate precipitations after a long dry season (due to high temperature). Therefore, it can have an effect on the soil properties (due to the evaporation of the water contained in the soil). This modification on soil properties raises a question of how such hydraulic structures (dams and dikes) could behave after the degradation of soil properties due to drought (water evaporation). This research investigated the vulnerability of core soils from three zoned dams in Morocco to internal erosion, particularly after the dam's core soil was submitted to the drying effect due to the drought (to simulate the global warming effect), causing desiccation. For this purpose, Hole Erosion Tests (HETs) were carried out on three kinds of core soils collected from the three dams aimed to assess their vulnerability to erosion after desiccation. The erosion results, analyzed through the erosion rate and soil resistance classification, showed an initial high resistance to internal erosion of tested soils, but the desiccation makes the core soils more sensitive to erosion (even in the filter presence), especially for Mazer dam whose core soil is a lean clay. So, a drought phase (which may be due to global warming) may threaten strongly the core soil resistance against erosion, leading to serious damage to dam stability when refilling occurs during floods.

**Keywords** Internal erosion · Filtration · Soil · Desiccation · Earthen dam

---

A. Jalil (✉) · A. Benamar  
Department of Civil Engineering, LOMC UMR 6294 CNRS-University of Le Havre Normandie,  
53 Rue de Prony, 76600 Le Havre, France  
e-mail: [ahmed.jalil87@gmail.com](mailto:ahmed.jalil87@gmail.com)

A. Jalil · E. T. Mohamed  
Department of Material Engineering, Ibn Tofail University of Kenitra, B.P 242, Kenitra, Morocco

## 1 Introduction

The last decade has seen significant global warming with longer periods of drought, due to global climate change. To this end, the soils undergo significant water evaporation as well as volume shrinkage, leading to serious damage to infrastructure [1]. Cracks exposed by desiccation resulting from water loss and volume shrinkage have a vital influence on the mechanical and hydraulic properties of soils, weaken the strength of the soil and can cause dam failures and lead to its collapse [2].

Lozada et al. [3] have shown through a simulation using a geotechnical centrifuge to show the influence of cracks resulting from desiccation by evaporation of water on the resistance and stability of soils (many failure mechanisms may occur depending on the depth of the cracks). Archer and Ng [4] proved the effects of temperature and relative humidity (thermal expansion of the soil) on a clay embankment through centrifuge modeling.

Furthermore, cracks in coatings can lead to a remarkable increase in the hydraulic conductivity of soils. Thus, shrinkage resulting from desiccation cracking is a real concern in the design and analysis of soil structures for various geotechnical engineering applications. Global warming leading to very long dry periods can threaten the stability of dams and dykes by reducing their resistance to internal erosion [5]. This disorder threatening the dams raises the question on the effect of the degradation of the properties of the soil and how this can affect the earthworks lifespan. Internal erosion is the leading cause of failure and incidents of levees, levees and dams worldwide. These hydraulic works may also be damaged exceptionally by overtopping during severe floods, or because of the sea level rise [6].

Internal erosion is a phenomenon that remains difficult to identify because of the many threats they present because it can easily initiate following a leak concentrated in transverse cracks, or in weakly compacted zones (significant permeability) [7]. The mechanics of internal erosion confirmed that the initiation of this phenomenon normally occurs when the water level of the reservoir reaches its highest level ever recorded (critical gradient) [8]. Indeed, the phenomenon that initiates locally and develops gradually is difficult to predict and represents the major causes of structural collapse. A break is often the result of successive situations and a combination of processes that accelerate the internal erosion mechanism. Fry et al. [9], Bonelli [10] showed that the mechanisms involved in internal erosion are multiple, different and complex, and depend on the nature of the materials and the flow conditions. Concerning pipe erosion, some authors have studied the role of compaction conditions on erosion characteristics  $k_{er}$  and  $\tau_c$  and process kinetics. Attom [11] showed that for the same density, the soil provides a higher erosion index when it is compacted in the wet side of the optimum water content. The research reported by Wahl [12] and Attom [11] also showed that along the compaction curve, the highest values of the erosion index are obtained at the compaction reference of the optimum Proctor. Wan and Fell [13] and Lim [14] have shown that the increase in initial water content leads to an increase in erosion leading to a better resistance to erosion. However, the magnitude of this increase is related to the soil nature. They also observed an increase

of erosion index when initial density increases. Benamar and Seghir [15] presented an analytical model based on the integration of the particle transport equation in a porous medium, and they showed that the detachability parameter decreases when the fines content increases. In order to properly investigate the suffusion process in porous media, Chetti et al. [16] implemented a three-dimensional numerical simulation of the coupling between fluid flow and internal erosion. Overall investigated parameters affecting internal erosion initiation and its progress, the drying effect of soil before seepage occurrence is not investigated. Due to climate change, long heat seasons raised in the last decade in North Africa. Therefore, many hydraulic structures (dams and levees) might suffer desiccation, which could affect the stability of dams against internal erosion. This paper presents the investigation of the effect of drying-induced shrinkage and desiccation, resulting from long dry seasons and rainfall shortage, on the vulnerability to internal erosion of three zoned dams in Morocco. In the area of studied Koudiat El Garn, Mazer and Moulay Boucheta dams, the rainfall data (Fig. 1) from the last decade indicated that the dam's areas have experienced a long drought which led to emptying two dam reservoirs, drying deeply the earthen dike and providing cracks that may be increased over time. This rainfall deficit has been almost generalized throughout the territory and has reached on average about -35% (in 2020), which caused the drop in the storage capacity of the dams (the average filling rate reached 34.2% in 2021, Fig. 2). Also the climate of Morocco in 2020 was marked by abnormally warm annual average temperatures, especially the areas from which the subject dams of our study originate (Fig. 3a, b, c), with a national annual average temperature anomaly of + 1.4 °C compared to the climatological normal over the period 1981–2010. Cracks spread typically from the soil surface downwards through the drying surface, where the matrix suctions are usually the most significant, and the constraints due to self-weight are minimal [17]. Today, the Koudiat El Garn and Mazer reservoirs are empty (Fig. 4a, b) whereas the reservoir of the Moulay Boucheta dam is below 20% of its total capacity due to a rainless period that has struck north Africa (Fig. 4c). When the reservoir levels decrease below the current level it will lead to the decrease in the structural reliability of the water intake structure. Generally, these embankment dams are not always subjected to significant hydraulic heads and remain largely unsaturated [5], therefore this will not seriously threaten their stability. However, during periods of flooding, embankment dams must withstand the considerable increase in water level on the outer face, as well as the corresponding changes in internal water pressure (and potential seepage). Therefore, a new filling of the reservoir can lead to more core susceptibility to internal erosion, especially in flood events. The influence of surface desiccation on embankment stability is one of the many uncertainties concerning the changes in physical processes and the trigger points of rupture in natural and artificial slopes in response to climate change [18]. The drying-induced soil desiccation effect on dam stability has been investigated in this study through Hole Erosion Tests of core soil from three dams.

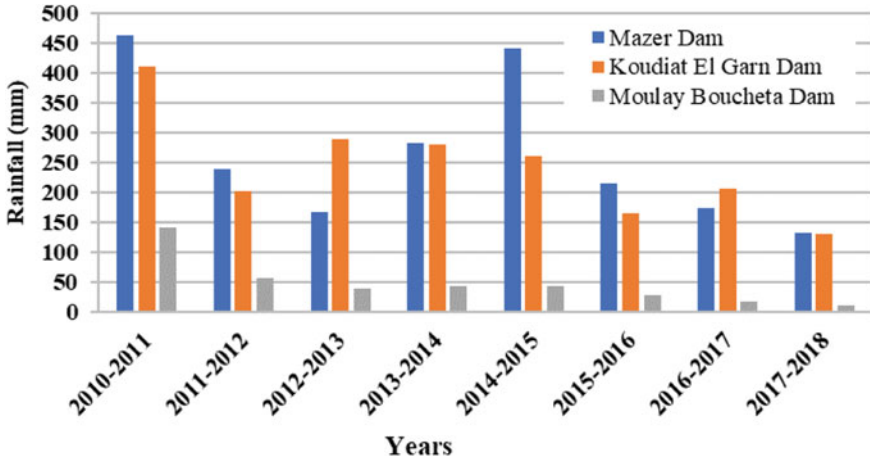


Fig. 1 Evolution of the rainfall in the area of dam location during last decade

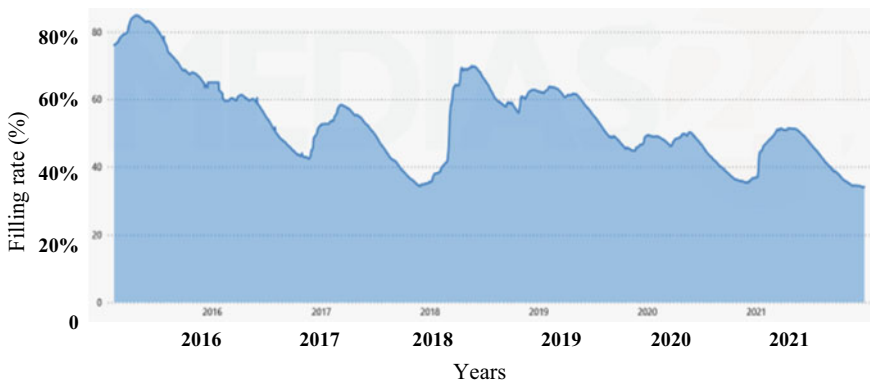
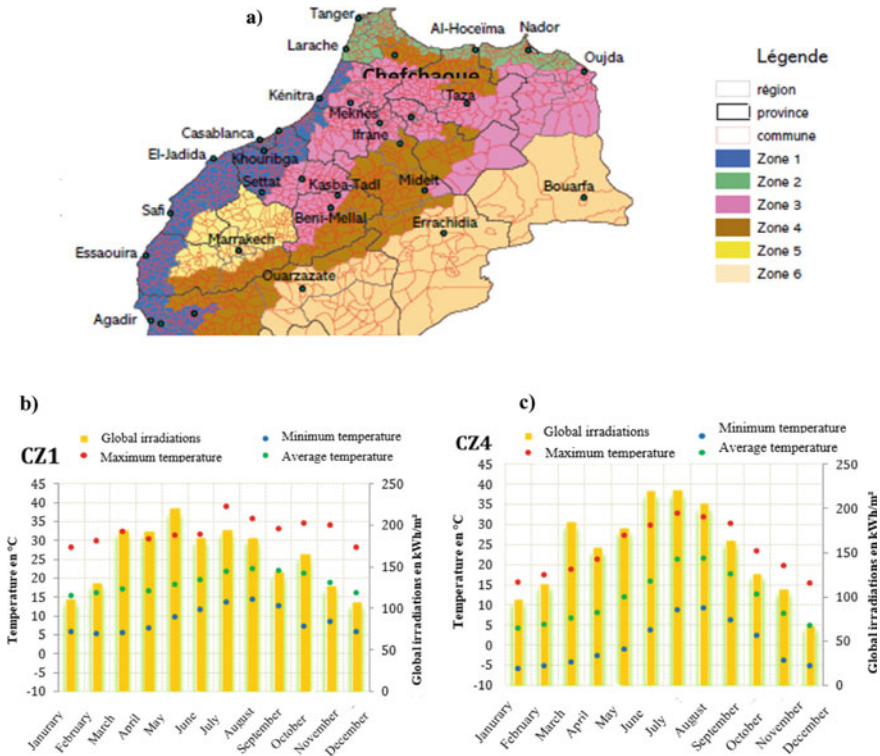


Fig. 2 Filling rate of dams in Morocco: evolution of the filling rate between 2015–2021

## 2 Materials and Methods

### 2.1 Dams and Materials Description

After the flooding events in 2002 in the region of Settât-Berrechid and their effects on industrial and agricultural fields, the arrangement program of Koudiat El Garn and Mazer’s dams and the warning system against floods were designed for floodplain preservation. Besides flood prevention, the aim is rather to guarantee irrigation of the lands located downstream covering an area of 2500 ha, and the recharge of groundwater, which has recorded a drop of 1 m per year. In 2011, Mazer dam was put into operation and Koudiat El Garn dam started operating in 2012. The site of



**Fig. 3** Ambient temperatures: **a** Maximum, minimum and average, and the monthly solar radiation on a horizontal plane of our three dams during a typical climatic year for: **b** Climatic zone number 1, **c** climatic zone number 4

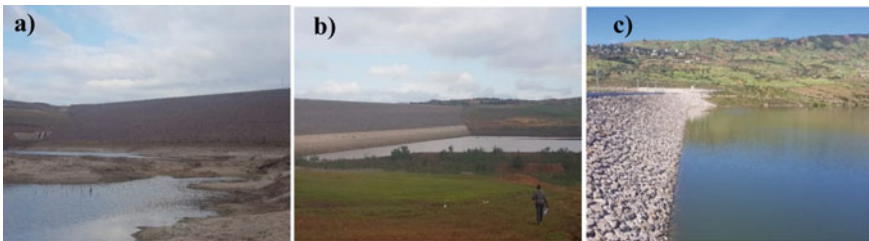


**Fig. 4** Evolution of the rainfall in the area of dam location during last decade. **a** Koudiat El Garn dam, **b** Mazer dam and **c** Moulay Boucheta dam

Moulay Boucheta dam is located about 12 km northwest of the city of Chefchaouen, and was put into operation in 2014.

These three-zoned dams include mainly a central core, a filter, upstream and downstream embankments and protections (Figs. 5 and 6).



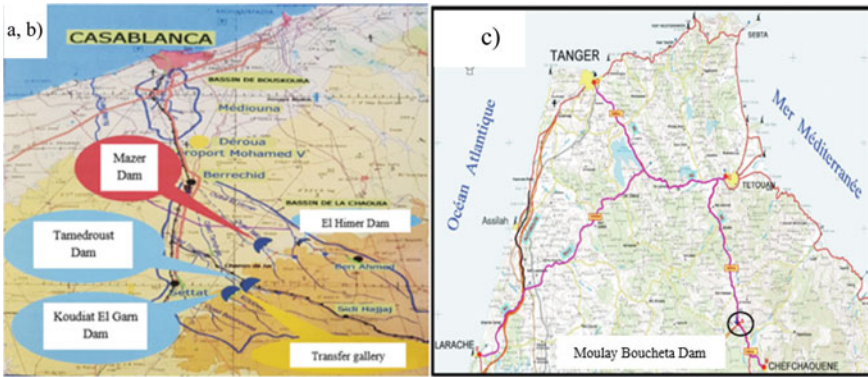


Fig. 5 A map depicting the location of a, b Koudiat El Garn dam and Mazer dam and c Moulay Boucheta dam

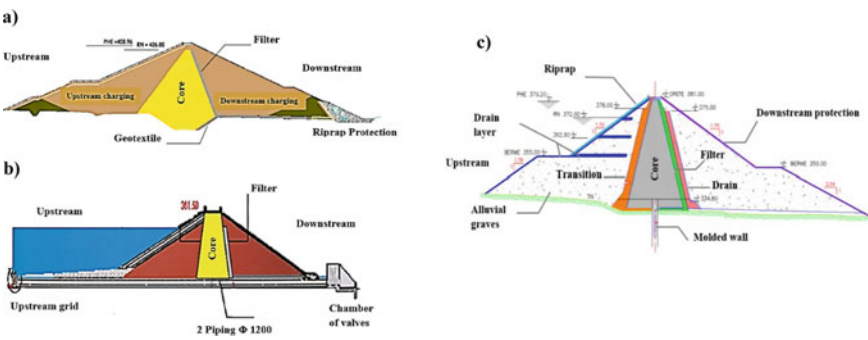


Fig. 6 A cut in the axis of the bottom drain of a Koudiat El Garn Dam, b Mazer Dam and c Moulay Boucheta Dam

The core material tested come from borrowings located in the areas of the reservoir from each of the three dams (Koudiat El Garn, Mazer, Moulay Boucheta). The preparation and the homogenization of the materials from point of view water content, and compactness respect the same conditions that those of the dam currently under way. Table 1 summarizes the geotechnical parameters of tested materials from the dam.

### 2.2 Experimental Setup and Test Procedure

The test apparatus involved a cylindrical plexiglass column of 140 mm inner diameter and 300 mm in length, a water graduated tank, a pump, and a pressure sensor at the inlet of the cell used to control the applied water pressure (Fig. 7). The cell was

**Table 1** Soils (core and filter) characteristics

Soil dam	Koudiat El Garn	Mazer	Moulay Boucheta
WL (%)	48	53	53
IP (%)	23	25	32
$\gamma_{\max}$ (t/m <sup>3</sup> )	17	17	17
Classification (ASTM)	Lean clay with sand	Lean clay	Lean clay
Clays (< 2 $\mu\text{m}$ ) ((%)	14.0	11.8	19.7
Silts (2–63 $\mu\text{m}$ ) (%)	64.4	75.8	78.8
Sand (63–2000 $\mu\text{m}$ ) (%)	21.6	12.4	1.5

connected to a water supply which provides a selected pressure in a range from 100 to 250 kPa [19, 20].

The hole erosion tests which consisted to introduce a controlled seepage into the soil hole and to measuring the erosion kinetics, aimed to evaluate the core soil erodibility at different hydraulic loads (pressures), before and after desiccation. For each core soil, four successive pressure steps (100, 150, 200, and 250 kPa) were applied and the erodibility was evaluated at each step. This experimental work aimed to study the behavior of soils with respect to the initiation and progression of internal erosion before and after desiccation, through the identification of the influence of pressure and hydraulic head variation, the nature and proportion of fines contained in the soil and also geotechnical parameters (water content). In this part of the experimental program carried out, we chose the Hole Erosion Test (HET) given that it is the most appropriate test to simulate the process of desiccation, which remains a little-studied phenomenon. To do this, test specimens were reconstituted with the optimum water content (20%), and then they were dried (in an oven at a temperature of 50 °C for 24 h) until drying, in order to study the effect of the water content decreasing below the critical value (desiccation), thus simulating periods of drought, and emptying of the reservoir. This is likely to occur because of the risk of drought in the dams' areas. However, during floods when the reservoir's water level increases rapidly and suddenly, cracks induced by the drought period (in the core soil) may lead to the dam's embankment experiencing internal erosion. As a result, through these tests, we will be able to assess the capacity of the soil to resist erosion at the base of the dam and its behavior after the water content is reduced significantly (until desiccation). The analysis of the results will allow to assess the vulnerability of the core soil to erosion, as well as to evaluate the sustainability of the dam.

Table 2 summarizes the test conditions with regards to soil parameters and applied pressure.

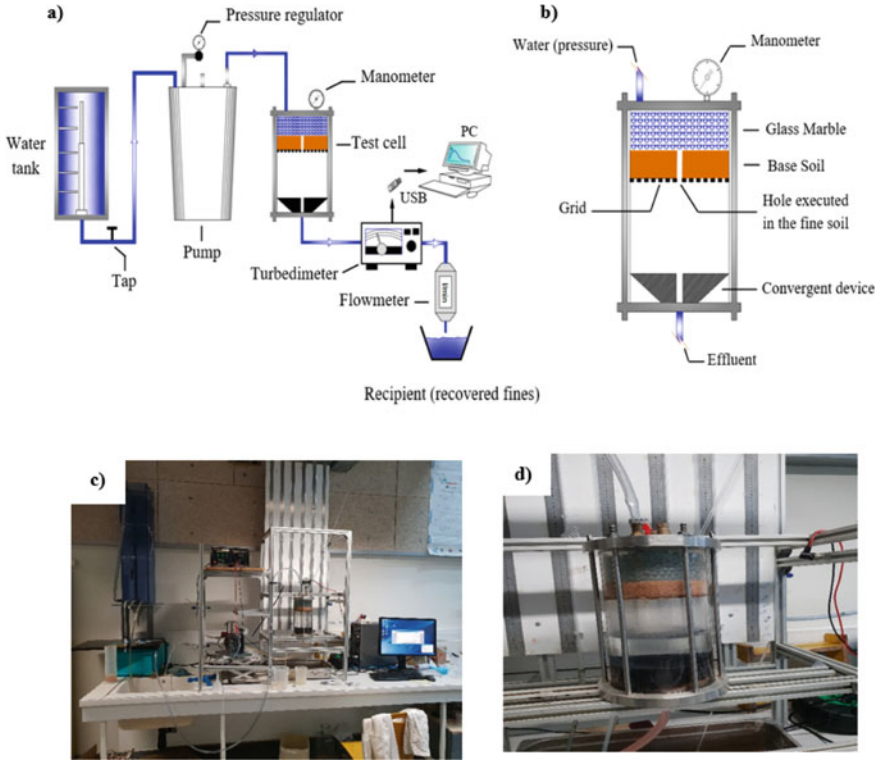


**Fig. 7** Schematic diagram of the experimental set up for hole erosion test (a), detailed view of test cell (b), overview of the set up (c), view of test cell in saturation phase (d)

**Table 2** Test parameters before and after desiccation

Base soil dam	Koudiat el Garn	Mazer	Moulay Boucheta
<i>Water content (%)</i>			
Before desiccation		20	
After desiccation	4.5	4.0	5.0
Hole diameter (mm)	15		
Applied pressure (kPa)	100–150–200–250		

### 3 Effect of Desiccation on Base Soil Erodibility

#### 3.1 Base Soil Erodibility from Hole Erosion Test

The recorded turbidity values led to derive through the correlation function of the outlet particle concentration. Using flow rate recordings, the erosion kinetics was deduced as the product of particle concentration and flow rate. The drawn curves in Fig. 8 showed the evolution of erosion kinetics over time, for both tests carried out before and after desiccation, for the three core soils. Overall, the erosion kinetics reached a maximal value rapidly before falling to a residual value, except for Mazer and Moulay Boucheta dams whose data remained at a very low constant value over time. The results clearly showed how seepage under a pressure of 100 kPa causes detachment of particles from the surface of the hole. The erosion kinetics before desiccation remained low for the three dams, but increased considerably after desiccation, especially for Koudiat El Garn and Mazer dams (Fig. 8b, d). Mazer dam appeared to be the most suffering internal erosion after desiccation as the erosion kinetics reached a very high value (2103 times the value before desiccation). This shows the effect of desiccation on the large detachment of particles and on the soil susceptibility against internal erosion (a quick particle erosion has been observed during the saturation phase before the test after desiccation, especially for Mazer dam). Therefore, this result proves that the more dryer was the core soil, the more it became susceptible to erosion [19, 20, 22], which promotes the detachment of particles much more quickly. However, it has also been found that erosion susceptibility differs from one dam to another either before or after desiccation. Mazer and Moulay Boucheta dams were the most resistant to erosion before desiccation, while after desiccation Mazer dam became the less resistant and Moulay Boucheta dam the most resistant against internal erosion. So, even though a core dam was well designed to be resistant to erosion, after desiccation it can suffer a drastic susceptibility to erosion. That is the case of Mazer dam whose core soil showed a lower clay content and a significant silt content which likely contributed to the easy detachment of silty particles after a strong drying.

The specimen was hydrated with varying water contents ranging from optimum to desiccation (4%). The curves Fig. 9 illustrate the evolution of erosion kinetics with regard to the resulting shear stress from the applied pressure, the values prior to and following desiccation. Figure 4 illustrates the evolution of the erosion rate of particles that were detached from the hole's surface over time, this shows a direct relationship between the erosion rate and the shear stress:  $\varepsilon = \tau$ . This clearly demonstrates how the pressure of 1 bar water flowing through the specimen causes the particles to be detached from the hole's surface. As depicted on the graphs, the kinetics of erosion before desiccation remained low during the first seconds of the initiation of the test, however, the rate of erosion after desiccation increased considerably [21–23]. This outcome indicates the influence of desiccation on internal erosion (a rapid particle erosion was observed during the saturation phase at desiccation). As a result, it

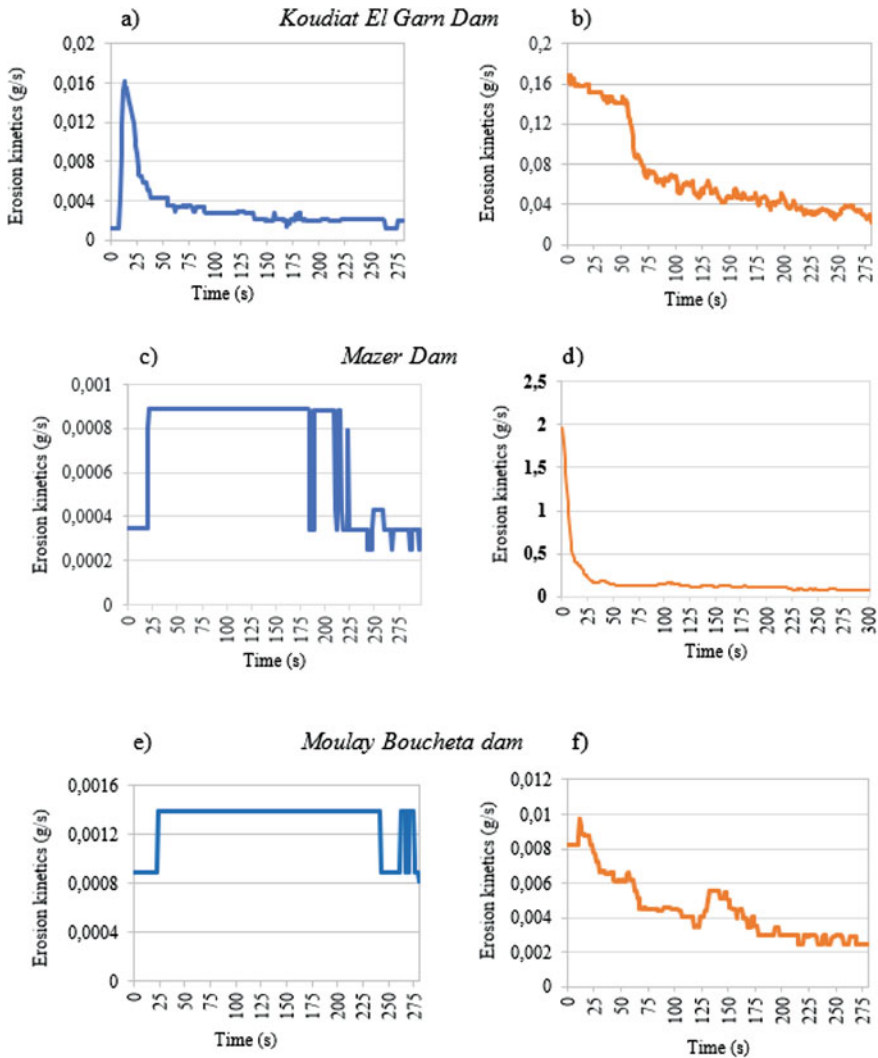


**Fig. 8** Time evolution of erosion kinetics in base soil at a pressure of 100 kPa before desiccation (a, c, e) and after desiccation (b, d, f)

demonstrates that the lower the water content of the specimen, the more susceptible the core soil is to erosion, which leads to the faster detachment of particles.

The results from Fig. 7 were presented using the linear erosion model [24],  $\tau_c$  and  $C_e$  were critical shear stress and erosion coefficient, respectively. Instead of the critical shear stress of the core soil prior to desiccation, which was extrapolated from the linear relationship, the value of soil following desiccation has been deduced from experience (due to the low involved value) when the lowest hydraulic load

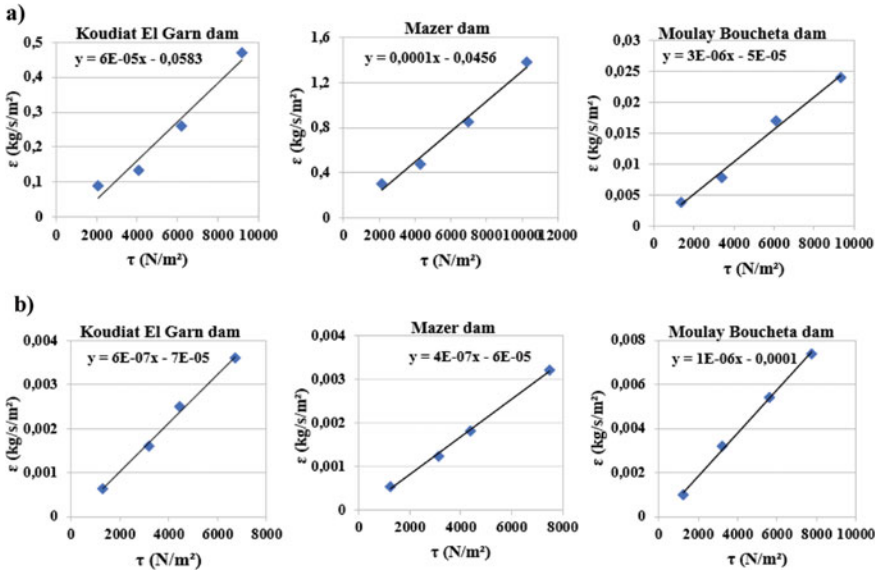


**Fig. 9** Evolution of erosion rate with applied pressure before desiccation (a) and after desiccation (b)

(0.06 m) is employed and a first erosion occurs. These specifications facilitate the characterization of the soil’s resistance to erosion. They are summarized in Table 3.

In order to address the vulnerability of tested soil as regards internal erosion, the above results (Table 3) were used for soil classification based on Hanson and Simon [25] criterion, indicating how long the soil resists to erosion before and after desiccation. Results (Fig. 10) indicated that the core soils are very resistant at optimum water

**Table 3** Erosion parameters of tested soil in the two configurations

Designation of test	Before desiccation	After desiccation
<i>Koudiat el Garn dam</i>		
$\tau_c$ (Pa)	117	11
$C_e$ (s/m)	$6 \times 10^{-7}$	$6 \times 10^{-5}$
$K_d$ (cm <sup>3</sup> /N s)	$353 \times 10^{-6}$	$3.53 \times 10^{-2}$
<i>Mazer dam</i>		
$\tau_c$ (Pa)	150	8
$C_e$ (s/m)	$4 \times 10^{-7}$	$1.32 \times 10^{-4}$
$K_d$ (cm <sup>3</sup> /N s)	$235 \times 10^{-6}$	$7.76 \times 10^{-2}$
<i>Moulay Boucheta dam</i>		
$\tau_c$ (Pa)	100	17
$C_e$ (s/m)	$10^{-6}$	$3 \times 10^{-6}$
$K_d$ (cm <sup>3</sup> /N s)	$588 \times 10^{-6}$	$1.7 \times 10^{-3}$

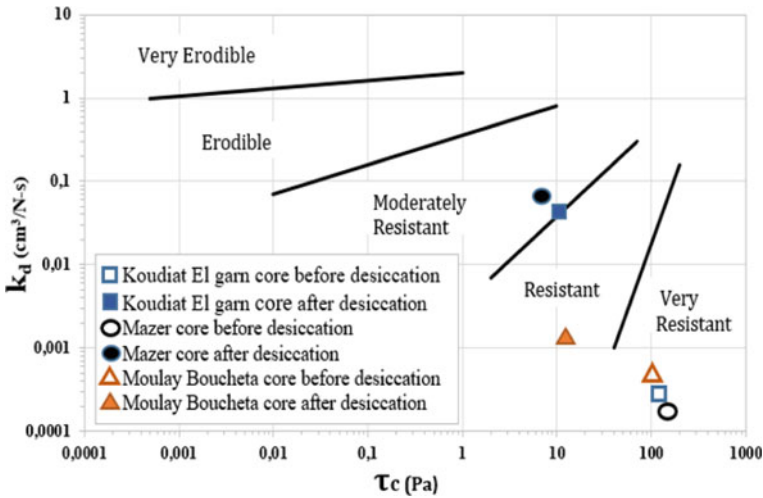


Fig. 10 Erodability classification of tested soil according to Hanson and Simon [25] diagram

content, but once desiccation was reached the soils became moderately resistant for Koudiat El Garn and Mazer dams [26], and resistant for Moulay Boucheta dam which showed strong resistance against erosion either before and after desiccation. So, the core soil is stable (low vulnerability to erosion) at optimum water content, but after the desiccation, the soil becomes highly sensitive to erosion. From the comparison of the measurements carried out on the amount of the eroded solid mass, whether before or after desiccation for core soil dams, we were able to demonstrate a consistency of the classifications obtained on erosion susceptibility.

From the analysis of the curves depicting the evolution of the diameter of the hole as well as the mass of eroded solids over time, before and after desiccation at different pressures, results before desiccation indicated that our soil had undergone extremely slow erosion. As a result, the diameter of the hole for the three dams is slightly increased (Fig. 9 before desiccation). However, the soil of the Mazer dam is more susceptible to erosion because of its lower water content (from 20 to 4% after desiccation) [26], this is taken into consideration the large quantity of mass that was eroded during and into the test end (Fig. 12), this led to the enlargement of the hole’s diameter over time (Fig. 11 after desiccation).

#### 4 Concluding Remarks

Hole erosion experiments have been conducted on samples from the base soil (core) of three dams (embankment and zoned dams) in Morocco to evaluate their susceptibility to erosion, specifically after drying. As a result, if the volume of rainfall in the area around the dam continues to decline, the likelihood of drought increases, which can

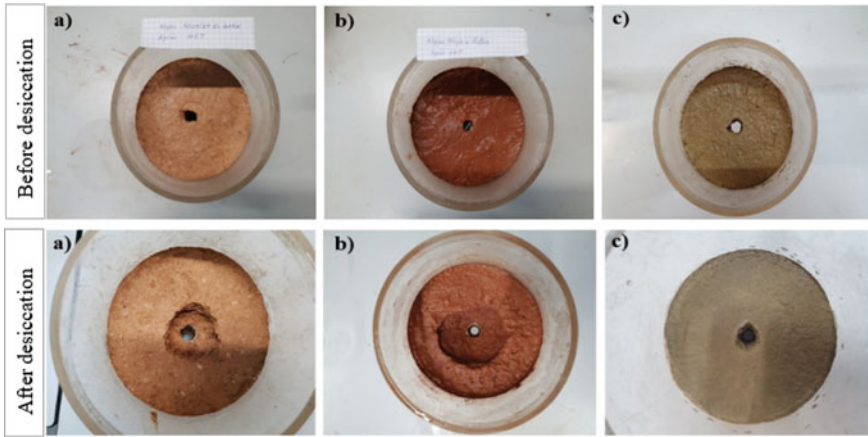


**Fig. 11** Pictures of the hole shape at the end of erosion test, before and after desiccation from Koudiat El Garn dam (a), Mazer dam (b), Moulay Boucheta dam (c)

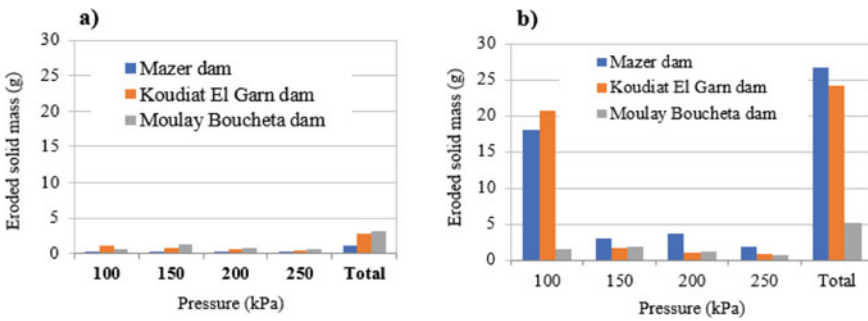


**Fig. 12** Evolution of cumulated eroded solid mass with applied pressure before desiccation (a) and after desiccation (b)

negatively affect the dam’s stability. In lab tests, the volume of water reduction was achieved in order to simulate the behavior of dams during droughts, this demonstrated the effect of desiccation on the hydraulic stability of dams, which led to cracks in the core of the dam. However, it has been observed through low water content (after desiccation) that the core soil becomes extremely susceptible to erosion, this is because once the drying process is complete, the increase in cracks results in a drastic decrease in the soil’s ability to resist erosion. From obtained results, we can expect a serious degradation of soil resistance against erosion if water content decreases drastically. The three core soils tested showed different behavior as regards to desiccation. Even though Mazer soil core suffered the weakest erosion before drying, it provided the most susceptibility to erosion after desiccation, as well as Koudiat El-Garn dam, owing likely to the lower clay content involved and the weak soil plasticity. Moulay-Boucheta core soil was the most resistant against erosion after



desiccation owing to its high plasticity and larger fines content. So, if the rainfall rate continues to decrease in the dam area, the risk of drought increases and can threaten the dam stability.

## References

1. Cui YJ, Gao YB, Ferber V (2010) Simulating the water content and temperature changes in an experimental embankment using meteorological data. *Eng Geol* 114:456–471
2. Zeng H, Tang CS, Cheng Q, Inyang HI, Rong DZ, Lin L, Shi B (2019) Coupling effects of interfacial friction and layer thickness on soil desiccation cracking behavior. *Eng Geol* 260:105–220
3. Lozada C, Caicedo BM, Thorel L (2015) Effects of cracks and desiccation on the bearing capacity of soil deposits. *Géotechnique Lett* 5(3):112–117
4. Archer A, Ng CWW (2018) Effects of temperature and relative humidity on a clay embankment: centrifuge modelling. *Géotechnique Lett* 8(2):138–143
5. Dyer M, Utili S, Zielinski M (2017) The influence of desiccation fine fissuring on the stability of flood embankments. *FRMRC Res Rep UR* 11:64
6. Duc DM, Hieu NM (2017) Analysis of sea-level rise impacts on sea dike stability in Hai Hau coast, Vietnam. *Int J Civil Eng* 15:377–389
7. Caldeira L (2019) Internal erosion in dams: studies and rehabilitation. *Int J Civil Eng* 17:457–471
8. ICOLD (2013) Internal erosion processes and engineering assessment. In: *COLD bulletin on internal erosion of existing dams, levees and dikes, and their foundations*, vol 1
9. France, Fry JJ, Vogel A, Royet P, Courivaud JR (1997) Internal erosion: typology, detection and repair. *Dams Reservoirs* 6:126
10. Bonelli S (2012) Geomaterials erosion. *LAVOISIER*
11. Atom M (2012) The effect of compaction and initial water content on soil erosion. In: *ICSE6 Paris*, pp 49–56
12. Wahl TL (2010) A comparison of the hole erosion test and jet erosion test. In: *Joint federal interagency conference on sedimentation and hydrologic modeling Las Vegas*, pp 1–12
13. Wan CF, Fell R (2002) Investigation of internal erosion and piping of soils in embankment dams by the slot erosion test and the hole erosion test. The University of New South Wales, Sydney, Australia, *UNICIV Rep. R-412*
14. Lim S (2006) Experimental investigations of erosion in variably saturated clays. Ph-D thesis report, University of New South Wales, Australia, p 197
15. Benamar A, Seghir A (2017) Physical and analytical modeling of internal erosion of fine particles in cohesionless soils. *J Porous Media* 20(3):205–216
16. Chetti A, Benamar A, Korichi K (2019) Three-dimensional numerical model of internal erosion. *Euro J Environ Civil Eng* 29(2):263–277
17. Morris PH, Graham J, Williams DJ (1992) Cracking in drying soils. *Can Geotech J* 29(2):263–277
18. Dijkstra TA, Dixon N (2010) Climate change and slope stability in the UK: challenges and approaches. *Q J Eng Geol Hydrogeol* 43:371–385
19. Jalil A, Benamar A, Ebn Touhami M (2020) Assessment of a dam vulnerability to internal erosion due to climate change in Morocco. *Innov Infrastruct Solutions* 5(2)
20. Jalil A, Benamar A, Ebn Touhami M (2021) Investigation of internal erosion susceptibility of core soil from three dams. *J Civil Eng Construct* 10(2):59–68
21. Jalil A, Benamar A, Ebn Touhami M (2021) Soil desiccation effect on internal erosion of earth dams in Morocco. In: *Proceedings of the 10th international conference on scour and erosion (ICSE-10)*, Arlington, Virginia, USA. In: Rice J, Liu X, McLroy M, Sasanakul I, Xiao M (eds) *ISSMGE website*, pp 1496–1505

22. Jalil A, Benamar A, Ebn Touhami M (2021) Internal erosion vulnerability of core soil due to drought: case study of three zoned dams. *SCIREA J Civil Eng Build Construct* 6(2):15–36. <https://doi.org/10.54647/cebc56065>
23. Jalil A, Benamar A, Ebn Touhami M (2021) Assessment of core soils vulnerability to internal erosion from three zoned dams, under drought effect due to climate change. In: *Advances in sustainable materials & technology*. Nova Science Publishers. <https://doi.org/10.52305/TTE Y2186>
24. Reddi LN, Lee IM, Bonala MVS (2000) Comparison of internal and surface erosion using flow pump tests on a sand-kaolinite mixture. *Geotech Test J GTJODJ* 23(1):116–122
25. Hanson GJ, Simon A (2001) Erodibility of cohesive streambeds in the loess area of the Midwestern. USA *Hydrol Process* 15(1):23–38
26. Jalil A, Benamar A, Ebn Touhami M (2019) Erosion—filtration analysis for assessing hydraulic instability of dams in Morocco and global warming effect. In: 2nd international conference on EGRWSE, University of Illinois-Chicago. In: Reddy KR, Agnihotri AK, Yukselen-Aksoy Y, Dubey BK, Bansal A (ed) *Sustainable environment and infrastructure*. Lecture notes in civil engineering, vol 90 Springer, pp 447–454

# Zeta Potential of Dispersed Nanocarbons by Sonication



Mohd Raihan Taha and Jamal Mansour Alsharif

**Abstract** Nanocarbons (NC) is a popular material with exceptional mechanical, electrical, and thermal properties. In geo-environmental applications, it has been studied in the past to absorb contaminants and its success depends on its dispersivity in soil–water systems. Usually surfactants were used to disperse chemicals in order to aid other required reactions. In this study, ultrasonic method was used to disperse the NC in distilled water and its zeta potential was studied. Two types of NC were used, i.e. carbon nanotube (CNT), and carbon nanofiber (CNF). Different amounts of the NC and water were used with sonication time of 2–12 min. The field-emission scanning electron microscopy (FESEM) was utilized to inspect the efficiency of the dispersion methodology. The result showed maximum zeta potential at 7 min sonication time for both CNT and CNF. The combination of this sonication time produces majority of high zeta potential readings yielding good dispersion stability or better. It is also showed that longer sonication time generally results in low zeta potential thus indicating the importance of getting the correct or optimum sonication time. In addition, the amount of NC in the solution must also be controlled. FESEM photos also indicate the importance of dispersion of NC in a soil-NC matrix in which the soil-NC undergoing regular mechanical mixing without sonication system results in a mixture of less dispersive stability rendering inefficient use of NC for its intended purposes.

**Keywords** Environmental geotechnics · Zeta potential · Dispersion · Sonication

---

M. R. Taha (✉) · J. M. Alsharif  
Universiti Kebangsaan Malaysia, Bandar Baru Bangi, 43600 Selangor, Malaysia  
e-mail: [profraihan@ukm.edu.my](mailto:profraihan@ukm.edu.my)

## 1 Introduction

Zeta potential ( $\zeta$ ) or electrokinetic potential is an important electrochemical characteristic of a clay. It measures the electrical potential at the shear plane of the electric double layer of clay-water suspension system. Theoretically, zeta potential is directly proportional to electrophoretic mobility and viscosity of solution, and inversely proportional to dielectric constant and Henry's function.

Nanocarbons (NC) have been studied and used in many applications including geoenvironmental engineering. Dispersion is one of the critical factors that strongly influence the properties of material-NC composites [1–4]. Since dispersion is related to adsorption and desorption efficiency of soil-NC system, zeta potential can be used to study soil-NC dispersion behavior.

Generally, NC have relatively high melting point close to 4000 K or 3675 °C [5], exhibiting a super hydrophobic property and chemically inert material [6], and have a strong tendency to agglomerate due to the presence of attractive van der Waals forces causing the fibers to tend to agglomerate preventing their dispersion in solvents [7, 8].

In soil-NC applications, it is important to ensure good dispersion of the NC so that efficient interaction can take place. For example for desorption of contaminants from soils, if the NC is allowed to clog together forming lumps, its exposure to the contaminants will be not be maximized and desorption will be difficult. Therefore, deagglomeration and subsequent distribution of NC within matrices is very important to ensure high interface exposure between interacting bodies.

The most commonly used procedure for dispersion is through the chemical route, i.e. the use of chemicals (mainly surfactants, polymers, functionalization, etc.) [9]. However, many of the chemicals used showed a negative effect on nanomaterials as they digest the fibers causing the fibers to become less effective. In addition, surfactants often cause bubbles to form in the composite materials reducing the strength of the end product [10].

The dispersion with nanomaterials are much complicated and sonication becomes very useful in aiding dispersion. The dispersion behavior of NCs with sonication depends on a few critical factors such as length of the nanomaterials, their entanglement density, volume fraction, duration sonication, etc. [11]. It has been reported Jiang et al. [12] that ultrasonication is external mechanical energy that helps the particles to overcome the attractive van der Waals forces at contact points or surfaces. They also reported that the NCs are negatively charged and tend to avoid coagulation by electrostatic repulsion above certain surface potentials, usually  $\pm 35$  mV. Consequently, by knowing the magnitude of the net surface potential, one can predict the possible aggregation behavior of CNTs [13]. In this study, mechanical (sonication) method have been studied to disperse NCs which was eventually used to examine its stability in soil–water system.

## 2 Materials and Methods

Two types of NCs were used i.e. carbon nanotube (CNT) and carbon nanofiber (CNF). These were the products of Arkema (France) and Pyrograf (USA), respectively. The CNT is marketed under trade name Graphistrength C100 is a multiwalled nanotube (MWNT) with dimensions of 1–10 microns in length and 10–15 nm in diameter (5–15 walls). CNF nanofiber material is a product designated as PR-24-XT-LHT. Some properties of the materials are provided in Table 1. The relative bulk size of CNT and CNF is shown in Fig. 1.

The Sonic Ruptor 250 Ultrasonic Homogenizer (USA) was used for sonication (Fig. 2). The ultrasonic tip used has a cylindrical-shaped medium-intensity ultrasonic processor with a diameter of 19 mm and a length of 10.5 cm. The device was operated

**Table 1** Properties of CNT and CNF used in this study

	Physical properties	Composition
CNT	<ul style="list-style-type: none"> <li>• Average diameter (nm) = 10–15</li> <li>• Average length (<math>\mu\text{m}</math>) = 1–10</li> <li>Apparent density (<math>\text{kg}/\text{m}^3</math>) = 50–150</li> <li>• Relative density (g/mL) at 25 °C = 2.1</li> <li>• Aspect ratio = 600–700</li> <li>• Applications = Reinforcements</li> </ul>	Carbon purity > 95%
CNF	<ul style="list-style-type: none"> <li>• Average Diameter, (nm) = 200</li> <li>• Average length (<math>\mu\text{m}</math>) = 50–200</li> <li>• Apparent density (<math>\text{kg}/\text{m}^3</math>) = 30–300</li> <li>• CVD carbon overcoat present on fiber = No</li> <li>• Nanofiber wall density, g/cc = 2–2.1</li> <li>• Aspect ratio = 1300–1500</li> <li>• Applications = Mechanical, and electrical</li> </ul>	Carbon purity > 98%

**Fig. 1** The relative bulk size of CNT and CNF

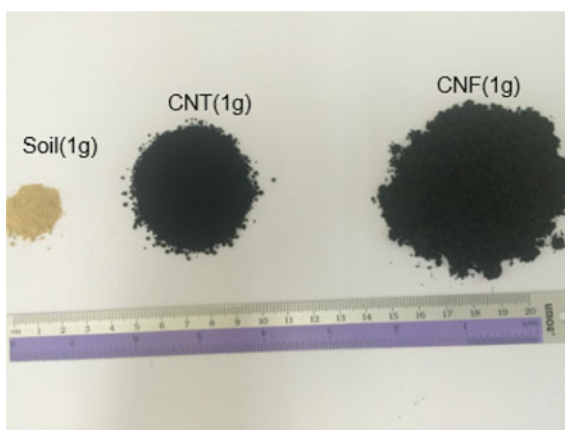


**Fig. 2** The sonic ruptor 250 ultrasonic homogenizer



at 50% of its maximum amplitude, delivering energy to the samples at a rate of 1900–2100 J/min. The energy was applied in cycles of 2 s to prevent the suspensions from overheating.

### 3 Results and Discussion

The results of the zeta potential ( $\zeta$ ) measurements for various testing combinations (obtained using the RSM Design-Expert v11.0 software) are tabulated in Tables 2 and 3. Based on Parveen et al. [14],  $\zeta$  of 0–5 mV indicates rapid coagulation of flocculation, 10–30 mV = incipient instability, 30–40 mV = moderate stability, 40–60 mV = good stability, > 60 mV = excellent stability.

For CNT, the results indicates that out of the 17 runs, 8 yields results of good stability or better ( $\zeta$  value greater than 40 mV). Out of these, sonication time of 7 min appeared to be the most favorable yielding excellent stability ( $\zeta = 62$  mV). Controlling sonication energy is important in order not to cause unwanted CNT particle breakages [15]. This study also showed that more sonication time (12 min in this case) generally results in low  $\zeta$ . So it is important that sonication time is controlled to achieve best results for dispersion stability. The most effective combination (Run #8 shown in Table 2) also results in the use of least amount of CNT (0.25 g) which is very advantageous considering the price of the material. A high amount of CNT also causes reduced water space in the system rendering low  $\zeta$ . Siljander et al. [16] also showed similar results and obtain highest conductivity (high  $\zeta$ ) for nanocellulose-CNT films with relatively low amount of CNT.

The results for CNF also show similarity with those of CNT. In addition to 8 runs resulting in good stability of better, the 7 min sonication time also produces

**Table 2** Results for CNT

Run#	A: Time (m)	B: CNT (g)	C: Water (ml)	$\zeta$ : (mV)
1	2	2.13	50	40
2	2	2.13	200	33
3	12	2.13	200	23
4	12	2.13	50	2
5	7	4	50	10
6	7	2.13	125	50
7	12	0.25	125	21
8	7	0.25	200	62
9	7	4	200	34
10	7	2.13	125	41
11	2	0.25	125	42
12	2	4	125	20
13	7	0.25	50	35
14	12	4	125	5
15	7	2.13	125	51
16	7	2.13	125	55
17	7	2.13	125	54

**Table 3** Results for CNF

Run#	A: Time (m)	B: CNT (g)	C: Water (ml)	$\zeta$ : (mV)
1	12	0.05	125	49
2	7	0.05	200	9.8
3	7	2	200	51
4	7	1.02	125	42
5	7	1.02	125	43.7
6	12	1.02	200	26.6
7	7	0.05	50	24
8	7	1.02	125	39.5
9	7	1.02	125	40
10	7	1.02	125	43
11	2	1.02	50	27
12	7	2	50	9.8
13	12	1.02	50	3.5
14	2	1.02	200	40
15	2	2	125	43
16	2	0.05	125	10.4
17	12	2	125	34

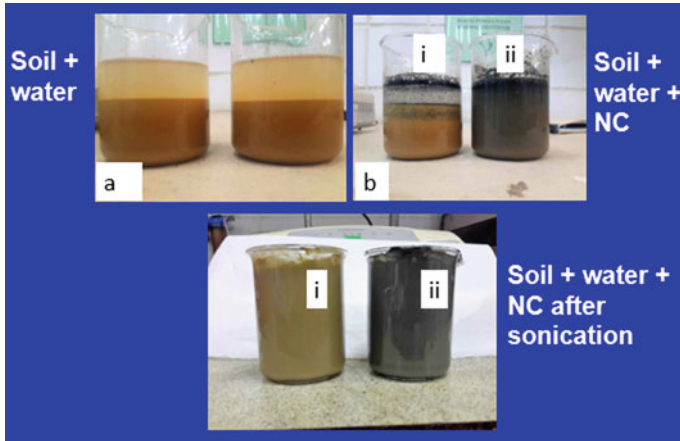


**Fig. 3** Stability of soil-NC mix before and after sonication (i) CNT (ii) CNF

good stability in the many combinations yielding the highest  $\zeta$  (51 mV). However, considering the amount of materials needed for good stability, the 12 min sonication time (Run#1 in Table 3) combination is more favorable as it uses much less CNF to attain almost similar  $\zeta$  values (49 mV). In general, it is found that the  $\zeta$  of CNT-water system is greater than that of CNF possibly due to greater density (larger size and longer) of the CNF.

Figure 3 illustrates the importance of dispersion of NC when in a soil-NC matrix. The soil-NC undergoing regular mechanical mixing (hand mix or using a stirrer) without sonication system shows a mixture of less stability. The homogenized mix as shown at the bottom of Fig. 3 is the product of sufficient sonication. It was also demonstrated that with sufficient sonication, this mix is stable after 30 days (Fig. 4). A higher soil–water ratio mix also show a more stable product. i.e. the water is less segregated and mostly remained within the matrix.

In many applications with nanomaterials, such as for soil improvement or remediation purposes, the high surface value of these nanomaterials due to its nano size is of prime importance. Its excellent reactivity comes from great surface exposure and its interactions with water and soil will be greatly affected if the form lumps and clod together in the matrix. In addition, disentanglement of the nanomaterials is very important so that it could also “reach out” and forming the required bridging process rendering the matrix stronger and more compact (Fig. 5). Thus, in order to disperse the nanomaterials, sonication is one of the possible routes especially in preventing other complex chemical reactions taking place with the use of other chemicals for dispersion.



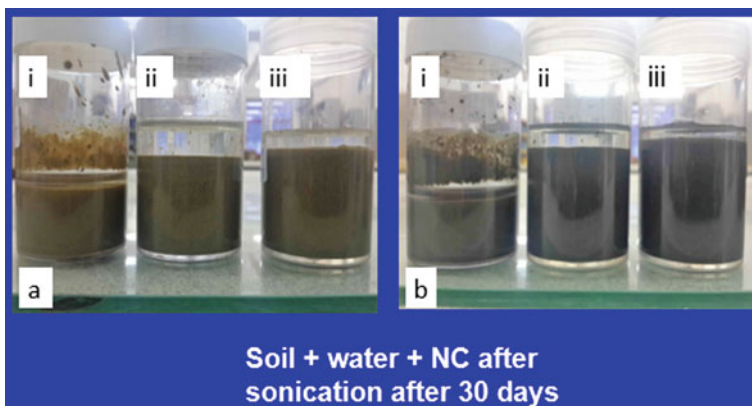


**Fig. 4** Stability of soil-CN mix with sonication after 30 days (a) CNT (b) CNF (i, ii, and iii indicates different soil–water ratios, i.e. soil–water ratios 1:1, 1:2, and 1:4)

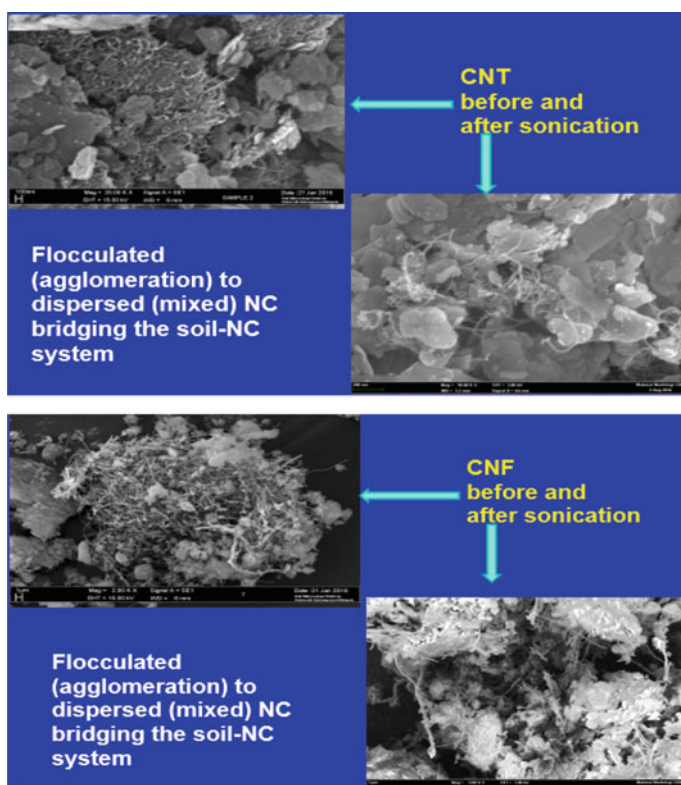


**Fig. 5** FESEM (field emission scanning electron microscope) photo of CNT and CNF before and after sonication

## 4 Conclusion

In this study, the application of sonication for dispersion of nanocarbons (NCs) in water is evaluated through measurement of the mixture zeta potential. Two type of NCs were used i.e. carbon nanotubes (CNT) and carbon nanofibers (CNF). These nanomaterials are made of pure carbon and are known to be insoluble in water making dispersion difficult to achieve. Amongst the variables chosen were sonication time, weight of nanomaterials and volume of water. The results show that under controlled conditions, a high zeta potential can be achieved and good to excellent dispersion can be obtained. Good dispersion is necessary in various geotechnical and geoenvironmental applications so that the surface area of the nanomaterials is fully exposed for the required interactions to take place efficiently.

**Acknowledgements** The authors gratefully acknowledge the Ministry of Education Malaysia for their financial support made through the Center for Research and Innovation Management (CRIM) of Universiti Kebangsaan Malaysia (UKM).

## References

1. Firoozi AA, Taha MR, Khan TA, Hejazi F, Firoozi AA, Alsharef JM (2019) A novel method for mixing nanomaterials with soil. *Nano Hybrids Compos* 25:46–48
2. Taha MR, Alsharef JMA (2018) Performance of soil stabilized with carbon nanomaterials. *Chem Eng Trans* 63:757–762
3. Taha MR, Alsharef JMA (2018) Effect of dispersion of nanomaterial on adhesion properties of soil using atomic force microscopy. *Int J Adv Mech Civil Eng* 5(2):8–12
4. Taha MR, Alsharef JMA, Khan AA, Aziz M, Gaber M (2018) Compressive and tensile strength enhancement of soft soils using nanocarbons. *Geomechd Eng* 16(5):559–567
5. Jorio A, Dresselhaus G, Dresselhaus MS (2007) Carbon nanotubes: advanced topics in the synthesis, structure, properties and applications. Springer, Heidelberg, p 720
6. Wang Z, Ci L, Chen L, Nayak S, Ajayan PM, Koratkar N (2007) Polarity-dependent electrochemically controlled transport of water through carbon nanotube membranes. *Nano Lett* 7(3):697–702
7. Alsharef JMA, Taha MR, Firoozi AA, Govindasamy P (2016) Potential of using nanocarbons to stabilize weak soils. *Appl Environ Soil Sci* 2016:9 Article ID 5060531
8. Alsharef JMA, Taha MR, Khan TA (2017) Physical dispersion of nanocarbons in composites—a review. *Jurnal Teknologi* 79(5):69–81
9. Ausman KD, Piner R, Lourie O, Ruoff RS, Korobov M (2000) Organic solvent dispersions of single-walled carbon nanotubes: toward solutions of pristine nanotubes. *J Phys Chem B* 104(38):8911–8915
10. Mo Y, Roberts RH (2013) Carbon nanofiber concrete for damage detection of infrastructure, Chapter 7. In: Maguire R (ed) *Advances in nanofibers*. InTechOpen, London
11. Sobolkina A, Mechtcherine V, Khavrus V, Maier D, Mende M, Ritschel M, Leonhardt A (2012) Dispersion of carbon nanotubes and its influence on the mechanical properties of the cement matrix. *Cement Concr Compos* 34(10):1104–1113
12. Jiang L, Gao L, Sun J (2003) Production of aqueous colloidal dispersions of carbon nanotubes. *J Colloid Interface Sci* 260(1):89–94
13. Vaisman L, Marom G, Wagner HD (2006) Dispersions of surface-modified carbon nanotubes in water-soluble and water-insoluble polymers. *Adv Func Mater* 16(3):357–363

14. Parveen S, Rana S, Fanguero R (2013) A review on nanomaterial dispersion, microstructure, and mechanical properties of carbon nanotube and nanofiber reinforced cementitious composites. *J Nanomater* 2013:1–19
15. Huang YY, Terentjev EM (2012) Dispersion of carbon nanotubes: mixing, sonication, stabilization, and composite properties. *Polymers* 4:275–295
16. Siljander S, Keinänen P, Rätty A, Ramakrishnan KR, Tuukkanen S, Kunnari V, Harlin A, Vuorinen J, Kanerva M (2018) Effect of surfactant type and sonication energy on the electrical conductivity properties of nanocellulose-CNT nanocomposite films. *Intl J Mol Sci* 19(6):1819

# Slope Stability Under Extreme Rainfall Conditions



Kübra Fitnat Ayvalik  and Seda Durukan 

**Abstract** It is known that natural or cut slopes are usually unsaturated soils. A slope may lose its current stability because of the decrease in matric suction due to the increase in water content. One of the reasons that can cause an increase in water content is rainfall, which is an environmental issue. The failure of a natural and/or cut slope triggered by a rainfall may cause environmental disasters resulting in fatal losses and injuries as well as economic damages. This study covers the stability of natural slopes under extreme rainfall conditions. During the stability analysis, a numerical analysis program was used which utilizes finite difference formulations. The slope model used in the study was designed to represent a classical natural slope dimensions and two different soil types were selected to compare; both are silty soils but having different suction characteristics and hydraulic conductivities. Three rainfall intensities have been selected and the two were from the recorded past events. The first is a long-term precipitation with low intensity, and the second and the third ones are short-term intensive precipitations, and all the rainfall models were acted individually with the same antecedent saturation degree. The factor of safety values was calculated for each situation and compared as well. As a result of the analysis, it has been seen that slope stability analysis of the unsaturated soils are very depended on their suction characteristics and hydraulic conductivities even though they have similar mechanical properties.

**Keywords** Slope stability · Landslides · Rainfall · Unsaturated soils

## 1 Introduction

Natural slopes are usually in unsaturated conditions having particularly steep slopes with very deep water table levels. Conventional approaches on slope stability suggested the evaluation of classical soil mechanics assumptions, however, the problem with the natural slopes is that slopes may lose their stability after subjected

---

K. F. Ayvalik · S. Durukan (✉)  
Manisa Celal Bayar University, Manisa, Türkiye  
e-mail: [seda.durukan@cbu.edu.tr](mailto:seda.durukan@cbu.edu.tr)

to a rainfall due to the increase in their saturation and so to the decrease in their suction stresses [1–3]. Thus, unsaturated soil mechanics approach is needed which includes the hydromechanical properties of the soil such as the hydraulic conductivity and the retention capacity. Careful attention is necessary when evaluating the stability of a natural slope and possibility of a landslide because of the fatal losses and undesired economic outcomes. The research of a possible landslide includes the rainfall characteristics of the site as well as the geological and geotechnical parameters. Some studies suggested practical landslide possibility approaches related only to the rainfall characteristics such as duration and intensity, however, it is obvious that soil properties may change the possibilities in every chance. Such early warning systems for possible landslides were suggested in literature regarding all the factors including the rainfall and soil properties [4–6].

Conventional technique to evaluate the landslides according to the rainfall threshold criteria, the thresholds are arranged by using scatter plots of rainfall intensity and duration or antecedent and daily rainfall settings [7–9]. Naidu et al., utilized cluster analysis method to demonstrate rainfall threshold triggering the landslides in Amboori, Kerala, India, which is a tropical area [6]. In the study, 2, 3 and 5-day antecedent rainfall clusters were modeled, and regression analysis was performed. When 5-day antecedent rainfall was zero, a single rainfall of 80.7 mm was found to trigger a landslide. In addition, almost 20% of triggering was found to be happened following the 5-day antecedent rainfall. The study suggested to use rainfall threshold criteria and also recommended to calculate the factor of safety values as well. Nazrien et al., investigated the effect of extreme rainfall events on riverbank slopes considering the historical rainfall data along with hydro-mechanical properties of the soil including the seepage analysis and factor of safety calculations [10]. According to the study, pore pressure distribution was found not only depended on rainfall infiltration and analysis type but also the geometry.

Kristo et al., investigated the historical rainfall of Singapore from two stations for the period of 1985–2009 and analyzed the rainfalls by duration with linear regression [5]. Due to the effect of climate change, an increase in the rainfall, in instance, longer durations was found. Regarding the past data a projection study was done, and possible rainfall intensities were determined. Factor of safety values were calculated for projected future data for years of 2003, 2050 and 2100 and, a significant decrease was found in factor of safety data for increasing years. Throughout the study, a simplified soil profile was modeled and calculated in SEEP/W for a typical residual soil along with its hydromechanical properties such as soil water characteristics curve (SWCC), hydraulic conductivity function (HCF) and classical strength characteristics.

Strong relations were found between rainfall and soil moisture conditions at an event of a landslide [11–14]. Godt et al., argued the relationship with antecedent rainfall and landslides [15]. According to the findings, even though the heavy rainfalls, conditions following a dry period were not likely found to cause a landslide while a relatively low intensity rainfall following a wet period did. A serious landslide took place in Italy, the Torgiovetto landslide, in 2003 [4]. After the landslide, many data had been collected with an extended monitoring work including the meteorological

and hydromechanical parameters. These measurements showed that still there were such movements in the wedge at heavy rainfall periods [16] and this was explained by the reduction in shear strength due to the increase in saturation and pore pressures caused by the rainfall. In addition, during the dry periods, the increase in water level was not sufficient enough to cause a landslide alone [16].

This study aims to investigate the behavior of a typical unsaturated slope under varying extreme rainfall conditions for two different soils having the same antecedent saturation degree. In this regard, a slope model was used to represent a classical natural slope in a numerical analysis program which utilizes finite difference formulations and, two different soil types were selected to compare; being both silty soils with different suction characteristics and hydraulic conductivities.

## 2 Materials and Method

A representative slope was modelled in the numerical analysis program, Fast Lagrangian Analysis of Continua (FLAC) which is a finite difference code software [17]. FLAC is able to run two-phase flow (tp-flow) of water and air in a 2D environment representing an unsaturated soil and computes the stability of a slope through deformation analysis. Two different soils were used during the analysis, soil1 was the one given in the manual of the FLAC, similarly, the slope geometry was also chosen as the one used in FLAC manual (see Fig. 1) and soil2 was the other soil sample used for comparison purposes. The geotechnical and hydromechanical properties of the soils used during the modelling study are presented in Table 1. For both soils the antecedent saturation degree was chosen to be the same which is 54%.

Three rainfalls were used in the models. The first one (R1) is a fictional long-term precipitation with relatively low intensity, and the second (R2) and the third (R3) ones were selected from the historical records as short-term intensive precipitations. Second and the third rainfall intensities were selected according to the historical extreme rainfall data given in the web site of Turkish State Meteorological Service [18]. The selected rainfalls are listed in Table 2.

Slope soil was arranged to have an antecedent saturation degree of 54% and then, the analyses to calculate the factor of safety were run. Afterwards, each precipitation was applied and analyzed for the final factor of safety values.

## 3 Results

Three rainfall intensities were used to understand and compare the soils' slope stability behavior under heavy precipitations. Initially the model was arranged to have a saturation degree of 54% according to the soil properties. Following, the factor of safety values for soil1 and soil2 were calculated and noted as the initial

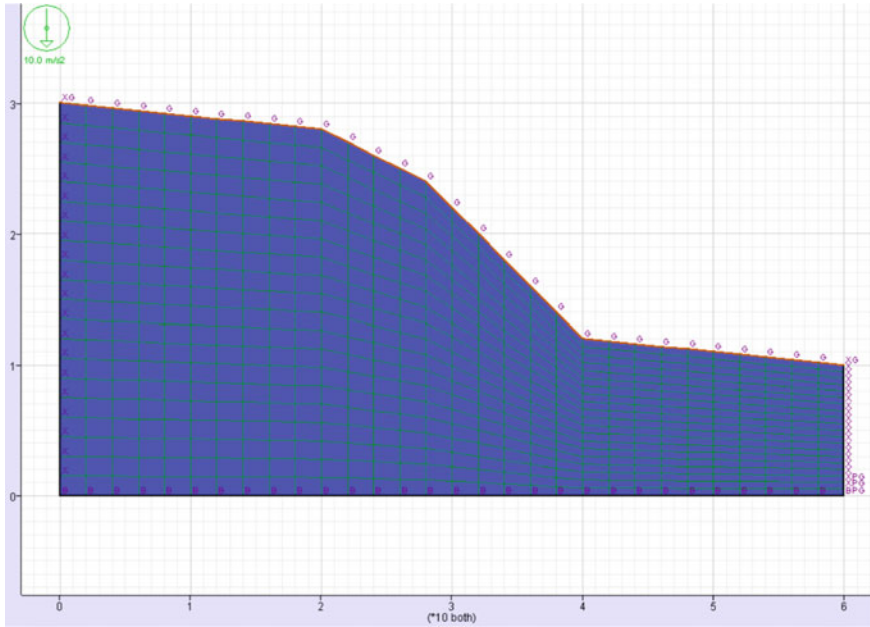


**Fig. 1** The slope model in FLAC

**Table 1** Some geotechnical and hydromechanical properties of the soils

Property	Soil1	Soil2
Dry density (kg/m <sup>3</sup> )	2000	1750
Drained cohesion (Pa)	0	5000
Drained friction angle (degrees)	30	28
Mobility coefficient (m <sup>2</sup> /(Pa-s))	10 <sup>-9</sup>	10 <sup>-10</sup>
Porosity	0.1	0.25
Van Genuchten parameter, a	0.336	0.304
Van Genuchten parameter, P <sub>0</sub> (MPa)	0.015	0.022
Antecedent saturation degree (%)	54	54
Initial pore pressure (Pa)	-45,203	-83,947

**Table 2** Rainfall intensities and durations

Rainfalls	Duration (min)	Intensity (mm)	Location	Date
R1	2880	120	Fictional	Fictional
R2	60	133.8	Bartın	2021
R3	15	70.7	Hopa	1998

state of the slopes. Afterwards, each rainfall was applied individually as precipitations to the upper layer. The analyses were run for different durations in order to determine whether the slope lost its stability under the actual rainfall duration or how much time it needed to lose its stability. As an instance, the initial and final visual presentations of soil1 representing before and after saturation degrees when subjected to R1 for 48 h in Fig. 2. Finally, the factor of safety results were gathered and presented in Table 3. Both soil1 and soil2 were found to be stable at the initial state where the saturation degree was 54%. However, the factor of safety value of soil1 (1.248) was lower than that of soil2 (1.646) at the initial phase. The initial pore pressures for soil1 and soil2 happened to be  $-45,203$  Pa and  $-83,947$  Pa, respectively. Considering the difference of pore pressures and similarity of mechanical properties, suction characteristics seemed to be effective on the factor of safety calculations.

Soil1 and soil2 under relatively low precipitation (R1) were stable at the end of 48 h even though soil1 reached the critical limit value. Actually, in many cases this situation should be considered as not safe and for practical purposes soil1 can be accepted as failed. In addition, soil2 was found to fail when the rainfall lasted at least 13 days which is far more from the actual realistic conditions. Both soils failed against R2 precipitation. Moreover, when the time needed for losing the stability was checked, it was seen that 19 min were enough for soil1 to lose its stability while 40 min were needed for soil2. The actual duration of R2 was recorded as 60 min. When the R3 precipitation was considered, soil1 lost its stability immediately in a couple of minutes while soil2 was still stable at the end of 15 min. The time needed to lose the stability for soil2 against R3 was found to be 30 min which may be considered as a possible duration for R3. When the dry densities of soil1 and soil2 were compared, it is seen that soil1 had a higher density. The mechanical properties were also different: no effective cohesion was defined for soil1 where a low amount of cohesion was set for soil2 and, the drained friction angles were also different but overall, the mechanical properties were not much far from each other. The critical difference was at their hydraulic conductivities and suction values such as air-entry value. Furthermore, the difference in the pore pressures of the soils at the initial state was almost twofold. Finally as a result, soil2 found to be more resistant to rainfall triggering landslides when compared to soil1.

## 4 Conclusions

The failure of a natural and/or cut slope triggered by a rainfall may cause environmental disasters resulting in fatal loses and injuries as well as economic damages. This study covers the stability of natural slopes under extreme rainfall conditions via numerical analysis using FLAC code. Three rainfall intensities have been selected: a long-term precipitation with relatively low intensity, and the second and the third ones being short-term intensive precipitations. All rainfall models acted separately with the same antecedent saturation degree which is 54%. Soil1 seemed to fail for



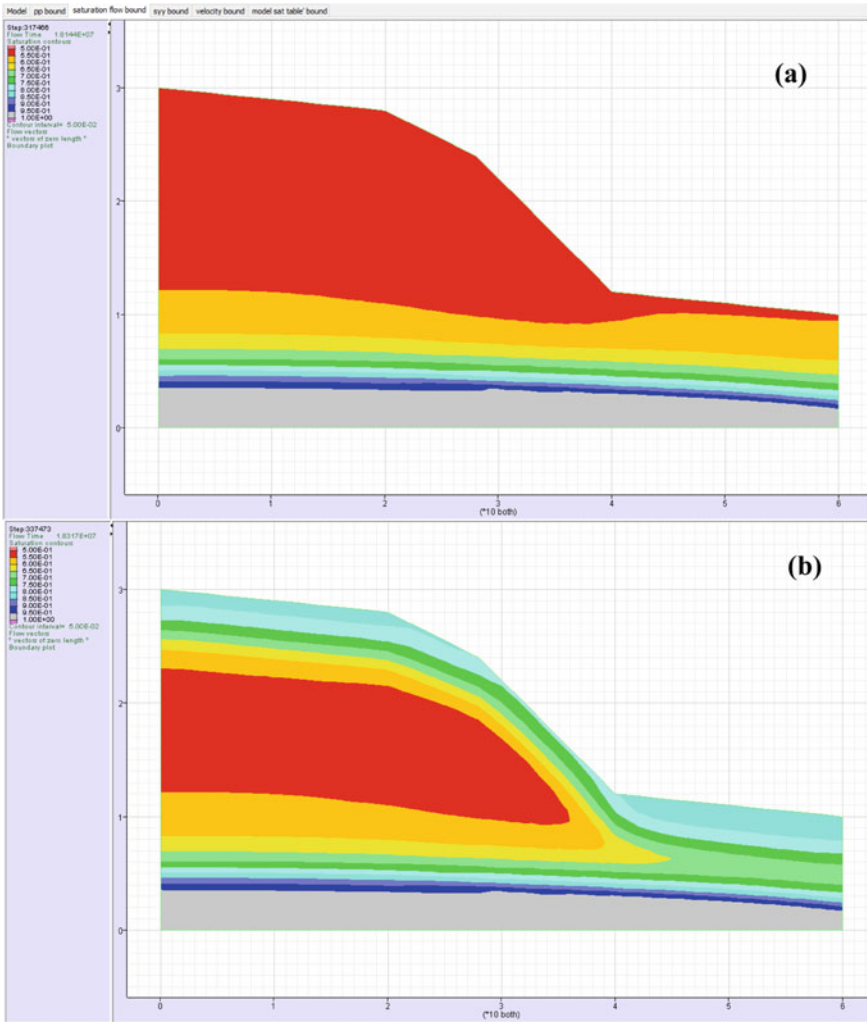


**Fig. 2** The saturation degree distribution of soil I **a** at its natural state before rainfall **b** after subjected to R1 for 48 h

**Table 3** Initial and final factor of safety (FoS) values of soils

Soil	FoS			
	Initial	R1 final	R2 final	R3 final
Soil1	1.248	1.088	< 1	< 1
Soil2	1.646	1.584	< 1	1.639

every rainfall conditions where soil2 remained stable for R1 and R3 precipitation conditions and failed under R2 conditions. Overall, soil2 was found to be more resistant to rainfall triggering landslides when compared to soil1 possibly due to the effect of the suction characteristics in terms of favorable contribution of negative pore pressures.

## References

1. Fredlund DG, Morgenstern NR, Widger RA (1978) The shear strength of unsaturated soils. *Can Geotech J* 15:313–321
2. Oh WT, Vanapalli S (2018) Undrained shear strength of unsaturated soils under zero or low confining pressures in the vadose zone. *Vadose Zo J* 17(1):180024
3. Zhang LL, Fredlund DG, Fredlund MD, Wilson GW (2014) Modeling the unsaturated soil zone in slope stability analysis. *Can Geotech J* 51(12):1384–1398
4. Intriери E, Gigli G, Mugnai F, Fanti R, Casagli N (2012) Design and implementation of a landslide early warning system. *Eng Geol* 147–148:124–136
5. Kristo C, Rahardjo H, Satyanaga A (2017) Effect of variations in rainfall intensity on slope stability in Singapore. *Int Soil Water Conserv Res* 5(4):258–264
6. Naidu S, Sajinkumar KS, Oommen T, Anuja VJ, Samuel RA, Muraliedharan C (2018) Early warning system for shallow landslides using rainfall threshold and slope stability analysis. *Geosci Front* 9(6):1871–1882
7. Gariano SL, Brunetti MT, Iovine G, Melillo M, Peruccacci S, Terranova O, Vennari C, Guzzetti F (2015) Calibration and validation of rainfall thresholds for shallow landslide forecasting in Sicily, southern Italy. *Geomorphology* 228(1):653e665
8. Marra F, Nikolopoulos EI, Creutin JD, Borga M (2016) Space-time organization of debris flows-triggering rainfall and its effect on the identification of the rainfall threshold relationship. *J Hydrol* 541(Part A):246e255
9. Ponziani F, Pandolfo C, Stelluti M, Berni N, Brocca L, Moramarco T (2012) Assessment of rainfall thresholds and soil moisture modeling for operational hydrogeological risk prevention in the Umbria region (central Italy). *Landslides*. <https://doi.org/10.1007/s10346-011-0287-3>
10. Nazrien Ng J, Mohd Taib A, Razali IH, Abd Rahman N, Wan Mohtar WH, A Karim O, Mat Desa S, Awang S, Mohd MS (2022) The effect of extreme rainfall events on riverbank slope behaviour. *Front Environ Sci* 10:859427
11. Ray RL, Jacobs JM (2007) Relationships among remotely soil moisture, precipitation and landslide events. *Nat Hazards* 43:211–222
12. Ray RL, Jacobs JM, Ballester TP (2011) Regional landslide susceptibility: spatiotemporal variations under dynamic soil moisture conditions. *Nat Hazards* 59:1317–1337
13. Ren D, Fu R, Leslie LM, Dickinson RE (2011) Predicting storm-triggered landslides. *Bull Am Meteorol Soc* 92:129–139
14. Salciarini D, Tamagnini C, Conversini P (2010) Discrete element modeling of debris-avalanche impact on earthfill barriers. *Phys Chem Earth* 35:172–181
15. Godt JW, Baum RL, Chleborad AF (2006) Rainfall characteristics for shallow landsliding in Seattle, Washington, USA. *Earth Surf Processes Landf* 31:97–110
16. Graziani A, Rotonda T, Tommasi P (2009) Stability and deformation mode of rock slide along interbeds reactivated by rainfall. In: *Proceedings of the first Italian workshop on landslides, Naples, Italy*, pp 62–71
17. FLAC, Itasca (2011) User's manual, FLAC 7.0. Itasca Consulting Group Inc., Minneapolis, Minnesota (USA)
18. Turkish state Meteorological Service Webpage. <https://mgm.gov.tr/veridegerlendirme/makimum-yagislar.aspx>. Last Accessed 25 May 2022

# Performance of Geocell Reinforced Expansive Soil Bed Under Circular Footing



Sanjeev Kumar , Sanjeev Naval, and Anil Kumar Sahu

**Abstract** This paper presents the results of laboratory model experiments on a circular foundation to better understand the performance of geocell reinforced expansive soil. The subsoil in this study was formed by naturally occurring expansive soil. To strengthen the soil bed, chevron-patterned geocells formed of polypropylene geotextile were used. Geocell mattress's height, geocell mattress's pocket size, and the geocell mattress's placement depth were all investigated in this testing program depth. In contrast to previous researchers, the reinforced bed's improved performance is determined to a settlement corresponding to the soil bed's failure settlement without reinforcement. The factors, non-dimensional, such as;  $I_f$  "bearing capacity improvement factor" and PRS% "settlement reduction factor", are used to evaluate the performance of reinforced beds. The use of geocell as a reinforcement caused a substantial bearing capacity increase as well as the decrease of footing settlement, as indicated by the test findings. The use of a geocell mattress of ideal proportions placed directly below the footing base increased the reinforced bed's bearing capacity greater than 200% and reduced footing settlement greater than 81%. The present study highlights the use of geocells toward the stabilization of the expansive soil.

**Keywords** Bearing capacity · Geocell mattress · Chevron pattern · Expansive soil · Circular footing

---

S. Kumar (✉)

Vaish Technical Institute, Rohtak, Haryana 124001, India

e-mail: [snjvbansal67@gmail.com](mailto:snjvbansal67@gmail.com)

S. Naval

DAV Institute of Engineering and Technology, Jalandhar, Punjab 144008, India

A. K. Sahu

Delhi Technological University, Delhi-110042, India

## 1 Introduction

Rapid urbanization necessitates the construction of structures on expansive soils. However, due to the shrinkage and swelling tendencies of these soils, it is difficult to construct any infrastructural facility atop them. The growth of infrastructure, particularly roads, railways, and buildings, is essential to the development of any location. Because these soils have extremely low shear strength, the performance of the buildings constructed atop them is a difficult task due to the risk of failures in bearing capacity and a significant consolidated settlement. To construct a stable and safe structure, the underlying expansive soil must be modified to enhance its carrying capacity. Stabilizing soils is among the most successful and dependable methods of increasing their strength because reinforcing soils improves the stability and bearing capacity while reducing settlement and lateral deformation [1–3]. Civil engineering projects are currently using a variety of materials in a number of shapes and approaches. The use of steel bars, fibers such as glass, polypropylene, polyesters, natural fibers such as palm, coir, jute, sisal, and so on has been acknowledged as an efficient soil reinforcement method [2, 4–6]. Metallic strips, meshes, polymeric fibers and grids have been widely utilized as planner reinforcement in the last few decades to strengthen foundations, highways, and the construction of wall [6–13]. Providing high strength geosynthetic reinforcement is yet another easy, quick, and cost-effective solution among the several stabilizing techniques available. Road construction accounts for approximately 80% of geosynthetics applications. The favorable effects of geosynthetic materials as reinforcement are primarily controlled by how they are utilized. Previously, the majority of research was conducted with geotextiles, geogrids, geomembranes, and geo-composites. However, there has been limited research undertaken with geocells in roadways on expansive soils. As a result, research on geocell reinforced pavements is required. The successful breakthrough in this area is the use of geocell, a three-dimensional confinement. A geocell mattress is a network of interconnected cells made of polymer geogrid strips. Geocells have been demonstrated to improve soil strength through limiting horizontal spreading, offering confinement, and resulting in the contained composite behaving more like rigid mattresses [14]. It intercepts the planes that may fail, and the rigidity of the mattress forces these deep into the underlying soil, thus increasing bearing capacity. Many researchers have already commented on the advantages of using geosynthetic materials as geocells.

Ghosh et al. [15] investigated the carrying capacity of a square footing lying atop pond ash and stabilized with jute geotextile. Latha et al. [16] conducted laboratory tests to investigate the geocell reinforcement benefits on the functioning of an earth embankment built atop a soft soil bed and to suggest a simple approach for designing a geocell-supported embankment. Through triaxial compression testing, Latha et al. [17] investigated the reinforcing form effects on geosynthetic reinforced sand strength increase. By conducting plate load tests on circular footing, Sitharam et al. [18] acquire a better understanding of how geocell reinforced soft soil, natural silty soil, and foundations behave under circular loading. Through large

scale model studies conducted according to similarity theory, Single cell reinforcement can increase load bearing capacity, stiffness, and percentage elastic deformation for each cycle, according to Pokharel et al. [19], however permanent deformation decreases. Dash [20] uses plate load tests on unreinforced and geocell reinforced sand beds to demonstrate the foundation soil's relative density effect on the geocell reinforcement behavior. Tafreshi and Dawson [21] conducted plate load experiments on strip footings installed on sand beds to determine bearing capacity when reinforced with geotextile that had the same characteristics as the geocell and planner form. Dash [22] used model plate load tests on strip footing to investigate the geocell reinforcement impact on sand bed load carrying ability. To assess the effect of subgrade layer strength, Biswas et al. [23] performed model load experiments on 150 mm diameter footing resting geocell reinforced foundation systems. To examine the geonet reinforcement impact on low compacted soft soil bearing capacity, Bazne et al. [24] used quantitative modeling and laboratory trials with varied compositions. Hegde and Sitharam [25] performed plate load testing and found that, where bamboo is abundant, both bamboo cells and bamboo grid as a reinforcement in planner form may be installed as a replacement for geocell and geogrid combinations. Indraratna et al. [26] used large-scale cubical triaxial experiments to compare the performance of unreinforced and reinforced sub ballast when subjected to cyclic loads. Shadmand et al. [27] studied load settlement characteristics of large footings, square shaped, using large scale loading tests on granular soils without and with geocell reinforcement, finding that geocell reinforced soils, like unreinforced soils, exhibit scale effect. Small-scale footing models cannot be readily compared to full-scale footings. Tavakoli and Motarjemi [28] investigated the soil's physical parameters' influence on the geocell reinforced granular soil interfacial properties by performing numerous large-scale direct shear tests. Kaur et al. [29] used numerical analysis to determine the geocell reinforced sand's bearing capacity and compared the findings to those obtained from a plate load test. The results of the program, Plaxis 3D, were found to be in accordance with those of the laboratory test. Kolathayar et al. [30] examined the bearing capacity and settlement characteristics of geocell, coir and HDPE, reinforced sand beds, as well as seashell sand beds, using many model plate load tests. The failure mechanism of geocells under tensile and shear loads was studied by Liu et al. [31], who presented the observed failure patterns as well as the development of consequences of practical geocell applications. Kuo and Chou [32] used three-dimensional FEM analysis to assess the geo-textile interlayer impact on flexible pavement performance. The study found that adding geo-jute to the mix enhances pavement performance by lowering stress, strain, and displacement at the subgrade's surface. Kolathayar et al. [33] performed model tests on clay beds stabilized with geocells fabricated from jute geotextile & sisal geotextile and compared the results obtained with those from the experiments on high density polyethylene geocell stabilized clay beds. Lal et al. [34] used plastic bottles and cut them to act as geocells for reinforcing sand. The results of the plate load tests indicated that compared to the unreinforced case, an improvement of 1.86 times over the geocell reinforced case were achieved. Kolathayar and Chitrachedu [35] evaluated the probability of using sand tire crumbs as an infill material compared to pure sand during the plate load

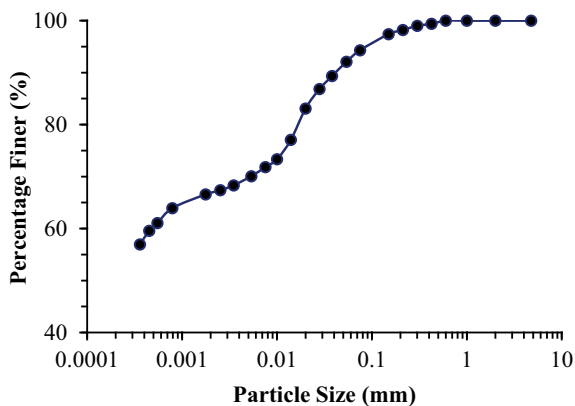
tests carried out on sand beds reinforced with high density polyethylene geocells and coir geocells. Gedela and Karpurapu [36] carried out numerical simulations using FALC<sup>3D</sup> software. The numerical simulations took into account an exact honeycomb shape as well as simplified geocell pocket shapes. The numerical modeling data was compared with the experimental data. Arvin et al. [37] carried out reduced-scale model tests on strip footing resting near an unreinforced and reinforced slope to investigate the bearing capacity and displacement behavior. During the experimentation, parameters like angle of slope, geocell embedment depth, geocell pocket size, and arrangement of double layer arrangement were discussed. Biswas et al. [38] conducted model tests and the influence of bamboo geocell and jute geocell with the provision of additional basal mat laid over the road pavement soft subgrade was investigated. The effect of different infill materials like sand, crushed aggregates, and recycled asphalt pavement was discussed. In the present research work, laboratory plate load tests were carried out using a model circular footing resting on a subgrade of geocell reinforced expansive soil. The main goal of the study is to demonstrate the benefit of using geocells as soil reinforcement to stabilize the expansive soil. During the research program, effect of different parameters like pocket size, height, and placement depth of geocell on the bearing capacity of a circular footing resting on expansive soil was considered.

## 2 Materials and Method

### 2.1 Materials

#### 2.1.1 Soil

The soil used in the study was a naturally occurring black cotton soil from the Banda district of Uttar Pradesh (India). It has a particle fraction percentage of 96% finer than 75 microns and a particle fraction percentage of 64.5% finer than 2 microns. Figure 1 depicts the particle size distribution curve. According to the Bureau of Indian Standard (BIS) Classification system, the expansive soil is classed as high plasticity clay and is denoted as CH. The soil's activity suggests that it is a normal active soil. Tests were conducted following procedures described in IS: 2720 and the index properties as listed in Table 1 were determined. A soil with greater activity, free swelling index, and plasticity normally has a higher tendency to swell. An X-ray diffraction analysis was conducted to determine the different minerals the procured soil contained. Figure 2 shows the result obtained from this analysis. This figure shows that the soil has quartz as a dominant constituent, while muscovite and talc are other major constituents.

**Fig. 1** Particle size distribution curve [39]**Table 1** Soil Properties [39]

Parameter	Value	
Specific gravity	2.63	
% Finer than 4.75 mm, %	100.00	
% Finer than 75 $\mu$ , %	94.00	
% Finer than 2 $\mu$ , %	64.50	
Liquid limit, %	87.24	
Plastic limit, %	37.56	
Plasticity index, %	49.68	
Free swelling index, %	72.50	
Activity	0.76	
Maximum dry density, kN/m <sup>3</sup>	14.85	
Optimum moisture content, %	22.50	
CBR, %	Unsoaked	6.28
	Soaked	1.82
Unconfined compressive strength, kN/m <sup>2</sup>	66.54	
Cohesion, kN/m <sup>2</sup> (uu Test)	33.27	

### 2.1.2 Geotextile

The geocell, a cellular confining structure, was fabricated from the woven polypropylene geotextile, PPMF-300, Fig. 3 and is available commercially. It was procured from M/s Filter Fabs, New Delhi, (INDIA). Different properties of the geotextile were determined following the procedures described in the relevant Indian Standard and are mentioned in Table 2.

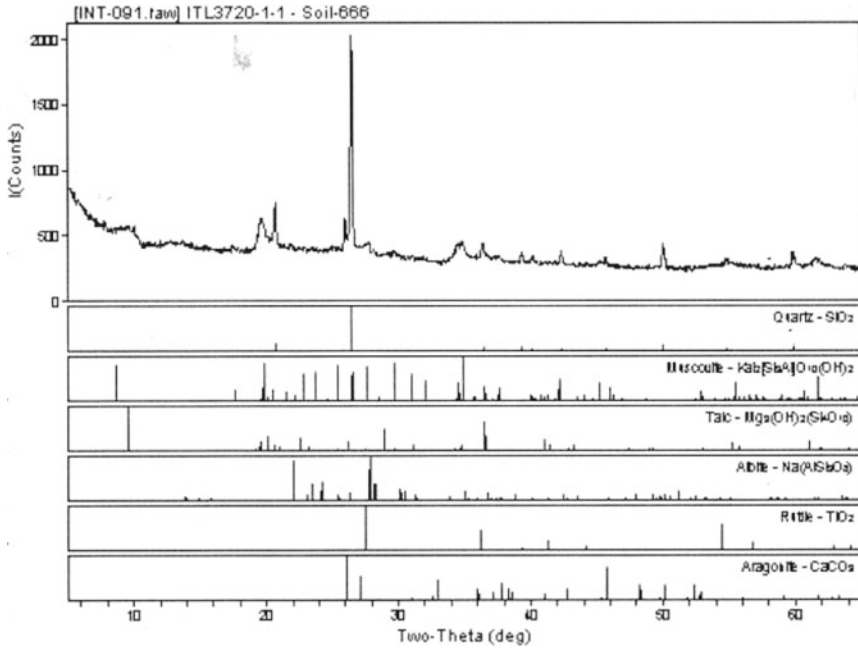
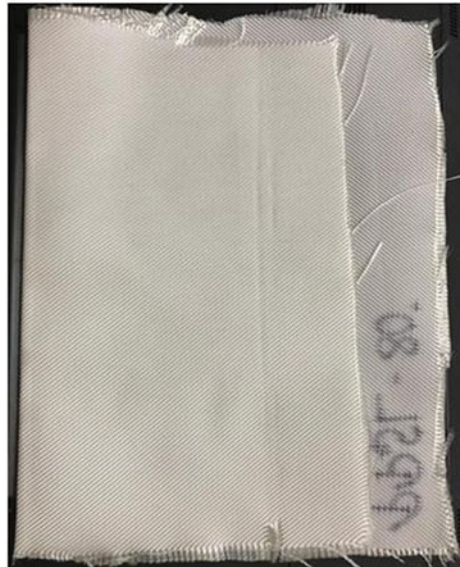


Fig. 2 X-ray diffraction analysis [40]

Fig. 3 Woven geotextile [40]





**Table 2** Geotextile Properties [40]

Parameter		Value
Thickness, mm		0.8
Weight per unit area, N/m <sup>2</sup>		3.4
Wide width tensile Strength, kN/m	WARP	80
	WEFT	70
Elongation at break, %	WARP	25
	WEFT	25
Joint strength, kN/m		13.4

## 2.2 Method

### 2.2.1 Test Setup

Laboratory plate load tests were conducted in a mild steel tank 1000 mm long, 1000 mm wide and 850 mm high. The yielding of the tank material, during loading of the model footing, was prevented through proper bracing of the tank sides with mild steel flats. A mild steel plate, 25 mm thick and 200 mm in diameter, was used as the model footing in this research programme. A thin sand layer mixed with epoxy glue was applied to the base of the model footing to roughen it [18, 21, 41–43]. A hydraulic jack, operated manually and resting against a reaction frame, was used to load the model footing. A pre-calibrated pressure gauge was mounted atop the pump, which was attached to the hydraulic jack, was used to measure the load increment applied to the model footing. Figure 4 shows the systematic diagram of the test setup.

**Fig. 4** Test setup of laboratory plate load test



### 2.2.2 Test Bed

Markings at a consistent distance of 50 mm along the test tank height were made to produce a test bed with uniform characteristics. Pulverized soil in the required quantity was blended with a specified amount of water to achieve the correct bulk density for each layer. To prevent loss of moisture content and to allow maturation, damp soil was then covered for 3–4 days. The matured wet soil was mixed one more time to ensure uniform water distribution before being placed in the test tank. Following soil placement in the tank, it was carefully leveled and compacted with a 48.9 N drop hammer of drop 450 mm to the requisite thickness using the reference markings made across the tank wall height. To ensure homogeneity of the prepared test bed, undisturbed samples were collected from numerous places during tank filling to determine the unit weight and moisture content of the compacted soil. Proctor's needle was used to check the same. As a result, sufficiently homogeneous test conditions were achieved during the testing program by carefully managing the moisture content and compaction effort.

### 2.2.3 Geocell Mattress

Strips of the required shape and size were cut from rolls of geotextile and joined in transverse and diagonal directions to make a chevron-patterned mattress, as shown in Fig. 5. Geocells with a chevron pattern perform better than those with a diamond pattern [41, 42, 44]. Nylon thread was used to stitch geotextile strips together in order to make geocell. To ensure that the tests were performed under uniform conditions, the number and length of stitches were kept constant for all geocells constructed during the testing session. The resulting geocell mattress was installed on the soil bed at the correct depth below the footing base, and its pockets were filled with damp soil. The soil in the geocell pockets was comparable to that in the subgrade layers underneath. Compaction in the geocell pockets was carefully regulated in order to achieve soil parameters identical to the underlying test bed. To determine the properties of compacted soil and to verify compaction quality, undisturbed soil samples were taken from a variety of locations within geocells.

### 2.2.4 Test Procedure

Reinforcement in the form of a geocell mattress was put atop the compacted earth bed across the entire plan area of the test tank. After filling the geocell mattress pockets with damp soil, the top surface was leveled, and the model footing, a 25 mm thick inflexible mild steel plate, was positioned along a predetermined alignment so that the load from the hydraulic jack could be applied with no eccentricity. To impart load, a hydraulic jack, operated manually, was inserted in between the footing and reaction frame. Between the footing surface and the hydraulic jack base, a mild steel plate 50 mm in diameter and 25 mm in thickness was inserted, thru which vertical

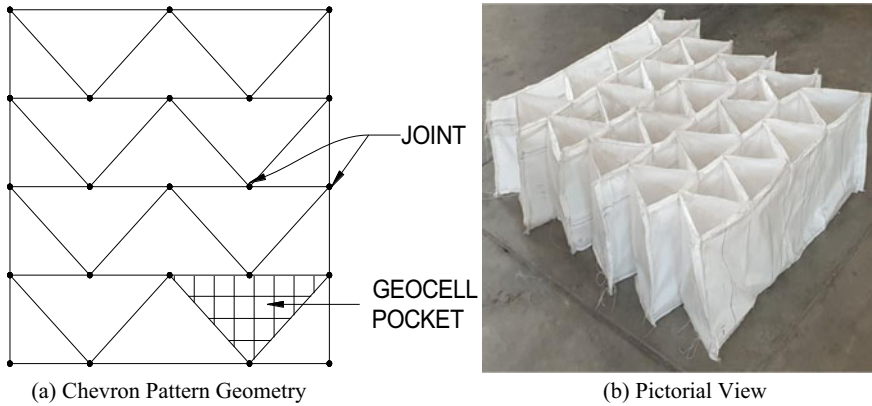


**Fig. 5** Geocell: chevron pattern

stresses were applied to the footing. A pre-calibrated pressure gauge mounted over the hydraulic jack pump was used to measure the applied load intensities. Loads were applied to the footing in increments, with a similar load in each increment, until failure or a settlement close to 50 mm was obtained. Footing settlement was measured using two dial gauges placed diametrically opposite one another along the footing's center line. Dial gauges were installed using steel beams resting on tank walls as a stable datum.

### 2.2.5 Test Parameters

The geometry of the problem under consideration in this research study is depicted in Fig. 6. All of the studies carried out throughout this research programme used a geocell mattress of the shape shown in Fig. 5. Four specific series of tests, as indicated in Table 3, were conducted by adjusting the parameters namely the placement depth ( $h$ ) beneath the footing base, the pocket size ( $d$ ), and the height ( $H$ ) of the geocell mattress. The diameter of an equivalent circle with an area equal to the opening of the geocell pocket is used to calculate the pocket size of the geocell. The series A tests were carried out on soil with no reinforcement, allowing for a direct comparison with the results of the series B, C, and D testing on geocell reinforced soil.

## 3 Results and Discussion

Figure 7 depicts the bearing pressure response behavior as a function of settlement for various geocell mattress heights. In the unreinforced instance, the bearing pressure-settlement curve slope is linear until a settlement of about 6% of the footing diameter

**Fig. 6** Test bed geometry

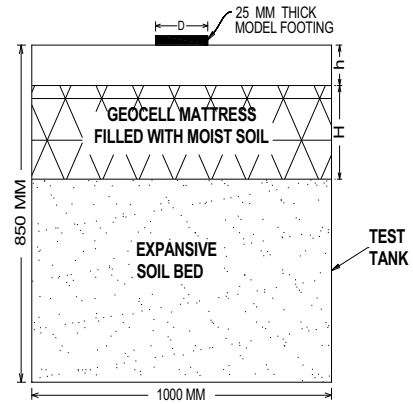


**Table 3** Details of model test programme

Test series	Reinforcement type	Test parameters
A	<i>Unreinforced</i>	Compacted at OMC
B	<i>Geocell</i>	
	Variable parameters	$h/D = 0, 0.05, 0.1, 0.2, 0.4, 0.6, 0.8, 1.0$
	Constant parameters	$H/D = 1, d/D = 1$
C	<i>Geocell</i>	
	Variable parameters	$d/D = 0.8, 1.0, 1.2, 1.4$
	Constant parameters	$H/D = 1, h/D = 0$
D	<i>Geocell</i>	
	Variable parameters	$H/D = 0.75, 1.25, 1.75, 2.25$
	Constant parameters	$d/D = 1, h/D = 0$

and decreases beyond that, suggesting that the footing is unable to sustain the additional applied pressure owing to soil bed failure. Furthermore, the response of the geocell reinforced cases demonstrates that as the bearing pressure-settlement curve approaches 10–12% of the footing diameter, a reduction in slope is observed. Beyond this settlement, the curve remains nearly steady, and the footing’s pressure bearing capability improves gradually. Because the foundation bed, consisting of geocell reinforced soil, continues to sustain additional applied loads, it can be assumed that by using geocell as reinforcement, no distinct failure was observed even up to a settlement of 25% of the footing diameter, the test’s terminal settlement. The ultimate bearing pressure at this settlement has grown to 2.45 times that of an unreinforced bed. Observations comparable to these were made in the majority of the other experiments. It could be because the existence of a geocell limits the soil, reducing the tensile stresses produced in the soil and so reducing the shape and size of the pressure bulb.

**Fig. 7** Bearing pressure—footing settlement response at different geocell mattress height

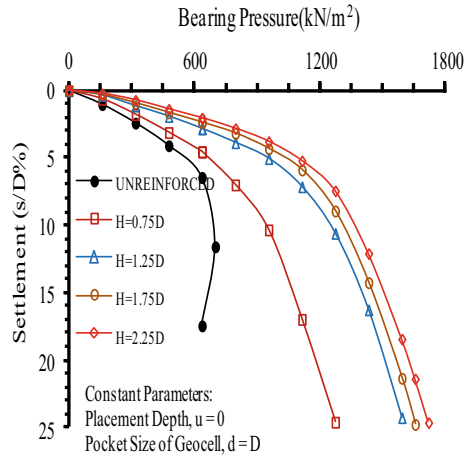
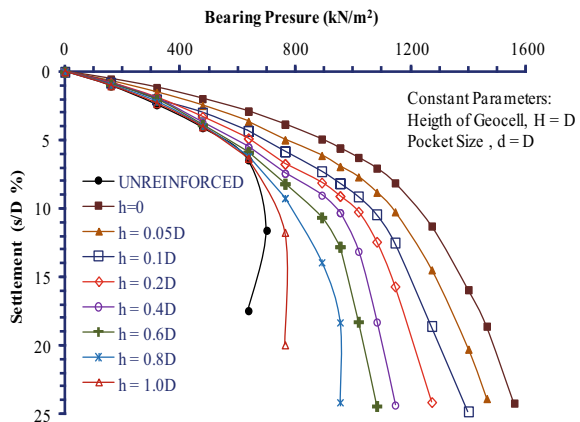


Figure 8 depicts the behavior of bearing pressure responses with footing settlement for different geocell mattress placement depths beneath the footing base. The bearing pressure-settlement curve behavior shows that for  $h/D$  ratios of 0.8 and 1, the ultimate bearing pressure is obtained distinctly, however, the footing continues to resist applied load until the experiment’s terminal settlement, for other  $h/D$  ratios. In both instances presented in Figs. 7 and 8, the bearing pressure-settlement curve remained linear until the footing settlement approached close to 5% in the unreinforced case and until 10–12% of the footing diameter for the geocell reinforced case, beyond which the curve slope diminished, showing that the composite, soil-geocell, began to break up locally due to the substantial settlement taking place under footing.

Sitharam et al. [18] found a similar finding for geocell reinforced soil beds, reporting a decrease in the slope of the pressure settlement curve at settlement near

**Fig. 8** Bearing pressure—footing settlement responses at different geocell mattress placement depths



10-15% of the footing diameter, following which the settlement slope remained practically constant while the footing bearing pressure continued to rise. The load bearing capability of the footing is reduced as a result of this phenomenon. No sign of failure for the geocell reinforced soil foundation bed was observed after this geocell reinforcement started resisting further applied load through mobilization of rigidity and anchorage derived from the adjoining stable soil mass, and for settlement approximately equal to 25% of the footing diameter. This could be because the reinforcing system operates as an interconnected cage with the geocell reinforcement. It drives an anchor from both sides of the loaded area due to frictional resistance. Furthermore, the geocell layer continues to support the footing even after shear failures of the soil mass inside the geocell pockets have occurred due to bending and shear rigidity. This function of the geocell layer is compared to that of a beam supporting a column in a structure. As a result, no unexpected failure was detected in soil reinforced by geocell reinforcement. This was confirmed when the geocell reinforcement was removed from the test tank after the testing were completed. Cell walls displayed buckling deformations that extended the full height of the geocell mattress, implying that the entire mattress behaved as a single unit.

With the inclusion of reinforcement, geocell mattress, the bearing capacity is analyzed using non-dimensional parameters such as (i) Bearing Capacity Improvement Factor, ( $I_f$ ) (ii) Percentage Reduction in Settlement, (PRS%). The bearing capacity improvement factor (this factor is just like the bearing capacity ratio chosen by Binquet and Lee [7] to evaluate increases in bearing capacity due to planner reinforcement, and it is also the same as the bearing capacity improvement factor ( $I_f$ ) adopted by the researchers [18, 21, 25, 41–43, 45] in the past for measuring the increase in bearing capacity) equates the bearing pressure of a bed reinforced with geocell reinforcement to a bed without reinforcement at a given footing settlement level. Mathematically:

$$I_f = \frac{\text{Bearing pressure of bed with geocell reinforced}}{\text{Bearing pressue of bed without geocell reinforced}} \quad (1)$$

The parameter percentage reduction in settlement, PRS%, which has been utilized by certain studies [18, 21] in the past, compares the settlement of a footing placed on a geocell reinforced bed to the settlement of a footing placed on an unreinforced bed at a given bearing pressure. Mathematically:

$$\text{PRS}\% = 1 - \frac{\text{Settlement of bed with geocell reinforced}}{\text{Settlement of bed without geocell reinforced}} \quad (2)$$

Footing settlement ( $s$ ), geocell mattress placement depth ( $h$ ), geocell mattress pocket size ( $d$ ), and geocell mattress height ( $H$ ) are all described as non-dimensional quantities in terms of  $D$ , the footing diameter, as ( $s/D$ ), ( $h/D$ ), ( $d/D$ ), and ( $H/D$ ) respectively.

The increase in soil bed bearing capacity due to reinforcement is generally calculated at a higher level of footing settlement, 35–50% of the footing width [18, 41–44].

In practice, this settlement level range cannot be too wide; thus, it may not be acceptable [21]. As a result, the current study improves the footing’s bearing capacity at a low settlement range,  $s/D = 12\%$ , which is equal to the ultimate failure pressure of a footing lying on an unreinforced soil bed.

### 3.1 Optimum Value of Geocell Mattress Placement Depth

Geocell mattress placement depth’s ( $h/D$ ) optimum value beneath the footing was investigated by performing the experiments listed in Table 3 under series B. During the tests, the parameter  $h/D$  was varied while the other parameters like  $H/D$  and  $d/D$  were held constant at 1.0, i.e. the footing diameter. Figures 9 and 10 depict the corresponding increase in bearing capacity.

For various placement depths ( $h/D$ ) of geocell mattresses, Fig. 9 shows the variation of BCIF ( $I_f$ ) with PRS(%). This figure reveals that the performance improvement in load bearing capacity and decrease in footing settlement increases continually as the geocell mattress placement depth is reduced. For depths ( $h/D$ ) less than 0.6, the performance improvement rate is greater. This implies that the soil mass within  $0.6D$  of the footing base is the most active and is more liable to be sheared. The comparatively stiff geotextile enters inside this depth when the geocell mattress placement depth is reduced, intercepting more slip planes and resulting in improved performance. Furthermore, when the geocell mattress is put very close to the footing base,  $h/D \leq 0.05$ , load bearing capacity and settlement reduction improve dramatically, as the footing rests almost completely on the stronger geocell mattress-soil composite. The rather stiff and rough geocell mattress provides friction and confinement to the soil resting over it, resulting in an increase in soil bed performance beyond  $0.6D$  placement depth of geocell mattress.

**Fig. 9** Variation of bearing capacity improvement factor with percentage reduction in settlement at various placement depths corresponding to ultimate bearing pressure and failure settlement of unreinforced bed

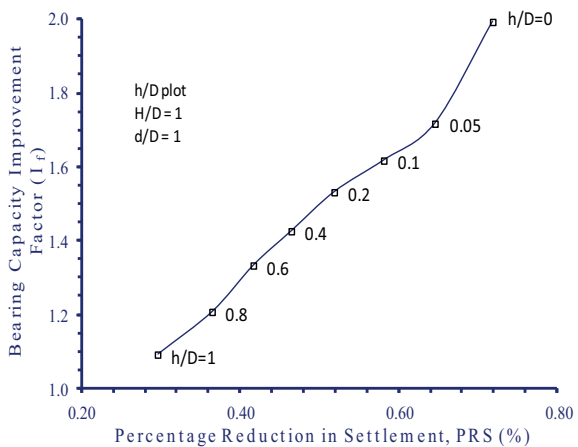
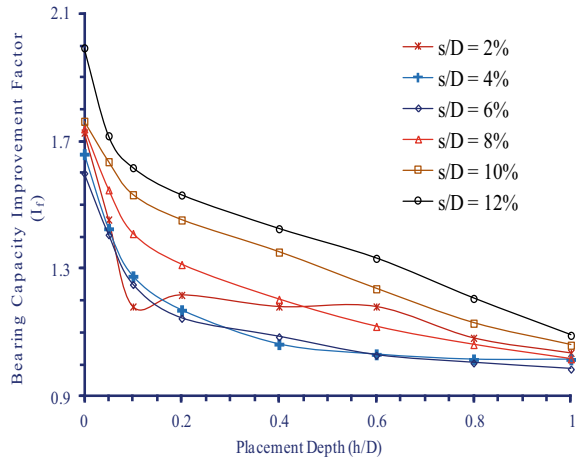


**Fig. 10** Variation of bearing capacity improvement factor with placement depth of geocell mattress at different footing settlement levels



Figures 9 and 10 show that as the geocell mattress placement depth below the footing base is reduced, the pressure bearing capability of the footing increases until it reaches its maximum value at  $h/D = 0$ . This finding is consistent with that of Sitharam et al. [18], who used geogrid to form geocells. The geocell reinforcement is a three-dimensional confining structure, and the soil lying freely in between the geocell mattress and footing base gets forced out under the pressure applied to the footing, resulting in a reduction in overall performance improvement. Furthermore, when the geocell mattress placement depth ( $h/D$ ) reached approximately equal to the footing diameter,  $h/D = 1$ , the effect of geocell reinforcement became negligible, and the reinforced bed behaved like an unreinforced bed. The pressure exerted by the footing on the soil mass beneath it may be the cause of this behavior. Because geocell placement is primarily focused on unreinforced soil bed at this depth, unreinforced failure mechanisms are more likely. When comparing the potential benefits of strengthening the sand bed with a planner and geocell kind of geotextile reinforcement, Tafreshi and Dawson [21] found similar results for geocell reinforcement.

### 3.2 Geocell Mattress Pocket Size Effect

The effects of different geocell mattress pocket sizes ( $d/D$ ) were determined by performing tests listed in Table 3 under test series C. The pocket size ( $d/D$ ) of the geocell mattress was altered during tests under this test series, while the values of other parameters such as  $H/D$  and  $h/D$  were kept constant at 1.0 and 0. Figure 11 depicts the variation of BCIF ( $I_f$ ) in relation to different geocell mattress pocket sizes. This plot demonstrates that when the geocell pocket size ( $d/D$ ) is reduced from 1.4 to 1.0, the improvement in bearing capacity occurs, but it reduces further when the pocket size is reduced to 0.8. Figures 12 and 13 demonstrate that increasing the



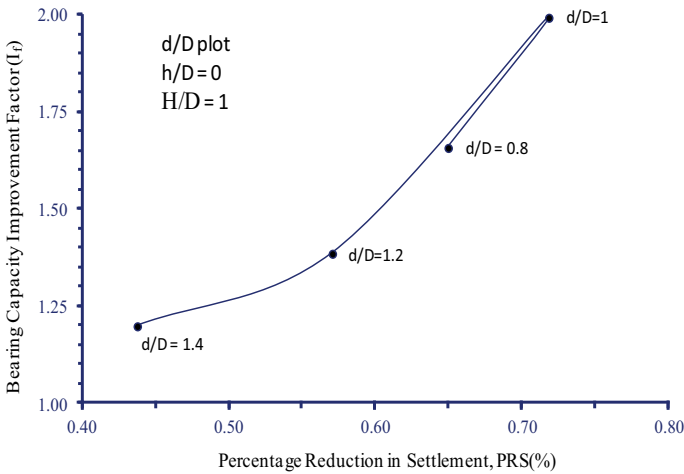


**Fig. 11** Variation in bearing capacity improvement factor with footing settlement factor for various geocell pocket sizes corresponding to ultimate bearing pressure and failure settlement of unreinforced bed

pocket size ( $d/D$ ) from 0.8 to 1.0 improves bearing pressure and percentage reduction in settlement. With each increase in pocket size, the performance improvement in footing’s settlement reduction and bearing capacity decreases dramatically. As a result, an optimal pocket size is reached when the ratio  $d/D$  equals unity, or 1. Figure 13 shows that when the pocket size ( $d/D$ ) is less than one, the settling reduction factor increases until reaches its maximum value when the pocket size becomes unity, i.e. equal to the diameter of the footing. When pocket size ( $d/D$ ) becomes greater than one, however, the settlement reduction factor falls again. This could be attributed to the confinement provided by the geocell pockets per unit volume, as well as an increase in the rigidity of the soil-geocell mattress composite.

### 3.3 Geocell Mattress Height Effect

Tests were performed under test series D of Table 3 to determine the effectiveness of geocell reinforcement in increasing bearing pressure and reducing soil bed settling because of an increase in geocell mattress height ( $H/D$ ) compared to an unreinforced bed. The height ( $H/D$ ) of the geocell mattress was varied in  $0.5D$  increments from  $0.75D$  to  $2.25D$ , while the  $u/D$  and  $d/D$  of the geocell mattress were held constant at 0 and 1 respectively. Figures 14 and 15 show the improvement in bearing capacity and percentage reduction in settlement as a result of this. Figure 16 shows the relationship between the percentage reduction in settling (PRS %) factor and the bearing capacity improvement ( $I_f$ ) factor. According to the plot, the improvement in the bearing capacity improvement factor ( $I_f$ ) is almost equivalent to the reduction in

**Fig. 12** Variation of bearing capacity improvement factor with geocell pocket size at various footing settlement levels

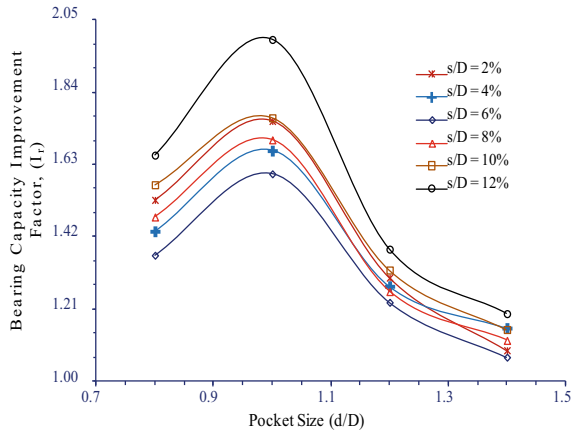
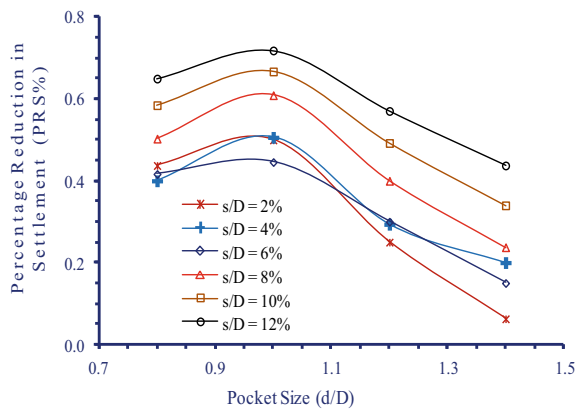


**Fig. 13** Variation of percentage reduction in settlement with geocell pocket size at various footing settlement levels



footing settling, PRS%, for each geocell mattress height. The inclusion of a geocell mattress improved the load bearing capacity and initial stiffness of the foundation bed significantly, as shown in Figs. 14 and 16. It’s also worth noting that the improvement in bearing capacity improvement factor ( $I_f$ ), as well as the percentage reduction in settlement (PRS%) factor, is greater at higher footing settlement levels, indicating that the reinforcing effectiveness of the geocell mattress improves with increased footing settlement. Both the factors, bearing capacity improvement factor ( $I_f$ ) and the percentage reduction in settlement (PRS%) factor, rise steadily until 1.25 height (H/D) of the geocell mattress. Performance improvement continues to improve as the geocell mattress height is increased, though at a reduced rate. Sitharam et al. [18], while analyzing the behavior of geocell reinforced soft clay foundations under circular footing, obtained similar kinds of results.

As the geocell mattress thickness is increased, the subsoil receives reduced footing pressure since the load is distributed over a broader area. Drag is created in the soil as a result of footing settling, which increases soil adhesion and interlocking resistance

**Fig. 14** Variation in bearing capacity improvement factor with geocell height at various footing settlement levels

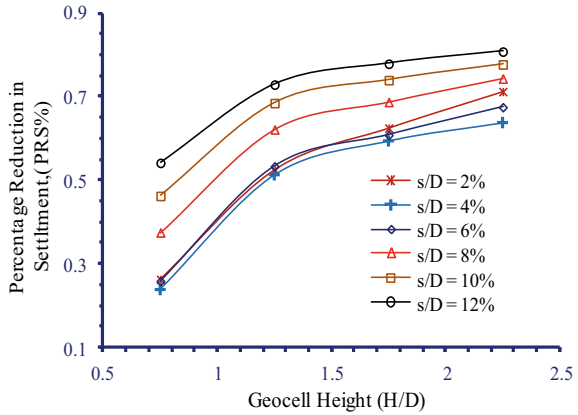
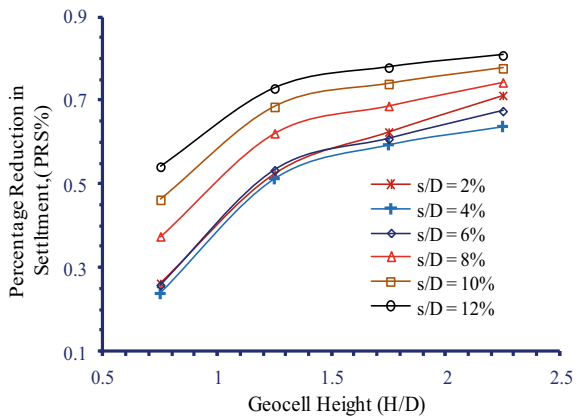


**Fig. 15** Variation of percentage reduction in settlement with geocell height at various footing settlement levels



enclosed in the geocell pocket. The improved footing performance as a result of the increased geocell mattress thickness is due to these two elements. The zone of soil influenced by footing pressure extends one to two times the footing width below the footing base, and this geocell mattress thickness,  $H/D = 1.25$ . Intercepts most of the potential failure zones, resulting in improved reinforced soil bed performance. With a great height,  $H/D = 1.75$  or more, the possible zone of failure is captured by the geocell reinforcement the least, resulting in a modest improvement in the soil bed's performance. As a result, a slight improvement in performance can be expected as the thickness of the geocell mattress approaches a value close  $2D$ . With geocell reinforced clay beds, Sitharam and Sireesh [46] achieved a value of 1.8. As a result, at  $1.75D$  and  $2.25D$  thicknesses of the geocell mattress, a minimal performance increase is noticed.

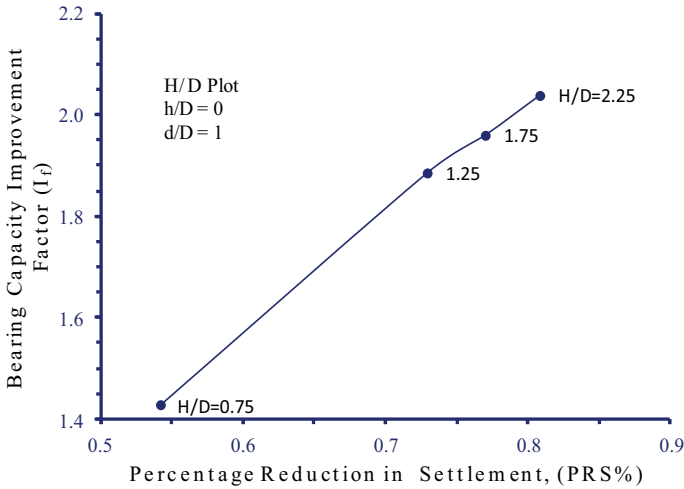


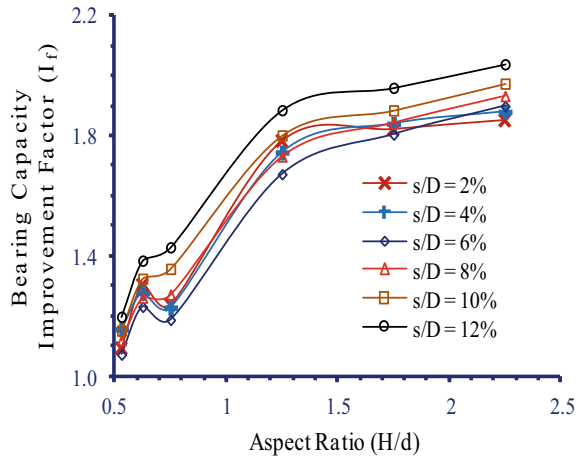
**Fig. 16** Variation in bearing capacity improvement factor with percentage reduction in settlement for different geocell mattress heights corresponding to ultimate bearing pressure and unreinforced bed failure settlement

### 3.4 Aspect Ratio Effect

The results of studies undertaken to determine the geocell mattress pocket size and height influence have been evaluated further in terms of geocell pocket aspect ratio,  $H/d$ . Figure 17 depicts the relationship between the aspect ratio and the bearing capacity improvement factor ( $I_f$ ). It can be noticed from this graph that as the geocell pocket aspect ratio increases, so does the footing load bearing potential. Until an aspect ratio 1.25, there is an increase in bearing capacity, but at aspect ratio 0.75, there is a dramatic loss in bearing capacity and beyond an aspect ratio 1.25, the rate of development in bearing capacity is only minimal. The abrupt dip in bearing capacity could be due to the fact that the geocell mattress behavior is similar to that of a geotextile layer until an aspect ratio equal to 0.75 and thereafter as the geocell mattress height increases, the bearing capacity improvement factor increases as well.

As a result, at aspect ratio 1.25, the greatest increase in bearing capacity enhancement can be attained. For embankments built with soft soils as well as reinforced with geocell, Krishnaswamy et al. [44] found that the optimal aspect ratio is unity, while Dash et al. [41] found that the optimum aspect ratio for strip footing lying on the geocell reinforced sand is 1.67. The numerous types of geosynthetic material used to create the geocells, the kind of soil chosen as the foundation soil, and the type of loading applied could all be contributing factors to the diversity in optimum aspect ratio values reported by different researchers.

**Fig. 17** Bearing capacity improvement factor - Geocell pocket aspect ratio response at different footing settlement levels



## 4 Conclusion

This research study presents the findings of model tests performed on a circular foundation put on expansive soil and reinforced with chevron-patterned geocells. The study's findings were assessed for bearing capacity enhancement and settlement decrease in a circular footing subjected to monotonic loading. Improvements in bearing capacity and footing settlement were observed at a settlement comparable to the footing's failure pressure, i.e. up to 12% of the footing width. The depth of the geocell mattress placement beneath the footing base, the size of the geocell pocket, the height of the geocell mattress, and the aspect ratio of the geocell pocket were all factors addressed in this research work. The following precise conclusions were reached once the study was completed:

- Using geocells as a load bearing reinforcement can significantly improve load bearing capacity and reduce settling of a foundation bed comprised of expansive soil.
- The pressure settlement response of the geocell reinforced soil bed is nearly linear for settlements until 10%-12% of footing diameter.
- Until terminal settlement equal to 25% of the footing diameter, there was no distinct failure of the geocell reinforced soil bed.
- When compared to the bearing pressure of an unreinforced bed at failure, an increase in bearing capacity of nearly 200% and an 81% reduction in settlement can be achieved.
- To get the most out of a geocell mattress with a chevron arrangement, install it just below the footing bottom,  $h/D = 0$ .
- A Geocell mattress with the ideal pocket size,  $d/D = 1$ , i.e. the diameter of the model footing, is believed to yield the best results.

- The performance gain is considerable at  $H/D = 1.25$ , but it is modest at  $H/D = 2$ , which is twice the footing diameter.
- The optimal aspect ratio for a geocell pocket supporting a circular footing is 1.25.

**Acknowledgements** This research article is based on research work carried out at the Civil Engineering Department of Vaish Technical Institute, Rohtak (Haryana), India. Furthermore, we are gratefully acknowledged the friendly forbearance and the unstinted help provided by Dr. R. S. Keserwani in helping with the test setup.

## References

1. Hausmann MR (1990) Engineering principles of ground modification. McGraw-Hill, New York
2. Prabakar J, Sridhar RS (2002) Effect of random inclusion of sisal fibre on strength behaviour of soil. *Constr Build Mater* 16(2):123–131
3. Yarbaşı N, Kalkan E, Akbulut S (2007) modification of the geotechnical properties, as influenced by Freeze–Thaw, of granular soils with waste additives. *Cold Reg Sci Technol* 48(1):44–54
4. Jin L, Wang G, Kamai T, Zhang F, Yang J, Shi B (2011) Static liquefaction behavior of saturated fiber-reinforced sand in undrained ring-shear tests. *Geotext Geomembr* 29(5):462–471
5. Santoni RL, Webster SL (2001) Airfields and roads construction using fiber stabilization of sands. *J Transp Eng* 127(2):96–104
6. Sharma R, Chen Q, Abu-Farsakh M, Yoon S (2009) Analytical modeling of geogrid reinforced soil foundation. *Geotext Geomembr* 27(1):63–72
7. Binquet J, Lee KL (1975) Bearing capacity tests on reinforced earth slabs. *J Geotech Geoenviron Eng* 101(12):124–1255
8. El Sawwaf MA (2007) Behavior of strip footing on geogrid-reinforced sand over a soft clay slope. *Geotext Geomembr* 25(1):50–60
9. Fragaszy RJ, Lawton E (1984) Bearing capacity of reinforced sand subgrades. *J Geotech Eng* 110(10):1500–1507
10. Guido VA, Dong K, Chang DK, Sweeney MA (1986) Comparison of geogrid and geotextile reinforced earth slabs. *Can Geotech J* 23(4):435–440
11. Hatami K, Bathurst RJ, Pietro PD (2001) Static response of reinforced soil retaining walls with nonuniform reinforcement. *Int J Geomech* 14:477–506
12. Khing KH, Das BM, Puri VK, Cook EE, Yen SC (1993) The bearing-capacity of a strip foundation on geogrid-reinforced sand. *Geotext Geomembr* 12(4):351–361
13. Léonard D, Vanelstraete A, Parewyck S (2002) Structural design of flexible pavements using steel netting as base reinforcement. *Int J Geomech* 2(3):291–303
14. Zhou H, Wen X (2008) Model studies on geogrid- or geocell-reinforced sand cushion on soft soil. *Geotext Geomembr* 26(3):231–238
15. Ghosh A, Ghosh A, Bera AK (2005) Bearing capacity of square footing on pond ash reinforced with jute-geotextile. *Geotext Geomembr* 23(2):144–173
16. Latha GM, Rajagopal K, Krishnaswamy NR (2006) Experimental and theoretical investigations on geocell-supported embankments. *Int J Geomech* 6(17):30–35
17. Latha GM, Murthy VS (2007) Effects of reinforcement form on the behavior of geosynthetic reinforced sand. *Geotext Geomembr* 25(1):23–32
18. Sitharam TG, Sireesh S, Dash SK (2007) Performance of surface footing on geocell-reinforced soft clay beds. *Geotech Geol Eng* 25(5):509–524

19. Pokharel SK, Han J, Parsons RL, Qian Y, Leshchinsky D, Halahmi I (2009) Experimental study on bearing capacity of geocell reinforced bases. In: Tuumluer, Al-Qadi (eds) Bearing capacity of roads, railways and airfields. Taylor & Francis, pp 1159–1166
20. Dash SK (2010) Influence of relative density of soil on performance of geocell-reinforced sand foundations. *J Mater Civ Eng* 22(5):533–538
21. Tafreshi SNM, Dawson AR (2010) Comparison of bearing capacity of a strip footing on sand with geocell and with planar forms of geotextile reinforcement. *Geotext Geomembr* 28(1):72–84
22. Dash SK (2012) Effect of geocell type on load-carrying mechanisms of geocell-reinforced sand foundations. *Int J Geomech* 12(5):537–548
23. Biswas A, Murali Krishna A, Dash SK (2013) influence of subgrade strength on the performance of geocell-reinforced foundation systems. *Geosynth Int* 20(6):376–388
24. Bazne MOA, Vahedifard F, Shahrokhbadi S (2014) the effect of geonet reinforcement on bearing capacity of low-compacted soft clay. *Infrastructure Geotechnology* 2(1):47–63
25. Hegde A, Sitharam TG (2015) Experimental and analytical studies on soft clay beds reinforced with bamboo cells and geocells. *Int J Geosynthetics Ground Eng* 1(2):1–11
26. Indraratna B, Biabani MM, Nimbalkar S (2015) Behavior of geocell-reinforced subballast subjected to cyclic loading in plane-strain condition. *J Geotech Geoenviron Eng* 141(1):04014081
27. Shadmand A, Ghazavi M, Ganjian M (2018) scale effects of footings on geocell reinforced sand using large-scale tests. *Civil Eng J* 4(3):497–508
28. Mehrjardi GT, Motarjemi F (2018) Interfacial properties of geocell-reinforced granular soils. *Geotext Geomembr* 46(4):384–395
29. Kaur A, Gill KS, Singh P (2018) Bearing capacity improvement using geocell reinforced sand. In: Proceedings of the 1st international conference on sustainable waste management through design, pp 160–169
30. Kolathayar S, Suja P, Nair V, Krishna S, Tamilarasi G (2019) Performance evaluation of seashell and sand as infill materials in HDPE and coir geocell. *Innov Infrastruct Solutions* 4(1):1–7
31. Liu Y, Deng A, Jaksak M (2019) Failure mechanisms of geocell walls and junctions. *Geotext Geomembranes* 47(2):104–120
32. Kuo CM, Chou FJ (2004) Development of 3-D finite element model for flexible pavements. *J Chin Inst Eng* 27(5):707–717
33. Kolathayar S, Sowmya S, Priyanka E (2020) Comparative study for performance of soil bed reinforced with jute and sisal geocells as alternatives to HDPE Geocells. *Int J Geosynthetics Ground Eng* 6(4):1–8
34. Lal D, Prasanna KL, Rao KR, Kamalekhar P, Bajrang J (2020) Effect of geocell on the behaviour of soil. In: IOP conference series: materials science and engineering, vol 998, no 1. IOP Publishing, p 012024
35. Kolathayar, S. and Chitrachedu, R.K., “Model Footing Tests on Sand Bed to Evaluate Efficiency of Tire Crumb as Infill Materials in Geocells” In *Advances in Geo-Science and Geo-Structures*, Springer, Singapore 253–259 (2022).
36. Gedela R, Karpurapu R (2021) Influence of pocket shape on numerical response of geocell reinforced foundation systems. *Geosynth Int* 28(3):327–337
37. Arvin MR, Heidari Soreshjani M, Khademhosseini A (2021) Behaviour of geocell-reinforced strip footings on slopes. *Geomech Geoen* 1–17
38. Biswas S, Hussain M, Singh KL (2021) Behaviour of jute and bamboo geocell with additional basal mat filled with different infill materials overlaying soft subgrade. *Int J Geosynthetics Ground Eng* 7(3):1–15
39. Kumar S, Sahu AK, Naval S (2020) Influence of jute fibre on CBR value of expansive soil. *Civil Eng J* 6(6):1180–1194
40. Kumar S, Sahu AK, Naval S (2021) Study on the swelling behavior of clayey soil blended with geocell and jute fibre. *Civil Eng J* 7(8):1327–1340
41. Dash SK (2001) Bearing capacity of strip footings supported on geocell-reinforced sand. *Geotext Geomembr* 19(4):235–256

42. Dash SK, Rajagopal K, Krishnaswamy NR (2001) Strip footing on geocell reinforced sand beds with additional planar reinforcement. *Geotext Geomembr* 19(8):529–538
43. Latha MG, Somwanshi A (2009) Effect of reinforcement form on the bearing capacity of square footings on sand. *Geotext Geomembr* 27(6):409–422
44. Krishnaswamy NR, Rajagopal K, Latha MG (2000) Model studies on geocell supported embankments constructed over a soft clay foundation. *Geotech Test J* 23(1):45–54
45. Hegde AM, Sitharam TG (2014) Effect of infill materials on the performance of geocell reinforced soft clay beds. *Geomech Geoeng* 10(3):163–173
46. Sitharam TG, Sireesh S (2006) Effects of base geogrid on geocell-reinforced foundation beds. *Geomech Geoeng* 1(3):207–216



# Recycling Excavated Clay to Produce ‘Sand-Like’ Material Through Sintering: Static Furnace Versus Rotary Kiln



S. Subramanian, J. W. Koh, J. M. Soh, S. H. Chew, K. E. Chua, Y. C. Tan, C. S. Teo, M. Y. C. Koh, and T. H. H. Cheung

**Abstract** Traditionally, sand is used as infilling material in land reclamation projects in Singapore. One-third of Singapore area is underlaid with marine clay deposits; hence, marine clay generated from underground excavation works for building and infrastructure developments is a significant source of excavated material in Singapore. Marine clay is not a suitable material for land reclamation due to its low permeability and high compressibility, which results in excessive settlements and low bearing capacity problems. Given the availability of excavated marine clay in Singapore, this study focuses on transforming marine clay into a “sand-like” reclamation fill material using a heat-treatment process called “Sintering”. Sintering is a thermal process where the clay is subjected to high temperature (850 °C), in which the weak mineral in clayey soil is transformed into a stronger mineral, i.e. transformation of kaolin to metakaolin. The end product of sintered clay product can be designed to process ‘sand-like’ properties. In order to achieve this high temperature, either a static furnace or a rotary kiln could be used. This paper focuses on the comparison of these two methods for this sintering process. The main objective of the study is to find the optimum operating conditions of the rotary kiln so that less heating energy is used to produce a ‘good’ quality sintered clay product. The test results indicate a positive mineral change when the temperature is maintained at 850 °C for 10 min in the kiln. The sintered clay products had a friction angle of about 39° and hydraulic conductivity around  $1 \times 10^{-3}$  m/s. Finally, the properties of sintered clay products produced from the rotary kiln and produced from the static furnace are compared.

**Keywords** Excavated clay · Land reclamation · Rotary kiln · Sintering · Static furnace

---

S. Subramanian · J. W. Koh · J. M. Soh · S. H. Chew

Department of Civil and Environmental Engineering, National University of Singapore, Singapore 117578, Singapore

K. E. Chua · Y. C. Tan · C. S. Teo · M. Y. C. Koh · T. H. H. Cheung (✉)

Building and Infrastructure Group, Housing and Development Board, Singapore 310480, Singapore

e-mail: [ceesusa@nus.edu.sg](mailto:ceesusa@nus.edu.sg)

## 1 Introduction

Sand is traditionally used as an infilling material for land reclamation project due to its ability to compact, high strength and drained properties. Due to the shortage of sand supply worldwide, there is a need to look for an alternative infilling material, such as marine clay.

One-third of Singapore land is underlaid with marine clay deposits (Kallang Formation). This marine clay generated from underground excavation works for building and infrastructure developments is a significant source of excavated material in Singapore. Marine clay, as it is, is not a suitable material for land reclamation due to its low permeability and high compressibility, which results in excessive settlements and low bearing capacity problems. Given the availability of excavated marine clay in Singapore, this study focuses on transforming marine clay into a “sand-like” reclamation fill material using a heat-treatment process called “Sintering”.

Sintering is a thermal process where the clay is subjected to high temperature (around 850 °C), in which the weak mineral in clayey soil is transformed into a stronger mineral, i.e. transformation of kaolin to meta-kaolin [1–4]. It can be designed such that the new sintered clay product has ‘sand-like’ properties, which can be used as infill material in the land reclamation project. In order to achieve this high temperature, either a static furnace or a rotary kiln could be used. The properties of sintered clay product produced through static furnace has already been studied in the early phase of the project. It was established that the sintering process indeed transformed marine clay into ‘sand-like’ material. While static furnace method may be suitable for controlled laboratory testing, it may not be sustainable for the industry-scale mass-producing process. Hence, other sintering method has to be found.

On the other hand, a rotary kiln is a cylindrical machine that rotates about its longitudinal axis and acts as a heat exchanger device [5]. This kiln is suitable for the high-intensity heating step of the sintering process. A rotary kiln is generally used to heat materials at temperatures high enough to bring about a chemical change, but the kiln can also be used as a rotary dryer to reduce the moisture content of materials [5]. The heat required for sintering is delivered to the material by lifting and overturning each sample moving through the kiln. The sample in the kiln moves both radially and axially. The radial motion is controlled by rotational speed (rpm) and the amount of sample inserted, while the axial motion is governed by the kiln’s inclination angle. Heat transfer to the material in the rotary kiln occurs in three different ways: (a) heat transfer to material by convection and gas radiation, (b) heat transfer to material by brick radiation, and (c) conductive heat transfer to material from brick [6].

Hence, this paper focuses on the suitability of using a rotary kiln for the sintering process and determining the rotary kiln’s optimum operating conditions. The properties of the sintered product from the rotary kiln are compared against sintered product from the static furnace.

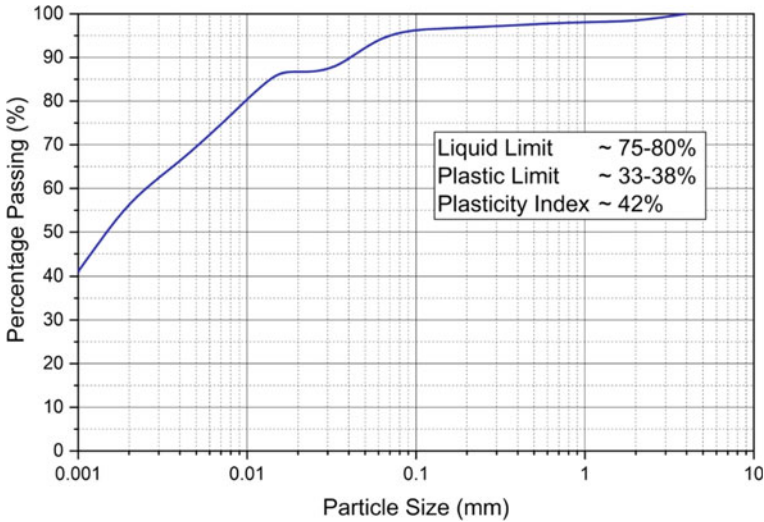


Fig. 1 Particle size distribution curve for SMC from TMSG

## 2 Material and Sample Preparation

### 2.1 Material Used

Singapore marine clay (SMC) used in this study is obtained from the excavated material sent to Tanah Merah Staging Ground (TMSG), a collection point for such material before deposition. Based on previous studies by NUS, “Soft Clay” is divided into two categories, namely “Soft Clay Type A” (SC-A, more sandy) and “Soft Clay Type B” (SC-B, more clayey and silty). The classification of these two categories is highlighted in the Particle Size Distribution (PSD) chart shown in Fig. 1. SC-B type soil is used for this study, represented by the solid line (soil sample from TMSG) in Fig. 1. The marine clay has an initial moisture content of 70–80% with Liquid Limit and Plastic Limit of 75–80% and 33–38%, respectively.

### 2.2 Sample Preparation

Sample preparation to obtain sintered product consists of several processes, namely screening, dewatering, granulating and sintering.

The SMC obtained from the site may consist of shells, tree roots, and other foreign materials. These materials must be removed before the sintering process. Also, any coarse sand present in the marine clay need to be removed. Sand is inert in the sintering process, which would result in a wastage of heat energy. Hence the

obtained marine clay must be wet sieved through a 1 mm sieve. The marine clay collected after sieving will have a moisture content greater than 100%.

The next process in sample preparation is dewatering, which will convert the marine clay from a slurry state to a near plastic limit state such that it could be rolled in a thread of 3 mm or for further granulation into the shape of a small ball. If the moisture content is too high, granulation becomes difficult as the marine clay is too soft and cohesive. On the other hand, it becomes harder to extrude the clay if the moisture is too low. A laboratory oven at 105 °C was used for dewatering the marine clay in the initial phase of the study. Dewatered marine clay is then turned into equivalent small balls of about 3 mm diameter by the granulation process.

This study used two types of sintering machines: a static furnace (Fig. 2) and a mini-rotary kiln (Fig. 3). The mini rotary kiln was constructed with a kiln drum made of silicon carbide, which has high conductivity and low expansion and can take up to 2000 °C. The kiln is designed to allow for adjustment in two important parameters, namely, sintering temperature and revolutions per minute.

The use of a static furnace for lab-scale production of ‘sand-like’ material was carried out previously [7]. The optimum operating condition was found to have a sintering temperature of 900 °C with a ramp rate of 300 °C/h and one-hour dwelling duration.

A study comparing the two differing sintering machines was made and their relative advantages and disadvantages were summarized and tabulated in Table 1.



Fig. 2 Picture of static furnace



**Fig. 3** Picture of **a** mini rotary kiln with control panel and **b** front view

**Table 1** Comparison of the static furnace and rotary kiln

Items	Static furnace	Rotary kiln
Heating process	The heat is transferred to the samples only through the convection process	The heat is transferred to the sample by all three modes of heat transfer—conduction, convection, radiation
Temperature heating sequence	Temperature will be ramping up to reach the target temperature. Once the target temperature is reached, there is a dwelling period followed by a cooling period	The target temperature and the retention can be controlled
Sample input/output	Samples are placed inside the furnace before starting the heating ramping stage when the furnace is at room temperature. The sintered product is collected after the cooling period	Samples are inserted into the kiln while the target temperature is reached. The sintered product is collected immediately after retention time
Parameters controlled	Sintering temperature, ramping rate, dwelling duration, and cooling down time	Sintering temperature, retention time, and rpm of rotation

### 3 Parameters Studies with Rotary Kiln Production

A series of sintering production studies were conducted using a rotating kiln and the marine clay mentioned, aiming to obtain a set of optimal operating parameters for such production. The parameters considered are sintering time (5, 10 and 15 min), kiln rotating frequency (36, 40, 44 and 48 rpm) and the initial mass of the sample (5, 10 and 15 g). Visual inspection and microscopic testing were carried out on the sintered products. As a first stage observation, visual inspection is carried out to determine whether the clay balls are completely sintered or un-sintered. The sintered samples are broken for inspection, and the colour of the sintered sample is noted down. A completely sintered s should have a uniform orange colour throughout. An

unsintered product is shown in grey colour. A partially sintered product is when the shell of the sintered sample is orange in colour while the core of the sample is still grey (marine clay original colour).

### ***3.1 Visual Inspection***

All the test series were carried out at 850 °C sintering temperature. The operating parameter and visual inspection results are tabulated in Table 2. For Test T0, where 5 g of sample was used with a sintering temperature of 850 °C, 36 rpm and 5 min of retention time, the results show that the sintered product was disintegrated after the retention time. This disintegration is because the clay balls have a moisture content of around 40% entering the rotary kiln at 850 °C; the water inside the clay vaporizes instantly and escapes the clay balls. This process of instant vaporization causes the clay balls to “explode”, resulting in an undesirable fragmented sintered product.

In the testing series, T1, T2 and T3, the initial moisture content is close to 0%, only the retention time varies (5, 10 and 15 min). Visual observation on T1 sintered product suggests that the surface of the clay balls is sintered, and the core of the sample is grey, suggesting that the retention time was too short for complete sintering. T2 and T3 sintered products seem to be completely sintered, indicating a minimum retention time required is about 10 min.











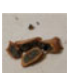
Testing series F0, F1, F2 and F3 were conducted with the rotation frequency of the rotary kiln at 0, 40, 44 and 48 rpm, respectively. All four test series have 10 min retention time. F0 simulates a static furnace, but the retention time of 10 min is too short for the sample to be fully sintered. Under F3 testing with 48 rpm, the samples are well sintered; however, some breakdown particles were observed due to particle-to-particle collision because of the high rotation speed. Both test series F1 and F2 with 40 and 44 rpm seem to produce well sintered and intact products.

Under M1 and M2 testing series, the initial mass of the sample is varied at 10 and 15 g, respectively, while the retention time is kept at 10 min, and rpm is kept as 40 rpm. The sintered product in M2 series is poorly sintered due to the excessive sample used. The presence of excessive clay samples blocks the heat, such that some samples do not receive adequate heat energy, thus resulting in a poor sintered product. M1 testing series with 10 g initial mass produces good quality, well-sintered product.

### ***3.2 Microscopic Inspection/Testing***

Based on the visual inspection in Sect. 3.1, unsatisfactory sintered clay products (T1, F0, F3 and M2) were removed from the microscopic study. Sintered products from the remaining test series (F1, F2, T2, T3 and M1) were then subjected to microscopic inspection through X-Ray diffraction (XRD) test to determine if a mineral transformation had occurred. Figure 4 shows the XRD results.

**Table 2** Visual inspection of parametric study using a rotating kiln

Test ID	Sample weight (g)	Moisture content-before sintering (%)	Rotating speed (rpm)	Retention time (mins)	Visual observation	Comments	*S/U
Original	–	~ 40	–	–		Original pre-dried sample (grey colour)	N.A
T0	5	~ 40	36	5		Sintered product "explodes" and breaks into small pieces	U
T1	5	~ 0	36	5		Some samples showed poor sintering	U
T2	5	~ 0	36	10		Clay sintered uniformly	S
T3	5	~ 0	36	15		Clay sintered uniformly	S
F0	5	~ 0	0	10		Not fully sintered	U
F1	5	~ 0	40	10		Clay sintered uniformly	S
F2	5	~ 0	44	10		Clay sintered uniformly	S
F3	5	~ 0	48	10		Inter-particle breaking is observed due to high rotating frequency	U
M1	10	~ 0	40	10		Clay sintered uniformly	S
M2	15	~ 0	40	10		Very poorly sintered	U

\* S—satisfactory, U—unsatisfactory

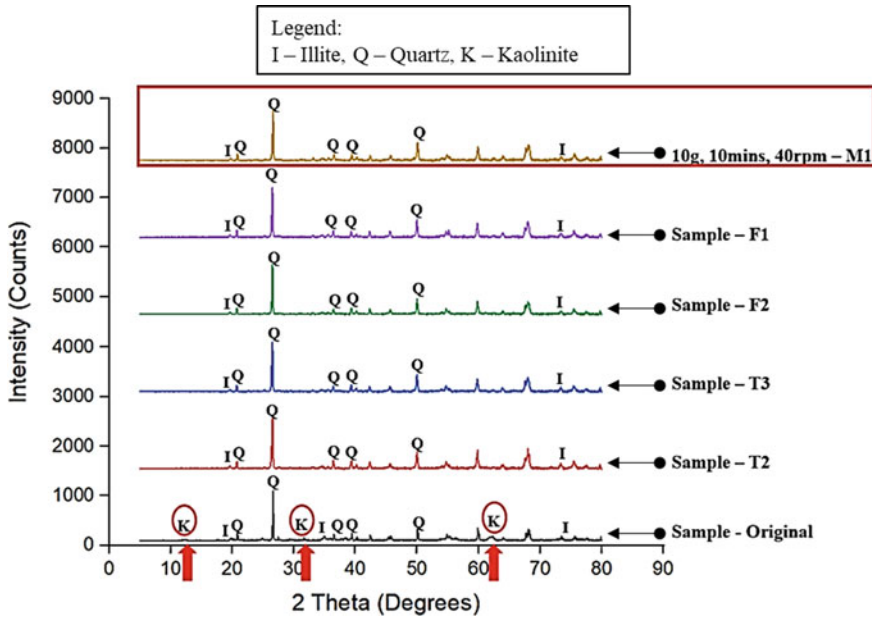


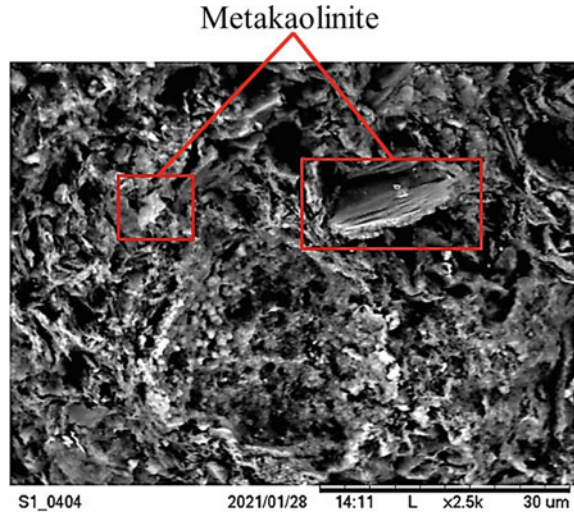
Fig. 4 X-ray diffraction (XRD) results on samples

The mineral phase transformation of kaolinite to metakaolinite is expected when the clay sample is subjected to a sintering temperature of 850–900 °C. As seen in Fig. 4, kaolinite was found in the original sample, which, upon sintering, is no longer detected by XRD testing. This change is consistent across all the samples deemed fully sintered by visual inspection. The presence of metakaolinite is not detected by XRD Test as it is an amorphous aluminosilicate (Panesar 2019) but can be identified using a Scanning Electron Microscope (SEM). Once it was established that kaolinite was no longer present in sintered clay sample by XRD testing, an SEM inspection was conducted to detect the presence of metakaolinite, if there is. Figure 5 shows the SEM picture of one sample, which clearly shows the presence of metakaolinite.

Thus, based on the visual observations XRD and SEM results, it can be concluded that parametric combinations F1, F2, T2, T3 and M1 will produce a well-sintered product. Among these well-sintered testing series, Test M1 is chosen to represent the optimum operating condition because more samples can be well sintered in a lesser duration, thereby being energy efficient and saving the operating cost.



**Fig. 5** Presence of metakaolinite in test M1



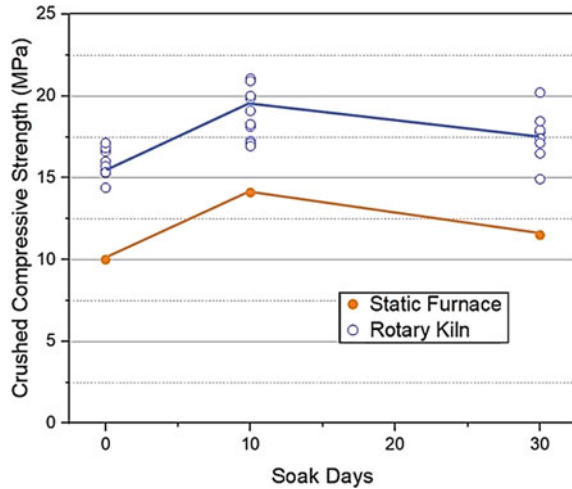
## 4 Comparison of Sintered Clay Properties Produced by a Static Furnace and Rotary Kiln

The optimum operating condition for the given rotary kiln was identified in this study to have a sintering temperature of 850 °C with a retention time of 10 min and an optimum initial mass of the sample of 10 g. Based on the previous study [7], the optimum operating condition for a static furnace was found to have a sintering temperature of 900 °C with a ramp rate of 300 °C/h and a dwelling period of 1 h. In this section, the mechanical properties of the sintered product produced using the static furnace and rotary kiln are compared. The properties considered are static compressive strength, permeability, and angle of internal friction of the sintered clay product.

### 4.1 Static Compression Strength

Zwick Roell Z100 universal testing machine with a maximum testing load of 100 kN was used in this study to obtain the ultimate compressive strength of sintered clay product. Ten (10) randomly chosen samples were subjected to the static compression test with a 1 mm/min strain rate. Besides the static compressive strength testing on the sintered product, another series of static compressive strength testing is carried out on sintered products soaked in saltwater for ten (10) days and 30 days. Soaking test is carried out to determine the effect of saltwater soaking (either no effect or detrimental) on the sintered product. The strength of the product produced using the static furnace, and rotary kiln is shown in Fig. 6.

**Fig. 6** Static Compressive strength of individual clay balls under un-soaked and soaked for various days in saltwater conditions

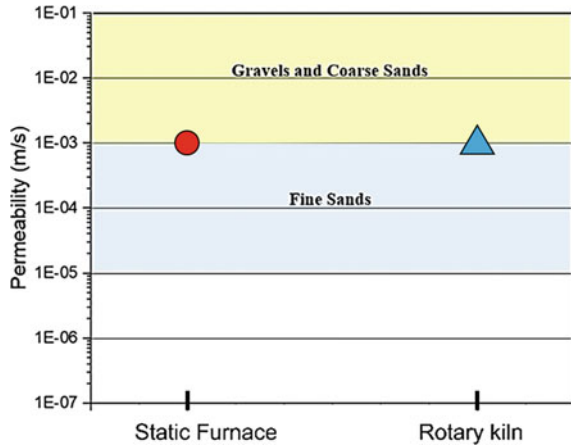


The results show that the strength of the sintered product produced using the rotary kiln is 5 MPa higher than the sintered produced using the static furnace for all un-soaked and soaked conditions consistently. This increase in strength of the sintered product from the rotary kiln could be due to the more effective heat transfer modes involved in the rotary kiln. The compression strength of the sintered product from the static furnace and rotary kiln increased when soaking under saltwater for about ten days, but the prolonged soaking after ten days reduced the compressive strength and back to un-soak value. A more detailed study will be conducted to validate this.

## 4.2 Permeability

Permeability of sintered product is an important parameter, as it would be used as an infilling material, which required good drainage characteristics. A constant head permeability test is carried out in accordance with ASTM D 2434–19 [8]. Figure 7 shows the permeability of sintered product from the static furnace and rotary kiln, which shows that the permeability of the sintered product is the same ( $k = 1 \times 10^{-3}$  m/s). Unlike static compressive strength, which depends on microscopic properties, the permeability of granular soil primarily depends on the packing arrangement and the particle size of the sintered product. The particle size and density of the sintered product were maintained to be the same, thereby leading to similar permeability results between sintered products. It is noted that the permeability of the sintered product lies in the range of fine to coarse sand.

**Fig. 7** Comparison of the permeability of sintered produced with static furnace and rotary kiln



### 4.3 Angle of Internal Friction

Shear strength is one of the important engineering properties of granular soil. A consolidated drained triaxial testing is carried out on the well-sintered product samples, and the friction angle is determined [9]. The sintered product from the rotary kiln had a friction angle of 39°. With this value of friction angle, the sintered product can be classified as coarse-grained uniform sand. The effective friction angle of sintered clay produced from the static furnace was 33.7°. A high friction angle of 39° is essential for a land reclamation material, and its classification also proves that the rotary kiln can sinter marine clay into a sand-like material effectively. The result also shows that the rotary kiln prototype can produce sintered clay of a higher friction angle than those produced by the static furnace. Thus, this sintered product can be deemed to have “sand-like” properties.

## 5 Conclusions

- (a) The study aims at converting excavated marine clay to ‘sand-like’ material using the sintering process. The use of a rotary kiln for the sintering process was studied in the current study. The optimum operating conditions of the rotary kiln to produce good quality, well-sintered products were identified. Then static compression test, constant head permeability test and triaxial testing were carried out to understand the properties of the sintered product. Finally, the mechanical properties of the sintered product obtained from the rotary kiln were compared against the mechanical properties obtained from the static furnace.

The study showed that the sintering temperature, kiln rotating frequency, retention time and initial mass of the sample could affect the quality of the sintered product. It was found that:

- i. High rotating frequency resulted in an inter-particle collision, and lower rotating frequency resulted in non-uniform sintering. 40 rpm was chosen as optimum for the kiln considered in this study.
  - ii. Feeding more samples at a given time would result in non-uniform sintering, and feeding fewer samples would waste energy. 10 g initial mass of samples was found to be optimum for the kiln used in this study.
  - iii. Lower retention time results in incomplete sintering. A retention time of 10 min was found to be sufficient for complete sintering in the kiln.
  - iv. A sintering temperature of 850 °C with 40 rpm, an initial mass of 10 g and retention time of 10 min was found to be optimum for the rotary kiln considered in this study.
- (b) This study also shows that the rotary kiln produces a better quality sintered product than that produced by a static furnace.
- i. The static compressive strength of individual sintered product from the rotary kiln is 5 MPa higher than that of the static furnace.
  - ii. The sintered product from both the rotary kiln and the static furnace has a permeability of approximately  $1 \times 10^{-3}$  m/s.
  - iii. The sintered produced from the rotary kiln has a friction angle of 39°, while the sintered product from the static furnace has a friction angle of 33.7°. Hence, it can be concluded that the rotary kiln produces better quality sintered product than the static furnace.
- (c) Thus, the sintered product can be termed as “sand-like” material.

**Acknowledgements** This research is supported by the National Research Foundation, Singapore, and Ministry of National Development, Singapore, under its Cities of Tomorrow R&D Programme (CoT Award No. COT-V3-2019-2). Any opinions, findings, conclusions, or recommendations expressed in this material are those of the author(s) and do not reflect the views of National Research Foundation, Singapore, and Ministry of National Development, Singapore.

## References

1. Katsuki H, Kim J, Kim SJ, Kim JY, Pee JH, Cho WS (2016) Influence of alumina content in the raw clay on the sintering behavior of Karatsu ware. *J Ceram Soc Jpn* 124:833–837. <https://doi.org/10.2109/jcersj2.16014>
2. Chen YF, Wang MC, Hon MH (2004) Phase transformation and growth of mullite in kaolin ceramics. *J Eur Ceram Soc* 24:2389–2397. [https://doi.org/10.1016/S0955-2219\(03\)00631-9](https://doi.org/10.1016/S0955-2219(03)00631-9)
3. Chargui F, Hamidouche M, Belhouchet H, Jorand Y, Doufnoune R, Fantozzi G (2018) Mullite fabrication from natural kaolin and aluminium slag. *Bol La Soc Esp Ceram y Vidr* 57:169–177. <https://doi.org/10.1016/j.bsecv.2018.01.001>

4. Cogswell JW, Neff H, Glascock MD (1996) The effect of firing temperature on the elemental characterization of pottery. *J Archaeol Sci* 23:283–287. <https://doi.org/10.1006/jasc.1996.0026>
5. Vijayan SN, Sendhilkumar S (2014) Industrial applications of rotary kiln in various sectors—a review. *Int J Eng Innov Res* 3:342–345
6. Arad S (2012) Victor Arad, heat transfer in rotary kiln from Deva cement factory. In: SGEM2012 12th international multidisciplinary scientific geoconference, 2012. <https://doi.org/10.5593/sgem2012/s04.v2003>
7. Koh JW, Sathyamoorthy S, Chew SH, Low KE, Chua KE, Tan YC, Soon TC, Lee JM, Koh MY (2022) Laboratory-scale production of 'sand-like' material from excavated soft soil. In: 7th international conference on geotechnology research engineering
8. ASTM-D2434–19 (2019) Standard test method for permeability of granular soils (constant Head). ASTM International. <https://doi.org/10.1520/D2434-19>.
9. ASTM D7181–11 (2011) Method for consolidated drained triaxial compression test for soils, D 7181. *Annu B Stand* 4

# Field Implementation of EAF Steel Slag Mixtures in Clayey Subgrade Stabilization



Irem Zeynep Yildirim  and Monica Prezzi 

**Abstract** Replacing traditional construction materials with industrial by-products can reduce their disposal in landfills, offering a sustainable geo-environmental solution. This study evaluates the feasibility of using various mixtures of EAF steel slag and other industrial by-products for their use as a suitable geo-material that can replace lime in subgrade stabilization applications. Field-test results and experiences gained in the implementation of the selected mixture in the field are presented. In the present study, clayey subgrade soils obtained from a potential stabilization site were blended with EAF steel slag (EAFSS)-Class C fly ash (CFA) and EAFSS-blast furnace slag (BFS) mixtures and tested in the laboratory. Proctor compaction curves and Atterberg Limits (ALs) of the mixtures were determined in the laboratory. The strength of the stabilized soil mixtures was determined through unconfined compression (UC) tests. Based on the results of the laboratory tests, the 7%EAFSS-3%CFA mixture was selected as the most suitable for lime replacement. The selected mixture was utilized in the field for a trial section of a pavement project. The dynamic cone penetrometer tests (DCPTs) performed 96 h after the subgrade compaction indicated the strength gain associated with the cementitious reactions and the effectiveness of the mixture in the stabilization of the clayey soil. The subgrade stabilized with EAFSS has been performing satisfactorily, discontinuities or visible signs of stress failure are not observed in the pavement sections constructed using the EAFSS-CFA mixture.

**Keywords** EAF steel slag · Blast furnace slag · Fly ash · DCPT · Subgrade stabilization

---

I. Z. Yildirim (✉)  
Bogazici University, Istanbul 34342, Turkey  
e-mail: [zyildirim@boun.edu.tr](mailto:zyildirim@boun.edu.tr)

M. Prezzi  
Purdue University, West Lafayette, IN 47907, USA

## 1 Introduction

Slag that is generated from recycling steel scraps in mini-mills is known as electric-arc-furnace steel slag (EAFSS). The slag generated in furnaces that are used to fine-tune steel slag is known as ladle furnace steel slag (LFSS). These slags are the main by-products from electric-arc-furnace (EAF) steel-making operations and they are typically stockpiled in the vicinity of the steel plants until they are sold for various industries. Some slag processors also prefer to store and market the blends of EAFSS and LFSS.

Due to the increased number and capacity of these recycling furnaces, EAFSS and LFSS output have been increasing accordingly and there has been significant research effort in the last two decades toward recycling these by-products. Generally, concerns related to volumetric instability have limited their utilization. The availability of a higher amount of unbound lime in LFSS indicates higher expansion potential that hinders its use as an aggregate [1, 2]. On the other hand, Santamaria et al. (2018) showed that swelling of pure coarse EAFSS can be alleviated quite easily after simple weathering treatment [3]. Yildirim, also compared the swelling response of EAFSS with LFSS and EAFSS-LFSS blends, and the results indicated a much lower swelling potential for EAFSS, compared to LFSS and its blends with EAFSS [4].

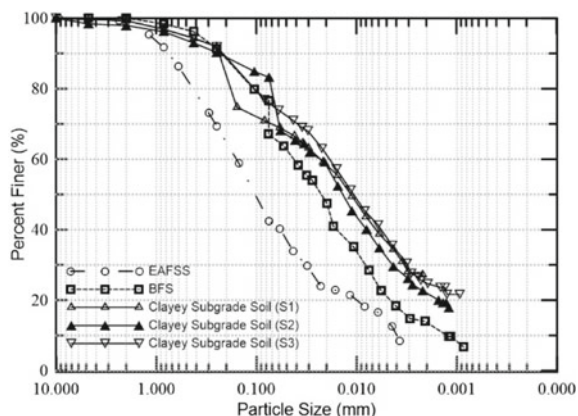
Creating value for EAFSS in pavement layers can reduce unnecessary stockpiling and landfills. Even though recent research has shown promising results for the use of coarser fractions as aggregate in asphalt and concrete pavements [5, 6] and in unbound and bound mixtures for road layers [7, 8] fine fractions of EAFSS remain underutilized. Similar to LFSS, the concerns related to larger surface area and higher exposure of CaO fraction in EAFSS can offer an opportunity for soil stabilization. This study evaluates the feasibility of replacing lime with mixtures of industrial by-products that incorporate EAFSS for soil stabilization. The most suitable EAFSS mixture was selected based on laboratory test results. The selected mixture was utilized to stabilize the clayey subgrade of trial sections of a pavement system in Indiana [9].

## 2 Subgrade Soils and Stabilization Materials

The construction of the ramps of a diamond interchange intersection in northern Indiana was selected as a suitable project for implementing EAFSS mixtures in a stabilization project. The subgrade soils collected from the southwest (SW) and northwest (NW) quadrants of the intersection at the site consisted of soft to stiff silty clays and silty clayey loam. The soil samples had lower strengths than the INDOT strength requirement (i.e., 275 kPa) indicating the need for stabilization [9, 10].

A nearby mini-mill in Crawfordsville, Indiana is the source plant for the EAFSS used in this study. For the implementation project, the material was processed and ground to a gradation with a maximum particle size of less than 2 mm. EAFSS is

**Fig. 1** Grain-size distribution of BFS, EAFSS, and soils used in the mixtures



not self-cementitious and hence, it was activated with either Class C fly ash (CFA) or blast furnace slag (BFS) to design a mixture that can be used in soil stabilization. Fine-grained CFA was obtained from a northern Illinois plant that burns bituminous coal and the BFS was received from an integrated mill near Gary, Indiana. The CFA consisted of mainly silt-size particles (i.e., 65% passing 45  $\mu\text{m}$ ). The grain-size distribution curves of EAFSS and BFS are provided in Fig. 1. Considering the economic feasibility of the project, the percentage of stabilization mixture was kept lower than or equal to 10% of the dry weight of the soil. One of the selection criteria in the design of these mixtures was to maximize the EAFSS in the mixture. The target two (2)-day UC strength for the stabilized subgrade was of about 550 kPa. Based on the results of initial trial test results, 7%EAFSS-3%BFS and 7%EAFSS-3%CFA mixtures were selected as suitable *stabilization materials* for further laboratory testing [10].

### 3 Laboratory Evaluation

Basic characterization tests (i.e., grain-size distribution, specific gravity, Atterberg limits) were performed on the clayey subgrade soils collected from the site. Proctor compaction tests and unconfined compressive strength (UC) tests were performed on the clayey subgrade soils per ASTM D698 [11] and ASTM D 2166 [12], respectively. Atterberg limits (AL) tests were performed on the soil-stabilization material mixtures to evaluate their plasticity index (PI) values. The effect of stabilization on the Proctor density—moisture content relationship was investigated through compaction tests performed on clayey soil-stabilization material mixtures. In order to determine the volumetric stability of the *in-situ* clayey subgrade soil and the clayey soil-stabilization mixtures, CBR swelling tests were monitored for ~ two (2) months at room temperature. The effectiveness of each mixture in stabilization was investigated through UC



**Table 1** Summary of laboratory characterization of subgrade soils

	PI	Fines (%)	O <sup>(1)</sup> (%)	Class	G <sub>s</sub> <sup>(3)</sup>	$\gamma_{d, \max}$ <sup>(4)</sup> kN/m <sup>3</sup>	w <sub>opt</sub> <sup>(5)</sup> (%)	q <sub>u</sub> <sup>(6)</sup> kPa
S1a	13	75	1.33	CL <sup>(2)</sup> /A-6 (8)	2.71	18.5	13	214–330
S1b	12	75	1.41	CL <sup>(2)</sup> /A-6 (7)				
S2	12	69	1.42	CL <sup>(2)</sup> /A-6 (6)				
S3	13	76	1.07	CL <sup>(2)</sup> /A-6 (9)				

Notes <sup>(1)</sup> Organic Content, <sup>(2)</sup> CL = Lean Clay with sand, <sup>(3)</sup> G<sub>s</sub> = Specific gravity, <sup>(4)</sup>  $\gamma_{d, \max}$  = maximum dry unit weight, <sup>(5)</sup> w<sub>opt</sub> = optimum moisture content, <sup>(6)</sup> q<sub>u</sub> = unconfined compressive strength

tests performed on compacted soil-stabilization material mixtures in general accordance with ASTM D5102-04 [13]. A shear strain rate of 1.5–2%/min was used for the mixtures in UC tests.

### 3.1 Subgrade Characteristics and Stabilization Requirement

The grain size distribution of the soils collected from the site, EAFSS, and BFS used in this research study are shown in Fig. 1. Table 1 summarizes the laboratory test results obtained for the clayey soils collected from the implementation site.

Some variations were observed in LL and PL of the soils tested. Nonetheless, the resulting PI of the samples were consistently in the 12–13 range. Based on these results, soils were classified as A-6 and lean clay with sand (CL) per AASHTO and ASTM classification systems. The average UC strength of the compacted samples was about 283 kPa, which was lower than the requirement. The data deducted from the boring logs for the top 1.5–2.0 m of the soil profile at the site was in agreement with our laboratory testing results. These soils exhibit high shrink-swell potential and have fair-to-poor subgrade rating and hence, the clayey soil at the site required stabilization to reach the target strength [10].

### 3.2 Characteristics of Clay-Stabilization Material Mixtures

The results of tests performed on the materials and the soil-stabilization material mixtures are summarized in Table 2. In this study, the soil stabilized with the selected mixtures generally exhibited higher LL and PL values than that of the *in-situ* clayey soil. On the other hand, the PI of the stabilized clay was almost identical to the PI of the *in-situ* clay. Typically, after stabilization, changes in the Atterberg limits are less pronounced in clays of low-to-moderate plasticity. The main goal of stabilization in this case study was the strength increase and accordingly, PI values of

the mixtures were deemed satisfactory. The standard compaction of the clayey-subgrade soil and clayey soil-stabilization material mixtures are shown in Fig. 2a. The compaction curves of the mixtures showed a similar change to those observed in lime-stabilized clays. The moisture-dry unit weight plot shifted right and down, showing the higher optimum moisture content ( $w_{opt}$ ) and lower maximum dry unit weight ( $\gamma_{d,max}$ ) of the mixtures. A stronger shift was observed for the soil-7%EAFSS-3% BFS mixture compared to the one observed for soil-7%EAFSS-3% CFA mixture [10]. CBR swelling response of the clayey soil and the mixtures are presented in Fig. 2b.

**Table 2** Summary of laboratory characterization materials and soil-stabilization mixture blends

Materials/soil-stabilization material mixtures	Atterberg limits			$G_s^{(4)}$	S. Proctor	
	LL <sup>(1)</sup>	PL <sup>(2)</sup>	PI <sup>(3)</sup>		$\gamma_{d,max}^{(5)}$ kN/m <sup>3</sup>	$w_{opt}^{(6)}$ (%)
EAFSS	NP	NP	NP	3.26		
CFA	NP	NP	NP	2.38		
BFS	NP	NP	NP	2.87		
S1	35	22	13	2.70	13	18.56
S1—7% EAFSS—3% BFS	39	25	14	2.75	16	16.94
S3	28–30	16–17	12–13	2.70		18.04
S3—7% EAFSS—3%CFA	35	22	13	2.74	15	

Notes <sup>(1)</sup> LL = liquid limit, <sup>(2)</sup> PL = plastic limit, <sup>(3)</sup> PI = plasticity index, <sup>(4)</sup>  $G_s$  = Specific gravity, <sup>(5)</sup>  $\gamma_{d,max}$  = maximum dry unit weight, <sup>(6)</sup>  $w_{opt}$  = optimum moisture content

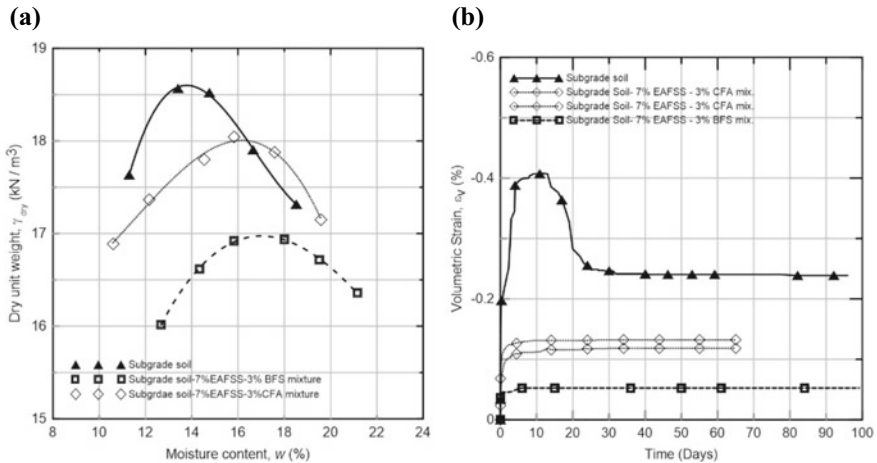


**Fig. 2** Soil-stabilization material mixtures: **a** compaction behavior **b** swelling response

The maximum volumetric strains ( $\epsilon_{v,max}$ ) of both soil-7% EAFSS-3%CFA and soil-7% EAFSS-3%BFS mixtures were lower than 0.15% (lower than the *in-situ* clayey soil). Both mixtures were able to alleviate the swelling of *in-situ* soils.

### 3.3 Strength-Gain Behavior of Soil-Stabilization Material Mixtures

Strength-gain behavior of the soil-stabilization material mixtures was determined through UC tests. Tests were performed on soil-7%EAFSS-3%CFA and soil-7% EAFSS-3%BFS mixtures that were cured for 1, 2, 4, 7, 14, and 30 days. Figure 3a shows the strength gain observed in the mixtures with respect to time. One (1)-day strength of both soil-7%EAFSS-3%CFA and soil-7%EAFSS-3%BFS mixtures were higher than the two (2)-day strength (i.e., 550 kPa) of the subgrade and hence, both mixtures were able to satisfy the criteria. A noticeable strength increase was observed for both of the mixtures tested as a function of curing time. Empirical equations (regression functions) are fitted to the experimental data. The UC strength ( $q_u$ ) of soil-7% EAFSS-3%CFA and soil-7%EAFSS-3%BFS mixtures cured for different times ( $t$  in days) can be predicted using Eqs. (1) and (2), respectively.

$$q_u = 760.06t^{0.0871} \quad (R^2 = 0.92) \tag{1}$$

$$q_u = 584.45t^{0.0432} \quad (R^2 = 0.92) \tag{2}$$

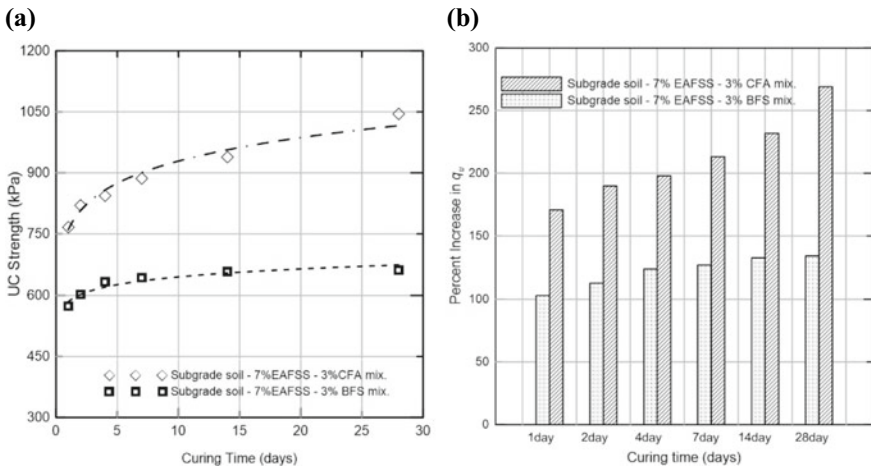


**Fig. 3** Strength gain behavior: **a** curing time versus UC strength of compacted mixtures **b** % UC strength increase with respect to reference with time

Strong cementitious reactions occurred in the soil-7%EAFSS-3%CFA mixture, accordingly the strength-gain with time was less pronounced in the soil-7% EAFSS-3%BFS mixture. This was attributed to the self-cementing characteristics of CFA. The % increase in strength gain with curing time for both mixtures are presented in Fig. 3b, assuming the *in-situ* clayey strength as a reference. Figure 3b shows that the strength of soil-7%EAFSS-3%CFA increases substantially (i.e., 270%) even after 14 days of curing time. The strength-gain behavior was different for the soil-7% EAFSS-3%BFS mixture (see Fig. 3b). For the soil-7%EAFSS-3%BFS mixture, the major portion of the strength increase was observed in the first seven (7) days of curing, and the strength gain was much less pronounced after the first week. The strength increase was only about 6% in the following three (3) weeks for the soil-7% EAFSS-3% BFS mixture [10].

Experimental results were evaluated together with the material availability, cost of preparation, and transportation of each mixture to the proposed implementation site and INDOT's local experience with stabilization. The 7%EAFSS-3%CFA mixture was selected as the economically most feasible and effective mixture for the implementation project.

## 4 Field Implementation

The minimum stabilized subgrade thickness is 1 ft (12-in.) per INDOT regulations. The subgrade of the 70-m section of the ramps located at the NW and SW quadrants of the diamond intersection at the implementation site was stabilized using 7%EAFSS-3%CFA mixture. The selected mixture was arranged off-site by blending 70% EAFSS-30%CFA (by weight) and brought to the field. The pre-mixed mixture was spread and thoroughly mixed with the clayey soils at the site using a truck with disks. Water was sprayed on the treated sections to bring the mixture to its  $w_{opt}$ . Compaction was facilitated with a sheepfoot roller with a minimum of five to six (5–6) passes and the finish grade was completed with a smooth-drum roller. The treated sections were protected from any disturbance from the traffic for about 72 h after compaction.

The quality control of the compacted subgrade was checked by dynamic cone penetration tests (DCPTs) on the NW and SW ramps on the sections of the subgrade stabilized with the 7% EAFSS-3%CFA mixture. On both ramps, DCPTs were performed ~ 1–3 h after completion of compaction. In the SW ramp stations, the NDCP values recorded for 0-to-6 in. (NDCP<sub>0~6"</sub>) and 6-to-16 in. (NDCP<sub>0~16"</sub>) penetration were in 8-to-18 and 17-to-24 ranges, respectively. In the NW ramp these counts were in 5-to-15 and 6-to-15 ranges, respectively. Figure 4a presents the distribution of these initial NDCP counts recorded in various stations. These NDCP values were most likely recorded prior to the occurrence of strong cementitious reactions. Even then both ramps could satisfy the criteria developed by the US DOT's untreated clayey soils. Two additional sets of DCPTs were performed on the SW ramp 96 h after compaction that are shown in Fig. 4b.

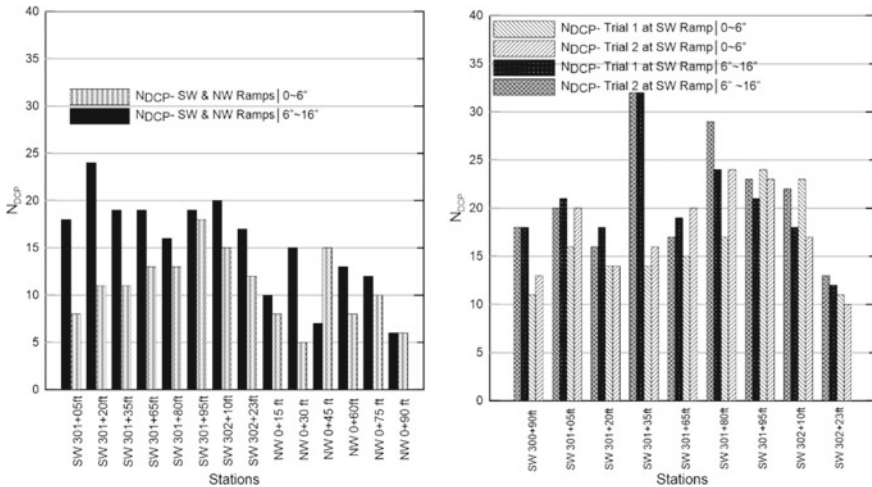


Fig. 4 NDCP a 1-to-3 h after compaction at SW and NW ramps b 96 h after recorded at SW ramps

The increase in the NDCP values with respect to time indicates the occurrence of cementitious reactions. Current INDOT specifications require a minimum average NDCP in the 16–20 range for modified soils [14]. Nonetheless, in this project, the average of the NDCP<sub>0''~6''</sub>, NDCP<sub>6''~12''</sub>, and NDCP<sub>16''~16''</sub>, values recorded 96 h after construction in the SW Ramp were 17, 14, and 21, respectively. The results of nuclear gage (NG) tests performed on five stations indicated relative compaction (RC) values in the 102.6% and 106.7% range that satisfied the minimum INDOT requirement: RC = 95–100% for field subgrade compaction [10]. Upon completion of field compaction quality tests, the subgrade was inspected to identify the presence of any weak or unsuitable zones. The subgrade surface was in intact condition and did not show any signs of cracks, discontinuities, or deformations before placement of the base course.

### 5 Conclusions

In this study, the feasibility of soil stabilization using material mixtures that incorporate electric-arc-furnace steel slag (EAFSS) was investigated. For this purpose, laboratory testing was performed on soil-7% EAFSS-3% CFA and soil-7% EAFSS-3% BFS mixtures. Stronger cementitious reactions and superior UC strength was observed in the 7%EAFSS-3%CFA mixture. Considering factors such as strength, local experience and economic feasibility, the 7%EAFSS-3%CFA mixture was used to improve the subgrade of the trial sections of a road construction project in which subgrade stabilization was required. The main steps of the subgrade construction included: (i) spreading the pre-mixed stabilization material mixture on the clayey

subgrade, (ii) diskings and water spraying, and (iii) compaction. For economic feasibility, the dry mixture was limited to 10% of the dry weight of subgrade soil, which was classified as CL. In order to determine the effectiveness of the stabilization, dynamic cone penetration tests (DCPTs) and nuclear gauge (NG) tests were performed on the subgrade. When DCPT tests performed on the SW ramp 3 and 96 h after compaction are compared, a visible increase is observed with time, indicating the improvement in the subgrade due to chemical reactions. The density values obtained from NG tests in the vicinity of DCPT locations correspond to relative compaction (RC) values higher than 100%, and hence field compaction was effective. When utilizing industrial by-products, environmental assessment including the leaching potential of the materials should be completed prior to use which was the case for this study. This study demonstrates that steel slag mixtures have the potential to be a cost-competitive alternative for soil stabilization, especially when the source of these industrial by-product is in the vicinity of the construction site.

**Acknowledgements** The authors are grateful for the financial support (FHWA/IN/ JTRP-2013/ SPR-3477), provided by the Indiana Department of Transportation (INDOT) and Edward C. Levy Co. (Levy) for the project. We convey our thanks to John Yzenas, Nayyar Zia Siddiki and Hobi Kim for their contributions to this study. The authors also appreciate the financial support provided by Bogazici University with BAP project number 16961.

## References

1. Shi C (2002) Characteristics and cementitious properties of ladle slag fines from steel production. *Cem Concr Res* 32(3):459–462
2. Yildirim IZ, Prezzi M (2015) Steel slag: chemistry, mineralogy, and morphology. In: Iskander M, Suleiman FM (eds) *IFCEE 2015*, March 17–21, geotechnical special publication No. 256, pp 2816–282. San Antonio, Texas
3. Santamaria A et al (2018) Dimensional stability of electric arc furnace slag in civil engineering applications. *J Clean Prod* 205:599–609
4. Yildirim IZ (2018) A comparative study on the compaction and swelling behavior of EAF-EAF ladle steel slags, *Zemin Mekaniği ve Geoteknik Mühendisliği 17. Ulusal Konferansı—ZMGM 17*, September 26–28, vol 2. İstanbul, pp 463–474
5. Ameri M, Hesami S, Goli H (2013) Laboratory evaluation of warm mix asphalt mixtures containing electric arc furnace (EAF) steel slag. *Constr Build Mater* 49:611–617
6. Ortega-López V et al (2018) Durability studies on fiber-reinforced EAF slag concrete for pavements. *Constr Build Mater* 163:471–481
7. Autelitano F, Giuliani F (2016) Electric arc furnace slags in cement treated materials for road construction: mechanical and durability properties. *Constr Build Mater* 113:280–289
8. Pasetto M, Baldo N (2018) Re-use of industrial wastes in cement bound mixtures for road construction. *Environ Eng Manag J* 17(2):417–426
9. Yildirim IZ et al (2013) Use of soil-steel slag-class-C fly ash mixtures in subgrade applications. Publication FHWA/IN/JTRP-2013/06. Joint Transportation Research Program, West Lafayette, Indiana. <https://doi.org/10.5703/1288284315188>
10. Yildirim IZ, Prezzi M (2022) Subgrade stabilisation mixtures with EAF steel slag: an experimental study followed by field implementation. *Int J Pavement Eng* 23(6):1754–1767. <https://doi.org/10.1080/10298436.2020.1823389>

11. ASTM D698–00a (2000) Standard test methods for laboratory compaction characteristics of soil using standard effort [12,400 ft-lbf/ft<sup>3</sup> (600 kN-m/m<sup>3</sup>)]. ASTM, West Conshohocken, PA
12. ASTM D2166/D2166M-16 (2016) Standard test method for unconfined compressive strength of cohesive soils. West Conshohocken, PA
13. ASTM D5102–04 (2004) Standard test method for unconfined compressive strength of compacted soil-lime mixtures. D5102–04, West Conshohocken, PA
14. INDOT (2015) Field testing of soil, granular soil, and coarse aggregate. Indiana Department of Transportation Office of Materials Management Office of Geotechnical Services, Indianapolis, Indiana

# An Experimental Investigation on Strength Behavior of Recycled Fine Aggregate (RCFA)-Treated Compacted Clayey Soils



Hashem Kishko, Z. Nil Kutlu, Aykut Şenol, and A. Onur Pehlivan

**Abstract** In geotechnical engineering applications, soils that exhibit plastic behavior over wide ranges of moisture content and liquid limits have the potential of low bearing capacity, settlement and potential of swelling/shrinking where they are generally considered to be as problematic soils. Although the compacted soils are commonly used in geotechnical engineering practice, compacted fine grained soils are not commonly preferred to be used for earthworks due to this plasticity in nature associated with complex hydro-mechanical behavior. Practicing engineers rely on using variety of design, construction and stabilization techniques to reduce these potential problems. In this aspect, promoting the use of recycled waste materials as improvement techniques and to make compacted fine grained soils usable by means of a stabilization becomes an important issue towards both for; proposing sustainable solutions and also sustainability for the construction of large infrastructures. Within scope of this study, shear strength properties for short term stability of compacted fine grained soils were tested to examine the convenience of adding—*recycled concrete fine aggregates*—for soil stabilization purpose to overcome these problems. The recycled concrete fine aggregates can be considered as a new material which were produced from crushing ready mix C16 concrete cast in 1250 × 2500 mm framework and after a curing period of 90 days. After crushing process, both coarse and fine aggregates were acquired. Since generally recycled coarse aggregates were used in structural concrete applications, only recycled fine aggregates were facilitated in soil stabilization. This paper gives a brief summary of the results of ongoing research on the shear strength behavior of non-treated and treated low plasticity clayey soil, emphasizing the effects of treatment parameters as: percent by weight of fine aggregate, and curing time. The results for the experimental analysis are reported showing the effect of fine aggregate addition on the strength behavior of compacted fine grained soil for relevant engineering applications.

---

H. Kishko · A. Şenol

Faculty of Civil Engineering, Istanbul Technical University, Istanbul 34469, Turkey

Z. N. Kutlu (✉) · A. O. Pehlivan

Faculty of Engineering and Natural Sciences, Maltepe University, Istanbul 34857, Turkey

e-mail: [zehranilkutlu@maltepe.edu.tr](mailto:zehranilkutlu@maltepe.edu.tr)



**Keywords** Recycled fine aggregate · Compacted clays · Soil stabilization · Treatment parameters

## 1 Introduction

Nowadays the essence for sustainable solutions to encounter some global threats such as global warming and climate change is a compelling necessity. While construction materials are being significantly used and being versatile in buildings and infrastructure, they have also a serious negative consequence on the environment. In addition to mining areas are being depleted over time, a large amount of energy is consumed to produce those mined natural aggregates. Thus, one of the viable solutions to preserve those sources is utilizing construction and demolition (C&D) waste as a partial or full replacement of natural aggregates in constructions.

Recycling of C&D wastes has been the ultimate advantageous and auspicious attempt towards remission of immense carbon emanation of the construction industry [1]. Over recent years, reusing of C&D materials in construction industry, concretely in embankments, road pavements, and backfills, has been the focus of attention for a large number of researchers. A major part of C&D wastes is concrete debris, which is the origin of recycled concrete aggregates (RCA) [2, 3]. In general terms, 65–80% of RCA is consisted of natural aggregates (NA), whereas 20–35% of cement mortar [4]. Using RCA as compacted aggregates in pavement bases and sub-bases gained wide engagement in recent decades [5–7]. However, mixing RCA with clayey soils to enhance the shear strength of subgrades have been rarely investigated.

Low strength, swelling, and high compressibility are common problems associated with clays. Literature is full of studies investigating the stabilization of clay soils with various additives such as cement, lime, and fly ash. The efficiency and selection of an additive rely on the type of soil and its field conditions. For the purpose of sustainability, adding RCA to soil was recently studied by many researchers [8–10]. They concluded that mixing C&D material with soil enhances the properties of soil alongside reducing environmental problems.

The purpose of this research study is to examine the effects of recycled concrete fine aggregates (RCFA) material and curing time on engineering properties of low plasticity clay. To achieve this goal, first, the properties of the clay and RCFA are introduced followed by the methodologies associated to investigate soil strength. Afterwards, results of compaction and unconfined compressive strength tests of pure clay only, and at various contents (5, 10, and 15%) of RCFA were evaluated.

## 2 Materials and Tests

### 2.1 Clay Soil

Initially, many geotechnical tests were performed to identify the clay. The measured geotechnical properties of the clay are summarized in Table 1. Atterberg limit and specific gravity tests were conducted according to [11, 12], respectively. As shown in Fig. 1, the grain size distribution was obtained in accordance with [13, 14]. Standard proctor test was used to determine maximum dry unit weight and the optimum moisture content of the soil by reference to [15]. Due to easily obtain samples at various experiments, miniature compaction tool calibrated to standard proctor test was utilized to obtain both the maximum dry unit weight and the optimum moisture content.

**Table 1** Geotechnical properties of soil

Liquid limit, %	34
Plastic limit, %	22
Plasticity index, %	12
$\gamma_{d-max}$ (kN/m <sup>3</sup> )	15.4
$\omega_{opt}$ , %	22
$G_s$	2.55
Passing 200 sieve (%)	100
Soil Type, USCS	CL

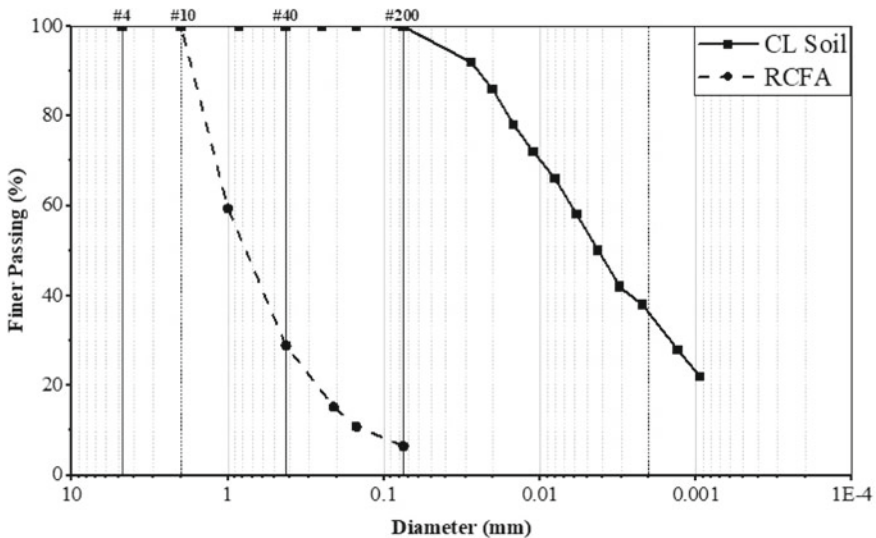
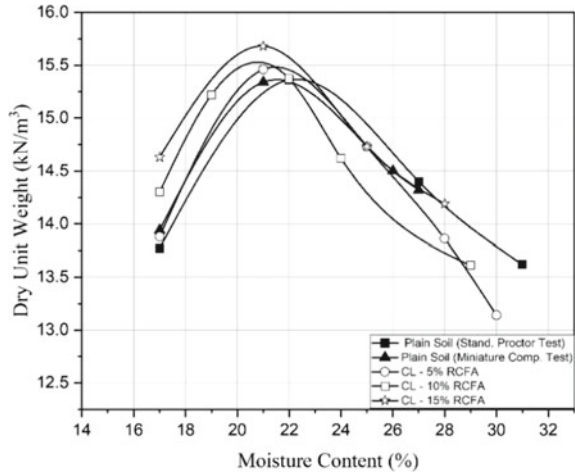


**Fig. 1** Size distribution of clay and RCFA

**Fig. 2** Compaction curves for plain soil and RCFA-clay mixtures



To calibrate this tool, standard proctor and miniature compaction tests were performed on the same sample by changing the number of blows and fall height until both curves have become close to each other as they are shown in Fig. 2.

## 2.2 Recycled Concrete Fine Aggregate (RCFA)

The recycled concrete was obtained from concrete blocks ( $1250 \times 2500$  mm) crushed after 90 days of casting for a specific research [16]. After crushing process, both coarse and fine aggregates were collected. While recycled coarse aggregates were mainly used in structural concrete applications, recycled fine aggregates were exclusively utilized in soil stabilization. Based on the research it was used for previously, the source concrete was C16 and had an average compressive strength reaching 20 MPa [16]. The specific gravity of RCFA was measured as 2.78 [12]. The gradation used in this experiment has a maximum particle size of 2 mm [13], as it is shown in Fig. 1.

## 2.3 Clay-RCFA Mixture

RCFA was mixed with clay as a proportion of this clay according to [17]. The adopted percentages of RCFA were 5%, 10%, and 15% by dry weight, respectively. Two approaches were endorsed, the first is to measure unconfined compressive strength (UCS) of the specimens immediately after the compaction, while the second is to measure UCS after 7 days of curing. Before mixing, both materials were oven dried. Then both were being mixed until the mixture appears uniform in color. Research

specimens, 50 mm in diameter and 100 mm in height, were constituted in three layers into a specially designed mold. The mold was being oiled to reduce friction. The ratio of specimens' diameter to maximum grain size was 25, which is more than the minimum of that limited by [18]. The specimens were extruded using a hydraulic specimen extruder machine, trimmed, weighed, measured, and wrapped in stretch film to be cured for 7 days in a moisture-proof container. After the identified curing period being reached, UCS test was performed on specimens in accordance with [18].

### 3 Results and Discussion

#### 3.1 Compaction Results

In this research, only for plain soil, both standard compaction and miniature compaction tests were performed in purpose of calibrating miniature compaction test to standard proctor compaction test. On the other side, for Clay-RCFA mixtures, only miniature compaction test was conducted at 5, 10, and 15% of RCFA for time-saving and less effort required. As it is shown in Fig. 2, it is noteworthy that an increase in RCFA percentage as for 5, 10 and 15%, leads to lower optimum moisture content and higher maximum dry unit weight. This may be emanated from some standpoints, these are: (i) mixing of soil with RCFA diminishes the surface area required to be moistened which conveys to reduction in optimum moisture content; (ii) occurring of hydration for residual unhydrated cement existed in RCFA helps to increase the bonding between clay-RCFA particles, thereby increasing soil density; (iii) the higher density of RCFA ( $G_s = 2.78$ ) compared to the clay ( $G_s = 2.55$ ), in like manner, contributes to boosting dry unit weight.

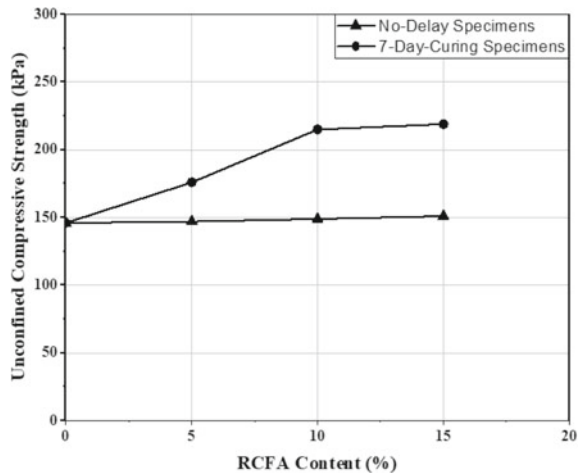
#### 3.2 Unconfined Compressive Strength

The results of unconfined compressive strength test in terms of axial stress are presented in Table 2. It can be seen from Fig. 3, while the specimens with RCFA measured immediately after the compaction show slight increase in axial stress in comparison to the plain soil, a considerable rise in UCS is noticed for specimens experienced humid curing. As an example of a mixture, i.e. RCFA = 15%, the curing duration leads to 50% increase in UCS after 7 days. A comparison between both curves shows that the curing duration is farther influential than that with no delay, hence demonstrating a time-based interaction of RCFA and soil particles. It is worth mentioning that high UCS values are observed at lower moisture content as compared to plain soil, specifically for no curing time specimens.

**Table 2** Unconfined compressive strength of soil samples treated with RCFA

Curing time (days)	RCFA content (%)	Unconfined compressive strength (kPa)		
		<i>w</i> = 18%	<i>w</i> = 22%	<i>w</i> = 26%
0	0	112	146	70
	5	147	141	95
	10	149	96	33
	15	151	89	49
7	0	112	146	70
	5	176	144	96
	10	215	146	74
	15	219	171	88

**Fig. 3** UCS with respect to RCFA content



From the results, it can be concluded that the percentage of RCFA does not play a significant role in increasing the strength of soil; nevertheless, initial moisture content and curing time are prime factors affecting the strength.

### 4 Conclusion

Sustainable development should be of urgent need in dealing with environmental problems. In regard to construction industry, utilizing recycled C&D materials as alternatives to natural aggregates can contribute to the reduction of environmental impacts. In this study, a series of geotechnical tests were performed to evaluate experimentally the effects of RCFA content and curing time on some geotechnical

properties and unconfined compressive strength of low plasticity clay. The following conclusions were drawn from the present research:

- i. Alike standard Proctor compaction test, utilizing miniature compaction test is to obtain maximum dry unit weight and optimum moisture content. Using miniature compaction apparatus, however, is more efficient regarding time and effort than using standard Proctor compaction apparatus.
- ii. Adding RCFA to clayey soil increases the maximum dry unit weight while the optimum moisture content decreases. This stems from diminishing the surface area required to be moistened for clay-RCFA mixture, the bonding occurred by the hydration of cement existed in clay-RCFA mixture, and the higher density of RCFA compared to the clay.
- iii. Curing process plays a great role in enhancing the strength. At 5% RCFA specimens with 7-day curing time shows that UCS is 20% greater compared to no-delay specimens. While UCS of 7-day cured specimens are 44% and 45% higher than no-delay specimens at 10% and 15% RCFA, respectively. Thus adding RCFA to clayey soil leads to a slight increase in UCS for no-delay specimens, and to a significant increase in UCS for specimens with curing time. While the strength was not enhanced noticeably for no-delay specimens compared to the plain soil, 21%, 47%, and 50% increase in the strength at percentages 5%, 10%, and 15% RCFA, respectively, were recorded in comparison to the plain soil.

## References

1. Nwakaire CM et al. (2020) Utilisation of recycled concrete aggregates for sustainable highway pavement applications; a review. *Constr Build Mater*
2. Pasandin AR, Pérez I (2015) Overview of bituminous mixtures made with recycled concrete aggregates. *Constr Build Mater* 74:151–161
3. Tam VW (2009) Comparing the implementation of concrete recycling in the Australian and Japanese construction. *J Clean Prod* 17(7):688–702
4. Kien TT et al. (2013) Recycling construction demolition waste in the world and in Vietnam. In: *The international conference on sustainable built environment for now and the future*, Hanoi
5. Rahman MA et al. (2015) Engineering and environmental assessment of recycled construction and demolition materials used with geotextile for permeable pavements. *J Environ Eng* 141(9)
6. Da Conceição Leite F et al. (2011) Laboratory evaluation of recycled construction and demolition waste for pavements. *Constr Build Mater* 25(6):2972–2979
7. Poon CS, Chan D (2006) Feasible use of recycled concrete aggregates and crushed clay brick as unbound road sub-base. *Constr Build Mater* 20(8):578–585
8. Kianimehr Marzieh et al (2019) Utilization of recycled concrete aggregates for light-stabilization of clay soils. *Constr Build Mater* 227:116792
9. Karkush MO, Yassin S (2019) Improvement of Geotechnical properties of cohesive soil using crushed concrete. *Civ Eng J* 5(10)
10. Jili Q et al. (2021) Characterization and comparison research on composite of alluvial clayey soil modified with fine aggregates of construction waste and fly ash. *Sci Eng Compos Mater* 83–95

11. Standard test methods for liquid limit, plastic limit, and plasticity index of soils (2017) ASTM D4318
12. Standard test methods for specific gravity of soil solids by water pycnometer (2017) ASTM D854-02
13. Standard test method for sieve analysis of fine and coarse aggregates (2017) ASTM C136-01
14. Standard test method for materials finer than 75- $\mu$ m (no. 200) sieve in mineral aggregates by washing (2017) ASTM C117-95
15. Standard test methods for laboratory compaction characteristics of soil using standard effort (12 400 ft-lbf/ft<sup>3</sup> (600 kN-m/m<sup>3</sup>)) (2017) ASTM D698-07
16. Pehlivan AO (2018) Investigation of fatigue and durability properties of concrete containing recycled concrete aggregate. Ph.D. Dissertation, Bogazici University
17. Standard practice for laboratory preparation of soil-lime mixtures using mechanical mixer (2017) ASTM D3551-17
18. Standard test method for unconfined compressive strength of compacted soil-lime mixtures (2017) ASTM D5102-96

# Sodium Borohydride Assisted Catalytic Reduction of Toxic Pollutants by Carbon and Nitrogen Based Poly-meric Compounds: A Review



Dimitra Das, Kalyan Kumar Chattopadhyay, and Somnath Mukherjee

**Abstract** Water pollution is one of the greatest concerns in today's world which needs immediate attention and strict regulatory surveillance to prevent its paramount adverse effects on the environment. Chemical pollutants discharged from countless industries like textiles and pharmaceuticals contribute extensively to contaminating freshwater resources of this planet whereby causing deleterious effects on all living organisms including human beings. Coloured dyes like Rhodamine B, Methyl Orange, Methylene Blue etc. and phenolic compounds like 4-Nitrophenol are a few of such pollutants whose degradation and complete removal from water-bodies are of utmost importance to avert pernicious environmental consequences. One of the most efficient techniques includes chemical catalytic reduction of these harmful pollutant compounds in the presence of sodium borohydride and appropriate catalyst materials, and this is a rapid degradation procedure moderated by the electron-relay effect. Polymeric compounds comprised of carbon and nitrogen elements are a distinctive class of materials that procured massive prominence in recent times owing to their prospective applications in numerous practical fields, including wastewater purification. Substantial porosity and surface area, non-toxic nature, low-cost and high-yield of production along with notable stability and durability are some of the remarkable features possessed by these materials which in turn make them a promising and efficient contestant for catalytic activities. The present article will try to abridge the findings of several reported literature that have dealt with the sodium borohydride induced catalytic reduction of toxic pollutants emitted from industrial plants by pure and doped carbon and nitrogen based materials.

**Keywords** Water purification · Chemical catalysis · Sodium borohydride · Toxic pollutants · Carbon and nitrogen based materials · Electron-relay effect

---

D. Das (✉) · K. K. Chattopadhyay  
School of Materials Science and Nanotechnology, Jadavpur University, Kolkata, India  
e-mail: [dimitradas248@gmail.com](mailto:dimitradas248@gmail.com)

S. Mukherjee  
Department of Civil Engineering, Jadavpur University, Kolkata, India



## 1 Introduction

Our planet is rapidly plummeting towards a severe environmental crisis due to pollution-related hazards. Advancement of human civilization has led to the enormous boom in the industrial sectors like textile, pharmaceuticals, printing, tanning, leather, explosives etc.; which in turn have massively contributed to the exhaustion and jeopardy of our natural resources accompanied with an extreme threat to our ecological system. Poisonous organic dyes which are essentially non-degradable in nature are discharged in gross amount into water environment from different industrial sources thereby causing drastic health risks in human beings and more severe menaces to aquatic organisms. A review by Hasanbeigi et al. reveals that textile manufacturing and dyeing industries are one of the primary generators of effluents in wastewater [1]. Another report by Kant et al. claims that approximately 3600 types of synthetic dyes are currently being produced by textile industries, most of which are extremely hazardous [2]. Out of the innumerable environmental devastations caused by textile industries, 80% of them are resulted from the discharge of pollutant dyes into aquatic bodies without undergoing regulatory treatment procedures [3]. Conventional water-treatment and purification procedures are not suitable enough for complete removal of these dyes because most of them are highly soluble in aqueous media [4]. A detailed study by Hassan et al. shows that India is one of the leading countries in manufacturing of dye products beside China owing to the ever-growing population in these two countries [4]. Synthetic dyes cause countless inimical effects on aquatic ecosystem by prohibiting the sunlight to pass through water, thus disturbing the natural photosynthetic activities of aquatic plants for oxygen production which in turn severely affect the lives of aquatic biota [5]. These dyes also cause substantial damage to human health by affecting skin, eyes, liver, stomach, reproductive and central nervous system and in cases of extreme exposure can cause carcinogenic effects [6]. Hence appropriate treatment of these dyes along with rigorous control on their emission before being discharged into fresh water-bodies is absolutely necessary to protect the environment from their hazardous effects.

There are several standard physical, chemical and biological procedures followed conventionally for the treatment of discharged pollutants, some of which include removal of synthetic dyes by adsorption technique [7], and partial or complete decomposition of dye compounds by advance oxidation processes (AOP) [8]. Other than these, Fenton, light assisted Fenton; and UV/visible/solar light induced photocatalytic degradation techniques deserve special mention owing to their facile applicability and appreciable rate of success [9–11]. Chemical precipitation methods, reverse osmosis, coagulation techniques employing alum, ferric sulphate, lime etc., membrane separation, ion-exchange, and bio-degradation of pollutants by micro-organisms are also some of the widely used methodologies engaged in waste-water purification [12–16]. Among all the above-mentioned procedures, adsorption and photocatalysis have been extensively availed for decreasing the concentration of

pollutants present in waste-water effluents and degrading the coloured dyes to non-toxic products respectively [17]. There are plenty of well-established adsorbent (like activated carbon, agricultural waste products obtained from rice husks, orange peels, fish scales etc.) and photocatalytic materials (like metal oxides and sulphides: TiO<sub>2</sub>, ZnO, CdS, ZnS etc.) which have been largely utilised for effective water purification owing to their high efficiency and cost-effective nature. However, these processes endure several drawbacks which restraint their implementation in practical fields. The fundamental limitation lies in the time taken for the toxic pollutants to be completely degraded or fully adsorbed by the catalyst or adsorbent respectively, which in most cases take considerable amount of time. Moreover, choice of materials for both these processes is another constraint since photocatalysis generally requires semiconductor materials having relevant band edges for dye degradation whereas adsorption demands highly porous materials possessing significant surface area.

In contrary, sodium borohydride (NaBH<sub>4</sub>) induced catalysis procedure is a relatively potent method for expeditious degradation of pollutants which is gradually finding relevance in waste-water remediation. The elementary concept of this method is a simple electron-relay process which occurs between the BH<sub>4</sub><sup>-</sup> ions and the pollutant complexes moderated by a catalyst. The faster the transport of electrons through the system, faster is the rate of degradation of the pollutants. As a result of this, very toxic contaminants can be rapidly degraded to innocuous end products. Till date, most of the researches performed on this procedure have utilized metal nanoparticles (like Au, Ag, Pd, Cu etc.) because of the high availability of free electrons on their surface. However, metal nanoparticles are required to be strongly anchored or embedded on a matrix (generally carbon and/or nitrogen polymeric-based, activated carbon, graphene, carbon nano-tubes/fibres etc.) to avert agglomeration of the nanoparticles and to enhance their catalytic performance [18].

Carbon and nitrogen (C–N) based polymeric materials are a promising class of functional materials which have been successfully implemented in numerous fields including energy related applications, optoelectronics, photovoltaics, and most importantly water purification. In this regard, 2D material like graphitic carbon nitride (C<sub>3</sub>N<sub>4</sub>/GCN) deserves special mention. This porous material has exotic properties which include appreciable thermal and chemical stability [19], impressive band edge potentials to facilitate catalytic reactions; and an exciting nitrogen rich triazine-based layered morphology which provides a strong support for immobilization of metal nanoparticles into the GCN matrix. GCN itself lacks active sites for adsorption of the pollutants on its surface, hence surface modification of GCN by incorporation of metal nanoparticles are frequently performed to activate the GCN surface for catalytic performances.

In this review article, the authors will mainly focus on the NaBH<sub>4</sub> assisted technique for pollutants degradation by primarily GCN and other carbon and nitrogen based polymeric materials.

## 2 Catalytic Reduction Procedure

For degradation of toxic pollutants by  $\text{NaBH}_4$ -induced procedure, the concentration of sodium borohydride is usually maintained at a higher value than that of the pollutants concentration. The kinetics of rate of degradation is thus a pseudo-first order type since it assumes that the concentration of  $\text{NaBH}_4$  remains unaltered throughout the reaction and hence does not influence the reaction rate. The rate of degradation is calculated following the pseudo-first order equation given by:

$$\ln\left(\frac{C_0}{C_t}\right) = kt \quad (1)$$

where,  $C_0$  = concentration of pollutant at time  $t = 0$

$C_t$  = concentration of pollutant at time  $t$ .

$k$  = pseudo-first order reaction rate constant obtained from the slope of the linear curve of  $[\ln(C_0/C_t)]$  plotted against time  $t$ .

The experimental procedure is comparatively much simpler and cost-effective than traditional photocatalysis or adsorption methods owing to the minimal requirements of equipment and catalyst amount. Initially, a solution of the pollutant of choice having a given concentration is prepared (let this be solution A having a concentration of  $10^{-5}$  M which is the stock solution). Next a stock solution (solution B) of  $\text{NaBH}_4$  is prepared having a concentration higher than that of solution A (let this be 0.001 M). A small amount of catalyst (let  $C$  mg) is first taken in a quartz cuvette, followed by the addition of some quantity of solution A (let 0.3 mL) and solution B (let 3 mL) in rapid succession. The quartz cuvette is immediately placed inside an UV-Vis spectrophotometer and the absorbance data is collected subsequently in second or minute time interval depending on how fast the reaction proceeds. With time, the intensity of the characteristic absorption peak of the particular pollutant gradually decreases which suggests the eventual reduction of the pollutant to end-products. The  $C_0$  and  $C_t$  values correspond to the absorption intensities at different time intervals, the plotting of which against time gives the rate constant values.

## 3 Different Types of Pollutants Present in Waste-Water

Presently, the aquatic ecosystem of the planet earth is in serious vulnerable situation owing to the alarming amount of pollutants being continuously discharged into the water environment from different industries. In this review article we will mainly discuss about some common dye compounds like Methyl Orange (MO), Rhodamine B (RhB) and Methylene Blue (MB) which are discharged from textile industries; and also about nitrophenol compounds whose main sources of emission are explosive, pesticides and leather industries. The sources, properties, and toxic effects of these

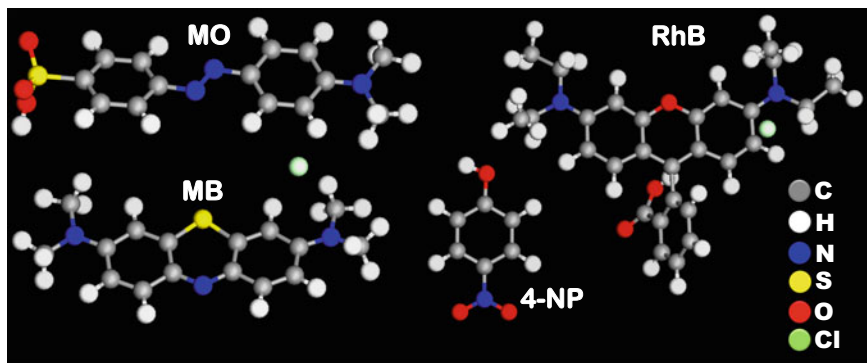


**Fig. 1** Chemical structure of different conventional toxic pollutants present in waste-water

pollutants are discussed in details below. Figure 1 shows the chemical structures of the respective pollutants.

### 3.1 Methyl Orange (MO)

MO is a frequently discharged hazardous effluent emitted primarily from textile industries and also from cosmetics, pharmaceuticals, and leather factories [20]. This azo dye is anionic in nature and has high solubility property. Moreover, the dye has non-biodegradable, carcinogenic and mutagenic properties which render its immense harmful nature towards aquatic organisms and human beings. It can cause diarrhea, vomiting effects, breathing problem, along with irritation in respiratory tract, skin and eyes. This dye has an intense orange color with the chemical formula  $C_{14}H_{14}N_3NaO_3S$  and a molecular weight of 327.33 g/mol. The aqueous solution of MO generates two absorption peaks as determined from UV–Vis spectrophotometer which are located at 464 and 265 nm. The delocalized  $\pi$  electrons of the azo bond ( $-N=N-$ ) give rise to the prominent peak at 464 nm whereas the aromatic ring of the dye molecule results in the hump at 265 nm [21]. During the  $NaBH_4$  assisted catalytic degradation experiment of MO dye by a suitable catalyst, as observed from the UV–Vis spectrum, the peak at 464 nm gradually decreases in intensity with time, whereas there is a visible shifting of the hump at 265–256 nm. Simultaneously, there is rapid change in the intense orange color of the dye solution to colorless. This occurs due to the destruction of the azo bond of MO to form the non-toxic products *N,N'*-dimethyl-*p*-phenylenediamine and sodium salt of sulphanilic acid at the end of the catalytic reactions [21].

### 3.2 Rhodamine B (RhB)

RhB dye belongs to the xanthene group of dyes and is cationic in nature. This toxic dye is majorly released from textile and paint industries along with significant emission from cosmetics and paper industries [22]. The potential health hazards of this dye to human beings include eye irritation leading to chemical conjunctivitis and injury to cornea, skin irritation upon contact with skin, gastrointestinal distress combined with diarrhea and vomiting, irritation in respiratory tract, along with carcinogenic effects [23]. This bright pink colored dye has the chemical formula  $C_{28}H_{31}ClN_2O_3$  and molecular weight of 479.02 g/mol. Due to its bright pink color, this dye exhibits an absorption peak near 554 nm in aqueous condition as observed from the UV spectrum. During the  $NaBH_4$  induced catalytic degradation procedure, there occurs simultaneous decrease in the intensity of the peak at 554 nm along with the origin of a peak at 237 nm with time. These phenomena suggest the breaking of the conjugated xanthene structure of RhB to form leuco-RhB along with the de-ethylation of RhB molecule [24]. Leuco-RhB is the non-toxic end product of the catalytic process.

### 3.3 Methylene Blue (MB)

MB is a bright blue colored cationic dye possessing thiazin group. This dye is primarily released into the water-bodies from textile and paper printing industries with alarming rate of emission from silk, cotton and fabric dyeing industries [25]. MB has the chemical formula  $C_{16}H_{18}ClN_3S$  and molecular weight of 319.85 g/mol. Because of its highly soluble nature in aqueous medium, impressive stability in varying conditions, and non-biodegradable nature, MB exhibits significant hazardous effects to human beings. These include gastrointestinal irritation, headache, dizziness, diarrhea, high blood pressure etc. Moreover, MB toxicity can also cause jaundice, local tissue necrosis, anemia, cyanosis and heart diseases [26]. MB in its unprotonated form exhibits two prominent absorption peaks at 611 and 663 nm as observed from its UV spectrum. During  $NaBH_4$  assisted catalytic procedure, in presence of a catalyst material, MB is rapidly degraded into its colorless end product leucomethylene blue.

### 3.4 Nitrophenol Compounds (NP)

These extremely hazardous groups of pollutants are primarily released from explosive industries and are treated as “priority pollutants” by most environmental organizations [27]. These compounds have significant usage in leather industries and also in industries manufacturing drugs, pesticides, fungicides, insecticides etc. The typical pollutants of this group include 2-NP, 3-NP and 4-NP out of which 4-NP is

considered to be the most hazardous. These pollutants have the chemical formula  $C_6H_5NO_3$  and molecular weight of 139.11 g/mol. These pollutants are believed to have carcinogenic and mutagenic effects on human beings. These compounds exhibit high solubility and stability in aqueous media due to which they are extremely difficult to be removed from water environment. Acute toxicity of nitrophenols can cause cyanosis, headaches, vomiting tendency, drowsiness, fatigue, irritation in eyes and skin etc. The aqueous solution of 4-NP is mild yellowish in color and gives an absorption peak around 316 nm. When  $NaBH_4$  is added into the pristine 4-NP solution, the solution rapidly turns bright yellowish in color due to the generation of 4-nitrophenolate ions, along with a visible shifting of the characteristic absorption peak to 400 nm. During the  $NaBH_4$  induced catalytic degradation procedure, there is gradual decrease in the intensity of this peak along with the formation of a new peak near 298 nm. The emergence of this peak along with the transformation of the yellow colored solution to colorless suggest the generation of 4-aminophenol as the non-toxic end product.

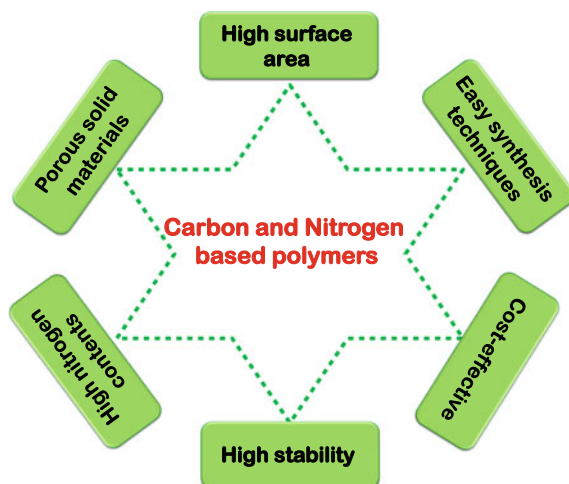
#### **4 Application of Carbon and Nitrogen Based Polymeric Materials in $NaBH_4$ Induced Catalytic Dye Degradation**

Metal NPs are easily embedded in polymeric matrices because of the rich functional groups of polymers ( $-OH$ ,  $-COOH$ ,  $-NH_2$  groups) which enable strong coordination bond formation with the metal NPs. GCN is a nitrogen rich polymeric material having a characteristic triazine core which acts as a suitable site for the incorporation of metal NPs. The lone pairs of nitrogen sitting at the edges of the triazine rings are excellent electron donors to form stable coordination complexes with the metal NP. Thus significant support and stability is provided to the metal NPs and in turn GCN becomes rich in catalytic active sites. Chemical catalytic reduction of toxic pollutants facilitated by  $NaBH_4$  has been an interesting research area for a long time. There have been innumerable research papers in this regard primarily dealing with metal nanoparticles (NPs) based catalysts for this type of catalytic reaction. However, this review article will only deal with the application of metal NPs doped carbon and nitrogen based materials with special focus on GCN (in its doped or composite form) for the  $NaBH_4$ -assisted reduction of pollutants. The lucrative properties of carbon and nitrogen based polymers are shown in a schematic representation in Fig. 2.

##### ***4.1 Catalytic Activity of Pristine and Doped C–N Based Polymeric Materials***

Gao et al. fabricated N-doped carbon nano-tubes from poultry feather wastes which could degrade 4-NP within 19 min and a rate constant value of  $2.1 \times 10^{-3} s^{-1}$  was

**Fig. 2** Properties of carbon and nitrogen based polymers



obtained [28]. Liu et al. utilized lignin and GCN as carbon source and nitrogen source respectively to fabricate nitrogen doped carbon which was subsequently employed for the rapid reduction of 4-Nitrophenol (4-NP) to 4-aminophenol (4-AP) within 50 s and having a rate constant value of  $4.77 \text{ min}^{-1}$  [29]. Edison et al. synthesized Ag NPs supported on N-doped carbon by hydrothermal method for the degradation of textile dyes like Methyl orange (MO) and Methylene Blue (MB) within 30 min and 15 min respectively [30]. The N-doped carbon support increased the stability of the Ag NPs thereby considerably improving the performance. Hayakawa et al. prepared nanocomposites based on Au NPs and dendrimers having  $-\text{NH}_2$  groups on the surface [31]. The as-prepared sample could reduce 4-NP within 18 min. Qiu et al. supported Au NPs on a conducting polymer nanotube, i.e. polypyrrole nanotube for effective catalytic degradation of 4-NP pollutant within 14 min [32]. The reaction rate constant value was calculated to be  $5.86 \times 10^{-3} \text{ s}^{-1}$ . Chang et al. reported synthesis of another type of conducting polymer, i.e. polyaniline nanofibres which they decorated with Ag NPs [33]. The as-synthesized nanocomposite in very small amount could degrade 4-NP within 3 min ( $k = 21.39 \times 10^{-3} \text{ s}^{-1}$ ). Ma et al. very recently developed a ternary composite comprised of  $\text{Ag}_3\text{PO}_4$ /Polypyrrole (PPy)/Polyaniline (PANI) for the degradation of both 4-nitrophenol and 2-nitroaniline [34]. 1 mg catalyst dosage resulted in the rate constant values of  $0.022 \text{ min}^{-1}$  and  $0.0053 \text{ min}^{-1}$  for 2-NA and 4-NP pollutants respectively. The composite synthesized at a ratio of 1:1 between PPy and PANI showed improved catalytic activity compared to the samples synthesized in other ratios since this composite catalyst exhibited impressive specific surface area accompanied by reduced pore size. Zhang et al. first synthesized fungal biochars and then introduced nitrogen doping in it for effective utilization of the sample in degrading 4-NP within 2 min [35]. The superior surface area of the catalyst ( $997 \text{ m}^2 \text{ g}^{-1}$ ) along with a high pore volume was the primary reasons for the impressive catalytic activity. With increase in the nitrogen content in the biochar, the catalytic

performance improved significantly and a rate constant value of  $7.26 \times 10^{-2} \text{ s}^{-1}$  was obtained. The nitrogen doping helped in providing more catalytic active sites in the biochar. Wang et al. developed two composite catalysts  $\text{Co}_3\text{O}_4/\text{N}$ -doped carbon and  $\text{Co-Co}_3\text{O}_4/\text{N}$ -doped carbon by sol-gel technique which exhibited  $\text{NaBH}_4$ -induced catalytic degradation of 4-NP [36]. It took 1.5 min to achieve complete reduction of 4-NP and the obtained rate constant value was  $2.29 \times 10^{-2} \text{ s}^{-1}$ . Mengying et al. synthesized two triazinyl-based covalent organic frameworks (COF) and introduced Pd clusters having a dimension of 0.8 nm into the pores of the as-synthesized COFs [37]. The composites could degrade 4-NP within 512 s and 365 s having rate constant values  $0.0102 \text{ s}^{-1}$  and  $0.0145 \text{ s}^{-1}$  respectively. They also performed the catalytic degradation of Mordant Green 17 (MG 17) dye in presence of  $\text{NaBH}_4$ . The two composites degraded MG 17 within 296 s and 1203 s respectively. In 2021, Subodh et al. reported the synthesis of a novel micro-spherical cross-linked covalent organic polymer with impressive surface to volume ratio [38]. The as-synthesized polymer named as TATF-COM was subsequently immobilized with Ag nanoparticles. This helped in prevention of agglomeration and in turn improved the recyclable property of the catalyst. The polymer was able to degrade 4-NP, 2,4-dinitrophenol (2,4-DNP), and 2,4,6-trinitrophenol (picric acid) within 120 s, 200 s, and 180 s respectively. Moreover the rate constant values increased with increase in the temperature gradient. A detailed list is provided in Table 1.

## 4.2 Catalytic Activity of GCN in Its Doped and Composite Forms

### 4.2.1 Doping of GCN

There are number of existing research articles on incorporation of noble metal NPs like Au, Ag, Pd into GCN for enhancement of catalytic activity in degradation of several toxic pollutants like MO, MB and 4-NP. Due to the exotic  $\pi$ -conjugated structure of GCN, it can not only adsorb NPs, but can also promote easy charge transfer throughout the molecule. Wang et al. and Veerakumar et al. anchored Ag NPs on GCN and Ag NPs on  $-\text{NH}_2$  functionalised GCN respectively for the catalytic degradation of 4-NP [39, 40]. Wang et al. reported a degradation time of 14 min whereas Veerakumar et al. could achieve complete degradation in as fast as 30 s. Like silver, gold NPs have also been supported on GCN matrix or made into nanocomposites with GCN for application in waste-water remediation. Bhowmik et al. reported the synthesis of very small Au NPs supported on GCN sheets which were efficiently utilized for the  $\text{NaBH}_4$ -assisted reduction of 4-NP [41]. They could achieve complete degradation in extremely short period of time (15 s). Nguyen et al. reported the fabrication of Au/GCN nanocomposite for utilization in the catalytic degradation of several nitrophenol compounds (2-NP, 3-NP, 4-NP, 2,4-NP, and 2,4,6-NP) [42]. They found that the performance of the catalyst was dependent on the initial



**Table 1** Catalytic activity of pristine and doped C–N based polymeric materials

Sample	Conc. of pollutant	Conc. of NaBH <sub>4</sub>	Catalyst Amnt	Time (min)	k (min <sup>-1</sup> )	Refs.
N–CNTs	4-NP: 3 mM (0.15 mL)	1.7 g/L (1 mL)	0.15 mg	19	0.126	[28]
NC	4-NP: 1.4 g/L (1.6 mL)	6.4 mmol	5 mg	0.83	4.77	[29]
NC–AgNPs	MB: 50 μM (2 mL)	0.005 M (0.95 mL)	0.05 mL	15	0.1581	[30]
	MO: 0.15 mM (2 mL)			30	0.0785	
PAMAM G5	4-NP: 3 mmol dm <sup>-3</sup> (0.1 cm <sup>3</sup> )	0.3 mol dm <sup>-3</sup> (0.1 cm <sup>3</sup> )	0.15 cm <sup>3</sup>	18	0.1446	[31]
PPyNTs/Au	4-NP: 4 mM (0.1 mL)	0.3 M (0.1 mL)	1 mg/mL (0.1 mL)	14	0.3516	[32]
AgNPs/PANINFs	4-NP: 5 mM (2 mL)	0.16 M (2 mL)	2.7 mg	3	1.2834	[33]
Ag <sub>3</sub> PO <sub>4</sub> /PPy/PANI	4-NP: 1 mM (5 mL)	0.01 M (20 mL)	1 mg	36	0.0053	[34]
	2-NA: 1 mM (5 mL)			120	0.022	
N doped fungal biochars	4-NP: 0.2 mM (20 mL)	200 mM (10 mL)	1 mg	2	4.356	[35]
Pd@COF–Ph	4-NP: 0.01 M (30 μL)	0.19 M (0.25 mL)	10 mg/mL (10 μL)	8.53	0.612	[37]
Pd@COF–BPh				6.08	0.87	
Ag@TATF–COM	4-NP: 25 mM (4 mL)	~ 100 (equiv.)	2 mg	2	1.356	[38]

concentration of the pollutants, pH, and presence of inorganic anions like Cl<sup>-</sup>, H<sub>2</sub>PO<sub>4</sub><sup>-</sup>, SO<sub>4</sub><sup>2-</sup>, NO<sub>3</sub><sup>-</sup> and HCO<sub>3</sub><sup>-</sup>. It took 10 min to completely degrade 4-NP along with a rate constant value of  $1.5 \times 10^{-2} \text{ s}^{-1}$ . Fu et al. also synthesized Au/GCN contact system for rapid reduction of 4-NP within 10 min and they obtained a rate constant of  $5.9362 \times 10^{-3} \text{ s}^{-1}$  [43]. Zhou et al. synthesized porous and ultrathin GCN nanosheets as a support for anchoring Au NPs on its surface [44]. The time taken for degradation of 4-NP was 200 s and the associated rate constant was calculated to be  $16.21 \times 10^{-3} \text{ s}^{-1}$ . Balakumar et al. uniformly assembled Au NPs on sulphur doped GCN to form a composite catalyst used for the degradation of 4-NP within 5 min and the corresponding 'k' value was  $0.796 \text{ min}^{-1}$  [45]. Many researchers have shown that bimetallic nanoparticle-based composites exhibit enhanced catalytic efficiency compared to single nanoparticles. In this regard, Fang et al. synthesized Pd/Au bimetallic NPs anchored on ultrathin GCN nanosheets which were able to

degrade 4-NP within 5 min [46]. Apart from Au and Ag NPs, there are also significant reports on immobilization of Pd NPs on GCN matrix. Zhao et al. developed platelet-like Pd/GCN nano-catalyst for efficient reduction of nitroarene compounds and they could achieve complete 4-NP degradation with 10 min with associated rate constant of  $0.00729 \text{ s}^{-1}$  [47]. Kumar et al. immobilized Pd NPs on nitrogen-rich GCN nanosheets for catalytic reduction of several pollutants including 4-NP, Methyl red (MR), MB and RhB within 60 s, 120 s, 80 s and 60 s respectively [48]. The corresponding rate constant values were calculated to be  $4.21 \times 10^{-3} \text{ s}^{-1}$ ,  $3.78 \times 10^{-3} \text{ s}^{-1}$ ,  $2.04 \times 10^{-3} \text{ s}^{-1}$ , and  $2.11 \times 10^{-3} \text{ s}^{-1}$  for 4-NP, MR, MB and RhB respectively. Apart from noble metal nanoparticles, GCN has also been decorated with other metal NPs like Cu and Ni along with their oxides or sulphides. Huang et al. anchored Cu NPs on GCN surface and utilized the as-prepared samples for efficient catalytic activity in degrading 4-NP within 360 s and obtained a rate constant value of  $1.86 \times 10^{-2} \text{ s}^{-1}$  [49]. Our group synthesized Ni doped GCN in different molar ratios and the best sample exhibited complete reduction of MO dye within 4 min [50]. The corresponding rate constant value was calculated to be  $1.421 \text{ min}^{-1}$  (Fig. 3).

Recently, our group has developed Cu-decorated and Ni-decorated GCN catalysts to degrade a wide range of pollutants conventionally present in waste-water [51]. We reported rapid degradation of 2-NP, 3-NP, 4-NP, MO, MR, RhB, MB, Congo Red (CR), Rose Bengal (RB) and a mixture of dyes within 5 min, 5 min, 3 min, 3 min, 4 min, 4 min, 4 min, 4 min, 3 min, and 7 min respectively by Cu decorated GCN catalyst. The corresponding rate constant values were calculated to

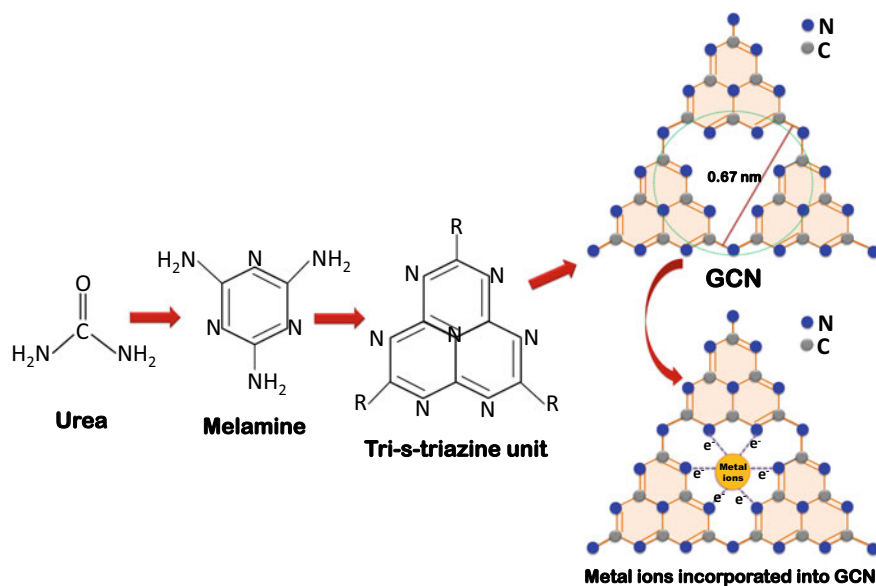


**Fig. 3** Gradual formation of GCN from raw precursor urea and schematic of metal ion incorporation into the GCN matrix

be  $0.8519 \text{ min}^{-1}$  (2-NP),  $1.8669 \text{ min}^{-1}$  (3-NP),  $1.1023 \text{ min}^{-1}$  (4-NP),  $2.1134 \text{ min}^{-1}$  (MO),  $1.4506 \text{ min}^{-1}$  (MR),  $1.3923 \text{ min}^{-1}$  (CR),  $1.6127 \text{ min}^{-1}$  (MB),  $1.9623 \text{ min}^{-1}$  (RhB),  $1.5216 \text{ min}^{-1}$  (RB), and  $0.3495 \text{ min}^{-1}$  (mixed dye). Moreover we performed detailed experiments to understand the effects of catalyst dosage,  $\text{NaBH}_4$  concentrations, pollutants concentrations and pH on the catalytic activities of the metal decorated GCN catalysts. We also carried out extensive first principles calculations to report the plausible mechanism of pollutant degradation by Cu-GCN sample. Saravanakumar et al. decorated GCN nanosheets with noble metal nanoparticles like Ag, Au, and Pd for rapid reduction of 4-NP by  $\text{NaBH}_4$  [52]. Among all the catalysts, Pd decorated GCN showed the best catalytic activity with a rate constant value of  $1.141 \text{ min}^{-1}$ . Ag-GCN, Pd-GCN, and Au-GCN could degrade 4-NP completely within 16 min, 4 min, and 6 min respectively. The main reason for the superior catalytic efficiency of Pd-GCN is due to the high electron density on its surface which facilitated faster transfer of electrons. GCN acted as a stabilizer which helped in the deposition of the noble metal nanoparticles on its two dimensional matrix. Nisha et al. reported the synthesis of a series of Cu doped GCN catalysts for catalytic hydrogenation of 4-NP [53]. The best sample with 1 wt% Cu content in GCN took 7 min to degrade 4-NP with a rate constant value of  $0.103 \text{ min}^{-1}$ . A detailed list is provided in Table 2.

#### 4.2.2 Heterojunctions of GCN

There are some interesting reports on synthesis of different types of heterojunctions or nanocomposites by coupling GCN with other compounds and their subsequent application in water purification. Ayodhya et al. synthesized a composite of  $\text{Ag}_2\text{S}$  and GCN which exhibited enhanced catalytic activity than both pristine GCN and  $\text{Ag}_2\text{S}$  [54]. The composite took 42 min to completely degrade 4-NP in presence of  $\text{NaBH}_4$ . They also varied the  $\text{NaBH}_4$  concentration to study the effect on  $\text{NaBH}_4$  on the catalytic activity. Yu et al. synthesized another type of nanocomposite based on Ag/GCN loaded carbon nanofibres by a combined procedure of electrospinning and carbonization [55]. The as-prepared sample took 50 min to achieve complete reduction of 4-NP to 4-AP with a rate constant value of  $0.094 \text{ min}^{-1}$ . A detailed experimentation and statistical optimization for the reduction of 4-NP by a tertiary composite catalyst  $\text{CeO}_2/\text{GCN}/\text{Ag}$  was reported by Pinheiro et al. [56]. Box-Behnken design of Response Surface Methodology was performed to study in-depth the effects of catalytic parameters like catalyst amount, reaction time,  $\text{NaBH}_4$  amount, and 4-NP concentration on the degradation activity of the composite catalyst. Time taken for complete degradation of 4-NP was 10 min. Verma et al. synthesized bi-functional ternary Ag-Cu<sub>2</sub>O-CuO/GCN composite catalysts for the reduction of 4-NP [57]. 97.8% of reduction was achieved within 4 min with a rate constant value of  $0.334 \text{ min}^{-1}$ . Effect of catalyst dosage and 4-NP concentration on the catalytic activity was also investigated. Mohammadi et al. reported the immobilization of Ag NPs on  $\text{Fe}_3\text{O}_4$ -polyallylamine decorated GCN substrate [58]. The nanocomposite was subsequently applied in the rapid reduction of textile dyes like MO and

**Table 2** Catalytic activity of GCN in its doped forms

Sample	Conc. of pollutant	Conc. of NaBH <sub>4</sub>	Catalyst Amnt	Time (min)	k (min <sup>-1</sup> )	Refs.
Ag/GCN	4-NP: 1.03 × 10 <sup>-4</sup> M (150 mL)	0.3 M (3 mL)	15 mg	14	0.186	[39]
Ag-NH <sub>2</sub> /GCN	4-NP: 1 × 10 <sup>-4</sup> M (3 mL)	0.3 M (0.1 mL)	3 mg/mL	0.5	9.564	[40]
Au-CN <sub>x</sub>	4-NP: 0.1 mM (3 mL)	0.3 mmol	5 mg	0.25	–	[41]
Au-GCN	2-NP, 3-NP, 4-NP: 10 mM (40 μL)	0.1 M (0.04–0.16 mL)	2 mg	10	0.9	[42]
Au-GCN	4-NP: 10 mg/L (50 mL)	0.1 g/mL (75 μL)	1 mg	10	0.356172	[43]
Au-GCN	4-NP: 0.1 mM (2 mL)	0.1 M (1 mL)	0.85 mg/mL (30 μL)	3.33	0.9726	[44]
Au@S-GCN	4-NP: 1 mM (10 mL)	1 mM (1 mL)	0.5 mg	5	0.751	[45]
Pd/ Au@GCN-N	4-NP: 14.37 mM (1 mL)	1.43 M (1 mL)	0.25 mg	5	0.7907	[46]
Pd-GCN	4-NP: 0.01 M (100 μL)	0.5 M (25 μL)	0.025 mg	10	0.4374	[47]
Pd/N-rich GCN	4-NP: 0.2 mM (0.2 mL)	0.4 M (0.5 mL)	0.02 mg	1	0.2526	[48]
	MR: 0.02 mM (0.2 mL)			2	0.1266	
	MB 0.02 mM (0.2 mL):			1.33	0.1224	
	RhB: 0.02 mM (0.2 mL)			1	0.2268	
Cu-GCN	4-NP: 0.01 M (40 μL)	0.5 M (80 μL)	0.05 mg	6	1.116	[49]
NiGCN	MO: 0.1 mM	0.1 M	1 mg	4	1.4219	[50]

(continued)

**Table 2** (continued)

Sample	Conc. of pollutant	Conc. of NaBH <sub>4</sub>	Catalyst Amnt	Time (min)	k (min <sup>-1</sup> )	Refs.
CuCN	2-NP: 1 mM (0.3 mL)	0.1 M (3 mL)	4 mg	5	0.8519	[51]
	3-NP: 1 mM (0.3 mL)	0.1 M (3 mL)	4 mg	5	1.8669	
	4-NP: 1 mM (0.3 mL)	0.1 M (3 mL)	4 mg	5	1.1023	
	MO: 0.1 mM (1 mL)	0.1 M (2 mL)	2 mg	3	2.1134	
	MR: 0.1 mM (1 mL)	0.1 M (2 mL)	2 mg	4	1.4506	
	CR: 0.1 mM (1 mL)	0.1 M (2 mL)	2 mg	4	1.3923	
	MB: 0.1 mM (1 mL)	0.1 M (2 mL)	2 mg	4	1.6127	
	RhB: 0.1 mM (1 mL)	0.1 M (2 mL)	2 mg	4	1.9623	
	RB: 0.1 mM (1 mL)	0.1 M (2 mL)	2 mg	3	1.5216	
Ag@GCN	4-NP: 1 mM	0.1 M	5 mg	16	0.301	[52]
Au@GCN				6	0.649	
Pd@GCN				4	1.141	
CN-Cu	4-NP: 0.01 M (0.05 mL)	0.5 M (2 mL)	0.5 mg	7	0.103	[53]

Rhodamine B (RhB) within 70 s and 100 s respectively. Qin et al. deposited Au NPs on polydopamine decorated GCN to develop an efficient catalyst which was able to degrade 4-NP within 1 min [59]. They further employed the catalyst for the catalytic reduction of several other pollutants like 2-NP, 2,4-DNP, MO, Congo red (CR), and Erichrome Black T (EBT) within 60 s, 80 s, 40 s, 180 s, and 120 s respectively. The rate constant value obtained for 4-NP reduction was  $0.0514 \text{ s}^{-1}$ . Kohantorabi et al. developed a ternary nanocomposite catalyst system comprising of Au NPs supported on CeO<sub>2</sub>/GCN [60]. The synergistic effect between the constituents of the composite catalyst led to the rapid reduction of 4-NP within 40 s. A 'k' value  $0.106 \text{ s}^{-1}$  was obtained accordingly. Gu et al. pointed out that morphological compatibility between the two constituents of a nanocomposite is essential to fabricate a "well-contacted interface" [61]. Hence they synthesized Pd nanosheets which they supported on GCN nanosheets to form an intimate interface between them. They utilized this composite for degradation of 4-NP within 6 min ( $k = 0.76 \text{ min}^{-1}$ ). Yang et al. designed a magnetic high-performance catalyst based on Pd/Fe<sub>3</sub>O<sub>4</sub>/GCN for the

catalytic degradation of 4-NP within 210 s in presence of  $\text{NaBH}_4$  [62]. The associated rate constant value was calculated to be  $0.0276 \text{ s}^{-1}$ . Aditya et al. [63] decorated perforated GCN nanosheets with  $\text{CuO-Cu}_2\text{O}$  whereas Mitra et al. [21] designed  $\text{Cu}_2\text{O/GCN}$  nanocomposites, both of which were utilized for rapid degradation of 4-NP and MO dye respectively. Aditya et al. could achieve maximum degradation of 4-NP within 4 min ( $k = 1.19 \text{ min}^{-1}$ ) and Mitra et al. reported complete reduction of MO within 4.75 min ( $k = 1.30 \text{ min}^{-1}$ ). Ayodhya et al. fabricated a nanocomposite based on  $\text{CuS}$  and GCN nanosheets which they exploited for the catalytic reduction of 4-NP within 50 min [64]. They achieved a rate constant value of  $0.023 \text{ min}^{-1}$ . Ayodhya et al. fabricated  $\text{GCN/Bi}_2\text{S}_3$  heterojunction by microwave synthesis technique and applied the as-synthesized sample in the degradation of 4-NP to 4-AP within 1 h [65]. The rate constant value was found to be  $0.016 \text{ min}^{-1}$ . Interestingly, the composite sample exhibited much higher catalytic efficiency than pristine GCN and  $\text{Bi}_2\text{S}_3$ . Ayodhya et al. synthesized another GCN based composite by supporting  $\text{ZnS}$  on GCN nanosheets [66]. The sample took 35 min to degrade 4-NP and the associated rate constant was calculated to be  $0.0275 \text{ min}^{-1}$ . Due to the interfacial charge transfer between GCN and  $\text{ZnS}$ , the degradation activity of the composite catalyst was found to be 4.1 times and 1.9 times higher than pristine GCN and  $\text{ZnS}$  respectively. Ayodhya et al. also designed a  $\text{GCN/CdS}$  composite by employing sonochemical method and they used the sample for fast reduction of 4-NP within 18 min [67]. The corresponding rate constant value was  $0.0388 \text{ min}^{-1}$ . The composite catalyst not only showed better catalytic efficiency than the base samples but also it was able to be reused up to 5 catalytic cycles. Kumar et al. developed a novel ternary nano-heterojunction based on  $\text{GCN/Bi}_2\text{O}_2\text{CO}_3/\text{CoFe}_2\text{O}_4$  which was utilized for the complete conversion of 4-NP to 4-AP within 5 min [68]. The rate constant was found to be  $13.05 \times 10^{-3} \text{ s}^{-1}$ . Yousaf et al. reported the synthesis of a composite catalyst comprising of  $\text{MnO}_2$  nanosheets and GCN fluffy sheets [69]. The composite could completely degrade 4-NP within 6 min with a rate constant value of  $0.734 \text{ min}^{-1}$  which was significantly higher than that of pristine GCN ( $0.00624 \text{ min}^{-1}$ ). As a result of intermixing  $\text{MnO}_2$  sheets with GCN network through pyrolysis method, many coordination sites were generated through  $\text{Mn-N-C}$  channels which helped in developing electron rich interfaces. These functioned as active sites and provided the synergistic effects required for the excellent catalytic activity. In 2022, Xiang et al. developed a hybrid composite consisting of  $\text{Cu}_2\text{O}$  nanoparticles supported on GCN and reduced graphene oxide (rGO) [70]. The composite achieved complete reduction of 4-NP to 4-AP within a minute. A rate constant value as high as  $6.33 \times 10^{-2} \text{ s}^{-1}$  was achieved for the best sample. The performance of the  $\text{Cu}_2\text{O/GCN-rGO}$  (60%) composite catalyst was better than  $\text{Cu}_2\text{O/rGO}$ ,  $\text{Cu}_2\text{O/GCN}$ , and  $\text{Cu}_2\text{O/GCN-rGO}$  (40%) composites. The synergetic effect between GCN and rGO helped in proper immobilization of the  $\text{Cu}_2\text{O}$  nanoparticles which in turn enhanced the catalytic performance in degradation of 4-NP. Antony et al. immobilized Pd nanoparticles on silyl functionalized GCN sheets for the catalytic degradation of several contaminants including 4-NP, MO and RhB [71]. 8 mg of catalyst could degrade 4-NP, MO, and RhB within 4 min, 5 min, and 1.5 min respectively. The corresponding rate constant

values obtained were  $2.06 \times 10^{-2} \text{ s}^{-1}$  (4-NP),  $0.807 \times 10^{-2} \text{ s}^{-1}$  (MO), and  $6.7 \times 10^{-2} \text{ s}^{-1}$  (RhB). A detailed list is provided in Table 3.

## 5 Plausible Mechanism of $\text{NaBH}_4$ -Induced Degradation of Pollutants

Extensive literature survey suggests that the  $\text{NaBH}_4$  induced catalytic degradation of toxic pollutants follow the Langmuir–Hinshelwood (L–H) adsorption model. The underlying concept of this mechanism is based on the phenomenon of electron-relay or electron-transfer between the reducing agent  $\text{NaBH}_4$  and the pollutant complexes which remain adsorbed on the surface of a potential catalyst material. The catalyst should be chosen in such a way so that it facilitates the easy and rapid transfer of electrons from the  $\text{BH}_4^-$  ions to the pollutants thereby reducing the pollutants to their non-toxic forms. During this process, a series of chemical reactions occur which have been described and/or predicted by many researchers till date.

In most cases, the catalytic reaction starts as soon as the  $\text{NaBH}_4$  molecule and the pollutant molecules come in contact with the catalyst material in the aqueous solution. Following the L–H mechanism, initially the proper adsorption of  $\text{NaBH}_4$  and pollutants on the catalyst has to be ensured.  $\text{NaBH}_4$  itself cannot perform any catalytic reduction in absence of a catalyst material since there exists a reaction kinetic barrier between  $\text{NaBH}_4$  and pollutants. This hinders the electron transfer between them. Hence is the necessity of a catalyst material which facilitates in the electron transfer by lowering the redox potential between  $\text{NaBH}_4$  and the hazardous pollutants. Sodium borohydride, in water medium, generates nucleophilic  $\text{BH}_4^-$  radicals through ionization. These radicals get adsorbed on to the catalyst surface and help in donating electrons to the system, and the catalyst functions as a mediator for relaying these electrons to the toxic pollutants adsorbed on its surface. This is a very basic outline of the mechanism that takes place during the catalysis. In reality, there are plenty of plausible pathways and chains of reactions through which the catalytic activity can proceed. In our recent work we have tried to explain the mechanism as clearly as possible following first principles calculations [51]. For this we have chosen three popular pollutants 4-NP, MO and MB.

To study the degradation mechanism of 4-NP, we considered two plausible pathways. When 4-NP ( $\text{C}_6\text{H}_4(\text{OH})\text{NO}_2$ ) undergoes reduction, it gets transformed to 4-AP ( $\text{C}_6\text{H}_4(\text{OH})\text{NH}_2$ ). There are a lot of confusions regarding the source of H atoms in the  $-\text{NH}_2$  group of 4-AP molecules. It seems highly possible that either  $\text{H}^-$  from  $\text{NaBH}_4$  or  $\text{H}^+$  from  $\text{H}_2\text{O}$  can act as the source of H atoms in 4-AP. However, it is to be noted that the nitro group ( $-\text{NO}_2$ ) of 4-NP is comprised of electron rich N and O atoms thereby making it a negatively charged centre. Thus it becomes quite evident that the  $\text{H}^-$  from  $\text{NaBH}_4$  cannot participate in the hydrogenation process of 4-NP due to the electrostatic repulsion between  $\text{H}^-$  and the negatively charged  $-\text{NO}_2$  group. However there are several reports where both  $\text{H}^+$  and  $\text{H}^-$  ions have been

**Table 3** Catalytic activity of GCN in its composite/heterojunction forms

Sample	Conc. of pollutant	Conc. of NaBH <sub>4</sub>	Catalyst Amnt	Time	k (min <sup>-1</sup> )	Refs.
Ag <sub>2</sub> S/GCN	4-NP: 2.5 mM (0.2 mL)	0.05–0.25 M (0.2 mL)	10 mg/L (80 μL)	42	0.0212	[54]
Ag/GCN loaded carbon nanofibres	4-NP: 3.45 mmol/L (50 mL)	0.64 g in 50 mL	50 mg	50	0.094	[55]
CeO <sub>2</sub> /GCN/Ag	4-NP: 0.025 mmol/L	35 mg	10 mg	10	–	[56]
Ag–Cu <sub>2</sub> O–CuO/GCN	4-NP: 100 ppm (1.5 mL)	0.01 M (1.5 mL)	0.05 mg	4	0.334	[57]
Ag NPs on Fe <sub>3</sub> O <sub>4</sub> –polyallylamine/GCN	MO: 10 ppm	0.1 M	2 mg	1.16	2.7	[58]
	RhB: 10 ppm	0.1 M	4 mg	1.67	2.46	
Au/Polydopamine/GCN	2-NP: 0.2 mM (15 mL)	10, 20, 40, 60, 80 mM (15 mL)	5 mg	1	2.904	[59]
	4-NP: 0.2 mM (15 mL)			1	3.084	
	MO: 0.2 mM (15 mL)			0.67	5.298	
	CR: 0.2 mM (15 mL)			3	1.17	
Au/CeO <sub>2</sub> /GCN	4-NP: 0.12 mM (2 mL)	0.04 M (250 μL)	1 mg	0.67	6.3768	[60]
Pd–GCN nanosheet	4-NP: 0.145 mM (2.5 mL)	1 M (50 μL)	5 mg	6	0.76	[61]
Pd/Fe <sub>3</sub> O <sub>4</sub> /GCN	4-NP: 0.01 M (0.1 mL)	0.5 M (25 μL)	0.1 mg	3.5	1.662	[62]
Copper Oxide/GCN	4-NP: 5 × 10 <sup>-5</sup> M (3 mL)	1.6 mM (3 mL)	1 mg	4	1.19	[63]
Cu <sub>2</sub> O/GCN	MO: 0.1 mM (3 mL)	2 × 10 <sup>-3</sup> mM (0.3 mL)	1 mg	4.7	1.3	[21]
GCN/CuS	4-NP: 1.26 × 10 <sup>-2</sup> mol/L (40 μL)	0.5 M (0.5 mL)	10 mg	50	0.023	[64]
GCN/Bi <sub>2</sub> S <sub>3</sub>	4-NP: 0.125 mM (4 mL)	0.1 M (2 mL)	25 mg	60	0.016	[65]
ZnS–GCN	4-NP: 0.1 mM (0.5 mL)	0.01 M (0.5 mL)	0.2 mg	35	0.0275	[66]

(continued)



**Table 3** (continued)

Sample	Conc. of pollutant	Conc. of NaBH <sub>4</sub>	Catalyst Amnt	Time	k (min <sup>-1</sup> )	Refs.
CdS/GCN	4-NP: 0.1 mM (1 mL)	10 mM (1 mL)	10 mg/L	18	0.0388	[67]
GCN/Bi <sub>2</sub> O <sub>2</sub> CO <sub>3</sub> /CoFe <sub>2</sub> O <sub>4</sub>	4-NP: 10 mM (2 mL)	0.05 M (20 mL)	–	5	0.783	[68]
MnO <sub>2</sub> /GCN	4-NP: 10 mM (60 μL)	0.1 M (8 mL)	1 mg/mL (1 mL)	6	0.734	[69]
Cu <sub>2</sub> O/GCN/rGO	4-NP: 5 mM (30 μL)	0.2 mol/L (75 μL)	0.2 mg/mL (30 μL)	1	3.798	[70]
GCN–Si@Pd	4-NP: 2.5 mM (10 mL)	0.15 M (10 mL)	–	4	1.236	[71]
	MO: 0.2 mM (25 mL)	0.15 M (10 mL)		6	0.4842	
	RhB: 0.2 mM (25 mL)	0.2 M (10 mL)		1.5	4.044	

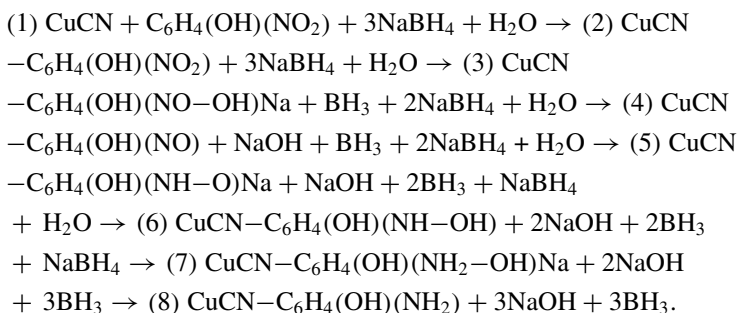
considered in the reaction pathway [72–74]. Bae et al. proposed the reaction pathway following H<sup>-</sup> of NaBH<sub>4</sub> as the hydrogen source [72]. After the initial adsorption of 4-NP on the catalyst material, the nucleophilic H<sup>-</sup> of NaBH<sub>4</sub> attacks the N atom of –NO<sub>2</sub> group to generate NHO<sub>2</sub><sup>-</sup> group. This NHO<sub>2</sub><sup>-</sup> group undergoes dehydroxylation to generate p-nitrosophenol which again gets converted to NHO<sup>-</sup> group by the transfer of the second H<sup>-</sup> from NaBH<sub>4</sub>. NHO<sup>-</sup> group is a strong Bronsted acid which induces the formation of NH<sub>2</sub>O group upon hydrolysis. At this stage p-hydroxyaminophenol is formed. This is followed by the reduction of NH<sub>2</sub>O group to NH<sub>3</sub>O<sup>-</sup> by the transfer of the third H<sup>-</sup> from NaBH<sub>4</sub>. Here the second dehydroxylation occurs thereby producing the non-toxic end product 4-AP. Thus the overall mechanism as suggested by Bae et al. is given as [72]:



Kong et al. performed isotope analysis to propose that the source of H in 4-AP comes from H<sub>2</sub>O rather than from NaBH<sub>4</sub> [73]. In the catalytic degradation experiment, NaBD<sub>4</sub> and D<sub>2</sub>O were used to replace NaBH<sub>4</sub> and H<sub>2</sub>O respectively and same experimental conditions were maintained. The standard set was maintained as NaBH<sub>4</sub> + 4-NP + Catalyst in H<sub>2</sub>O solution. It was observed from the selected ion chromatogram of deprotonated 4-AP that when NaBH<sub>4</sub> was replaced by NaBD<sub>4</sub> keeping the other factors constant, the intensity of the recorded signal remains same as that of the standard set. However when H<sub>2</sub>O was replaced by D<sub>2</sub>O keeping other factors same, then the intensity of the ion chromatogram signal of 4-AP increases with time. This indicated that H<sup>-</sup> of NaBH<sub>4</sub> does not contribute to the final product 4-AP. Thus they proposed the reaction pathway where one H adsorbs on one of the O atoms

of the nitro  $-\text{NO}_2$  group of 4-NP thus forming a single  $-\text{OH}$  like structure attached to the  $-\text{NO}$ . Next, another H gets adsorbed on this complex by attaching with the other O atom of the nitro group thereby resulting in two OH groups attached to the N atom (dihydroxyl-like structure). In the next step, upon hydroxyl dehydration, one water ( $\text{H}_2\text{O}$ ) molecule will be removed, as a result of which 4-nitrosophenol molecule will be formed. Again another H atom comes and gets attached to the  $-\text{NO}$  group thereby forming a  $-\text{NOH}$  group. This is followed by attachment of another H atom to this complex to form  $-\text{NHOH}$  group. Subsequently another water molecule is released at this stage leaving behind an  $-\text{NH}$  group. Finally a hydrogen atom joins to this cluster to finally form the  $-\text{NH}_2$  group of the 4-AP end product.

Recently we have reported both the reaction pathways for degradation of 4-NP by Cu decorated GCN [51]. Since the fundamental criterion for the initiation of the catalytic activity involves the proper adsorption of 4-NP pollutant on the catalyst surface; so in our work we studied the favourable adsorption configuration by attaching the 4-NP molecule on the surface of Cu decorated GCN in two different configurations: (i) N atom of  $-\text{NO}_2$  group of 4-NP is attached to the catalyst surface, (ii) O atom of  $-\text{OH}$  group of 4-NP is attached on the catalyst surface (Fig. 4a). To corroborate the experimental findings, we also attached 4-NP molecule in these two configurations on the surface of pristine GCN. It was observed that only a weak van der Waals interaction exists between 4-NP and bare GCN, thus 4-NP could not be adsorbed on the GCN surface. This was also evident from the experiments conducted on pure GCN which showed no signs of catalytic activity in degrading 4-NP in presence of  $\text{NaBH}_4$ . From first principles calculations, it was seen that configuration (ii) gave slightly better adsorption energies compared to configuration (i). Next we carried out the calculations of the reaction pathways following  $\text{H}^+$  and  $\text{H}^-$  as hydrogen sources in 4-AP from  $\text{H}_2\text{O}$  and  $\text{NaBH}_4$  respectively for both the configurations. For the pathway following  $\text{H}^-$  as the source of H, in case of configuration (ii), a significant energy barrier was visible from the free energy diagrams. However, a minute surmountable energy barrier is observed in case of configuration (i), otherwise the reaction proceeds effortlessly. This energy barrier occurs due to electrostatic repulsion of  $\text{H}^-$  by  $-\text{NO}_2$  group which need to be overcome for smooth proceeding of the catalytic activity. The chain of reactions involving the  $\text{H}^-$  ions as depicted from first principles calculations for configuration (i) are given below [51]:



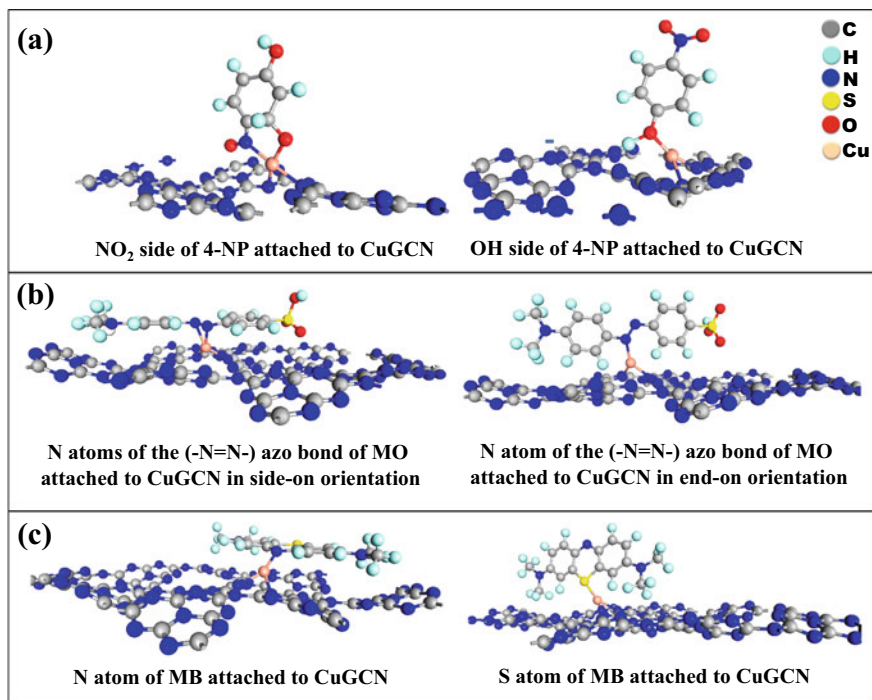
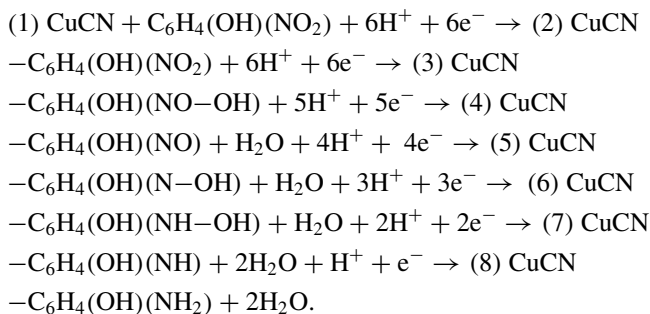


**Fig. 4** Attachment of conventional pollutants like, **a** 4-NP, **b** MO, and **c** MB on model sample Cu decorated GCN via different configurations [51]

In this case, the reaction barrier occurs between the intermediate steps (4) and (5).

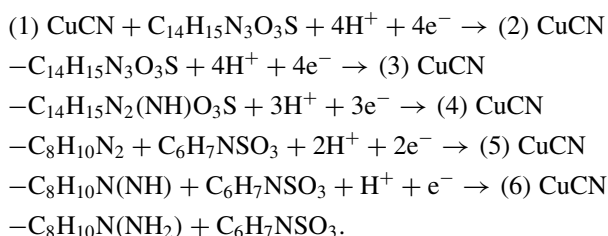
For the plausible reaction pathway following  $\text{H}^+$ , similar to the  $\text{H}^-$  case, significant amount of energy barrier was observed in case of configuration (ii). However, for configuration (i), the chain of reactions proceeds in exothermic nature which indicates the spontaneity of the reaction pathway. The mechanism is given as follows [51]:



From the above mentioned two pathways, it is clearly observed that the reaction mechanism is most favourable for configuration (i) with  $\text{H}^+$  as the source of hydrogen

in the end product 4-AP. This in turn suggests that H<sub>2</sub>O instead of NaBH<sub>4</sub> is the facile source of H in the 4-AP molecule. There are still on-going researches to pin-point the plausible mechanism that occurs during the reduction of 4-NP to 4-AP. However, to the best of our knowledge, we have tried to put forward a feasible pathway that may shed light into the catalytic reaction mechanism.

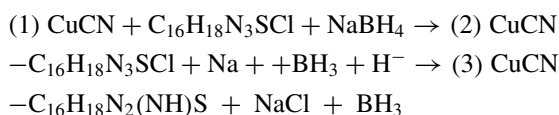
Similar to 4-NP, we had also carried out the first principles study of the degradation mechanism of other two conventional pollutants MO and MB in our recent work [51]. Like 4-NP, both MO and MB exhibited very weak adsorption on pristine GCN which in turn corroborated the experimental results. However, for Cu decorated GCN sample, Cu proved to be an efficient active site for pollutants adsorption through strong chemical interaction. For the adsorption of MO on catalyst surface, the most advantageous configuration was found to be the one where one N atom of the (–N = N–) azo bond of MO attaches with the Cu atom of Cu–GCN (Fig. 4b). The reaction pathway follows H<sup>+</sup> as the hydrogen source from H<sub>2</sub>O in the case of MO degradation and is given as [51]:



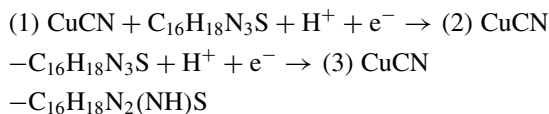
The end products of MO degradation were N, N'-dimethyl-p-phenylenediamine (C<sub>8</sub>H<sub>10</sub>N(NH<sub>2</sub>)) and sulphanilic acid (C<sub>6</sub>H<sub>7</sub>NSO<sub>3</sub>). Out of the 6 steps in the reaction pathway, the sulphanilic acid product was formed after the 3rd step involving the H<sup>+</sup> coupling and electron transfer. The MO degradation mechanism followed a spontaneous exothermic process.

For MB dye degradation, two types of adsorption configurations of MB on the catalyst surface were studied: one with the N atom of MB attached with Cu atom of Cu–GCN and the other with S atom of MB attached on Cu of Cu–GCN (Fig. 4c). It is also to be noted that the chemical structure of MB has one anionic N atom in the middle and two cationic N atoms at the ends. Better exothermic adsorptions were observed in two cases: when the middle anionic N atom interacts with Cu and the S atom interacts with Cu. Weak adsorption was observed when the cationic end N atoms were adsorbed on Cu. In this case, due to the cationic property of MB, the pathway for degradation of MB follows both H<sup>–</sup> and H<sup>+</sup> as H sources from NaBH<sub>4</sub> and H<sub>2</sub>O respectively to form the end product Leuco MB.

The reaction mechanism involving H<sup>–</sup> is given as [51]:



The reaction mechanism involving  $H^+$  was studied for both the configurations where either N or S of MB were attached on Cu–GCN and the pathway is as follows [51]:



Both the catalytic reaction mechanisms involving  $H^+$  and  $H^-$  ions as hydrogen sources were spontaneous in nature. For  $H^+$  pathway, the degradation reaction was more feasible in the case where S site of MB was attached on Cu–GCN as compared to the configuration where middle N of MB was attached on the catalyst. Again for the  $H^-$  pathway, spontaneous catalytic reaction was observed when N site of MB was attached on Cu site of GCN. Through these first principles analyses we have tried to provide plausible degradation mechanisms of some the conventional pollutants present in waste-water by metal-doped GCN catalyst material. A schematic representation of  $\text{NaBH}_4$ -assisted catalytic degradation of 4-NP, MO, and MB pollutants and their respective end products are shown in Fig. 5.

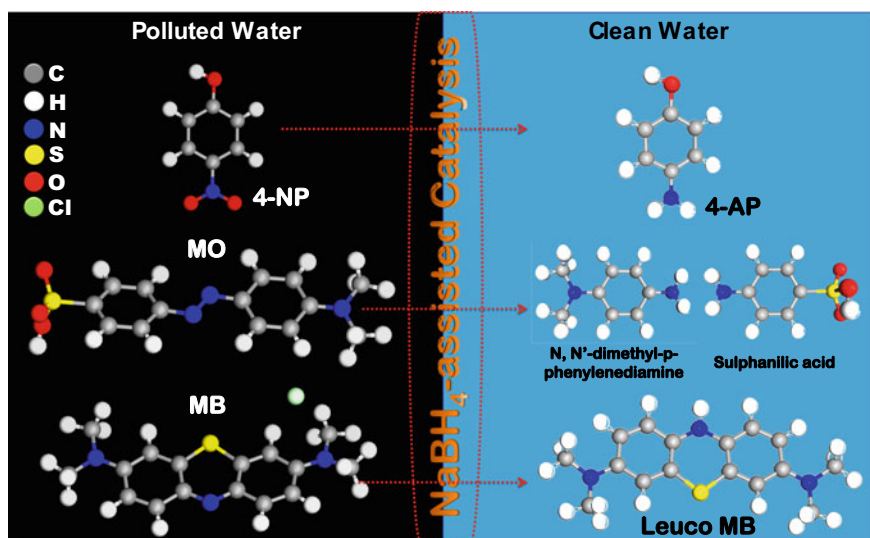


**Fig. 5** Schematic representation of  $\text{NaBH}_4$ -assisted catalytic degradation of 4-NP, MO, and MB pollutants and their respective end products

## 6 Conclusion

In the present review article, we have discussed about the potential application of carbon and nitrogen based polymeric materials for  $\text{NaBH}_4$  assisted catalytic reduction of several conventional hazardous pollutants emitted into water environment from various industries. Our primary focus was on the utilization of GCN, a special class of nitrogen-rich two dimensional layered materials, as a promising contestant for waste-water remediation. We have discussed in details about improving the catalytic activity of GCN by incorporating metal ions into its matrix or fabricating heterojunctions and nanocomposites with other potential semiconducting materials. Noble metal nanoparticles incorporated GCN samples exhibited superior catalytic activity in degrading wide range of toxic pollutants.  $\text{NaBH}_4$ -induced catalysis procedure proved to be a very facile, cost-effective, efficient reduction technique for ultra-fast degradation of pollutants as compared to other conventional methods. We have tried our best to provide some insight into the reduction mechanism of some common pollutants like 4-NP, MO, and MB by a model sample Cu doped GCN. The role of  $\text{NaBH}_4$ ,  $\text{H}_2\text{O}$  and the catalyst material was discussed in details. In conclusion, this review article brings forth extensive literature survey which was conducted to provide a support to carry out research works in the field of  $\text{NaBH}_4$  assisted catalytic degradation by carbon and nitrogen based polymers in their various forms.

## References

1. Hasanbeigi A, Price L (2015) A technical review of emerging technologies for energy and water efficiency and pollution reduction in the textile industry. *J Clean Prod* 95:30–44
2. Kant R (2011) Textile dyeing industry an environmental hazard. *Nat Sci* 4(1)
3. Lellis B, Fávoro-Polonio CZ, Pamphile JA, Polonio JC (2019) Effects of textile dyes on health and the environment and bioremediation potential of living organisms. *Biotechnol Res Innov* 3(2):275–290
4. Hassan MM, Carr CM (2018) A critical review on recent advancements of the removal of reactive dyes from dyehouse effluent by ion-exchange adsorbents. *Chemosphere* 209:201–219
5. Lambert SJ, Davy AJ (2011) Water quality as a threat to aquatic plants: discriminating between the effects of nitrate, phosphate, boron and heavy metals on charophytes. *New Phytol* 189(4):1051–1059
6. Aquino JM, Rocha-Filho RC, Ruotolo LA, Bocchi N, Biaggio SR (2014) Electrochemical degradation of a real textile wastewater using  $\beta\text{-PbO}_2$  and DSA<sup>®</sup> anodes. *Chem Eng J* 251:138–145
7. Thangamani KS, Andal NM, Kumar ER, Saravanabhavan M (2017) Utilization of magnetic nano cobalt ferrite doped *Capra aegagrus hircus* dung activated carbon composite for the adsorption of anionic dyes. *J Environ Chem Eng* 5(3):2820–2829
8. Verma P, Samanta SK (2018) Microwave-enhanced advanced oxidation processes for the degradation of dyes in water. *Environ Chem Lett* 16(3):969–1007
9. Xu XR, Li HB, Wang WH, Gu JD (2004) Degradation of dyes in aqueous solutions by the Fenton process. *Chemosphere* 57(7):595–600
10. Shaban M, Abukhadra MR, Ibrahim SS, Shahien M (2017) Photocatalytic degradation and photo-Fenton oxidation of Congo red dye pollutants in water using natural chromite—response surface optimization. *Appl Water Sci* 7(8):4743–4756

11. Nezamzadeh-Ejehieh A, Khorsandi S (2014) Photocatalytic degradation of 4-nitrophenol with ZnO supported nano-clinoptilolite zeolite. *J Ind Eng Chem* 20(3):937–946
12. Tan BH, Teng TT, Omar AM (2000) Removal of dyes and industrial dye wastes by magnesium chloride. *Water Res* 34(2):597–601
13. Chincholi M, Sagwekar P, Nagaria C, Kulkarni S, Dhokpande S (2014) Removal of dye by adsorption on various adsorbents: a review. *Int J Sci Eng Technol Res* 3:835–840
14. Karcher S, Kornmüller A, Jekel M (2002) Anion exchange resins for removal of reactive dyes from textile wastewaters. *Water Res* 36(19):4717–4724
15. Vijayageetha VA, Rajan AP, Arockiaraj SP, Annamalai V, Janakarajan VN, Balaji MS, Dheenadhayalan MS (2014) Treatment study of dyeing industry effluents using reverse osmosis technology. *Res J Recent Sci* 3(ISC-2013):58–61
16. Fu Y, Viraraghavan T (2001) Fungal decolorization of dye wastewaters: a review. *Bioresour Technol* 79(3):251–262
17. Yagub MT, Sen TK, Afroze S, Ang HM (2014) Dye and its removal from aqueous solution by adsorption: a review. *Adv Coll Interface Sci* 209:172–184
18. Zhang P, Shao C, Zhang Z, Zhang M, Mu J, Guo Z, Liu Y (2011) In situ assembly of well-dispersed Ag nanoparticles (AgNPs) on electrospun carbon nanofibers (CNFs) for catalytic reduction of 4-nitrophenol. *Nanoscale* 3(8):3357–3363
19. Sakaushi K, Antonietti M (2015) Carbon-and nitrogen-based porous solids: a recently emerging class of materials. *Bull Chem Soc Jpn* 88(3):386–398
20. Munagapati VS, Yarramuthi V, Kim DS (2017) Methyl orange removal from aqueous solution using goethite, chitosan beads and goethite impregnated with chitosan beads. *J Mol Liq* 240:329–339
21. Mitra A, Howli P, Sen D, Das B, Chattopadhyay KK (2016) Cu<sub>2</sub>O/g-C<sub>3</sub>N<sub>4</sub> nanocomposites: an insight into the band structure tuning and catalytic efficiencies. *Nanoscale* 8(45):19099–19109
22. Dahri MK, Kooh MRR, Lim LB (2016) Remediation of rhodamine B dye from aqueous solution using Casuarina equisetifolia cone powder as a low-cost adsorbent. *Adv Phys Chem* 2016
23. Ismail M, Khan MI, Khan SB, Khan MA, Akhtar K, Asiri AM (2018) Green synthesis of plant supported CuAg and CuNi bimetallic nanoparticles in the reduction of nitrophenols and organic dyes for water treatment. *J Mol Liq* 260:78–91
24. Ma S, Chen X, Zhao B, Li L, Fu W (2018) Rapid degradation of rhodamine B via poly(dopamine)-modified membranes with silver nanoparticles. *Chem Eng Technol* 41(1):149–156
25. Hou C, Hu B, Zhu J (2018) Photocatalytic degradation of methylene blue over TiO<sub>2</sub> pretreated with varying concentrations of NaOH. *Catalysts* 8(12):575
26. Li Y, Du Q, Liu T, Peng X, Wang J, Sun J, Wang Y, Wu S, Wang Z, Xia Y, Xia L (2013) Comparative study of methylene blue dye adsorption onto activated carbon, graphene oxide, and carbon nanotubes. *Chem Eng Res Des* 91(2):361–368
27. Narayanan KB, Sakthivel N (2011) Heterogeneous catalytic reduction of anthropogenic pollutant, 4-nitrophenol by silver-bionanocomposite using *Cylindrocladium floridanum*. *Bioresour Technol* 102(22):10737–10740
28. Gao L, Li R, Sui X, Li R, Chen C, Chen Q (2014) Conversion of chicken feather waste to N-doped carbon nanotubes for the catalytic reduction of 4-nitrophenol. *Environ Sci Technol* 48(17):10191–10197
29. Liu Y, Xu H, Yu H, Yang H, Chen T (2020) Synthesis of lignin-derived nitrogen-doped carbon as a novel catalyst for 4-NP reduction evaluation. *Sci Rep* 10(1):1–14
30. Edison TNJI, Atchudan R, Karthik N, Balaji J, Xiong D, Lee YR (2020) Catalytic degradation of organic dyes using green synthesized N-doped carbon supported silver nanoparticles. *Fuel* 280:118682
31. Hayakawa K, Yoshimura T, Esumi K (2003) Preparation of gold–dendrimer nanocomposites by laser irradiation and their catalytic reduction of 4-nitrophenol. *Langmuir* 19(13):5517–5521
32. Qiu L, Peng Y, Liu B, Lin B, Peng Y, Malik MJ, Yan F (2012) Polypyrrole nanotube-supported gold nanoparticles: an efficient electrocatalyst for oxygen reduction and catalytic reduction of 4-nitrophenol. *Appl Catal A Gen* 413:230–237

33. Chang G, Luo Y, Lu W, Qin X, Asiri AM, Al-Youbi AO, Sun X (2012) Ag nanoparticles decorated polyaniline nanofibers: synthesis, characterization, and applications toward catalytic reduction of 4-nitrophenol and electrochemical detection of H<sub>2</sub>O<sub>2</sub> and glucose. *Catal Sci Technol* 2(4):800–806
34. Ma J, Deng H, Zhang Z, Zhang L, Qin Z, Zhang Y, Gao L, Jiao T (2022) Facile synthesis of Ag<sub>3</sub>PO<sub>4</sub>/PPy/PANI ternary composites for efficient catalytic reduction of 4-nitrophenol and 2-nitroaniline. *Colloids Surf A: Physicochem Eng Aspects* 632:127774
35. Zhang Y, Xiao X, Chen B (2022) Facile nitrogen doping in fungal hyphae-derived biochars via cooperation of microbial culture and pyrolysis for efficient catalytic reduction of 4-nitrophenol. *Chemosphere* 300:134526
36. Wang H, Ma YJ, Shen Y, Zhang C, Yang J, Li P (2022) Facile sol-gel route for designing of Co<sub>3</sub>O<sub>4</sub>/N-doped carbon and Co-Co<sub>3</sub>O<sub>4</sub>/N-doped carbon nanomaterials with unexpected high catalytic performances toward hydrogenation reduction of 4-nitrophenol. Retrieved from SSRN, 4087346
37. Fan M, Wang WD, Zhu Y, Sun X, Zhang F, Dong Z (2019) Palladium clusters confined in triazinyl-functionalized COFs with enhanced catalytic activity. *Appl Catal B: Environ* 257:117942
38. Subodh, Prakash K, Masram DT (2020) Silver nanoparticles immobilized covalent organic microspheres for hydrogenation of nitroaromatics with intriguing catalytic activity. *ACS Appl Polym Mater* 3(1):310–318
39. Wang X, Tan F, Wang W, Qiao X, Qiu X, Chen J (2017) Anchoring of silver nanoparticles on graphitic carbon nitride sheets for the synergistic catalytic reduction of 4-nitrophenol. *Chemosphere* 172:147–154
40. Veerakumar P, Dhenadhayalan N, Lin KC, Liu SB (2017) Silver nanoparticles modified graphitic carbon nitride nanosheets as a significant bifunctional material for practical applications. *ChemistrySelect* 2(4):1398–1408
41. Bhowmik T, Kundu MK, Barman S (2015) Ultra small gold nanoparticles–graphitic carbon nitride composite: an efficient catalyst for ultrafast reduction of 4-nitrophenol and removal of organic dyes from water. *RSC Adv* 5(48):38760–38773
42. Nguyen TB, Huang CP, Doong RA (2019) Enhanced catalytic reduction of nitrophenols by sodium borohydride over highly recyclable Au@graphitic carbon nitride nanocomposites. *Appl Catal B: Environ* 240:337–347
43. Fu Y, Huang T, Jia B, Zhu J, Wang X (2017) Reduction of nitrophenols to aminophenols under concerted catalysis by Au/g-C<sub>3</sub>N<sub>4</sub> contact system. *Appl Catal B: Environ* 202:430–437
44. Zhou X, Li Y, Xing Y, Liu X, Yu X, Yu Y (2020) Comparison of the catalytic properties of Au nanoparticles supported on different two-dimensional carriers. *J Phys Chem Solids* 142:109438
45. Balakumar V, Kim H, Ryu JW, Manivannan R, Son YA (2020) Uniform assembly of gold nanoparticles on S-doped g-C<sub>3</sub>N<sub>4</sub> nanocomposite for effective conversion of 4-nitrophenol by catalytic reduction. *J Mater Sci Technol* 40:176–184
46. Fang W, Deng Y, Tang L, Zeng G, Zhou Y, Xie X, Wang J, Wang Y, Wang J (2017) Synthesis of Pd/Au bimetallic nanoparticle-loaded ultrathin graphitic carbon nitride nanosheets for highly efficient catalytic reduction of p-nitrophenol. *J Colloid Interface Sci* 490:834–843
47. Zhao Y, Tang R, Huang R (2015) Palladium supported on graphitic carbon nitride: an efficient and recyclable heterogeneous catalyst for reduction of nitroarenes and Suzuki coupling reaction. *Catal Lett* 145(11):1961–1971
48. Kumar Y, Rani S, Shabir J, Kumar LS (2020) Nitrogen-rich and porous graphitic carbon nitride nanosheet-immobilized palladium nanoparticles as highly active and recyclable catalysts for the reduction of nitro compounds and degradation of organic dyes. *ACS Omega* 5(22):13250–13258
49. Huang S, Zhao Y, Tang R (2016) Facile fabrication of a Cu@g-C<sub>3</sub>N<sub>4</sub> nanocatalyst and its application for the aerobic oxidations of alkylaromatics and the reduction of 4-nitrophenol. *RSC Adv* 6(93):90887–90896
50. Das D, Banerjee D, Mondal M, Shett A, Das B, Das NS, Ghorai UK, Chattopadhyay KK (2018) Nickel doped graphitic carbon nitride nanosheets and its application for dye degradation by chemical catalysis. *Mater Res Bull* 101:291–304



51. Das D, Das BK, Sarkar R, Mukherjee S, Chattopadhyay KK (2022) Copper and nickel decorated g-C<sub>3</sub>N<sub>4</sub> as superior catalysts for reduction of toxic pollutants: a combined experimental and theoretical approach. *Appl Surf Sci* 580:152137
52. Saravanakumar K, Priya VS, Balakumar V, Prabavathi SL, Muthuraj V (2022) Noble metal nanoparticles (M<sub>x</sub> = Ag, Au, Pd) decorated graphitic carbon nitride nanosheets for ultrafast catalytic reduction of anthropogenic pollutant, 4-nitrophenol. *Environ Res* 212:113185
53. Nisha V, Moolayadukkam S, Paravannoor A, Panoth D, Chang YH, Palantavida S, Hinder SJ, Pillai SC, Vijayan BK (2022) Cu doped graphitic C<sub>3</sub>N<sub>4</sub> for p-nitrophenol reduction and sensing applications. *Inorg Chem Commun* 142:109598
54. Ayodhya D, Veerabhadram G (2019) Synthesis and characterization of g-C<sub>3</sub>N<sub>4</sub> nanosheets decorated Ag<sub>2</sub>S composites for investigation of catalytic reduction of 4-nitrophenol, antioxidant and antimicrobial activities. *J Mol Struct* 1186:423–433
55. Yu B, Liu Y, Jiang G, Liu D, Yu W, Chen H, Li L, Huang Q (2017) Preparation of electrospun Ag/g-C<sub>3</sub>N<sub>4</sub> loaded composite carbon nanofibers for catalytic applications. *Mater Res Express* 4(1):015603
56. Pinheiro D, Devi KS, Jose A, Karthik K, Sugunan S, Mohan MK (2020) Experimental design for optimization of 4-nitrophenol reduction by green synthesized CeO<sub>2</sub>/g-C<sub>3</sub>N<sub>4</sub>/Ag catalyst using response surface methodology. *J Rare Earths* 38(11):1171–1177
57. Verma A, Kumar S, Chang WK, Fu YP (2020) Bi-functional Ag-CuxO/gC<sub>3</sub>N<sub>4</sub> hybrid catalysts for the reduction of 4-nitrophenol and the electrochemical detection of dopamine. *Dalton Trans* 49(3):625–637
58. Mohammadi P, Heravi MM, Sadjadi S (2020) Green synthesis of Ag NPs on magnetic polyallylamine decorated g-C<sub>3</sub>N<sub>4</sub> by *Heracleum persicum* extract: efficient catalyst for reduction of dyes. *Sci Rep* 10(1):1–10
59. Qin L, Huang D, Xu P, Zeng G, Lai C, Fu Y, Yi H, Li B, Zhang C, Cheng M, Zhou C (2019) In-situ deposition of gold nanoparticles onto polydopamine-decorated g-C<sub>3</sub>N<sub>4</sub> for highly efficient reduction of nitroaromatics in environmental water purification. *J Colloid Interface Sci* 534:357–369
60. Kohantorabi M, Gholami MR (2018) Fabrication of novel ternary Au/CeO<sub>2</sub>@g-C<sub>3</sub>N<sub>4</sub> nanocomposite: kinetics and mechanism investigation of 4-nitrophenol reduction, and benzyl alcohol oxidation. *Appl Phys A* 124(6):1–17
61. Gu K, Pan X, Wang W, Ma J, Sun Y, Yang H, Shen H, Huang Z, Liu H (2018) In situ growth of Pd nanosheets on g-C<sub>3</sub>N<sub>4</sub> nanosheets with well-contacted interface and enhanced catalytic performance for 4-nitrophenol reduction. *Small* 14(33):1801812
62. Yang Y, Tang R (2018) Magnetically recyclable Pd/Fe<sub>3</sub>O<sub>4</sub>/g-C<sub>3</sub>N<sub>4</sub> as efficient catalyst for the reduction of nitrophenol and suzuki-miyaura reaction at room temperature. *Chem Lett* 47(4):544–547
63. Aditya T, Jana J, Pal A, Pal T (2018) One-pot fabrication of perforated graphitic carbon nitride nanosheets decorated with copper oxide by controlled ammonia and sulfur trioxide release for enhanced catalytic activity. *ACS Omega* 3(8):9318–9332
64. Ayodhya D, Veerabhadram G (2019) Influence of g-C<sub>3</sub>N<sub>4</sub> and g-C<sub>3</sub>N<sub>4</sub> nanosheets supported CuS coupled system with effect of pH on the catalytic activity of 4-NP reduction using NaBH<sub>4</sub>. *FlatChem* 14:100088
65. Ayodhya D, Veerabhadram G (2021) Microwave-assisted fabrication of g-C<sub>3</sub>N<sub>4</sub> nanosheets sustained Bi<sub>2</sub>S<sub>3</sub> heterojunction composites for the catalytic reduction of 4-nitrophenol. *Environ Technol* 42(6):826–841
66. Ayodhya D, Veerabhadram G (2019) Stable and efficient graphitic carbon nitride nanosheet-supported ZnS composite catalysts toward competent catalytic performance for the reduction of 4-nitrophenol using NaBH<sub>4</sub>. *Mater Today Sustain* 5:100015
67. Ayodhya D, Veerabhadram G (2020) Ultrasonic synthesis of g-C<sub>3</sub>N<sub>4</sub>/CdS composites and their photodegradation, catalytic reduction, antioxidant and antimicrobial studies. *Mater Res Innov* 24(4):210–228
68. Kumar A, Kumar A, Sharma G, Ala' a H, Naushad M, Ghfar AA, Guo C, Stadler FJ (2018) Biochar-templated g-C<sub>3</sub>N<sub>4</sub>/Bi<sub>2</sub>O<sub>2</sub>CO<sub>3</sub>/CoFe<sub>2</sub>O<sub>4</sub> nano-assembly for visible and solar assisted

- photo-degradation of paraquat, nitrophenol reduction and CO<sub>2</sub> conversion. *Chem Eng J* 339:393–410
69. Yousaf AB, Zavahir S, Zeb A, Michalcova A, Kasak P (2022) Nanostructural synergism as Mn-N-C channels in manganese (IV) oxide and fluffy g-C<sub>3</sub>N<sub>4</sub> layered composite with exceptional catalytic capabilities. *J Colloid Interface Sci* 610:258–270
  70. Xiang Z, Wang X, Xu L, Wang Z, Meng J, Zhang J, Zhao J, Wang H (2022) Synthesis of cuprous oxide nanoparticles on graphitic carbon nitride and reduced graphene oxide and their catalytic performance toward the reduction of 4-nitrophenol. *J Mater Sci* 57:2424–2435
  71. Antony AM, Kandathil V, Kempasiddaiah M, Shwetharani R, Balakrishna RG, El-Bahy SM, Hessien MM, Mersal GA, Ibrahim MM, Patil SA (2022) Graphitic carbon nitride supported palladium nanocatalyst as an efficient and sustainable catalyst for treating environmental contaminants and hydrogen evolution reaction. *Colloids Surf A: Physiochem Eng Aspects* 647:129116
  72. Bae S, Gim S, Kim H, Hanna K (2016) Effect of NaBH<sub>4</sub> on properties of nanoscale zero-valent iron and its catalytic activity for reduction of p-nitrophenol. *Appl Catal B: Environ* 182:541–549
  73. Kong X, Zhu H, Chen C, Huang G, Chen Q (2017) Insights into the reduction of 4-nitrophenol to 4-aminophenol on catalysts. *Chem Phys Lett* 684:148–152
  74. Wang Z, Su R, Wang D, Shi J, Wang JX, Pu Y, Chen JF (2017) Sulfurized graphene as efficient metal-free catalysts for reduction of 4-nitrophenol to 4-aminophenol. *Ind Eng Chem Res* 56(46):13610–13617

# Arsenate Adsorption on Goethite Nanorods in the Presence of Geochemical Constituents



Leila Alidokht , Öznur Karaca , and Nasser Shirzadeh 

**Abstract** The present study describes the adsorption kinetics of arsenate ( $\text{As}^{\text{V}}$ ) from solution by synthetic goethite nanorods (GN) in the presence of clay mineral, calcite, and leonardite-derived humic acid (HA). Batch experiments were performed at different pH values (5.5, 7, 8.5) to obtain the adsorption kinetics of  $\text{As}^{\text{V}}$  using  $1 \text{ g L}^{-1}$  GN,  $120 \text{ mg L}^{-1}$  HA,  $4 \text{ g L}^{-1}$  calcite, and  $20 \text{ g L}^{-1}$  kaolinite. Experiments containing calcite were only performed at pH values 7 and 8.5. The initial concentration of As was kept at  $100 \mu\text{M}$ . Results showed that GN adsorbs near 50–70% As, depending on pH, and the reaction kinetics can be described by a pseudo-second-order model. Adsorption efficiency and the rate decreased with increasing alkalinity, indicating competition for sorption sites between  $\text{As}^{\text{V}}$  and  $\text{OH}^-$  on GN. Calcite and HA showed no efficiency toward the adsorption of As within the studied time range. Slight As adsorption efficiency ( $\approx 14\%$ ) by kaolinite was observed at pH 5.5. In all studied pH values, the presence of HA, kaolinite, and calcite significantly inhibited the efficiency and rate of As removal by GN. Limited As adsorption in the presence of HA is probably due to the blockage of GN reactive surface sites by HA. In a system containing kaolinite and GN, the overall As removal rate was controlled by the lowest adsorbent. Interaction effects between kaolinite and calcite, calcite and HA, and kaolinite and HA on the removal of As were statistically insignificant.

**Keywords** Goethite nanorods · Arsenate · Adsorption · Geochemical constituents · Kinetics

---

L. Alidokht (✉) · Ö. Karaca · N. Shirzadeh  
Department of Geological Engineering, Faculty of Engineering, Çanakkale Onsekiz Mart University, Çanakkale, Turkey  
e-mail: [l.alidokht@gmail.com](mailto:l.alidokht@gmail.com)

Ö. Karaca  
e-mail: [oznurkaraca@comu.edu.tr](mailto:oznurkaraca@comu.edu.tr)

## 1 Introduction

In the last few decades, metal(loid)s contamination of water and soils has become a global problem and is likely to increase worldwide with growing industrial and agricultural activities. Due to the risk of their accumulation in the human food chain, metal(loid)s are considered highly eco-toxic substances. They can enter the environment through both pedogenic and anthropogenic processes. However, anthropogenic activities have been identified as the major sources of metal(loid)s contamination [1–3].

Arsenic can pose severe risks for human health and ecological systems and is classified as a Class-1 carcinogen by the World Health Organization (WHO). If its concentration exceeds  $55 \text{ mg kg}^{-1}$  and  $50 \text{ } \mu\text{g L}^{-1}$  in soil and water, respectively, then it is known to have toxic effects on both humans and plants [4]. Two chemically active species of As are mostly known for their toxicity. Arsenite ( $\text{As}^{\text{III}}$ ) is primarily present in reducing environments, whereas arsenate ( $\text{As}^{\text{V}}$ ) is in oxidizing environments, with the former being the more toxic and mobile form [5]. Arsenic may be leached from the soil and cause contamination of groundwater and/or taken by crops and possibly enter the food chain [6].

Arsenic (in both of its common  $\text{As}^{\text{III}}$  and  $\text{As}^{\text{V}}$  states) has shown a high tendency to strongly bind to (hydrated) Fe oxides (as monodentate or bidentate inner-sphere complexes), even at very low concentrations. Nanoscale iron oxides are one of the principal sorbents of these oxyanions in soils and waters. Several studies have confirmed that iron and iron oxide nanoparticles can be used to remove  $\text{As}^{\text{V}}$  [7–9]. In this context, engineered goethite ( $\alpha\text{-FeOOH}$ ) nanorods (GN) have shown a high affinity toward  $\text{As}^{\text{V}}$  oxyanion. While there has been substantial research on the removal of  $\text{As}^{\text{V}}$  by iron oxide minerals from contaminated soils, there are, to the best of our knowledge, no studies that investigate 1) the effect of geochemical constituents on the efficiency and kinetics of  $\text{As}^{\text{V}}$  adsorption onto GN in an aqueous solution. This information is mandatory before designing a remediation methodology and field applications.

More recently, novel groundwater remediation techniques utilize the sportive properties of iron oxides to stabilize inorganic contaminants in groundwater through Permeable Adsorptive Barriers (PABs). The performance of PABs significantly depends on the geochemical composition of groundwater. Various geochemical constituents, such as natural organic matter (NOM), carbonate species, and clay minerals, may impose their impacts. Therefore, we aimed to investigate the effects of geochemical constituents including humic acid (HA) (extracted from Leonardite), calcite, and clay mineral (kaolinite) on the efficiency, and kinetics of  $\text{As}^{\text{V}}$  adsorption onto synthesized GN in an aqueous solution in a batch system.

## 2 Materials and Methods

### 2.1 Synthesis of Goethite ( $\alpha$ -FeOOH) Nanorods

Goethite nanorods were prepared following the method described by Jaiswal et al. [10]. 50.0 g of an analytical grade of  $\text{Fe}(\text{NO}_3)_3 \cdot 9\text{H}_2\text{O}$  was dissolved in a half-liter of de-ionized water in a 1 L plastic container. The solution was hydrated for 24 h at pH 1.6 with continuous stirring with a magnetic stirrer. Then 2.5 M KOH solution was added dropwise until the solution attains a pH of 12. The resulting suspension was aged for 5 days in a thermostatic oven at 60 °C. The goethite paste was then oven-dried at 60 °C. Characterization of prepared iron oxide was performed using XRD and SEM techniques.

### 2.2 Extraction of Humic Acid from Leonardite

Leonardite was used as a source of HA. The International Humic Substances Society (IHSS) method, with a small modification, was used for the extraction of HA. Leonardite was air-dried, grounded, and passed through a 0.15 mm sieve. 0.5 M sodium hydroxide was added to leonardite in a solid to solution ratio of 1:10. The suspension was mixed for 24 h, and then the supernatant was collected through centrifugation. The collected solution was acidified (pH  $\approx$  1) using 6 M of hydrochloric acid (HCl) (Scharlau Co.). The suspension was allowed to stand overnight at 4 °C. Precipitates (HA) were separated from the solution by centrifugation and then re-dissolved by the addition of a minimum volume of 0.1 M potassium hydroxide (KOH) and potassium chloride (KCl) salt. Suspended solids were removed by centrifugation, and HA was precipitated by adding 0.6 M HCl to pH  $\approx$  1 and left overnight at 4 °C. The supernatant was discarded, and HA was suspended in 0.1 M HCl/0.3 M hydrofluoric acid (HF) and shaken for 16 h at room temperature. Precipitates were washed several times with deionized water, and finally, obtained HA was freeze-dried. FTIR analyses of the solid HA were carried out using Shimadzu 8400 S FTIR spectroscopy (Japan). The C, H, N, and S content of HA was determined by Costech Elemental Combustion System (ECS) 4010 CHNS analyzer (Italy), and the elemental and content of O (in wt%) were calculated by difference. Extracted HA was characterized using FTIR and CHNS analyses [11].

### 2.3 Batch Experiments of $\text{As}^{\text{V}}$ Adsorption on GN

In the first series of experiments, adsorption of  $\text{As}^{\text{V}}$  on GN in the absence or presence of HA, calcite, and/or kaolinite was measured with batch adsorption experiments. Stock solutions of  $\text{Na}_2\text{HAsO}_4$  were added to a 1 L flask containing 1.2 g  $\text{L}^{-1}$  GN

(with or without  $120 \text{ mg L}^{-1}$  HA,  $4 \text{ g L}^{-1}$  calcite,  $20 \text{ g L}^{-1}$  kaolinite) in a background electrolyte solution of  $0.01 \text{ M CaCl}_2$  to achieve a total initial As the concentration of  $0.1 \text{ mM}$ . The initial pH of  $\text{As}^{\text{V}}$  solutions was adjusted to 5.5, 7, and 8.5 using  $0.1 \text{ N HCl}$  and  $\text{NaOH}$  solutions. The second series (control runs) was performed to evaluate the effect of HA, calcite, and kaolinite on the concentrations of As in the absence of GN. Suspensions were agitated, and at various time intervals, a  $2 \text{ mL}$  sample was taken, and the residual concentration of  $\text{As}^{\text{V}}$  was determined using ICP-OES. Batches containing calcite were carried out at pH 7 and 8.5. Prior to use, the calcite was equilibrated with the calcite-equilibrate solution at pH 7 or 8.5, according to the method described by Sørensen et al. [12]. The experimental data were analyzed using various kinetic models, including zero-order, pseudo-first-order, pseudo-second-order, and diffusion parabolic, to determine the best model fitting our data.

### 3 Results and Discussion

#### 3.1 GN Characterization

The X-ray diffractogram shown in Fig. 1 confirmed that the synthesized material was goethite iron oxide, with the characteristic five peaks at  $21.7$ ,  $33.7$ ,  $37.17$ ,  $53.77$ , and  $59.52$  degrees. SEM images (Fig. 1) show nanorods of goethite particles.

#### 3.2 Characterization of HA

According to the elemental analysis, nitrogen, carbon, hydrogen, sulfur, and oxygen content of extracted HA were as 1.1, 45.31, 3.11, 0.75, and 49.17%, respectively. The N/C atomic ratio of 0.024 shows that the samples belong to low-rank coal. In addition, the H/C atomic ratio of 0.068 indicates that the extracted humic acid may originate from vascular plant material rather than from fungal/bacterial organic matter. The FTIR spectra exhibit typical major peaks of HA (Fig. 2). The strong and broad absorption band at  $3467 \text{ cm}^{-1}$  assigns to H-bonded OH groups. Observed absorption bands in the regions of  $2929 \text{ cm}^{-1}$  and  $2865 \text{ cm}^{-1}$  probably arise from aliphatic and methoxy groups, respectively. Absorption in  $1660 \text{ cm}^{-1}$  refers to the  $\text{C}=\text{O}$  of amide groups and quinone ketones. A relatively weak peak at  $1269 \text{ cm}^{-1}$  may belong to nitrates ( $\text{R}-\text{O}-\text{NO}_2$ ),  $=\text{C}-\text{O}-\text{C}$  groups and possibly  $\text{P}=\text{O}$  vibrations and  $\text{C}-\text{O}$  of phenolic groups. Additionally, the absorption band in  $754 \text{ cm}^{-1}$  arises from aromatic  $\text{C}-\text{H}$  (less substituted rings). The FTIR results evidently showed the predominance of OH, COOH and COO groups as the most characteristic features HA [11].

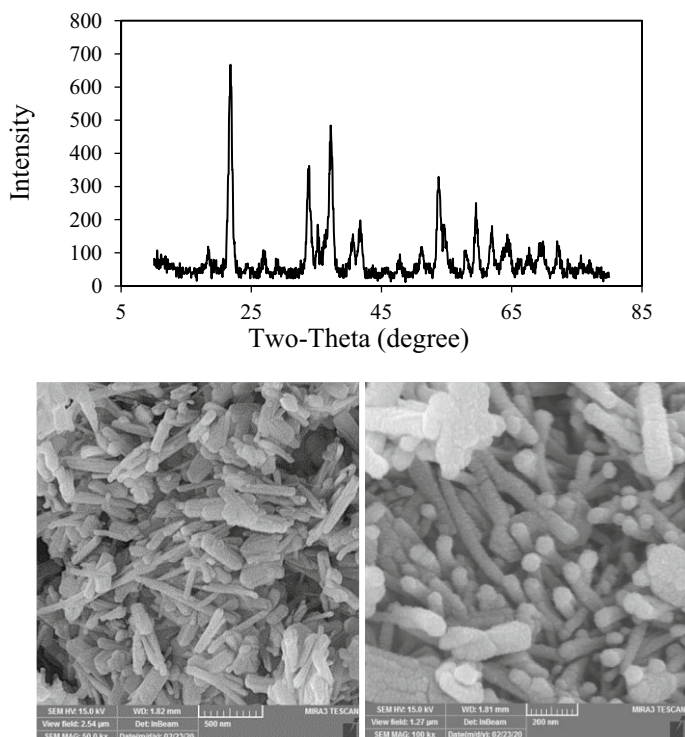


**Fig. 1** XRD pattern and SEM images of synthesized goethite nanorods

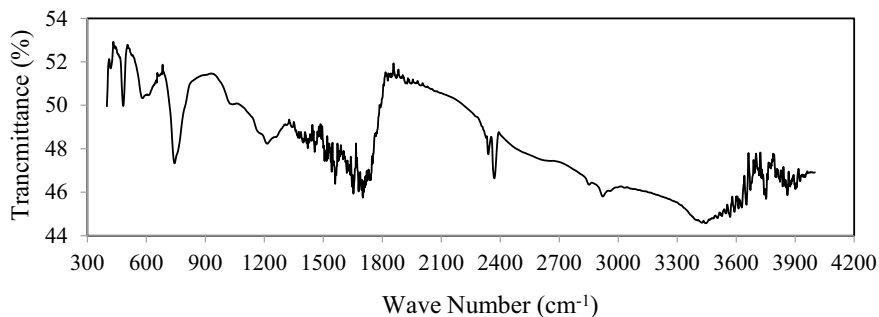


**Fig. 2** FTIR spectra of HA derived from leonardite

### 3.3 Arsenate Adsorption

The adsorption of arsenate on GN, kaolinite, calcite, and HA at different pH values are shown in Fig. 3. Results demonstrated that adsorption of As by GN is a rapid reaction, and more than 80% of the reaction takes place within the first 10 min. Adsorption of

As by kaolinite, calcite, and HA was very slow and inefficient reaction. This is consistent with Jacobson and Fan [13]. In the presence of HA and calcite, As adsorption was only about 10% at pH 5.5 and 7, respectively. Kaolinite showed 3.5, 10, and 13% adsorption efficiency at pH 8.5, 7, and 5.5, respectively. As expected, adsorption on all materials decreases with increasing pH. It should be considered that the arsenate adsorption mechanism on GN and kaolinite possibly involves surface complexation with the hydroxyl groups at the mineral surface, as well as anion exchange reactions with the sulphate ions present in the structure. At low pH values, the surface groups of iron oxide and kaolinite are mainly positively charged, which will favor the interactions between the arsenate and the mineral groups. The pH increase in the suspensions will produce a decrease in the amount of positively charged surface groups, and therefore a decrease in the arsenate adsorption is expected.

For calcite-containing samples,  $\text{As}^{\text{V}}$  forms inner-sphere surface complexes via corner-sharing with Ca octahedra. Although the adsorption efficiency of calcite was very low, a slight change in As adsorption capacity was observed by decreasing pH from 8.5 to 7. In the presence of HA, no  $\text{As}^{\text{V}}$  adsorption was observed at pH 7 and 8.5. The concentration of residual As was slightly decreased by decreasing the solution pH to 5.5. Functional groups such as carboxyl, hydroxyl, and amino groups, as well as other N- and S-containing groups on undissolved HA, have the potential to sorb anionic molecules at low pH values. As pH increases, adsorption of  $\text{As}^{\text{V}}$  by HA decreases due to increased electrostatic repulsion between negatively charged

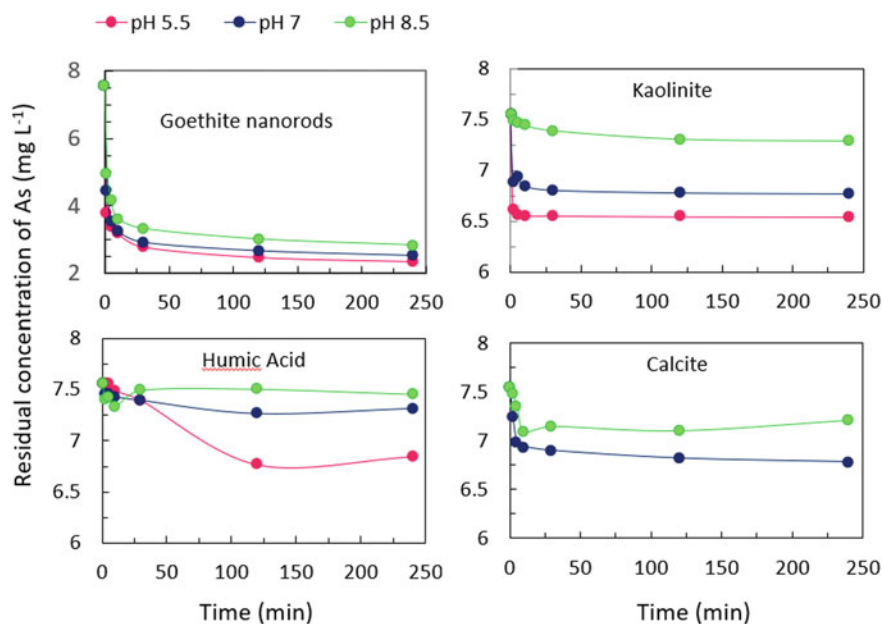


**Fig. 3** Changes in  $\text{As}^{\text{V}}$  concentration with time during its reaction with geochemical constituents at various pH values



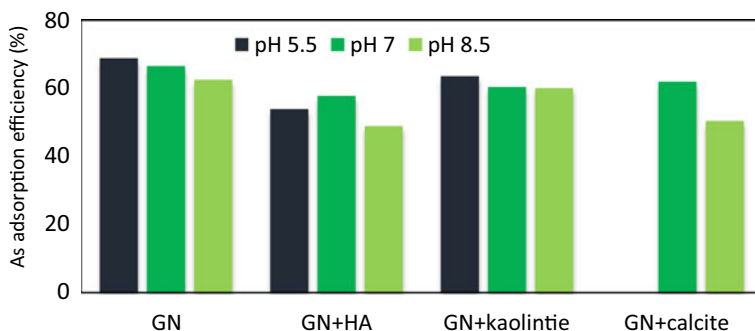


**Fig. 4** Effect of co-application of geochemical constituents and goethite nanorods on the adsorption of  $\text{As}^{\text{V}}$

HA functional groups and  $\text{As}^{\text{V}}$  ions. However, the dissolution of HA at high pH values and the formation of soluble complexes with As could be another reason for the observed results.

Leonardite was used as a source of HA. The International Humic Substances Society (IHSS) method, with a slight modification, was used for the extraction of HA.

The results of the co-application of geochemical constituents with goethite nanorods indicated that the presence of HA, kaolinite, and calcite significantly decreases the rate and extent of As removal by goethite nanorods. Although kaolinite and calcite had shown a slight As removal efficiency, their combination with goethite nanorods decreases the overall As removal efficiency. Results are shown in Fig. 4.

The kinetic parameters of examined models are represented in Table 1. Results indicated that the PSO equation is the best of the various kinetic equations studied, as evidenced by the overall highest value of  $R^2$  and the lowest value of SE. Data conformance from the pseudo-second-order model is also shown in Fig. 5. Our results indicated that the adsorption rate of arsenate by GN and in the presence of geochemical constituents can be well approximated by pseudo-second-order reaction concerning the initial pH of the solution.

Goethite has a higher sorption affinity for high polar carboxylic functional moieties on humic acid. Adsorption of HA on the goethite blocks active sites of the goethite surface, and therefore, arsenate adsorption efficiency decreases [14]. Studies have shown that the presence of fulvic acid (FA) and HA can decrease arsenate adsorption to a range of minerals and soils [15–19]. Weng et al. [14] studied arsenate and FA or HA interactions on the goethite surface. They found that the adsorption of FA and HA led to the desorption of arsenate and, accordingly, a substantial increase in arsenic. They also reported that the adsorption of both FA and HA was mutually reduced by competition with arsenate. Weng et al. [14] speculated that the main mechanism explaining the effects of natural organic matter on arsenic speciation is site and electrostatic competition. Moreira et al. [20] reported similar results when examining the adsorption of arsenate, phosphate, and humic acids on acicular

**Table 1** Parameters of PFO, PSO, parabolic diffusion, and elovich kinetic models

	pH	Pseudo-second order			Pseudo-first order			Diffusion parabolic			Elovich			
		$k_2$	$R^2$	SE	$k_1$	$R^2$	SE	$k_d$	$R^2$	SE	$\alpha$	$\beta$	$R^2$	SE
GN	5.5	0.27	0.991	0.189	0.70	0.966	0.381	0.23	0.418	1.500	120	2	0.994	0.151
	7	0.23	0.994	0.139	0.45	0.95	0.269	0.35	0.450	1.430	100	2	0.981	0.263
	8.5	0.13	0.997	0.097	0.35	0.973	0.296	0.38	0.518	1.249	250	2.4	0.972	0.300
GN + kaol	5.5	0.11	0.996	0.120	0.30	0.981	0.250	0.30	0.529	1.273	30	1.9	0.949	0.418
	7	0.02	0.991	0.175	0.08	0.991	0.185	0.26	0.741	1.008	50	2.3	0.721	1.046
	8.5	0.08	0.994	0.143	0.20	0.982	0.258	0.30	0.617	1.195	10	1.9	0.880	0.668
GN + HA	5.5	0.26	0.974	0.235	0.60	0.935	0.376	0.35	0.500	1.047	180	3.0	0.999	0.043
	7	0.2	0.981	0.220	0.30	0.915	0.472	0.25	0.499	1.149	105	2.5	0.997	0.075
	8.5	0.07	0.988	0.152	0.16	0.961	0.283	0.30	0.699	0.786	205	3.3	0.886	0.484
GN + cal	7	0.14	0.985	0.223	0.30	0.950	0.408	0.36	0.518	1.276	260	2.5	0.962	0.355
	8.5	0.13	0.995	0.102	0.40	0.952	0.317	0.25	0.561	0.960	210	3.1	0.963	0.277

goethite nanoparticles obtained from acid mine drainage. The inhibitory effect of HA on the adsorption of As<sup>V</sup> by FeO nanoparticles has also been demonstrated by Giasuddin et al. [21].

However, our findings on the influence of calcite on the As<sup>V</sup> adsorption by goethite were inconsistent with Liu et al. [22] reports. They found that As<sup>V</sup> removal by goethite increases in the presence of bicarbonate, resulting from buffering effects and bicarbonate-induced iron corrosion and CaCO<sub>3</sub> formation in solution. Although CaCO<sub>3</sub> is known as an adsorbent of As<sup>V</sup> [22, 23], due to its low reaction rate, it acts as a rate-limiting factor in the adsorption process of As<sup>V</sup> by goethite and declines the adsorption efficiency in a specific time scale.

The experimental data were fitted into the various kinetic models, including pseudo-first-order (PFO) (Eq. 1), pseudo-second-order (PSO) (Eq. 2), diffusion parabolic (Eq. 3), and Elovich (Eq. 4). Evaluation of goodness of fit of kinetic models was conducted using least-square regression analysis and calculation of standard error of the estimate.

$$q_t = q_e(1 - e^{-k_1 t}) \quad (1)$$

$$q_t = \frac{q_e^2 k_2 t}{q_e k_2 t + 1} \quad (2)$$

$$q_t = q_e - k_d t^{1/2} \quad (3)$$

$$q_t = \left(\frac{1}{\beta}\right) \ln(\alpha\beta) + \left(\frac{1}{\beta}\right) \ln t \quad (4)$$

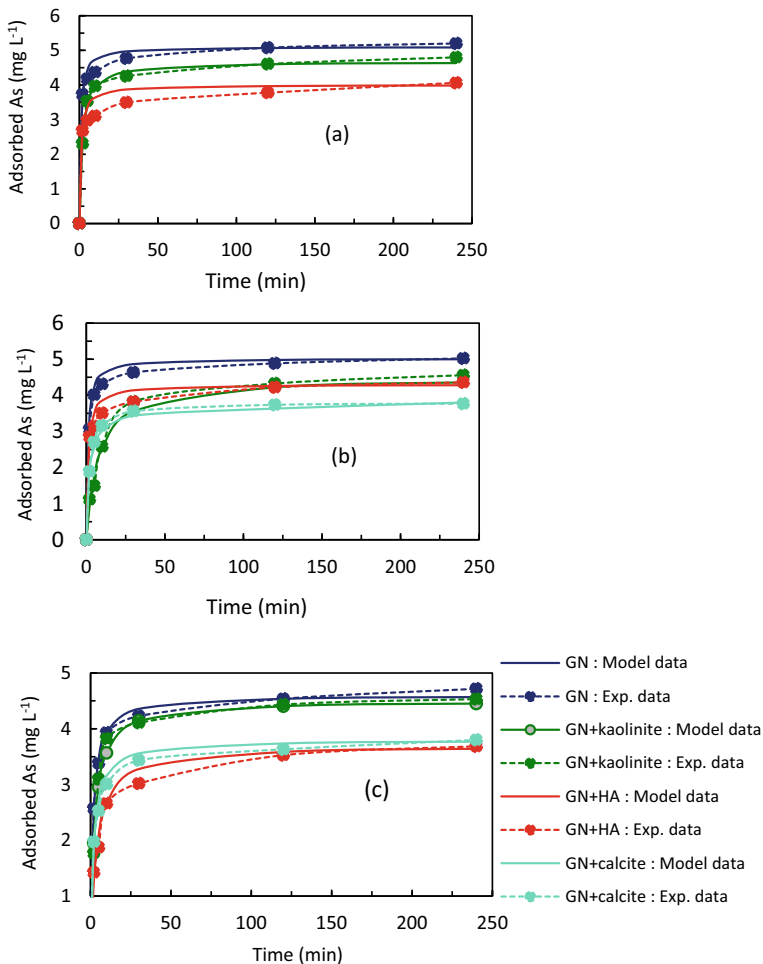


**Fig. 5** Pseudo second-order kinetic plots of adsorption of arsenate on goethite nanorods in the presence of geochemical constituents

where,  $q_t$  is the adsorbed amount of solute at time  $t$ ,  $q_e$  is the adsorbed amount of solute at equilibrium,  $k_1$ ,  $k_2$ , and  $k_d$  refer to the rate constants of PFO, PSO, parabolic diffusion, and Elovich models, respectively.  $\alpha$  and  $\beta$  are constants referring to the initial adsorption rate and desorption constant, respectively.

According to the data given in Table 1, the pseudo-second-order model was the best kinetic model, as evidenced by the highest determination coefficient ( $R^2$ ) and the lowest standard error of the estimate (SE). The residual As<sup>V</sup> concentration as a function of reaction time and corresponding pseudo-second-order kinetic models are shown in Fig. 5. In the case of the pseudo-second-order model, the rate constant decreased by increasing the initial pH of the solution. For other examined models,

however, a fluctuating trend was observed. Considering that several studies on sorption processes have reported a strong correlation between a pseudo-second-order kinetic model with chemisorption, it suggests that the chemisorption mechanism also played an important role during the arsenate sorption onto goethite iron oxide [24]. Although the presence of geochemical constituents decreased the extent and the rate of As<sup>V</sup> adsorption by GN, it did not alter the mechanism of the reaction. It is suggested to investigate the effect of concentrations of geochemical constituents on the mechanisms of As<sup>V</sup> removal by goethite on a molecular scale for a better understanding of the mechanisms of the adsorption process.

## 4 Conclusion

In this study, goethite nanorods were prepared by precipitation method and used for arsenate adsorption from an aqueous solution. Kaolinite, calcite, and humic acid were selected as three major geochemical constituents and were investigated for their effect on the efficiency and the rate of arsenate adsorption by goethite. The results indicated that freshly synthesized goethite nanorods were highly efficient and rapid in arsenate removal. The extent of arsenate adsorption depended on the solution's initial pH and the presence of geochemical constituents. High pH values and the presence of kaolinite, calcite, or humic acid significantly decreased the rate and efficiency of arsenate adsorption by goethite. The adsorption followed pseudo-second-order kinetics. The adsorption mechanism is mainly dominated by electrostatic interaction and chemical binding of arsenate with surface functional groups of goethite.

**Acknowledgements** This research was supported by Çanakkale Onsekiz Mart University Scientific Research Coordination Unit with the project no. FHD-2021-3803.

## References

1. Karaca O, Reddy KR (2014) Environmental assessment of mine tailings: Can-Etili Basin (Turkey) as a case study. In: Proceedings of 14th international multidisciplinary scientific geoconference and expo (SGEM 2014). Albena Resort, Bulgaria
2. Karaca O, Cameselle C, Bozcu M (2019) Opportunities of electrokinetics for the remediation of mining sites in Biga peninsula, Turkey. *Chemosphere* 227:606–613
3. Usman ARA, Lee SS, Awad YM, Lim KJ, Yang JE, Ok YS (2012) Soil pollution assessment and identification of hyperaccumulating plants in chromated copper arsenate (CCA) contaminated sites, Korea. *Chemosphere* 87:872–878
4. Wan X (2020) Review on remediation technologies for arsenic-contaminated soil. *Front Environ Sci Eng* 14(2):24
5. Wang HT, Ding J, Xiong C, Zhu D, Li G, Jia XY, Zhu YG, Xue XM (2019) Exposure to microplastics lowers arsenic accumulation and alters gut bacterial communities of earthworm *Metaphire californica*. *Environ Pollut* 251:110–116

6. Lyubun YV, Pleshakova EV, Mkandawire M, Turkovskaya OV (2013) Diverse effects of arsenic on selected enzyme activities in soil–plant–microbe interactions. *J Hazard Mater* 262:685–690
7. Shipley HJ, Engates KE, Guettner AM (2011) Study of iron oxide nanoparticles in soil for remediation of arsenic. *J Nanopart Res* 13:2387–2397
8. Montalvo D, Vanderschueren R, Fritzsche A, Meckenstock RU, Smolders E (2018) Efficient removal of arsenate from oxic contaminated water by colloidal humic acid-coated goethite: batch and column experiments. *J Clean Prod* 189:510–518
9. Alidokht L, Anastopoulos I, Ntarlagiannis D, Soupios P, Tawabini B, Kalderis D, Khataee AR (2021) Recent advances in the application of nanomaterials for the remediation of arsenic-contaminated water and soil. *J Environ Chem Eng* 9:105533
10. Jaiswal A, Banerjee S, Mani R, Chattopadhyaya MC (2013) Synthesis, characterization and application of goethite mineral as an adsorbent. *J Environ Chem Eng* 1:281–289
11. Alidokht L, Oustan S, Khataee A (2021) CrVI reductive transformation process by humic acid extracted from bog peat: effect of variables and multi-response modeling. *Chemosphere* 263:128221
12. Sørensen HU, Postma D, Jakobsen R, Larsen F (2008) Sorption and desorption of arsenate and arsenite on calcite. *Geochim Cosmochim Acta* 72:5871–5884
13. Jacobson AT, Fan M (2019) Evaluation of natural goethite on the removal of arsenate and selenite from water. *J Environ Sci* 76:133–141
14. Weng L, Riemsdijk WHV, Hemstra T (2009) Effects of fulvic and humic acids on arsenate adsorption to goethite: experiments and modeling. *Environ Sci Technol* 43:7198–7204
15. Bowell RJ (1994) Sorption of arsenic by iron-oxides and oxyhydroxides in soils. *Appl Geochem* 9(3):279–286
16. Gustafsson JP (2006) Arsenate adsorption to soils: modelling the competition from humic substances. *Geoderma* 136(1–2):320–330
17. Ko I, Davis AP, Kim JY, Kim KW (2007) Effect of contact order on the adsorption of inorganic arsenic species onto hematite in the presence of humic acid. *J Hazard Mater* 141(1):53–60
18. Simeoni MA, Batts BD, McRae C (2003) Effect of groundwater fulvic acid on the adsorption of arsenate by ferrihydrite and gibbsite. *Appl Geochem* 18(10):1507–1515
19. Xu H, Allard B, Grimvall A (1988) Influence of pH and organic substance on the adsorption of As(V) on geologic materials. *Water Air Soil Pollut* 40(3–4):293–305
20. Moreira RFPM, Vandresena S, Luiza DB, Joséa HJ, Pumab GL (2017) Adsorption of arsenate, phosphate and humic acids onto acicular goethite nanoparticles recovered from acid mine drainage. *J Environ Chem Eng* 5:652–659
21. Giasuddin ABM, Kanel SR, Choi H (2007) Adsorption of humic acid onto nanoscale zerovalent iron and its effect on arsenic removal. *Environ Sci Technol* 41(6):2022–2027
22. Liu TZ, Rao P, Mak MKS, Wang P, Lo IMC (2009) Removal of co-present chromate and arsenate by zero-valent iron in groundwater with humic acid and bicarbonate. *Water Res* 43(9):2540–2548
23. Alexandratos VG, Elzinga EJ, Reeder RJ (2007) Arsenate uptake by calcite: macroscopic and spectroscopic characterization of adsorption and incorporation mechanisms. *Geochim Cosmochim Acta* 71(17):4172–4187
24. Ho YS, McKay G (1999) Pseudo-second order model for sorption processes. *Process Biochem* 34(5):451–465

# A Case Study on Piping as a Mechanism Causing Collapse of an Earth Dam



Ayşenur Altınsoy  and Gürkan Özden 

**Abstract** The design of dams used in drinking, utility, irrigation water supply, and energy production are a subject that needs to be studied meticulously so that the resulting product would be optimum without harming the environment as much as possible. The dam causes the formation of a new ecosystem in the region where it is built and, accordingly, the establishment of a balance between nature and the dam. The collapse of the dam in the ecosystem where the downstream region is located will cause severe damage such as loss of life, deterioration of the balance of the ecosystem, and flooding of habitats. Studies have shown that the failure rate of earth-fill dams is relatively high compared to other types of dams. The reasons for the failure of earthen dams can be listed simply as (1) overtopping, (2) piping, (3) poor management, and (4) natural disasters. The triggering of the piping mechanism, which has an important place among the possible causes of collapse, was investigated within this study's scope of a case history. In Idaho, the USA, the zoned earth-rock fill type Teton Dam with a body height of 93 m from the river bottom is thought to be an example of piping that may have been triggered because of faulty construction and possibly design practices. This dam has been studied in detail in the literature regarding piping and the consequences of the damage. The dam's collapse had heavy consequences: 11 people and 16,000 livestock died, three towns were evacuated, electricity production stopped, and irrigation water supply was interrupted. It has been long speculated that piping was triggered in the natural ground below the core (below the cut-off), which was not protected by a filter. In this study, Teton Dam was modeled numerically to demonstrate the gradual development of piping mechanism better.

**Keywords** Piping · Earth dam · Case study · Finite element modelling

---

A. Altınsoy (✉)

Graduate School of Natural and Applied Sciences, Department of Civil Engineering, Dokuz Eylül University, Izmir, Turkey

e-mail: [aysenur.altinsoy@ogr.deu.edu.tr](mailto:aysenur.altinsoy@ogr.deu.edu.tr)

G. Özden

Faculty of Engineering, Department of Civil Engineering, Dokuz Eylül University, Izmir, Turkey

## 1 Introduction

Some of the parameters to be considered in the design of a dam can be given as the constructed dam would be sustainable, the damage to the environment is kept at a minimum level, it is designed in harmony with the ecosystem, and it has sufficient safety. Considering the increasing construction costs and the damage caused to the environment by reinforced concrete dams the most suitable option for dam construction may be considered as earth-fill type dams. This is especially true from the carbon footprint point of view [1]. However, sustainability of earth-dams is of utmost importance since collapse of earth-fill dams may result in loss of life, upsetting the balance of the ecosystem and causing floods. Examples to such case include the failure of the Teton Dam in Idaho and the Baldwin Hills Dam in Los Angeles.

Studies have shown that the failure rate of earth-fill dams is relatively high compared to other dams. The reasons for the collapse of earthen dams can be listed simply as (1) overflow, (2) piping, (3) mismanagement, and (4) natural disasters. Among these possible causes of collapse, the piping mechanism occupies a more significant percentage than the others [2]. For this reason, one of the issues to be addressed in the earth-fill dam design is the piping mechanism. The piping mechanism is a form of seepage erosion, defined as the washing of fines by failing to resist the drag forces generated by hydraulic loads. Various terms have been used to classify this seepage erosion [3–5]. Boiling, which is one of the terms used in this sense, can be defined as the loosening of a significant soil volume in parallel with the seepage flow and the loss of strength of the soil. Hydraulic fracturing, another expression, is known as dividing the soil by succumbing to the pore water pressure and breaking it into pieces. Internal erosion is the movement of small grains through a matrix of larger grains. On the other hand, the word piping refers to the local development of void channels in discontinuities in the ground (low specific gravity, cracked and fissured structure, high fine grain size content, etc.). Separate seepage lines starting from the dam's downstream side combine to create high seepage pressures. The erosion process progresses backward, and flow lines with unnatural irregular shapes are formed on the ground. This phenomenon may cause severe damage to the dam body with a loss of strength in the core material. Static or dynamic loads can also pay the way to the piping mechanism.

Within the scope of this study, Teton Dam, which was examined in detail in the literature, was modeled numerically using finite element method, the development of excess pore water pressure from the analysis results was examined, and accordingly, the development of the piping mechanism was investigated under static loads (Table 1).

**Table 1** Summary of failure causes for the four typical earth-dam types [2]

Technical deficiencies						
Earth dam type	Overtopping	Piping	Others	Poor management	Disasters	Sum
Homogeneous earth fill	13	22	2	1	–	38
Zoned earth fill	3	6	–	–	–	9
Earth fill with core wall	8	2	1	–	1	12
Concrete faced earth fill	–	2	–	–	–	2

## 2 Modelling of Piping Mechanism

A relatively simple approach to investigate triggering of piping is to trace the hydraulic gradient until it gets close to the critical one, which is expressed by Eq. 1. This methodology was employed by some researchers in the past [6].

$$v = k \cdot i \quad (\text{Darcy's Law}) \quad i \rightarrow i_{cr} = \frac{\gamma'}{\gamma_{water}} \tag{1}$$

In the above given equation,  $v$  represents the velocity of the water particles (L/T),  $k$  parameter stands for the permeability of the soil (L/T), and  $i$  represents the hydraulic gradient. It is assumed that the piping mechanism will start when the hydraulic gradient ( $i$ ) calculated from here exceeds the critical hydraulic gradient ( $i_{cr}$ ). The  $\gamma'$  and  $\gamma_{water}$  are the effective unit weight of the soil and unit weight of water, respectively. Studies have shown that hydraulic fracturing can occur in regions where the hydraulic gradient is less than 1 [7]. In line with the research, the threshold value of the hydraulic gradient was taken as 70% of the critical hydraulic gradient in this study.

In this study, firstly, the numerical model of the Teton Dam was formed in stages to assign gravity loads as usual for majority of geotechnical problems. Then, the water level on the upstream side was defined followed by steady state flow analysis. By examining the hydraulic gradient values from the results obtained, the portion of the finite element geometry with  $i > 0.7i_{cr}$  were replaced with a soil material with higher permeability and lower shear strength parameters. The analysis continued iteratively until the condition  $i > 0.7i_{cr}$  was not met within the model geometry. A python code developed specifically for this purpose was used throughout the iteration. The logic of the algorithm was similar to the one used for analysis of a model dam [8].



### 3 Teton Dam

Teton Dam is a zoned earth-rock fill dam with a body height of 93 m, built on the Teton River in eastern Idaho. It collapsed during the first filling of its reservoir on June 5, 1976. The collapse of the Teton Dam caused 11 deaths and \$400 million in damage. Although the consequences of this great disaster are heavy, it is an event from which important lessons were learned. After the dam's failure, a panel was formed to examine the possible causes of failure, and necessary investigations were made. Research on the geology of the construction area has shown that the rocks under the dam foundation are composed of volcanic-origin basalt and rhyolite rock types and have a suitable structure for developing the piping mechanism due to its high layer permeability. In addition, it has been observed that the dam material was dominated by erosive silt used as filling material, which was later considered as suitable for the development of erosion and piping mechanism. It has been reported that seepage of this material may have caused backward erosion, and erosion may have occurred in terms of direct contact with water through cracks [9–11]. Considering all these, it is clear that the rhyolite under the dam and the fine marine origin silt used as the zone filling materials are insufficient to avoid piping due to their high permeability (Fig. 1).

Research results showed that; (1) The contact surfaces of the core region of the dam with the jointed rock on which the dam body was placed could not be adequately sealed and made impermeable by grouting (Fig. 2). (2) An appropriate filter layer was not provided to prevent the core material from being dragged into any unsealed opening by the effect of seeping pore water.



**Fig. 1** Photograph of Teton Dam failure [11]



Fig. 2 Vertical joints crossing alignment where grout cap is missing between [11]

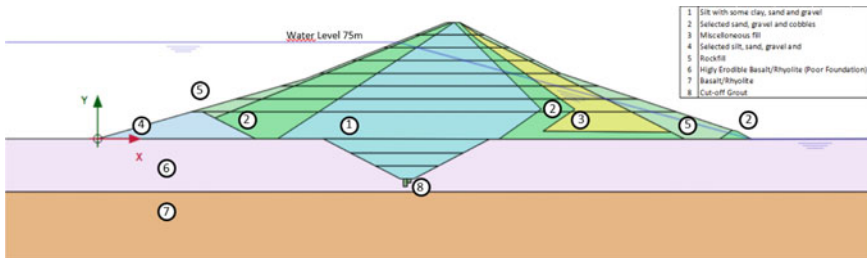


Fig. 3 The finite element model constructed for the analysis of the Teton Dam

### 4 Two-Dimensional Analysis

A commercially available 2D finite element software was used in the analysis. The model created according to the idealized geometry of the Teton Dam used in the analysis is given in Fig. 3. The material models and parameters used in the zones and foundation of the dam are presented in Table 2. The analyzes were carried out using effective stress based mechanical soil-rock parameters.

### 5 Results and Discussions

According to the results of the first stage analysis, where iterations were not performed yet, the maximum achieved hydraulic gradient was calculated as = 2.749 and the factor of safety  $F_s = 1.159$ . According to these results, it was observed that the piping mechanism could be initially triggered around the cut-off grout (Fig. 4).

**Table 2** Material parameters used in the analysis

<i>Hardening soil</i>											
	$\gamma_{unsat}$ kN/ m <sup>3</sup>	$\gamma_{sat}$ kN/ m <sup>3</sup>	Drainage type	$e_{init}$	k m/day	$E_{50}^{ref}$ MPa	$E_{oed}^{ref}$ MPa	$E_{ur}^{ref}$ MPa	$c'$ kPa	$\phi$ ( $^{\circ}$ )	$\psi$ ( $^{\circ}$ )
Zone-1	16.5	18.8	Und(A)	0.26	$4.32 \times 10^{-3}$	37.5	37.5	112.5	75	37	6.7
Zone-2	20	21	Und(A)	0.50	$8.12 \times 10^{-3}$	50	50	150	0	40	10
Zone-3	17	18	Und(A)	0.50	$4.32 \times 10^{-2}$	37.5	37.5	112.5	75	37	6.7
Zone-4	16	17	Und(A)	0.50	0.864	15	15	45	0	40	10
Zone-5	18.5	19.5	Drained	0.50	8.64	15	15	45	0	40	10
<i>Mohr–Coulomb</i>											
	$\gamma_{unsat}$ kN/ m <sup>3</sup>	$\gamma_{sat}$ kN/ m <sup>3</sup>	Drainage type	$e_{init}$	k m/day	$E'$ GPa	$\nu$	Tensile kPa	$c'$ kPa	$\phi$ ( $^{\circ}$ )	$\psi$ ( $^{\circ}$ )
Zone-6	21	22	Und(A)	0.45	$226 \times 10^{-3}$	0.298	0.26	–	10	38	8
Zone-7	25	26	Und(A)	0.15	$8.64 \times 10^{-6}$	6.0	0.20	3000	700	30	0
Zone-8	22	22	Non-porous	0.30	$8.64 \times 10^{-6}$	20	0.20	135	350	39	9.4

These results agree with the data in studies and reports on the causes of the Teton Dam failure. Following the first stage, the material parameters of the zones where  $i \geq 0.7icr$  were replaced by weak soil parameters as defined in Table 3 since soils with high hydraulic gradients near boiling conditions would attain much lower shear strength. The path to be followed by the piping mechanism is given in Fig. 5. As a result of the development of the piping mechanism, the safety factor calculated by the strength reduction method was reduced to  $F_s = 0.40$ . Failure points computed in the analysis section are given in Fig. 6. One may notice that the locations of the failure points match well with the critical failure locations (cut-off grout and dam body), for which considerations were made in the reports authored following the dam’s collapse. The most vital difficulty encountered in the numerical determination of the piping line was the reconstruction of the finite element mesh at the first stage. This problem was avoided by using the code written in python language. The code was created in such a way that it proceeds to the next step by dividing the groundwater flow rates formed after each stage by the permeability of the relevant soil zones, calculating the hydraulic gradient ( $i$ ), comparing the values found with the  $icr$  values, and assigning weak soil to the meshes where the condition was not met.

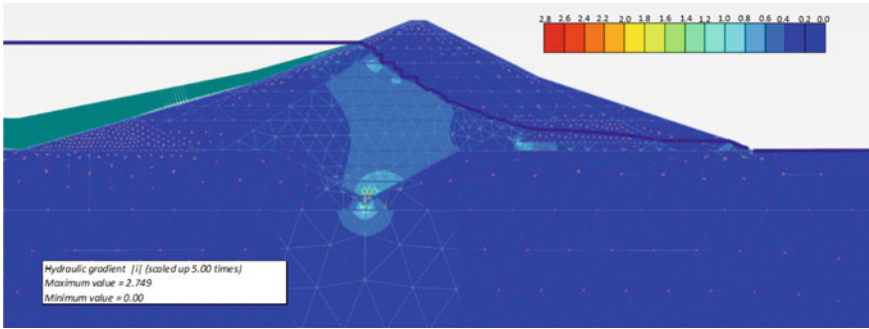


**Fig. 4** Hydraulic gradient values calculated following initial stage analysis

**Table 3** Weak zone parameters used in the analysis

	$\gamma_{\text{unsat}}$ kN/m <sup>3</sup>	$\gamma_{\text{sat}}$ kN/m <sup>3</sup>	Drainage type	$e_{\text{init}}$	k m/day	$E_{50}^{\text{ref}}$ MPa	$E_{\text{oed}}^{\text{ref}}$ MPa	$E_{\text{ur}}^{\text{ref}}$ MPa	$c'$ kPa	$\phi$ ( $^{\circ}$ )
Weak zone-1	16.5	18.85	Drained	0.26	0.1128	37.5	37.5	112.5	2	20
Weak zone-2	20	21	Drained	0.50	0.2624	50	50	150	1	20

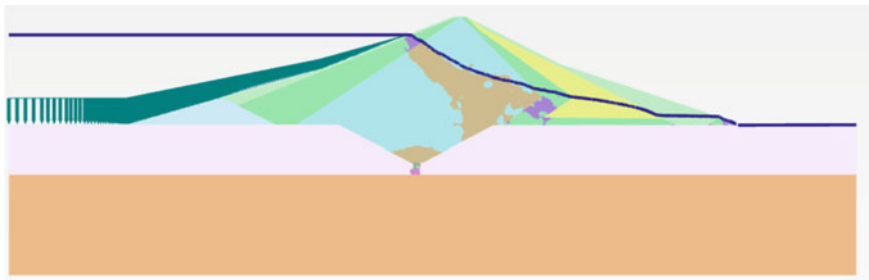


**Fig. 5** The resulting piping pattern

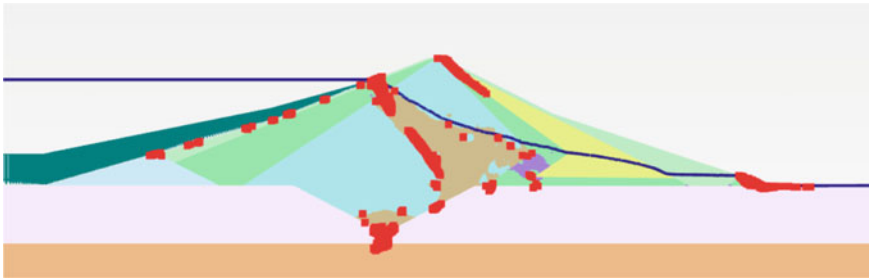


**Fig. 6** Failure points after the final stage analysis

## 6 Conclusions

The case histories encountered in the literature regarding dam failures show that piping and hydraulic fracturing are among the most prominent collapse mechanisms. Analyses conducted for the Teton Dam, a spectacular example of piping-related failures, proved that this mechanism could be foreseen using a relatively simple numerical methodology provided that reliable soil data such as shear strength and permeability parameters were available. The engineers are more stressed than ever about designing and constructing structures, including cost-effective earth dams with low carbon footprints. However, technical requirements shall never be bypassed to reach this goal. For instance, it is understood from the analysis results that the use of silt or clayey silt, although more cost-effective, in the core material should be avoided. In addition, it is seen that the layer called ‘Zone-2’ is almost as impermeable as the core zone, preventing water drainage and causing high hydraulic gradients. The use of unsuitable material in this zone resulted from borrowing it from a nearby quarry for cost reduction. If this layer had been built with an adequate permeability to act as a filter, excessive pore water pressures in the core region would have been safely discharged. Analyses also show that particular attention should be paid to the cut-off grout injection during the design and application stages. It may be concluded that successful realization of large-scale civil engineering projects is a complex task requiring an optimization among cost reduction, low carbon footprint, and sustainable aspects of the design process.

## References

1. Zhang S, Pang B, Zhang Z (2015) Carbon footprint analysis of two different types of hydropower schemes: comparing earth-rockfill dams and concrete gravity dams using hybrid life cycle assessment. *J Clean Prod* 103:854–862. <https://doi.org/10.1016/j.jclepro.2014.06.053>
2. Zhang L, Xu Y, Jia JS (2009) Analysis of earth dam failures: a database approach. *Georisk* 3(3):184–189. <https://doi.org/10.1080/17499510902831759>
3. Terzaghi K, Peck RB (1956) *Soil mechanics in engineering practice*. Wiley, New York, London, Sydney
4. Jaworski GW, Seed HB, ve Duncan JM (1981) Laboratory study of hydraulic fracturing. *J Geotech Eng Div* 107(6):713–732
5. Lubochkov EA (1962) Piping resistant non cohesive soils. *Isvestia VN II G* 71, pp 61–89
6. Gattinoni P, Francani V (2009) A tool for modeling slope instability triggered by piping. *Int J Geol Environ Eng*
7. Hubbert MK, Willis DG (1957) Mechanics of hydraulic fracturing. *Trans Soc Petrol Eng AIME* 210:153–163
8. Sharma RP (2013) Case histories of earthen dam failures. In: *International conference on case histories in geotechnical engineering*. Retrieved from <https://scholarsmine.mst.edu/icchge/7ic chge/session03/8>
9. Seed HB, Leps TM, Duncan JM, Bieber RE (1976) Hydraulic fracturing and its possible role in the Teton Dam failure. Appendix D of Report to U.S. Dept. of the Interior and State of Idaho on Failure of Teton Dam by Independent Panel to Review Cause of Teton Dam Failure, pp D1–D39

10. U.S. Department of the interior Teton Dam failure review group (1977). Failure of Teton Dam, a report of findings
11. U.S. Department of the interior Teton Dam failure review group (1980) Failure of Teton Dam, final report

# A Global Review of Environmental Management System Implementation in Construction Industry



Hasan Eteraf , Zahra Delshad, and Viktoria Mikita

**Abstract** Significant advancements in company structure and management have been accomplished in recent years. Many causes have contributed to the creation of quality control and environmental management systems as a competitive strategy for enterprises, including the rising needs of customers and the globalization of world markets. In comparison to other professional sectors, the construction industry has been sluggish to respond to environmental issues and implement Environmental Management Systems (EMS). As our understanding of the environment grows and a more sustainable approach is needed, the construction sector faces several problems. Time, money, and quality have historically been the limiting factors in building projects, but it has become increasingly important to include environmental factors as well. One of the primary problems that designers and project managers face nowadays is focusing on environmental factors. The body of knowledge on the issue of environmental management in the construction industry was gathered and analyzed in this study with the goal of determining the state of the art. Barriers to the adoption of the ISO 14001 standard in the construction sector were also highlighted, based on different locations throughout the world.

**Keywords** Construction · Environmental management systems · ISO 14001 · Sustainable construction · Global review

## 1 Introduction

The contemporary world is fast progressing thanks to advances and technology, and environmental indicators show that the building sector is one of the most significant providers of trash to the environment [1]. Worldwide targets have been set to enhance the world's sustainability, and international coordination standards, management tools, and classification systems are needed to steer the construction sector in the correct direction [2]. Many international construction firms utilize a variety of

---

H. Eteraf (✉) · Z. Delshad · V. Mikita  
University of Miskolc, Miskolc, Hungary  
e-mail: [hghassan@uni-miskolc.hu](mailto:hghassan@uni-miskolc.hu)

© The Author(s), under exclusive license to Springer Nature Singapore Pte Ltd. 2023  
Y. Yukselen-Aksoy et al. (eds.), *Sustainable Earth and Beyond*, Lecture Notes in Civil Engineering 370, [https://doi.org/10.1007/978-981-99-4041-7\\_37](https://doi.org/10.1007/978-981-99-4041-7_37)

419

standards, such as those developed by the International Organization for Standardization (ISO), the world's biggest creator of voluntary international standards. (ISO Central, Secretariat, 2012). The goal of applying ISO standards in the construction business is to improve management control, customer service, resource optimization, communication, work coordination, and environmental protection [3]. ISO 14001 (Environmental management), ISO 9001 (Quality management), and ISO 26000 (Sustainability management) are ISO standards linked to sustainability in the construction sector (Social management). Standards are a collection of procedures that explain how people who follow them might attain desired product characteristics, marketing, and process improvement. These standards are used by many players all around the world to achieve distinct objectives. Standards are governed procedures that result in collaboration, coordination, and instructions. These might be thought of as rules that explain what the adopter should do in specific scenarios. When these guidelines are applied to a large number of adopters, the adopters will begin to behave in a consistent manner, resulting in uniformity among individuals and organizations [4].

## **2 Environmental Management System and ISO 14001**

An Environmental Management System (EMS) is a mechanism that assists a company in achieving its environmental objectives by reviewing, evaluating, and improving its environmental performance on a regular basis [5]. The premise is that this continuous analysis and evaluation will reveal possibilities for the organization's environmental performance to be improved and implemented. The EMS does not specify a minimum level of environmental performance that must be met; instead, each organization's EMS is adapted to its own goals and targets.

Despite the fact that there have been several EMS initiatives throughout the years, ISO 14001 is the first attempt to define a worldwide EMS standard [6]. In 1996, the ISO 14001 standard was published, building on the success of the ISO 9000 series. The ISO 14001 standard was modeled after a number of national environmental management standards. The standard was developed in the organizational framework of the 1990s, a period marked by the intensification of the drive toward a green production and consumption model [7]. ISO 14001 acceptance and benefits are depending on a wide range of dependent variables, such as business model enhancement, competitiveness, reduction of waste, and staff dedication. There is no actual agreement on how to assess environmental performance, which might be based on a variety of non-comparable metrics. In this view, depending on the criteria and factors utilized, the examination of ISO 14001 effects might provide a variety of outcomes [8].



### 2.1 EMS in Construction Industry

Although environmental management systems are a relatively new issue in the construction industry, current research supports the necessity for construction businesses to explore designing and implementing such systems. According to the latest statistics published in 2020, ISO 14001 accreditation has been granted to over 348,000 firms in 176 countries in different sectors. In more detail, in the field of construction, there are 58,751 organizations in 116 countries that have received ISO 14001 certification. China is leading the world with over 8000 certifications. Compared to the other countries, Japan, Spain, Romania, and Italy have had the highest number of I 14001 certificates issued in construction sector, respectively (Fig. 1) [9].

### 3 Methodology

This article used a comprehensive literature review and accompanying meta-analysis in line with commonly established standards. The benefits of this approach include the fact that it is an efficient and systematic means of summarizing the results of several investigations, as well as providing adequate transparency of results [10]. Key phrases such as environmental management system, ISO 14001, and construction industry were searched for in this study using internet databases. This was done methodically, first by acquiring an overview of the environmental management status in the construction industry globally, and then by narrowing the searches to geographic locations relevant to the meta-analysis criteria. The review was enhanced using

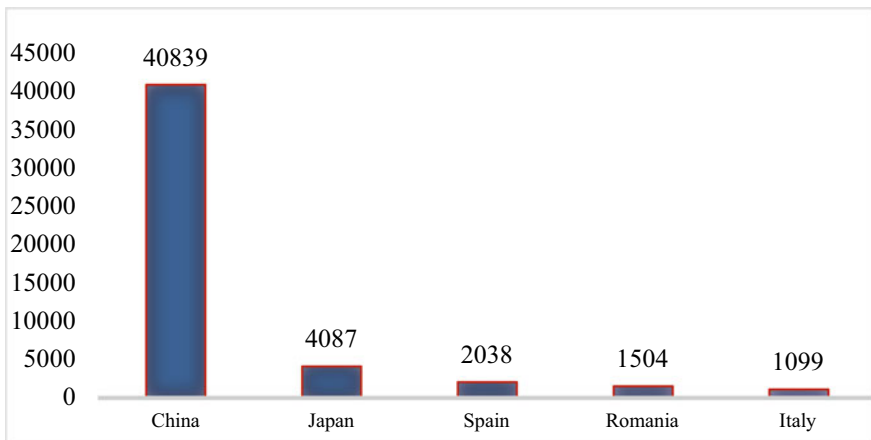


**Fig. 1** The first five countries which have the most ISO14001 certificates in construction sector (Source [11])

repeated literature sweeps with iterative intensification of search parameters based on emergent themes to build a mosaic of international EMS and other environmental initiative implementation.

### 4 Global Overview of ISO 14001 Implementation

According to ISO survey in 2020, ISO 14001 is implemented in 39 sectors, Construction has the most ISO 14001 certifications, followed by wholesale and retail trade, electrical and optical production. This segmentation demonstrates the significance of having ISO 14001 for specific industries and enterprises (Fig. 2). Also, the first five sectors with the numbers of ISO 14001 certificates have been shown in Fig. 3.

The goal of this section is to provide an overview of ISO 14001 implementation in the construction sector in various parts of the world. The findings demonstrate the increased adoption of this standard within this sector as a result of rising expectations from the whole spectrum of internal and external stakeholders. Figure 4 shows the proportion of ISO14001 certificates implemented in different regions in relation to whole. As it can be seen the East Asia and Pacific and also Europe have the most certificates. In the following, the sub-sections are organized in line with the current state of the accessible literature for certain international locations [12].

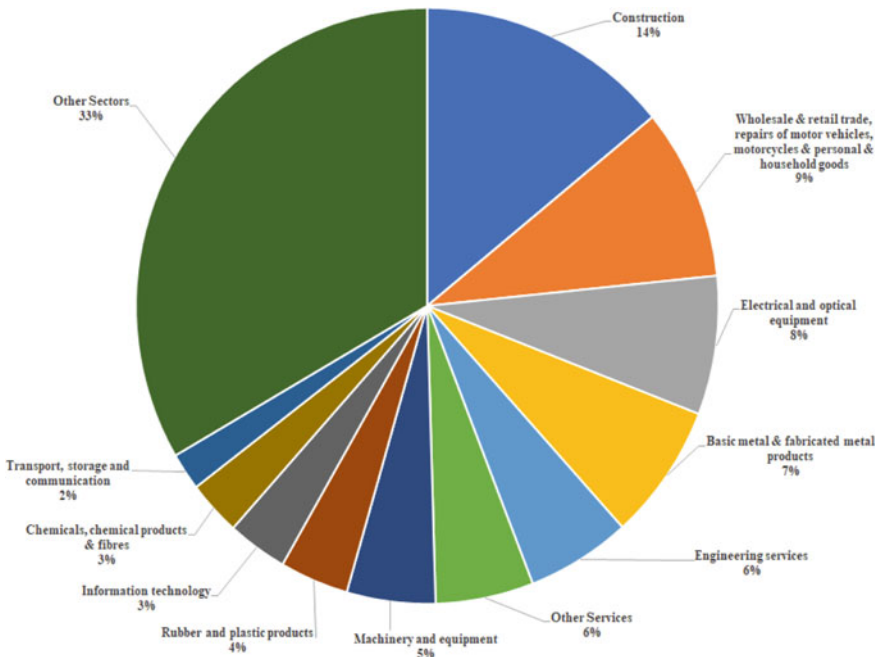


Fig. 2 Sectors with ISO 14001 certificates

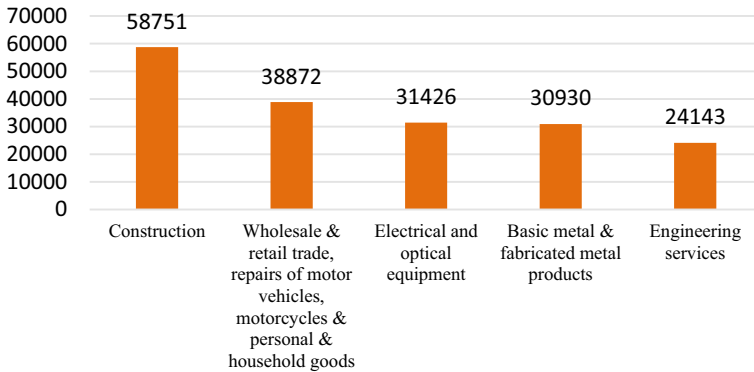


Fig. 3 The first five Sectors which have the most ISO14001 certificates

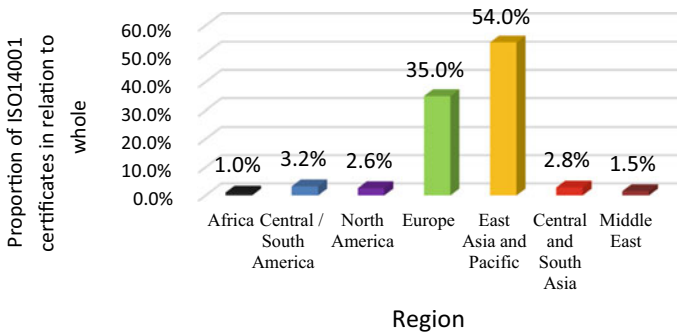


Fig. 4 Proportion of ISO 14001 certificates implemented in different regions in relation to total number

The International Organization for Standardization (ISO) has revealed the findings of its study on Management System Standard Certifications 2020, revealing a 11.48% rise in valid ISO 14001 certifications compared to 2019. Since the focus of this study is on the construction industry, by summarizing the reported scattered data, the number of certificates issued in this field is broken down into different global locations in Fig. 5 [13].

As can be seen in the graph, most of the certificates issued belong to Asia and Oceania, but it should be noted that more than 40,000 of these belong to China.

### 4.1 Viewpoint of East, Central and South Asia Plus Pacific

Since 2005, ISO 14001 certification Issued in regions of East, Central and South Asia, along with pacific, has been higher than the other continents of the world.

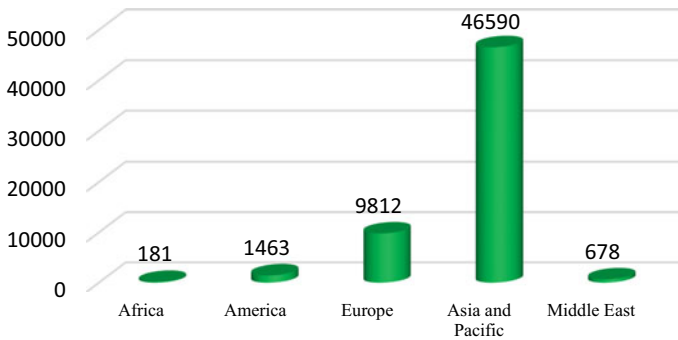


**Fig. 5** Number of ISO 14001 certificates for construction sector in different international locations

Before that, however, Europe had the largest share. According to data released by the International Organization for Standardization from 1999 to 2017, there was a 546% growth by 2017 in number of companies used ISO 14001 which are located in central and south of Asia in comparison to 1999. Similarly, an increase of 449% was reported for East Asia and Pacific.

By 2020, construction firms accounted for the biggest share of the **Chinese** economy's total business volume. According to a 2012 study done in China, organizations certified to ISO 9001 and ISO 14001 achieved benefits such as increased capacity to find a sustainable competitive advantage [14]. However, obstacles in properly implementing the systems were also identified, particularly in regard to resource limitations such as time, manpower, and money. Motouh discovered that EMS implementation based on the ISO 14001 framework may enhance an organization's everyday environmental actions and performance. The poll also discovered that the need to improve a company's image among the community and investors was the primary motivation for ISO 14001 implementation, followed by the need to raise staff understanding of environmental concerns [15]. According to the findings of another study in 2009, EP adoption has a favorable influence on environmental performance in the construction sector in two ways. First, by incorporating EP into building projects, the enterprise may get environmental credibility. Environmental legitimacy indicates that the organization's environmental activities and projects are regarded to be environmentally responsible and beneficial. Construction companies are frequently expected to take steps to reduce noise, landfill trash, and fugitive dust, as well as to use clean transportation and to green the surrounding area [16]. A recent study in China shows that the knowledge and abilities of a project team, rather than government laws, are the primary motivators for the application of EP in construction projects. EP deployment has been shown to improve both environmental and organizational performance [17]. In 2015, research was conducted in **Malaysia** to investigate the critical aspects of EMS implementation, such as environmental aspects and impacts, Good Environmental Practice to be developed on construction sites, and the level of awareness or understanding among site staffs on ISO 14001 EMS implementation in their organizations. It was discovered that the successful

implementation of ISO 14001 EMS is mostly dependent on the comprehension of the personnel [18]. The **Australian** government publishes a brochure giving instructions for corporations and contractors to first minimize and then eliminate garbage generated by construction and demolition operations. Waste management has become a big challenge, especially because the building industry accounted for 38% of all trash created in Australia in 2007 [19]. A study was performed to assess construction firms' opinions of the impact of ISO 14000 adoption on their operations in **Singapore**. Major issues were identified, and recommendations were given for the future development of environmental management systems (EMS) in the Singapore construction sector. There are indications that environmental concerns will lead to significant changes in building industry methods. For example, the environmentally concerned end-purchaser and building user is projected to develop in Singapore in the near future. Furthermore, the clients' external environment may drive them to demonstrate their commitment to environmental preservation by adding significant elements in their projects and facilities [20]. A life-cycle evaluation of a sustainable building sector in **India** revealed that a complex web of stakeholders must be examined, and ISO 14001 should be prioritized if the aim of sustainability is to be met. Given that India's GDP is expected to increase by double digits, that 50% of building project raw materials are generated from natural resources, and that 50% of all created garbage in India originates from construction projects, the need for action is evident. The outcome was that the building sector in India should employ the best possible technology, acquire locally accessible materials, assure environmentally friendly design at all stages, apply energy-efficient methods, decrease risks, and strive to connect the whole supply chain [21]. According to the CIRC assessment, cost-cutting practices in the **Hong Kong** local construction sector result in the bare minimum of promises by construction players to improving environmental performance. Implementing environmental management initiatives will, without a doubt, incur expenditures [22]. One of the primary reasons why many contractors do not use an EMS is financial concerns. For example, the implementation of ISO 14000 and HK-BEAM will entail additional expenditures for equipment, staff training, human resources, and environmental technologies, such as water treatment and the use of noise-barrier materials [23].

## **4.2 Viewpoint of Europe**

Europe was able to increase its number of companies under ISO 14001 by 200% between 2000 and 2017, which is less than the same in Asia and the Pacific. Since 2013, it has been observed that the issuance of ISO 14001 certification in Europe has almost stopped, and unfortunately, even in 2017, it experienced an 8% decrease compared to the previous year.

The **Dutch** construction sector is being pushed by the government to become more progressive and sustainable. The cases in the **United Kingdom** demonstrated that the hurdles to EMS adoption were considerable; nevertheless, they may be overcome

by using a variety of steps. The solutions included senior management commitment and the spread of that sentiment throughout the organization, training to increase awareness and staff competence with the issues, clear communication of rationale and benefits, operational staff engagement and ownership, and clear objectives and targets in those parts of the new systems that have the greatest impact on operations [24]. The main challenges for implementing environmental management systems at construction projects in **Turkey** include in being very quick and rigid schedules for construction projects, an extremely competitive environment with low margin ratios for contractors, and lower levels of validity in the construction sector compared to other industrial sectors. In addition, there are gaps in waste management and environmental systems [25]. At the current stage of development in Latvia, as well as across the world, the concept of sustainable development has a significant impact on the enterprise operations. According to a poll of construction enterprises in Latvia, the predicted improvement in the organizations' image is a key motivating reason for implementation. Legal compliance might be tough to achieve, yet it works effectively in everyday practice. The two most critical issues in developing EMS into Sustainability Management Systems are to enhance the synchronization between the EMS and the organization's strategy and to increase the learning process and direct engagement of all workers [26]. The majority of **Slovenian** construction firms have implemented EMS. There are fewer SMEs with an EMS than bigger organizations; SMEs view the needed documentation supporting the EMS as excessive and a key impediment to its adoption. In reality, these findings are significant because they may serve as the foundation for future initiatives to promote EMSs inside construction SMEs [27]. According to the conclusions of a **Swedish** research, an assignment management system and environmental management should be linked into a single system. To promote accessibility, the system must be speedy and contain a good search function. For executing environmental duties, appropriate tools such as checklists, templates, and instructions are required. Furthermore, personnel must have a sufficient understanding of sustainability to be able to apply the tools and succeed in sustainable management. There should also be a feedback option for employees that encourages them to offer thoughts and comments that will add to the company's knowledge sharing [28]. The use of EMSs in construction Industry of **Madrid** looked to be more of a formality, only a means of preserving the Environmental Management System's accreditation. It was more of a way of completing the rules for submitting an offer to contracting organisms than a sign of any genuine commitment to improve construction enterprises' environmental performance [29]. The major reasons for adopting ISO 14001 at construction businesses in **Estonia**, according to Stonia, are (1) to stay competitive, (2) to improve corporate image, and (3) to deal with environmental challenges, and a lack of funds for implementation is not regarded a barrier. Furthermore, it has been demonstrated that most businesses have difficulties in adopting ISO 14001, which are mostly connected to human resources such as working habits, staff awareness, and attitudes toward environmental concerns [30].

### 4.3 *Viewpoint of America*

According to an ISO survey on the American continent, only 1284 enterprises had the ISO 14001 certificate in 1999; however, this number has climbed to 18,318, demonstrating a tremendous growth.

Construction businesses pursuing certification may face challenges such as employee opposition to paperwork, the effort of establishing the system across many project sites, and the inexperience of auditors in the **United States** with assessing construction operations. It's unknown why the adoption of ISO 14001 standards in the building industry in the United States has been so slow. The expense of certification, ambiguity about the good environmental consequences of ISO 14001 certification in construction enterprises, and a lack of understanding about environmental concerns are all possible preliminary factors. According to an empirical research done in the **United States**, the most significant barriers to adopting the ISO 14001 standard are expensive certification costs and a lack of other available resources [31]. Local and regional business assistance in the form of programs appears to help pragmatic operations managers grasp some of the complicated standards in the **Canadian** construction sector, particularly for small and medium-sized firms (SMEs) [32]. During the last decade, significant efforts have been made to reduce the environmental effect of construction projects in South America. The findings, however, differ throughout regions and even cities within the same nation. Many construction businesses in **Colombia** are devoting significant resources to successfully penetrate worldwide markets by providing their clients' requests in sustainable ways. At the same time, several institutions have a long-term interest in sustaining cutting-edge research units focused on various environmental challenges. The lack of financial incentives, lack of integrated design, and affordability are the main barriers to sustainable construction in **Chile**, whereas tax reduction incentives for companies based on their level of investment effort in construction industry would be a key government action to support sustainable [33]. In **Mexico**, ISO 14001 certification grew from 63 plants in 1999 to 1701 in 2017. According to a research, the ISO 14001 program in Mexico attracts unclean factories under regulatory pressure—not only reasonably clean ones—but has little long-term influence on their regulatory compliance [34].

### 4.4 *Viewpoint of Africa*

Due to the data published by ISO, the regional share of ISO 14001 certificates issued in 1999 for Africa continent compared to the rest of the world was 0.9%, which increased to 1% in 2017. Thus, despite the dramatic increase in the number of certificates issued—from 129 in 1999 to 3083 in 2017—in Africa, this continent still has a small share, which might be caused by different reasons.

A study in **Egypt** looked into the challenges of implementing ISO 14001 in the construction industry. The four biggest impediments to ISO 14001 implementation in the contractor's group were a lack of government pressure, EMS startup costs, a lack of customer requirements/supports, and high implementation costs in declining order of frequency. Obstacles to ISO 14001 implementation were also noted in the consultants group. The key ones were EMS setup costs, a lack of government pressure, a lack of client demand/support, and high implementation costs in declining order of frequency [35]. Announced a ban for poor environmental management are not a significant external motivator of EMS in **Kenyan** construction enterprises. This is due to corruption as well as the severity of the sanctions. Because of the sector's existing culture and attitude toward environmental stewardship, environmental policies are not a major internal impetus for EMS adoption and implementation. The fragmented nature of the industry, as well as the price-based economy, have an impact on EMS adoption since bids are granted to the lowest bidder, and the image of construction enterprises is not particularly important to them, therefore corporate social and environmental duties take a second seat [36]. In **South Africa** the absence of legal enforcement of the EMS as a necessary requirement in the construction sector, the lack of in-house expertise, and the expense of implementing the EMS ISO 14001 standard were identified to be the most important impediments to EMS implementation in the construction industry. This might be attributed to the fact that sustainable construction practices are still relatively new in African construction [37]. Sustainable building must be adopted and implemented, and players in the construction sector are hopeful about the good effects sustainable construction may have on the economy, environment, and society. Another study in South Africa found that there are a number of aspects connected to stakeholders' competence, opportunity, and incentive that need to be improved in order to boost the adoption and implementation of sustainable building techniques. Beliefs about consequences, knowledge, social influences, skills, and beliefs about capabilities were identified as five key target domains that can be used to develop behavior change interventions, such as interventions aimed at adopting circular economy principles or agile and lean principles to improve SC adoption and implementation among construction industry stakeholders [38]. About **Algeria**, despite the government's efforts and resources to apply the idea of sustainable development to all active sectors, it is highlighted that there is still a scarcity of sustainable architecture in the building sector. It appears that developing and implementing an environmental strategy to the promotion of sustainable buildings that is appropriate for Algeria is a must. However, in order to achieve appropriate land management, the choice of construction implantation site should be given top priority. It is also proposed that the existing national legal and regulatory framework be strengthened by enacting implementing laws and regulations, as well as establishing controls and monitoring of their implementation [39].



## 4.5 *Viewpoint of the Middle Eastern Countries*

With its rising population and improving tourist industry, the Middle East is seeing increased demand for infrastructure, development, and construction projects of all types, from retail to offices to residential. Middle Eastern nations have begun to establish their own green building rules, which reflect their particular conditions and market demands, based on worldwide building criteria such as Leadership in Energy and Environmental Design and the BRE Environmental Assessment Method. Like the rest of the world, in 2017 Middle Eastern countries have had more numbers of corporate engagement with environmental management system especially ISO 14001 rather than it used to be in 1999.

The best international H&S practice is applied in the **UAE** and information availability is appropriate. Many managers are committed to environmental management and the H&S of their employees, but there are some barriers and critical success factors to be addressed to assure continued improvement. There is potential for improving environmental and health and safety performance [40]. External factors such as a scarcity of skilled sustainability professionals, green suppliers and developers, a lack of government support, a lack of public awareness and demand, and market uncertainty are all major barriers to the implementation of an environmental management system in the UAE construction sector. External obstacles have an impact on internal barriers. To overcome the external hurdles, it is up to the state and federal governments in the **UAE** to develop an environmental management system strategic plan. People should be empowered to make sustainable choices, and they should be encouraged to engage actively in the conception, planning, and implementation of Environmental management system policies, according to the strategic plan. Government strategies should be developed to encourage competent professionals, suppliers, and developers to relocate to the region [41]. According to a study conducted in **Iran**, top management commitment and support, environmental specialist assistance, environmental legislation, training and awareness, and maintenance and improvement costs are the most important critical sub-factors of ISO 14001 implementation in the construction industries in Iran. As a result, ISO 14001 emphasizes senior management commitment and support for a successful implementation. A useful framework for assessing the effectiveness of ISO 14001-based environmental management system (EMS) installation was also created, which can be used in any firm [42]. As evidenced by the low significance indices, contracting businesses in **Lebanon** are not implementing many good environmental practices. Due to the economic crisis and severe competition in a relatively limited market, contractors in Lebanon are attempting to reduce profit margins. As a result, any sustainable activities that can lower their incurred costs, such as avoiding material wastes, storage expenses, and the reuse of excavated material to reduce dumping costs, are prioritized. Furthermore, environmental rules and policies are still low in all industries. As a result, the legislative body has a critical role to play in developing the appropriate legal framework to safeguard all parties' interests and encourage a broader adoption of sustainable building techniques; this can only be accomplished

if the government takes the lead in this area. In developing nations, it is common to delegate entire duty to the local administration. True, the government is a key factor in such transformations, but all stakeholders should be involved and strive to balance long-term gains with short-term ones. As a result, all stakeholders should look at the industry on a macro basis and aim to create best practices that suit everyone's present and future interests [43]. putting the notion of sustainability into practice In the **Kuwait** construction sector, construction is low; consequently, more action and strategies to enhance and support this idea are needed in order for it to be utilized effectively in future projects. The biggest hurdle to the application of sustainability construction techniques in Kuwait was shown to be a lack of understanding; the Kuwaiti government must take measures in terms of developing standards, rules, and incentives to encourage sustainability construction [44]. In **Oman**, sustainable construction methods are still in their infancy. However, putting these principles in place might help the country thrive by lowering resource use, such as electricity and water, and protecting the environment. In Oman, several prospects for environmentally friendly development have been found. The government may be forced to spend more in renewable energy sources if oil output is limited. Following sustainable building standards may save both development and operations costs, in addition to lowering environmental negative effects. This might be a huge help to the country's attempts to offer enough cheap accommodation across the Sultanate, as well as the government's ambition to make Oman a more enticing tourism destination. Because Oman's local government is the country's largest investor in the construction industry, developing sustainability regulations and tactics tailored to its demands will assure profitability. Cost effectiveness, project delays, limited availability of green materials and equipment, lack of knowledge and awareness, and a lack of environmental regulation are among the most major problems related with the application of sustainable building techniques in Oman. The government has taken steps through the Research Council, but additional funding and incentives are needed [45].

## 5 Conclusion

The large and rising support base for continual improvements in the construction sector has been proved by this worldwide study. With each passing day, EMS's position inside various industrial sectors becomes stronger, and the construction industry is no exception. EMS adoption and certification are increasingly becoming a need for industry survival. It also clearly demonstrates that implementing an environmental management system in a construction firm has had a major positive influence on many firms. Even in industrialized countries such as the United States and China, the notion of an environmental management system is still relatively new. However, it is still advised that main companies in the United States, the United Kingdom, and other developed and developing countries acquire ISO 14001 certification. By doing so, a construction company can establish comprehensive laws and regulations, as well as self-protect the implementation of environmental management in the context of

construction management. In addition, certain benefits and challenges to ISO 14001 implementation in the construction sector throughout the world were examined in this research. Increased management expenses, a lack of trained personnel, a lack of collaboration among subcontractors, restricted chances for product variety, a lack of customer support, government restrictions, uncertainty regarding marketing benefits, and employee non-awareness are just a few of the difficulties identified. EMS implementation, on the other hand, provides benefits such as improved sustainability, noise control, waste recycling, customer trust, environmental awareness, and business image, as well as a competitive advantage. In conclusion, the benefits of ISO 14001 certification in construction appear to outweigh the disadvantages. Implementing the suggested improvements may have the effect of broadening and optimizing the application of these standards. Nonetheless, the ISO 14001 family of standards has only recently been implemented in the construction industry, as it has been in all other industries. More time and experience with the standards may be required before more conclusive judgments about the application of ISO 14001 in the construction business can be reached. To expedite the growth, adoption, and implementation of EMS, more effort must be put into raising awareness. It is suggested to continue the education and work with academic institutions and research and development activities. It may utilise technical tools to identify better answers to various environmental issues confronting the construction sector, as well as to foster healthy competition and higher profit margins across the board.

## References

1. Chan YH, Lee BC, Lee JC (2014) Sustainability in the construction industry in Malaysia: the challenges and breakthroughs. *Int J Econ Manag Eng* 8(4):1218–1222. <https://doi.org/10.5281/zenodo.1094747>
2. Lou EC, Goulding JS (2008) Building and construction classification systems. *Archit Eng Des Manag* 4(3–4):206–220. <https://doi.org/10.3763/aedm.2008.0079>
3. Turk AM (2009) The benefits associated with ISO 14001 certification for construction firms: Turkish case. *J Clean Prod* 17(5):559–569. <https://doi.org/10.1016/j.jclepro.2008.11.001>
4. Brunsson KH (2002) Management or politics—or both? How management by objectives may be managed: a Swedish example. *Financ Accountability Manag* 18(2):189–209. <https://doi.org/10.1111/1468-0408.00150>
5. Cascio J (1996) The ISO 14000 handbook. CEEM Information Services, New York. <https://doi.org/10.1061/~ASCE/1052-3928~2005/131:3~208/>
6. Darnall N (2006) Why firms mandate ISO 14001 certification. *Bus Soc* 45(3):354–381. <https://doi.org/10.1177/0007650306289387>
7. Heras-Saizarbitoria I (2021) ISO 9001, ISO 14001, and new management standards. Springer
8. Boiral O, Guillaumie L, Heras-Saizarbitoria I, Tayo Tene CV (2018) Adoption and outcomes of ISO 14001: a systematic review. *Int J Manag Rev* 20(2):411–432. <https://doi.org/10.1111/ijmr.12139>
9. ISO Survey of certifications to management system standards
10. Littell J (2008) Systematic reviews and meta-analysis. Oxford University Press, New York. <https://doi.org/10.1093/acprof:oso/9780195326543.001.0001>
11. ISO Survey (2020) Retrieved July 02, 2022, from <https://www.iso.org/the-iso-survey.html>
12. ISO (2017) Retrieved July 02, 2022, from <https://www.iso.org/the-iso-survey.html>

13. ISO (2020) Retrieved July 02, 2022, from <https://www.iso.org/the-iso-survey.html>
14. To WM, Lee PK, Billy TW (2012) Benefits of implementing management system standards: a case study of certified companies in the Pearl River Delta, China. *TQM J*. <https://doi.org/10.1108/17542731211191195>
15. Matouq M (2000) A case-study of ISO 14001-based environmental management system implementation in the People's Republic of China. *Local Environ* 5(4):415–433. <https://doi.org/10.1080/713684893>
16. Bortree DS (2009) The impact of green initiatives on environmental legitimacy and admiration of the organization. *Public Relat Rev* 35(2):133–135. <https://doi.org/10.1016/j.pubrev.2009.01.002>
17. Li Y, Ding R, Sun T (2019) The drivers and performance of environmental practices in the Chinese construction industry. *Sustainability* 11(3):614. <https://doi.org/10.3390/su11030614>
18. Yusoff S, Nordin R, Yusoff H (2015) Environmental Management Systems (EMS) ISO 14001 implementation in construction industry: a Malaysian case study. *Issues Soc Environ Account* 9(1):18–31
19. Zuo J, Zhao ZY (2014) Green building research—current status and future agenda: a review. *Renew Sustain Energy Rev* 30:271–281. <https://doi.org/10.1016/j.rser.2013.10.021>
20. Ofori G, Briffett C IV, Gang G, Ranasinghe M (2000) Impact of ISO 14000 on construction enterprises in Singapore. *Constr Manag Econ* 18(8):935–947. <https://doi.org/10.1080/014461900446894>
21. Pati P, McGinnis S, Vikesland PJ (2014) Life cycle assessment of “green” nanoparticle synthesis methods. *Environ Eng Sci* 31(7):410–420. <https://doi.org/10.1089/ees.2013.0444>
22. CIRC (Construction Industry Review Committee) (2001) Construct for excellence. Report of the Construction Industry Review Committee, CIRC, Hong Kong. <https://doi.org/10.1080/0146190802259043>
23. Shen LY, Tam VW (2002) Implementation of environmental management in the Hong Kong construction industry. *Int J Project Manag* 20(7):535–543. [https://doi.org/10.1016/S0263-7863\(01\)00054-0](https://doi.org/10.1016/S0263-7863(01)00054-0)
24. Zutshi A, Creed A (2015) An international review of environmental initiatives in the construction sector. *J Clean Prod* 1(98):92–106. <https://doi.org/10.1016/j.jclepro.2014.06.077>
25. Akyurek A, Agdag ON (2017) Evaluation of environmental management system implementation in construction projects. *Eur Sci J Spec Ed* 322–331
26. Tambovceva T, Geipele I (2011) Environmental management systems experience among Latvian construction companies. *Technol Econ Dev Econ* 17(4):595–610. <https://doi.org/10.3846/20294913.2011.603179>
27. Šelih J (2007) Environmental management systems and construction SMEs: a case study for Slovenia. *J Civ Eng Manag* 13(3):217–226. <https://doi.org/10.1080/13923730.2007.9636440>
28. Valldor Blücher M (2014) Environmental management in the Swedish construction industry—suggestions for improved knowledge management
29. Rodríguez G, Alegre FJ, Martínez G (2011) Evaluation of environmental management resources (ISO 14001) at civil engineering construction worksites: a case study of the community of Madrid. *J Environ Manag* 92(7):1858–1866. <https://doi.org/10.1016/j.jenvman.2011.03.008>
30. Inno M (2005) Assessment of the ISO 14001 implementation process in Estonian certified construction companies
31. Khalid T (2003) Pre-service high school teachers' perceptions of three environmental phenomena. *Environ Educ Res* 9(1):35–50. <https://doi.org/10.1080/1350462030303466>
32. Searcy C, Morali O, Karapetrovic S, Wichuk K, McCartney D, McLeod S, Fraser D (2012) Challenges in implementing a functional ISO 14001 environmental management system. *Int J Qual Reliab Manag*. <https://doi.org/10.1108/02656711211258526>
33. Newbold J (2006) Chile's environmental momentum: ISO 14001 and the large-scale mining industry—case studies from the state and private sector. *J Clean Prod* 14(3–4):248–261. <https://doi.org/10.1016/j.jclepro.2004.05.010>

34. Blackman A (2012) Does eco-certification boost regulatory compliance in developing countries? ISO 14001 in Mexico. *J Regul Econ* 42(3):242–263. <https://doi.org/10.1007/s11149-012-9199-y>
35. Abd Elkhalek HA, Aziz RF, Omar AF (2015) Implementation of environmental management systems in construction industry. *Int J Educ Res* 3(7):407–432
36. Onkangi NR, Nyakondo NS, Mwangi P, Ondari L, Wachira B (2018) Environmental management systems in construction projects in Kenya: barriers, drivers, adoption levels. *Rwanda J Eng Sci Technol Environ* 1(1). <https://doi.org/10.4314/rjeste.v1i1.8S>
37. Esse AM (2019) Implementation of environmental management system in South African construction industry: advantages and barriers
38. Marsh RJ, Brent AC, De Kock IH (2021) Understanding the barriers and drivers of sustainable construction adoption and implementation in South Africa: a quantitative study using the theoretical domains framework and COM-B model. *J S Afr Inst Civ Eng/Joernaal van die Suid-Afrikaanse Instituut van Siviele Ingenieurswese* 63(4):11–23. [https://hdl.handle.net/10520/ejc-civileng\\_v63\\_n4\\_a2](https://hdl.handle.net/10520/ejc-civileng_v63_n4_a2)
39. Tebbouche H, Bouchair A, Grimes S (2017) Towards an environmental approach for the sustainability of buildings in Algeria. *Energy Procedia* 1(119):98–110. <https://doi.org/10.1016/j.egypro.2017.07.053>
40. Alhanouti A, Farrell P (2021) Complementary implementation of best practice in environmental management with health and safety; context of the United Arab Emirates construction industry. *Renew Energy Environ Sustain* 6:20. <https://doi.org/10.1051/rees/2021015>
41. Balasubramanian S (2012) A hierarchical framework of barriers to green supply chain management in the construction sector. <https://doi.org/10.5539/jsd.v5n10p15>
42. Hessami HZ, Golsefid-Alavi M, Shekaf SM, Mavi RK (2012) Evaluation of success factors of ISO 14001-based EMS implementation and ranking the cement industry using the TOPSIS method. *J Appl Environ Biol Sci* 2(10):523–530
43. Majdalani Z, Ajam M, Mezher T (2006) Sustainability in the construction industry: a Lebanese case study. *Constr Innov*. <https://doi.org/10.1108/14714170610710613>
44. AlSanad S (2015) Awareness, drivers, actions, and barriers of sustainable construction in Kuwait. *Procedia Eng* 1(118):969–983. <https://doi.org/10.1016/j.proeng.2015.08.538>
45. Saleh MS, Alalouch C (2015) Towards sustainable construction in Oman: challenges and opportunities. *Procedia Eng* 1(118):177–184. <https://doi.org/10.1016/j.proeng.2015.08.416>

# Changes Over Time in Geotechnical and Geoenvironmental Properties of a Recycled Construction and Demolition (C&D) Waste



Castorina S. Vieira , Paulo M. Pereira , and Nuno Cristelo 

**Abstract** In recent years, several studies and applications of recycled aggregates coming from Construction and Demolition (C&D) waste have been carried out, but the knowledge related to the long-term behaviour of these alternative materials is still fairly limited. Granulometric changes of recycled C&D materials, due to the breakage of particles induced by compaction and weather conditions, and the consequent modifications in their properties are frequently pointed out as an important issue regarding their field application. In order to study the evolution of the geotechnical and geoenvironmental properties of C&D recycled materials, small trial embankments were constructed with a mixed fine-grain C&D waste (0–10 mm). After 24 months of exposure to real weather conditions, the material was collected and the initial laboratory campaign was repeated. This paper compares geotechnical properties and the geoenvironmental behaviour of the original (as provided by the recycling plant) and collected C&D materials. The geotechnical assessment included particle size distribution, minimum and maximum void ratios and Proctor compaction parameters. The geoenvironmental characterization was achieved by laboratory leaching tests and pH assessment. The constituents of the recycled C&D waste were also evaluated. The results of this study pointed out that the changes over time of the geotechnical properties are not relevant. The geoenvironmental characterization showed that there are no environmental concerns related to groundwater contamination.

**Keywords** C&D waste · Geotechnical properties · Long-term behaviour

---

C. S. Vieira (✉) · P. M. Pereira  
CONSTRUCT, Faculty of Engineering, University of Porto, R. Dr. Roberto Frias, S/N, 4200-465  
Porto, Portugal  
e-mail: [cvieira@fe.up.pt](mailto:cvieira@fe.up.pt)

N. Cristelo  
CQ-VR, Department of Engineering, University of Trás-Os-Montes E Alto Douro, Vila Real,  
Portugal

## 1 Introduction

Several studies and applications of recycled aggregates coming from C&D wastes have been carried out over the last years. Most of these studies are performed with selected recycled materials (crushed concrete, crushed ceramics, reclaimed asphalt,...), that exhibit a distinct behaviour from the mixed recycled aggregates that recycling plants are generally able to supply in large quantities. Furthermore, most of these studies do not address the long-term behaviour of these alternative materials.

The influence of the compaction method on hydraulic and mechanical characteristics of two types of C&D materials (crushed bricks and recycled concrete aggregate) are discussed by [1]. The present study is not directly focused on the effects of compaction on recycled aggregates behaviour but intends to analyse the effects on geotechnical and geoenvironmental properties induced by their exposure to real weather conditions (in this case for 24 months).

The knowledge related to the long-term behaviour of recycled materials is still fairly limited. This study as part of a broader research project represents a first step towards increasing the knowledge in this domain.

## 2 Materials and Methods

The material studied is a fine-grain recycled C&D waste, provided by a Portuguese recycling plant located in the outskirts of Figueira da Foz (Portugal), which mainly results from the recycling process of C&D waste coming from renovation and maintenance works on small residential buildings and cleaning illegal deposits of C&D wastes. Figure 1 shows the visual appearance of the C&D waste before going into the recycling process (Fig. 1a) and the fine-grain recycled material after processing (Fig. 1b).

At the recycling plant, three different recycled materials are produced: a fine-grain recycled material (0–10 mm), a coarse recycled aggregate (10–30 mm) and an all-in recycled aggregate (0–40 mm). The first one, as it is a material with a high fines content, is less accepted in the market and therefore its viability for geotechnical applications has been studied. In the present study the fine-grain material is used.

The material properties and its constituents will be presented in Sect. 3.

Small trial embankments were constructed with two main purposes: to study the degradation induced by these recycled materials on the short-term tensile behaviour of three different geosynthetics [2, 3]; and, to evaluate the changes in the geotechnical and geoenvironmental properties of the recycled C&D material after exposure to real weather conditions. Figure 2a illustrates one of the embankments construction phases and Fig. 2b shows the appearance of the embankments prior to exhumation of the geosynthetics samples (i.e. prior to their deconstruction).

More details on the embankments can be found in a previous publication [2].



**Fig. 1** Visual appearance of: **a** the C&D waste at the recycling plant; **b** fine-grain recycled C&D material



**Fig. 2** Small trial embankments: **a** construction–compaction of the layers; **b** after 24 months of construction

Twenty-four months after construction, the embankments were dismantled and a sample of the filling material was collected for a new laboratory characterization. Throughout this text, the original recycled material (as provided by the recycling plant) is named “initial C&D” material, while the material collected from the embankments is designated as “collected C&D” material.

The particle size distribution of the initial C&D material was first determined following the European Standard EN 933-1 [4] for aggregates. However, as this recycled aggregate has significant fines content, the particle size distribution was also determined according to ISO/TS 17892-4 [5], including sieving and sedimentation.

The constituents of the initial C&D material were estimated following the stipulated in the European Standard EN 933-11 [6] for coarse recycled aggregate. The results and applicability of this standard will be discussed in Sect. 3.

Minimum and maximum void ratios of initial C&D and collected C&D material were determined following ASTM D4253 [7] and ASTM D4254 [8], respectively.



In order to obtain the dry density-moisture content relationship, Modified Compaction Proctor tests were performed in accordance with the European Standard EN 13286-2 [9].

The potential release of dangerous substances by the recycled material was assessed through laboratory leaching tests following the European Standard EN 12457-4 [10]. The leaching tests were carried out at a liquid to solid ratio of 10 l/kg ( $L/S = 10$ ) on initial C&D material and on the collected material.

### 3 Results and Discussion

The constituents of the initial C&D material, evaluated before the construction of the trial embankments) are shown in Fig. 3. It should be noted, however, that the standard EN 933-11 [6] applies to coarse recycled aggregates, so only particles with dimensions greater than 4 mm are classified. As the separation of particles and their classification of particles is a manual procedure, it is not humanly possible to classify the finer fractions.

Figure 3a shows the classification of the coarse particles, i.e., only referring to particles with dimension larger than 4 mm. However, since this fraction represents only around 14% of the particles, the results were corrected for a more realistic classification (Fig. 3b).

The predominant materials, for the particles possible to classify, are concrete, mortar, unbound aggregates and natural stones, as well as, a significant amount of masonries.

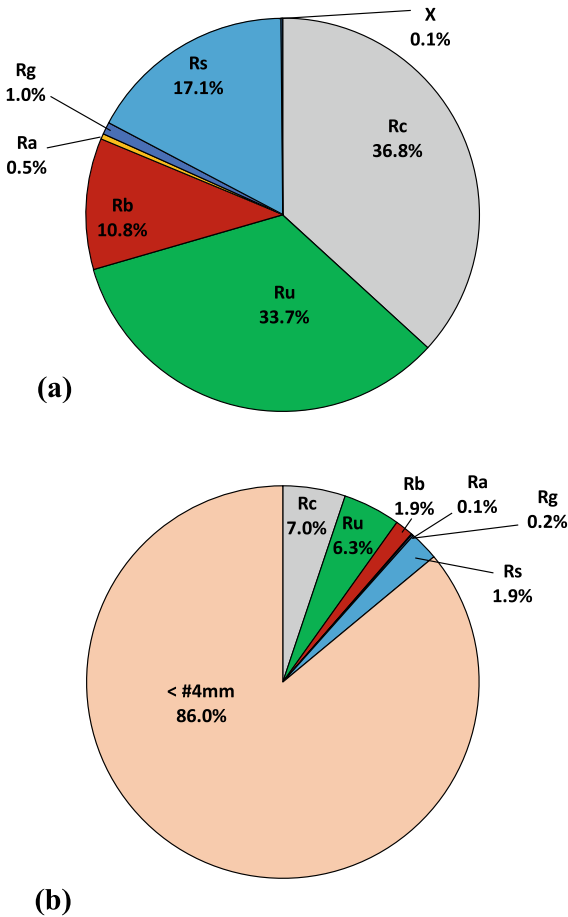
Figure 4 compares the particle size distribution of the initial and collected C&D materials. From the analysis of Fig. 4, it is clear that particle breakage occurred, i.e. the material tested after 24 months became finer. Particles with dimension bellow 2 mm (maximum sand size particles) increased from 71.5 to 86.2%. Fine content (particles smaller than 0.063 mm) raised from 11.7 to 20.4%.

The fine content of the soils currently used in embankments construction (frictional fill) is commonly limited to 15% [11], so the breakage of particles over time can be an issue with influence on the permeability of the recycled C&D material. This effect is currently being studied.

Comparing the values of the effective particle size,  $D_{10}$ , defined as the soil diameter at which 10% of the material weigh is finer, for both materials (see Table 1), one can conclude that this grading characteristic decreased about 2.7 times. The medium grain size,  $D_{50}$ , has halved.

The Proctor compaction curves for both materials are illustrated in Fig. 5. As expected, since the fines content of the C&D material after 24 months of exposure to weather conditions has increased, the maximum dry density decreased and the optimum moisture content increased.

Table 1 summarizes the physical and mechanical properties evaluated in the current study.



Rc: concrete, concrete products, mortar, concrete masonry units; Ru: unbound aggregate, natural stone, hydraulically bound aggregate; Rb: clay masonry units, calcium silicate masonry units, aerated non-floating concrete; Ra: bituminous materials, Rg: glass; Rs: soils; X: other materials.

**Fig. 3** Constituents of the initial C&D material: **a** for the fraction larger than 4 mm (following the standard [6]; **b** for the overall sample

The results of the laboratory leaching test carried out on the initial and collected C&D materials, as well as the acceptance criteria for leached maximum concentration for inert landfill according to [12] are presented in Table 2.

The leaching tests revealed that, for the initial C&D material only the sulphate (SO<sub>4</sub>) exceeded the maximum value established by [12] for inert materials (1000 mg/kg dry matter). The recycled C&D material collected from the embankments exhibited a significant decrease of the sulphate and dissolved solids contents. All the other potential contaminants are well below the limits.

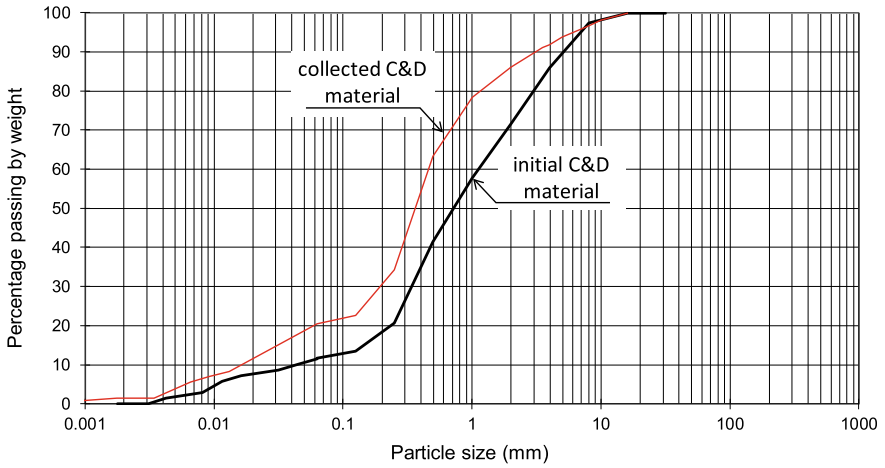


**Fig. 4** Particle size distribution of the initial and collected C&D material

**Table 1** Some physical and mechanical properties of the initial and collected C&D materials

Parameter	Initial C&D material	Collected C&D material
D <sub>10</sub> (mm)	0.043	0.016
D <sub>50</sub> (mm)	0.72	0.36
Minimum void ratio, e <sub>min</sub>	0.434	0.414
Maximum void ratio, e <sub>max</sub>	0.877	0.891
Maximum dry density (Mg/m <sup>3</sup> )	1.96	1.92
Optimum moisture content, OMC (%)	12.7	13.5

D<sub>10</sub> and D<sub>50</sub> characteristic grain diameters.

**Fig. 5** Proctor compaction curves

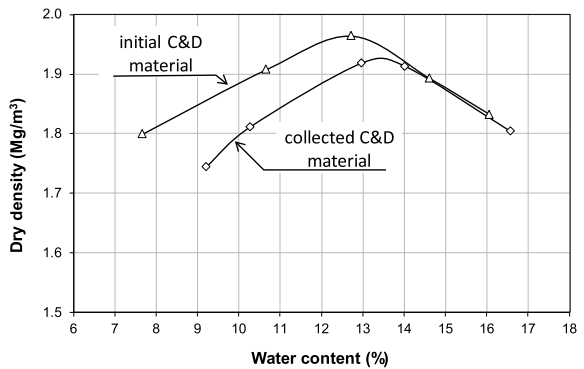


**Table 2** Results of laboratory leaching test and limits to inert landfills (adapted from [3])

Parameter	Initial C&D material (mg/kg dry matter)	Collected C&D material (mg/kg dry matter)	Acceptance criteria—Inert landfill [12]
Arsenic, As	0.013	0.020	0.5
Lead, Pb	< 0.01*	< 0.01*	0.5
Cadmium, Cd	< 0.003*	< 0.003*	0.04
Chromium, Cr	< 0.01*	< 0.01*	0.5
Copper, Cu	0.029	0.041	2
Nickel, Ni	0.01	< 0.01*	0.4
Mercury, Hg	< 0.002*	< 0.002*	0.01
Zinc, Zn	< 0.1*	< 0.1*	4
Barium, Ba	0.069	0.085	20
Molybdenum, Mo	0.036	0.011	0.5
Antimony, Sb	0.011	< 0.01*	0.06
Selenium, Se	< 0.02*	< 0.02*	0.1
Chloride, Cl	19	< 6*	800
Fluoride, F	< 1.5*	1.6	10
Sulphate, SO <sub>4</sub>	<b>2100</b>	630	1000
Dissolved Organic Carbon, DOC	25	29	500
Dissolved Solids, DS	3030	1510	4000

\* limit of quantitation (LoQ)

The pH value of the leachate also decreased from alkaline (pH = 8.3) for the initial C&D material to slightly acidic (pH = 6.8) for the material exposed to weather conditions. These changes can be explained by the decrease in leachate concentration over time.

## 4 Conclusions

The results of this study pointed out that the exposure of a mixed (non-selected) fine-grain recycled C&D material to real weather conditions for 24 months has led to the degradation of its grain size and consequent change in its geotechnical properties. It is important to mention that the breakage of the particles may also be attributed to the construction of the trial embankments and collection of samples.

The geoenvironmental characterization carried out through laboratory leaching tests showed that there are no environmental concerns related to the use of this recycled C&D material in geotechnical works. The value of sulphate of the initial

C&D material exceeded the threshold stipulated by European legislation regarding inert materials. However, according to the same Directive if the waste does not meet only this limit, it may still be considered as complying with the acceptance criteria, as long as the sulphate leaching does not exceed 6000 mg/kg at L/S = 10 l/kg (liquid/solid).

The results presented in this paper are part of a broader research project. Broadening and more comprehensive conclusions can be expected in future publications.

**Acknowledgements** This work was financially supported by: Project PTDC/ECI-EGC/30452/2017—POCI-01-0145-FEDER-030452—funded by FEDER funds through COMPETE2020—Programa Operacional Competitividade e Internacionalização (POCI) and by national funds (PIDDAC) through FCT/MCTES; Base Funding—UIDB/04708/2020 of the CON-STRUCT—Instituto de I&D em Estruturas e Construções—funded by national funds through the FCT/MCTES (PIDDAC).

## References

1. Yaghoubi E, Disfani MM, Arulrajah A, Kodikara J (2017) Impact of compaction method on mechanical characteristics of unbound granular recycled materials. *Road Mater Pavement Des* 19(4):912–934. <https://doi.org/10.1080/14680629.2017.1283354>
2. Vieira CS, Pereira PM (2015) Damage induced by recycled construction and demolition wastes on the short-term tensile behaviour of two geosynthetics. *Transp Geotech* 4:64–75. <https://doi.org/10.1016/j.trgeo.2015.07.002>
3. Vieira CS, Pereira PM (2021) Short-term tensile behaviour of three geosynthetics after exposure to recycled construction and demolition materials. *Constr Build Mater* 273:122031. <https://doi.org/10.1016/j.conbuildmat.2020.122031>
4. EN 933-1 (2009) Tests for geometrical properties of aggregates—part 1: determination of particle size distribution—sieving method. CEN
5. ISO/TS 17892-4, CEN ISO/TS 17892-4 (2004) Geotechnical investigation and testing—laboratory testing of soil—part 4: determination of particle size distribution
6. EN 933-11 (2009) Tests for geometrical properties of aggregates—part 11: classification test for the constituents of coarse recycled aggregate. CEN
7. ASTM D 4253 (2006) Standard test methods for maximum index density and unit weight of soils using a vibratory table. American Society for Testing Materials, USA
8. ASTM D 4254 (2006) Standard test methods for minimum index density and unit weight of soils and calculation of relative density. American Society for Testing Materials, USA
9. EN 13286-2 (2002) Unbound and hydraulically bound mixtures—part 2: test methods for laboratory reference density and water content—proctor compaction. CEN
10. EN 12457-4 (2002) Characterisation of waste—leaching—compliance test for leaching of granular waste materials and sludges—part 4: one stage batch test at liquid to solid ratio of 10l/kg for materials with particle size below 10 mm (without or with size reduction). CEN
11. BS 8006-1 (2010) Code of practice for strengthened/reinforced soils and other fills. British Standard Institution, p 260
12. Council Decision 2003/33/EC (2003) Council decision establishing criteria and procedures for the acceptance of waste at landfills pursuant to article 16 of and annex II to directive 1999/31/EC. Official J Eur Union L11/27

# Removal of Phosphate from Stormwater Runoff Using Bench Scale Constructed Wetland



Harsh Pipil, Shivani Yadav, Sonam Taneja, Harshit Chawla,  
Anil Kumar Haritash, and Krishna R. Reddy

**Abstract** Stormwater runoff originating from agricultural fields, garden, green belts, parks, etc. is susceptible to carry along phosphate in dissolved form in it. Presence of phosphate can lead to eutrophication in water the receiving bodies even if its concentration is  $< 0.1$  mg/l. Natural or cultural eutrophication has led to significant adverse effect on water quality around the globe. The present study was undertaken to determine the efficacy of *Phragmites* based constructed wetland for the removal of phosphate from stormwater runoff under Indian conditions. The study was conducted under natural environmental conditions to evaluate the role of meteorological parameters. It was observed that *Phragmites* based wetland could efficiently remove the phosphate from stormwater with an efficiency as high as 96% at hydraulic retention time (HRT) of 24 h. The increase in ambient temperature increases the phosphate removal efficiency of *sp*. It leads to the conclusion that *Phragmites* removes phosphates from synthetically prepared stormwater runoff in a CW cell which it is a sustainable and eco-friendly technique to remove phosphate from stormwater runoff. This process does not require energy from external source is required for its operation.

**Keywords** Phragmites · Constructed wetland · Stormwater · Runoff · Phosphate

---

H. Pipil (✉) · S. Yadav · S. Taneja · H. Chawla · A. K. Haritash  
Department of Environmental Engineering, Delhi Technological University, Bawana Road,  
Shahbad Daulatpur, Delhi 110042, India  
e-mail: [harsh\\_phd2k19@dtu.ac.in](mailto:harsh_phd2k19@dtu.ac.in)

K. R. Reddy  
Department of Civil, Materials, and Environmental Engineering, University of Illinois, Chicago,  
IL 60607, USA

## 1 Introduction

India is second most populous and seventh largest country in world in terms of its land mass which is approximately 2.4% of world's total land [1]. Most of the Indian population lives in rural India, though a significant migration of population towards urban India was seen in last few decades. This has increased burden on existing water resources due to limited water resources. Uneven distribution of rainfall, change in land use pattern and climate change has caused scarcity of freshwater [2]. Rainwater is considered as the source of purest form of water but its interaction with earth's surface makes it polluted and unfit for use. As a consequence, stormwater runoff contains suspended impurities such as silt, sand, clay, and floating impurities like plastics, tree branches and leave. It also contains dissolved impurities in it such as nutrients and heavy metals [3, 4]. Among the nutrients such as phosphate and nitrate, former one is a critical pollutant that can lead to eutrophication of receiving water body such as a lake or a pond in urban areas [5]. Studies in India has shown that stormwater runoff contains phosphate in urban stormwater runoff [6, 7]. Despite of being contaminated, the strength of pollutants and impurities in stormwater runoff is relatively lesser than domestic wastewater. Stormwater can be treated before it can get further contaminated. Thus, it is necessary to use water purification technique to treat this stormwater runoff. This will help in reducing the demand and supply gap of freshwater. The technique Water Sensitive Urban Design (WSUD) have been successfully implemented in developed countries like United States of America, Canada, Australia and New Zealand, etc. [8]. There is an urgent need for the development and exploration for feasibility of WSUD techniques such as gross pollutant trap (GPT), vegetated swale, rain garden, wetlands, tree pits, etc. in developing country like India [9]. This present study focuses on removal of phosphate from synthetically prepared stormwater runoff.

## 2 Methods and Materials

### 2.1 Wetland Configuration and Its Analysis

The present study was undertaken on a bench scale constructed wetland (CW) cell, located in Delhi Technological University, Delhi. *Phragmites* were planted in CW cell built up of brick masonry which was CW cell was 110 cm long, 80 cm wide with height of 45 cm. Depth of bed substrate was of 35 cm with 10 cm of free board (Fig. 1). Substrate had specific gravity (G) 2.7, void ratio ( $e$ ) 0.67 and bulk density ( $\rho$ ) of 1782 kg/m<sup>3</sup>. The substrate was filled with homogenous mixture of sand, silt and gravel to provide the scope for easy root penetration, and better hydraulic conductivity through the bed without difficulty. Initially, 20 plants were planted uniformly distributed in CW cell which increased to 180 plants at the end of study. The cell was flushed with distilled water until no phosphate was obtained in effluent

before the start of experiment. Stormwater runoff was prepared synthetically using analytical grade (AG) di-hydrogen orthophosphate ( $\text{KH}_2\text{PO}_4$ ) for varying influent  $\text{PO}_4^{3-}$  concentration (5, 10 and 20 mg/l). It was fed into the cell from the top daily and effluent was collected after hydraulic retention time (HRT) of 24 h from the outlet valve provided at the bottom. Available phosphate (AP) and total phosphate (TP) analysis was carried out for both influent and effluent collected daily using spectrophotometric method (Labtronics make LT-290 Model spectrophotometer). Ratio of ferric ion ( $\text{Fe}^{3+}$ ) to ferrous ion ( $\text{Fe}^{2+}$ ) was also studied to determine the redox conditions pertaining in the system and the possibility of phosphates being getting bound to iron present in substrate. Observations of pH, electrical conductivity (EC) and total dissolved solids (TDS) were analysed using the Orion Make (USA, Model: A329) multi-meter.

The phosphate removal efficiency was calculated using the Eq. 1

$$\text{Removal efficiency}(\%) = \frac{(C_i - C_f)}{C_i} \times 100 \tag{1}$$

where,  $C_i$  is initial phosphate concentration (mg/l),  $C_f$  is phosphate concentration after HRT of 24 h at effluent end (mg/l).

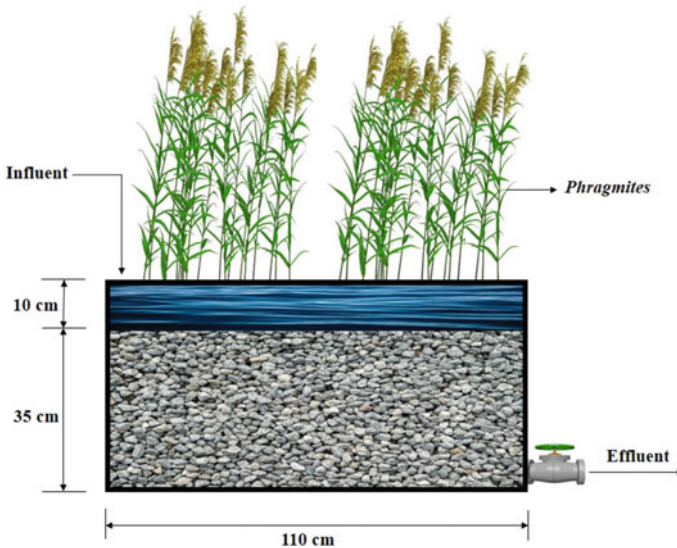


**Fig. 1** Schematic description of configuration of CW cell used during the study



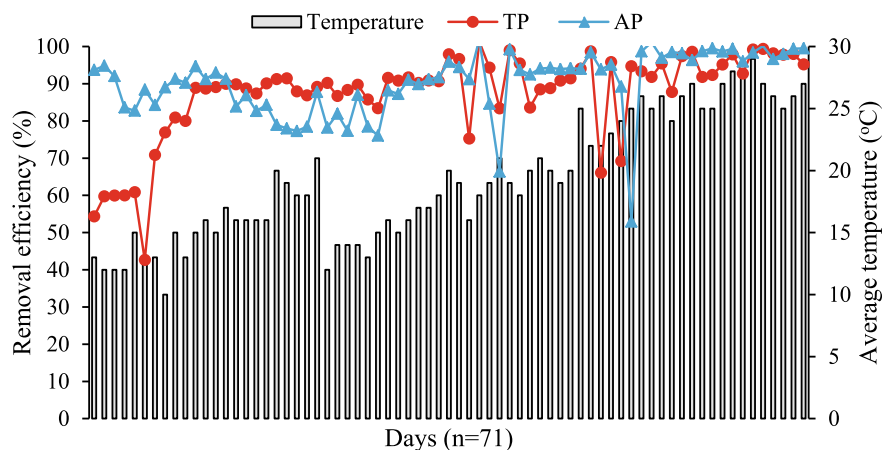


**Fig. 2** Available and total phosphate removal efficiency (%) with average ambient temperature ( $^{\circ}\text{C}$ ) during study

### 3 Results and Discussion

#### 3.1 General Observations

The ambient minimum, maximum and average temperature for Delhi, India, was noted during the present study. The temperature ranged between 2 and 42  $^{\circ}\text{C}$ . The average minimum and maximum temperature was found to be of order 13.6  $^{\circ}\text{C}$  and 26.8  $^{\circ}\text{C}$ , respectively. This represents the sub-tropical climatic conditions in India under which the study was undertaken. Average temperature profile along with available phosphate (AP) and total phosphate (TP) removal efficiency is represented in Fig. 2. The average sunshine hours also ranged between 8 and 10 h. Wet precipitation (mm) was received in small spells during the study which had negligible influence on the study due to dilution. It was also observed that the phosphate removal efficiency varied with temperature.

#### 3.2 AP Removal Study

The available phosphate removal follows the trend summer > spring > winter > autumn (Figs. 3 and 4). It can be attributed towards the increase in average daily sunshine hours, rise in ambient temperature that has enhanced the water updraft of plant *sp.* which resulted in increase in evapotranspiration. The metabolic activity of the plant also increases in the presence of sunlight through photosynthesis. This highlights possible reason for enhanced AP removal efficiency in summers. The increase in daily sunshine hours resulted in increase in AP removal efficiency in

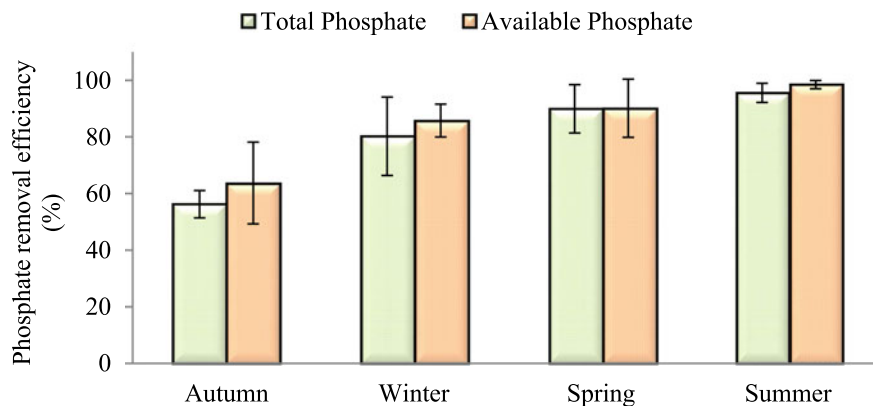


**Fig. 3** Average available phosphate (AP) and total phosphate (TP) removal efficiency in various seasons during study

summer season, while its removal efficiency was least in autumn season. Also, the removal efficiency of AP is greater than TP. This attributes to easy availability of AP in synthetic stormwater runoff from CW cell. Also, adsorption by bed substrate as well as plant uptake are the possible mechanism towards the removal of phosphate from CW cell. Studies have shown the bed sediments gets saturated of nutrient with time and thus, cannot remove the nutrient from stormwater runoff for longer duration [10, 11]. In the present study, the AP removal efficiency increased with increase in sunshine hours and ambient average temperature. Thus, not only bed substrate was involved in removal of AP but plants also played a significant role in its removal efficiency.

### 3.3 TP Removal Study

The TP removal efficiency also follows the trend summer > spring > winter > autumn (Figs. 3 and 4). However, AP removal efficiency > TP removal efficiency since, AP is more readily available to taken up by the plants while TP remains in bound form and cannot be easily taken up by the plant. TP removal was maximum in summer while it is lowest in autumn. This can be attributed towards the sunshine hours and average ambient temperature. In summer season, the maximum temperature rose to 42 °C with increased daily sunshine. This has led to increased photosynthetic activity and metabolism of plant. Also, the increase in updraft of phosphate from CW cell in summer enhanced the TP removal as compared to other seasons.

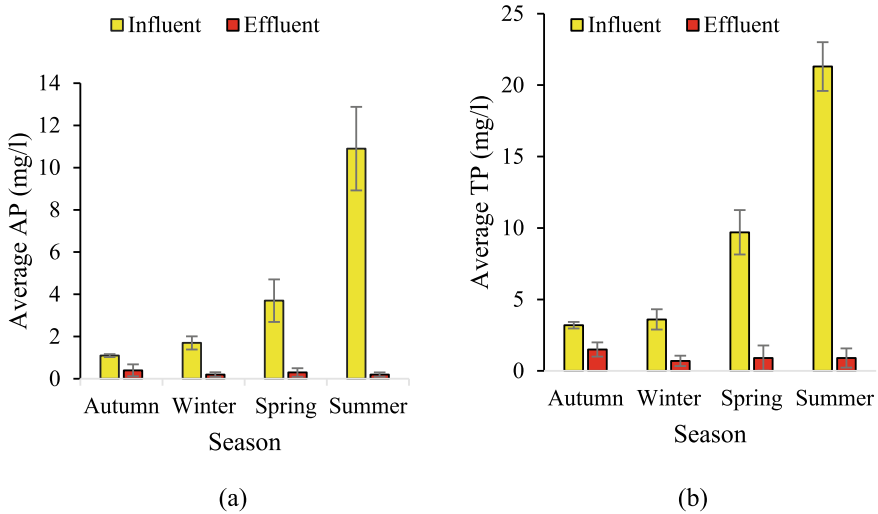


**Fig. 4** Seasonal variation of average concentration of, **a** available phosphate (AP); and **b** total phosphate (TP)

### 3.4 Reduction–Oxidation Study

Redox conditions persisting in the CW cell was analysed on the basis of ferric to ferrous ratio. It was found that the ratio of ferric to ferrous ion ( $\text{Fe}^{3+}/\text{Fe}^{2+}$ ) is  $< 1.0$ . Higher ferrous values than the ferric ion concentration shows that reducing conditions are dominating in the CW cell during the study. During reducing condition, the iron present in the form of ferrous in substrate of the wetland cell will not bind with the phosphate. This relates to the fact that the phosphates are not removed by bed sediments by its combination with iron.

## 4 Conclusion

It can be concluded that *Phragmites* can survive in wide range of temperature in Indian sub-tropical weather conditions. This plant can effectively remove the phosphates over a wide range of influent concentration which shows its ability towards shocks and its threshold capacity. The plant *sp.* survived, multiplied and its density also increased in CW cell. Overall, phosphate removal efficiency followed the trend autumn  $<$  winter  $<$  spring  $<$  summer season for both available phosphate (AP) and total phosphate (TP). There is a positive co-relation between its efficiency to remove phosphate and the increase in influent phosphate concentration. The removal efficiency also increased with the increase in average ambient temperature and sunshine hours which is related to more updraft of water by plant. Also, rise in temperature and sunshine

hours increased the photosynthesis and metabolic activities of plant. The ratio of ferric to ferrous ion ( $\text{Fe}^{3+}/\text{Fe}^{2+}$ ) is  $< 1.0$  which shows that reducing conditions are dominating in the CW cell. The plant *sp.* can be harvested to make manure from it since it has phosphate present in it. It can also be used as sink of carbon through carbon sequestration and can be used for thatching in rural India. Also, the overall process of phosphate removal does not require any energy input from external sources. Thus, it can be said that the process is sustainable towards removal of phosphate from urban stormwater runoff.

## References

1. Profile: National portal of India. <https://www.india.gov.in/india-glance/profile>. Accessed on 18 June 2022
2. Vialle C, Sablayrolles C, Lovera M, Jacob S, Huau MC, Montrejaud-Vignoles M (2011) Monitoring of water quality from roof runoff: Interpretation using multivariate analysis. *Water Res* 45(12):3765–3775. <https://doi.org/10.1016/j.watres.2011.04.029>
3. Hwang HM, Fiala MJ, Park D, Wade TL (2016) Review of pollutants in urban road dust and stormwater runoff: part 1. Heavy metals released from vehicles. *Int J Urban Sci* 20(3):334–360. <https://doi.org/10.1080/12265934.2016.1193041>
4. Yang YY, Lusk MG (2018) Nutrients in urban stormwater runoff: current state of the science and potential mitigation options. *Curr Pollut Rep* 4(2):112–127. <https://doi.org/10.1007/s40726-018-0087-7>
5. Haritash AK, Dutta S, Sharma A (2017) Phosphate uptake and translocation in a tropical *Canna*-based constructed wetland. *Ecol Process* 6:12. <https://doi.org/10.1186/s13717-017-0079-3>
6. Arora AS, Reddy AS (2013) Multivariate analysis for assessing the quality of stormwater from different urban surfaces of the Patiala city, Punjab (India). *Urban Water J* 10(6):422–433. <https://doi.org/10.1080/1573062X.2012.739629>
7. Pipil H, Haritash AK, Reddy KR (2022) Spatio-temporal variations of quality of rainwater and stormwater and treatment of stormwater runoff using sand–gravel filters: case study of Delhi, India. *Rend Lincei. Sci Fis Nat* 33(1):135–142. <https://doi.org/10.1007/s12210-021-01038-5>
8. Hoban A (2019) Water sensitive urban design approaches and their description. In: *Approaches to water sensitive urban design*. Woodhead Publishing, pp 25–47. <https://doi.org/10.1016/B978-0-12-812843-5.00002-2>
9. Pipil H, Yadav S, Taneja S, Chawla H, Haritash AK, Reddy KR (2022) Water sensitive urban design (WSUD) for treatment of storm water runoff. In: *Proceedings of international conference on innovative technologies for clean and sustainable development (ICITCSD–2021)*. Springer, Cham, pp 49–61. [https://doi.org/10.1007/978-3-030-93936-6\\_5](https://doi.org/10.1007/978-3-030-93936-6_5)
10. Haritash AK, Sharma A, Bahel K (2015) The potential of *Canna lily* for wastewater treatment under Indian conditions. *Int J Phytorem* 17(10):999–1004
11. Nandakumar S, Pipil H, Ray S, Haritash AK (2019) Removal of phosphorus and nitrogen from wastewater in *Brachiaria*-based constructed wetland. *Chemosphere* 233:216–222. <https://doi.org/10.1016/j.chemosphere.2019.05.240>

# Stabilization of Expansive Soil Using Rice Husk Ash



Krupansh Patel  and Bhargav Tewar 

**Abstract** The concept of Sustainable development in construction industry brings in the use of waste and recycled materials procured from different or same sectors. Rice Husk ash is an agricultural waste generated from boilers using Rice Husk as fuel and is obtained as a by-product. Rice Husk burnt at 550–800°C produce greyish white colored rice husk ash, which contains around 92–93% silica by weight. In this study, Rice Husk ash is mixed in different proportions with Black cotton soil to study the effects on its engineering properties like Atterberg's limits, Free swell Index, Specific gravity, Unconfined compressive strength, Standard proctor and California bearing ratio. It is observed that the swelling and shrinkage potential of Black cotton soil is exponentially decreased from 53% without RHA addition to 5.46% at Black cotton soil + 30% RHA addition and from 49% without RHA addition to 29% at Black cotton soil + 30% RHA addition respectively. While, California bearing ratio of soil in soaked conditions has increased from almost 6% without RHA addition to 10% at Black cotton soil + 30% RHA addition. From the results obtained, it can be inferred that Rice husk Ash has positive impact on engineering properties of black cotton soil. This mix can be recommended for Village/district roads and hilly roads. Blending Rice Husk Ash with expansive black cotton soil paves way for sustainable construction besides economic benefits.

**Keywords** Rice husk ash · Free swell · Expansive soil · Shrinkage limit · California bearing ratio

## 1 Introduction

This study focuses on stabilization of expansive soil while taking experimenting on black cotton soil (BCS) as an example. The area of soil in India is around 520,000 km<sup>2</sup>, which is about 16% of the area of India. This puts it in the list of one of the majority soil deposits in India. It exhibits high swelling and shrinkage potential in the presence

---

K. Patel (✉) · B. Tewar  
CEPT University, Ahmedabad, India  
e-mail: [krupansh.patel.btech17@cept.ac.in](mailto:krupansh.patel.btech17@cept.ac.in)

© The Author(s), under exclusive license to Springer Nature Singapore Pte Ltd. 2023  
Y. Yukselen-Aksoy et al. (eds.), *Sustainable Earth and Beyond*, Lecture Notes in Civil Engineering 370, [https://doi.org/10.1007/978-981-99-4041-7\\_40](https://doi.org/10.1007/978-981-99-4041-7_40)

451

and absence of moisture content which can result in low soil bearing capacity [1]. This property of BCS results from the presence of the clay mineral montmorillonite, which is primarily responsible for the expansive nature of the soil. Water penetrating the interlayer molecular gaps and associated adsorption causes montmorillonites to expand much more than other clays [2]. The soil stabilization process improves the physical attributes of expansive soils in terms of strength, durability and other geotechnical characteristics. It can be done by mixing of admixtures and through compaction by mechanical means which increase strength and cohesion of soil. As, the major properties of soil on which the construction is concerned are swelling potential and shrinkage factor (volume) and California bearing ratio (CBR) and unconfined compressive strength (UCS). Apart from these, few factors like durability and permeability also play a significant role [3]. Construction of roads, buildings or any infrastructure projects to be built would face structural problems and require high maintenance, thus increasing overall project cost.

As the need for sustainable development is rising, using waste and industrial by-products in soil stabilization for road, buildings and infrastructure constructions is an area to explore. This is due to high availability of industrial wastes and by-products and relatively less reuse or proper disposal systems. Rice Husk Ash (RHA) is one such waste, which is pozzolanic in nature having high percentage of silica content [3].

## **2 Materials**

### ***2.1 Black Cotton Soil***

Black cotton soil is the result of weathered basaltic rocks solidified from lava. It swells in presence of moisture and develops cracks during absence or at very less moisture content [4]. The black cotton soil has high water holding capacity and is fertile due to which cotton cultivation can be done on it. Black cotton soil is poorly graded and has higher percentage of clay content, especially montmorillonite which is responsible for expansive nature of soil. The soil sample is collected from a village near Dholka, Gujarat, India, at a depth of 1.0m depth from the ground level.

### ***2.2 Rice Husk Ash***

Rice Husk ash is an agricultural industry waste initially produces as Rice Husk separated from rice paddy. Rice mills generate large amounts of rice husk. The rice husk is then used as fuel in the boilers for power generation and processing of rice paddy. Generally, Rice Husk Ash produced from burning of rice husk is obtained in one or more than one type of chemical composition combination, depending up on

**Table 1** Chemical composition of rice husk ash

Chemical composition	Weight (%)
Silica (SiO <sub>2</sub> )	91.59
Iron oxide (Fe <sub>2</sub> O <sub>3</sub> )	0.21
Calcium oxide (CaO)	1.58
Magnesium oxide (MgO)	0.53
Carbon (C)	4.8
Alumina (Al <sub>2</sub> O <sub>3</sub> )	0.82
Sodium oxide (Na <sub>2</sub> O)	0.13
Potassium oxide (K <sub>2</sub> O)	0.34

the degree of heat under which the rice husk is burnt. Rice husk contains about 75% organic matter and remaining 25% of the husk is converted into ash when burnt [5]. The Rice Husk Ash is obtained from a local trader in Bavla, Gujarat, India. This is burnt at a temperature range of 550–800 °C. The chemical composition of Rice Husk Ash is also obtained from the trader, which contains about 91% silica (Table 1).

### 3 Testing Plan and Methodology

#### 3.1 Soil Type Identification

The sample of BCS was initially tested for Atterberg Limits and Free swell index test to check if the soil is actually black cotton soil, by checking if the values of plasticity index and liquid limit lie in ‘CH zone’ (Clay zone with high plasticity) in Casagrande’s Plasticity chart (Fig. 1).

#### 3.2 Scope of Study

Further, tests like compaction test (Standard Proctor test), California bearing ratio test, shear strength test (Unconfined compressive strength test) and specific gravity test are performed as per standard protocols IS 2720 (Part 5)—[6], IS 2720 (Part 6)—[7], IS 2720 (Part 7)—[8], IS 2720 (Part 40)—[9], IS 2720 (Part 10)—[10] and IS 2720 (Part 16)—[11]. These tests are divided into two parts to identify Physical and Engineering properties of soil (Table 2).

Tests were conducted on untreated soil and compared with treated soil at different percentages i.e., BCS + 10% RHA, BCS + 20% RHA, BCS + 30% RHA.

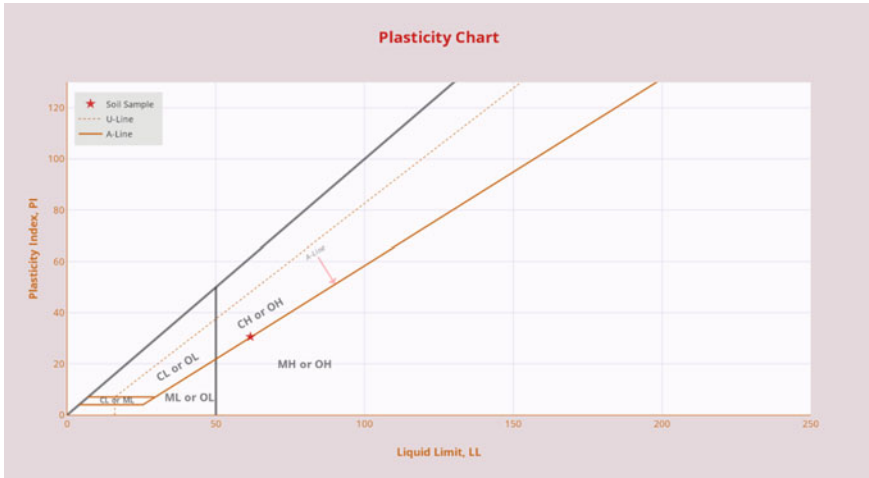


**Fig. 1** Casagrande’s plasticity chart for black cotton soil

**Table 2** Scope of study of different properties of black cotton soil

Tests	Atterberg’s limits	Free swell index	Standard proctor	UCS test	CBR test
Physical properties	Liquid limit (%)	Swelling potential (%)			
	Plastic limit (%)				
	Shrinkage limit (%)				
Engineering properties			MDD (g/cc)	Shear strength (Kg/cm <sup>2</sup> )	Unsoaked CBR (%)
			OMC (%)	Cohesion of soil (Kg/cm <sup>2</sup> )	Soaked CBR (%)

## 4 Results and Discussions

### 4.1 Atterberg’s Limits

The fine grain soil is categorized using the liquid limit and plastic limit values, giving us idea about the soil’s on-site consistency. When determining the foundation’s permitted bearing capacity and settlement, it is also used to forecast the soil’s consolidation qualities. It also correlates to engineering properties like compressibility, permeability and shear strength [12]. The test was done according to IS 2720 (Part 5)—[6] and IS 2720 (Part 6)—[7].The liquid limit and plasticity index values decrease with increase in % of RHA in soil, minimum plasticity index is attained



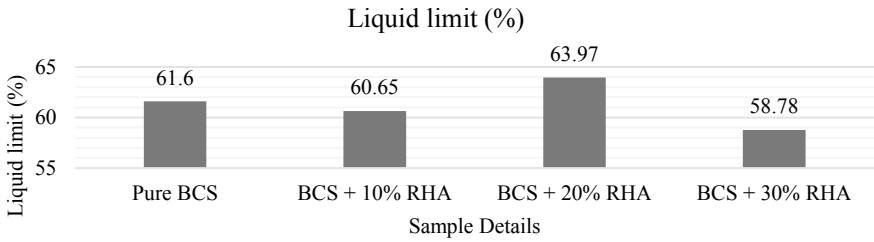


Fig. 2 Comparison of liquid limit of soil at varying percentages of RHA

from the mix BCS + 30% RHA, decreasing by almost 57% in value compared to untreated BCS, while the minimum value liquid limit is attained from the mix BCS + 30% RHA, decreasing by almost 5% only and the plastic limit value increase with addition of RHA and maximum attained at BCS + 30% RHA, increasing by almost 32% in value compared to untreated BCS. Volumetric shrinkage also decreased with increase in % of RHA; minimum value being attained from mix BCS + 30% RHA which is almost 41% less compared to untreated BCS (Figs. 2, 3, 4 and 5).

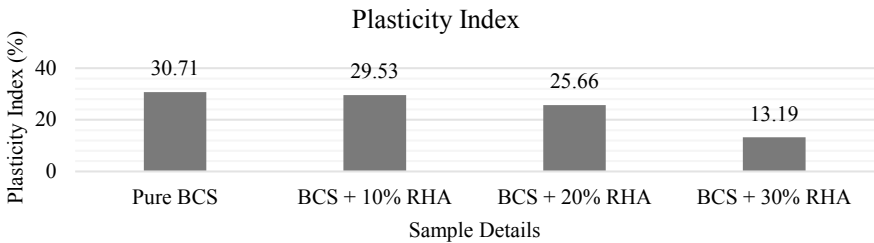


Fig. 3 Comparison of plasticity index of soil at varying percentages of RHA

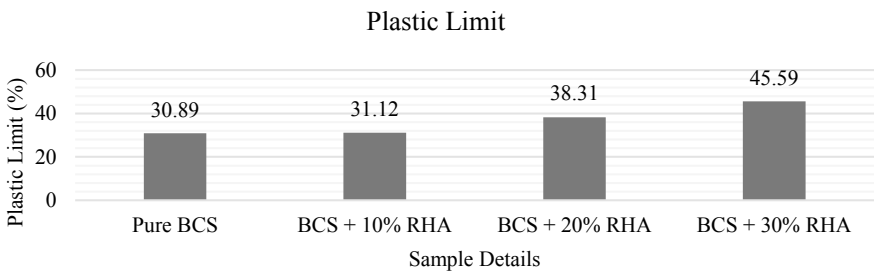
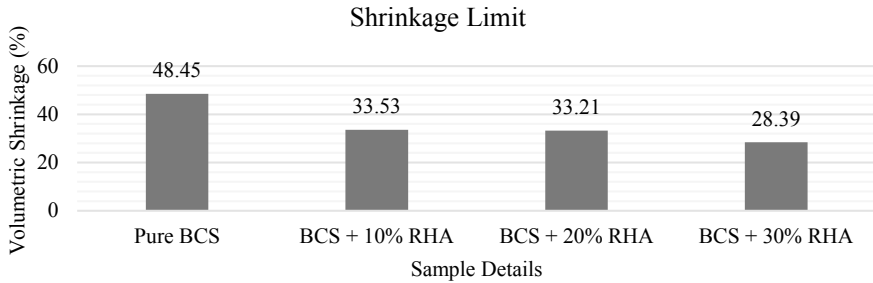
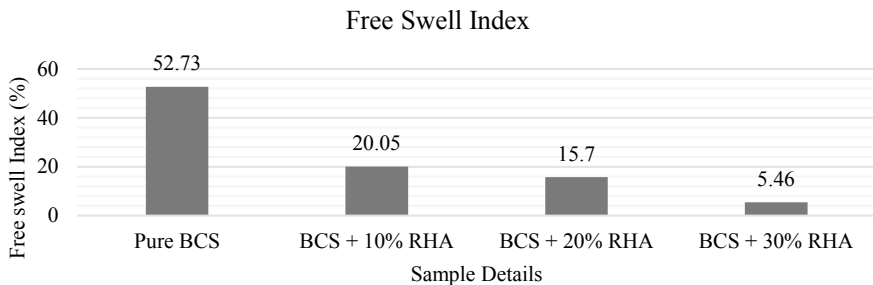


Fig. 4 Comparison of plastic limit of soil at varying percentages of RHA



**Fig. 5** Comparison of volumetric shrinkage of soil at varying percentages of RHA



**Fig. 6** Comparison of free swell index values of soil at varying percentages of RHA

## 4.2 Free Swell Index

Free swell index is used to determine the potential of a soil to swell. The test is done according to IS 2720 (Part 40)—[9]. The free swell index decreased by almost 90% for the mix BCS + 30% RHA. As BCS has really high swelling potential leading to high volumetric changes, such significant reduction in swelling index can be helpful in construction. This can be attributed to the presence of free CaO in RHA which reacts with clay and generate physical forces between the particles decreasing the swelling [12] (Fig. 6).

## 4.3 Standard Proctor Test

This test's objective is to establish the appropriate moisture content to utilise while compacting the soil in the field and the degree of density that may be anticipated as a result. The test was done according to IS 2720 (Part 7)—[8]. Addition of RHA to soil decreased the maximum dry density (MDD) of the treated soil compared to untreated soil and optimum moisture content (OMC) increased with increase in RHA content. The minimum MDD is achieved for mix BCS + 30% RHA which is almost

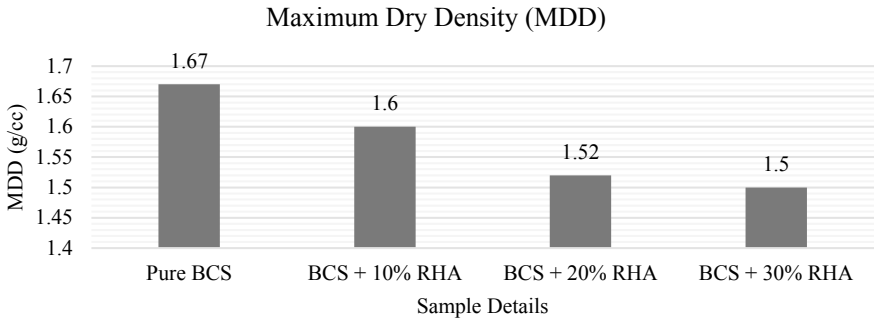


**Fig. 7** Comparison of MDD of soil at varying percentages of RHA

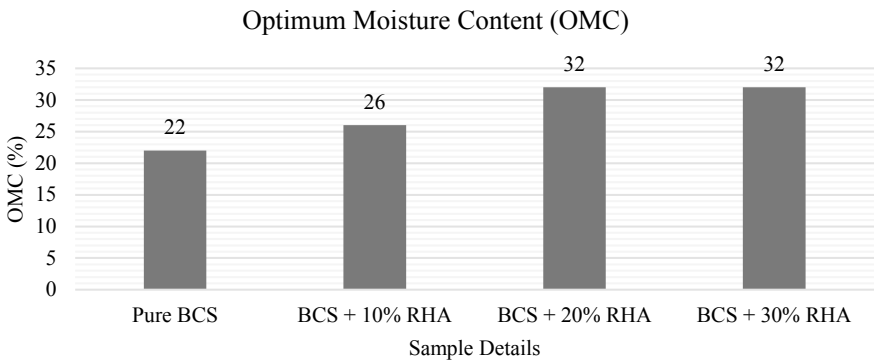


**Fig. 8** Comparison of OMC of soil at varying percentages of RHA

10% less than MDD untreated BCS. While the OMC of mix BCS + 30% RHA is the highest and almost 31% more than that for untreated BCS (Figs. 7 and 8).

#### 4.4 Unconfined Compressive Strength

The test is used to find the unconfined compression strength in terms of total stress. Unconfined compression strength test can help determine resistance offered by clayey or cohesive soil. The test helps to determine the utmost important property of soil that is shear strength. This is the key feature for the soil load transfer. The test is done according to IS 2720 (Part 10)—[10]. With addition of RHA in black cotton soil it was observed that, with increase in % RHA content, Unconfined shear strength and cohesion of soil both decreased by almost 64% which is very high. It was observed during mixing of RHA to black cotton soil that the soil is losing its cohesiveness while also behaving like sandy soil due to addition of RHA (Fig. 9).

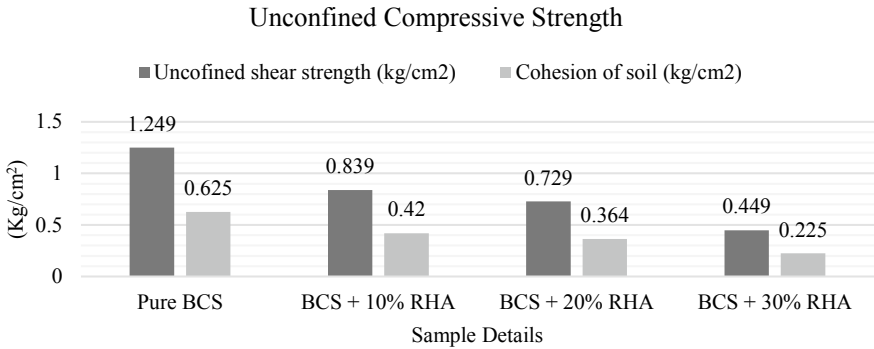


**Fig. 9** Comparison of shear strength and cohesion values of soil at varying percentages of RHA

### 4.5 California Bearing Ratio

This test done to determine the strength of the subgrade soil. The test is done according to IS 2720 (Part 16)—[11]. With addition of RHA in BCS it was observed that with increase in % of RHA, unsoaked CBR value decreased by about 28% of the mix BCS + 30% RHA compared to untreated BCS. This can be correlated with the results obtained in standard proctor test wherein decrement of MDD was observed along with increment in OMC. This indicates loss in bearing strength of BCS under unsoaked conditions. While, under soaked conditions, with increase in % RHA content, CBR value increase by almost 43% for mix BCS + 30% RHA compared to untreated BCS. This indicates that with addition of RHA, black cotton soil performs better in strength parameters under soaked conditions, which is a major improvement considering poor performance of black cotton soil in soaked conditions (Figs. 10 and 11).

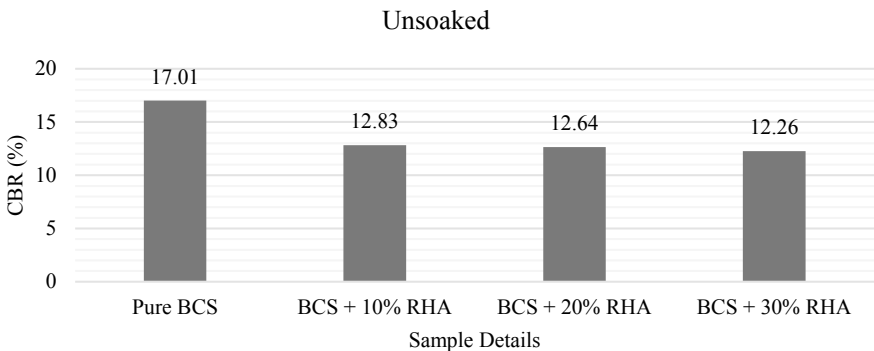


**Fig. 10** Comparison of CBR values at varying percentages of RHA in unsoaked conditions

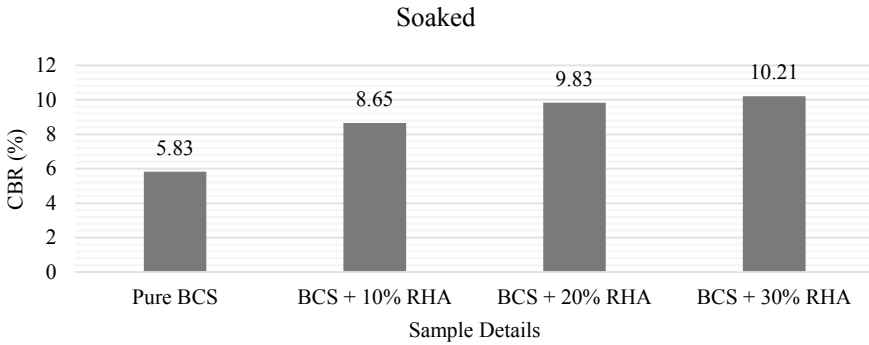


Fig. 11 Comparison of CBR values at varying percentages of RHA in soaked conditions

### 5 Conclusions

From the research conducted, it can be said that addition of Rice Husk Ash has significantly improved certain properties while the others have decreased, based on the results it can be concluded that the mix BCS + 30% RHA can be called the optimum mix for this particular soil. It can be concluded that:

1. The plasticity index of the optimum mix decreased by 57%.
2. Major improvement is seen in volumetric shrinkage which decreased by 41% for optimum mix.
3. For optimum mix, MDD decreased by 10% and OMC increased by 31% thus, resulting in decrease in unsoaked CBR value by 28% and Shear strength and cohesion by 64%.
4. For optimum mix, Soaked CBR value increased by 43% which improves the poor engineering property of BCS under soaked conditions.
5. Lastly, the major issue of high volumetric change due to its swelling potential is decreased by 90% for optimum mix.

Stabilizing soil using waste like RHA can be highly economical solution for subgrade of road embankments. According to IRC 37—2012, stabilized soil can be used for district roads, hilly region roads, rural/ village roads and roads connecting ports where water locking in soil is a problem. This can reduce the need of removal of BCS by stabilizing the soil on site. This can help in sustainable development in construction industry.

### References

1. Karatail TR, Wambua Kaluli J, Kabubo C, Thiong’o G (2016) Soil stabilization using rice husk ash and natural lime as an alternative to cutting and filling in road construction. *J Constr Eng Manag ASCE* 143:04016127-1–04016127-5.17. Author F, Author S (2016) Title of a

- proceedings paper. In: Editor F, Editor S (eds) Conference 2016, LNCS, vol 9999. Springer, Heidelberg, pp 1–13
2. Nelson JD, Miller DJ (1992) Expansive soils, problems and practice in foundation and pavement engineering. Wiley, New York. Author F (2010) Contribution title. In: 9th International proceedings on proceedings. Publisher, Location, pp. 1–2
  3. Anwar Hossain KM (2011) Stabilized soils incorporating combinations of rice husk ash and cement kiln dust. *J Mater Civ Eng* 23(9):1320–1327. [https://doi.org/10.1061/\(asce\)mt.1943-5533.0000310](https://doi.org/10.1061/(asce)mt.1943-5533.0000310)
  4. Qureshi MA, Mistry HM, Patel VD (2015) Improvement in soil properties of expansive soil by using copper slag. *Int J Adv Res Eng Sci Technol (IJAREST)* 2(7):125–130
  5. Prakash J, Kumara K, Kumar V (2017) Stabilization of soil using rice husk ash. *Int J Innov Res Sci Technol Eng (IJRSET)* 6
  6. IS 2720 (Part 5) (1985) Determination of liquid and plastic limits. Bureau of Indian Standards
  7. IS 2720 (Part 6) (1972) Determination of shrinkage factors. Bureau of Indian Standards
  8. IS 2720 (Part 7) (1980) Determination of water content-dry density relation using light compaction. Bureau of Indian Standards
  9. IS 2720 (Part 40) (1977) Determination of free swell index of soils. Bureau of Indian Standards
  10. IS 2720 (Part 10) (1991) Determination of unconfined compressive strength test. Bureau of Indian Standards
  11. IS 2720 (Part 16) (1987) Laboratory determination of CBR. Bureau of Indian Standards
  12. Raj R, Banupriya S, Dharani R (2016) Stabilization of soil using rice husk ash. *Int J Comput Eng Res (IJCER)* 6

# Geotechnical Characterization Methodology of Water Treatment Sludge for Production of Liner Material



Leonardo Marchiori , Maria Vitoria Morais , António Albuquerque ,  
and Victor Cavaleiro 

**Abstract** Clayey soils and geosynthetic materials are used as low hydraulic conductivity layers and environmental protection barriers in civil engineering works for storing wastes as covering and bottom impermeabilization layer structures, known as liners. Future shortage of clay materials and geosynthetic's high costs are usual problems, aligned with the need of prevention of environmental impacts associated to wastes by industry infiltrating into groundwater, sustainable solutions are needed. The reuse of industrial waste materials follows directives of the circular economy when this application is expected to reduce construction costs, help preserve natural resources, reduce the use of synthetic materials, reuse industrial waste materials, and contribute to sustainability. Water treatment sludges (WTS) are generated by water treatment plants mainly from periodic washing of the sedimentation tanks and filters and seems to be suitable for a geomaterial replacement. To make it feasible, the most significant factors that need more investigations are index properties, physical and mechanical behavior, chemical compaction and resistance, hydraulic conductivity, and leaching potential. A methodology for different ratios of WTS, soil, and with or without additive needing, along with a laboratorial analysis of water treatment sludge sample were proposed to ensure the expected results and parameters for liner alternative material.

**Keywords** Industrial waste(s) valorization · Hydraulic barrier(s) · Waterproofing · Earthwork(s) · Water treatment sludge(s)

---

L. Marchiori (✉) · M. V. Morais · A. Albuquerque · V. Cavaleiro  
Universidade da Beira Interior, Covilhã, Portugal  
e-mail: [leonardo.marchiori@ubi.pt](mailto:leonardo.marchiori@ubi.pt)

FibEnTech, Covilhã, Portugal

GeoBioTec, Aveiro, Portugal

# 1 Introduction

## 1.1 Waste Valorization

Waste is any substance discarded or which had the intention or obligation to discard and the called industrial waste is that produced by industrial activity such as mining operations, water treatment plants, thermal processes, and factories' waste generation. Solid and semi-solid waste from water and effluent treatment facilities are water treatment sludges (WTS), or water treatment residuals, or waterwork wastes, mainly any waste from water treatment plant (WTP) [1]. Since United Nations (UN) Conference on the Human Environment in 1972, known as the Stockholm Conference, UN has been designing and planning initiatives around the preservation of the environment, other worldwide events as ECO-92, also known as Rio-92, which used the first report as a basis, has become more frequent and treated as national and global problems, indicating its importance. Direct reuse, remanufacturing, and reprocessing to produce biological and chemical conversion products, fuel source and land reclamation are the main strategies, emerging a change in society's attitudes, resulting in investments for development of beneficial reuse of industrial by-products [2]. Other industrial wastes, such as blast furnace and boiler slag, fly and bottom coal ash wastes and other materials have been used as road construction materials and continues to grow due to its great performance and financial numbers. In view of this possible and viable application, started to investigate the rejected products for other applications in civil engineering.

A potential for the valorization of industrial waste is the application of some of them as barrier materials for waterproofing earthworks for the storage of solid waste (SW) and wastewater. However, for this application, it is needed investigation over different areas in geotechnical engineering, chemical compatibility and long-term behavior, laboratorial tests can achieve mechanical properties, chemical and mineralogical composition, in addition to conducting geotechnical characterization, hydraulic and leaching experiments, proving several parameters. Important physical characteristics include specific weight, moisture content, particle size distribution, compacted porosity of residues, oxides composition, and biological and chemical resistance properties [1]. The identification of appropriate geo-applications for an industrial waste is the most crucial step, requiring consideration of its properties and a comprehensive knowledge and understanding of geotechnical construction, in addition to economic and environmental regulations [3].

## 1.2 Hydraulic Barriers

The process to qualify a waste material as a sustainable barrier for waste disposal is divided in many aspects and complex phases, their role in a liner is to prevent some behaviors of clays that, because of its plasticity, usually cause differential settlement,



volume changes and possibly cracking allowing leaching through the barrier. These phases can be condensed by 2 bigger ones: (1) selection, characterization, physical and chemical, and testing of solid industrial wastes that are non-hazardous and with disponible, always making comparisons with clays and/or clayey soils, after analysis (2) should be evaluated the performance, mechanical and hydraulic, of several clay-waste mixtures to define optimum moisture.

Clays and geosynthetic layers like compacted clay liner (CCL) or geosynthetic-clay liner (GCL) have low hydraulic conductivity and are used as environmental protection barriers in geotechnical engineering works like solid waste landfill, wastewater ponds and mining ponds, being cover and bottom liners [2–14]. Basal liners are generally built with natural clay soils, due to their characteristics of high strength and low hydraulic conductivity, however, it is increasingly difficult to find locally available clay soils that satisfy the necessary engineering properties [11]. In addition, several solid industrial wastes appear to have physical and chemical characteristics similar to clays and continue to be discarded in soils, water or landfills, contributing to significant negative environmental impacts and not being recycled or recovered [8].

Those liners' properties can be summarized in, mainly low hydraulic conductivity, less than  $1 \times 10^{-9}$  m/s; enough strength to support the weigh above it, depending on the disposed material; deformation during service without cracking or rupture and self-healing properties; chemical compatibility with the disposed, and high cation exchange capacity; and an important issue for development countries and work owners with not many resources, easy construction with low-cost materials.

## 2 Properties Review

### 2.1 *Water Treatment Sludge as Liners*

WTS are mainly sludges from periodic washing of the sedimentation tanks and filters, called water treatment sludges (WTS) [15], its chemical and mineralogy are basically compound for silica, around 20%, and aluminum, 60%, and iron, 5%, looking similar to aluminum silicates as clays like kaolin [16]. According to Fourier transform infrared spectroscopy (FTIR) analysis, WTS has almost 70% of similarity with clay soils [16], because of the main presence of kaolinite, a common clay mineral [17, 18]. Dehydrated and treated, chemically or incinerated, sludges and muds from WTP also have the potential to be alternative materials for liners instead of clays [19], with a severe attention for its hazardousness especially for high organic matter content and mainly because of its permeability, compaction, durability and workability in constructions [20].

Gonçalves et al. [21] mixed dehydrated WTS with clayey soils with 1:0.5 and 1:1 ratio and with sand, 1:0.25 ratio, reaching at least  $1 \times 10^{-9}$  m/s after compaction showing viability for landfill liner material. Corroborating, [7] concluded that samples of WTS from Cubatão, São Paulo, are thixotropic, a phenomenon of reversible time-dependent decrease of viscosity, namely when it is sheared for some time, the viscosity decreases, however, when the shear is stopped, the viscosity of the system is restored, the undrained shear increased five times since the immediate measure, although remain needs treatment to achieve adequate shear strength. Other ratios have been tested, just like mixtures with other wastes and clays, [22] found optimum moisture of clay, WTS and calcium carbide residue of 40:40:20 ratio, WTS principally affected the hydraulic conductivity and compressive strength, reaching hydraulic conductivity of  $6.6 \times 10^{-9}$  m/s and a 56-day compressive strength of 2.95 MPa. Tests were conducted with a comprehensive investigation into the use of WTS in unconfined compressive strength and the retraction behavior of kaolinite clay, samples were added to kaolinite by the dry weight of clay and showed an increase in strength within WTS addition. An increase in the curing period resulted in an increase in the resistance to unconfined compression and a reduction in the shrinkage potential.

Research on the hydraulic conductivity of water treatment sludge is lacking, however, it has the potential to be used as a covering material in landfills, but it can also be studied as a bottom material if it presents hydraulic conductivity lower than  $10^{-9}$  m/s.

### 3 Laboratorial Methodologies

#### 3.1 Sampling

The sampling procedure was conducted as follows based on Theory of Sampling [23]:

1. samples of approximately 50 kg must be collected and stored in plastic boxes tagged with a composite code, the collection date, the donor company, and the site's coordinates.
2. transport from collection place to the Soil Mechanics, Geotechnics, Environmental, Sanitation, and/or Chemical Laboratories which will store the materials and performed the tests
3. approximately 50% of the total sample stored as replacement material, also used in mixtures, and the other 50% dehydrated and determined raw material water content
4. the dehydrated portion of the sample was divided for laboratory tests according to each standard and amounts

### 3.2 *Index Properties and Physical Characterization Methods*

The standard adopted for the separation of soil samples and residual materials can follow the guidelines of the [24]. Also, from that standard were determinate the water content ( $w$ ) of the samples using the 105–110 °C oven for 24 h.

Granulometry is the measurement of the particle size distribution of the grains of soils, it is defined as the distribution by weight percentage of soil particles in accordance with their dimensions, summarizing the nomenclature according to size is clay (<0.005 mm), silt (0.005–0.075 mm), sand (0.075–4.5 mm), gravel (4.5–75 mm), rock (75–300 mm) and cobbles (>300 mm). For fine particles such as clays, characterized for those which pass for sifting process that pass through the #200 sieve (0.075 mm), the sedimentation method used is from [25], or even laser analysis. Classification for composites follows the one for soil like Unified Soil Classification System (USCS) [26].

For index properties determination, solid particles specific gravity ( $G_s$ ), by pycnometer method [27] can be used. Besides, consistency, or Atterberg, limits were determined following standards [28, 29] for liquid and plastic limits respectively, only for the fraction of the soil that passes through the #40 sieve (0.425 mm). Casagrande shell method for liquidity index ( $w_L$ ) and molded sample by hand on a glass plate for plasticity index ( $w_P$ ), and the difference between those values is the plasticity index (PI). Plasticity is a very important characteristic of fine soils; it describes the capability of the soil to suffer irreversible deformation without break or crumble. In general, depending on the quantity of water, or humidity, the soil can be in one of the states of plasticity, liquid, plastic, semi-solid and solid. Decreasing the amount of a liquid state soil, it became a plastic, decreasing volume until the solid state be reached [30].

### 3.3 *Mechanical Behavior Methods*

Compaction is the process of increase density of the soil grouping the particles with reduction of air volume, there is no significant decrease of water [30]. Compacted clay liners are used as basal and cover for landfills, the compaction act decreasing the void index consequently increasing the hydraulic conductivity. Compaction curves of soils are essential for practical and a trustworthy analysis for field compaction quality [31]. The Proctor test described on [32] provide compaction curve and saturation curve, index properties such as optimal water content ( $w_{opt}$ ), maximum dry weight ( $\gamma_{max}$ ) and, in addition can determine void index ( $e$ ), porosity ( $n$ ) and saturation index ( $S$ ).

Terzaghi formulated an equation, for the one-dimensional consolidation case, that relates the change in pore pressure ( $\Delta u$ ), time ( $t$ ), and the depth ( $z$ ) of a soil element subjected to a stress ( $\Delta \sigma$ ) uniformly distributed over an infinite area of soil, and presents the solutions of the consolidation equation by two dimensionless quantities, the time factor ( $T_v$ ) and the average degree of consolidation ( $U_v$ ) within consolidation

coefficient ( $c_v$ ), for practical terms, it is adopted for the end of the consolidation when  $T_v$  equals to 1 and the consolidation reaches 90%. Looking to determine the consolidation coefficient, two traditional methods are used, Taylor and Casagrande, to predict the speed at which the soil settles. Taylor method uses the square root of time on the x-axis to fit a tangent line, obtaining degrees of consolidation 0 and 90%. The Casagrande Method, on the other hand, plot time in logarithm scale, and uses an extension of the instantaneous consolidation part to obtain 0%, and two tangent lines, one in the primary consolidation and another in the secondary consolidation, where the intersection between them is the 100% point. Both methods seek to obtain the equivalent of 50% of the consolidation and its respective time.

Coulomb and Mohr strength theory express shear strength ( $\tau_f$ ) in terms of cohesion ( $c$ ) and friction angle ( $\varphi$ ) and utilizing Terzaghi concept of effective stress, parameters  $c'$  and  $\varphi'$  can be determined from triaxial tests. Triaxial tests consist in a cylindrical specimen enclosed in flexible membranes between a loading cap and a pedestal for drainage and axial load, this enclosed into a water pressure chamber. The load is applied in two stages, in the first, the water in the chamber confines the specimen and the second is applied axial load from a constant rate press. Theoretically, triaxial should apply three stresses, one for each axis, although in practice using cylindrical samples, there is a axial symmetrically resulting in  $\sigma_1 \geq \sigma_2 = \sigma_3$ , the major and axial stress being  $\sigma_1$  and the fluid pressure from the cell being  $\sigma_2 = \sigma_3$ . Consolidated undrained assembly must not allow drainage during application of deviator stress.

For liner simulation, consolidated undrained (CU) triaxial tests were performed, the first stage is saturation and consolidation, where the specimen wets and consolidate at confining pressure ( $\sigma_c'$ ) and in the second stage, when drainage is not permitted but pore pressure may be measured. Different pressures are applied called deviator stress ( $\sigma_d$ ), at least three, to generate a Mohr–Coulomb line or determine the effective stress path due parameterizations.

### 3.4 Chemical Composition Methods

Cation exchange capacity (CEC) is proportionally inversed to mineral grain size particles [18]. Clay Activity values higher than 27 meq/100 g correspond to high chemical activity [17]. CEC is determined by the ammonium acetate method buffered to pH = 7. X-Ray Diffractometry (XRD), X-Ray Fluorescence (XRF) and Scanning Electron Microscopy (SEM) are the main chemical and mineralogical characterization techniques used.

In XRD, each mineral species is characterized by a systematic arrangement atomic (or ion) specific, with characteristic crystalline planes that can diffract X-rays. The diffraction of X-rays by atoms in a crystalline plane produces characteristic patterns when recorded (angles and intensities). These diffraction patterns are used as a fingerprint in the identification of mineral species, producing a series of dots or lines, called bands. The XRF consists of the incidence of an X-ray beam on a sample, making with its electrons being ejected from the layers close to the nucleus, The vacancies

created are filled by electrons from the outermost layers, emitting X-rays (fluorescent or secondary), whose energies correspond to the difference between the energies of the levels and sublevels of the transitions. Each type of atom has a characteristic and unique X-ray spectrum that is used as a comparison for identification. The intensity of the FRX of a certain wavelength is related to the concentration of the element that emitted it. FRX analysis is semi-quantitative and provides the chemical composition expressed as the oxides of the elements. The Scanning Electron Microscope (SEM) is one of the most versatile instruments to obtain information on the morphology of minerals. When they have detectors that capture characteristic X-rays by energy dispersion (Energy Dispersive Spectroscopy—EDS), they are called MEV-EDS, and provide information about the chemical elements that compose them. The SEM produces images with a three-dimensional appearance, a direct result of the great depth of field and allows the examination in successive increases, with great depth of focus, combining information from electronic and optical images. According to other authors, the main reason for its use is the high resolution obtained when observing the samples.

### ***3.5 Hydraulic Performance Methods***

The methodology for permeability analysis in laboratory is very simple, although differs according to the soil to be studied, falling head permeameter is used for low permeability soils such as clays, and constant head permeameter for high permeability soils, like sands. Falling head permeability can be measure from upward or downward through the soil, however, downward flow can transport fines and occurring clogging of the sample. The sample to be studied is inserted into a measured cylinder with a cross section ( $A$ ) and specimen height ( $L$ ), this cylinder is connected through tubes to another graduated cylinder with a cross section ( $a$ ) that contains water to a certain level. At a certain initial moment ( $t_1$ ), there is a certain hydraulic load according to the height ( $h_1$ ), at another moment ( $t_2$ ) there is another hydraulic load ( $h_2$ ), following [33].

Low hydraulic conductivity plays an important role in the applicability of WTS to landfilling [8]. But, due to the lack of research, it needs field application, mechanical stabilization, and long-term behavior. In addition to varying greatly according to the region and the source of the water to be treated, prior characterization must always be performed.

## 4 Conclusions

For future investigations over waste-based composites with soils, like water treatment sludge valorization in different ratios with or without additives, to achieve liner requirements, the author suggestion mixtures in Table 1 and laboratorial tests in Table 2, following literature’s path.

Besides that, must performed field small scale experimental liners, testing its compaction, compression resistance, and field permeability, also long-term behavior can be tested due to chemical and thermal resistances (wet-dry, freeze-thaw cycles, leaching resistance and biological degradation). Those characteristics should qualify the material as liner.

**Table 1** Potential mixtures ratios for WTS, soils and additives for liner feasibility

Soil:Waste ratio	Soil:Waste ratio (if low ratios behave similar)	Soil:Waste:Additive ratio (choosing the best performance composite)
100:0%		+ 2.5% of additive taking 1.25% of each + 5% of additive taking 2.5% of each + 10% of additive taking 5% of each
20:80%	75:25%	
15:85%	50:50%	
10:90%	25:75%	
05:95%		

**Table 2** Potential laboratorial tests methodology for residues application in liners

<i>Geotechnical</i>	<i>Mechanical</i>
Specific gravity (Density)	Compaction (Normal proctor)
Consistency limits (Atterberg)	Consolidation (Oedometric)
Particle Size Distribution (Sieve and laser)	Triaxial (Consolidated undrained)
<i>Chemical</i>	<i>Hydraulic</i>
Cation exchange capacity	Permeability (Falling head)
Mineralogy (X-Ray diffraction)	
Microstructure (Scanning electron microscope)	Leachability (Batch and column)
Composition (Energy dispersive spectrometry)	

## References

1. Tchobanoglous G, Theisen H, Vigil S, George T, Samuel V (1993) Integrated solid waste management: engineering principles and management issues. McGraw-Hill Companies, Incorporated
2. Abichou T, Edil TB, Benson CH, Tawfiq K (1998) Beneficial reuse of foundry sands in construction of hydraulic barrier layers. Geotechnical Special Publication, pp 186–200. [https://doi.org/10.1061/40756\(149\)13](https://doi.org/10.1061/40756(149)13)
3. Abichou T, Benson CH, Edil TB (2000) Foundry green sands as hydraulic barriers: laboratory study. Geotect Geoenviron Eng 0241:657–666. [https://doi.org/10.1061/\(ASCE\)1090-0241\(2000\)126](https://doi.org/10.1061/(ASCE)1090-0241(2000)126)
4. Abichou T, Benson CH, Edil TB (2002) Foundry green sands as hydraulic barriers: field study. J Geotechn Geoenviron Eng 128:206–215. [https://doi.org/10.1061/\(ASCE\)1090-0241\(2002\)128:3\(206\)](https://doi.org/10.1061/(ASCE)1090-0241(2002)128:3(206))
5. Rubinos DA, Spagnoli G (2018) Utilization of waste products as alternative landfill liner and cover materials: a critical review. Crit Rev Environ Sci Technol 48:376–438. <https://doi.org/10.1080/10643389.2018.1461495>
6. Rubinos D, Spagnoli G, Barral MT (2015) Assessment of bauxite refining residue (red mud) as a liner for waste disposal facilities. Int J Min Reclam Environ 29:433–452. <https://doi.org/10.1080/17480930.2013.830906>
7. Tsubawa JK, Pereira KFS, Boscov MEG (2017) Thixotropy of sludge from the Cubatão water treatment plant, Brazil. Geotechnical Frontiers GSP 280:842–851. <https://doi.org/10.1061/9780784480472.090>
8. Agamuthu P (2013) Landfilling in developing countries. Waste Manage Res 31:1–2. <https://doi.org/10.1177/0734242X12469169>
9. Devarangadi M, Shankar MU (2020) Correlation studies on geotechnical properties of various industrial byproducts generated from thermal power plants, iron and steel industries as liners in a landfill—a detailed review. J Cleaner Prod 261:121207. <https://doi.org/10.1016/j.jclepro.2020.121207>
10. Fall M, Célestin J, Sen HF (2010) Potential use of densified polymer-pastefill mixture as waste containment barrier materials. Waste Manage 30:2570–2578. <https://doi.org/10.1016/j.wasman.2010.07.016>
11. Guney Y, Cetin B, Aydilek AH, Tanyu BF, Koparal S (2014) Utilization of sepiolite materials as a bottom liner material in solid waste landfills. Waste Manage 34:112–124. <https://doi.org/10.1016/j.wasman.2013.10.008>
12. Kraus JF, Benson CH, Van Maltby C, Wang X (1997) Laboratory and field hydraulic conductivity of three compacted paper mill sludges. J Geotechn Eng 123:654–662. [https://doi.org/10.1061/\(ASCE\)1090-0241\(1997\)123:7\(654\)](https://doi.org/10.1061/(ASCE)1090-0241(1997)123:7(654))
13. Osinubi KJ, Eberemu AO (2010) Desiccation induced shrinkage of compacted lateritic soil treated with blast furnace slag. Geotech Geol Eng 28:537–547. <https://doi.org/10.1007/s10706-010-9308-6>
14. Palmer BG, Edil TB, Benson CH (2000) Liners for waste containment constructed with class F and C fly ashes. J Hazard Mater 76:193–216. [https://doi.org/10.1016/S0304-3894\(00\)00199-0](https://doi.org/10.1016/S0304-3894(00)00199-0)
15. Gimenez Boscov ME, Hems PS (2020) Some topics of current practical relevance in environmental geotechnics. Soils Rocks 43:461–495 <https://doi.org/10.28927/SR.433461>
16. Bashar NAM, Zubir ZH, Ayob A, Alias S (2016) Water treatment sludge as an alternative liner for landfill site: FTIR and XRD analysis. In: AIP Conference Proceedings, American Institute of Physics Inc. <https://doi.org/10.1063/1.4965082>
17. Coelho GMR (2016) Avaliação da capacidade reativa de uma lama de ETA para a remoção de metais pesados de escorrências rodoviárias, Universidade da Beira Interior
18. Kyncl M (2008) Opportunities for water treatment sludge re-use, GeoSci Eng LIV:11–22
19. Balafoutas G (1999) Bottom ash from pollutant migration in landfills. In: Waste management and research

20. Bashar NAM, Zubir ZH, Ayob A, Alias S (2016) Water treatment sludge as an alternative liner for landfill site: FTIR and XRD analysis. In: AIP conference proceedings, p 1774. <https://doi.org/10.1063/1.4965082>
21. Gonçalves F, de Souza CHU, Tahira FS, Fernandes F, Teixeira RS (2017) Incremento de lodo de ETA em barreiras impermeabilizantes de aterro sanitário. *Revista DAE* 65:5–14. <https://doi.org/10.4322/dae.2016.018>
22. Prakongwittaya W, Asavapisit S, Piyaphanuwat R (2020) Reuse of calcium carbide and water treatment residues in the bottom clay liner of a municipal solid waste landfill. *Environ Progr Sustain Energy* 39:e13434. <https://doi.org/10.1002/ep.13434>
23. Tsugawa JK, Monte R, Eugênia M, Boscov G, Tsugawa JK, Fernandes E, Sabino DS, Gimenez Boscov ME (2019) Importance of composing representative samples according to the theory of sampling (TOS) for the reuse of water treatment sludge. In: *Geotechnical engineering in the XXI century: lessons learned*, pp 2450–2457 <https://doi.org/10.3233/STAL190314>
24. ABNT, NBR-6457 - Amostras de solo - preparação para ensaios de compactação e ensaios de caracterização, Rio de Janeiro (2016)
25. ABNT, NBR 7181 - Soil - Sieve Particle Analysis (2016), p 13
26. ASTM International, Standard Practice for Classification of Soils for Engineering Purposes (Unified Soil Classification System) ASTM Standard Guide (2011), pp 1–5
27. ABNT, NBR 6508 - Grãos de solos que passam na peneira 4,8 mm - Determinação da Massa Específica (1984), p 8
28. ABNT, NBR 6459 - Solo - Determinação do limite de liquidez (2016)
29. ABNT, NBR 7180 – Solo - Determinação do limite de plasticidade (2016)
30. Craig R (2007) *Mecânica dos solos*
31. Yaghoubi E, Arulrajah A, Yaghoubi M, Horpibulsuk S (2020) Shear strength properties and stress–strain behavior of waste foundry sand. *Constr Build Mater* 249:118761. <https://doi.org/10.1016/j.conbuildmat.2020.118761>
32. ABNT, NBR 7182 - Solo- Ensaio de Compactação (2016)
33. ISO17892-11(2019) *Geotechnical investigation and testing—laboratory testing of soil—Part 11: permeability tests*



# A Low-cost Setup to Evaluate the Performance of a Methanotrophic Activity in Bio-augmented Systems at a Laboratory Scale



Nivedita Sana, Dali Naidu Arnepalli, and Chandraraj Krishnan

**Abstract** There is a need to develop methane mitigation strategies to curb the increasing global warming and restrict the global rise in temperature to below the threshold of 2 °C, per the Paris Agreement's goals. Methanotrophs represent an attractive natural sink, for they can fix even atmospheric methane concentrations by assimilating it into biomass. Despite the emergence of several mitigation systems based on methanotrophs such as biocovers, biofilters, and biotarps to curtail methane emissions from landfills, there is still insufficient evidence to support their effectiveness. The simulation of low-grade methane emissions to study bio-augmented systems in laboratory conditions requires mixing methane and air at very low flow rates. Achieving such low gas flow rates requires sophisticated mass flow controllers, which are expensive. Thus, one of the major factors in impeding high throughput research on methane biomineralization is designing the experimental setups for screening organisms and materials for bio-augmented systems. This study designed and validated a low-cost continuous column flow system for mixing methane and air in appropriate proportions simulating landfill gas flow conditions. Coir mat bio-augmented with *Methylosarcina* sp. LC4 as a biotarp prototype was tested in these continuous flow setups. The performance of the prototype was evaluated based on the methane removal efficiency. An Arduino-based MQ4 methane sensor and DHT11 humidity and temperature sensor were installed in the headspace of the column for online monitoring of the outlet gas. Thus, an indigenously designed, low-cost setup was successfully used to assess the performance efficiency of a bio-augmented coir-based biotarp prototype at a laboratory scale.

**Keywords** Gas mixing setup · Methane biomineralization · Bubble counter · Low-cost setup

---

N. Sana · D. N. Arnepalli (✉)  
Department of Civil Engineering, Indian Institute of Technology, Chennai 600036, India  
e-mail: [arnepalli@iitm.ac.in](mailto:arnepalli@iitm.ac.in)

C. Krishnan  
Department of Biotechnology, Indian Institute of Technology, Chennai 600036, India  
e-mail: [kcraj@iitm.ac.in](mailto:kcraj@iitm.ac.in)

## 1 Introduction

The unabated emissions of greenhouse gases, including carbon dioxide and methane, have already caused multiple observed changes in the climate system [1]. Methane has seen the highest-fold increase in atmospheric concentrations of all greenhouse gases since pre-industrial times, contributing to as much as 30% of global warming [2]. However, methane has a much shorter lifetime of a decade compared with centuries for CO<sub>2</sub>. Thus, curbing methane emissions is an opportunity for short-term relief from the disruptive effects of global warming. The global methane assessment has found that cutting human-caused methane by 45% this decade would restrict the global rise in temperature to below the threshold of 2 °C, per the Paris Agreement goals [3]. Currently, anthropogenic activities contribute to over 60% of the worldwide methane budget, of which more than 30% is contributed by municipal solid waste landfills and dumpsites [4, 5]. Despite the efforts worldwide to harness landfill methane for energy generation, only 60%–90% of the methane emitted from the engineered landfill is captured [6]. Methane capture and utilization from landfill gas become economically nonviable when its concentration drops below 20% v/v. In this scenario, the landfill gas is destroyed by high-temperature flaring, contributing to global warming in carbon dioxide emissions [7].

Methanotrophs are methane-oxidizing bacteria that can assimilate methane at atmospheric concentrations as low as 1.84 ppmv [8]. Although several mitigation systems based on methanotrophs such as biocovers, biofilters, biowindows, and biotarps have been developed to curtail its emissions from landfills, there is still insufficient evidence to support their effectiveness [6]. The current systems mostly use nonspecific microbial communities, such as active sludge as natural inoculum, which leads to inconsistent performances. At the same time, studies with pure methanotrophs are limited to a few laboratory studies [9]. The necessity to understand and design bio-augmented systems to arrest low-grade methane is now greater than ever.

The simulation of low-grade methane emissions to study bio-augmented systems in laboratory conditions requires mixing methane and air at low flow rates. Since methane is a flammable and explosive gas, the mixtures of methane and air cannot be stored and are generally done in-situ. The typical flow rates for column experiments emulating these systems range from 0.5 to 50 ml/min. Achieving such low gas flow rates requires mass flow controllers, which are expensive. Thus, one of the major factors in impeding high throughput research on methane biomineralization is designing the experimental setups for screening organisms and materials for bio-augmented systems.

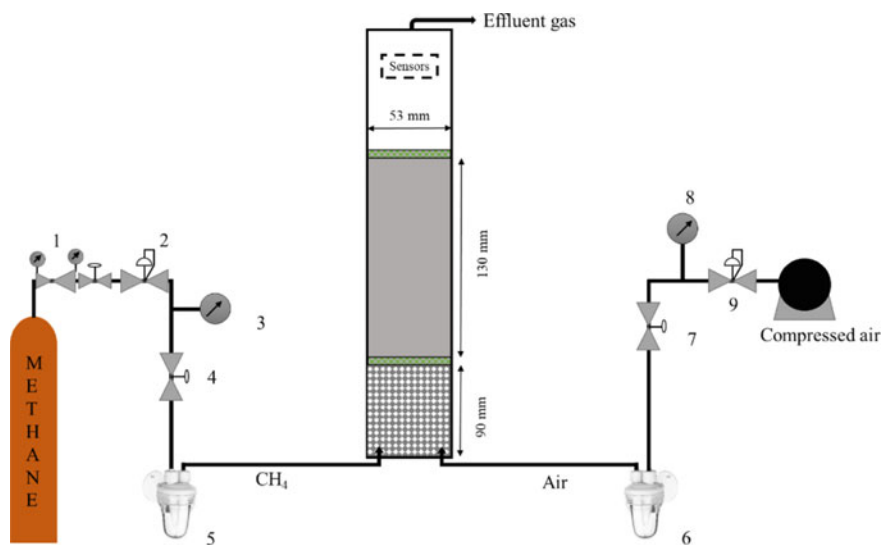
## 2 Materials and Methods

### 2.1 Setup for Flow Control and Regulation

A combination of pressure regulators controlled the flow rates of the gases to be mixed to bring down the inlet pressure of the gas to the desired value, followed by an inline flow control valve (Fig. 1). High purity methane cylinder (> 99.999%, 130 bar) and compressed airline (8 bar) were used as the source for respective gases. The pressure of the methane gas from the source is maintained constant at a set value (0.5–1 bar) by two pressure reducers in series; a two-stage cylinder regulator in series with a pressure regulator (LR-D-MAXI, FESTO, Germany). A single pressure regulator (LR-D-MAXI, FESTO, Germany) was used for compressed air to reduce the pressure to the set value of 0.5–1 bar. The pressure gauge downstream is used to monitor the absolute pressure. The pressure regulator is manually adjusted to account for pressure variations caused by the gas flow. The flow control valve (Mercury pneumatic, India) regulates the gas flow rate passing through the bubble counter. An acrylic bubble counter (ISTA, China) with a check valve was used in the present study. Water was used as the liquid in the bubble counter and was added intermittently to account for the loss due to evaporation and to maintain a constant water level. Polyurethane pneumatic tubing (8 mm outer diameter and 6 mm inner diameter) was used for all the gas flow channels.

### 2.2 Calibration of the Bubble Counter

The water displacement technique collected the volume of the gas flowing out of the bubble counter. A calibrated 50 ml burette having 12.7 mm diameter with a stopcock was filled with water and carefully inverted over a tray containing water. The outlet from the bubble counter was introduced into the submerged open end of the burette. The water displaced per unit time was calculated by recording the difference in the water meniscus level at the measurement's beginning and end. Since the height of the water-filled burette is nominal, the rate of water displaced can be approximated as the gas flow rate. Simultaneously, the number of bubbles generated in the bubble counter per unit time was manually enumerated. The correlation between the number of bubbles per unit of time and the gas flow rate was determined at different gas flow rates. All the experiments were carried out in triplicates. Correlations for both methane and air at various inlet pressures were obtained.



- 1 – Two-stage cylinder pressure regulator  
 2, 9 – Pressure regulator  
 3, 8 – Pressure gauge  
 4, 7 – Flow control valve  
 5, 6 – Bubble counter

**Fig. 1** Schematic layout of the low-cost continuous column flow system

### 2.3 *Mixing of the Gases and Validation by Gas Chromatography*

At an inlet pressure of 0.5 bar, based on the bubble count per unit time of methane and air, the flow rates of individual gases were determined. The gas streams were allowed to flow through the column setup for homogenous mixing. The gases were mixed in different ratios by varying their flow rates. The % CH<sub>4</sub> (v/v) was predicted using Eq. 1.

$$\% \text{CH}_4 \left( \frac{v}{v} \right)_{\text{predicted}} = \frac{\text{Flow rate of CH}_4}{\text{Flow rate of CH}_4 + \text{Flow rate of air}} \quad (1)$$

The mixed gas was collected in a 50 ml test tube by water displacement technique and then sealed by a silicone sleeve stopper septum underwater. Collected gas samples were analyzed by gas chromatography according to the protocol described by us previously [10]. The % CH<sub>4</sub> predicted values were compared with the values obtained by the gas chromatography to validate the protocol for mixing the gases.

## 2.4 Column Setup

The RO housing used in the water purification systems was repurposed for the column setup simulating a landfill biotarp at a laboratory scale. The height of the column was 300 mm. Bottom 90 mm of the column was filled with plastic balls for homogeneous mixing of methane and air. The height of the packing material to be used as a biotarp is 130 mm. The packing material used here is coir, previously used to immobilize methanotrophs for methanol production [11]. A perforated disc separated the headspace and the column packing. The headspace of the column had a pre-calibrated DHT11 temperature and humidity sensor and an MQ4 methane sensor installed in it. The details of the column setup are given in the schematic diagram (Fig. 1).

## 2.5 Calibration of MQ4 Sensor

MQ4 gas sensor is a metal oxide semiconductor-based sensor that detects methane gas concentrations in air. The sensing element of the MQ4 sensor has a fixed resistance in clean air ( $R_0$ ). This resistance decreases in the presence of methane ( $R_s$ ). Furthermore, the ratio of these resistances ( $R_s/R_0$ ) can be used to determine the methane concentration in the air.

In addition, a fixed resistance ( $R_L$ ) is connected in series with the sensing element. In the presence of methane, the voltage drop ( $V_0$ ) across  $R_L$  is measured as analog output from this sensor.  $V_0$  is further used to calculate  $R_s$  using Eq. 2.

$$V_0 = 5 \times \frac{R_L}{R_L + R_s} \quad (2)$$

Several pre-determined methane mixtures obtained by mixing methane and air at appropriate flow rates described previously were used to calibrate the sensors. The sensor was flushed with clean air before each reading. The analog output from the MQ4 sensor was read using an Atmega328 Arduino nano (Fig. 2). The code for the collection of data simultaneously from the DHT11 and MQ4 sensors is presented in Fig. 3.

## 2.6 Column Operation

Column setup simulating an engineered landfill cover was operated for ten days. At the beginning of the experiment, the packing material in the column, i.e., coir, was inoculated with 60 ml of *Methylosarcina* LC4 cells grown, harvested, and resuspended in fresh NMS media ( $OD_{600} = 0.6$ ) and allowed free drainage [10]. The column was then supplied with 0.6 ml/min methane and 15 ml/min air mixed in situ

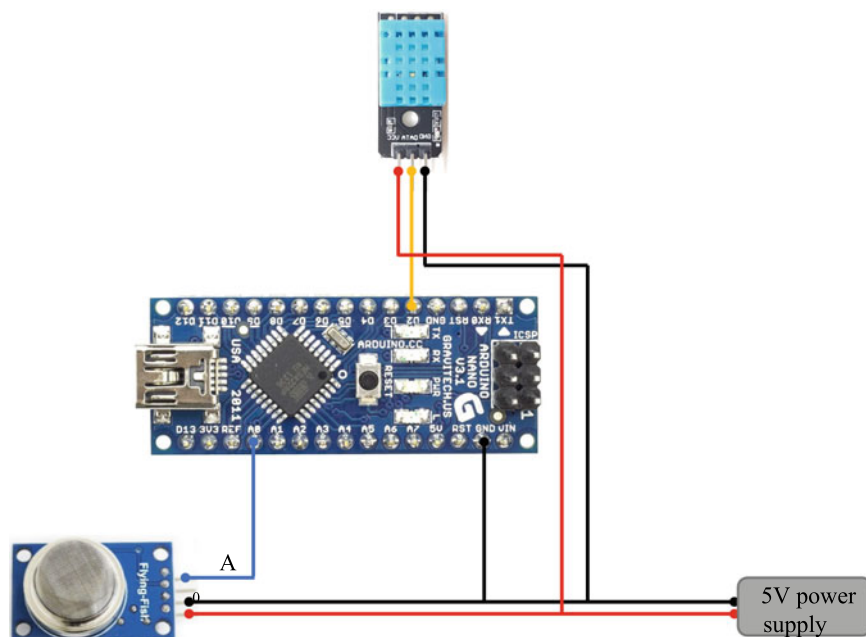


**Fig. 2** Connection diagram of Atmega328 Arduino nano based MQ4 methane sensor and DHT11 temperature and humidity sensor

by the arrangement described previously. The effluent gases were monitored using the installed sensors as well as gas chromatography.

### 3 Results and Discussion

#### 3.1 Calibration of the Bubble Counter

An indigenously developed apparatus achieved a continuous supply of methane and air at desired flow rate and concentration (Fig. 1). The pressure before the flow meter must be high enough to ensure that the pressure drops downstream have an almost negligible effect. The inlet pressure varied from 0.5 to 1 bar. The flow rate of the gas passing through the bubble counter was determined by collecting the outlet gas underwater in a graduated burette. The bubble's radius formed in the bubble counter is correlated to pressure difference by the simplified Laplace pressure equation (Eq. 3).

$$\Delta P = 2 \times \left( \frac{2\gamma}{R} \right) \quad (3)$$

where R is the radius of the bubble and  $\gamma$  is the surface tension.

```

#include <dht.h>
dht DHT1;
#define DHT11_PIN1 2
void setup()
{
  Serial.begin(9600);
  Serial.println("LABEL,Date,Time,V1,T1,H1 ");
}

void loop()
{
  double S1;
  DHT1.read11(DHT11_PIN1);
  Serial.print("DATA,DATE,TIME,");
  double V1=0;

  for (int i=0;i<500;i++)
  {
    V1= V1+analogRead(A0);      //MQ4 sensor gives an analog output in the range
    1-1024
  }
  S1=(V1/500)*5/1024;          //The analog output is converted to voltage
  Serial.print(S1);
  Serial.print(",");
  Serial.print(DHT1.temperature); //DHT11 sensor gives a digital output
  Serial.print(",");
  Serial.println(DHT1.humidity);
  delay(60000);
}

```

**Fig. 3** Code for data collection from DHT11 and MQ4 sensors using Arduino

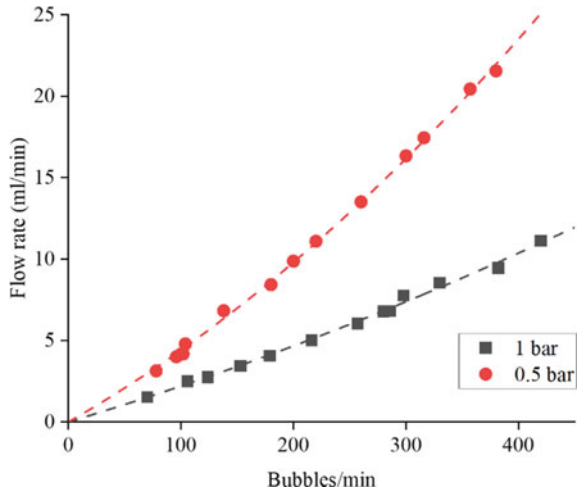
In the case of air, with the increase in the inlet pressure from 0.5 to 1 bar, the number of bubbles for the same airflow volume almost doubled (Fig. 4). The correlations between flow rate and the number of bubbles at inlet pressures of 0.5 and 1 bar are given by Eqs. 4 and 5, respectively.

$$y = 0.03924x + (4.8845 \times 10^{-5})x^2 \quad (4)$$

$$y = 0.02071x + (1.30094 \times 10^{-5})x^2 \quad (5)$$

In the case of methane, since the source was at high pressure, two pressure reducers were required to bring the pressure down to the required values. The number of bubbles for a specific flow rate did not change significantly with the change in pressure (Fig. 5). The correlations between flow rate and the number of bubbles at inlet pressures of 0.5 and 1 bar are given by Eqs. 6 and 7, respectively.

**Fig. 4** Flow rate versus bubble count per unit of time for air at 0.5 and 1 bar of pressure



$$y = 0.0367x + (4.0013 \times 10^{-5})x^2 \tag{6}$$

$$y = 0.03858x + (6.13554 \times 10^{-5})x^2 \tag{7}$$

**Fig. 5** Flow rate versus bubble count per unit of time for methane at 0.5 and 1 bar of pressure

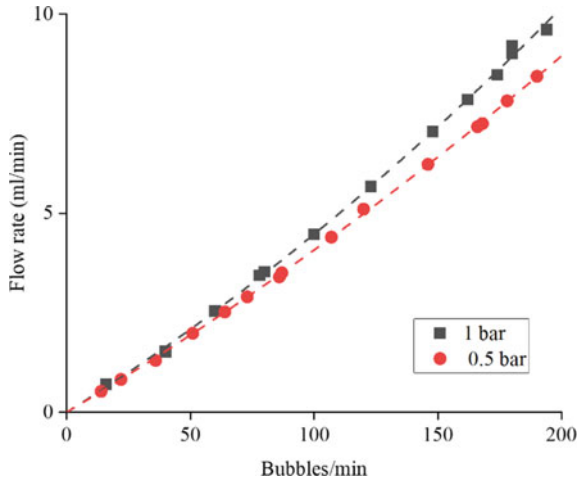
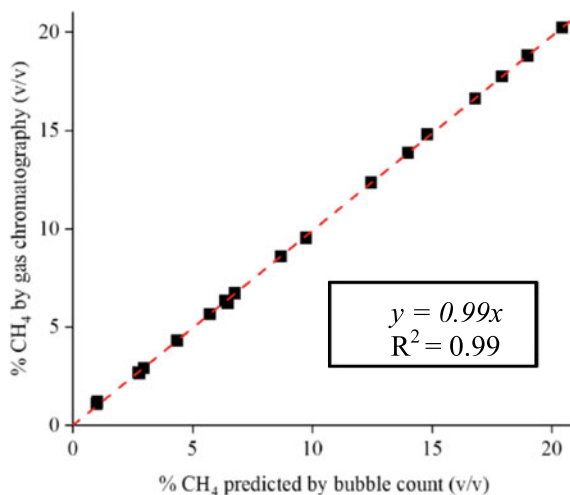




**Fig. 6** Correlation between % CH<sub>4</sub> (v/v) obtained by gas chromatography and that predicted by the bubble count



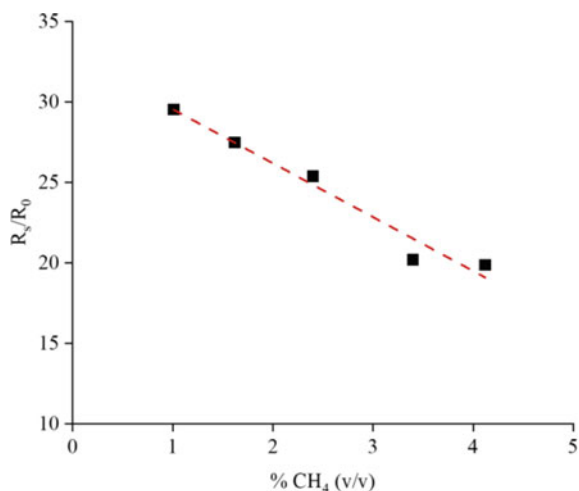
### 3.2 *Mixing of Gases Air and Methane*

Constant inlet pressure of 0.5 bar was maintained for the subsequent experiments involving mixing gases. The flow rate of the gases (air and methane) was set according to the previously obtained correlations from the bubble count. The gas flows were passed through a column setup filled with plastic balls to ensure uniform mixing of the gases. The outlet gas from the column setup was collected in 50 ml test tubes by water displacement technique and sealed with silicone septa. The gas chromatography further analyzed the outlet gas collected in the test tubes. Several pre-determined methane concentrations (% CH<sub>4</sub> predicted) obtained by mixing methane and air at different flow rates were verified using gas chromatography (Fig. 6).

### 3.3 *MQ4 Methane Sensor Calibration*

MQ4 methane sensor was installed in the headspace of the column setup and separated from the column's packing material by a perforated disc. Before each measurement, the MQ4 sensor was manually flushed with air. MQ4 sensor was not intended to measure the methane concentrations accurately but to observe the relative changes in methane concentrations in the outlet. A correlation between  $R_s/R_0$  and the preset methane concentrations was obtained. However, this correlation varied slightly with each MQ4 sensor. A representative correlation of an MQ4 sensor is shown in Fig. 7. Similar correlations have been obtained in previous studies [12, 13].

**Fig. 7** Methane oxidation and removal efficiency of bio-augmented coir column setup



### 3.4 Column Operation

The decrease of methane in the outflowing gas from the column bio-augmented with *Methylosarcina* LC-4 was monitored by an MQ4 sensor, and gas samples were collected in 50 ml test tubes by water displacement and closed with septa for further analysis by gas chromatography. Methane oxidation by methanotrophs immobilized in the column setup was monitored for ten days and is presented in Fig. 7. The methane oxidation increased to a maximum of 176 g/m<sup>2</sup>, corresponding to methane removal efficiency of 60% on day 6, and declined later, probably due to depletion of nutrients.

## 4 Conclusion

A low-cost working setup for regulating and measuring low flow rates of methane-air mixtures was designed, calibrated, and validated. The system was also used to continuously study the biomineralization of methane in a biotarp prototype for ten days. Based on this prototype, multiple column setups can be deployed for the high-throughput screening of organisms and materials for methane fixation and further valorization.

## References

1. UNEP homepage. <https://www.unep.org/explore-topics/climate-action/what-we-do/climate-and-clean-air-coalition>. Last accessed 2022/6/9.
2. CCAC homepage. <https://www.ccacoalition.org/en/news/new-ipcc-report-bolsters-evidence-methane-reductions-are-key-preventing-climate-catastrophe>. Last accessed 2022/6/9
3. UNEP (2021) Climate and clean air coalition: global methane assessment: benefits and costs of mitigating methane emissions. UN Environment Programme, Nairobi
4. Huber-Humer M, Gebert J, Hilger H (2008) Biotic systems to mitigate landfill methane emissions. *Waste Manage* 26(1):33–46
5. Kirschke S, Bousquet P, Ciais P, Saunois M, Canadell JG, Dlugokencky EJ et al (2013) Three decades of global methane sources and sinks. *Nat Geosci* 6:813–823
6. Sadasivam BY, Reddy KR (2014) Landfill methane oxidation in soil and bio-based cover systems: a review. *Rev Environ Sci Biotechnol* 13:79–107
7. Ménard C, Ramirez AA, Nikiema J, Heitz M (2012) Biofiltration of methane and trace gases from landfills: a review. *Environ Rev* 20:40–53
8. Cai Y, Zheng Y, Bodelier PLE, Conrad R, Jia Z (2016) Conventional methanotrophs are responsible for atmospheric methane oxidation in paddy soils. *Nat Commun* 7(1):1–10
9. Sahoo KK, Goswami G, Das D (2021) Biotransformation of methane and carbon dioxide into high-value products by methanotrophs: current state of art and future prospects. *Front Microbiol* 12:1–9
10. Nivedita S, Arnepalli DN, Krishnan C (2021) Kinetics and stoichiometry of an efficient methanotroph *Methylosarcina* sp. LC-4 isolated from a municipal solid waste dumpsite. *J Environ Eng* 147(5):04021011
11. Patel SKS, Kalia VC, Joo JB, Kang YC, Lee JK (2020) Biotransformation of methane into methanol by methanotrophs immobilized on coconut coir. *Bioresour Technol* 297:122433
12. Riddick SN, Mauzerall DL, Celia MA, Kang M, Bandilla K (2020) Variability observed over time in methane emissions from abandoned oil and gas wells. *Int J Greenhouse Gas Control* 100:103116
13. Nagahage ISP, Nagahage EAAD, Fujino T (2021) Assessment of the applicability of a low-cost sensor-based methane monitoring system for continuous multi-channel sampling. *Environ Monit Assess* 193(8):1–14

# An Assessment Focused on the Waste Energy Recovery by Co-processing of Oil Spilled in the Blue Amazon



Érica Machado da Silva Guerreiro  and André Felipe Simões 

**Abstract** In August 2019, an oil spill from marine shipping occurred in the area known as Blue Amazon—a vast maritime space of 5.7 million km<sup>2</sup>—between the northeast and southeast regions of Brazil. It collected more than 5000.00 tons of waste from the coast, treated, and applied as a Refuse Derived Fuel (RDF) in co-processing industries. In such context, this article presents an analysis focused on the co-processing of waste material in a cement kiln from the oil spill on the Brazilian coast. This study is predominantly theoretical and bibliographical since it is presented secondary data obtained from external access to public documents, dissertations, thesis, official reports, and scientific articles. It was observed that the application of waste as a substrate in industrial processes, either as a fuel or as thermal power generation, proved to be technically and economically viable, in addition to having the capacity to replace fossil fuel derivatives and reduce greenhouse gas emissions. Moreover, RDF shows to be a promising application of waste-to-energy since it allows the energy recovery of the amount of waste that would previously be disposed of in landfills without being recycled or treated.

**Keywords** Oil spill · Blue Amazon · Co-processing · Waste-to-energy · Refuse derived fuel

## 1 Introduction

Blue Amazon, as shown in Fig. 1, is an extensive maritime space of 5.7 million km<sup>2</sup> of great strategic importance that comprises the sum of the Exclusive Economic Zone and the Continental Shelf of Brazil, which includes maritime areas, rivers and lakes under Brazilian jurisdiction. The name “Blue Amazon” is associated with an analogy between the riches existing in the sea and those of the Amazon, the world’s biggest tropical rainforest [1].

---

É. M. da Silva Guerreiro (✉) · A. F. Simões  
Institute of Energy and Environment of the University of São Paulo – IEE/USP, Av. Prof. Luciano Gualberto 1289, São Paulo 05508-900, Brazil  
e-mail: [ericaguerreiro@usp.br](mailto:ericaguerreiro@usp.br)



Fig. 1 Blue Amazon's map [2]

In August 2019, one of the biggest environmental disasters in Brazil caused by an oil spill from a marine shipping. Due to its extent and impacts, it is considered the most serious environmental disaster ever recorded in tropical coastal regions [3]. This oil spill began to appear on the waters of Paraíba's state and, subsequently, extended for about 1000 km of the Brazilian Coast [4] in the northeast and southeast regions between the states of Maranhão and Rio de Janeiro [5]. From August/2019 to March/2020, 11 states, 130 municipalities and 1009 locations were affected by the oil spill [6], as illustrated in Fig. 2.

Co-processing is a successful practice of Refuse Derived Fuel (RDF) application, in which urban waste of physicochemical characteristics equivalent to the original raw material is burned during clinker (main component of cement manufacturing) production in rotary kilns of the cement industry [7]. To achieve more sustainable and international quality standards, many cement industries have been partially replacing coke (oil derived) for RDF during the co-processing of waste as an alternative fuel for energy and material recovery proposals.

The oil collected from the Brazilian coast was applied as Refuse Derived Fuel to replace petroleum coke in co-processing industries, proving to be a promising alternative for energy recovery, capable of transforming residues with no recycling potential into a high calorific power raw material for another industrial process. The article aims to present analysis on the co-processing of waste material in a cement



Fig. 2 Locations on the Brazilian coast affected by oil spill from 30/08/2019 to 19/03/2020 [6]

kiln from the oil spill in the Brazilian blue amazon based on official reports and secondary data.

## 2 Methodology

This article is predominantly theoretical and bibliographical since it is presented secondary data obtained from external access to public documents, studies, official reports and scientific articles through Science Direct and Scielo databases. Reflections and analysis are presented about the energy use of the amount of waste collected on the Brazilian coast in order to bring to light the co-processing process as an interesting waste-to-energy technology, capable of reusing waste with no recycling potential.

### 3 Discussion and Analysis

Researchers from the Laboratory of Computational Methods in Engineering (LAMCE) at the Federal University of Rio de Janeiro (UFRJ) identified three possible regions of the oil spill origin, according to the spread of ocean currents on the Brazilian coast from information obtained until September/2019: (1) approximately 350 km from the coast of the state of Paraíba; (2) 600 km from the border between the states of Pernambuco and Alagoas; (3) 400 km from the border between the states of Alagoas and Sergipe [8]. Figure 3 shows the direction of the oil spill movement.

The following scenario of disorganization, inefficient communication, and the absence of a health crisis cabinet led to a mobilization of thousands of volunteers (such as artisanal fishermen and local residents) unprotected by equipment and vulnerable to contamination by oil derivatives—such as benzene and aromatic hydrocarbon. Thus, exposing the lack of financial resources and the fragility of the country's emergency health actions [9].

According to internal data from the Brazilian Navy, responsible for investigating this environmental crime, 5379.76 tons of waste were collected—30% of which was oil. The collected oil presented a carcinogenic substance, either by inhalation, ingestion or direct contact [10] and therefore, it was packaged in bags—as shown in Fig. 4.

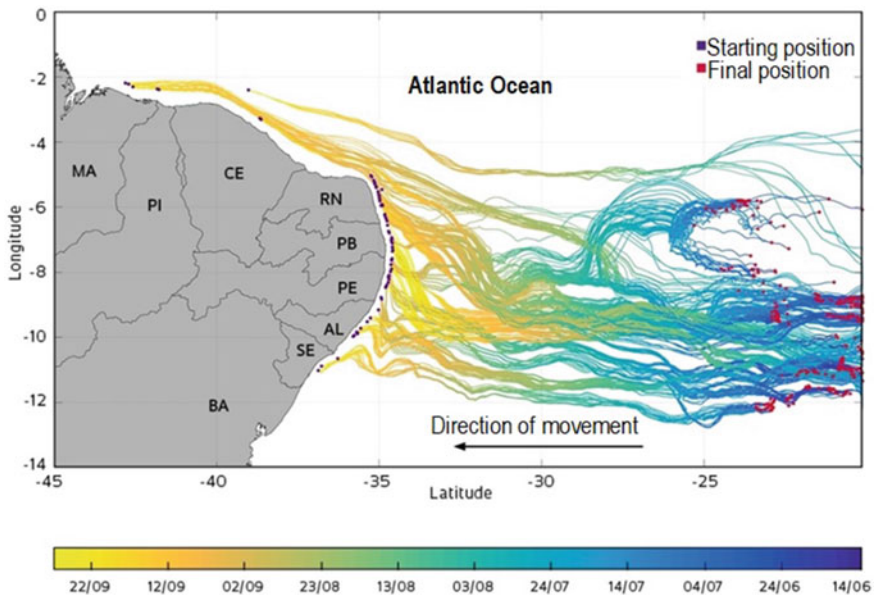


Fig. 3 Oil spill trajectories [8]



**Fig. 4** Collection and packaging of crude oil in bags [10]. *Photo* Sidney Vieira

Analyses performed by gas chromatography (fingerprinting) indicated the possibility of the material being crude oil due to its light hydrocarbon fraction loss by evaporation [11]. The waste material was a highly weathered heavy crude oil with high viscosity properties, high concentrations of medium and long-chain hydrocarbons, and very low concentrations of aromatic hydrocarbons [12].

A team from the Geosciences Institute (IGEO) of the University of Bahia analyzed the chemical composition by gas chromatography coupled to mass spectrometry (charge/mass ratio comparison standard of ion 191) of an oil sample collected on the coast of the state of Bahia in October/2019. Such analysis indicated a high geochemical similarity to an oil of Venezuelan origin [8, 11], as shown in Fig. 5; whose hypothesis was also confirmed by Petrobras.

After the oil spill process in a marine environment, it is initiated a sequence of changes in the chemical composition of the product (known as weathering). And, subsequently, the prediction of behavior and destination of the oil are influenced by certain factors such as the amount of oil spill, its initial physical and chemical characteristics, duration, and the climatic conditions and oceanographic hydrodynamics [13].

In addition to the uncountable environmental and financial damages, choosing appropriate treatment and destination for those tons of oil spilled on the coast was necessary instead of final disposal in landfills. Therefore, the amount of waste was mainly collected by volunteers and reused for energy purposes as raw material in cement kilns. Through external access to public data of the Brazilian Institute of Environment and Renewable Natural Resources (IBAMA), the oil collected was destined to cement kilns with license for co-processing, such as Votorantim Cimentos—in the



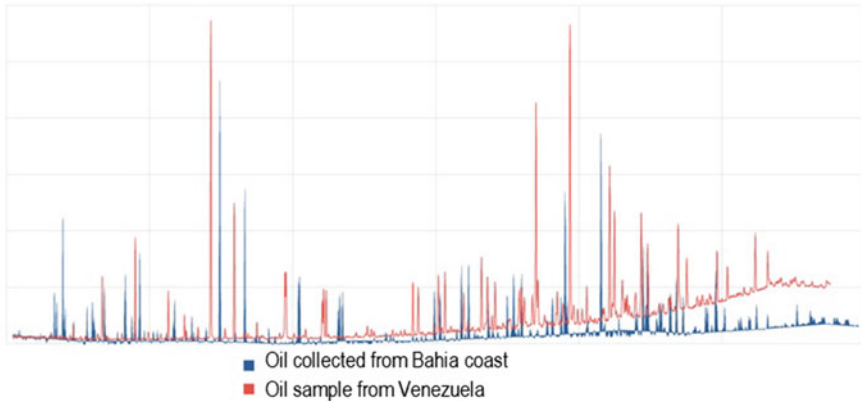


**Fig. 5** Comparison of the compositions of oil samples from Venezuela and those collected on the coast of Bahia [8]

units of Laranjeiras (located in Sergipe state) and Sobral (located at Ceará state)—and Mizu Cimentos—in Baraúna (located at Rio Grande do Norte state)—for energy purpose in their respective industries. After treatment, part of the oil collected on the coast of Ceará state was reused as an alternative fuel at the Apodi Cement Factory, being completely destroyed inside the kiln by a heat up to 2000 °C [14].

It is worth mentioning that to achieve a successful RDF production, some prerequisites are desired:

- Waste used for alternative fuel purpose need to maintain its basic parameters regularity, such as particle size, high calorific value, moisture, and ashes;
- Waste with the potential to substitute raw materials in another process needs to achieve similar characteristics to the original components used in the industry;
- Homogeneous characteristics of RDF are critical and can be obtained at the end of the blending stage;
- The RDF pre-treatment unit needs to be located near and integrated into the consumption unit due to transportation costs and long-term contracts.

During clinker production, calcium oxide reacts in the kiln at high temperatures (1400–1500 °C) with silica, alumina and ferrous oxide to form silicates, aluminates, and ferrites that compose the clinker—which is cooled and then ground with gypsum and some additives in order to produce cement [15]. The waste processing in rotary kilns is under conditions of high temperature, alkalinity, oxidizing atmosphere, favorable mixture of gases and products, and ideal residence time (> 2 s) for the destruction of hazardous waste [16], avoiding possible problems with dioxins and furans. The activity of waste co-processing in rotary kilns for clinker production is licensed in Brazil by Conama Resolution 499/20 [17] (Conama—“*Conselho Nacional do Meio Ambiente*”—is the Brazilian Environment Council).

The RDF production is one of the main waste-to-energy processes, in which waste goes through several treatment stages until it is transformed into a substrate with great

potential of replacing fossil fuels—such as coke and coal—and which can be used as raw material in other industries processes without changing the final quality of product [18]. Therefore, the original concept is to recover energetically the waste that was supposed to be previously disposed of in landfills without any kind of reuse and/or recycling.

The RDF is a term applied to high calorific value materials (generally, 18 Mega-joules per kilogram) recovered after the waste collection, sorting and treatment stages [19]. The calorific value of one ton of oil is equivalent to four tons of waste, so if this amount of waste was energetically reused it could avoid atmospheric emissions released by fossil derivative burning [20]. Thus, the use of waste in industrial processes, especially in co-processing, reduces fossil derivatives consumption and, consequently lowers carbon dioxide emissions.

Of the seven cement plants in the Northeast region, five received the oil residue collected on the coast, and therefore, the waste was used as an alternative fuel in cement kilns instead of being disposed in landfills [21]. Part of the amount collected on the Brazilian coast was also sent to the treatment center Ecoparque Pernambuco (located in the State of Pernambuco), which received in just two days around 100 tons of waste and then, it was mixed with another types of waste and after two stages of grinding transformed into a blend of high energy potential to be used as a fuel in industries [22] (Figs. 6, 7).

With this, it is possible to observe the co-processing of oil in cement kilns presented itself as a viable and feasible technology for energy recovery of the amount



**Fig. 6** Receiving of oil collected from the Brazilian Coast at Ecoparque Pernambuco [22]. *Photo* Bobby Fabisak



**Fig. 7** Mixture and grinding processes for blend transformation [22]. *Photo Bobby Fabisak*

of waste from the oil spill on the Brazilian Coast in 2019. The RDF process collected such waste and was treated and transformed into raw material in the industry. It is worth pointing out that the Refuse Derived Fuel is obtained after a preheat treatment stage. Therefore, it is not an alternative to landfills (type of final disposal) but rather a waste energy recovery technology.

## 4 Conclusions

The present article showed that co-processing presents itself as a technology with excellent development potential for waste energy recovery, especially concerning cement kilns. The study showed the oil collected on the Brazilian coast from a crude oil spill was transformed into refuse derived fuel (RDF) and applied as raw material in cement industries. Thus, the application of high calorific value waste as a substrate in industrial processes, either as a fuel or as thermal power generation, proved to be feasible and viable, and also can replace fossil fuel derivatives and reduce GHG emissions. Finally, the production of RDF shows to be a promising application of waste-to-energy since allows the energy recovery of the amount of waste that would previously be disposed of to landfills without being recycled or treated.

**Acknowledgements** This study was financed in part by the Coordenação de Aperfeiçoamento de Pessoal de Nível Superior—Brasil (CAPES)—Finance Code 001. For those who believe in science.

## References

1. BRASIL (2022) Ministério da Defesa. Marinha do Brasil. SISGAAZ: Proteção e Monitoramento das Águas Jurisdicionais Brasileiras. <SisGAAZ: Proteção e Monitoramento das Águas Jurisdicionais Brasileiras/Marinha do Brasil>. Accessed 29 April 2022
2. SISGAAZ (2015) Sistema de Gerenciamento da Amazônia Azul. Brasília. <DefesaNet - SisGAAZ - Amazônia Azul: Brasil confirma sua influência do outro lado do Atlântico>. Accessed 28 April 2022
3. Brum HD, Campos-Silva JV, Oliveira EG (2020) Brazil oil spill response: government inaction. *Science* 367(6474):155–156
4. IBAMA (2020) Instituto Brasileiro do Meio Ambiente e dos Recursos Naturais Renováveis. Ministério do Meio Ambiente. Cartilha informativa sobre a trajetória do acidente. Brasília. <cartilha\_v2.indd (ibama.gov.br)>. Accessed 30 April 2022
5. BRASIL (2020) Ministério da Defesa. Marinha do Brasil. Brasília. <DefesaNet - SisGAAZ - MB - Investigação Lançamento de Óleo>. Accessed 29 April 2022
6. IBAMA (2020) Instituto Brasileiro do Meio Ambiente e dos Recursos Naturais Renováveis. Ministério do Meio Ambiente. Localidades afetadas. Brasília. <2020-03-19\_LOCALIDADES\_AFETADAS.pdf (ibama.gov.br)>. Accessed 30 April 2022
7. PLANSAB (2019) Plano Nacional de Saneamento Básico. Ministério do Desenvolvimento Regional. Caderno Temático Recuperação Energética de Resíduos Sólidos Urbanos. Caderno coordenado pelo Deutsche Gesellschaft für Internationale Zusammenarbeit (GIZ) com apoio da Technische Universität Braunschweig. Brasília
8. Fioravanti C (2019) Os caminhos da mancha. Pesquisa FAPESP. <Os caminhos da mancha: Revista Pesquisa Fapesp>. Revista Pesquisa Fapesp. Accessed 01 May 2022
9. Pena PGL, Northcross AL, Lima MAG, RÊGO RCF (2020) The crude oil spill on the Brazilian coast in 2019: the question of public health emergency. Thematic section: public health emergencies in debate. *Cadernos de Saúde Pública* 36(2):e002301019
10. Araújo ME, Ramalho CWN, Melo PW (2020) Pescadores artesanais, consumidores e meio ambiente: consequências imediatas do vazamento de petróleo no Estado de Pernambuco, Nordeste do Brasil. *Cadernos de Saúde Pública* 36(1)
11. UFBA (2019) Universidade Federal da Bahia. Análises do Lepetro/Igeo indicam correlação entre óleo encontrado nas praias do Nordeste e petróleo venezuelano. Bahia. <[https://ufba.br/ufba\\_em\\_pauta/analises-do-lepetroigeo-indicam-correlacao-entre-oleo-encontrado-nas-praias-do](https://ufba.br/ufba_em_pauta/analises-do-lepetroigeo-indicam-correlacao-entre-oleo-encontrado-nas-praias-do)>. Accessed 30 April 2022
12. IBAMA (2020) Instituto Brasileiro do Meio Ambiente e dos Recursos Naturais Renováveis. Ministério do Meio Ambiente. Orientação técnica: vistoria de acompanhamento e limpeza do litoral. Brasília. <<https://www.ibama.gov.br/phocadownload/emergenciasambientais/2019/manchasdeoleo/10.pdf>>. Accessed 30 April 2022
13. BRASIL (2020) Ministério da Defesa. Marinha do Brasil. Informações sobre o óleo. Disponível em. <Informações sobre o Óleo/Marinha do Brasil>. Accessed 29 April 2022
14. ABCP (2019) Associação Brasileira de Cimento Portland. São Paulo. <<https://abcp.org.br/oleo-de-praias-sera-coprocessado-pela-industria-de-cimento/>>. Accessed 01 May 2022
15. Kaddatz KT, Rasul MG, Rahman A (2013) Alternative fuels for use in cement kilns: process impact modelling. *Proc Eng* 56:413–420
16. Rocha SDF, Lins VFC, Santo BCE (2011) Aspectos do coprocessamento de resíduos em fornos de clínquer. *Engenharia Sanitária Ambiental* 16(1):1–10
17. BRASIL (2020) MMA: Ministério do Meio Ambiente. Resolução Conama 499, de 06 de outubro de 2020. Dispõe sobre o licenciamento da atividade de coprocessamento de resíduos em fornos rotativos de produção de clínquer. Diário Oficial da União. Brasília, 2020. BRASIL
18. Lamas WQ, Palau JCF, Camargo JR (2013) Waste materials co-processing in cement industry: ecological efficiency of waste reuse. *Renew Sustain Energy Rev* 19:200–207
19. BNDES (2014) Banco Nacional de Desenvolvimento Econômico e Social. Análise das Diversas Tecnologias de Tratamento e Disposição Final de Resíduos Sólidos Urbanos no Brasil, Europa,

- Estados Unidos e Japão. Fundação de Apoio ao Desenvolvimento da Universidade Federal de Pernambuco (FADE/UFPE). BNDES
20. Cardoso MT (2019) Regulação em aproveitamento energético de resíduos: proposições para o Brasil com base no estudo de caso sueco. 2019. 242 f. Tese (doutorado). Instituto de Energia e Ambiente, Universidade de São Paulo. São Paulo
  21. ABCP (2020) Associação Brasileira de Cimento Portland. São Paulo. <&lt;<https://coprocessamento.org.br/oleo-no-litoral-o-destino-dos-residuos-retirados-das-praias/&gt;>>. Accessed 01 May 2022
  22. Vieira F (2019) Saiba para onde vai e o que é feito do óleo do desastre ambiental do Nordeste. Jornal do Commercio, 22 out 2019. <<https://jc.ne10.uol.com.br/canal/cidades/cienciamambiente/noticia/2019/10/22/saiba-para-onde-vai-e-o-que-e-feito-do-oleo-do-desastre-ambiental-do-nordeste-391047.php>>. Accessed 03 May 2022

# Sulfate Contamination in Groundwater Nearby Reclaimed Waste Management Site: Case Study



Eugeniusz Koda , Anna Podlasek , Magdalena Daria Vaverková ,  
and Petra Martínez Barroso 

**Abstract** The most common form of sulfur (S) occurring in water is sulfate ( $\text{SO}_4^{2-}$ ).  $\text{SO}_4^{2-}$  is widely distributed in natural environment in concentrations ranging from a few to several thousand milligrams per liter and plays an important role in biogeochemical cycles. As the  $\text{SO}_4^{2-}$  salts are often major contaminants in water, there is a real need to perform scientific research aiming at the investigation of sources, transport and fate of  $\text{SO}_4^{2-}$  to maintain the safety of the environment and human health. The aim of presented study was to assess the groundwater contamination by  $\text{SO}_4^{2-}$  originating from the waste management site (Lubna landfill) located in Poland. The investigation of  $\text{SO}_4^{2-}$  sources and changes in  $\text{SO}_4^{2-}$  concentrations in groundwater was performed on the basis of monitoring network of piezometers. The research provides the outcomes of a long-term groundwater quality analysis and the insights on temporal changes of this parameter. The monitoring results were compared with the Polish standards, and the quality of groundwater within the Lubna landfill and its vicinity were assessed. The application of remedial works was also discussed as a solution for the reduction of further contamination.

**Keywords** Landfill · Pollution · Groundwater · Monitoring · Reclamation

---

E. Koda (✉) · A. Podlasek · M. D. Vaverková  
Department of Revitalization and Architecture, Institute of Civil Engineering, Warsaw University of Life Sciences – SGGW, Warsaw, Poland  
e-mail: [eugeniusz\\_koda@sggw.edu.pl](mailto:eugeniusz_koda@sggw.edu.pl)

A. Podlasek  
e-mail: [anna\\_podlasek@sggw.edu.pl](mailto:anna_podlasek@sggw.edu.pl)

M. D. Vaverková  
e-mail: [magdalena\\_vaverkova@sggw.edu.pl](mailto:magdalena_vaverkova@sggw.edu.pl)

M. D. Vaverková · P. M. Barroso  
Department of Applied and Landscape Ecology, Faculty of AgriSciences, Mendel University in Brno, Brno, Czech Republic  
e-mail: [petra.barroso@mendelu.cz](mailto:petra.barroso@mendelu.cz)

## 1 Introduction

Landfilling is still the most common method of disposing the municipal solid wastes (MSW). Nevertheless, there are a number of environmental nuisances related to landfilling.

Above all, disposal of MSW in landfills constitutes a considerable source of groundwater pollution and therefore landfills have been identified as one of the major threats to water resources [1]. Harmful impact of landfills is visible to both surface and groundwater resources which results from the toxicity of the leachate and its subsequent migration [2, 3].

In recent years, there have been several studies conducted to assess pollution level at the landfill sites and their surroundings [4–8]. Basically, such studies concerned the monitoring of the concentrations of pollution indicators in groundwater and then comparison of measured values with the standards for respective contaminant.

In case of landfills, the sulfate ion ( $\text{SO}_4^{2-}$ ) is, next to the chloride ion ( $\text{Cl}^-$ ), the basic indicator of the penetration of pollutants into groundwater.  $\text{SO}_4^{2-}$  is the basic form of S in groundwater. The form of S compounds in waters strongly depends on oxidation–reduction conditions. Under oxidative conditions,  $\text{SO}_4^{2-}$  is stable and usually is not adsorbed. Nevertheless, under strongly reducing conditions, it can undergo biochemical reduction to hydrogen sulfide ( $\text{H}_2\text{S}$ ) and sulfides ( $\text{S}^{2-}$ ).

Moreover, it is commonly revealed that a serious source of  $\text{SO}_4^{2-}$  in shallow groundwater is the oxidation of S introduced through anthropogenic activities, such as in the process of burning fossil fuels and smelting metals or in the process of mining waste storage. The source of  $\text{SO}_4^{2-}$  can also be the oxidation of organic S contained in soil as well as in sewage and municipal waste landfills. Generally, every type of human activity involves the emission of volatile, liquid or solid waste containing  $\text{SO}_4^{2-}$  or S compounds capable of processing into  $\text{SO}_4^{2-}$  [9].

Areal sources of  $\text{SO}_4^{2-}$  contamination mainly concern MSW and industrial waste landfills. High  $\text{SO}_4^{2-}$  concentrations are, for example, observed in the vicinity of ash landfills (on average 670 mg/L, maximum 2300 mg/L), mining and industrial landfills (up to 3000 mg/L) or MSW landfills (340–3000 mg/L) [10].

Several studies on groundwater quality assessment near landfills revealed that increased concentrations of  $\text{SO}_4^{2-}$  might be attributed to the leachate effluents. This phenomena was confirmed by Abd El-Salam and Abu-Zuid [11] who performed monitoring studies within the landfill site in Egypt. The mentioned authors showed that due to leachate impact, the concentrations of  $\text{SO}_4^{2-}$  measured in groundwater were at the level higher than 543 mg/L.

Alam et al. [12] pointed out that the reason due to which groundwater within the landfill area had been found as polluted was the migration of leachate. Lebedeva et al. [13] also pointed out that the high content of  $\text{SO}_4^{2-}$  in groundwater, as a product of the microbial activity, might be observed in the areas of reclaimed landfill.

The objective of this study was to characterize the quality of groundwater near the Lubna landfill in Poland, with a special attention given to  $\text{SO}_4^{2-}$  as one of the primary indicator of groundwater pollution.

## 2 Materials and Methods

### 2.1 Description of the Study Site

The Lubna landfill is an embankment type structure, located approximately 30 km south from the city of Warsaw, Poland (Fig. 1).

The area of the landfill belongs to Góra Kalwaria district, and partially (the north-east corner of the landfill) to the Konstancin-Jeziorna district. It covers an area of approximately 22 ha, and the height of the landfill is almost 60 m. The nearest western surroundings of the landfill are wastelands with grassland plants. Further from the landfill, there are forest, grasslands and arable fields.

The storage of MSW in the Lubna landfill began in 1978 in a wetland area which was not prepared for landfilling purposes. Therefore, since 1996, reclamation works have been carried out and included the construction of the cut-off wall around the landfill, leachate drainage system, berms and degassing and mineral capping system. The cut off-wall of 0.6 m thickness and length of ca. 2000 m composed of bentonite material. The depth of the cut-off wall (5.5–17.0 m) depended on hydrogeological conditions, therefore it was installed c.a. 2.0 m below impermeable soil layers.

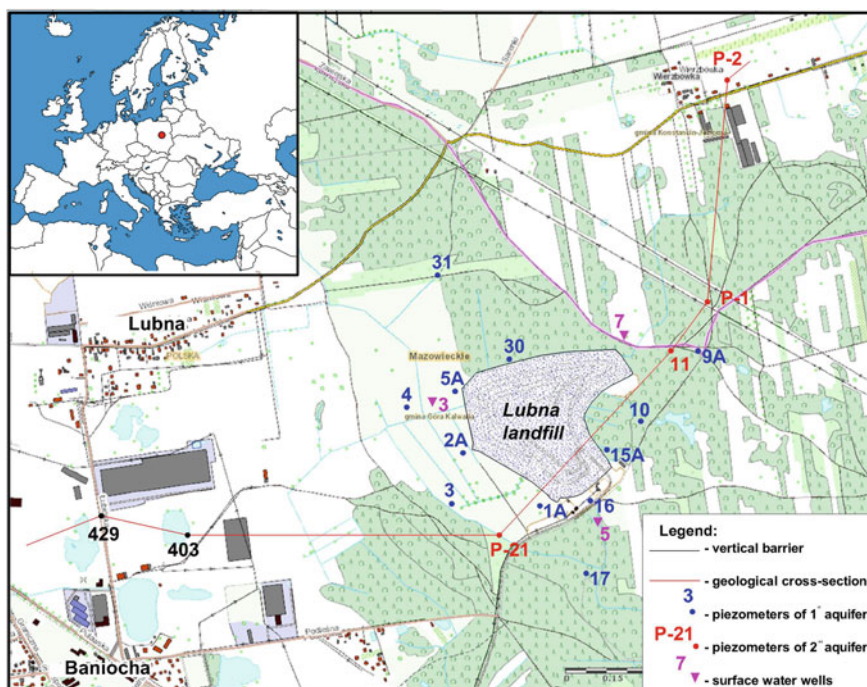


Fig. 1 Location of the Lubna landfill and its monitoring network



There are two quaternary aquifers observed at the landfill site. The first level of groundwater table is located within topsoil consisting of fluvioglacial sands. The depth of groundwater table in this level was measured in the range 0.1–1.8 m. The second aquifer is located within a layer of Masovian interglacial saturated sands of 40 m thickness and is a primary usable level (Quaternary). It is separated from the first aquifer by two layers of boulder clay. The groundwater table was measured at the depth of 10–11 m (piezometer P-21 located upstream the landfill) and at the depth of 24.5–27 m (piezometer P-1 and P-2 located downstream the landfill).

Measurements in existing piezometers indicate that the directions of water flow are mainly to the north-west and south-east. These directions are susceptible to seasonal oscillations that depend on the groundwater level of the first aquifer horizon. The monitoring network of the Lubna landfill consists of twelve shallow piezometers and four deep wells (P-1, P-2, 11, P-21), providing records since 1994. The monitoring network of the first aquifer consists of three piezometers located on the east side (9A, 10, 15A), seven piezometers within the zone of groundwater discharge from the landfill concerning three on the south (1, 16, 17) and four on the west (2A, 3, 4, 5A). There are also two piezometers (30 and 31), located to the north where the groundwater inflow was indicated. The observations conducted during the monitoring period allowed for tracking changes of groundwater quality and assessment of the efficiency of reclamation works carried out at that site.

## 2.2 *Sampling and Experimental Analysis*

The samples were collected from the piezometers located within the Lubna landfill site using an immersed pump. Each pumping was performed with measurements of parameters: pH, temperature and electrical conductivity. Since 2006, the samples were collected once every six months, and between 2007 and 2010 the frequency was doubled, with respect to the time schedule adopted according to the Polish standards.

Due to the landfill closure in March 2011, the measurements were again limited to one every six months. Groundwater samples were collected into smoked glass bottles and stored in the laboratory refrigerator until the analysis.  $\text{SO}_4^{2-}$  were measured by a gravimetric method and then, the assessment of groundwater quality was based on a comparison of  $\text{SO}_4^{2-}$  concentration in collected samples with levels required by the Polish law [14].

## 3 Results and Discussion

Regarding the requirements for a good chemical status of groundwater, pointing out the maximum allowable concentration of  $\text{SO}_4^{2-}$  at the level of 250 mg/L, it can be stated that mean concentrations observed in piezometers located at the east side from the Lubna landfill did not show alarming values. Both, before and after the

construction of the cut-off wall, the mean concentrations measured are within the range of acceptable values (Table 1). For piezometers located in the south site (zone of groundwater discharge), it was observed that significant temporal fluctuations of  $\text{SO}_4^{2-}$  concentrations occurred. Changes of  $\text{SO}_4^{2-}$  concentrations in groundwater, with regard to temporal aspects, can be also linked to the groundwater level changes. It was indicated that if the groundwater level was higher, the lower concentration of  $\text{SO}_4^{2-}$  was observed. Similar phenomena of the dependence of pollutant concentrations and groundwater level was presented by Koda et al. [6, 15]. The maximum concentrations of  $\text{SO}_4^{2-}$  in selected piezometers exceeded the permissible level. Nevertheless, the mean values measured during the monitoring period did not exceed the allowable 250 mg/L and therefore are within the range of good chemical status.

The maximum concentrations of  $\text{SO}_4^{2-}$  measured in piezometers located in the west side (discharge zone) are at higher level than acceptable. The maximum concentrations observed in these piezometers are up to four times higher than the permissible limit. Mean values of  $\text{SO}_4^{2-}$  concentrations are higher than 250 mg/L only in piezometers 2A and 3. For other piezometers located in the west side, at the direction of groundwater discharge, the average concentrations of  $\text{SO}_4^{2-}$  are lower than 250 mg/L and in overall indicate a good groundwater chemical status observed in that site.

The concentrations of  $\text{SO}_4^{2-}$  measured in the north site, at the direction of groundwater inflow, indicate no exceeding above the limit. By means of  $\text{SO}_4^{2-}$  concentrations, the observed values are characteristic for a good groundwater chemical status and indicate no impact of external sources on groundwater quality within the landfill area.

**Table 1** Statistical summary of  $\text{SO}_4^{2-}$  concentrations (mg/L) in groundwater before and after the cut-off wall installation

Piez	Location	Before				After			
		Min	Max	Mean	SD	Min	Max	Mean	SD
9	East	16	140	73.33	40.29	4.39	923	216.50	159.61
10		21	146	69.33	37.46	6.36	196	70.35	47.73
15A		–	–	–	–	2.00	569	115.53	122.88
1	South (discharge zone)	34	225	117.38	69.38	4.90	374	140.50	73.08
16		–	–	–	–	22.80	630	207.60	108.48
17		–	–	–	–	29.04	562	201.11	76.64
2A	West (discharge zone)	53	153	97.75	34.30	53.10	1090	<b>626.48</b>	245.53
3		53	470	165.22	149.42	53.00	795	<b>310.35</b>	228.51
4		16	293	123.53	93.78	12.00	312	135.42	59.82
5A		26	206	139.00	66.80	15.40	704	137.10	106.43
30	North (inflow)	–	–	–	–	9.00	168	50.40	45.29
31		–	–	–	–	9.96	122	40.15	26.59

Considering changes of  $\text{SO}_4^{2-}$  concentrations in time, a statement can be made that a progressive improvement of groundwater quality is observed after the closure of the cut-off wall introduced in the area, as a part of the reclamation work carried out at the landfill. This can be observed in each piezometer in the zone of groundwater discharge on the west side of the landfill, with the exception of the period when the transitory increase occurred due to groundwater level changes. The fluctuations in  $\text{SO}_4^{2-}$  concentrations in groundwater at the south side of the landfill also show the decreasing manner with time, with some peaks observed during the monitoring period. In general, the concentrations of  $\text{SO}_4^{2-}$  measured in groundwater samples collected from the south side of the landfill are characteristic for the second and the third class of groundwater quality. Temporarily, the groundwater in that area is considered to be highly polluted (5th class of groundwater quality).

The greatest diversity of the range of  $\text{SO}_4^{2-}$  concentrations in groundwater is observed for the piezometers located in the east side of the Lubna landfill. There is a strong probability that it can be attributed to the closest vicinity to the arable fields and landfill's facilities that can pose the external source of  $\text{SO}_4^{2-}$  contamination to groundwater. Based on the performed monitoring studies, it can be said that the analyzed shallow aquifer was contaminated by the landfill leachate and contaminants, washed out from rainfall water, coming from infiltration through the wastes disposed on the landfill from 1978 to 1998.

The results of monitoring records from the piezometers located in the north from the landfill indicate that the groundwater in the inflow direction is not contaminated by  $\text{SO}_4^{2-}$ . The concentrations observed there are in the range characteristic for the good chemical status.

It was also revealed that currently observed concentrations of  $\text{SO}_4^{2-}$  in each piezometer located within the landfill site indicate the good status of groundwater quality (Table 2). Moreover, the quality of groundwater in the vicinity of piezometers 10 at the east side and 31 at the north side of the landfill are characteristic for the first class of groundwater quality according to Regulation of the Ministry of Marine Economy and Inland Navigation of Poland [14]. Currently measured  $\text{SO}_4^{2-}$  concentrations also reflect the conditions of improving the quality of the groundwater in the Lubna landfill after introducing the cut-off wall and adopting other reclamation works.

Similar findings, based on the long-term monitoring studies at the Polish landfill site, as in our research, were acquired by Janas and Zawadzka [16] and ascertained that  $\text{SO}_4^{2-}$  concentrations are susceptible to significant temporal changes. The mentioned authors observed the fluctuations of  $\text{SO}_4^{2-}$  concentrations in groundwater in the range between 200 and 1400 mg/L, which means that in some points of monitoring period, the groundwater at the landfill site was highly polluted (5th class of groundwater quality). This was justified as a result of a direct penetration of leachate from the landfill to the groundwater.

For comparison, studies performed by Han et al. [17] revealed that the concentrations of  $\text{SO}_4^{2-}$  in groundwater at the landfill sites in China were observed at the level even up to 3160 mg/L, whereas the average concentrations of this ion in groundwater were equal to 141 mg/L. It indicates that the concentrations of  $\text{SO}_4^{2-}$  in groundwater

**Table 2** Actual concentrations of  $\text{SO}_4^{2-}$  in groundwater within the Lubna landfill site

Piez	Location	Sulfate concentration (mg/L)	Chemical status
9	East	149.0	Good
10		64.0	
15A		229.0	
1	South (discharge zone)	160.0	
16		128.0	
17		80.0	
2A	West (discharge zone)	175.0	
3		166.0	
4		40.0	
5A		103.0	
30	North (inflow)	72.0	
31		63.0	

show significant fluctuations with peaks observed at the levels many times higher than the acceptable 250 mg/L. Nevertheless, taking into consideration the average observed values for groundwater samples collected from the Chinese landfill sites, it can be stated that  $\text{SO}_4^{2-}$  in groundwater observed due to leachate migration do not contribute a serious problem to groundwater quality.

## 4 Conclusions

Systematically collected monitoring data of the Lubna landfill indicate that the landfill itself contributes a source of  $\text{SO}_4^{2-}$  contamination to groundwater.

It was proved that the application of the cut-off wall around the landfill had a positive impact on the groundwater quality and the levels of pollution indicator in groundwater. The process of improving the status of groundwater quality was extended in time, but currently the concentrations of  $\text{SO}_4^{2-}$  show that the groundwater within the landfill site has a good chemical status and no penetration of leachate from the landfill is observed. In some parts of the study site, the concentrations are typical for the first class of groundwater quality and in the range of the geochemical background. According to collected monitoring data, there is also a temporal pattern of  $\text{SO}_4^{2-}$  concentration fluctuations observed in the study area, strictly related to the changes of groundwater level. The monitoring results presented in this research clearly indicate efficiency of the cut-off wall application and its crucial role in protecting the soil–water environment from  $\text{SO}_4^{2-}$  migration within the landfill area.

Following outcomes of presented study it would be recommended to perform reclamation works, with a special attention given to the application of the cut-off

walls surrounding landfills, to prevent the migration of leachates to further distances from the landfill and to reduce the concentrations of pollutants in groundwater.

## References

1. Vaverková MD, Adamcová D, Zloch J, Radziemska M, Boas Berg A, Voběrková S, Maxianová A (2018) Impact of municipal solid waste landfill on environment: a case study. *J Ecol Eng* 19(4):55–68. <https://doi.org/10.12911/22998993/89664>
2. Przydatek G, Kanownik W (2019) Impact of small municipal solid waste landfill on groundwater quality. *Environ Monit Assess* 191:169. <https://doi.org/10.1007/s10661-019-7279-5>
3. Dominijanni A, Manassero M (2021) Steady-state analysis of pollutant transport to assess landfill liner performance. *Environ Geotech* 8(7):480–494. <https://doi.org/10.1680/jenge.19.00051>
4. Kapelewska J, Kotowska U, Karpińska J, Astel A, Zieliński P, Suchta J, Algrzyrna K (2019) Water pollution indicators and chemometric expertise for the assessment of the impact of municipal solid waste landfills on groundwater located in their area. *Chem Eng J* 359:790–800. <https://doi.org/10.1016/j.ccej.2018.11.137>
5. Koda E, Sieczka A, Osinski P (2016) Ammonium concentration and migration in groundwater in the vicinity of waste management site located in the neighborhood of protected areas of Warsaw. Poland. *Sustain* 8:1253. <https://doi.org/10.3390/su8121253>
6. Koda E, Miszkowska A, Osinski P, Sieczka A (2020) Heavy metals contamination within restored landfill site in Poland. *Environ Geotech* 7:512–521. <https://doi.org/10.1680/jenge.18.00031>
7. Przydatek G (2019) Multi-indicator analysis of the influence of old municipal landfill sites on the aquatic environment: case study. *Environ Monit Assess* 191:773. <https://doi.org/10.1007/s10661-019-7814-4>
8. Podlasek A, Jakimiuk A, Vaverková MD, Koda E (2021) Monitoring and assessment of groundwater quality at landfill sites: selected case studies of Poland and the Czech Republic. *Sustain* 13:7769. <https://doi.org/10.3390/su13147769>
9. Venkatesan G, Swaminathan G (2009) Review of chloride and sulphate attenuation in ground water nearby solid-waste landfill sites. *J Environ Eng Landsc* 17(1):1–7. <https://doi.org/10.3846/1648-6897.2009.17.1a-Ig>
10. Szczepańska J, Twardowska I (2004) Mining waste. In: Twardowska I (ed) *Solid waste: assessment, monitoring and remediation*, waste management series, vol 4. Elsevier, Amsterdam, pp 319–385
11. Abd El-Salam MMA, Abu-Zuid GI (2015) Impact of landfill leachate on the groundwater quality: a case study in Egypt. *J Adv Res* 6:579–586. <https://doi.org/10.1016/j.jare.2014.02.003>
12. Alam P, Sharholy M, Ahmad K (2020) A study on the landfill leachate and its impact on groundwater quality of Ghazipur Area, New Delhi, India. In: Kalamdhad A (eds) *Recent developments in waste management*. Lecture notes in civil engineering, vol 57. Springer, Singapore, pp 345–358
13. Lebedeva YY, Kotiukov P, Lange I (2020) Study of the geo-ecological state of groundwater of metropolitan areas under the conditions of intensive contamination thereof. *J Ecol Eng* 21(2):157–165. <https://doi.org/10.12911/22998993/116322>
14. Regulation of the Ministry of Marine Economy and Inland Navigation of Poland Dated 11 October 2019 on the criteria and method of evaluating the underground water condition. *Journal of Laws* No. 2148, 1–9 (in Polish). <http://prawo.sejm.gov.pl/isap.nsf/download.xsp/WDU20190002148/O/D20192148.pdf>. Accessed 03 April 2020
15. Koda E, Osinski P, Kolanka T (2013) Flow numerical modeling for efficiency assessment of vertical barriers in landfills. In: Manassero M, Dominijanni A, Foti S, Musso G (eds) *Coupled phenomena in environmental geotechnics*. CRC Press, London, pp 693–698

16. Janas M, Zawadzka A (2018) Assessment of the monitoring of an industrial waste landfill. *Ecol Chem Eng S* 25(4):659–669. <https://doi.org/10.1515/eces-2018-0044>
17. Han Z, Ma H, Shi G, He L, Wei L, Shi Q (2016) A review of groundwater contamination near municipal solid waste landfill sites in China. *Sci Total Environ* 569–570:1255–1264. <https://doi.org/10.1016/j.scitotenv.2016.06.201>

# Challenges in Teaching Geoenvironmental Engineering Course



Luis F. M. Ribeiro, Jyoti K. Chetri, and Krishna R. Reddy

**Abstract** Geoenvironmental engineering is a multidisciplinary field which focuses on providing engineering solutions to the environmental problems such as subsurface contamination. It requires knowledge of multiple disciplines such as geotechnical engineering, chemistry, biology, and environmental engineering. The growing events of environmental pollution have resulted in rapid advancements in the field of geoenvironmental engineering. Many advanced subsurface containment and remediation technologies have been developed. However, academic progression of geoenvironmental engineering is not in line with the professional advancement. Geoenvironmental engineering is not taught as a formal course in many academic institutions across the world. There are many challenges faced by the academic institutions to introduce and teach geoenvironmental engineering as a formal course. There is a need to devise strategies and methodologies to teach geoenvironmental engineering course in academic institutions. In this study, several challenges in teaching geoenvironmental engineering course were identified and ranked based on a survey. The survey was distributed among the professionals and academics working in the field of geoenvironmental engineering. Two main categories of challenges were identified: implementation challenges and acceptance challenges. Five challenges under each category were shortlisted and were ranked on a scale of 1–5, 1 being the least important and 5 being the most important, in the survey. The collected data were analyzed in terms of the rankings assigned by the group of respondents via the multi-criteria decision technique TOPSIS, which allowed ranking the challenges. Top three challenges in each category were selected as the basis for devising strategies and methodologies for introducing and teaching geoenvironmental engineering course. Not having expertise to teach geoenvironmental engineering was found to be the most critical challenge which needs to be addressed for successful implementation of geoenvironmental engineering course in academic institutions.

---

L. F. M. Ribeiro  
University of Brasília, Brasília, DF 70910.900, Brazil

J. K. Chetri · K. R. Reddy (✉)  
University of Illinois at Chicago, Chicago, IL 60607, USA  
e-mail: [krreddy@uic.edu](mailto:krreddy@uic.edu)

**Keywords** Geoenvironmental engineering · Teaching challenges · Implementation challenges · Acceptance challenges · TOPSIS

## 1 Introduction

Rapid industrialization and economic growth, especially during the twentieth century, resulted in the production and release of various chemicals and their by-products into the environment, leading to the contamination of air, water, and soils. These contaminants affected the ecosystem and eventually harmed human health and the environment. The growing events of environmental pollution have resulted in rapid advancements in the field of geoenvironmental engineering.

With the increased attention, environmental concerns have become a new aspect of geotechnical engineering. Indiscriminate waste disposal practices and resulting contamination issues have resulted in rapid advances in the fields of geotechnical engineering and environmental engineering. Geotechnical engineers often play an important role in the investigation and characterization of soils and rocks, and suitable hosts for waste repositories. The subsurface environmental problems also require an understanding of the chemical characteristics of the subsurface and the ability to design pollution control or remediation using environmental engineering skills. A combined experience of geotechnical engineering and environmental engineering is required to address various aspects of these problems.

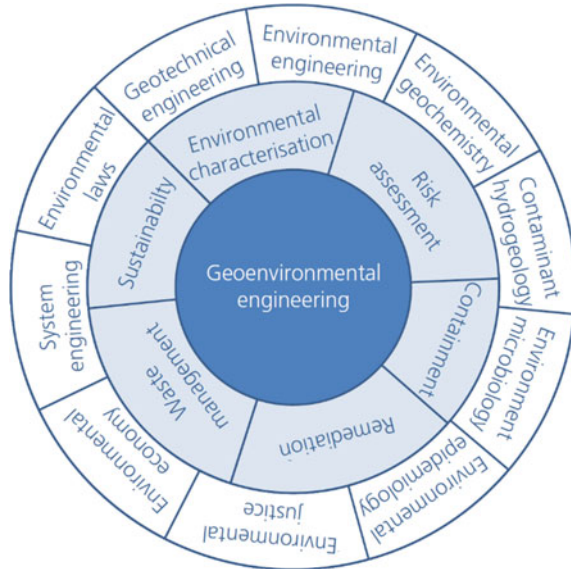
Thus, in the early 1990s, geoenvironmental engineering emerged as a new specialty of civil engineering. This new engineering covers the behavior of soils, rocks, and groundwater and their interactions with contaminants, as well as addressing problems of hazardous and nonhazardous waste management and contaminated sites.

Geoenvironmental engineering has evolved as a broad multidisciplinary field that focuses on providing engineering solutions to environmental problems. It should be noted that environmental geotechnics is referred to a narrow field which deals with the application of classical geotechnical engineering to environmental problems, specifically addressing geotechnical aspects such as settlement, slope stability, seepage, etc. However, geoenvironmental engineering is a broad field, and it requires multidisciplinary knowledge such as geotechnical engineering, environmental engineering, environmental geochemistry, contaminant hydrogeology, environmental microbiology, environmental risk assessment, environmental economics, environmental justice, systems engineering, environmental laws, and sustainability.

Figure 1 illustrates this complexity and multidisciplinary knowledge regime covered by geoenvironmental engineering. The academic progression of geoenvironmental engineering is not on par with the professional geoenvironmental engineering advancements. Geoenvironmental engineering is not taught as a formal course in many academic institutions around the world. Faculty often find themselves unprepared for teaching such an emerging and multidisciplinary course. There



**Fig. 1** Multidisciplinary knowledge related to geoenvironmental engineering [1]



are many challenges faced by academic institutions in developing and teaching geoenvironmental engineering as a formal course.

The objective of this work is to evaluate the main problems, challenges, and deficiencies in the teaching of geoenvironmental engineering. This work aims to develop strategies and methodologies that can enable and improve the quality of geoenvironmental engineering courses in academic institutions.

## 2 Methodology

### 2.1 Data

The methodology involved conducting an online survey with an established questionnaire. The questionnaire was designed to understand the academic or professional experience of the respondents in the field of geoenvironmental engineering, awareness of the scope/field of geoenvironmental engineering, faculty engagement, awareness of the topics covered in the geoenvironmental engineering courses, specific format in which the syllabus must be prepared, and the need for any formal procedures to start the course and curriculum in an academic institution. The topics included in the questionnaire were based on the text book *Geoenvironmental Engineering: Site Remediation, Waste Containment, and Emerging Waste Management Technologies* [2]. Table 1 presents the important topics covered in the geoenvironmental engineering course.

**Table 1** Important topics covered in geoenvironmental engineering course [2]

Topics	
(a) Introduction to geoenvironmental engineering	(b) Pertinent environmental laws and regulations
(c) Chemical background	(d) Composition of soils and soil properties
(e) Groundwater flow	(f) Geochemistry background
(g) Subsurface contamination: sources, contaminants, regulations, and remediation approach	(h) Contaminant transport and fate
(i) Risk assessment and remedial strategy	(j) Contaminated site characterization
(k) Soil and groundwater remediation technologies	(l) In situ waste containment
(m) Landfill regulations, siting and configurations	(n) Sources and characteristics of wastes
(o) Groundwater monitoring	(p) Waste containment liner systems, leachate collection and removal systems and liner design, final cover systems, landfill gas generation and management
(q) Beneficial use of waste materials: recycling	(r) Surface impoundments
(s) Bioreactor landfills	(t) End uses of closed landfills
(u) Subaquatic sediment waste: in situ capping	

The survey was conducted online through Google forms. The teaching challenges were classified into two categories: implementation challenges, and acceptance challenges. Under each category, five major challenges were listed as shown in Tables 2 and 3, and the respondents were asked to rank them on a scale of 1–5; 1 being the least important and 5 being the most important. The respondents were divided according to the years of teaching and professional experience into three groups: more than 10 years of experience; between 5 and 10 years of experience; and < 5 years of experience. It was considered that the greater the experiences, the greater their ability to know the real challenges in their field and, therefore, greater weightage given to their feedback. So, faculty/professionals with more than 10 years of experience (Group 1) received 50% weightage, respondents with 5–10 years of experience (Group 2) received 30%, and respondents with < 5 years of experience (Group 3) received 20% weightage in the analysis. The average ranking of each group of respondents for each challenge were used in the data analysis.

**Table 2** Implementation challenges

Symbol	Implementation challenge
IC1	Not having expertise to teach geoenvironmental engineering
IC2	Not having a good textbook and/or teaching material
IC3	Not having an option to add a new course to existing curriculum
IC4	Lack of multidisciplinary/interdisciplinary knowledge
IC5	Faculty and curriculum being restrictive to their own classical discipline (geotechnical/environmental engineering)

**Table 3** Acceptance challenges

Symbol	Acceptance challenge
AC1	Not knowing the scope of geoenvironmental engineering
AC2	Not knowing the relevance/importance of the course in addressing the current global challenges
AC3	Lack of projects that encourage students to participate in the course
AC4	Lack of awareness and/or urgency of learning and addressing geoenvironmental problems
AC5	Lack of awareness among students about future career opportunities

## 2.2 Data Analysis

The survey data were analyzed by the Technique for Order of Preference by Similarity to the Ideal Solution (TOPSIS). TOPSIS is a multicriteria decision analysis method, which was originally developed by Hwang and Yoon [3] in 1981, and with further development by Yoon [4], Hwang et al. [5], and Yoon and Kim [6]. According to Lee and Eom [7], multicriteria decision-making tool (MCDM) is a very important tool for dealing with unstructured problems that contain multiple and conflicting goals. The MCDM as TOPSIS was applied in this study to rank different challenges.

The strength of the TOPSIS methodology to other MCDM techniques is the use of negative and positive criteria simultaneously in decision making. The closest alternative to the positive ideal solution and the furthest from the negative ideal alternative is selected. Thus, it is possible to provide a more realistic form of modeling compared to other non-compensatory methods [8]. The other advantage of TOPSIS is the possibility of ordering alternatives considering different analysis criteria denoting different degrees of importance by weights. This characteristic of TOPSIS increases the efficiency of decision making [9].

In summary, TOPSIS is a compensatory aggregation technique that compares a set of alternatives by identifying weights for each criterion, normalizing scores for each criterion, and calculating the geometric distance between each alternative and the ideal alternative and, consequently, the best score in each criterion.

Each of the ten challenges (five implementation challenges and five acceptance challenges) had scores assigned by each survey respondents' group. Based on the survey, score of 1 was considered the least important, and score of 5 was the most important. The symbols used to represent the implementation and acceptance challenges used in the TOPSIS analysis are shown in Tables 2 and 3.

The ordering of challenges using the TOPSIS technique was performed by following the routine proposed by Hwang and Yoon [3] which is explained as follows:

Step 1. This step is characterized by the structuring of the D matrix, the decision matrix. This matrix is characterized by the alternatives associated with n attributes (or criteria). The elements ( $x_{ij}$ ) were identified by an alternative (i) and by an analysis criterion (j). In this research, the alternatives correspond to the 10 challenges adopted, separated into two categories of five challenges: implementation and acceptance challenges, and the criteria correspond to the three groups of respondents. Two matrices with 15 values were thus obtained. According to Hwang and Yoon [3], the mathematical representation of the matrix D is shown in Eq. 1.

$$D = \begin{bmatrix} x_{11} & x_{12} & \dots & x_{1n} \\ x_{21} & x_{22} & \dots & x_{2n} \\ \dots & \dots & \dots & \dots \\ x_{m1} & x_{m2} & \dots & x_{mn} \end{bmatrix} \tag{1}$$

Step 2. This step involves construction of the normalized decision matrix which transforms the various dimensions of attributes into non-dimensional attributes. Thus, each criterion is divided by the norm of the total outcome vector of the considered criterion. The  $r_{ij}$  element of the normalized decision matrix R can be calculated using Eq. 2 as per Hwang and Yoon [3] and attains a matrix form shown in Eq. 3. Consequently, each attribute has the same unit length of vector.

$$r_{ij} = x_{ij} / \sqrt{\sum_{i=1}^n x_{ij}^2} \tag{2}$$

$$R = \begin{bmatrix} r_{11} & r_{12} & \dots & r_{1n} \\ r_{21} & r_{22} & \dots & r_{2n} \\ \dots & \dots & \dots & \dots \\ r_{m1} & r_{m2} & \dots & r_{mn} \end{bmatrix} \tag{3}$$

Step 3. In this step, the weightages are considered to construct the weighted normalized matrix. This matrix can be calculated by multiplying each column of the matrix R with its associated weight  $w_j$  shown in Eq. 4 [3]:

$$v_{ij} = w_j r_{ij} \tag{4}$$

The new matrix obtained is called Matrix V. In this work, the weightages  $w_j$  assigned were 50% for Group 1, 30% for Group 2, and 20% for Group 3 of survey respondents. The normalized weighted decision matrix V takes the form as shown in Eq. 5.

$$V = \begin{bmatrix} v_{11} & v_{12} & \dots & v_{1n} \\ v_{21} & v_{22} & \dots & v_{2n} \\ \dots & \dots & \dots & \dots \\ v_{m1} & v_{m2} & \dots & v_{mn} \end{bmatrix} \tag{5}$$

Step 4. This step involves the determination of positive ( $v_j^+$ ) and negative ( $v_j^-$ ) ideal solutions and calculate the Euclidean distance for each alternative. The  $v_j^+$  and  $v_j^-$  ideal solutions are the maximum and minimum values, respectively of the normalized weighted matrix (V), for each of the challenge criterion. According to Hwang and Yoon [3], the Euclidean distance from the positive and negative ideal solutions are represented by Eqs. 6 and 7, respectively.

$$S_i^* = \left[ \sum_j (v_{ij} - v_j^+)^2 \right]^{1/2} \tag{6}$$

$$S_i' = \left[ \sum_j (v_{ij} - v_j^-)^2 \right]^{1/2} \tag{7}$$

Step 5. This step involves calculation of relative proximity to the ideal solution,  $C_i^*$  indicator. This indicator allows ordering the challenges rankings according to the interviewees' perceptions. It is noteworthy that the values of  $C_i^*$  must be between 0 and 1. The  $C_i^*$  indicator was calculated using Eq. 8 as proposed by [3].

$$C_i^* = \frac{S_i'}{S_i^* - S_i'} \tag{8}$$

Step 6. This step involves ranking the preference order: A set of alternatives can now be sorted according to the descending order of  $C_i^*$ . The ones with the shortest distance to the ideal solution are inferred as the best alternative. This procedure is applied to the survey data collected in this study.

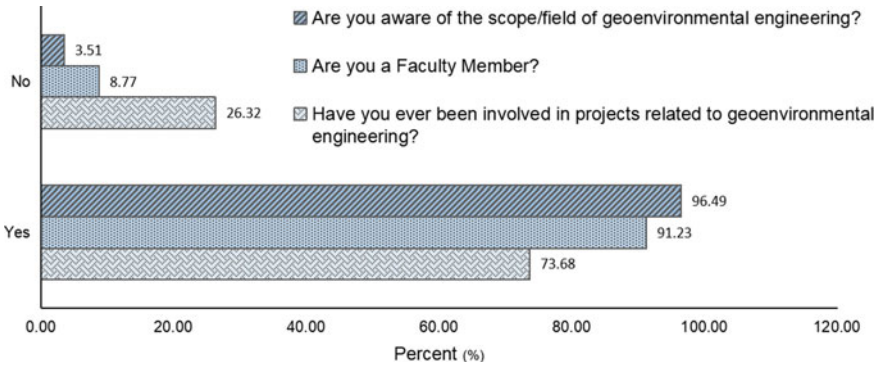


Fig. 2 Awareness of respondents on geoenvironmental engineering

### 3 Results and Discussions

#### 3.1 Demographics of Survey Respondents and Scope of Geoenvironmental Engineering

The demographics of the survey respondents comprised of civil engineering (80.7%), environmental engineering (8.8%), and other engineering majors such as construction, computer, geological, geotechnical, and structural engineering (10.5%). It should also be noted that 52.6% of the respondents had more than ten years of experience, 17.5% had 5 to 10 years of experience, and 24.6% had 1–5 years of experience, and only 5.3% had < 1 year of experience. Figure 2 shows the percentages of respondents that were aware of geoenvironmental engineering. Most of the participants were aware of the scope/field of geoenvironmental engineering.

#### 3.2 Ranking of Challenges Based on TOPSIS Technique

Tables 4 and 5 show the average scores assigned by each group of respondents for the five challenges under each challenge category.

The values in Tables 4 and 5 were normalized using Eq. 2 and the values are shown in Tables 6 and 7, respectively.

The normalized values in Tables 6 and 7 were multiplied by the weightages assigned to each group of respondents using Eq. 4. The weighted values are shown in Tables 8 and 9.

Tables 10 and 11 present the values of positive ideal solution and the negative ideal solution which are basically the maximum and minimum values of the normalized scores of each challenge categories shown in Tables 8 and 9.

**Table 4** Average scores of implementation challenges attributed by each group of respondents

Challenge	> 10 Years (G1)	5–10 Years (G2)	1–5 Years (G3)
IC1	3.47	3.70	3.80
IC2	3.63	4.10	2.90
IC3	2.63	1.50	3.00
IC4	3.23	3.50	3.80
IC5	3.27	3.40	3.30

**Table 5** Average scores of acceptance challenges attributed by each group of respondents

Challenge	> 10 Years (G1)	5–10 Years (G2)	1–5 Years (G3)
AC1	2.73	3.60	3.00
AC2	2.80	3.70	3.10
AC3	3.53	3.40	3.80
AC4	3.17	3.60	3.40
AC5	3.47	3.80	3.90

**Table 6** Normalized scores of implementation challenges

Challenge	> 10 Years (G1)	5–10 Years (G2)	1–5 Years (G3)
IC1	0.47	0.49	0.50
IC2	0.50	0.55	0.38
IC3	0.36	0.20	0.40
IC4	0.44	0.47	0.50
IC5	0.45	0.45	0.44

**Table 7** Normalized scores of acceptance challenges

Challenge	> 10 Years (G1)	5–10 Years (G2)	1–5 Years (G3)
AC1	0.39	0.44	0.39
AC2	0.40	0.46	0.40
AC3	0.50	0.42	0.49
AC4	0.45	0.44	0.44
AC5	0.49	0.47	0.50

**Table 8** Weighted normalized scores related to implementation challenges

Challenge	> 10 Years (G1)	5–10 Years (G2)	1–5 Years (G3)
IC1	0.24	0.15	0.50
IC2	0.25	0.16	0.08
IC3	0.18	0.06	0.08
IC4	0.22	0.14	0.10
IC5	0.22	0.14	0.09

**Table 9** Weighted normalized score related to acceptance challenges

Challenge	> 10 Years (G1)	5–10 Years (G2)	1–5 Years (G3)
AC1	0.19	0.13	0.08
AC2	0.20	0.14	0.08
AC3	0.25	0.13	0.10
AC4	0.22	0.13	0.09
AC5	0.25	0.14	0.10

**Table 10** Positive and negative ideal solution for implementation challenges

Solution criteria	> 10 Years (G1)	5–10 Years (G2)	1–5 Years (G3)
Positive ideal solution	0.25	0.16	0.10
Negative ideal solution	0.18	0.06	0.08

**Table 11** Positive and negative ideal solution for acceptance challenges

Solution criteria	> 10 Years (G1)	5–10 Years (G2)	1–5 Years (G3)
Positive ideal solution	0.25	0.14	0.10
Negative ideal solution	0.19	0.13	0.08

The values in Tables 10 and 11 are used to calculate the distances of the positive and negative ideal solution (Eqs. 6 and 7, respectively) and are shown in Tables 12 and 13. These tables also show the value of coefficient ( $C_i^*$ ) which was obtained using Eq. 8. This coefficient is the indicator of the relative proximity to the ideal solution. This indicator allows ordering the challenges according to the respondents' perceptions.

Based on the values of the coefficient ( $C_i^*$ ), the implementation challenges and acceptance challenges were rank ordered as shown in Tables 14 and 15, respectively.

**Table 12** Distances from the positive ideal solution ( $S_i^*$ ), distances from the negative ideal solutions ( $S_i'$ ) and coefficient  $C_i^*$  for implementation challenges

Challenge	$S_i^*$	$S_i'$	$C_i^*$
IC1	0.02	0.11	0.85
IC2	0.02	0.12	0.84
IC3	0.13	0.00	0.02
IC4	0.04	0.09	0.72
IC5	0.04	0.09	0.69



**Table 13** Distances from the positive ideal solution ( $S_i^*$ ), distances from the negative ideal solutions ( $S_i'$ ) and coefficient  $C_i^*$  for acceptance challenges

Challenge	$S_i^*$	$S_i'$	$C_i^*$
AC1	0.06	0.01	0.11
AC2	0.06	0.01	0.18
AC3	0.02	0.06	0.80
AC4	0.03	0.03	0.53
AC5	0.00	0.06	0.93

**Table 14** Ranking of implementation challenges

Rank	$C_i^*$	Symbol	Challenge
1	0.85	IC1	Not having expertise to teach geoenvironmental engineering
2	0.84	IC2	Not having a good textbook and/or teaching material
3	0.72	IC4	Lack of multidisciplinary/interdisciplinary knowledge
4	0.69	IC5	Faculty and curriculum being restrictive to their own classical discipline (Geotechnical/environmental engineering)
5	0.02	IC3	Not having an option to add a new course to existing curriculum

**Table 15** Ranking of acceptance challenges

Rank	$C_i^*$	Symbol	Challenge
1	0.93	AC5	Lack of awareness among students about future career opportunities
2	0.80	AC3	Lack of projects that encourages students to participate in the course
3	0.53	AC4	Lack of awareness and/or urgency of learning and addressing geoenvironmental problems
4	0.18	AC2	Not knowing the relevance/importance of the course in addressing the current global challenges
5	0.11	AC1	Not knowing the scope of geoenvironmental engineering

Based on the  $C_i^*$  values, “not having the expertise to teach geoenvironmental engineering”; “not having a good textbook and/or textbooks”, and “the lack of multidisciplinary/interdisciplinary knowledge” were considered the top three implementation challenges. “Lack of awareness among students about future career opportunities”, “lack of projects that encourage students to participate in the course”, and “lack of awareness and/or urgency to learn and face geoenvironmental problems” were the top three acceptance challenges.

“Not having the expertise to teach geoenvironmental engineering” and “Lack of awareness among students about future career opportunities” were the topmost implementation challenge and acceptance challenge, respectively. These challenges represent a recognition of the geoenvironmental engineering importance and the value of promoting better training of students and professionals. It reveals the perceptions of

faculty about the importance of multidisciplinary associated with the challenges of broad knowledge of issues related to the environment.

On the other hand, the lack of awareness of students about future career opportunities, the most important acceptance challenge, reflects the lack of knowledge of the geoenvironmental engineering problems and applications. Geoenvironmental issues still seem to be in a distant universe whose unawareness often leads to disregard of their great importance.

## 4 Conclusions

As the importance of geoenvironmental engineering is increasing, there is a growing need for including geoenvironmental engineering in the academic courses. In this study, the challenges to teach geoenvironmental engineering were identified and ranked to evaluate the most important challenges that need to be addressed for successful implementation of this course in academic institutions. The study reveals that there is a need for the faculty to understand the scope of the course and embrace the multidisciplinary of this course and develop those skills to successfully teach this course in the academic institutions.

Another important aspect was the unawareness of the students about the future prospects of the geoenvironmental engineering career opportunities. The most valuable aspect of this research was the recognition of the importance of geoenvironmental engineering and the need to improve the quality of the curriculum. Better training of professionals, improvement of the curriculum, and use of good textbook represent the great strategies to follow for the advancement of geoenvironmental engineering.

**Acknowledgements** The financial support for this project was received from the University of Illinois at Chicago. Luis Fernando Martins Ribeiro is grateful for the funding from the Research Foundation of the Distrito Federal, Brazil (FAP-DF) to conduct postdoctoral research at UIC.

## References

1. Reddy KR (2014) Evolution of geoenvironmental engineering. *Environ Geotech* 1(3):136–141
2. Sharma HD, Reddy KR (2004) *Geoenvironmental engineering: site remediation, waste containment, and emerging waste management technologies*. John Wiley & Sons, Inc., Hoboken, New Jersey, p 992
3. Hwang CL, Yoon K (1981) *Multiple attribute decision making: methods and applications*. Springer-Verlag, New York
4. Yoon K (1987) A reconciliation among discrete compromise situations. *J Oper Res Soc* 38(3):277–286
5. Hwang CL, Lai YJ, Liu TY (1993) A new approach for multiple objective decision making. *Comput Oper Res* 20(8):889–899

6. Yoon KP, Kim WK (2017) The behavioral TOPSIS. *Exp Syst Appl* 89:266–272
7. Lee SM, Eom HB (1990) Multiple-criteria decision support system: the powerful tool for attacking complex, unstructured decisions. *Syst Pract* 3(1):51–65
8. Singh RK, Gupta A, Kumar A, Khan TA (2016) Ranking of barriers for effective maintenance by using TOPSIS approach. *J Qual Maint Eng* 22(1):18–34
9. Lima Junior FR, Carpinetti LCR (2015) A comparison between the TOPSIS and fuzzy-TOPSIS methods to support multi-criteria decision making for supplier selection. *Gestão Produção São Carlos* 22(1):17–34

# Nanoremediation of Lindane Contaminated Soils



Liang Zhao, Jyoti K. Chetri , Raksha Rai, Luis Fernando Martins Ribeiro, and Krishna R. Reddy 

**Abstract** The application of nanoscale zero-valent iron (nZVI) for remediation of soils contaminated by organic pollutants has drawn great attention, mainly owing to its relatively low cost and low toxicity. The present study investigated the degradation of lindane ( $\gamma$ -HCH) by two types of nZVIs, NANO FER 25S (N25S) and NANO FER STAR (NS). Three types of soils (field sand, kaolin, and glacial till) were spiked with 50 mg/kg lindane and were treated using different concentrations of N25S and NS. The highest lindane removal rate obtained was 99.99% using 10 g/L N25S in kaolin. Similarly, a near complete removal of lindane was achieved in the field sand using 4 g/L NS and 4 g/L N25S with removal rates of 99.9 and 99.7%, respectively. A considerable portion of the lindane may have possibly been lost through volatilization during the process of spiking, resulting in an unexpected decrease of the initial lindane concentration from 50 to 37, 38, and 28 mg/kg in field sand, kaolin, and glacial till samples, respectively. It is concluded that the degradation efficiency of lindane increased with increasing nZVI concentration and maximum degradation was achieved in kaolin by NS and N25S. The results show that the average degradation rate was higher with N25S than NS due to better contact and uniformity of the N25S suspension than the NS solution prepared from the NS powder.

**Keywords** Nanoremediation · Lindane · nZVI nanoparticles · Halogenated organic contaminants

---

L. Zhao · J. K. Chetri · R. Rai · L. F. M. Ribeiro · K. R. Reddy (✉)  
University of Illinois at Chicago, Chicago, IL 60607, USA  
e-mail: [krreddy@uic.edu](mailto:krreddy@uic.edu)

L. F. M. Ribeiro  
University of Brasilia, Brasilia, DF 70910.900, Brazil

## 1 Introduction

Nanotechnology is an emerging technology with wide applications in various fields. It has shown great potential as a remediation technique for polluted soils, especially persistent organic pollutants (POPs) such as pesticides and insecticides. The conventional remediation methods based on physical, chemical, and biological processes are found to be ineffective to achieve complete remediation of pesticides and insecticides contamination. Hence, there is a need to develop nanotechnology-based alternative methods for the complete remediation of pesticides and insecticides contaminants from the environment. Nanoremediation has the potential to provide some beneficial alternative to the current practices of site remediation.

Lindane or  $\gamma$ -hexachlorocyclohexane (also known as  $\gamma$ -HCH and  $\gamma$ -BHC) is an organochlorine insecticide, that severely affects public health and the environment. Lindane's production is forbidden in many countries due to its high toxicity, mobility, and persistence, bioaccumulation, and recalcitrant characteristics in the atmosphere, groundwater, and soil [1].  $\alpha$ -HCH,  $\beta$ -HCH,  $\gamma$ -HCH, and  $\delta$ -HCH are the prime isomers of hexachlorocyclohexanes (HCHs).  $\gamma$ -HCH is used for insecticidal applications, and is thus responsible for cumulative toxic effects through bioaccumulation in food chain.

Lindane is strictly banned for agricultural use in the countries that signed The countries that signed Stockholm Convention on POPs have banned the use of lindane in agricultural applications; however, lindane is still being used in cosmetic and pharmaceutical applications in many countries across the globe, for example in shampoos. India and China have been reported as one of the prime sites for lindane production [1]. Between 1950 and 2000, approximately 600,000 tons of lindane was supposed to be used in agriculture, medicine and other industries across the globe. It is estimated that there is approximately 1,600,000–1,900,000 million tons of HCH residues present globally [2]. Table 1 shows the selected studies that reported residual lindane concentrations in the environment across the world.

Thus, the requirement for exploring methods and techniques to decontaminate soils impacted by  $\gamma$ -HCH is growing. Previous researchers studied electrokinetic remediation [3], phytoremediation [4], nanoremediation, and bioremediation techniques on the degradation of organochlorine contaminants, especially lindane, in soils and groundwater. Among them, nanoremediation has appeared as a novel and efficacious solution for environmental remediation which is suitable for a broad range of contaminants like chlorinated compounds, hydrocarbons, and organic compounds [3].

nZVI is an ideal electron donor, which acts as a precursor to iron oxides due to the spontaneous oxidation of Fe(0) in the aqueous form to Fe(II) and Fe(III). One of the possible reactions involving halogenated organic compound and zero valent iron is shown in Eq. 1.

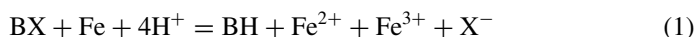


**Table 1** Residual lindane in the environment

Location	Concentration	References
Sao Paulo, Brazil	30.0–72.8 (pg/m <sup>3</sup> )	[7]
Mar Del Plata, Argentina	0.28–3.7 (pg/m <sup>3</sup> )	[7]
Bolivian Andes	0.3–42 (pg/m <sup>3</sup> )	[7]
Egaila, Kuwait	38.6 (pg/m <sup>3</sup> )	[8]
Shuwaikh, Kuwait	112 (pg/m <sup>3</sup> )	[8]
Abdali, Kuwait	78.1 (pg/m <sup>3</sup> )	[8]
Yangtze River Delta, China	0.9 (ng/g)	[7]
Jinjiang River, China	5.861 (ng/g)	[10]
Taihu Lake, China	1.98 (ng/L)	[11]
Bohai Riverine Sediment, China	0.26 (ng/g)	[12]
Bohai Marine Sediment, China	0.02 (ng/g)	[12]
Haihe River, China	92.3 (ng/L)	[13]
Yellow River, China	94.0 (ng/L)	[13]
Huaihe River, China	97.4 (ng/L)	[13]
Southeast Drainage Area Rivers, China	97.3 (ng/L)	[13]
Beijing Park, China	0.5327 (ng/g)	[5]
Guanting Reservoir, China	0.2 (ng/g)	[14]
Macau Coastal Water, China	5.33 (ng/L)	[15]
Meiliangwan Bay, China	3.35 (ng/L)	[16]
Hangzhou Wet Deposition, China	24.15 (ng/L)	[17]
Lake Tai, China	4.2 (ng/g)	[17]
Jinhan Bay, China	2.2 (ng/g)	[17]
Tianjin, China	5.5 (ng/g)	[18]

Nanoremediation involves the use of reactive nanomaterials, such as nZVI, for the transformation and detoxification of contaminants. The use of nZVI is found to be effective for degrading organic pollutants such as organochlorine pesticides compounds, and chlorinated organic compounds. Application of nanoparticles in remediating various pollutants in the environment has been explored. Li et al. [5] highlighted the methods of synthesis and characterization of nZVI and its used in the remediation of organic and inorganic pollutants. The authors pointed out that zero valent iron (ZVI) can be effective electron donors and hence, Pb, Cd, Ni, and Cr are subjected to the reduction by ZVI nanoparticles. Similarly, San Román et al. [6] reported lindane degradation by laboratory-synthesized polymer-stabilized iron

nanoparticles in aqueous solution. Results showed that these nanoparticles possess excellent dechlorination performance.

Dominguez et al. [19] studied degradation of lindane in soil, water and ground-water using five commercial iron microparticles with different physical and chemical properties. HCH isomers revealed dissimilar behaviors and dechlorination order ( $\gamma > \alpha > \delta > \beta$ ) as per the axial/equatorial location of the chlorines.  $m\text{Fe}^{-1}$  was the most active iron source. San Román et al. [20] explored the use of nZVI and polymer stabilized nanoparticles for lindane degradation and developed analytical methods to analyze and detect lindane and its degradation by-products. San Román et al. [20] found that the SPE–GC/MS method provides low detection limits, high recovery (above 95%) and it is an important tool for kinetic studies of the degradation process for each polymer used, while HS–SPME–GC/MS has demonstrated to be a successful tool for the extraction and assessment of volatile degradation by-products.

Rawtani et al. [21] collated the degradation potential of nZVI and polymer-stabilized nZVIs and presented the prime mechanism for lindane degradation to be dehydrohalogenation. nZVI is currently the most widely used nanoparticles among all the available nano particles [22]. Metal nanoparticles, such as NANOFER 25S (N25S) suspension and NANOFER STAR (NS) powder are among the few commercially available nZVI particles made in Europe and have the capability for effective remediation of soils and groundwater contamination.

Zhuang et al. [23] assessed the remediation abilities of one of the types of NANOFER particles to degrade polybrominated diphenyl ethers (PBDEs) and organic pollutants. Zhuang et al. [23] concluded that N25S could debrominate selected environmentally abundant PBDEs. However, a small number of studies in the past have investigated the abilities of NANOFER to degrade lindane-contaminated soils. Some researchers explored the effect of iron nanoparticles on the surrounding environment. Table 2 summarizes important physical and chemical properties of  $\gamma$ -HCH or lindane. The main objectives of this study are to evaluate the lindane removal capacities of various forms of nanoiron and investigate the effect of soil types on the lindane removal capacities of nanoiron.

## 2 Materials and Methods

### 2.1 Soils Characterization

Three different types of soils were tested in this study: (a) field sand; (b) kaolin; (c) glacial till. Field sand, known as Three River Sand, was obtained from Wisconsin, USA, and kaolin from Fisher Scientific (Waltham, MA, USA). Glacial till represents typical field clayey soil encountered in and around Chicago and was obtained from Zion, IL, USA. The physio-chemical characteristics of soils were determined as

**Table 2** Physical and chemical properties of lindane ( $\gamma$ -HCH)

Properties	Lindane ( $\gamma$ -HCH)
Molecular formula	$C_6H_6Cl_6$
Molecular weight	290.830
Boiling point	311 °C [24]
Melting point	112.5 °C [25]
Solubility in water	6.6 mg/L at 25 °C [26]
Solubility in acetone	> 200 g/L at 25 °C [27]
Solubility in hexane	12.6 g/L at 20 °C
Specific gravity	1.85 [28]
Corrosivity	Corrosive to metals [28]
Color/form	White crystalline powder [29]
Stability	Stable under recommended storage conditions [25]
EPA toxicity classification	Class II [30]

per American Society for Testing and Materials (ASTM) standard procedures. The results are shown in Table 3. Figure 1 shows the grain size distribution of all the soils tested.

**Table 3** Physio-chemical properties of the three soils used in this study

Properties	ASTM method	Field sand	Glacial till	Kaolin
Specific gravity	ASTM D854	2.65	2.59	2.36
Grain size distribution:	ASTM D422			
Gravel (%)		0.3	0	0
Sand (%)		99.6	40.3	0
Fines (%)		0.1	59.7	100
Atterberg limits:	ASTM D4318			
Liquid limit (%)		Non-plastic	34	39
Plastic limit (%)		–	16	27
Plasticity index (%)		–	18	12
USCS classification	ASTM D2487	SP	CL (sandy lean clay)	CL
Moisture content (%)		0.20	1.20	0.80
Organic content (%)	ASTM D2974	0.6	2.2	3.3
Hydraulic conductivity (cm/s)	ASTM D2434	$1.02 \times 10^{-1}$	$2.59 \times 10^{-8}$	$8.34 \times 10^{-9}$
pH (1:1)	ASTM D4972	7.8	6.8	7.5



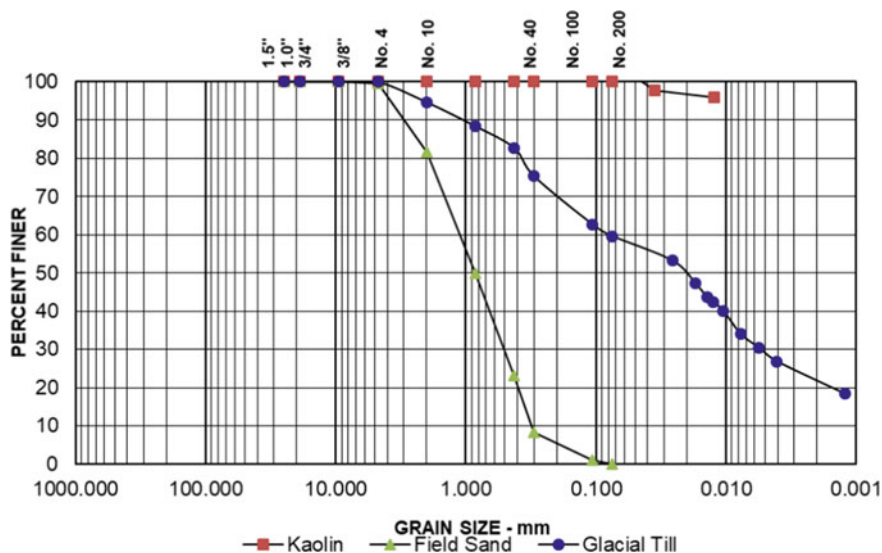


Fig. 1 Grain size distribution of field sand, kaolin, and glacial till

## 2.2 Zero-Valent Iron Nanoparticles

In this study, a commercial stabilized dispersion of N25S and a powder of NS obtained from NANO IRON, s.r.o., Židlochovice, Czech Republic were used. The mean diameter of N25S was 50–60 nm, ZVI content was 14–18%, the magnetite ( $\text{Fe}_3\text{O}_4$ ) content 2–6%, carbon (C) 0–1%, surfactant 3%, and water 77%. The pH of the nZVI suspension was  $12.2 \pm 0.1$ . NS was a dry air-stable, flammable powder which contains 65–80% of Fe(0) and 20–35% of iron oxide. The surface of nanoparticles was stabilized by a thin layer of iron oxide, preventing nZVI from oxidation. Nanoparticles were used immediately after receipt.

## 2.3 Spiking Procedure

The soils were sieved through 2 mm sieve and dried at room temperature (25 °C). A stock solution of lindane was prepared by dissolving 50 mg of lindane in acetone (100 mL) and methanol (100 mL) solution. The lindane stock solution was homogeneously mixed with 1000 g of each soil. The spiked soils were then stored at room temperature in the environmental fume hood for over two weeks.

## 2.4 Batch Treatment Tests

For the tests with N25S suspension, 5 g of each soil was mixed with N25S solution to achieve the targeted initial nZVI concentrations of 0, 4, 10, 20, 50, 75, and 100 g/L. The samples were shaken in a mechanical shaker for uniform mixing and allowed to react for 24 h at room temperature.

For the tests with NS powder solution, at first NS solution was prepared from the NS powder. 20% aqueous slurry was prepared by adding 100 g of dry NS powder to 400 ml distilled water. The NS powder was added slowly to the distilled water with continuous stirring on a magnetic stirrer. The mixing was conducted in a closed bottle to minimize the exposure of fresh air to the slurry and prevent possible oxidation of nZVI. The properly dispersed slurry was homogeneous, and the slurry was transferred into a PET bottle and left at room temperature for 48 h to allow stabilization of the slurry. The gas pressure developed in the slurry bottle was released by opening the bottle after 48 h. The NS slurry bottle was then sealed and stored in the refrigerator (2–4 °C).

Seven different solutions were prepared with concentrations of 0, 4, 10, 20, 50, 75, 100 g/L of nZVI -soil mixtures for the three types of soils, totaling 42 sets of samples including duplicates for the batch experiments. Subsequently, samples were shaken for 24 h at room temperature then centrifuged (4000 rpm, 10 min) to separate the solids. At the end of the process, soil samples were analyzed using GC–MS at STAT Analysis, Chicago, IL.

## 3 Results and Discussions

The effect of nZVI dosage on the degradation/dechlorination of lindane was studied in field sand, kaolin and glacial till at a room temperature of 25 °C. The pH of the soils was 8.04, 7.79, and 7.73 for field sand, kaolin, and glacial till, respectively. Lindane removal rate approached 100% in the field sand with NS as well as with N25S (Fig. 2). For both types of nZVI, the lindane removal rate increased with the increasing dosage of nZVI. In the field sand, the best lindane removal rate was obtained at the concentration of 75 g/L for NS and 100 g/L for N25S, which are 99.97 and 99.92%, respectively.

In kaolin, concentrations equal or > 10 g/L of NS or N25S led to lindane removal rate close to 100% (Fig. 3). However, the rate of degradation of lindane was slightly higher for N25S than for NS. This difference in removal could be due to the uniformity of the N25S suspension as compared to the NS solution.

Lindane removal rate reached 97.70% with NS and 99.93% with N25S in glacial till at the concentration of 4 g/L (Fig. 4). The higher removal rate for N25S suggests that the dechlorination of lindane by iron particles occurs at the metal surface. In this sense, it can be considered that the N25S suspension has larger contact area in contrast to the NS solution that was prepared from the powder form.

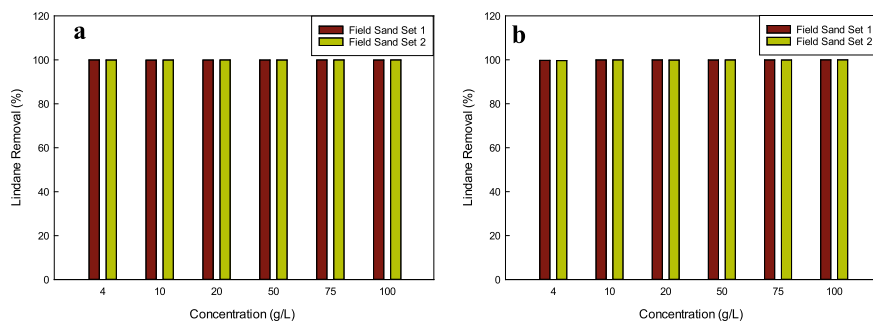


**Fig. 2** Lindane removal rate in field sand using nZVI **a** NS and **b** N25S at different concentrations

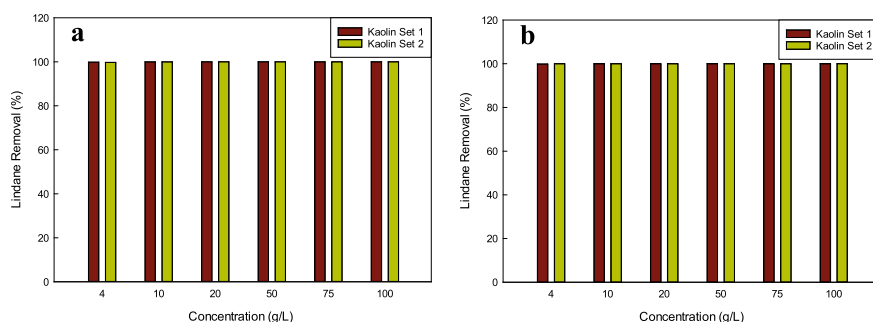


**Fig. 3** Lindane removal rate in kaolin using nZVI **a** NS and **b** N25S at different concentrations

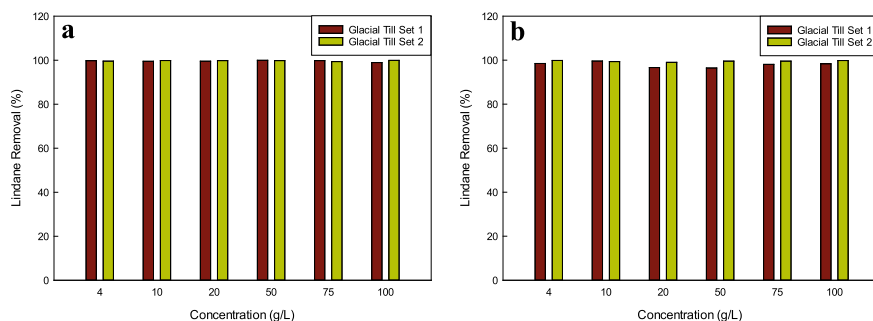


**Fig. 4** Lindane removal rate in glacial till using nZVI **a** NSTAR and **b** N25S at different concentrations

A comparison of residual lindane concentrations in field sand, kaolin, and glacial till is shown in Fig. 5. Lindane was degraded nearly completely by nZVI NS and N25S at 4 g/L and higher concentrations (Fig. 5). However, the lindane concentration at 20 g/L N25S in the glacial till slightly increased and then decreased for the concentrations higher than 20 g/L. This variation is considered within the range

of experimental error. The degradation efficiency increases with the increase in the initial concentration of nZVI. At 10 g/L N25S, nearly 100% lindane degradation was observed in field sand, kaolin, and glacial till. Lindane concentration decreased rapidly when the nZVI increased from 0 to 4 g/L which could be attributed to the fact that with the increase in the initial concentration, the availability of surface reactive sites of nZVI become larger, because of which, the percent of lindane molecules undergoing degradation reduces.

Lindane removal rates were significantly higher for both types of nZVIs NS and N25S (Fig. 6). The average degradation rate is slightly higher for N25S than NS, possibly due to the contact rate and uniformity of the N25S suspension performing better than the NS solution which was prepared from the NS powder. The lindane removal rate increased with the increase of nZVI dosage. The lindane removal rates were 99.95, 99.99, and 99.43% in field sand, kaolin, and glacial till, respectively with 100 g/L NS solution and 99.96, 99.99, and 99.07% in field sand, kaolin, and glacial till, respectively with 100 g/L N25S suspensions. Clearly, a higher nZVI dosage leads to higher dechlorination of lindane.

It should be noted that some portion of the lindane spiked to the soils during the process of artificial contamination was lost through volatilization and other pathways

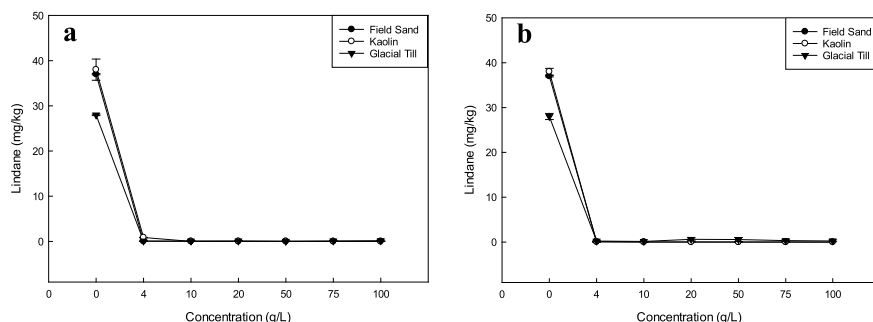


**Fig. 5** Effect of nZVI **a** NS and **b** N25S concentration on residual lindane concentrations in different soils

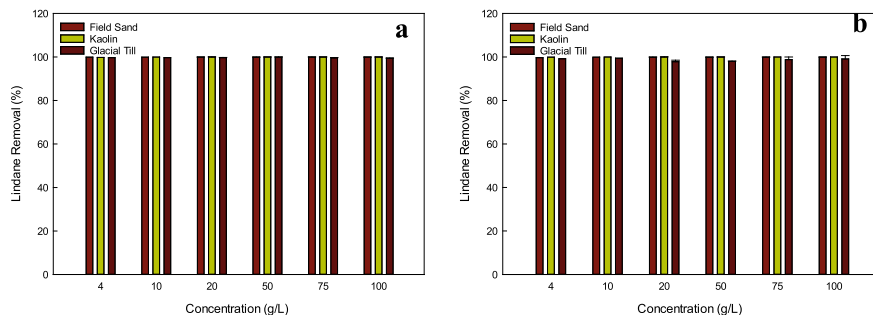


**Fig. 6** Lindane removal rates in three different soils using nZVI **a** NS and **b** N25S

based on the test results of unexpected decrease of initial lindane concentration in field sand, kaolin, and glacial till samples from 50 to 37 mg/kg, 38, and 28 mg/kg, respectively.

The test results show a clear relationship between lindane degradation and nZVI dosage. For the field sand, the NS concentration of 4 g/L resulted in 99.94% reduction of lindane, which is slightly lower than the 99.68% reduction by N25S. It was observed that even a low dose of nZVI (4 g/L) was efficient, stable and cost-effective agent for lindane remediation. Therefore, it is concluded that nZVI can be used for the effective remediation of lindane contaminated soil.

The potential mechanism for lindane degradation has been shown to be dehydrohalogenation or dichloroelimination [19, 20, 31]. The reactivity of the reactant and the relative position of chlorines on the cyclic structure determine the pathway of the reaction. There are different possible pathways of lindane degradation by nZVI. One pathway begins with a dehydrochlorination reaction which consists of concurrent elimination of one chlorine and one hydrogen from an adjacent carbon atom with the formation of gamma-2,3,4,5,6-pentachloro-1-cyclohexene (PCCH) and releasing of hydrogen chloride. PCCH further transforms into 1,2,4-trichlorobenzene (TCB), and subsequently dichlorobenzene (DCB) which may further degrade to benzene. Another possible pathway includes dichloroelimination of  $\gamma$ -HCH to tetrachloro-cyclohexadiene (TeCCH) which involves the elimination of two chlorine atoms from two adjacent carbon atoms along with the formation of carbon double bond and release of chloride. TeCCH may further degrade to dichloro-cyclohexadiene (DCCHD) and eventually chlorobenzene (CB) or benzene [31].

## 4 Conclusions

The present study aimed to evaluate the efficacy of nZVI for the degradation of lindane ( $\gamma$ -HCH) in three different types of soils (field sand, kaolin, and glacial till), using two different types of nZVI (NS and N25S). The results demonstrated near complete lindane dechlorination in all soils tested with NS or N25S, indicating that nZVI is highly effective for lindane degradation. The nearly complete degradation of lindane at 4 g/L NS or N25S in field sand, kaolin, and glacial till, indicates the potential of nZVI to degrade lindane at low concentrations (< 4 g/L). Additional testing is warranted to determine the optimal low nZVI concentration to degrade lindane. However, before a definitive conclusion can be drawn regarding the implementation of this technology in the field, additional work to study its applicability, such as rich organic matter soils with a high affinity for lindane, is needed.

**Acknowledgements** The financial support for this project was received from the University of Illinois at Chicago. Luis Fernando Martins Ribeiro is grateful for the funding from the Research Foundation of the Distrito Federal, Brazil (FAP-DF) to conduct postdoctoral research at UIC.

## References

1. Humphreys EH, Janssen S, Heil A, Hiatt P, Solomon G, Miller MD (2007) Outcomes of the California ban on pharmaceutical lindane: clinical and ecologic impacts. *Environ Health Perspect* 116(3):297–302
2. Vijgen J, Yi LF, Forter M, Lal R, Weber R (2006) The legacy of lindane and technical HCH production. *Organohalogen Comp* 68:899–904
3. Reddy KR, Darko-Kagya K, Al-Hamdan AZ (2011) Electrokinetic remediation of chlorinated aromatic and nitroaromatic organic contaminants in clay soil. *Environ Eng Sci* 28(6):405–413
4. Salam JA, Hatha MA, Das N (2017) Microbial-enhanced lindane removal by sugarcane (*Saccharum officinarum*) in doped soil-applications in phytoremediation and bioaugmentation. *J Environ Manag* 193:394–399
5. Li XQ, Elliott DW, Zhang WX (2006) Zero-valent iron nanoparticles for abatement of environmental pollutants: materials and engineering aspects. *Crit Rev Solid State Mater Sci* 31(4):111–122
6. San Román I, Galdames A, Alonso ML, Bartolomé L, Vilas JL, Alonso RM (2016) Effect of coating on the environmental applications of zero valent iron nanoparticles: the lindane case. *Sci Total Environ* 565:795–803
7. Rauert C, Harner T, Schuster JK, Eng A, Fillmann G, Castillo LE, Pozo K (2018) Air monitoring of new and legacy POPs in the Group of Latin America and Caribbean (GRULAC) region. *Environ Pollut* 243:1252–1262
8. Gevao B, Porcelli M, Rajagopalan S, Krishnan D, Martinez-Guijarro K, Alshemmari H, Zafar J (2018) Spatial and temporal variations in the atmospheric concentrations of “Stockholm Convention” organochlorine pesticides in Kuwait. *Sci Total Environ* 622:1621–1629
9. Sun J, Pan L, Zhan Y, Lu H, Tsang DC, Liu W, Zhu L (2016) Contamination of phthalate esters, organochlorine pesticides and polybrominated diphenyl ethers in agricultural soils from the Yangtze River Delta of China. *Sci Total Environ* 544:670–676
10. Yu Y, Li Y, Shen Z, Yang Z, Mo L, Kong Y, Lou I (2014) Occurrence and possible sources of organochlorine pesticides (OCPs) and polychlorinated biphenyls (PCBs) along the Chao River, China. *Chemosphere* 114:136–143
11. Qu CS, Chen W, Bi J, Huang L, Li FY (2011) Ecological risk assessment of pesticide residues in Taihu Lake wetland, China. *Ecol Model* 222(2):287–292
12. Zhong G, Tang J, Zhao Z, Pan X, Chen Y, Li J, Zhang G (2011) Organochlorine pesticides in sediments of Laizhou Bay and its adjacent rivers, North China. *Mar Pollut Bull* 62(11):2543–2547
13. Gao J, Liu L, Liu X, Lu J, Zhou H, Huang S, Spear PA (2008) Occurrence and distribution of organochlorine pesticides—lindane, p, p'-DDT, and heptachlor epoxide: in surface water of China. *Environ Int* 34(8):1097–1103
14. Wang T, Lu Y, Shi Y, Giesy JP, Luo W (2007) Organochlorine pesticides in soils around Guanting Reservoir, China. *Environ Geochem Health* 29(6):491–501
15. Na T, Fang Z, Zhanqi G, Ming Z, Cheng S (2006) The status of pesticide residues in the drinking water sources in Meiliangwan Bay, Taihu Lake of China. *Environ Monit Assess* 123(1–3):351–370
16. Zhou R, Zhu L, Yang K, Chen Y (2006) Distribution of organochlorine pesticides in surface water and sediments from Qiantang River, East China. *J Hazard Mater* 137(1):68–75
17. Nakata H, Hirakawa Y, Kawazoe M, Nakabo T, Arizono K, Abe SI, Ding X (2005) Concentrations and compositions of organochlorine contaminants in sediments, soils, crustaceans, fishes and birds collected from Lake Tai, Hangzhou Bay and Shanghai city region, China. *Environ Pollut* 133(3):415–429
18. Gong ZM, Xu FL, Dawson R, Cao J, Liu WX, Li BG, Tao S (2004) Residues of hexachloro-cyclohexane isomers and their distribution characteristics in soils in the Tianjin area, China. *Arch Environ Contam Toxicol* 46(4):432–437

19. Dominguez CM, Rodriguez S, Lorenzo D, Romero A, Santos A (2016) Degradation of hexachlorocyclohexanes (HCHs) by stable zero valent iron (ZVI) microparticles. *Water Air Soil Pollut* 227(12):446
20. San Román I, Alonso ML, Bartolomé L, Galdames A, Goiti E, Ocejo M, Vilas JL (2013) Relevance study of bare and coated zero valent iron nanoparticles for lindane degradation from its by-product monitorization. *Chemosphere* 93(7):1324–1332
21. Rawtani D, Khatri N, Tyagi S, Pandey G (2018) Nanotechnology-based recent approaches for sensing and remediation of pesticides. *J Environ Manag* 206:749–762
22. Patil SS, Shedbalkar UU, Truskewycz A, Chopade BA, Ball AS (2016) Nanoparticles for environmental clean-up: a review of potential risks and emerging solutions. *Environ Technol Innov* 5:10–21
23. Zhuang Y, Jin L, Luthy RG (2012) Kinetics and pathways for the debromination of polybrominated diphenyl ethers by bimetallic and nanoscale zerovalent iron: effects of particle properties and catalyst. *Chemosphere* 89(4):426–432
24. Haynes WM (2014) *CRC handbook of chemistry and physics*. CRC Press, New York
25. Willett KL, Ulrich EM, Hites RA (1998) Differential toxicity and environmental fates of hexachlorocyclohexane isomers. *Environ Sci Technol* 32(15):2197–2207
26. Lotse EG, Graetz DA, Chesters G, Lee GB, Newland LW (1968) Lindane adsorption by lake sediments. *Environ Sci Technol* 2(5):353–357
27. MacBean C (2008) *e-Pesticide Manual*. Alton (UK). British Crop Protection, Council. Glyphosate (1071-83-6)
28. Barsan ME (2007) NIOSH pocket guide to chemical hazards
29. Lewis RJ (1996) *Sax's dangerous properties of industrial materials*, vol 8. New York
30. Benimeli CS, Fuentes MS, Abate CM, Amoroso MJ (2008) Bioremediation of lindane-contaminated soil by *Streptomyces* sp. M7 and its effects on *Zea mays* growth. *Int Biodeter Biodegrad* 61(3):233–239
31. Singh R, Misra V, Mudiam MKR, Chauhan LKS, Singh RP (2012) Degradation of  $\gamma$ -HCH spiked soil using stabilized Pd/Fe0 bimetallic nanoparticles: pathways, kinetics and effect of reaction conditions. *J Hazard Mater* 237:355–364

# Water Treatment Sludge as Geotechnical Liner Material: State-of-Art



Leonardo Marchiori , António Albuquerque , and Victor Cavaleiro 

**Abstract** The periodical cleaning of the decanters at the plant generates solid wastes called water treatment sludges (WTS), a chemical compound similar to aluminum silicates. WTS's properties have been studied for geotechnical purpose and it seems to be suitable for producing liner materials for landfills, dams, ponds, and lagoons which store and prevent soil's infiltration of residues. Liners are usually shaped of soil and geosynthetics, their main properties required are compaction, compressibility and shear strength, chemical compatibility, and hydraulic conductivity. WTS to be considered as a soil substitute, it must be function like a soil, thus, for developing alternative materials, physical, chemical, mechanical, and hydraulic characterization laboratorial parameters are the first step to make viable its reuse. In this sense, the study aims to review the literature over the above-mentioned parameters in order to evaluate WTS as liner material. This review concluded that WTS have high heterogeneity in chemical and mechanical behavior due source of water and treatment processes. WTS' water affinity affects plasticity behavior, and its incorporation into soils seems to contribute for a composite with pozzolanic characteristics, low specific gravity, finer granulometry, and mechanical stabilization. Although need attention on its chemical compatibility, the influence on shear resistance—increasing internal effective friction angle and decreasing cohesion—and the optimum ratio of introduction within soils for an alternative liner material. Nonetheless, there are lacks in literature over hydraulic conductivity, and long-term behavior, the use of the material in practice must be preceded by pilot tests or experimental landfills.

**Keywords** Water treatment sludge · Liner · Geotechnical material · Waterproofing · Review

---

L. Marchiori (✉) · A. Albuquerque · V. Cavaleiro  
Universidade da Beira Interior, Covilhã, Portugal  
e-mail: [leonardo.marchiori@ubi.pt](mailto:leonardo.marchiori@ubi.pt)

FibEnTech, Covilhã, Portugal

GeoBioTec, Covilhã, Portugal



## 1 Introduction

Water treatment plants (WTP) operations basically consisting of capture, chemical coagulation, flocculation, decantation, filtration, and disinfection of the water, natural or residual, several minerals are used on that process, as Ca, Mg, Na, K, Fe, chlorides, nitrates, and nitrites. Cornwell [1] developed WTS estimative for WTP that use alum or ferric coagulant for the removal of suspended solids, the sludge production ( $S$ ) can be estimated along plant flow ( $Q$ ) in ML/d and quantities in mg/L of alum ( $Al$ ) or iron ( $Fe$ ) coagulant, suspended solids ( $SS$ ) and additional chemicals ( $A$ ) as polymer, clay, lime and activated carbon, by (1) and (2), respectively:

$$S = Q \times (0.44Al + SS + A) \quad (1)$$

$$S = Q \times (0.29Fe + SS + A) \quad (2)$$

Its chemical and mineralogy are basically compound for silica around 20%, aluminum 60%, and iron 5%, looking similar to aluminum silicates [2–4]. These chemical compounds are derived from the coagulants, principally aluminum sulphate ( $Al_2(SO_4)_3$ ) and ferric chloride ( $FeCl_3$ ), and also from alkalizing or acidifying agents to control the water pH. WTS is characterized by a black slurry due activated carbon in water treatment processes. According to Kyncl [4], WTS sludge can be divided in several types: caught in trash-racks; saline water from ion exchange recovery; wastewater produced in preparation of chemicals; polymeric flocculant clarification sludge; decarbonization sludge; sludge from removal of iron and manganese from groundwater; filter washing slurry; and the most common from floc suspensions of iron and alumina oxides from settlement tanks and clarifiers, the last one contains much water and it is called alumina sludge. The water industry produces daily tones WTS, in which a single water treatment plant WTP produces approximately 100,000 ton/year [5], its disposal costs are around US\$100/ton [6]. Their disposal methods are in sanitary landfills, discharging into steams and ocean barging and being reutilized in sewage treatment plants.

WTS's properties seem to be suitable for producing liner materials [7] and for reinforcing weakened clay soils [8, 9], other studies evaluated lime sludge and concluded as possible fill material for road construction, moreover the sludge is used for phosphorus removal in wastewater treatment and for cement production as admixtures [4]. Dehydrated and treated, chemically or incinerated, sludges and muds from WTP also have the potential to be alternative materials for liners instead of clays [10] with a severe attention for its hazardousness especially for residual water and mainly because of its permeability, compaction, durability, and workability in constructions [2], so, a more sustainable destination for WTS is its use in earthworks and as landfill lining. However, due to its high-water content and plasticity, the investigation of WTS's workability in construction procedures is mandatory. United Nations (UN) directive [11] established sustainable objectives for the future, thus, the valorization of WTS within soils for reinforcement and liner application minimize

the waste disposal problem, while at the same time moving the society towards a more sustainable future. In addition to an environmentally friendly approach, following the circular economy principles, it seems to be cheaper than current solutions that extract natural materials and generate more waste in synthetics industry.

WTS geotechnical properties have been studied for the past decades and summarized by Roque da Silva [12] as cover and bottom for industrial and sanitary landfills and road pavement sub-bases and bases, containment structures, embankments, and trench filling; in construction industry as ceramic material and as aggregates for mortars and cementitious elements; and in sanitation as coagulant and pollutant control in sewage treatment. Ahmad et al. [13] encouraged recovery, recycling and reuse of sludge called 3 R's conception, reviewing the abovementioned applications, for coagulant recovery; despite having a lower cost and reducing disposal, it requires complex and limited laboratory recovery.

It also shows to be efficient in removing heavy metals and turbidity, but it has high costs, the use as adsorbent is efficient for P removal, but it needs studies for other elements. For substrate in wetlands, it improves the removal of P and N, however it still needs investigation, and as sewage dewatering has improved its consolidation and dewatering, but it still has high costs and logistics problems. In addition, for cement production, its chemical composition and cementitious properties are similar to cement but implicate a retardation of settling and add deleterious components affecting mechanical properties, therefore it can generate lightweight aggregates or even suiting for non-structural concrete as sand, although requiring high temperatures which can pollute, reduce compressive strength and increase water retention. And, at last, for agriculture purpose, it improves soil aggregation, water permeability, but it is a risk of metal accumulation.

For these applications, the main properties required are compaction, compressibility and shear strength, chemical compatibility, and hydraulic conductivity, Dayton and Basta [14] concluded that for a WTS to be considered as a soil substitute, it must be function like a soil, thus, for developing alternative materials, physical, chemical, mechanical, and hydraulic characterization and knowledge about geotechnical parameters are the first step to make viable the reuse of WTS. Besides, for an adequate environmental characterization, solubilization and leaching tests are methods used for classification and diagnosis for quantification of the transferred material to environment, solubilization is a dissolution mechanism of a given material in water, and leaching is the potential transference of organic and inorganic substances through the material.

## ***1.1 Bibliometric Analysis***

This research was done in 3 of the main databases for bibliometric and data analysis, Google Scholar, Scopus and Web of Science, for title, abstract and keywords, the search was performed using Boolean OR, keywords truncated as it follows: “water

treatment sludge\*” OR “water treatment residu\*” OR “alum sludge\*” OR “waterwork sludge\*” OR “waterwork residu\*” was searched and resulted in 7310, 1769 and 1512 scientific works, for Google Scholar, Scopus and Web of Science, respectively. Publications started since 1970 and showed a growing relevance of the subject in recent years, this research was carried out with the aim of designating and characterizing the studied residue. The main subjects are from Environmental Science and Engineering with more than half of the works, corroborating the relevance for the studied area.

When combining the above-mentioned with other keywords, using Boolean AND, separately, for “characteristic\*”, “production”, “quantities”, looking to evaluate the main parameters when analyzing WTS. However, to search deeper into the area of research, again with Boolean AND, separately, for “landfill\*”, “wetland\*”, “liner\*”, “earthwork\*”, and “pond\*”. For landfilling and constructed wetlands, there are more works comparing to liners and earthworks, and even more for stabilization and mining ponds.

The most frequent keywords of the downloaded data in Scopus around WTS were performed with a bibliometric analysis software “VOSviewer” (<https://www.vosviewer.com> accessed January 2022) while version 1.6.17 was used in this study. VOSviewer is a software tool specifically developed for building and viewing bibliometric networks, built based on keyword co-occurrence, sources, bibliometric coupling, co-citation, or co-authorship relationships. Items are presented in Fig. 1 as circles for viewing, while their sizes depend on the importance of each term.

## 2 Geotechnical Characteristics

WTS physical characteristics are directly involved with understanding of the material state, liquid or solid, because of its high moisture content and its use when dehydrated. The WTS liquid phase is composed by free water, not associated with solid particles and which surrounds the solid residue; interstitial water, between molecular structure voids; capillary water, maintained by surface tension; and the hydration water when the positive pole of the water molecules approaches the negative charges of the WTS colloids [15]. The relationship with water has an important factor in WTS properties, [15] observed WTS subjected to dry–wet (D–W) and freeze–thaw (F–T) cycles and its plasticity decrease, grain size increase and greater undrained shear strength along cycles. Due moisture content and compaction method affects hydraulic conductivity and shear strength, WTS sample water content and interaction must be very carried analyzed.

The granulometry difference between WTS samples is determined by the nature of particles in the water, and coagulation, flocculation, and sedimentation efficiency, in addition to removal techniques [16], the weather station at the time of sampling, and the initial moisture of the sample [17]. The specific gravity depends mainly on the mineralogical composition, generally the WTS present values lower than 2.70–2.85 [17], typical values for clay minerals.

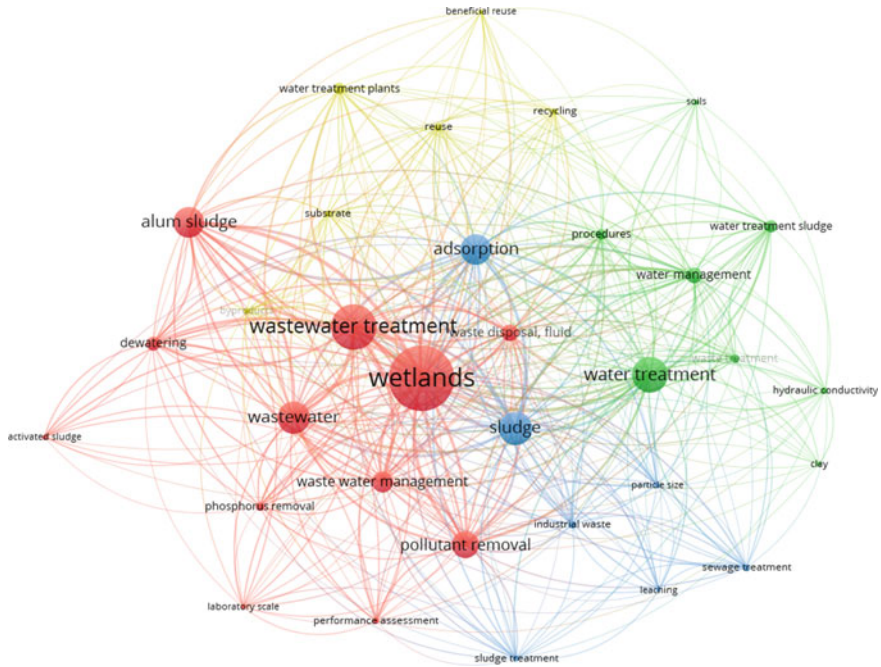


Fig. 1 Keyword co-occurrence net by VOSviewer

WTS have high water content and usually plasticity due affinity of alum for water and sometimes very low specific gravity comparing to soils, value below 2.0 [18], but some studies found WTS’ plasticity varying abusively with IP values around NP-670 [15], mostly in natural samples show plastic behavior, like fine-grained soils, and dehydrated present granular and non-plastic characteristics. According to Basim [15], water content variation is the greatest cause in geotechnical properties impacts, altering its floc structure, particle size and ion concentration and complex formation. Besides, [15] concluded an influence of age and weather in WTS samples, fresh and new ones have high plasticity comparable to montmorillonite, however when subjected to weathering, they lost plasticity and water affinity, also showed differences in several parameters such as density, shear strength and consolidation parameters. Another factor that impacts plasticity is F–T cycles, Basim [15] found plastic samples becoming non-plastic when imposed to one or more cycles and referred this change of plasticity and granulometry due dehydration because of cementitious action of the colloids and binding properties due calcium, iron, and aluminum oxide presence and [18] attached this significant plasticity decrease due alum is a precipitating agent. If needed, plasticity can be altered by anti-plasticizer as micas, sands, or coal fly ashes [16].

Table 1 was design by the author reviewing literature’s index properties to illustrate the difference between WTS explaining divergent processes of treatment and chemical composition of the water utilized, the data are ordered from the highest GS

to the lowest, including their respective plasticity limit values, liquidity and consequently their plasticity index, the variance is explicit according to the material worked and the dewatering technique already portrayed, with very high plasticity indexes to non-plastic for samples with the same specific density range.

**Table 1** Physical properties

References	G <sub>S</sub> (-)	W <sub>L</sub> (%)	W <sub>P</sub> (%)	PI (%)
Montalvan and Boscov [21]	2.9	239	81	158
Silva and Hemsí [22]	2.8	228–156	85–75	154–71
Zekkos et al. [23]	2.7	38	32	6
Gonçalves et al. [24]	2.7	–	NP	NP
Basim [15]	2.7–1.7	690–53	228–NP	670–NP
Dąbska [25]	2.8–2.7	63–58	41–34	31–17
Shah et al. [26]	2.8	55	21	34
	2.7	54	27	27
	2.6	48	28	20
	2.6	42	29	13
	2.6	40	30	10
	2.5	43	NP	NP
Scapin et al. [27]	2.7	40	20	20
	2.6	42	30	12
	2.6	43	36	7
	2.4	–	NP	NP
	2.5	–	NP	NP
Montalvan [17]	2.4	536	236	300
Roque da Silva [12]	2.4	536	236	300
Dehydrated		–	NP	NP
O’Kelly and Quille [28]	2.0–1.8	550–430	325–240	290–105
O’Kelly [18]	1.9	490	240	250
Arulrajah et al. [29]	1.8	110	80	30
Aydilek et al. [30]	1.8	–	NP	NP
Wolff et al. [16]	–	79	57	22
Bağrıçık and Güner [31]	–	98	45	53
Machado and Müller [32]	–	–	NP	NP

### 3 Chemical, Mineralogical and Morphological Composition

According to Bashar [2], WTS has almost 70% similarity in chemical composition with clayey soils. Caniani et al. [19] noticed the presence of hydroxides, originated from coagulating agents, colloids, organic matter, and inorganic precipitates, meanwhile does not show substances that could be dangerous for the environment. The main oxides of WTS are alumina ( $\text{Al}_2\text{O}_3$ ), silica ( $\text{SiO}_2$ ) and iron ( $\text{Fe}_2\text{O}_3$ ), varying its percentage due methodologies and coagulant utilized in water treatment processes, the one with higher alumina, indicates aluminum coagulant, and others which used ferric coagulant have higher iron content, high silica ( $\text{SiO}_2$ ) content can create the possibility for pozzolanic activity, and Wang et al. [20] stated that in consolidation tests, pozzolanic reaction may depress the diffuse double layer and causing dispersion flocculating as result of free water drainage. The amorphous and porous nature of Al and Fe hydroxides makes the sludge a possible adsorption site for majority of anions [13].

In general, studied WTS that have neutral or acid pH due mostly to very low organic matter in its composition, and slightly alkaline when have addition of chemicals and conditioning during treatment processes [28]. pH is important because it affects the leaching of metals and the biodegradation of organic matter [17]. Gonçalves et al. [24] considered higher organic carbon and organic matter content in WTS than in clayey soils, as the material contains a concentration of elements found in the soil and, eventually, algae and bacteria from the water. Basim [15] concluded that W–D or F–T cycle have no impact in organic matter content, and chemical analysis, elemental or in oxides. Usually, it has high loss on ignition (LOI), between 40 and 60% [28], that is related to clayey mineral, hydroxides, and organic matter [16]. Rodríguez et al. [33] referenced heavy metals presence habitually observed in concentrations much lower than the minimum values allowed but need a rigid analysis both from the sludge and the treated water, as they may have been contaminated with precipitates or pollutants.

Mineralogy and chemical compositions differences among calcium, aluminum and iron sludges are expected to influence the physical, chemical, and geotechnical characteristics of the sludge [23]. Clayey minerals presence can impact several WTS's properties as plasticity, shrinkage or swelling, cohesion and cation exchange capacity, consequently compaction and consolidation characteristics. Presence of organic matter and heavy metals in WTS composition consequently decrease and increase specific gravity, respectively [15], thus, leaching is not a concern for ground-water and soil contamination [23], such as heavy metals that are below international limits [34].

Ahmad et al. [5] found through x-ray diffraction (XRD) tests an absent well-crystalline phase and thus considering WTS having amorphous structure. Diffractogram studies indicate mainly quartz ( $\text{SiO}_2$ ), large amounts for alum sludge [34], and others clayey mineral such as kaolinite, calcite, muscovite, chlorite, gibbsite, goethite, and micas, explained by the water source bedrock. For the crystalline phase, the  $\text{Al}_2\text{O}_3$  content was associated with kaolinite ( $\text{Al}_2\text{Si}_2\text{O}_5(\text{OH})_4$ ) and

gibbsite ( $\text{Al}(\text{OH})_3$ ),  $\text{Fe}_2\text{O}_3$  with hematite ( $\text{Fe}_2\text{O}_3$ ), magnetite ( $\text{Fe}_3\text{O}_4$ ) and goethite ( $\text{FeO}(\text{OH})$ ), and  $\text{SiO}_2$ , to quartz, present among the suspended solids in raw water [12]. Ahmad et al. [13] found that aged sludge exhibited similar XRD characteristics to fresh sludge indicating that the crystallization did not occur during the ageing process. WTS presented metakaolin, a highly reactive pozzolan material, obligatory when calcinated in its crystallography, [34] classified alum sludge as Class N (natural) pozzolan material due viable replacement in concrete. Lime ( $\text{CaO}$ ), when present or added, leads to three types of chemical reactions, first cation exchange with an immediate reduction in plasticity, second, carbonation, a reaction that originates calcite ( $\text{CaCO}_3$ ), and pozzolanic reactions [35]. Calcite and graphite (C) explain lime as coagulant and high LOI [16], related to the decomposition of organic matter. Amorphous material is usually related to humid compounds and aluminum/iron oxides and hydroxides.

Table 2 synthesize chemical characteristics of WTS, it demonstrates the difference in the percentages of aluminum, silica, and iron oxides, respectively, ordered by the largest amount of  $\text{Al}_2\text{O}_3$  as it is an important component for liner production, these discrepancies show the coagulants used in the process of water treatment, these sludges are differentiated between alum or ferric sludge, and according to [22] both can contribute to geotechnical properties. Furthermore, it shows the difference between cation exchange capacity (CEC), pH and organic matter percentages for studied sludges, properties of importance regarding chemical compatibility due ability to hold positively charged ions when acting as liner. Also, [3] concluded that CEC is proportionally inversed to mineral grain size particles, the more clayey the soil, the lower its CEC, high CEC denote potentially high holding capacity of contaminants.

Table 3 summarized that typical mineralogy when all studied WTS presented quartz, most kaolinite, some muscovite and other in lower quantities gibbsite, goethite, and calcite, among others uncommon minerals.

Along with crystallography, elemental and oxides composition, the morphology of the composites can help distinguish elements distribution through the sample, scanning electron microscope (SEM) is the normally used methodology, SEM analysis for WTS identify it as a filling material into soil incorporation, providing a finer granulometry and more homogeneous mixture, which corroborate the particle size distribution [36]. An example of SEM image is showed in Fig. 2.

## 4 Mechanical Resistance

Compaction standards using Normal or Modified Proctor proved to be very difficult due a very dense block of material is formed when WTS is by itself, having no workability [12, 39] that explains mixtures with soils. Shah et al. [26] concluded that by incorporating WTS in soil as stabilizer can reduce field compaction effort and costs. Wang et al. [20] found unusual shape of compaction curves for WTS by itself, showing no optimum values, the dry density increased along with higher water

**Table 2** Chemical properties

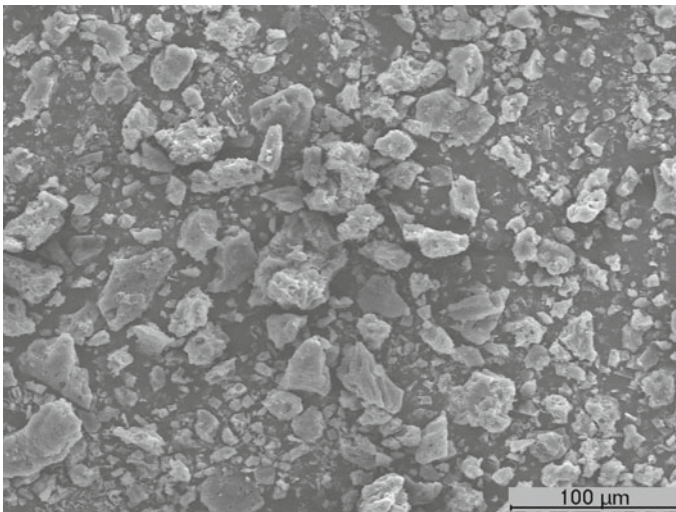
References	Al <sub>2</sub> O <sub>3</sub> (%)	SiO <sub>2</sub> (%)	Fe <sub>2</sub> O <sub>3</sub> (%)
Coelho [3]	60	25	5
Shah et al. [26]	38	29	15
Montalvan [17]	37	4	17
Gomes Ramirez et al. [37]	35	42	5
Thermally treated [37]	42		
Roque da Silva [12]	30	5	12
Wolff et al. [16]	30	38	1
de Godoy et al. [38]	27	52	12
Gomes Ramirez et al. [37]	25	27	18
Rodríguez et al. [33]	18	30	5
Ahmad et al. [5]	14	53	5
Montalvan and Boscov [21]	9	18	46
Basim [15]	8–28	7–11	3–14
Bağrıçık and Güner [31]	2	16	48
References	CEC (meq/100 g)	pH (–)	OM (%)
Dayton and Basta [14]	56.5–13.6	5–8	1–15
Montalvan [17]	32.5	7	2
Montalvan and Boscov [21]	25.5	7	3
Gonçalves et al. [24]	8.9	5	3
Roque da Silva [12]	7.3	6	27

contents, although when mixed with sandy soils or lime the one-hump compaction was obtained, concluding that when upon drying, particles attract strongly together forming flocs and when dried and rewetted, it loses its cohesion behaving like granular material. This one-hump compaction curve was also obtained by [15] utilizing wet to dry method, diverging from the usual dry to wet method, logically explained due WTS's high water content and difficult workability. [12, 17, 18, 40] tested mixtures with different ratios of WTS incorporating sandy and clayey soils and presented maximum dry unit weight decreasing and optimum water content



**Table 3** Mineralogical properties

References	Quartz	Kaolinite	Muscovite	Gibbsite	Calcite	Goethite
Gonçalves et al. [24]	✓	✓	✓	✓		✓
Montalvan and Boscov [21]	✓	✓	✓			✓
Montalvan [17]	✓	✓	✓	✓		✓
de Godoy et al. [38]	✓	✓	✓			
Bashar et al. [2]	✓	✓				
Roque da Silva [12]	✓	✓		✓		
Gomes Ramirez et al. [37]	✓	✓				✓
Basim [15]	✓				✓	✓
O'Kelly [18]	✓				✓	
Wolff et al. [16]	✓			✓		
Rodríguez et al. [33]	✓				✓	
Machado and Müller [32]	✓					

**Fig. 2** SEM of WTS

increasing with increasing WTS content, explained by the increment in fines due WTS' fine granulometry.

Mixtures can be an effective way to valorize WTS for soil amendment, [24] tried 35% and 50% amount of WTS with clayey soil, and 20% with sandy soil, for waterproofing barriers layers reaching acceptable compaction characteristics, other authors [17, 26, 27, 32] mixed clays and sands in ratios between 2 and 50% and tested compaction searching for incorporation as liners materials, bottom and top layers, soft soils reinforcements or just to improve geotechnical properties of soils.

Wang et al. [20] found similar consolidation behavior to treated and untreated, but initial void ratio lower for treated ones, attributable to the decreased water content within additives, although both resulting high compression indexes and recompression very low due its dispersive structure, most WTS's  $C_c$  values are between 0.20 and 0.50 and  $C_s$  among 0.01–0.07. Hydraulic conductivity from oedometer tests decrease along with void ratio, according to [30] when comparing to natural clays, WTS have higher consolidation rate and permeability due high-water content, explaining the  $k$ -void relationship.

The WTS are highly compressible, [28] consolidation test program concluded for WTS, that primary consolidation occurs due to dissipation of excess pore pressure and it was dominant during the early load stages, and the secondary compression due to the realignment of the solids became increasingly dominant at higher stresses as consequence to the significant reduction in the hydraulic conductivity, several authors noticed that WTS generated a certain amount of gas, which interfered and sometimes prevented the consolidation process due to test long duration. Anisotropic consolidation aims to reproduce more realistic field conditions, as it is known that the stress state in the field is generally anisotropic, although triaxial tests with isotropic densification are more widespread [17].

Studies [31] resulted in an optimum mixing ratio of 10% of WTS increasing the bearing capacity of clay soil by 1.69 times along with an optimum reinforcement thickness of height/diameter ( $H/D$ ) = 2.25, furthermore found consolidation settlements decreased by up to 62%, probably due high amount of silica minerals that becoming a gel which connect the soils' grains blocking voids and consequently increase the bearing capacity.

For liner simulation, consolidated undrained (CU) triaxial tests are performed and according to [18], WTS' shear resistance is enhanced firstly by the aggregation of the clay particles into larger flocs and the deactivation of water by the alum, and secondly by the binding together of these flocs into clusters by the long-chained polyelectrolyte molecules. Wang et al. [20] tested untreated WTS in CU triaxial compression and it behave as a consolidated soil with high sensitivity explained for its high plasticity, and high friction angle, literature  $\phi'$  values are mostly 35–45°, low shear strength and cohesion, [41] reported  $\phi'$  values for alum WTS are high compared with the values generally associated with high-plasticity organic clays as montmorillonite. Basim [15] determined an increase relationship between compressive strength and solids content, characteristic of normally consolidated clay [18]. Also, [18] attached the failure line that best-fit WTS was through the origin ( $c' = 0$ ). For practical analysis, undrained shear strength ( $S_u$ ) is taken as half the maximum deviator stress in triaxial cells. For waste landfills, undrained shear strength must be more than 40 kPa [17].

Additionally, [20, 42] concluded that samples of WTS are thixotropic, a phenomenon of reversible time-dependent decrease of viscosity, namely when it is sheared for some time, the viscosity decreases, however, when the shear is stopped, the viscosity of the system is restored, the undrained shear increased five times since the immediate measure, although remain needs treatment to achieve adequate shear strength. There is a significant variation in the undrained shear strength according to

water content, alum WTS tends to have marginally higher shear strength values than iron WTS [41].

Tests on WTS were conducted with a comprehensive investigation into the use of lime sludge, which use lime as coagulant, in unconfined compressive strength (UCS) and the retraction behavior of commercially available kaolinite clay, different ratios were added to kaolinite by the dry weight of the clay and showed that, with the increase of WTS content, the UCS value increased initially, followed by a slight decrease, an increase in the curing period resulted in an increase in the resistance to UCS, in addition, an increase of WTS led to a reduction in the shrinkage potential. Basim [15] found a relevant difference in sampled drying conditions, for dry to wet condition,  $S_u$  and dry density decreased when moisture content increased, and for wet to dry, the opposite relation,  $S_u$  increased with  $w$  until certain value, then  $S_u$  decreased. Furthermore, [22] found an exponential relationship between  $S_u$  and solid contents ( $s$ ) for WTS through (3):

$$S_u = 0.018 \times (e^{13.5s}) \quad (3)$$

Table 4 presents mechanical parameters like optimal values of compaction, moisture, and dry specific weight, for WTS and WTS-soil mixtures within the mixture's percentages, either with clays or sands, for laboratory tests using standard or modified compaction. Data are ordered to evaluate the sludge in its purest state, thus WTS ratio decrease. Optimum moisture content are mainly around 15–35%, although according to dehydration method of samples, it can rise to 160%, when WTS compaction parameters are analyzed from dry to wet, it behave like a soil within one-hump compaction curve reaching 15–35% values, besides that when treated the opposite way, wet to dry like usually it's done for soils, compaction curve are more like a linear progression linked with higher values for moisture content [18, 20]. Also summarized consolidation and compressibility parameters as compression and swell coefficients ( $C_c$  and  $C_s$ , respectively), in order of least compressive samples, lower to higher  $C_c$  values, and the conclusion is when adding WTS compacted mixtures were more compressible than the soils. More WTS content results in higher compressibility of the mixtures, such behavior was expected since WTS addition causes reduction of dry unit weight and increases plasticity [17]. Additionally, it gathered the values of cohesion and friction angle organized by decreasing WTS percentages, reducing the amount of sludge in the mixtures, thus, it was possible to observe that increasing WTS in the soils' mixtures, the cohesion decreased, and the friction angle increased, corroborating with other studies justified by WTS' loss of plasticity, decreasing cohesion, and increasing strength by filling voids due to its fine portion. Furthermore, Wang et al. [20] concluded that this strength can be achieved by enhancing density by consolidation and/or compaction.

**Table 4** Mechanical properties

References	wopt (%)	$\rho_d, opt (g/cm^3)$	WTS ratio (%)	Mixture
Dąbska [25]	29–38	1.3–1.4	100%	–
Fei et al. [23]	30	1.4	100%	–
Silva and Hemsli [22]	38	1.4	100%	–
Arulrajah et al. [29]	50	0.9	100%	–
O’Kelly [18]	160	3.6	100%	–
Gonçalves et al. [24]	33	1.4	35%	Clay
	32	1.5	50%	
	15	1.8	20%	
				Sand
Scapin et al. [27]	27	1.4	15%	Clay
	34	1.3	25%	Clay
	36	1.3	35%	Clay
	48	1.1	50%	Clay
Montalvan and Boscov [21]	12–17	1.7–1.9	20%	Sand
Machado and Müller [32]	16	1.8	5%	Clay
	20	1.7	20%	Clay
Shah et al. [26]	18	1.7	2%	Clay
	18	1.8	4%	Clay
	17	1.8	6%	Clay
	18	1.8	8%	Clay
	18	1.8	10%	Clay
	17	1.7	12%	Clay
References	Cc (–)	Cs (–)	WTS ratio (%)	Mixture
Montalvan [17]	0.1	0.02	5%	Sand
	0.2	0.03	6%	
	0.3	0.04	7%	
	0.4	0.05	8%	
	0.5	0.07	11%	
O’Kelly and Quille [28]	0.10–0.80	0.01	100%	–
Montalvan and Boscov [21]	0.13	0.02	20%	Sand
Roque da Silva [12]	0.21	0.06	15%	Sand
	0.16	0.03	20%	
	0.22	0.04	25%	
O’Kelly [18]	0.20–0.28	0.04–0.06	100%	–
Aydilek et al. [30]	0.20	0.06	100%	–
Fei et al. [23]	0.54	0.03	100%	–

(continued)

**Table 4** (continued)

References	wopt (%)	$\rho_d, \text{opt}$ (g/cm <sup>3</sup> )	WTS ratio (%)	Mixture
Arulrajah et al. [29]	0.56–0.64	0.04	100%	
References	$c'$ (kPa)	$\varphi'$ (°)	WTS ratio (%)	Mixture
O'Kelly [18]	0	39	100%	–
O'Kelly and Quille [41]	0	39–44	100%	–
Arulrajah et al. [29]	1–23	33–40	100%	–
Basim [15]	0–36	16–35	100%	–
Roque da Silva [12]	6	38	15%	Sand
	13	35	20%	
	6	38	25%	
Montalvan [17]	12	38	15%	Sand
	6	39	20%	
	10	38	25%	
	14	36	35%	

## 5 Hydraulic Performance

Gonçalves et al. [24] mixed dehydrated WTS with clayey and sandy soils reaching satisfactory  $k$  after compaction showing viability for landfill liner material. Low permeability is due to the  $\text{Al}(\text{OH})_3$  present in the WTS [20] and also associated with the microstructure of the sludge flocs [18]. Gonçalves et al. [24] observed that mixtures with soil: WTS ratios of 1:0.25, 1:0.5 and 1:1 presented  $k$  in between  $10^{-8}$  and  $10^{-7}$  cm/s, suitable for use in landfill works as low permeability materials, furthermore, highlighted that the WTS' gravel granulometry did not significantly change the permeability of the soils in the mixtures, since this was noticeably reduced during the compaction process, the clods of the WTS were broken when compacted.

Bentonite is a clay mineral from the group of montmorillonites widely used in geotechnical works due to its low permeability, [32] tested the permeability of bentonite-WTS mixtures and found a reduction up to  $10^{-2}$  cm/s, finding minimum values for barriers ( $10^{-7}$  cm/s) when increasing the sludge ratio by 20%, in short, the replacement of bentonite by WTS can be seen as a benefit due to the reduction of mineral extraction and production impacts without loss in hydraulic performance. A study over influences of WTS' hydraulic conductivity [25] measured long-term performances and showed  $k$  values increasing when with NaOH and HCl solutions and decreasing with tap and distilled water, and an important and practical reduction when measured with waste leachate, reaching  $10^{-7}$  cm/s of permeability while water content around 25–35% and compaction degree between 95 and 105% as requirement.

Triaxial permeability tests are another effective way to obtain the hydraulic conductivity, but attention is needed during procedure, [17] indicated that lack of initial saturation would cause permeability to increase rather than to decrease over

time, caused by a possible migration of colloids inside the sample, eventually causing partial clogging, consequently reducing flow rate, other possibility stated was clay's particle dispersion while internal swelling. Thus, the main cause of permeability and flow rate changes when under stress are particles migration, void ratio redistributions and clogging, physical, biological, and chemical.

The hydraulic conductivity ( $k$ ) is usually determined using standard or modified Proctor compaction energy and measured in rigid wall permeameters using falling head testing. Although, [18, 20] established in consolidation tests through oedometer a relation valid for void ratio ( $e$ ) values between 7 and 17 for hydraulic conductivity through (4):

$$k = (2.13 \times 10^{-15}) \times e^{6.15} \quad (4)$$

Table 5 summarizes WTS samples incorporated or not in soils and ordinated by decreasing their hydraulic conductivity, in addition an evaluation of their applicability in earth works using liners was made. The minimum and most adopted value for hydraulic barriers is  $k < 10^{-7}$  cm/s, these collected data verifies the heterogeneity of the sludge, which can be waste material valorized in different proportions, from 5 to 100%, always depending on its physical, chemical, and geotechnical, however, as mentioned, these characteristics change significantly according to the sludge sample, its chemical processes in the WTP and the raw water composition. Dąbska [25] found for WTS by itself  $k$  around  $10^{-9}$  cm/s over [29] only  $10^{-5}$  cm/s, a difference in the order of 4 significant figures, identifying divergent materials. Roque da Silva [12], Montalvan [17], Ferreira [40], Tsugawa et al. [42] studies were analyzed, and a possible pattern was found, it conclude that WTS can be used as landfill bottom or cover liners when mixed with soils with lower hydraulic conductivity in ratios between 5 and 20% of dry mass.

## 6 Conclusions

Low hydraulic conductivity plays an important role in the applicability of water treatment sludge to landfill covers [42, 43], however, it has the potential to be used as a covering material in landfills, but it can also be studied as incorporation as bottom material if it presents low hydraulic conductivity,  $< 10^{-7}$  cm/s. For liner application, WTS must have enough strength to support the disposal and construction loads induced. Thus, WTS has shown a possible strand within soils and landfill liners, enhancing specific geotechnical characteristics while valorizing disposable material.

The literature's review concluded:

- Water affinity of WTS is a very important factor, if the sample is treated with dry-wet procedure, it behaves in an opposite way to wet-dry treatment, influencing parameters as its liquidity, plasticity, shrinkage, and CEC.

**Table 5** Hydraulical properties

References	k (cm/s)	WTS ratio (%)	Mixture	Liner
Arulrajah et al. [29]	$1 \times 10^{-5}$	100%	–	
Fei et al. [23]	$3 \times 10^{-6}$	100%	–	
Machado and Müller [32]	$8 \times 10^{-7}$	5%	Clay	
	$6 \times 10^{-7}$	20%	Clay	
O’Kelly [18]	$2 \times 10^{-7}$	100%	–	
O’Kelly and Quille [28]	$1 \times 10^{-7}$	100%	–	✓
Roque da Silva [12]	$8 \times 10^{-8}$	15%	Sand	✓
	$3 \times 10^{-7}$	20%	Sand	
Gonçalves et al. [24]	$6 \times 10^{-8}$	35%	Clay	✓
	$3 \times 10^{-8}$	50%	Sand	✓
	$5 \times 10^{-7}$	20%	Sand	
Scapin et al. [27]	$5 \times 10^{-8}$	15%	Clay	✓
	$8 \times 10^{-8}$	25%	Clay	✓
	$3 \times 10^{-7}$	35%	Clay	
Montalvan [17]	$6 \times 10^{-8}$	3%	Sand	✓
	$4 \times 10^{-7}$	4%	Sand	
	$3 \times 10^{-8}$	6%	Sand	✓
Dąbska [25]	$6 \times 10^{-9}$	100%	–	✓

- WTS has also exposed their variability in granulometric and geotechnical characteristics according to the region, the source of the water to be treated, the water treatment plant processes, chemical added and dewatering method.
- It seems to contribute with pozzolanic characteristics, due to their inherent high amount of silica minerals, creating a silica-gel that connects grains and structural layers while minimizing porosity within the soil, increasing its bearing capacity.
- High aluminum content is the responsible for its low specific gravity makes it possible to reduce the final weight of the mixture, which can reduce potential costs and transport effort.
- WTS’ mineralogy is mainly quartz and kaolinite, which are utilized in liners.
- WTS have high compressibility, needing attention for possible differential settlements.
- WTS influence shear resistance increasing friction angle and decreasing cohesion. Enough strength can be achieved by enhancing density with consolidation and/or compaction effort.
- Hydraulic conductivity is the most important factor for liners, apparently, mixing WTS between 5 and 20% of dry mass in soils with a lower hydraulic conductivity,

is an effective way for their valorization as waterproofing layers in earth works, liners.

Although, due to lack of research, it needs more investigation and attention on:

- Laboratory tests over mechanical stability, hydraulic conductivity, and long-term behavior.
- An individual analysis of WTS' permeability must be carried for each region, and its geotechnical performance is an obligatory evaluation, searching for characteristic patterns.
- The analysis of geotechnical properties attested to the potential use of the mixtures, however, the use of the material in practice must be preceded by pilot tests or experimental landfills.

## References

1. Cornwell DA (2006) Water treatment residuals engineering. AWWA Research Foundation and American Water Works Association
2. Bashar NAM, Zubir ZH, Ayob A, Alias S (2016) Water treatment sludge as an alternative liner for landfill site: FTIR and XRD analysis. In: AIP conference proceedings. American Institute of Physics Inc., New York. <https://doi.org/10.1063/1.4965082>
3. Coelho GMR (2016) Avaliação da Capacidade Reativa de uma Lama de ETA para Remoção de Metais Pesados de Escorrências Rodoviárias. Universidade da Beira Interior
4. Kyncl M (2008) Opportunities for water treatment sludge re-use. *GeoSci Eng LIV* 147:11–22
5. Ahmad T, Ahmad K, Alam M (2016) Characterization of water treatment plant's sludge and its safe disposal options. *Proc Environ Sci* 35:950–955. <https://doi.org/10.1016/j.proenv.2016.07.088>
6. Tsugawa JK, Romano RCO, Pileggi RG, Boscov MEG (2019) A rheological approach for the evaluation of geotechnical use of water treatment sludge. In: *Environmental science and engineering*. Springer, Berlin Heidelberg, pp 264–272. [https://doi.org/10.1007/978-981-13-2221-1\\_24](https://doi.org/10.1007/978-981-13-2221-1_24)
7. Marchiori L, Albuquerque A (2020) Critical review of industrial solid wastes as barrier material for impermeabilization of storage waste facilities. In: *SUM2020: 5th symposium on urban mining and circular economy*
8. Marchiori L, Studart A, Albuquerque A, Cavaleiro V, Silva A (2021) Geotechnical characterization of water treatment sludge for liner material production and soft soil reinforcement. *Mater Sci Forum* 1046:83–88
9. Baker RJ, van Leeuwen J, White DJ (2005) Applications for reuse of lime sludge from water softening
10. Okoli RE, Balafoutas G, Okoli RE (1999) Bottom ash from sludge cake as a barrier material to pollutant migration in landfills. *Waste Manag Res* 17:288–295
11. United Nations (n.d.) The 2030 agenda for sustainable development. <https://doi.org/10.1201/b20466-7>
12. Roque da Silva A (2021) Comportamento Geotécnico de Misturas de Areia Argilosa Laterítica e Lodo de Estação de Tratamento de Água Taiapuêba, Município de Suzano. Universidade de São Paulo, São Paulo
13. Ahmad T, Ahmad K, Alam M (2016) Sustainable management of water treatment sludge through 3'R' concept. *J Clean Prod* 124:1–13. <https://doi.org/10.1016/j.jclepro.2016.02.073>



14. Dayton EA, Basta NT (2001) Characterization of drinking water treatment residuals for use as a soil substitute. *Water Environ Res* 73:52–57. <https://doi.org/10.2175/106143001X138688>
15. Basim SC (1999) Physical and geotechnical characterization of water treatment plant residuals. Institute of Technology, New Jersey
16. Wolff E, Schwabe WK, Landim AB, Vitorino MD, dos Santos WL (2007) A Substituição de Argila por Lodo de ETA na Produção de cerâmica Vermelha. In: Proceedings of the 51º congresso Brasileiro de Cerâmica, Salvador, BA
17. Montalvan ELT (2021) Geotechnical properties of mixtures of water treatment sludge and residual lateritic soils from the State of São Paulo. Universidade de São Paulo
18. O’Kelly BC (2006) Geotechnical properties of a municipal water treatment sludge incorporating a coagulant, Dublin
19. Caniani D, Masi S, Mancini IM, Trulli E (2013) Innovative reuse of drinking water sludge in geo-environmental applications. *Waste Manag* 33:1461–1468. <https://doi.org/10.1016/j.wasman.2013.02.007>
20. Wang MC, Hull JQ, Jao M (1992) Stabilization of water treatment plant sludge for possible use as embankment material.pdf. *Transp Res Rec* 15:36–43
21. Montalvan ELT (2016) Boscov MEG (2016) Geotechnical characterization of a soil-water treatment sludge mixture. *Geo-Chicago GSP* 57:418–427
22. Silva AS, Hemi PS (2018) Efeito do teor de sólidos na resistência ao cisalhamento de um lodo de ETA visando seu uso em cobertura diária de aterros sanitários. In: XIX congresso Brasileiro de Mecânica Dos Solos e Engenharia Geotécnica, Salvador, BA
23. Fei X, Zekkos D, Li L, Woods R, Sanford L (2017) Geo-characterisation of lime water treatment sludge. *Environ Geotech* 4:209–219. <https://doi.org/10.1680/jenge.15.00028>
24. Gonçalves F, de Souza CHU, Tahira FS, Fernandes F, Teixeira RS (2017) Incremento de lodo de ETA em barreiras impermeabilizantes de aterro sanitário. *Revista DAE* 65:5–14. <https://doi.org/10.4322/dae.2016.018>
25. Dąbska A (2019) Hydraulic conductivity of compacted lime-softening sludge used as landfill liners. *Water Air Soil Pollut* 230:280. <https://doi.org/10.1007/s11270-019-4281-z>
26. Shah SAR, Mahmood Z, Nisar A, Aamir M, Farid A, Waseem M (2020) Compaction performance analysis of alum sludge waste modified soil. *Constr Build Mater* 230:116953. <https://doi.org/10.1016/j.conbuildmat.2019.116953>
27. Scapin J, Santos EF, Pinheiro RJB (2021) Análise de Misturas de Lodo de ETA com Solo Siltoso da Região de Santa Maria - RS, in: LETA2021 - 1º Encontro Nacional de Lodo de Estação de Tratamento de Água, pp 6–9
28. O’Kelly B, Quille M (2009) Compressibility and consolidation of water treatment residues. *Waste Resour Manag* 162:85–97. <https://doi.org/10.1680/warm.2009.162.2.85>
29. Arulrajah A, Disfani MM, Suthagaran V, Bo MW (2013) Laboratory evaluation of the geotechnical characteristics of wastewater biosolids in road embankments. *J Mater Civil Eng* 25:1682–1691. [https://doi.org/10.1061/\(asce\)mt.1943-5533.0000739](https://doi.org/10.1061/(asce)mt.1943-5533.0000739)
30. Aydilek AH, Edil TB, Fox PJ (1999) Consolidation characteristics of wastewater sludge. *Geotechnics of High Water Content Materials*. ASTM STP 1
31. Bağrıaçık B, Güner ED (2020) An experimental investigation of reinforcement thickness of improved clay soil with drinking water treatment sludge as an additive. *KSCE J Civil Eng* 24:3619–3627. <https://doi.org/10.1007/s12205-020-0111-5>
32. Machado MFB, Müller MCR (2019) Avaliação das características geotécnicas do lodo de estação de tratamento de água frente à bentonita. Universidade Do Extremo Sul Catarinense, pp 1–18
33. Rodríguez NH, Ramírez SM, Varela MTB, Guillem M, Puig J, Larrotcha E, Flores J (2010) Re-use of drinking water treatment plant (DWTP) sludge: characterization and technological behaviour of cement mortars with atomized sludge additions. *Cement Concr Res* 40:778–786. <https://doi.org/10.1016/j.cemconres.2009.11.012>
34. Owaid HM, Hamid R, Taha MR (2014) Influence of thermally activated alum sludge ash on the engineering properties of multiple-blended binders concretes. *Constr Build Mater* 61:216–229. <https://doi.org/10.1016/J.CONBUILDMAT.2014.03.014>

35. Silva AS, Hemi PS (2021) Adição de Cal a um Lodo de ETA Visando Melhoria da Resistência para Uso em Cobertura Diária de Aterros Sanitários. In: LETA2021 - 1º Encontro Nacional de Lodo de Estação de Tratamento de Água
36. Marchiori L, Studart A, Albuquerque A, Pais LA, Boscov ME, Cavaleiro V (2022) Mechanical and chemical characterization of soil-water treatment sludge mixtures for liner production. *Open Civil Eng J*
37. Gomes Ramirez K, Possan E, Bittencourt PRS, Carneiro C (2018) Colombo M (2018) Physico-chemical characterization of centrifuged sludge from the Tamanduá water treatment plant (Foz do Iguacu, PR). *Rev Matér* 23:521. <https://doi.org/10.1590/S1517-707620180003.0521>
38. de Godoy LGG, Rohden AB, Garcez MR, da Costa EB, Da Dalt S (2019) Andrade JJO (2019) Valorization of water treatment sludge waste by application as supplementary cementitious material. *Constr Build Mater* 223:939–950. <https://doi.org/10.1016/J.CONBUILDMAT.2019.07.333>
39. Marchiori L, Studart A, Morais MV, Albuquerque A, Cavaleiro V (2021) Avaliação do Potencial de Utilização de Resíduo de ETA como Impermeabilizante de Obras de Terra para a Contenção de Resíduos. In: LETA2021 - 1º Encontro Nacional de Lodo de Estação de Tratamento de Água, pp 58–60
40. Ferreira KSM (2020) Comportamento Geotécnico de Misturas de Argila Laterítica com Lodo de Estação de Tratamento de Água para Uso em Obras de Terra. Universidade de São Paulo
41. O'Kelly BC (2010) Quille ME (2010) Shear strength properties of water treatment residues. *Proc Instit Civil Eng Geotech Eng* 163:23–35. <https://doi.org/10.1680/geng.2010.163.1.23>
42. Tsugawa JK, Pereira KFS, Boscov MEG (2017) Thixotropy of sludge from the Cubatão water treatment plant. Brazil. *Geotech Front GSP* 167:842–851. <https://doi.org/10.1061/9780784480472.090>
43. Raheem A, Sikarwar VS, He J, Dastyar W, Dionysiou DD, Wang W, Zhao M (2018) Opportunities and challenges in sustainable treatment and resource reuse of sewage sludge: a review. *Chem Eng J* 337:616–641. <https://doi.org/10.1016/j.cej.2017.12.149>